Development of novel catalytic materials with low content of precious metals for the after-treatment of automobile exhaust gas

Jianxiong Wu

Thèse

Université de Lille

Ecole Doctorale ED SMRE

présenté par **JIANXIONG WU**

en vue de l'obtention du titre de

DOCTEUR EN CHIMIE

Spécialité Molécules et Matière Condensée

Sujet de thèse

Development of novel catalytic materials with low content of precious metals for the after-treatment of automobile exhaust gas

Soutenu le 13 Septembre 2019

Thesis supervised by	Pascal GRANGER	Supervisor
	Christophe DUJARDIN	Co-supervisor
	Jean-Philippe DACQUIN	Advisor

JURY

Antonella GLISENTI, Professeur, Université de Padova	Rapporteur
Philippe VERNOUX, Docteur, IRCELYON	Rapporteur
Catherine BATIOT DUPEYRAT, Professeur, Université de Poitiers	Examinateur
Rose-Noëlle VANNIER, Professeur, ENSCL	Examinateur
Pascal GRANGER, Professeur, Université de Lille	Directeur de thèse
Christophe DUJARDIN, Professeur, ENSCL	Co-directeur de thèse
Jean-Philippe DACQUIN, Maître de conférence, Université de Lille	Invité

Table of Contents

Acknowledgements

The past three years at University of Lille have been a rewarding and unforgettable experience in my life. During this period I had the chance to meet and cooperate with many talented people to discover jointly the exciting field of automobile catalysts. Involved in a multinational European research program, I witnessed the complete process for the development of the next-generation automobile exhaust catalytic system and felt personally the profound effect it brings on our daily life. I would not have been able to make this journey without the generous help from so many people to whom I feel deeply grateful.

Firstly, I would like to thank the European Commission for financing the PARTIAL PGMs project within which this research is carried out. Secondly, I would like to express my sincere gratitude to the jury committee: namely Professor Rose-Noëlle Vannier for chairing my thesis defence, Professor Catherine Batiot Dupeyrat, Professor Antonella Glisenti and Doctor Philippe Vernoux for judging the quality of my work. I would like to acknowledge the jury committee not only for the insightful comments and remarks, but also for the hard questions which incented me to widen the scope of my research from a variety of perspectives.

I hearby extend my heartfelt thanks to my supervisors: Professor Pascal Granger, Professor Christophe Dujardin and Doctor Jean-Philippe Dacquin for providing me an opportunity to complete my PhD thesis. I still remember the first day we met in the DeNO$_x$ group. At the beginning, I was a bit shy leaning against the corridor wall without saying a word. Your warm reception and witty remarks closed quickly the distance between us and made me feel at home. I would like to express my sincere gratitude to Pascal who is a mild, thoughtful and knowledgeable man always full of energy and passion. He provided crucial guidance at key moments in my research while at the same time allowing me to work independently most of the time. His valuable suggestions, deep insights and selfless support helped me greatly at various stages of my research, including the writing of this thesis. His immense knowledge, endless enthusiasm for scientific discoveries and wholehearted commitment to higher education cause exemplified the real dedication to one's beloved career. His spirit of professionalism and lifelong dedication will always keep inspiring me to pursue excellence in whatever I do over the course of my career development. Moreover, my hearty thanks goes to Christophe who is extremely kind, caring, patient and always supportive of me no matter what difficulties I encountered during my PhD life. He always believed in me and encouraged me even when I was not that confident in myself in moments of difficulties. Without his unwavering support and encouragement, I would not have been able to complete this thesis in time. Also, I would like to thank sincerely Jean-Philippe, a charming and enthusiastic man who, despite his own busy schedule, is always ready to lend a hand to whomever in need of help. In a word, all of you showed a role model for me. After having got along with you for a couple of years, I realized how priviledged I am to get the chance to work together with some of the most brilliant minds in this field. I feel forever grateful to all of you and I have already started to miss you.

Acknowledgements

A very special gratitude goes out to all the PARTIAL PGMs project partners, especially Antonella Glisenti from University of Padova, Pegie Cool and Tim Van Everbroeck from University of Antwerp, Emiel Hensen and Long Zhang from Eindhoven University of Technology, Emily Price and David Thompsett from Johnson Matthey, Cristina Salazar and Daichi Campo from Lurederra. I would thank you all for the stimulating discussions and fruitful collaborations on the related subjects. My sincere gratitude is reserved for Anke Schöen. Her preliminary work paved a way to the successful completion of my PhD thesis. My sincere thanks also goes to the PARTIAL PGMs project colleagues in UCCS, namely, Jean-François Paul, Shreya Nandi, Elise Berrier, Anne-Sophie Mamede. It was really fantastic to have the opportunity to work together with you in this challenging yet significant project. In addition, a special gratitude goes to Professor Sébastien Royer who gave me access to the laboratory and experimental facilities of the MATCAT group. This dissertation would not be possible without his precious support and assistance.

I am also grateful to the following laboratory staff, namely, Laurence Burylo, Simon Pardis, Martine Trentesaux, Olivier Gardoll, Nora Djelal (UCCS), Joëlle Thuriot Roukos (REALCAT), Catherine Cordier (UMET) and Sandra Casale (LRS-UPMC) for kindly performing various analyses. I also extend my hearty thanks to the master student Marie-Christine Boegli and the laboratory technician Loic Dubois, with whom I worked in the past few years as a co-supervisor. Your sincere words and creative ideas have been an important source of inspiration during my PhD life and I greatly enjoyed working with you.

Likewise, I would like to express my sincere thanks for all the support I received from my friends in UCCS. Just to name a few of them (please forgive me for not being able to list all of them): Charlotte Desjacques, Hermann Siaka, Shuo Chen, Hélori Salembier, Peixin Li, Yin Xu, Yaqian Wei, Guanfeng Liang, Dichao Shi, Guillaume Pomalaza, Mélissandre Richard, Bang Gu, Jin Sha, Jérémy Dhainaut, Carmen Ciotonea, Bakytzhan Yeskendir, Nisrine Hammi, Parnian Peyrovi, Grece Abdallah, Tanushree Kane, Shilpa Sonar, Maya Ibrahim, Juliana Aparicio, Xiang Yu, Yuanshuang Zheng, Xiu Liu, Yanping Chen, Liwei Hou and many others. The joyful days and cheerful moments we spent together as well as the stressful and sleepless nights we worked hard before deadlines will always be treasured in my memory. With your company and support, I will never walk alone in the pursuit of knowledge and truth.

Last but not the least I would like to thank my beloved parents: Wenguang Wu and Wenjie Yan, to whom I feel deeply indebted for ever. Like many Chinese students of my generation, I am the only child of my family. My parents have dedicated their entire lifetime to nurture and educate me, never asking for anything in return. They sacrificed so much for bringing me up that I can never pay them back for all that they have done for me throughout my life. As a phrase goes, the most beautiful thing in this world is to see our parents smiling and knowing that we are the reason behind that smile. I hope that I have not let my parents down so far and that they would be able to talk about me with pride.

To my dearest parents and friends, for their unconditional love and support.

Acronyms, abbreviations and symbols

$\square$	anionic vacancy
O_s^*	Active oxygen species
3DOM	Three-dimensionally Ordered Macroporous material
A	pre-exponential factor
Å	Ångström
ADP	Ammonia-driven Deposition Precipitation
AOS	average oxidation state
BE	Binding Energy
BET	Brunauer-Emmett-Teller
BJH	Barret-Joyner-Halenda
BSE	Back Scattered Electron
CA	Citric Acid
CC	Closed-Coupled configuration
CCD	Charge-Coupled Detector
CCM	Conventional Citric Method
CCT	Colloidal Crystal Templating
CEDI	Charge-Enhanced Dry Impregnation
COP	Coprecipitation
CRT	Continuously Regenerating Trap
d	spacing between diffracting planes
D	Dispersion of precious metal
DMAC	N, N-dimethylacetamide
DOC	Diesel Oxidation Catalyst
DOSC	Dynamic Oxygen Storage Capacity
D_p	aerodynamic diameter of particulate matter
DPF	Diesel Particulate Filter
$d_{Rietveld}$	crystallite size calculated from Rietveld refinement

Acronyms, abbreviations and symbols

E_{app}	apparent activation energy
EDS	Energy-Dispersive X-ray Spectroscopy
EG	Ethylene Glycol
EGR	Exhaust Gas Recirculation
Eq.	equation
F_{A0}	inlet molar flowrate of reactant A
FCC	face-centered cubic lattice
FSP	Flame Spray Pyrolysis
GDI	Gasoline Direct Injection
GHSV	Gas Hourly Space Velocity
GPF	Gasoline Particulate Filter
H_2-TPR	H_2 Temperature Programmed Reduction
ICP-AES	Inductively Coupled Plasma Atomic Emission Spectroscopy
IS	isomeric shift
IWIM	Incipient Wet Impregnation Method
k	reaction rate constant
K	chemical equilibrium constant
K	Kelvin
KE	kinetic energy
K_α	Copper K-alpha X-ray energy (8.04 keV)
LEAN	lean condition
LHD	Light-Heavy Duty
$m_{catalyst}$	catalyst weight
MCP	mechanochemical processing
MPI	Multi-Point Injection
NEMCA	Non-faradaic Electrochemical promotion of Catalysis
NGV	Natural Gas Vehicle
O_2-TPD	O_2 Temperature Programmed Desorption
$O_{ads.}$	adsorbed oxygen
$O_{lattice}$	lattice oxygen
OSC	Oxygen Storage Capacity
PFI	Port Fuel Injection

Acronyms, abbreviations and symbols

PGM	Platinum Group Metal
PM	Particulate matter
PMMA	polymethyl methacrylate
PN	particulate number
PS	polystyrene
Q_0	total volumetric feed flowrate
Q_s	quadrupole splitting
r	radius
REE	Rare Earth Element
RICH	rich condition
rpm	rotation per minute
$r_{specific}$	specific reaction rate
s	adsorption site
S	selectivity
SCR	Selective Catalytic Reduction
SEM	Scanning Electron Microscopy
SSA	Specific Surface Area
STOI1	first stoichiometric condition
STOI2	second stoichiometric condition (return test)
T	temperature
t	tolerance factor
TMAOH	tetramethylammonium hydroxide
TPR	Temperature Programmed Reaction
TWC	Three Way Catalyst
UF	Under-floor configuration
vol.	volume
wt.	weight
X	conversion
$X_A(T)$	conversion of reactant A corresponding to a certain temperature T
XAFS	X-ray Absorption Fine Structure
XPS	X-ray Photoelectron Spectroscopy
XRD	X-ray diffraction

Acronyms, abbreviations and symbols

Y	yield
α-oxygen	suprafacial oxygen
β-oxygen	intrafacial oxygen
$\Delta E_{splitting}$	energy difference of multiplet splitting
θ	incident angle of the incoming beam
λ	air to fuel ratio
λ	wavelength of incident beam
ν	stoichiometric coefficient
ρ	density
χ	electronegativity

Abstract

The current study aims to develop novel catalytic materials for the post-treatment of exhaust gas stemming from gasoline engines. The Three Way Catalyst (TWC) is generally considered as a mature and reliable technology capable of removing simultaneously the main pollutants present in the automobile exhaust gas: CO, HC and NO_x. The existing TWC system relies heavily on the significant use of Platinum Group Metals (PGMs) and Rare Earth Elements (REEs). However, the high-cost and scarcity of the conventional PGM-based TWC system constitutes an obstacle for the cost reduction of exhaust gas treatment technology as well as a severe burden on natural resource. Another drawback of conventional TWC is associated with the sintering of precious metals in the process of catalyst operation and unsatisfactory N_2 selectivity during NO_x reduction. Therefore, alternative solutions are required which should ideally allow a substantial reduction of PGMs usage without sacrificing significantly the catalytic performance.

The goal of this study is to evaluate the feasibility of applying perovskite-type materials as an alternative to the replacement of conventional TWC system. The main approach employed is composition optimization of perovskite-type materials, including creation of non-stoichiometry in the chemical composition, partial substitution in A or B site and addition of small amount of PGMs. Influence of partial substitution in A or B site as well as the synergistic effect of dual substitutions in both A and B site were investigated. Results showed that Cu doping in B site could enhance oxidation of CO and C_3H_6 while Mn doping had a noticeable promoting impact on NO reduction under stoichiometric conditions. Small amount of PGM loading combined with doping of Cu or Mn could enhance remarkably the redox properties of the lanthanum ferrite perovskite. Ca doping in A site affected the dispersion and diffusion of precious metals across the perovskite substrate. The PGM-loaded perovskite catalysts outperformed the commercial benchmark catalyst in terms of higher NO conversion and N_2 selectivity in stoichiometric condition in the operating temperature range of the TWC system but the $deNO_x$ activity during cold-start process remains a big challenge.

Keywords:
automotive emission control, 3 way catalyst, perovskite, CO oxidation, HC oxidation, $deNO_x$

Résumé

La présente étude vise à développer de nouveaux matériaux catalytiques pour le post-traitement des gaz d'échappement provenant de moteurs à essence. Le catalyseur trois voies (CTV) est généralement considéré comme une technologie mature et fiable capable d'éliminer simultanément les polluants principaux présents dans les gaz d'échappement des voitures: CO, HC et NO_x. Le système de CTV existant repose largement sur l'utilisation importante de métaux du groupe du platine (MGP) et d'éléments de terres rares (ETR). Cependant, le coût élevé et la rareté du système de CTV conventionnel à base de MGP constituent un obstacle à la réduction des coûts de la technologie de traitement des gaz d'échappement ainsi qu'un lourd fardeau sur les ressources naturelles. Un autre inconvénient du système de CTV conventionnel est lié au frittage de métaux précieux dans le processus de fonctionnement du catalyseur et à la sélectivité insatisfaisante d'azote lors de la réduction des NO_x. Par conséquent, des solutions alternatives sont nécessaires, qui devraient idéalement permettre une réduction substantielle de l'utilisation de MGP sans sacrifier de manière significative les performances catalytiques.

Le but de cette étude consiste à évaluer la faisabilité de l'utilisation de matériaux de type perovskite comme alternative au remplacement de systèmes de CTV conventionnels. L'approche principale utilisée est l'optimisation de la composition de matériaux de type perovskite, notamment la création d'une non-stœchiométrie dans la composition chimique, la substitution partielle dans le site A ou site B et l'ajout d'une faible quantité de MGP. L'influence de la substitution partielle dans le site A ou site B ainsi que l'effet synergique des doubles substitutions dans les sites A et B ont été étudiés. Les résultats ont montré que le dopage de Cu dans le site B pouvait augmenter l'oxydation de CO et de C_3H_6, tandis que le dopage de Mn avait un impact déterminant sur la réduction du NO dans des conditions stœchiométriques. Une faible quantité de charge de platinoïdes combinée avec le dopage de Cu ou de Mn améliore remarquablement les propriétés redox de perovskite de type ferrite de lanthane. Le dopage de Ca dans le site A a entraîné un impact significative sur la dispersion et la diffusion partielle de métaux précieux dans la structure de la perovskite. Les performances obtenues sur ces nouveaux systèmes sont supérieures à celles obtenues sur un catalyseur de référence commercial en termes de conversion de NO et de sélectivité d'azote plus élevée dans des conditions stœchiométriques dans la plage de températures de fonctionnement du système de CTV, mais l'activité de $DeNO_x$ au cours du processus de démarrage à froid reste un défi majeur.

Mots clés: Catalyseur trois voies, perovskite, $DeNO_x$, oxydation de CO, oxydation de C_3H_6

Chapter I. Context and general introduction

Air quality deterioration resulting from automobile exhaust emission has been a serious concern since as early as 1970s owing to the rapid increase of vehicles [M.V. Twigg 2007] The main reason for air pollution caused by gasoline engine waste gas is that the non-perfect combustion of petroleum-sourced fuels results in the production of hazardous pollutants such as CO and unburned HC. Besides, formation of nitric oxide (NO_x) usually takes place in the combustion chamber due to the presence of oxygen. [N.A. Henein 1976; L.J. Muzio 1997; J.W. Hwang 1999] Oxidation and reduction reactions need to occur at the same time in order to convert the abovementioned three types of contaminant to harmless products. Up to now, Three Way Catalyst (TWC) has been widely applied in exhaust control of gasoline engines since more than four decades. Three way catalytic converter is generally believed as the most mature and effective approach to eliminate simultaneously CO, HC and NO_x at air-to-fuel ratio close to stoichiometric value near 14.7. The most common components of the modern commercial TWC formulations consist of Platinum Group Metals (PGMs) as active phase, porous support (i.e. γ-alumina) and some additives based upon Rare Earth Element (REE) (i.e. lanthanum oxide, ceria, ceria-zirconia). The major drawbacks of PGMs lie in their high cost, volatility and poor thermal stability whereas REE is regarded as strategic resources due to their scarcity and uncertainty of supply which poses a risk on the sustainability of automobile industry. These materials have been classified by European Union as Critical Raw Materials (CRM). The increasing price and severe shortage of supply of CRM calls for urgent reduction of their usage in the TWC in the coming years from both economic and strategic point of view. To find alternatives with low cost, low CRM content, high activity for pollutant conversion and good thermal stability potentially capable of replacing current TWC formulations has been an ultimate goal in recent studies regarding automobile exhaust control. Extensive efforts have been made towards development of innovative materials with reduced amount of CRM while being capable of removing effectively contaminants facing the implementation of more stringent environmental legislations.

This study is carried out within the framework of EU-funded project PARTIAL-PGMs whose goal is to develop new type of automobile post-treatment system while achieving the ambition of minimization of expensive and scarce materials. More specifically, the aim of significant reduction of 35% PGMs and 20% rare earth element is expected to attain while at the same time keeping gaseous pollutants and soot level below the limits stipulated by the harsh EU regulations. To realize such target, one possible strategy would be the employment of a Gasoline Particulate Filter (GPF) coated with materials comparable to the existing TWC. The main scheme involves integrating the GPF with TWC through smart design and then placing the coupled GPF/TWC entity in the appropriated position within the catalytic converter of gasoline engines in order to fabricate the 2nd generation GPF/TWC hybrid automotive post-treatment system. This system possesses many advantages: Firstly, a continuous combustion of soot will be achieved and effective elimination of particulate matter will be envisaged thanks to the introduction of GPF. Secondly, the compact configuration allows rapid light-off at low temperature and reduced emission during cold-

start process. Regeneration of soot would be available at lower temperature (c.a. 100°C). Thirdly, the small volume of the device would not only reduce notably the cost but also facilitate the installation in the exhaust pipeline. More importantly, a significant cut on the usage of PGMs and REE is anticipated through innovative design and optimization of nanostructured materials via chemistry and engineering approaches.

Mixed oxides with perovskite-type structure have been proposed as a potential substitute for the existing PGM-based TWC due to their unique advantages. The low cost, good oxidation activity, high thermal stability and tunable properties makes perovskite an ideal candidate for environmental catalysis application. The flexible composition and high structural tolerance allows a wide range of combination of catalytically active transition metals through partial substitution in A or B site. [K.K. Hansen 2001; L.G. Tejuca 1989]What's more, it is reported by previous studies that perovskite could favor the redispersion of noble metals on the surface through ex situ redox thermal treatment. [A. Schön 2015; Y. Wu 2015; J.P. Dacquin 2010, 2011] Soot oxidation can be reinforced thanks to the enhanced mobility of surface and lattice oxygen. [P. Ciambell 2001; R. Jiménez 2010; D. Fino 2003]. These distinctive attributes meet the EU requirements for future three way catalytic materials. In this sense, research on the feasibility of using perovskite as replacement material for the conventional PGM-based TWC will be of great significance.

The main objective of this study is to explore the possibility of applying perovskite as active phase to the post-treatment of gasoline engine exhaust gas. Redox properties of perovskite would be tailored by means of substitution in A or B site in order to achieve optimized three way catalytic activity while maintaining the usage of PGMs and REE within the permitted level.

One of the main drawbacks associated with perovskite-type material is the low selective reduction of nitric oxides in stoichiometric condition. Small amount of noble metal is therefore indispensible in order to attain effective NO_x abatement in the real driving condition where air-to-fuel ratio fluctuates near 14.7. It should be pointed out that the current lowest noble metal loading in TWC meeting Euro 6 standard is already less than 1 g/L, which serves as a benchmark that should be taken into account when designing formulations of PGM-perovskite composite materials.

Through rational design of the catalyst and optimization of the specification and operating conditions of the filter, a highly effective GPF/TWC prototype that can meet future strict emission regulations will finally be delivered.

This manuscript will report the development of alternative TWC compositions with the aim to get more insights into the specificities of perovskite based materials recognized for their flexibility and the possibily to tune their redox and thermal properties through the accommodation of a wide number of active elements thanks to their structural properties. Accordingly particular attention will be paid to the ḷoading with low amount of PGM, i.e. rhodium and palladium. This manuscript will be composed of 9 chapters.

After a detailed examination of the state of the art and the description of experimental protocols and physicochemical techniques in the experimental section, the results will be presented and discussed in four different parts.

The first part A corresponding to chapter IV. is related to the catalytic properties of supported palladium on ceria-zirconia mixed oxide as benchmark catalysts.

Part B composed of to chapters V. and VI. are related to the intrinsic properties of dual substituted stoichiometric and non stoichiometric ferrite materials. Particular attention will be paid to the difference observed in terms of surface properties and related catalytic properties after iron substitution by copper and manganese.

Part C and D will report the impact of palladium and rhodium incorporation on the catalytic properties. It will be found that PGM can assist oxidation reactions but more importantly can compensate the weakness of perovskite to reduce efficiently NO_x to nitrogen in stoichiometric conditions showing that the composite materials thus obtained can outperform the performances recorded on the commercial benchmark catalysts.

At the end a general conclusion will emphasize the breakthrough achieved in this study.

Reference

[P. Ciambell 2001] P. Ciambelli, S. Cimino, L. Lisis, M. Faticanti, G. Minelli, I. Pettiti, P. Porta. Applied Catalysis B: Environmental, 2001, 33:193–203.

[J.P. Dacquin 2010] J.P. Dacquin, M. Cabié, C.R. Henry et al. Journal of Catalysis, 2010, 270:299–309.

[J.P. Dacquin 2011] J.P. Dacquin, C. Lancelot, C. Dujardin, P. Granger. Journal of Physical Chemistry C, 2011, 115:1911–1921.

[D. Fino 2003] D. Fino, N. Russo, G. Saracco, V. Specchia. Journal of Catalysis, 2003, 217:367–375.

[K.K. Hansen 2001] K.K. Hansen, E.M. Skou, H. Christensen et al. Journal of Catalysis, 2001, 199:132-140.

[N.A. Henein 1976] N.A..Henein. Progress in Energy and Combustion Science, 1976, 1(4):165–207.

[J.W. Hwang 1999] J.W. Hwang, H.J. Kal, M.H. Kim et al. SAE technical paper series, 1999, 1999-01-0195.

[R. Jiménez 2010] R. Jiménez, R. Zamora, G. Pecchi, X. García, A.L. Gordon. Fuel Processing Technology, 2010, 91:546–549.

[L.J. Muzio 1997] L.J. Muzio, G.C. Quartucy. Progress in Energy and Combustion Science, 1997, 23:233–66.

[A. Parlak 2005] A. Parlak, H. Yasar, C. Hasimoglu, A. Kolip. Applied Thermal Engineering, 2005, 25(17–18):3042–3052.

[F. Payri 2006] F. Payri, J. Benajes, J. Arrègle, J.M. Riesco. Oil & Gas Science and Technology-Revue d'IFP Energies nouvelles, 2006, 61(2):247–258.

[A. Schön 2015] A. Schön, C. Dujardin, J.P. Dacquin, P. Granger. Catalysis Today, 2015, 258:543–548.

[L.G. Tejuca 1989] L.G. Tejuca, J.L.G. Fierro, J.M.D. Tascón et al. Advances in Catalysis, 1989, 36:237–328.

[M.V. Twigg 2007] M.V. Twigg. Applied Catalysis B: Environmental, 2007, 70:2–15.

[Y. Wu 2015] Y. Wu, C. Dujardin, C. Lancelot et al. Journal of Catalysis, 2015, 328:236–247.

Chapter II. Literature review

2.1. Three-Way Catalyst: an established technology for exhaust post-treatment

Emission control of automotive exhaust is of great importance on a global level to tackle the problem of air pollution. Engine exhausts are a complex mixture. Several examples of exhaust compositions for some common engine types are listed in Table 2.1. [J. Kašpar 2003]. It must be pointed out that real compositions of engine exhaust vary substantially due to the contribution of a great number of affecting factors.

Table 2.1. Example of exhaust compositions for two- and four-stroke, diesel and lean-four-stroke engines. Reference [J. Kašpar 2003] with permission.

Exhaust components and conditions[a]	Diesel engine	Four-stroke spark ignited-engine	Four-stroke lean-burn spark ignited-engine	Two-stroke spark ignited-engine
NO_x	350–1000 ppm	100–4000 ppm	≈1200 ppm	100–200 ppm
HC	50–330 ppm C	500–5000 ppm C	≈1300 ppm C	20,000–30,000 ppm C
CO	300–1200 ppm	0.1–6%	≈1300 ppm	1–3%
O_2	10–15%	0.2–2%	4–12%	0.2–2%
H_2O	1.4–7%	10–12%	12%	10–12%
CO_2	7%	10–13.5%	11%	10–13%
SO_x	10–100 ppm[b]	15–60 ppm	20 ppm	≈20 ppm
PM	65 mg/m^3			
Temperatures (test cycle)	r.t.–650 °C (r.t.–420 °C)	r.t.–1100 °C[c]	r.t.–850 °C	r.t.–1000 °C
GHSV (h^{-1})	30,000–100,000	30,000–100,000	30,000–100,000	30,000–100,000
λ (A/F)[d]	≈1.8 (26)	≈1 (14.7)	≈1.16 (17)	≈1 (14.7)[e]

Note:

a N_2 is reminder.

b For comparison: diesel fuels with 500 ppm of Sulphur produce about 20 ppm of SO_2

c Close-coupled catalyst

d λ defined as ratio of actual A/F to stoichiometric A/F, λ=1 at stoichiometry (A/F=14.7)

e Part of this fuel is employed for scavenging of the exhaust, which does not allow to   define a precise definition of the A/F

Among these components, CO, HC and NO_x are the most hazardous gaseous pollutants. Since 1982, the Three-Way Catalyst (TWC) has been extensively applied to the post-treatment of exhaust gas from gasoline engines. The name of TWC is derived from the ability to remove simultaneously as-mentioned three major pollutants present in the exhausts. [J. Kašpar 2000] TWC works at air-to-fuel (A/F) ratio close to stoichiometry (14.7) in order that all three pollutants could be converted at the same time. [J. Kašpar 2000]. A closed-loop emission control system is employed to keep the A/F ratio as close to stoichiometry as possible.(Fig. 2.1.) [J. Kašpar 2000]. In brief, two λ sensors (oxygen sensor) are mounted in the closed-loop control system: one placed upstream and the other placed downstream of the catalytic converter. The amount of air is constantly measured and the fuel injection is adjusted automatically by the electronic automation system which relies on the feedback signal from the λ sensor located upstream of the catalytic converter. A/F fluctuations can be detected by comparing the signal difference between the two λ sensors. Extensive variations

of A/F ratio can be avoided by an On-Board Diagnostics (OBD) which presumes that a narrow A/F window at the stoichiometric point is the fingerprint of an effective TWC system. [J. Kašpar 2003].
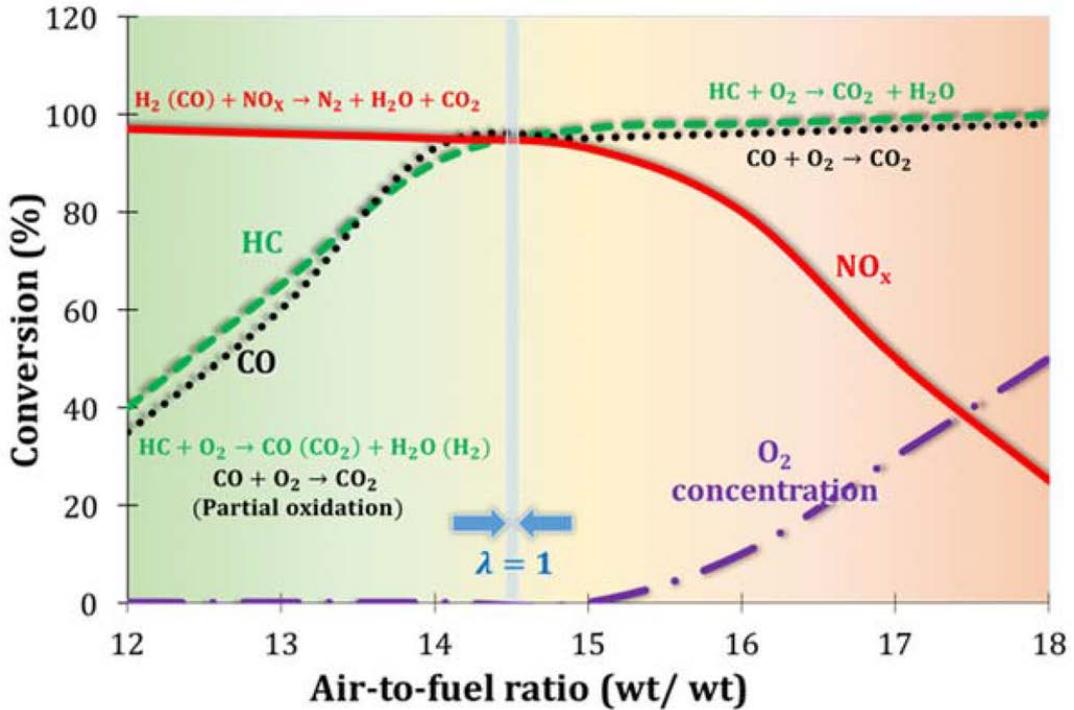
Fig. 2.1. Three-way catalytic (TWC) converter profile for conversion vs. air-to-fuel ratio. From [Q. Zheng 2015] with permission.

The main reactions taking palce within a TWC converter are listed below [J. Kašpar 2003]:

Oxidation reactions:

$$2CO + O_2 \rightarrow 2CO_2 \qquad\qquad (eq.\, 2-1)$$

$$C_mH_n + \left(m + \frac{n}{4}\right)O_2 \rightarrow mCO_2 + \frac{n}{2}H_2O \qquad\qquad (eq.\, 2-2)$$

$$2H_2 + O_2 \rightarrow 2H_2O \qquad\qquad (eq.\, 2-3)$$

NO reduction reactions:

$$C_mH_n + \left(2m + \frac{n}{2}\right)NO \rightarrow \left(m + \frac{n}{4}\right)N_2 + mCO_2 + \frac{n}{2}H_2O \qquad (eq.\, 2-4)$$

$$CO + NO \rightarrow \frac{1}{2}N_2 + CO_2 \qquad\qquad (eq.\, 2-5)$$

$$H_2 + NO \rightarrow \frac{1}{2}N_2 + H_2O \qquad\qquad (eq.\, 2-6)$$
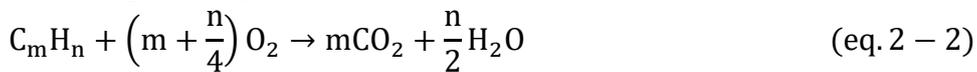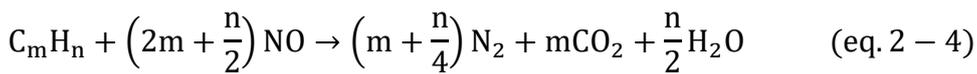
Water-Gas Shift(WGS) reaction:

$$CO + H_2O \rightarrow CO_2 + H_2 \qquad\qquad (eq.\, 2-7)$$

Steam reforming reaction:

$$C_mH_n + 2mH_2O \rightarrow mCO_2 + \frac{(n + 4m)}{2}H_2 \qquad\qquad (eq.\, 2-8)$$
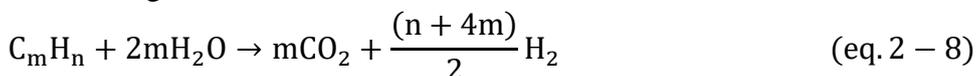
A point worth noting is that apart from nitrogen, side products such as nitrous oxide and ammonia could also be produced depending on reaction conditions:

$$C_mH_{2(1-2m)} + 2NO \rightarrow N_2O + mCO_2 + (1-2m)H_2O \qquad (eq. 2-9)$$
$$C_mH_{2(1-2m)} + NO \rightarrow NH_3 + mCO_2 + (1-2m)H_2O \qquad (eq. 2-10)$$
$$CO + 2NO \rightarrow N_2O + CO_2 \qquad (eq. 2-11)$$
$$H_2 + 2NO \rightarrow N_2O + H_2O \qquad (eq. 2-12)$$
$$H_2 + \frac{2}{5}NO \rightarrow \frac{2}{5}NH_3 + \frac{2}{5}H_2O \qquad (eq. 2-13)$$
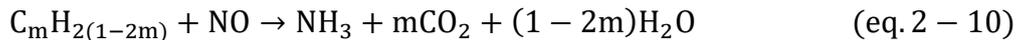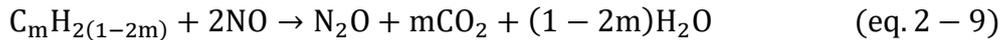
Nitrous oxide is usually formed during cold start process (equation 9, 11, 12) whereas ammonia can be generated in large amount under rich-burn condition due to the excess of HC and H_2 (equation 10 et 13).[P. Granger 2001, 2004; J.H. Wang 2015]

Typically, TWC is composed of : [W.G. Shim 2011; P. Lucena 1999; J. Kašpar 2003]

(a) monolithic honeycomb substrate (i.e. metal, ceramic): The biggest advantage of metal monolith lies in their high conductivity and low heat capacity; ceramic monolith such as cordierite($2MgO \cdot 2Al_2O_3 \cdot 5SiO_2$) has been widely applied because of their low cost. [J. Kašpar 2003] Recently particular attention has been paid to solid foams as a possible solution to replace honeycomb monolith. [P. Dimopoulos Eggenschwiler 2009]

(b) porous support: Alumina has been extensively employed as support thanks to its high surface area and exceptional thermal stability. γ-Al_2O_3, δ-Al_2O_3, θ-Al_2O_3 have all been reported to be used in the TWC converter. [J.R. Anderson 1975]

(c) active phase: Conventional active phase is mainly relied on precious metals(i.e. Pt, Pd, Rh).The main problems linked with precious metals are their scarcity, high cost as well as deactivation. In light of the as-stated inconveniences, alternative approaches need to be developed.

(d) additives: some additives function as promoters in favor of the TWC performance. It has been confirmed that ceria-based materials demonstrated beneficial effects on the TWC. Detailed explanations about the promotional effects are given in literatures. [J. Kašpar 2000; K.C. Taylor 1984; A. Trovarelli 1996] Nowadays, CeO_2-ZrO_2 is extensively employed due to its excellent thermal stability.

An ideal TWC converter is expected to possess a number of qualities, including high activity and selectivity, fast light-off, high thermal stability, high oxygen storage capacity. [J. Kašpar 2003] Recently, to achieve higher energy efficiency, the ratio of air/fuel fed into internal combustion engines higher than 14.7 (the stoichiometric value) is suggested. However, high ratio of air/fuel usually results in the low NO reduction efficiency of TWC in such a fuel-lean condition. Consequently, development of a new generation of TWC to improve the NO reduction activity in oxygen-rich condition poses new challenges for researchers and engineers. [L.F. Chen 2005].

2.2. Four-Way Catalytic system: a solution to meet future emission standards

Nowadays, more stringent standards concerning automotive exhaust emissions have been set. In the latest Euro 6 regulation, a stricter upper limit has been stipulated not only for the

gaseous pollutants (i.e. CO, CH, and NO_x) but also for the particulate matter (PM). Recent European legislations with respect to gasoline and diesel car exhaust emissions are succinctly summarized in Table 2.2. In comply with Euro6 standards which came into effect as of September 2014, particulate number (PN) was restricted to less than 6×10^{11} PN/km both for gasoline positive ignition engines and diesel compression ignition engines.

Table 2.2. Summary of EU emission standards for passenger cars

Stage	Date	CO	HC	HC+NOx	NOx	PM	PN
		g/km					#/km
Positive Ignition (Gasoline)							
Euro 1†	1992.07	2.72 (3.16)	-	0.97 (1.13)	-	-	-
Euro 2	1996.01	2.2	-	0.5	-	-	-
Euro 3	2000.01	2.30	0.20	-	0.15	-	-
Euro 4	2005.01	1.0	0.10	-	0.08	-	-
Euro 5	2009.09[b]	1.0	0.10[d]	-	0.06	0.005[e,f]	-
Euro 6	2014.09	1.0	0.10[d]	-	0.06	0.005[e,f]	6.0×10^{11} [e,g]
Compression Ignition (Diesel)							
Euro 1†	1992.07	2.72 (3.16)	-	0.97 (1.13)	-	0.14 (0.18)	-
Euro 2, IDI	1996.01	1.0	-	0.7	-	0.08	-
Euro 2, DI	1996.01[a]	1.0	-	0.9	-	0.10	-
Euro 3	2000.01	0.64	-	0.56	0.50	0.05	-
Euro 4	2005.01	0.50	-	0.30	0.25	0.025	-
Euro 5a	2009.09[b]	0.50	-	0.23	0.18	0.005[f]	-
Euro 5b	2011.09[c]	0.50	-	0.23	0.18	0.005[f]	6.0×10^{11}
Euro 6	2014.09	0.50	-	0.17	0.08	0.005[f]	6.0×10^{11}

Note: a. until 1999.09.30 b. 2011.01 for all models c. 2013.01 for all models d. and NMHC=0.068 g/km e. applicable only to vehicles using DI engines f. 0.0045 g/km using the PMP measurement procedure g. 6.0×10^{12} 1/km within first three years from Euro6 effective dates [Adapted from: https://www.dieselnet.com/standards/eu/ld.php]

In respect of the increasingly severe legislations imposed, more sophisticated exhaust after-treatment systems with higher efficiency and durability have to be developed. A catalytic system that is able to eliminate at the same time gaseous pollutants (CO, unburnt hydrocarbons and NO_x) as well as particulate matter is therefore regarded as a suitable solution to meet future emission regulations.

As to the gasoline engine emission, compared to conventional gasoline engines such as Port Fuel Injection (PFI) or Multi-Point Injection (MPI), Gasoline Direct Injection (GDI) has demonstrated significant advantages in terms of fuel economy, gain in performance, better drivability and lower CO_2 emissions resulted from evolution of the engine combustion mode [W. Piock 2011; S. Philipp 2013]. In light of the distinctive strengths, GDI has experienced a substantial increase of market share in recent years and is expected to replace largely conventional gasoline engines to become the mainstream of next-generation gasoline engines. Nevertheless, it was suggested that GDI engines typically emit 10-40 times more particles (by mass) than PFI engines and over one-thousand times in number (PN). Vehicles equipped with GDI engines are reported to emit roughly two orders or even higher of magnitude of the ultrafine particles than the PFI engines [P. Whitaker 2011]. Despite the benefits of reduced fuel consumption and CO_2 emissions, a higher emission of particulate matter (PM) remains the biggest obstacle to overcome for GDI technology in comparison with conventional gasoline engines (i.e. PFI, MPI), necessitating a widespread application of Gasoline

Particulate Filter (GPF). It has been estimated that by 2030, PM produced from GDI will be more than those of diesel engines [European Environment Agency report]. As can be seen in Fig. 2.2., current Euro5 GDI engines exceeds the proposed Euro6 PN standard and additional efforts are still required to meet more stringent criteria.

Also, it is well known that diesel engines are characterized by higher fuel combustion efficiency compared to gasoline engines. However, some serious drawbacks associated with diesel emissions are very evident. The main issues related to diesel engines are the emission of NO_x and particulate matter (PM). Several technologies have been developed to the address the former issue, including SCR, NSR and LNT. In the case of PM, a Diesel Particulate Filter(DPF) is required. Indeed, a Diesel Particulate Filter(DPF)is considered the only feasible solution for diesel after-treatment technology which can comply with future stricter requirement for PM emission[T. Körfer 2008; T.V. Johnson 2010.] A detailed comparision of particulate number and particulate mass for gasoline and diesel engines is illustrated in Fig. 2.2..
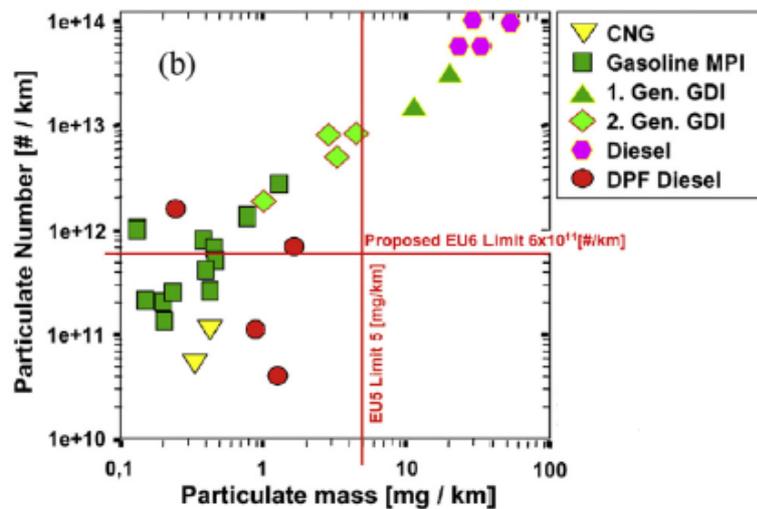

Fig. 2.2. Comparison of particulate number and particulate mass emissions for gasoline and diesel engines(Adapted from P. Whitaker 2011)

PM is a complex mixture consisting of solid phase and condensate materials.[B. Guan 2015]. Inorganic carbon and metal ashes are the main components of solid phase whilst boiling hydrocarbons, water and sulfuric acid constitute the condensates.[E. Vouitsis 2003; H. Burtscher 2005]. Correspondingly, the total diesel particulate matter (PM) is made up of four major fractions: (a) elemental carbon (solid, i.e. soot) (b) soluble organic fraction (SOF, solid or liquid substances finely distributed in gases) generated by fuel and engine lubricant oil (c) sulfates (hydrated sulfuric acid, metal sulfates and liquid, depending on the sulfur content of the fuel) (d) ash (inorganic materials) [B. Guan 2015]. It should be emphasized that the specific composition of PM may vary over a large extent and rest with many factors such as the employed fuel and oil, the engine design, the real operating conditions and the management strategies. [A.K. Agarwal 2007; D.R. Tree 2007; M.M. Maricq 2007). The typical composition and structure of diesel engine PM is represented in Fig. 2.3.
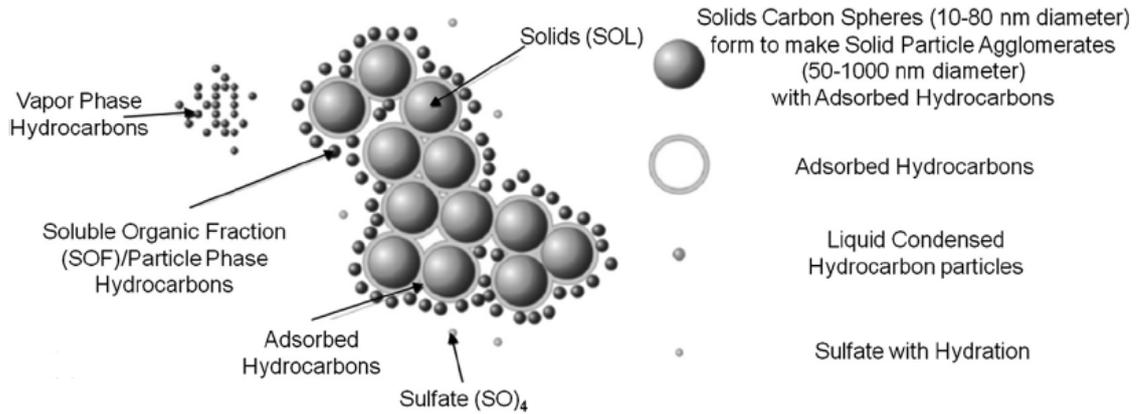
Fig. 2.3. typical chemical composition and structure of diesel engine particulate matter [R. Prasad 2010; D.B. Kittelson.1998; H. Burtscher 2005]

According to their aerodynamic diameters D_p, soot particles are divided into five categories. The classification of soot particles are listed in Table 2.3.

Table 2.3. classification of soot particles based on aerodynamic diameters[D.B. Kittelson 1998; A.K. Agarwal 2007]

Particle classification	aerodynamic diameter D_p
large particles	$D_p> 10\mu m$
coarse particles (PM 10)	$2.5\ \mu m<D_p<10\ \mu m$
fine particles (PM 2.5)	$0.1\ \mu m<D_p<2.5\ \mu m$
ultra-fine particles (PM 0.1)	$0.05\ \mu m<D_p<0.1\ \mu m$
nanoparticles	$D_p<0.05\ \mu m$ (or $D_p< 50$ nm)

The contribution of different soot particles to PM and PN is shown in Fig. 2.4. It is noteworthy that although present in the greatest number, the very smallest particles consisting of the nuclei mode contribute little to the total mass. By contrast, particulate mass is dominated by less yet heavier larger particles making up the accumulation mode. [H. Burtscher 2005]. Smaller particles have been revealed to be the most hazardous to human health. [R. Prasad 2010; Z.D. Ristovski 2012]. As a consequence, not only the mass but also the number of particulates have been specified in vehicle emission legislations.
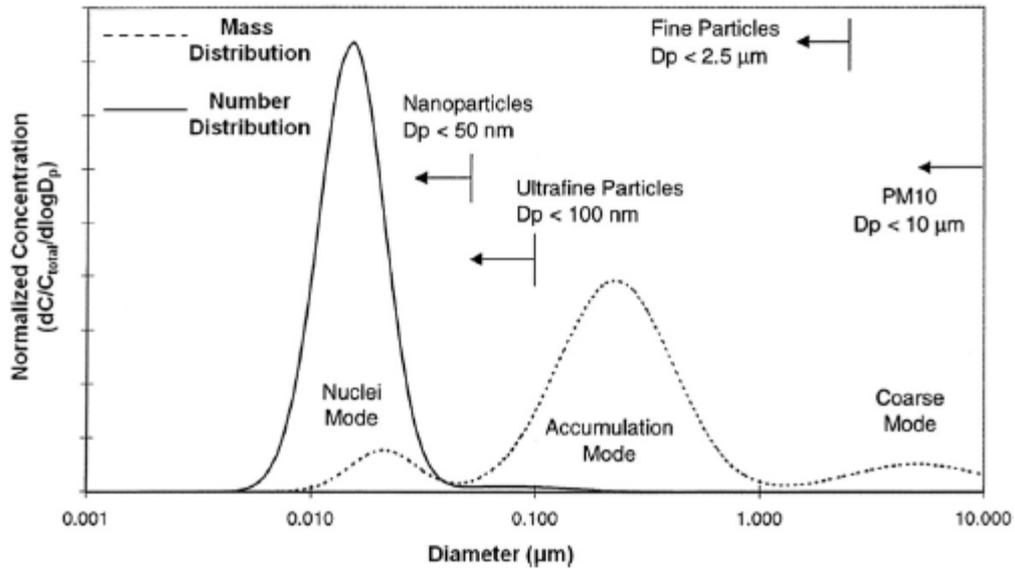
Fig. 2.4. Illustration of mass- and number-based concentration of typical particle size distribution from diesel exhaust. Reprinted with permission of [H. Burtscher H. 2005; M.M. Maricq 2007].

Ceria-based catalysts have been widely studied for soot oxidation.[S. Liu 2015]. Four kinds ceria-based catalysts have been reported most applicable: (1) $Ce_xZr_{1-x}O_2$ with high cerium content(x>0.76) (2)rare earth metals modified ceria, especially Pr (3) transition metals modified ceria (i.e Mn, Cu) (4) Ag//CeO$_2$ [S. Liu 2015].

To address the problem of particulate matter emission, a Particulate Filter (PF) is inevitably required. PF has been proven to be quite effective in controlling PM emissions of diesel automobiles. Fig. 2.5. shows the structure of a wall-flow particulate filter and corresponding coated substrate.
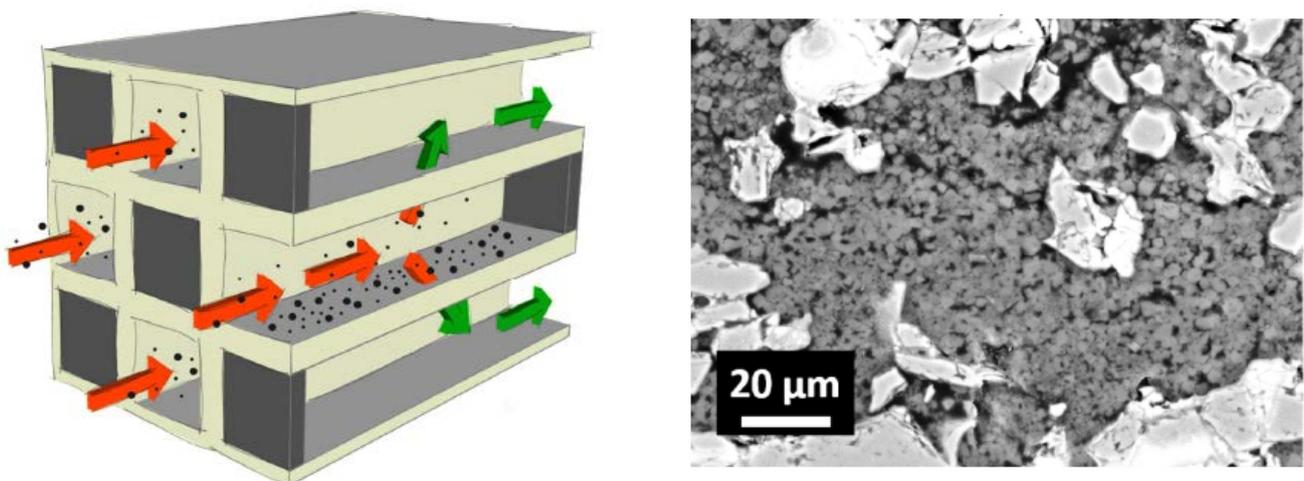

Fig. 2.5. Structure of particulate filter (PF). left: schematic of wall-flow particulate filter right: SEM of washcoat (black: pores; dark grey: SCR washcoat; lightgrey: SiC substrate). Sample used: SCR/SiC 1.9 g/m^3 adapted from [M. Václavík 2017) with permission.

However, plugging of PF due to the continuous use under real driving conditions is the most common problem. Regeneration of the PF is thus a crucial step to maintain the high

efficiency of soot removal. [J. Kašpar 2003] The regeneration of PF is usually done by burning soot deposited on the filter. Fig. 2.6. shows the principle of the continuously regenerating trap (CRT) for diesel particulate removal [J. Kašpar 2003].
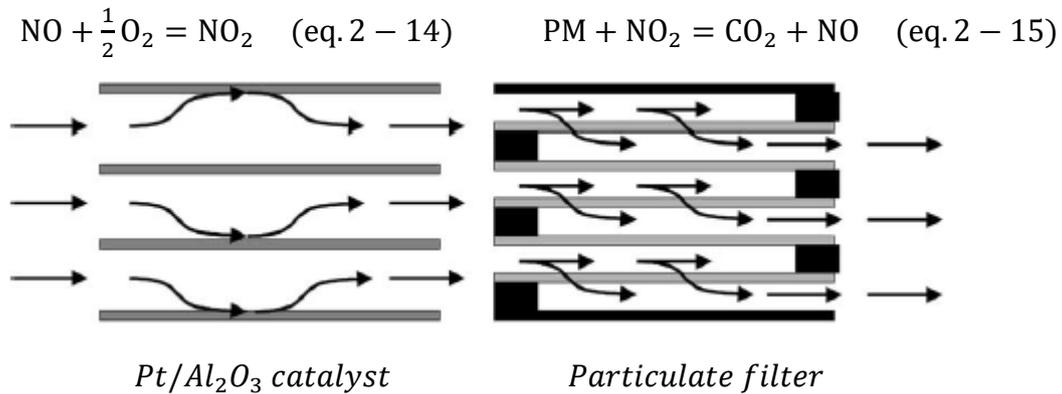
$$NO + \frac{1}{2}O_2 = NO_2 \quad (eq.\, 2-14) \qquad PM + NO_2 = CO_2 + NO \quad (eq.\, 2-15)$$

$$Pt/Al_2O_3\ catalyst \qquad\qquad Particulate\ filter$$

Fig. 2.6. working principle of continuously regenerating trap (CRT) with permission from[J. Kašpar 2003].

2.3.   Construction of the Four-Way Catalytic system:

In the context of increasingly stringent legislations, current exhaust gas after-treatment technologies must be combined in tandem with particulate filters to achieve simultaneous removal of gaseous pollutants (CO, unburnt hydrocarbons and NO_x) and particulate matter. Thus, a catalytic system capable of eliminating simultaneously CO, HC, NO_x and particulate matter is labelled as a Four-Way Catalytic system. Several schemes have been worked out to act as potentially practical designing plans for the future Four-Way Catalytic system. A non-exhaustive overview about the Four-Way Catalytic system is presented below.
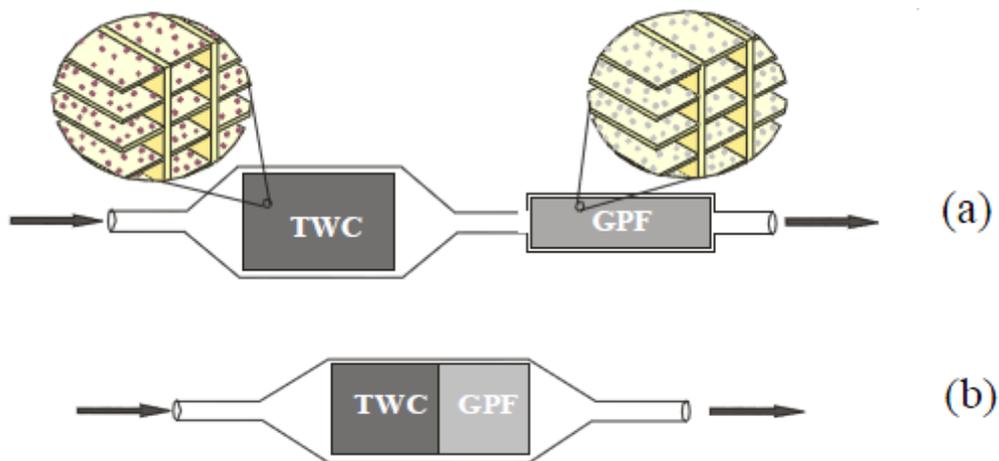
2.3.1. GPF/TWC coupling

Fig. 2.7. Different integration mode of the first-generation GPF/TWC coupling (a) under-floor(UF) configuration (b) closed-coupled(CC) configuration.

GPF+TWC has been reported as one the most promising integrated catalytic systems for gasoline vehicles that are able to meet strict Euro6 regulations. Fig. 2.7. is the schematic show of different integration mode of the first-generation GPF/TWC coupling.

In light of the effectiveness of particulate filter in terms of PM emission reduction, some studies have been conducted to investigate the feasibility of applying particulate filter to GDI engine for the sake of reducing significantly the emission of PM. [R. Zhan 2010] Basically, the prevailing configurations of the first-generation GPF/TWC are as follows:

(a) **Under-floor (UF) configuration** In under-floor (UF) configuration, the GPF is located behind the TWC. Occasional active regeneration of the GPF is required due to relatively low temperature ($<250\,℃$) environment, especially under urban driving condition. [D. Greenwell 2013] It should be noted that soot emission in such configuration becomes more obvious under repeated start-stop operations in minus zero ambient temperatures.

(b) **Close-coupled (CC) configuration** In this configuration, the GPF is directly attached to the TWC. Placed close to the TWC in a hot environment, the GPF is able to make fully use of the exhaust thermal energy. Therefore, a higher energy-efficiency can be achieved and in particular active regeneration is not needed. Typically, greater emissions of gaseous pollutants (CO, HC, and NO_x) occur during cold-start process.

Johnson claimed that emission performance could be improved when the CC configuration was transformed to downstream UF configuration [T.V. Johnson 2014]. Zhan stated that GPF in a UF position displayed higher PM/PN filtration efficiencies for all PN size range in comparison with those of the same GPF placed in a CC position. [R. Zhan 2010] The author attributed the higher filtration efficiencies to the formation of soot cake which was facilitated by the low temperature of GPF at UF position. [R. Zhan 2010] Still, it must bear in mind that in the UF configuration the GDI is expected to be able to provide temperatures sufficient for the active regeneration the GPF. Another point which is essentially to be noted is that in the case of active regeneration with excess O_2 of a soot-loaded GPF, it is vital to make sure that excess O_2 will not jeopardize the upstream TWC performance for the sake of maintaining effective removal of CO, HC and NO_x under stoichiometric air-to fuel ratio. [T. Chan 2013; D. Rose 2013; K.F. Hansen 2014]. It was found that GPF backpressure decreased 25% when it was placed downstream of the TWC as a result of ash effect.[C. Morgan 2012; D. Greenwell 2013]

It must be emphasized that despite the similarity of basic design, some important characteristic discrepancies between GPF and DPF cannot be overlooked. According to Saito[C. Saito 2011], less soot accumulation on the GPF was ascertained compared to that on DPF due to the much lower PM emission of the GDI engine. Hence, the PM filtration efficiency of the GPF was lower than that of the DPF due to the lack of soot layer formed on the PF wall during operation. On the contrary, the exhaust temperature and flow rate of the GDI engine tend to be higher than those of the diesel engine, resulting in increased pressure drop across a wall-flow GPF. [A. Williams 2006]. A thin wall and low cell density filter concept is therefore applicable to ensure lower pressure drop [T.V. Johnson 2014]

What's more, the combination of a blended system wherein TWC is coated on the substrate of GPF has been proposed an option for the design of the 2nd generation GPF/TWC

coupling. Some advantages of such design can be exemplified: firstly, the integration of the GPF and TWC into a single compact device allows a significant reduction of the volume, easier to be packed into exhaust pipelines. Secondly, continuous combustion of soot could be realized thanks to the distinctiveness of the GDI engine. Besides, higher energetic efficiency and lower cost can be expected. The development of the 2nd generation GPF/TWC is now underway.

Based upon the above analysis, technical parameters of the GPF/TWC coupling still need to be optimized to achieve the removal of gaseous pollutants and the filtration of PM with highest efficiencies and lowest backpressure. Meanwhile, it is quite essential to combine the after-treatment system with engine emission control strategies in order to gain desirable effectiveness of the GPF without damaging significantly the TWC performance. [B. Guan 2014]

2.3.2. DPF-DOC-SCR integration

DOC+SCR+DPF`or DOC+DPF+SCR

Recently, an Exhaust Gas Recirculation (EGR) engine with low engine-out NO_x has been proposed to be integrated with an after-treatment system composed of a DOC, a DPF and an SCR catalyst to achieve an improved emission reduction performance.[P. Tennison 2004] In general, two configuration architectures can be implemented: either DOC+SCR+DPF (in which the SCR is placed upstream of the DPF) or the DOC+DPF+SCR (in which the SCR is placed downstream of the DPF) [A. Gurupatham 2009].

As to the former configuration DOC+SCR+DPF, a better performance during cold-start process will be available. Thanks to its proximity to the engine, the SCR will be warmed up quickly during cold-start operations to offer a better low-temperature activity and maintain best NO_X reduction performance.[B. Guan 2014] Moreover, high-temperature excursions stemming from downstream regeneration of active DPF can protect the SCR catalyst, which presents the possibility of employing a broader selection of SCR catalysts and enable to proceed the use of vanadium-based SCR catalysts that have been proven effective to meet Euro IV and Euro V standards. [B. Guan 2014]. In addition, another advantage of such configuration is that the DPF can be used as NH_3 slip catalysts for the upstream SCR system. By contrast, the main drawback of such configuration consists in the drastic suppression of passive DPF regeneration caused by the low level of NO_x following the SCR system, leading to worse fuel economy.[I. Gekas 2009] This configuration takes advantage of the fast light-off of the upstream SCR catalyst to meet the very harsh cold-start NO_x restrictions and has been applied mainly to light-heavy duty (LHD) vehicles.

Another configuration of integration is the DOC+DPF+SCR. Several benefits of this configuration can be exemplified: (1) since the DPF is placed closer to the engine, the passive DPF regeneration performance can be enhanced and the fuel penalty of the active DPF regeneration can be lowered owing to higher temperature. (2) the DOC outlet NO_2 could be potentially utilized by DPF to boost passive regeneration of collected soot (3) an improved cleanness and durability of SCR catalyst can be envisioned due to the removal of soot upstream [P. Tennison 2004] Such configuration offers an improved fuel efficiency with higher engine-out NOx, essential for passive regeneration of DPF. [B. Guan 2014]

Notwithstanding, some flaws associated with such configuration should not be neglected. (1) Since the SCR catalyst is located relatively in a cool environment during the cold-start process of the engine, heat transfer will be hindered due to the thermal storage of the DPF, which delays dramatically the arrival of hot exhaust gas to downstream components and results in slower "light-off" of the catalytic system and undesirable NO_x reduction performance. This phenomenon has been observed more evident in larger engines. (2) The complete consummation of NO_2 resulting from soot oxidation by NO_2 in the upstream DPF reduces significantly the amount of NO_2 available to the SCR system. [B. Guan 2014] (3) the thermal ageing of SCR catalyst might be exasperated due to the controlled or uncontrolled PM regeneration. As a consequence, only the non-vanadium catalyst can be applied, such as FeZ and CuZ SCR catalysts because of their higher tolerance to thermal ageing [I. Gekas 2009; A. Vressner 2010].

In short, the DOC+SCR+DPF configuration is more suitable to meet stringent cold-start requirements but penalty of fuel economy resulting from the lack of passive DPF regeneration remains a negative issue. [B. Guan 2014] In comparison, the DOC+DPF+SCR configuration would need higher EGR ratio at cold-start and low-load conditions when confronted to the same cold-start requirement. Nevertheless, the DPF is expected to undergo full-time passive regeneration at high load conditions. [B. Guan 2014]

2.3.3. SCRF (SCR coated DPF)

As a matter of fact, the SCR catalyst can be washcoated onto the wall-flow DPF to form a compact system in combination of characteristics of both SCR and DPF. Such a system is referred to as SCRF or SCRT as it combines the functions of SCR and DPF in a single device. [B. Guan 2014]. Fig. 2.8. is the schematic of physical and chemical processes taking place in a single wall-flow substrate channel of the SCRF[J.H. Lee 2009; W.Y. Tang 2013]. Channel morphologies of SCR/DPF with different SCR catalyst loading amount are illustrated in Fig. 2.9. [K.G. Rappé 2014]
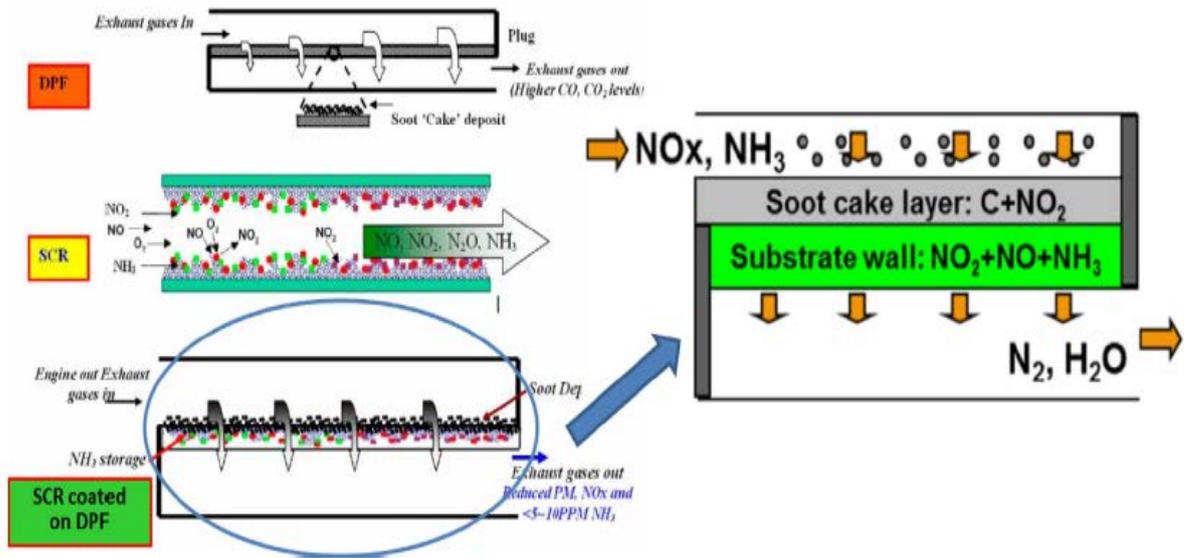
Fig. 2.8. Schematic of physical and chemical processes taking place in a single wall-flow substrate channel of the SCRF [J.H. Lee 2009; W.Y. Tang 2013].
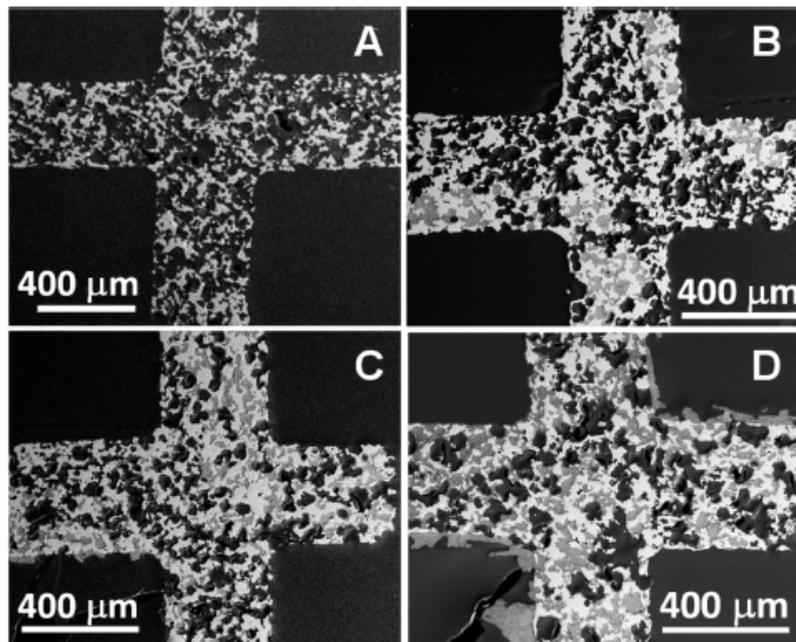

Fig. 2.9. SEM image of (A) clean DPF (B) SCR/DPF with 60 g/L SCR catalyst loading (C) SCR/DPF with 90 g/L SCR catalyst loading (D) SCR/DPF with 150 g/L SCR catalyst loading (reproduced from [K.G. Rappé 2014]).

A number of features associated with SCRF system makes it on the most advanced technologies for diesel exhaust after-treatment facing the prospect of more stringent regulations [B. Guan 2014]:

(1) Placed closer to the engine, the SCRF takes full advantages of the heat discharged from the engine, leading to a higher DPF regeneration efficiency and less thermal loss. Hence, a more rapid light-off of the "deNO$_x$" function can be realized.

(2) Due to the fact that conventional SCR system can be reduced or even discarded, the packaging space and weight will be substantially cut down, allowing an attenuated cost of the exhaust system

(3) Additional SCR catalyst volume can be attached without enlarging tremendously packing space so that the SCRF becomes an energy-efficient and cost-saving system capable of removing simultaneously NO_x and soot. [E. Ngan 2011;M. Naseri 2011]

However, not all kinds of SCR catalysts can be applied to SCRF system. The first requirement for SCR catalysts coated on DPF is their thermal stability to endure excess heat generated during active DPF regeneration. Only zeolite-based SCR formulations are thereby applicable. Besides, a satisfying deNO$_x$ performance should be guaranteed in the temperature range of 200-350℃ for urban utilization. Also, uncontrolled NO_x emissions must be disposed of during active DPF regeneration process (450-700°C).[M. Naseri 2011] CuZ SCR catalysts have been widely studied due to their excellent thermal robustness and deNO$_x$ performance. Under steady-state condition, a deNO$_x$ efficiency of over 90% has been achieved on the CuZ SCR catalyst across a wide temperature window [J.H. Lee 2009]. G. Cavataio reported that CuZ SCR catalyst showed a 70-90% deNO$_x$ efficiency even at inlet temperature of 560-630℃ during active SCRF soot regeneration. Equally important, no obvious deNO$_x$ efficiency was observed when the as-mentioned SCRF catalyst is subjected to soot regenerations after 100 DTI at 800℃ and 30 DTI at 1000°C respectively. [G. Cavataio 2009]. It has been revealed by previous studies that a NO_x conversion as high as 86% could be attained by using SCRF catalysts during cold-start FTP test, manifesting the potential of SCRF catalysts to meet future strict NO_x emission standards. [B. Guan 2014]

Several parameters should be taken into account to avoid significant pressure drop: firstly, the washcoat amount and its location inside the pores of the filter materials must be well designed since both soot efficiency and pressure drop are related to such parameters (as is shown in Fig. 2.10.). Besides, the ratio of NO_2/NO_x should be maintained within a reasonable range to ensure an acceptable deNO$_x$ performance during passive DPF regeneration. In addition, as discussed before, SCR catalyst should exhibit high thermal stability and resistance to poisoning. It has been established that CuZ with chabazite (CHA) structure (such as Cu-SSZ-13, Cu-SAPO-34) demonstrates better activity and selectivity compared to bench-mark Cu-ZSM-5 and Cu-beta catalysts. [D.W. Fickel 2010, 2011]
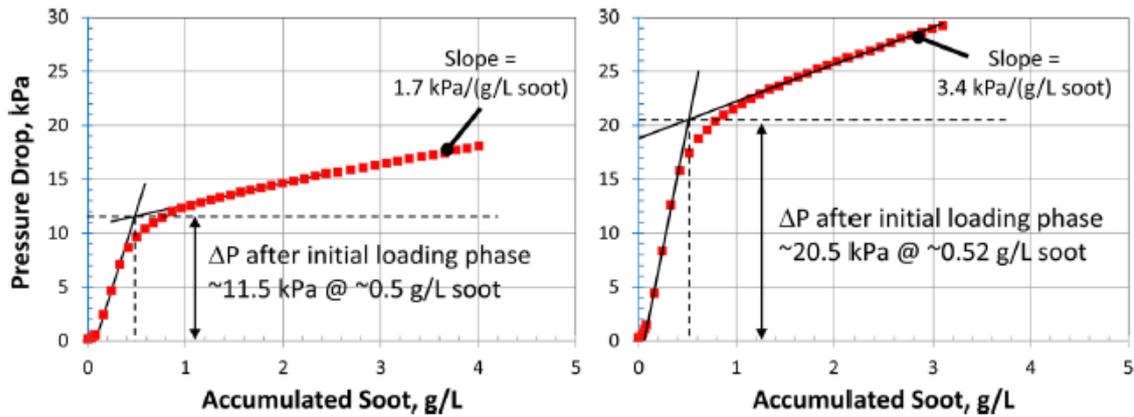
Fig. 2.10. Soot-loading characteristics of 90 (left) and 150 g/L (right) SCR/DPF samples configured such that catalyst was present predominantly on the upstream portion of the filter microstructure and on the inlet channel wall (for the 150 g/L sample) [K.G. Rappé 2014]

The major drawback of the SCRF system resides in the restriction of SCR catalyst loadings on the wall-flow substrate of the DPF because of pressure drop constraint. [B. Guan 2014]. It is therefore necessary to optimize the trade-off regarding wall-flow substrate porosity pressure drop, wash coat loading intensity and filtration efficiency to yield best overall performance. [B. Guan 2014] A. Kawakami reported a hybrid technology in which membrane filtration technology was coupled to porous material. The result was quite encouraging in that the introduction of membrane technology enhanced initial filtration efficiency of the porous wall-flow substrate and pressure drop was greatly reduced[A. Kawakami 2012; Y. He 2009]. Another point worth noting is that a competitive relation exists between the passive soot regeneration of DPF and the reduction of NO_x since these two reactions compete for the consumption of NO_2. In most cases, kinetic rates of SCR reactions were much faster than those of passive soot oxidation [M. Naseri 2011]. Moreover, deNOx performance might be inhibited due to soot loading on SCRF as the latter prevents the contact of NH_3 and NO_x with active sites of SCR catalysts, [B. Guan 2014] although contrary results have also been reported [M. Castagnola 2011].

The SCRF concept is likely to become increasingly prevalent as it presents a major step towards the miniaturization of the catalytic system for diesel exhaust after-treatment.

2.3.4. Natural Gas Vehicle three-way catalyst(NGV-TWC)

Natural Gas Vehicle (NGV) is characterized by very low amount of PM emission comparted to gasoline and diesel vehicles. Nevertheless, the main drawback of NGV lies in the residual emission of methane which is characteristically refractory to break down due to the high bond energy of C-H (439.3 kJ mol^{-1}).[B.C. Enger 2008] Pd-Rh three way catalysts and Pt-Pd oxidation catalysts have been widely applied to NGV emission control under stoichiometric(λ =1) and lean-burn condition (λ =1.3), respectively. It has been proved that compared to lean-burn condition, stoichiometric condition is more favorable to the improvement of emission abatement performance since the removal of NO_x and methane is much easier under such condition. Moreover, the presence of water and low-concentration sulfur (<0.5 ppm) would lead to an enhanced resistance of the catalyst to poisoning. Lean-

burn condition has been attested to be advantageous to the combustion of methane at low temperature. A critical issue related to the NGV catalyst is the thermal stability of oxidic palladium which is susceptible to decomposition at high temperature. Hence, particular attention should be paid to the equilibrium of $PdO_x \rightleftarrows Pd^0$. The combination of Pd-Pt was suggested to be beneficial to the improvement of the thermal stability as well as the robustness against sulfur poisoning of the NGV catalyst. [P. Granger 2017]

Palladium has been considered as the benchmark catalyst for methane oxidation. Activation of methane is supposed to take place on site pairs composed of surface PdO and surface Pd (Fig. 2.11.). [P. Gélin 2002]High Pd loading (>200 g ft^{-3}) is usually required for the sake of compensating the activity loss engendered by thermal sintering. [A. Raj 2016] Recent studies are mainly focused on threes aspects: (1) mechanism of thermal deactivation at high temperature (2) development of catalytic system with better resistance to sulfur poisoning (3) improvement of low-temperature activity during engine cold-start. [P. Gélin 2002]
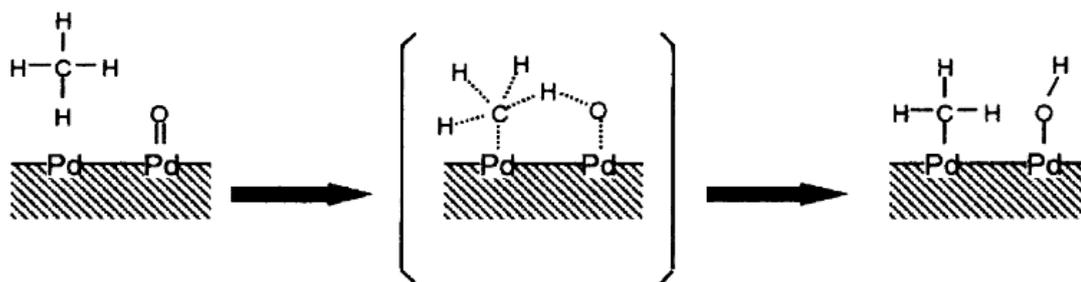
Fig. 2.11. Reaction scheme for the activation of methane on a surface Pd–PdO site pair. Adapted from[P. Gélin 2002] with permission.
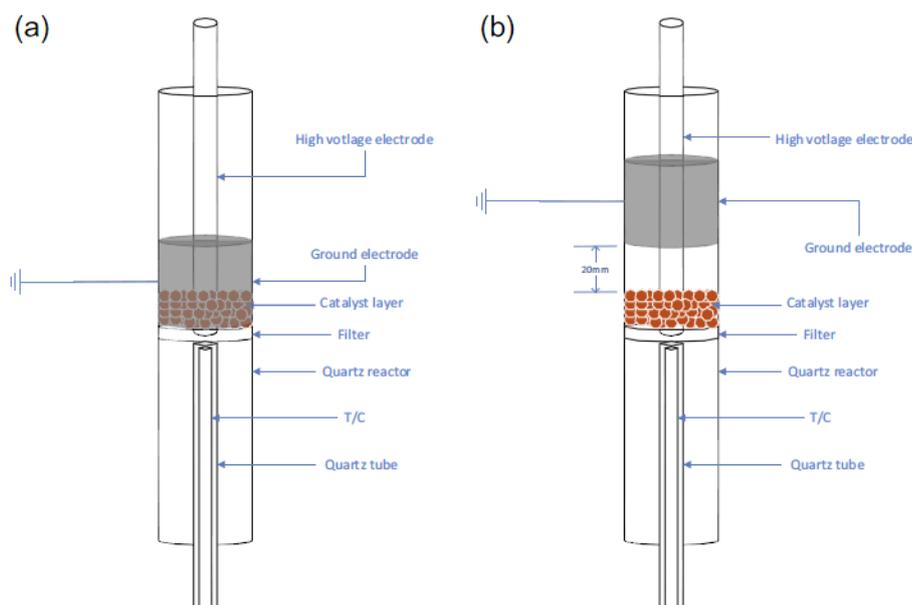
Fig. 2.12. (a) In-plasma catalysis reactor configuration (b) Post-plasma catalysis reactor configuration[H. Lee 2015].

Methane oxidation on a plasma-catalysis hybrid system was studied by H. Lee [H. Lee 2015]. Depending on the loading position of the catalyst, two different configurations of the hybrid system were proposed: in-plasma catalysis (wherein the catalyst is placed in the

discharge zone) and post-plasma catalysis (wherein the catalyst is placed after the discharge zone) (Fig. 2.12.). The author claimed that a synergistic effect was found for the in-plasma configuration, demonstrating a quicker "light-off" of methane oxidation and a lower CO selectivity. Consequently, complete methane oxidation was achieved even at room temperature when 2 wt.% Pd/Al_2O_3 oxidation catalyst was employed. However, such synergy was not detected in the post-plasma configuration. In addition, electrochemical method has also introduced to assist the catalytic activity of methane oxidation. This method is based upon the concept of non-faradaic electrochemical promotion of catalysis (NEMCA) discovered by Stoukides [M. Stoukides 1981]. By applying a potential between the working electrode (consisting of the catalyst supported on a solid electrolyte) and the counter electrode (deposited on the same solid electrolyte), the metal-support interaction can be monitored.[P. Granger 2017] The effect of electrochemical promotion of catalysis on methane combustion was systematically studied by F. Matei [F. Matei 2013].It was established that impregnation of Pd on highly porous $YSZ(Y_2O_3$-stabilized-ZrO_2, an oxygen ion conductor) led to a much more active catalyst compared to that typically deposited on dense YSZ, with an increased catalytic rate as much as one order of magnitude.(Fig. 2.13.) The author attributed the improvement of catalytic performance to the much higher dispersion of palladium on porous electrolytes.
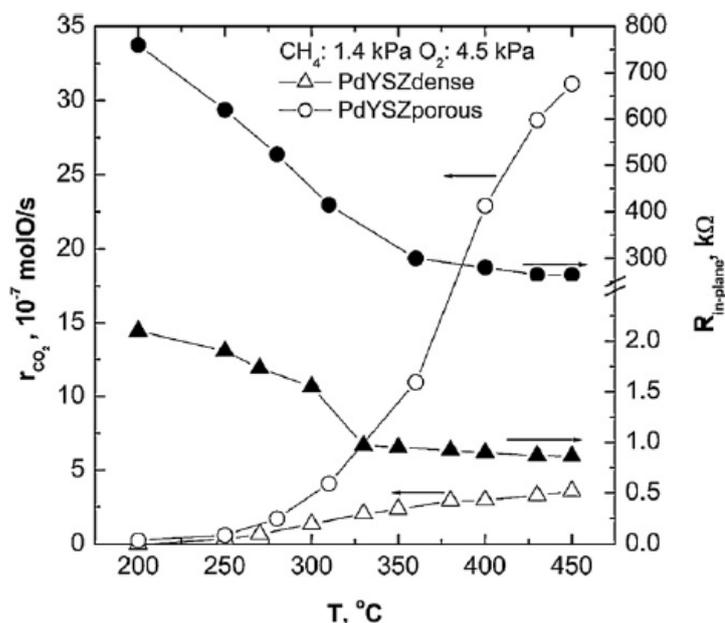
Fig. 2.13. Effect of the temperature on methane conversion, CO_2 formation rate and in-plane resistance of the Pd catalyst deposited on dense and on porous YSZ. Conditions:$P_{CH_4} = 1.4\ kPa$, $P_{O_2} = 4.5\ kPa$, F = 200 ml/min. [Reproduced with permission from F. Matei 2013]

One of the major obstacles in methane conversion consists in the deactivation caused by coke deposition. [P. Granger 2017]. It is accepted that such problem can be bypassed with the help of application of materials with good Oxygen Storage Capacity (OSC) properties. Perovskites with superb OSC can be acquired via the stabilization of unusual oxidation states of transition metals and the creation of oxygen vacancies, which is usually achieved by means of substitution on A or B site. Meanwhile, previous studies have indicated the

beneficial effect of perovskite-based material on stabilizing PdO. Eyssler asserted that depending on the calcination temperature and reaction temperature, a delicate equilibrium existed between the fraction of active PdO exposed on the $LaFeO_3$ surface and the fraction of Pd^{n+} dissoluted in the Pd-$LaFeO_3$ solid solution. [A. Eyssler 2011] The author further discovered that below 700 ℃, catalytic activity was in accordance with Pd^{2+} species present on the surface of $LaFeO_3$. The higher the thermal treatment temperature, the lower the Pd dispersion, resulting in a diminished accessibility of PdO-surface and active centers. The author concluded that 2 wt.% Pd/$LaFeO_3$ outperformed the conventional Pd/Al_2O_3 in terms of stabilizing active PdO at high temperature. [A. Eyssler 2011]. It was widely recognized that the self-regenerative mechanism of perovskites can protect noble metals (i.e. Pt, Pd, Rh) from sintering by inhibiting the particle growth. Yoon [D.Y. Yoon 2015] studied the thermal stability of Pd-containing $LaAlO_3$ catalyst. A strong Pd-La interaction was clarified to induce the electron transfer from La to Pd. As a result, a higher electron density of Pd was identified, probably responsible for the enhancement of thermal stability of PdO when subjected to high temperature.

NGV is assumed to be an alternative for conventional gasoline or diesel vehicles to meet future harsh legislation requirements. The concept of NGV can be concretized through either CNG or LNG. Further amendments are still needed to cut the cost while improving the overall performance of the NGV prior to its large-scale application, in particular dealing with issues of deactivation caused by thermal ageing, water or poisoning (especially sulfur) as well as methane slip at low temperature. [A. Raj 2016]

2.4. Perovskite as modern Three Way Catalyst

Although three-way catalytic converters have been established as the most effective engine exhaust gas post-treatment system in the past decades, plenty of problems have emerged in the practical application, such as their high cost owing to the increasingly tight supply of precious metals, the deactivation issues as well as the difficulty and complexity of recycling process. More attention is being paid to the development of new materials as possible alternatives to precious-metal based TWC.

Perovskite is referred to oxides with the chemical formula of ABO_3 or A_2BO_4. In the typical ABO_3 structure, A cations are 12-fold coordinated and B cations are 6-fold coordinated with nearby oxygen anions. The larger cations A and surrounding oxygens form a face-centered cubic lattice(FCC) in which the smaller cations B occupy the octahedral sites[Y.M. Chiang 1997]. A cations are usually alkaline elements, alkaline earth elements or lanthanide series whereas B cations can be transition metals with 3d, 4d or 5d electronic configuration[L.G. Tejuca 1993] The limit of cationic radii is $r_A > 0.090\ nm$ for A cations and $r_B > 0.051\ nm$ for B cations, respectively.
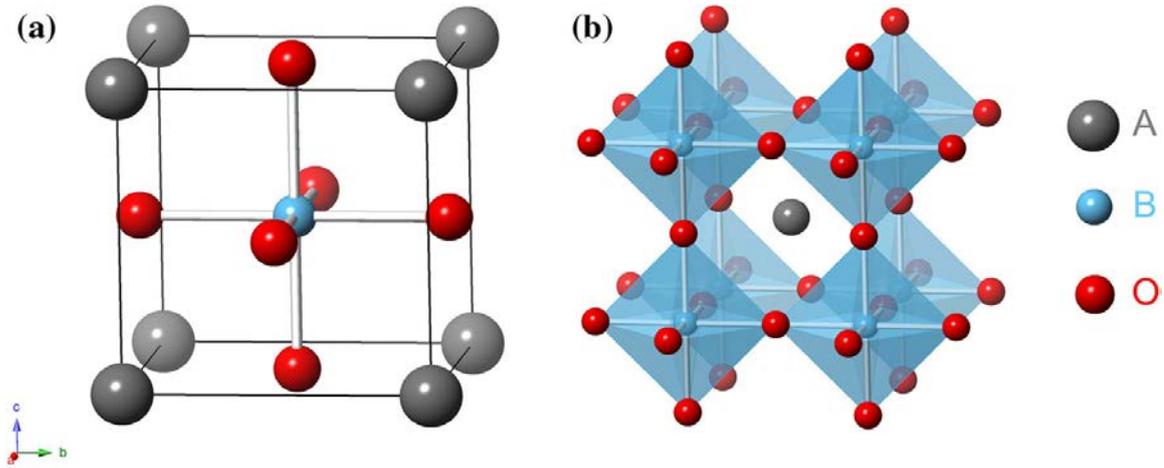
Fig. 2.14. Schematic plot of ideal (cubic) structure of ABO_3 perovskite a-lattice, b-polyhedrons(reproduced with permission of [H. Du 2015]).

The tolerance factor (also called the Goldschmidt factor) is an empirical factor introduced to indicate the ion accommodation capability of the perovskite structure. [V.M. Goldschmidt 1926]

$$t = \frac{r_A + r_O}{\sqrt{2}(r_B + r_O)} \qquad (eq.\,2-16)$$

r_A – radius of A site cation

r_B – radius of B stie cation

r_O – radius of oxygen anion

Theoretically, perovskite structure could be maintained as long as the tolerance factor is kept within the range of $0.75 \leq t \leq 1$. In the ideal cubic structure of highest symmetry, A cation, B cation and oxygen anion have contact with each other. The ideal structure occurs only when the tolerance factor gets close to 1.0 at high temperature. A t value lower than 1.0 gives rise to a structure with less symmetry. When t<0.75 the crystal exists in the form of ilmenite. While when t >1.0 the crystal becomes hexagonal symmetry such as calcite or aragonite [M. A. Pena 2001]. In the majority of cases, deviations from the ideal structure are known, including orthorhombic, rhombohedral, tetragonal, monoclinic and triclinic(lowest symmetry) lattice systems.[C.P. Khattak 1979; J.B. Goodenough 1970, 1974] these distorted structures are present predominantly at room temperature but could transform to cubic structure at high temperature. According to Pena[M.A. Pena 2001], deviations from cubic structure may result from the distortion of cubic unit cell or an enlargement of the cubic unit cell or a combination of both.

An advantageous characteristic of perovskite oxides is their structural flexibility to accommodate a wide range of ions both on A and B site, allowing them to be chemically tailored with the aim to endow themselves with specific features. Cations both on the A site and B site could be substituted with various types of metal cations with same or different radii or valences in order to modify the physicochemical properties and subsequent catalytic performance of the material[R.J.H. Voorhoeve 1976, 1977; M.A. Pena 2001]. It is therefore possible to conduct partial substitution on A and B site on the premise that electroneutrality principle and geometrical requirement are met. Due to their good structure adaptability and

tunability, multiple formulas of substituted perovskite could be formed, including simple compounds such as $A^{1+}B^{5+}O_3$, $A^{2+}B^{4+}O_3$, $A^{3+}B^{3+}O_3$ and complex compounds such as $A(B'_{1-y}B''_y)O_{3\pm\delta}$, $(A'_{1-x}A''_x)BO_{3\pm\delta}$, $(A'_{1-x}A''_x)(B'_{1-y}B''_y)O_{3\pm\delta}$, etc.

Ruddlesden-Popper series of layered oxides

Certain metals (i.e. La_2CuO_4) only form Ruddlesden-Popper oxides(RP oxides) rather than the perovskite with typical ABO_3 structure. The Ruddlesden-Popper phase (RP phase) is composed of n consecutive perovskite layers (ABO_3) alternating with rock-salt layer (AO) along the crystallographic c-axis direction[Dongkyu Lee 2017]. A cation is located at the boundry between two types of layers with a coordination number of 9 while B cation is situated in the center of octahydron formed with nearby 6 oxygen anions. The general formula of RP oxides can be expressed as $A_{n+1}B_nO_{3n+1}$ (n≥1) or more specifically as $(AO)\cdot(ABO_3)$ where n represents the number of connected layers of vertex-sharing BO_6 octahedra[I.D. Brown 1992] When n=1, A_2BO_4 structure is formed, i.e. La_2CuO_4 ;When n>1 additional ABO_3 blocks are introduced between two rock-salt layers to form complex oxides with multiple stacked octahedral layers[Dongkyu Lee 2017].

2.4.1. Related reaction mechanisms on perovskites:

2.4.1.1.   Oxidation reactions for CO and HC:

Low-temperature oxidation: CO oxidation

It is established that CO oxidation follows a suprafacial mechanism that usually takes place at low temperature. Oxygen contained in the material is consumed constantly in the course of reaction, which should be replenished by the oxygen dissociated from gas phase so that the reaction could go on smoothly. [N. Guilhaume 1997]. Zhang-Steenwinkel [Y. Zhang-Steenwinkel 2004] studied the kinetics of CO oxidation on $La_{0.8}Ce_{0.2}MnO_3$. In general, 4 major steps are involved:

$$O_2 + 2s \underset{k_2}{\overset{k_1}{\rightleftharpoons}} 2O_s \qquad K_1 = \frac{k_1}{k_2} \qquad\qquad \text{(eq. 2-17)}$$

$$CO + s \underset{k_{-2}}{\overset{k_2}{\rightleftharpoons}} CO_s \qquad K_2 = \frac{k_2}{k_{-2}} \qquad\qquad \text{(eq. 2-18)}$$

$$CO_s + O_s \underset{k_{-3}}{\overset{k_3}{\rightleftharpoons}} CO_{2s} \qquad K_3 = \frac{k_3}{k_{-3}} \qquad\qquad \text{(eq. 2-19)}$$

$$CO_{2s} \overset{k_4}{\rightarrow} CO_2 + s \qquad\qquad\qquad \text{(eq. 2-20)}$$
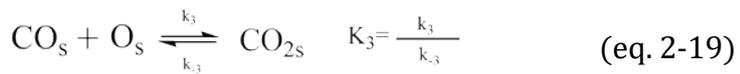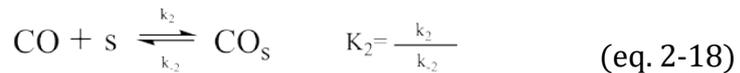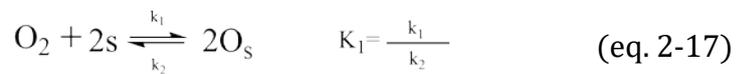
where

 s − adsorption site

Equation (2-18) is considered as the rate-determining step. An equilibrium exists between adsorbed CO and CO in the gas phase. The depletion of adsorbed oxygen would be refilled by oxygen from the gas phase. Reaction rate can be derived:

$$R = NK_4 \frac{K_1^{1/2} K_2 K_3 P_{CO} P_{O_2}^{1/2}}{1 + K_1^{1/2} P_{O_2}^{1/2}} \qquad (eq. 2-21)$$

According to equation (19), the CO oxidation reaction is first order in respect to CO and 0-0.5 order in respect to oxygen (0 order when exposed to high oxygen pressure). [Y. Zhang-Steenwinkel 2004]

High-temperature oxidation: CH_4 oxidation

In contrary to CO, CH_4 oxidation is administered by the intrafacial mechanism which occurs at higher temperature following the Mars-van-Krevelen mechanism [S. Keav 2014]. In the intrafacial mechanism, as–mentioned suprafacial mechanism is still valid yet the oxygen vacancies can be replenished either by oxygen dissociated from the gas phase or by oxygen migrated from the bulk due to the oxygen mobility of the perovskite. [S. Royer 2014].

Reaction rate of methane oxidation on perovskite is given by Pena (M. A. Pena 2001):

$$R = \frac{K_2 P_{CH_4} (K_{O_2} P_{O_2})^{1/2}}{1 + (K_{O_2} P_{O_2})^{1/2}} + k_1 P_{CH_4} \qquad (eq. 2-22)$$

For perovskite, $(K_{O_2} P_{O_2})^{1/2} \ll 1$, equation (20) can be simplified as :

$$R = K_2 P_{CH_4} (K_{O_2} P_{O_2})^{1/2} + k_1 P_{CH_4} \qquad (eq. 2-23)$$

where

K_2 indicates the contribution of surface oxygen to the kinetics of methane oxidation while k_1 reflects the contribution of bulk oxygen migrated to the surface of catalyst to the kinetics of methane oxidation. [S. Royer 2014].

It is widely acknowledged that methane oxidation is first order with respect to methane. Although controversies have arisen, first-order kinetics with respect to oxygen for methane oxidation have been accepted by a number of researchers. [J. Kirchnerova 2002; M. Bosomoiu 2008; V. Szabo 2003]

Kinetic study of methane oxidation on $La_{0.9}Ce_{0.1}CoO_3$ perovskite was conducted by Auer[R. Auer 2002]. 4 major steps were proposed by the author:

$$CH_4 + s \underset{k_{-0}}{\overset{k_0}{\rightleftharpoons}} CH_{4s} \qquad (eq. 2-24)$$

$$O_2 + s \underset{k_{-0}}{\overset{k_0}{\rightleftharpoons}} O_{2s} \overset{k_1'}{\longrightarrow} O_s^* \text{ (fast)} \qquad (eq. 2-25)$$

$$CH_4 + O_s^* \xrightarrow{k_2} I_s + O_s^* \xrightarrow{k_2'} P_s \quad \text{(fast)} \qquad \text{(eq. 2-26)}$$

$$P_s \underset{k_{-3}}{\overset{k_3}{\rightleftharpoons}} P_{gas} \qquad \text{(eq. 2-27)}$$
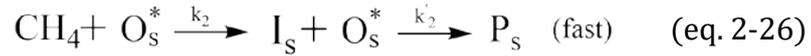
where

s − adsorption site

O_s^* − active oxygen species, such as $O^-, O^{2-}, O_2^-, O_2^{2-}$

I_s − intermediate

P_s − $CO_2 + H_2O$

Equation (25) is the rate-determining step. Based upon Mars and van Krevelen mechanism, reaction rate is expressed as:

$$R = \frac{k_1 k_2 P_{O_2} P_{CH_4}}{k_1 P_{O_2} + {}^{\nu} k_2 P_{CH_4} + \dfrac{{}^{\nu}{}_P k_1 k_2}{k_3} P_{O_2} P_{CH_4}} \qquad (\text{eq. } 2-28)$$

Where

ν − stoichiometric coefficient of O_2

${}^{\nu}{}_P$ − stoichiometric coefficient of products

2.4.2. Perovskite for soot oxidation

The possibility of using perovskite for diesel soot oxidation has been investigated by many researchers.[S. Hernandez 2012; P. Ciambelli 2001; J.L. Hueso 2008; L.M. Petkovic 2011; R. Jiménez 2010; D. Fino 2003; N. Russo 2005; D. Hari Prasad 2012; X. Wang 2012] In summary, catalytic activity of perovskite for soot oxidation are related to several intrinsic properties: (i) surface and bulk oxygens mobility (ii) activity at high temperature (iii) high thermal stability (iv) spillover mechanism involving the enrichment of suprafacial oxygen species (α-oxygen) with oxygenated species on the surface of soot particles[P. Ciambelli 2001; R. Jiménez 2010; D. Fino 2003].$LaCoO_3$, $LaNiO_3$, $LaFeO_3$ have been revealed capable of oxidizing soot below 445°C[A. Mishra 2017]

Studies of $L_{0.6}Sr_{0.4}BO_3$ (B=Fe, Mn, Ti) perovskite on soot oxidation were conducted by W.Y. Hernández [W.Y. Hernández 2015]. It was shown that $L_{0.6}Sr_{0.4}FeO_3$ and $L_{0.6}Sr_{0.4}MnO_3$ presented better soot oxidation activity than $L_{0.6}Sr_{0.4}TiO_3$. Furthermore, the author concluded that $L_{0.6}Sr_{0.4}MnO_3$ was suitable to oxidize soot at low oxygen partial temperatures due to the abundant presence of Mn^{4+}.[W.Y. Hernández 2015]

2.5. Oxygen Storage Capacity (OSC)

In light of the fact that TWC runs in the presence of fluctuation of air-fuel ratio around 14.7 in real exhaust emissions, oxygen amount is expected to variate periodically so that λ could be maintained as close to 1 as possible. In order to buffer the perturbation of reaction atmosphere induced by the fluctuation of air-to-fuel ratio in real driving conditions, the TWC

must have the ability to store oxygen in lean condition and release oxygen in rich condition quickly enough with the aim to compensate for the temporary imbalance of oxidants and reductants in the exhaust emission and broaden the operating window during constant lean/rich transformation. [J. Bickel 2016]. Accordingly, this ability is called Oxygen Storage Capacity (OSC) of the material. [D. Duprez 2001]. Oxgygen Storage Capacity(OSC) has been considered one the most crucial factors governing TWC activity. The conversion efficiency of TWC is closely dependent on the oxygen storage capacity(OSC), the storage and release kinetics and the current oxidation state of the material.[J. Bickel 2016] More specifically, the oxygen storage capability of material can be evaluated by two indices: Oxygen Storage Capacity (OSC) and Dynamic Oxygen Storage Capacity (DOSC). The former indicates the amount of oxygen thermodynamically available while the latter refers to the amount of oxygen kinetically available during transient conditions. [J.H. Wang 2015]

2.5.1. CeO$_2$-based OSC materials

At the beginning, CeO$_2$ had been used in the conventional TWC converter as OSC material. CeO$_2$ stores oxygen in oxidative atmosphere and release oxygen in reductive atmosphere as described by the following reversible reaction [S. Matsumoto 2004]:

$$CeO_2 \rightleftharpoons CeO_{2(1-x)} + xO_2 \qquad\qquad (eq.\,2-29)$$

where $0 \leq x \leq 0.25$
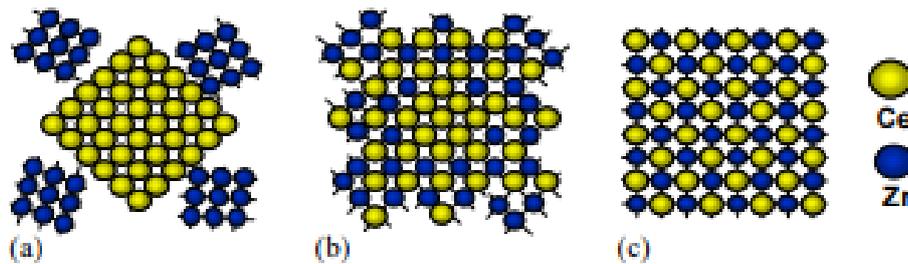
Fig. 2.15. Illustration of different atomic configurations of CeO$_2$-ZrO$_2$ mixed oxides(CZ) (a) M-CZ, a mixture of CeO$_2$, ZrO$_2$ and CeO$_2$-ZrO$_2$ solid solution (b) S-CZ, a solid solution of CeO$_2$ and ZrO$_2$ (c) R-CZ, a solid solution of CeO$_2$ and ZrO$_2$ with a pyrochlore-type structure in which Ce and Zr atoms are arranged in a regular manner[S. Matsumoto 2004].
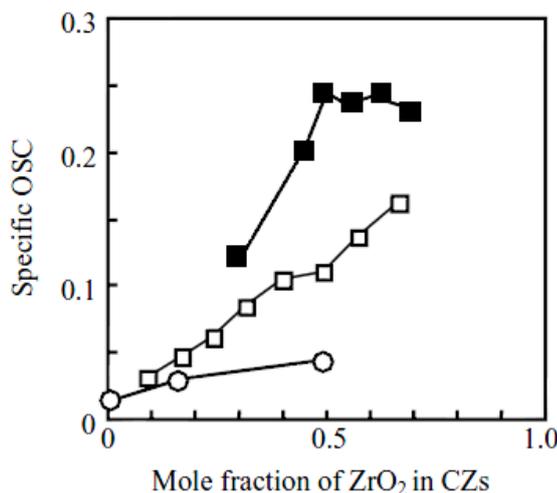
Fig. 2.16. Specific OSC (the amount of OCS per mole of Ce) of CeO_2-ZrO_2 mixed oxide (CZ) as a function of ZrO_2 content. (◯) M-CZ; (□) S-CZ; (■) R-CZ. The amount of OSC was the moles of oxygen released when these materials were treated at 1173K in air for 15 min, followed by reduction under a stream of 20% hydrogen in nitrogen at 773 K[S. Matsumoto 2004].

At present, OSC material is based upon ceria-zirconia mixed oxides $Ce_xZr_{1-x}O_2$ (CZ) modified by a variety of components. [J. Bickel 2016]. Ceria provides the cyclic oxygen storage-release function and Zr is often doped so that the resistance to sintering of ceria could be strengthened and the thermal stability of the $Ce_xZr_{1-x}O_2$ solid solution could be enhanced [Q. Zheng 2019] It was revealed that OSC of $Ce_xZr_{1-x}O_2$ mixed oxides is determined by both elementary composition and textural properties (i.e. pore volume and pore size distribution). Three types of CZ configurations are known to exist (Fig. 2.15.), namely the M-CZ(Fig. 2.15. a), S-CZ(Fig. 2.15. b) and R-CZ(Fig. 2.15. c). R-CZ with pyrochlore-type structure was identified as the one with best OSC compared to M-CZ and S-CZ at the premise of the same ZrO_2 fraction in the solid solution, as is shown in Fig. 2.16. Moreover, among the two metastable tetragonal phases t and t'', the t'' phase appeared better redox properties.(Fig. 2.17.) [M. Yashima 1994]. Recently, a ceria zirconia support with core-shell structure was reported by M. Ozawa[M. Ozawa 2017]
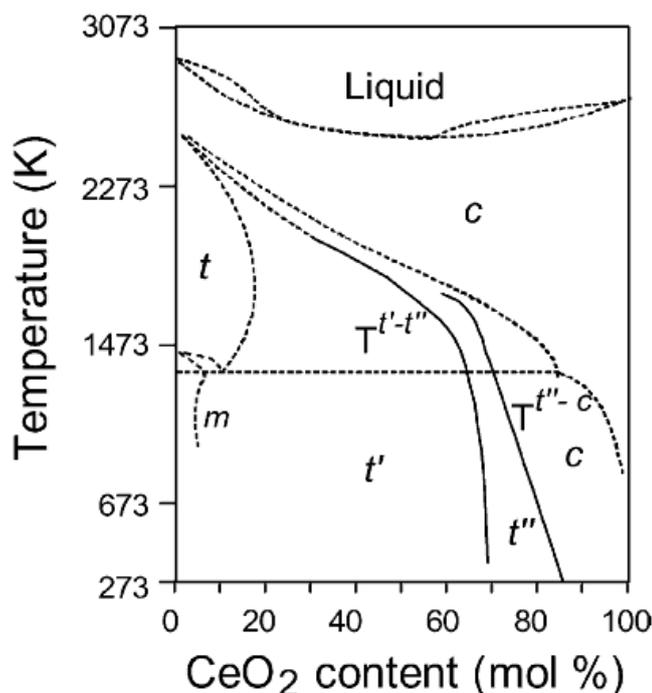
Fig. 2.17. Experimental phase diagram of CeO_2-ZrO_2 system (Adapted from [M. Yashima 1994] with permission).

2.5.2. Perovskite-type OSC materials

Thanks to their intrinsic oxygen mobility and thermal stability, perovskites have been extensively investigated as potential alternatives for conventional TWCs in the past decades. It was established that perovskite with $ABO_{3-\delta}$ formula displayed significant swings with regard to the oxygen non-stroichiometry δ by means of reacting with oxygen present in gas phase[S. Royer 2005 a; A. Klimkowicz 2014]. Structure defect, arising from partial substitution on A site and B site, has been verified to improve oxygen mobility and subsequent OSC properties. It was also disclosed that the OSC of perovskite depended mainly on the characteristic of B cations rather than A cations although the latter plays a more important role in the structural stabilization by affecting charge-valence balance and vacancy density.[Q. Zheng 2019; Z. Say 2014]. Basically, 2 types of oxygen species that are catalytically active co-exist in a perovskite-type oxide[Fig. 2.18. Y. Noboru 1981]: Suprafacial oxygen species(α-oxygen, such as O_2^{2-}, O_2^-) and Intrafacial oxygen species(β-oxygen such as O^{2-}). The former refers to oxygen adsorbed on the surface of oxides and are available at low-temperature range(generally below 600℃). In contrast, the latter are oxygen present in bulk of lattice which are inclined to be activated at high temperature (above 600℃) and take part in catalytic reaction according to Mars-van-Krevelen mechanism[S. Keav 2014] . CO oxidation by molecular oxygen is recognized to take place through a suprafacial process[R.J.H. Voorhoeve 1976; L.G. Tejuca 1989; J.L.G. Fierro 1990]. NO reduction follows an Intrafacial mechanism[R.J.H. Voorhoeve 1974, 1975, 1976; M.A. Pena 2001; J.L.G. Fierro 1990] As to oxidation of unburnt hydrocarbons by molecular oxygen, either suprafacial or intrafacial mechanism could reign depending on both the characteristic of hydrocarbons and the composition of perovskite. The combustion of propylene and iso-

butene on $LaBO_3$(B=Cr, Mn, Fe, Co and Ni) at 250°C was verified by G. Kremenić [G. Kremenić 1985] to follow a suprafacial mechanism. In the case of methane oxidation, it was widely acknowledged that methane oxidation was dominated by a suprafacial mechanism below 800°C whilst an intrafacial mechanism was regarded as the predominant one above 800°C [H. Arai 1986]. Toluene combustion on $LaFeO_3$ and $YFeO_3$ was presumably dominated by a suprafacial mechanism despite the fact that an intrafacial mechanism cannot be excluded as far as the latter oxide was concerned. [M. Markova-Velichkova 2013]
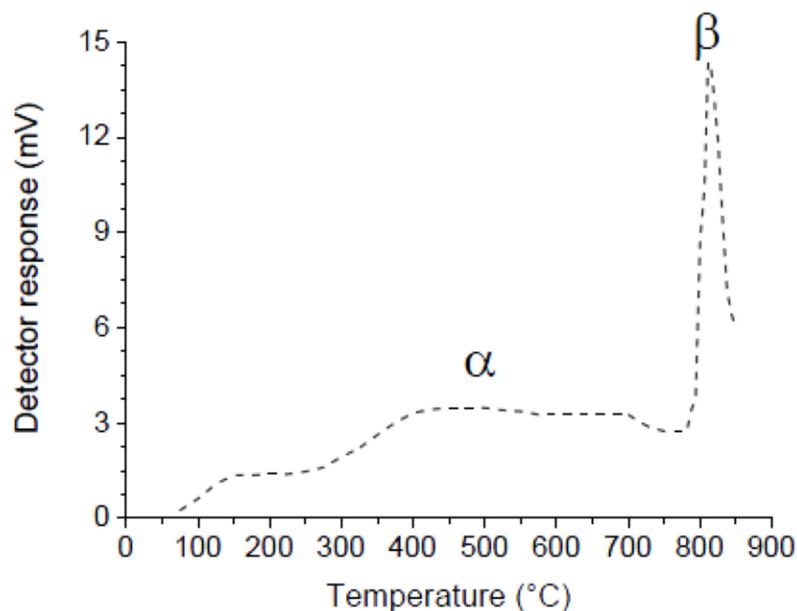
Fig. 2.18. Oxygen temperature-programmed desorption on $La_{0.6}Sr_{0.4}CoO_3$ the broad desorption peak in the low-temperature zone corresponds to α-oxygen species; the sharp desorption peak in the high-temperature zone corresponds to δ-oxygen species[Y. Noboru 1981].

Liu[L. Liu 2016]claimed that particle substitution on A site only had negligible effect on the OSC of perovskite with general formula ABO_3(A=La, Ba, Sr; B=Cr, Mn, Fe, Co, Ni, Cu) whereas the electronegativity of metals on B site exhibited significant influence of the OSC. An inverted volcano plot was observed [Fig. 2.19. L. Liu 2016] The author concluded that 3d transition metal B site electronegativity is suited to serve as a descriptor for evaluating OSC of perovskites.

Catalytic activity of a series of nanocrystalline perovskite of general formula $AA'BB'O_3$((A=La, A'=Ca, Sr, Y, Ce; B=B'=Mn, Fe, Co, Ni)) as TWC has been studied by S. Kelly [K. Simmance 2019]. It was suggested that $La_{1-x}Sr_xBO_3$ perovskites cannot provide accessible OSC rapidly enough to respond to varying transient conditions of exhaust emissions. The author concluded that the catalytic activity of perovskites is dominated by the reactivity of B-O bond on the surface of material rather than bulk properties such as oxygen mobility as evidenced by the fact that a non-correlation between the perturbed TWC activity and oxygen storage capacity was demonstrated.
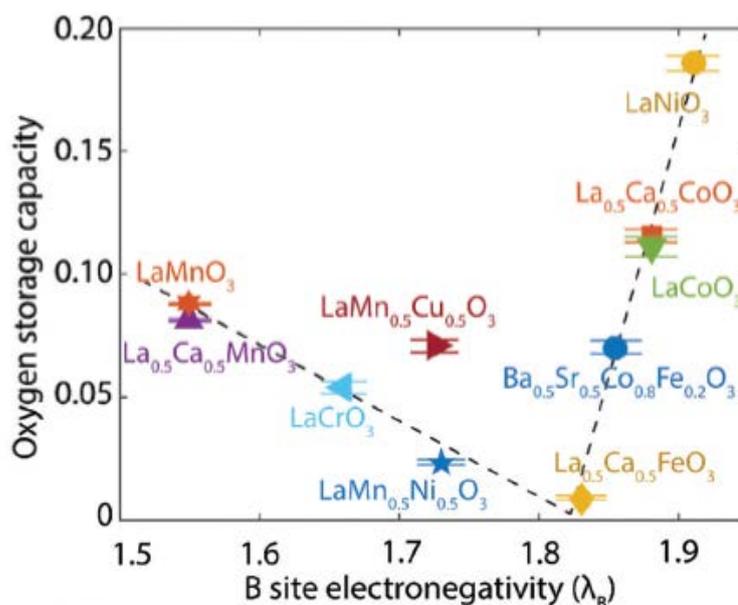
Fig. 2.19. Oxygen Storage Capacity (OSC) plotted versus B site electronegativity of perovskite ABO_3 [L. Liu 2016].

Nevertheless, one of the biggest drawbacks of perovskite-based material is their low specific surface area (SSA), leading to a poor activity at low temperature range. The optimization of synthesis method has been proven effective to overcome the as-mentioned problem. Until now, many new developments have been achieved to improve the textural properties of perovskites, such as the fabrication of three-dimensionally ordered macroporous (3DOM) perovskite system through colloidal crystal templating (CCT) route. In addition, a significant breakthrough has been attained in terms of manipulating the morphology via the screening of appropriate surfactant so that surface planes with highest intrinsic activity can be preferentially exposed to reactants.[P. Granger 2017]. Likewise, the development of meso-macropore networks allows the minimization of diffusion limitations, resulting in desirable performance at low temperature, as is shown on $La_{0.6}Sr_{0.4}MnO_3$ for methane combustion. [F. Huang 2018]

2.6. Metal dispersion

Metal dispersion is defined as the proportion of metal atoms exposed at the surface of metal crystallites with regard to total number of metal atoms. [X. Zhu 2013]. Metal atoms exposed at the surface are considered as catalytically active sites. One of the goals of synthesis optimization is to increase the amount of metal active sites. A number of strategies can be used to gain a better noble metal dispersion on the TWC. Meher [S.K. Meher 2013] invented a surfactant reduction method using ethylene glycol as surfactant to synthesize an Pt/CeO_2 catalyst characterized by ultra-fine dispersion of Pt on tuned morphology of ceria. Such catalyst presented excellent catalytic activity for CO oxidation.(Fig. 2.20)
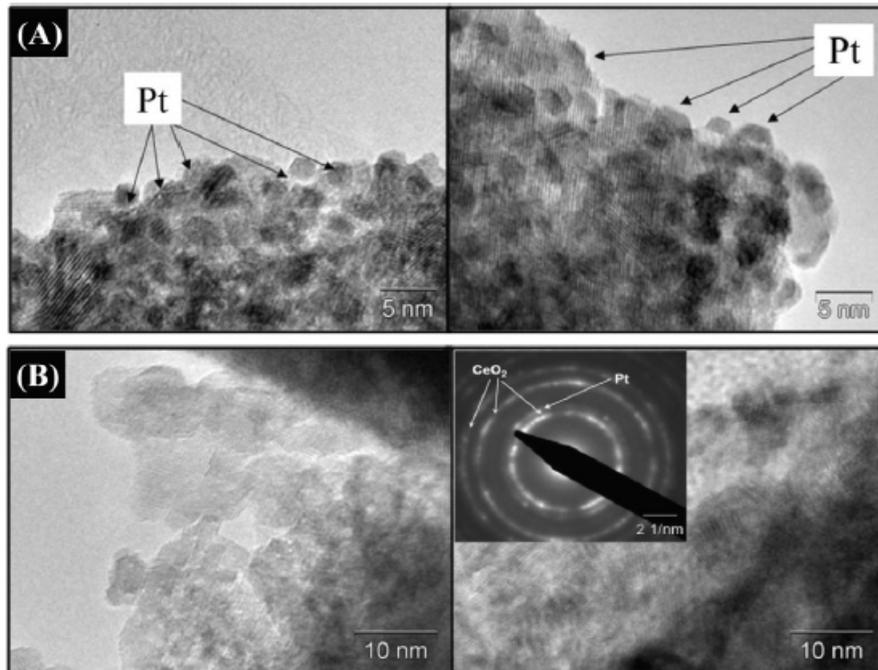
Fig. 2.20. HRTEM images of (A) Pt/CeO$_2$-CH IMP(conventional imgregnation) (B) Pt/CeO$_2$-CH EGR(ethylene glycol reduction)The inset in B shows the SAD information of CeO$_2$ and Pt in the corresponding sample. [S.K. Meher 2013]

In addition, synthesis of core-shell type CeO$_2$/ZrO$_2$ was realized by M. Ozawa [M. Ozawa 2017]. In his work, ceria nanoparticles were first precipitated on pure zirconia surface. After heat treatment at 800 °Cin air for 3 h, a CZ support with core-shell structure was obtained (Fig. 2.21.), which provided large number of active sites and higher OSC. Hence, a high dispersion of Pt and Rh on the as-prepared core-shell CZ was observed, resulting in outstanding activity for oxidation of CO and C$_3$H$_6$ as well as for NO reduction.
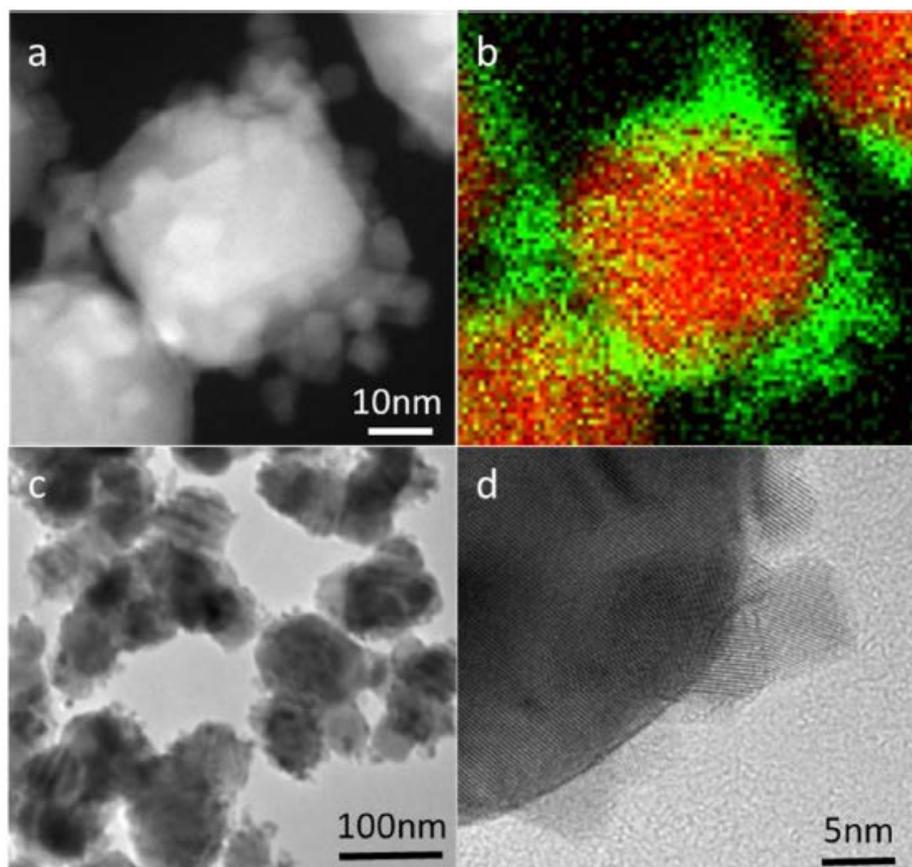
Fig. 2.21. Transmission electron microscopy analysis of CeO_2/ZrO_2 support: (a) STEM image of a core-shell type CeO_2/ZrO_2 particle, (b) EDS elemental mapping of corresponding area to (a), (c) TEM image of CeO_2/ZrO_2 samples under low magnification, (d) TEM image of interface region in a composite particle. [M. Ozawa 2017]

X. Zhu[X. Zhu 2013] introduced a facile way to improve metal dispersion on support by means of Charge-Enhanced Dry Impregnation(CEDI). This method is based on electrostatic adsorption mechanism of supports, which has been suggested for the synthesis of ultra-small (1-2 nm) noble and base metal nanoparticles over various oxide and carbon supports.[J.R. Regalbuto 1999; M. Schreier 2004; L. Jiao 2008; L. D'Souza 2007; X. Hao 2011]. By acidifying or basifying sufficiently the impregnation solution, surface of the support could be charged and electrostatic adsorption would be activated. The core of this technology is to well anticipate the initial pH needed for the impregnation solution. For supports with high point of zero charge, the impregnation solution should be acidified. In contrast, for supports with low point of zero charge, the impregnation solution should be basified for the purpose of launching electrostatic adsorption. It was demonstrated that this CEDI method improved vastly the dispersion of Pt on Pt/C, Pt/SiO_2 and Pt/Al_2O_3 catalysts. In light of the simplicity and effectiveness of this method, the author further concluded that it can be extended to a wide range of materials in order to achieve better metal dispersion on carbon and oxide supports(i.e. carbon black, alumina, magnesia, silica, niobia, anatase titania). [X. Zhu 2013]

The role of citric acid (CA) on Pt dispersion on porous supports was investigated systematically by T. Cheng[T. Cheng 2017]. According the author, addition of citric acid in the preparation process of catalyst contributed to the dispersion of Pt and enhanced

significantly TWC catalytic performance. The best Pt dispersion was acquired with molar ratio Pt/CA=2:1.

For Pd-only TWC, the dispersion, chemical state and thermal stability of active Pd species rely on the interaction between Pd and the support [A. Cao 2010; M. Shen 2009]. L.Lan[L. Lan 2018 a] reported a $Pd/CZ/Al_2O_3$ catalyst with optimized configuration (simply expressed as $Ce0_{.7}Zr_{0.3}O_2/Pd/Al_2O_3$ and $Pd/Ce_{0.7}Zr_{0.3}O_2/Pd/Al_2O_3$). It was noticed by the author that with regard to the former, Pd was predominately distributed on Al_2O_3 and Pd species could migrate from Al_2O_3 towards the surface of CZ grains upon ageing. Still, as to the latter, Pd species were highly dispersed on CZ in the form of Pd^{2+} when exposed to the same ageing treatment, combined with larger amount of oxygen vacancies formed adjacent to the Pd/CZ interface. The author concluded that a better dispersion of Pd could be achieved through adjusting synthesis procedures. The same author also reported that when CZ/Al_2O_3 support was thermal treated at 300°C prior to introduction of Pd species, a special $Pd/CZ/Al_2O_3$ catalyst with Pd semi-embedded in CZ/Al_2O_3 can be obtained due to the Pd-CZ interaction. Hence, higher Pd dispersion, more oxidative Pd^{2+} species and larger amount of oxygen vacancies were observed compared to conventional $Pd/CZ/Al_2O_3$ TWC. These features can still be maintained even after ageing in air at 1000°C during 5h. [L. Lan 2018 b]. Likewise, J. Deng[J. Deng 2018] found that incorporation of Zr, Y and La into ceria lattice was beneficial to generate structure defects on the CZ surface. A superior TWC performance was thereby attained resulting from the higher Pd dispersion and larger amount of active Pd^{2+} species.

A. Satsuma[A. Satsuma 2012] proposed a new method for the synthesis of Ru/CeO_2 catalyst, combining calcination in air at 700°C and then reduction in H_2 at 400. The catalyst prepared in this way was characterized by a high dispersion of Ru with particle size of around 2 nm on CeO_2 surface and showed exceptional activity for CO oxidation, which was attributed by author to the self-dispersion mechanism of Ru, in which 3 major steps were involved: (i) oxidation of Ru metal into RuO_2 during calcination in air. (ii)dispersion of nano-sized, oxidized Ru particle onto CeO_2 surface with the formation of Ru-O-Ce bond.(iii) reduction of external surface of Ru particle in a flow of H_2 at relatively low temperature.

G. Perin[G. Perin 2017] developed a novel nanocomposites made of $CuO/LaNiO_3$ using CuO as active phase and LaNiO3 as active support. CuO nanoparticles were deposited on the surface of $LaNiO_3$ perovskite by means of ammonia-driven deposition precipitation (ADP) method. Various characterization tools confirmed that CuO was only deposited on the surface of $LaNiO_3$ as highly dispersed phase which gave rise to a significantly enhanced activity for NO reduction as well as higher N_2 selectivity. Later, the same research group extended this method to fabricate $CuO/LaCoO_3$ nanocomposites. Similar results were obtained in that the highly dispersed CuO on $LaCoO_3$ surface resulted in better activity for NO reduction, although slightly inferior to that of $LaNiO_3$.[M. Pacella 2018] By comparing the as-mentioned two nanocomposites, the author assumed that deposition of CuO on nickelates had better effect on NO reduction while deposition of CuO on cobaltites was most favorable to oxidation activity.[M. Pacella 2018]

M. Shen[M. Shen 2012] reported that phosphorus doping led to moderate improvement of Pd dispersion on the support for conventional $Pd/\gamma-Al_2O_3$ TWC, both on the fresh[Fig. 2.22.] and aged[Fig. 2.23.] catalysts. The author made a conclusion that active phosphorus

species existed as P-O-Al units at the surface and that the mutual stabilization effects between Pd clusters and as-stated P-O-Al units played an key role not only in anchoring Pd firmly on the surface active sites but also in limiting the phase segregation of $AlPO_4$ from γ-Al_2O_3 matrix under harsh ageing conditions, resulting in better Pd dispersion and hydrothermal resistance.
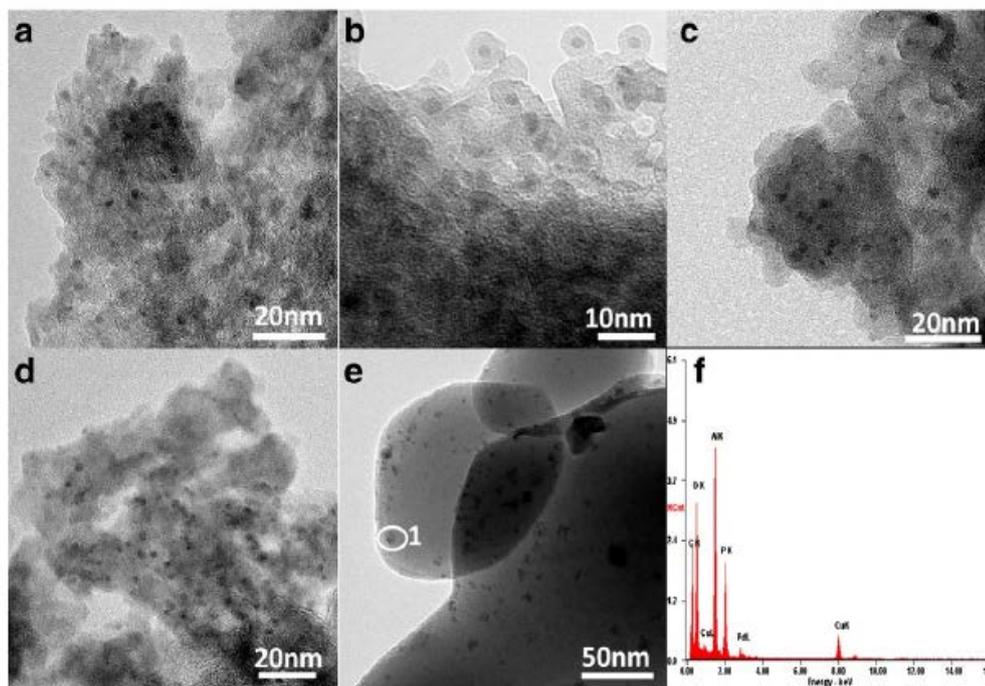
Fig. 2.22. TEM images of the fresh palladium supported catalysts. (a) Pd/G005-F (b) Pd/G105-F (c) Pd/G305-F (d) Pd/G505-F (e) Pd/AlPO$_4$-F and (f) EDX-spectra from region 1. Reproduced with permission from [M. Shen 2012].
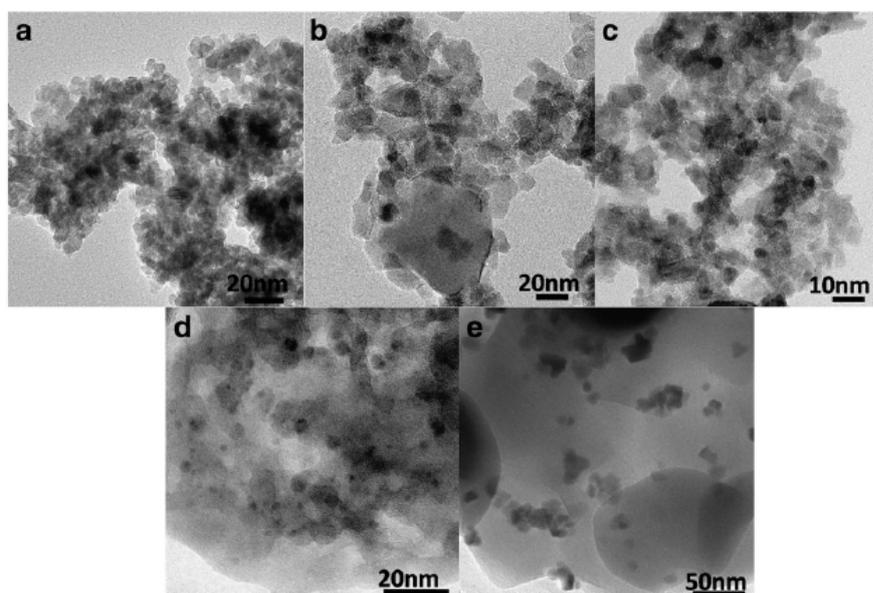
Fig. 2.23. TEM images of the aged palladium supported samples. (a) Pd/G005-A (b) Pd/G105-A (c) Pd/G305-A (d) Pd/G505-A and (e) Pd/AlPO$_4$-A. [M. Shen 2012]

Previous studies on PGM-containing TWC have ascertained that thermal treatments involving gases (i.e. oxygen and hydrogen) had an influence on the dispersion of noble metals on alumina supports.[R.M.J. Fiedorow 1976, 1997; J.E. Stulga 1980; T.J. Lee 1984]. Redispersion of was achieved through the formation and spitting of noble metal oxides that formed fin metallic clusters after reduction.[H. Birgersson 2004 a]. The same author observed that both catalytic activity and metal dispersion can be altered by adding chlorine to oxygen stream during thermal regeneration.[H. Birgersson 2004 a]. As a consequence, not only the metal dispersion was improved but also losses of noble metals was prevented thanks to the formation of volatile MO_xCl_y [H. Birgersson 2004 b] It can be said that redispersion of noble metal is feasible owing to the fact that addition of gaseous chlorine mixtures could provoke a restructuring of noble metal catalysts through the formation of the mobile Pt/PdO_xCl_y complex[H. Lieske 1983; G. Lietz 1983; G. Tonetto 2001; K. Foger 1985 a]. It was clarified by Foger [K. Foger 1985 b] that 3 major steps were involved in the redispersion process: (i) the formation of a volatile halide (ii) redistribution of the halide on the support surface (iii) readsorption of the halide and the formation of stable surface complexes.

The influence of reduction/reoxidation conditions on the metal dispersion in Rh/CeO_2 catalyst was investigated by S. Bernal[S. Bernal 1998]. Based upon the result obtained by computer simulation, the author inferred that metal dispersion of aforementioned catalyst was more sensitive to the reduction treatment than to the reoxidation treatment and rhodium redispersion could only be seen at higher temperatures of 1073K and 1173K. [S. Bernal 1998]

2.7.   Self-regenerative mechanism of perovskite-metal

The self-regeneration phenomenon of perovskite-type catalysts was introduced for the first time by Y. Nishihata[Y. Nishihata 2002]. In his experiment, $LaFe_{0.57}Co_{0.38}Pd_{0.05}O$ was used as the so-called "intelligent catalyst" to compare with the conventional Pd-impregnated γ-Al_2O_3 catalyst. Tolerance to aging as well as catalytic activity prito to and after aging of the as-mentioned catalysts were examined by a series of methods. It was manifested that perovskite-based $LaFe_{0.57}Co_{0.38}Pd_{0.05}O_3$ catalyst afforded an extraordinary heat resistance capability compared to Pd-impregnated γ-Al_2O_3 catalyst. From the images of transmission electron microscopy (Fig. 2.24. b), it was shown that after ageing at 900°C during 100 h, the particle size of palladium of perovskite-based catalyst increased only to a limited extent, evidenced by small metallic particles with diameters of 1-3 nm. On the contrary, an enormous increase of the particle size of the Pd/alumina catalyst was observed when exposed to the same ageing conditions, reaching up to 120 nm. The reason for this phenomenon was attributed by the author to the capability of Pd-perovskite catalyst to suppress remarkably the growth of metallic particles. Furthermore, the aged Pd-perovskite catalyst displayed a much higher catalytic activity compared with the Pd/alumina one. After ageing at 900 °Cduring 100h, the Pd-perovskite catalyst retained high catalytic activity whilst catalytic activity of the Pd/alumina decreased dramatically by around 10%, as illustrated in Fig. 2.25.
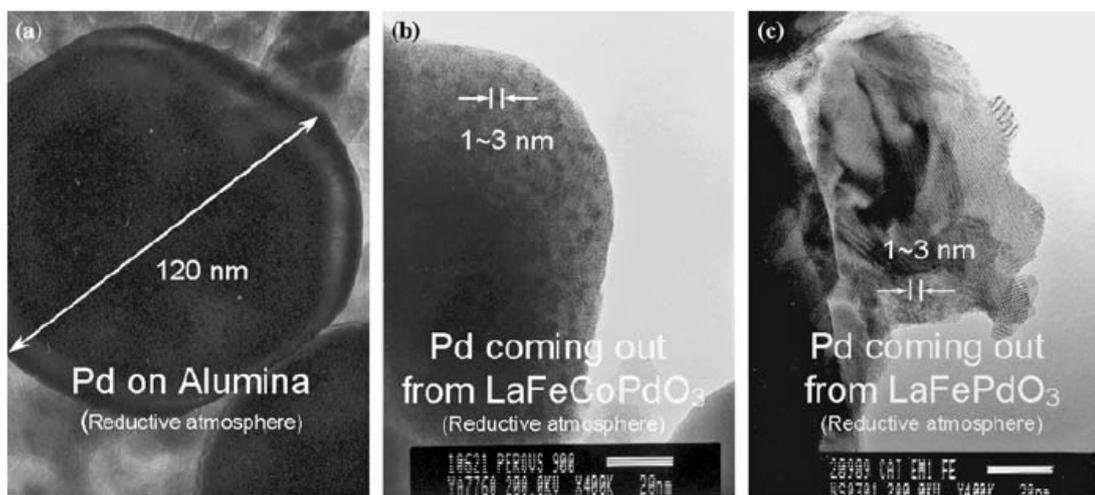
Fig. 2.24. TEM images of a)Pd/alumina b) $LaFe_{0.57}Co_{0.38}Pd_{0.05}O_3$ c)$LaFe_{0.95}Pd_{0.05}O_3$ after ageing at 900℃ for 100h.
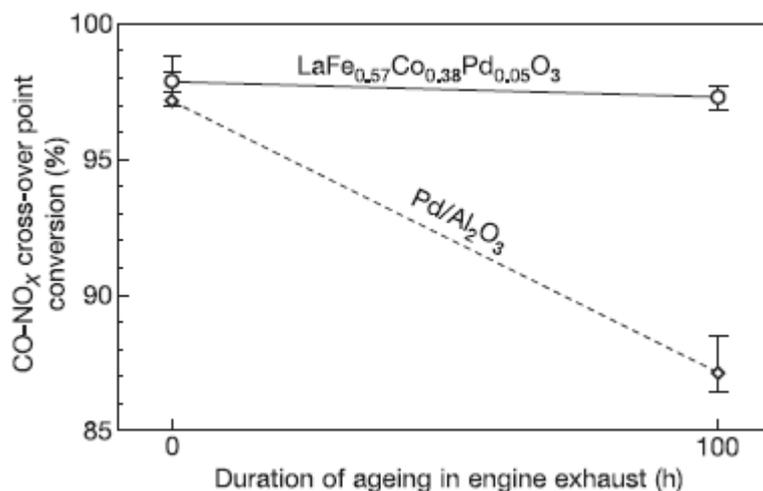
Fig. 2.25. Catalytic activity of $LaFe_{0.57}Co_{0.38}Pd_{0.05}O_3$(Pd-perovskite catalyst) and Pd-impregnatedγ-Al_2O_3 (Pd/alumina catalyst) during the ageing process at 900℃ lasting 100h. The conversion efficiency was investigated three times for each sample by the sweep test. The symbol represents the CO-NO_x cross-over point conversion (With air-to-fuel ratioλ=1) and error bars signify corresponding maximum and minimum values.(picture reproduced with permission of Y. Nishihata 2002)

Based on the above findings, the author believed that Pd might be able to move back and forth between the B-site of the perovskite structure and the metal particle lattice site in respond to redox fluctuations typical of the real exhaust emissions [Y. Nishihata 2002]. The concept of "intelligent catalyst" was thereby put forward by the same author, stemming from the fact that Pd could move reversibly into and out of the perovskite lattice during oxidative-reductive cycles, avoiding the growth and agglomeration of palladium metallic particles and leading to subsequently an improved catalytic activity even after ageing at high temperature. [Y. Nishihata 2002]

Similar results have been testified by the same research group[Y. Nishihata 2005] on the cobalt-free Pd-perovskite with the formula $LaFe_{0.95}Pd_{0.05}O_3$. Apart from the reversible "entering-segregating" behavior of palladium into and out of the perovskite lattice, the author also proposed that iron plays an important role both in stabilizing the perovskite structure and in suppressing the agglomeration and growth of palladium particles. The "Self-regeneration" mechanism of Pd-perovskite catalyst was then elucidated in detail by H. Tanaka[H. Tanaka 2005] which can be described shortly as follows(Fig. 2.26.): the palladium atom could move back and forth between the inside and the outside of the perovskite lattice during redox cycles. On one hand, in oxidative atmosphere, palladium atoms would enter into the perovskite lattice and occupy the B-site within the perovskite structure in the form of palladium cations(i.e.Pd^{3+} or Pd^{4+}) to participate in the oxidation of CO and unburnt hydrocarbons; on the other hand, in reductive atmosphere, palladium would segregate instinctively from the perovskite lattice and exist in the form of small, fine palladium metallic particles (Pd^0, 1-3 nanometers in diameter) dispersed on the surface. That is to say, the perovskite structure could be maintained throughout a redox cycle whereas the local structure around Pd varies periodically in a repetitive pattern. Since the migration behavior of palladium is completely reversible and could occur in a wide range of temperatures (i.e. from 200°C to 1050°C), it inhibits the agglomeration and growth of palladium particles and prevents small palladium particles from becoming bigger ones, thereby avoiding the sintering of palladium when exposed to high temperature and retaining good catalytic activity under severe conditions.
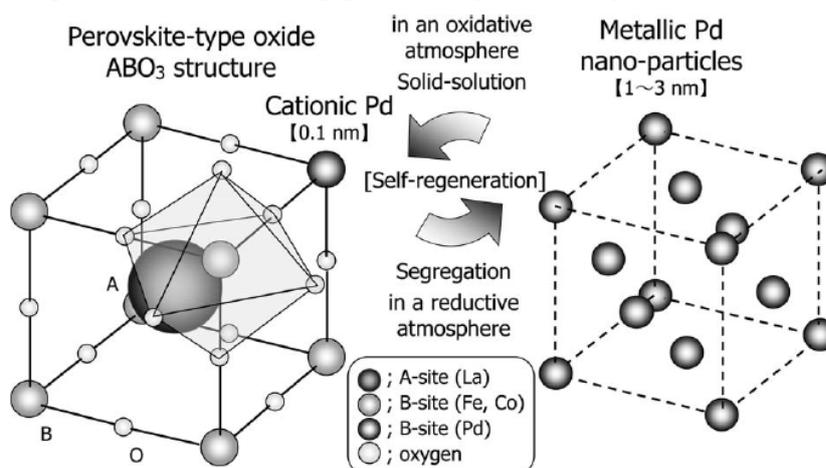
Fig. 2.26. schematic diagram of the intelligent catalyst, demonstrating the reversible movement of palladium metal in and out of the perovskite lattice during redox fluctuation [H. Tanaka 2004].

According to M. Taniguchi et al., a higher metallic Pd concentration on the surface than in the bulk evidenced by XPS implied that Pd segregation in the reductive atmosphere stars first near the surface, followed by the segregation of Pd from the bulk of the perovskite framework [M. Taniguchi 2004; M. Uenishi 2005; H. Tanaka 2004]. Besides, it was also suggested that the Pd self-regeneration function could occur at temperature range as low as 100-300°C [H. Tanaka 2005]. What's more, the structural change of Pd is very rapid. It was proven by the in-situ DXAFS that the transient time for the structural change around Pd was merely a few seconds at 600°C. [H. Tanaka 2005]

M. Taniguchi[M. Taniguchi 2007] extended the self-regeneration concept initially discovered in Pd-perovskite to other perovskite-type oxides. It was confirmed by author that self-regenerative function was observed not only in the Pd-perovskite, but also in the Rh-perovskite and the Pt-perovskite as well.[Fig. 2.27. M. Taniguchi 2007] Similar to palladium, rhodium and platinum exhibited a comparable pattern of moving in and segregating out of the perovskite lattice in a reversible way in a redox cycle as well as outstanding suppression effect on the agglomeration and growth of either rhodium or platinum grains, respectively. A universal technology was accordingly proposed for designing such a "Super intelligent catalyst". [M. Taniguchi 2007].
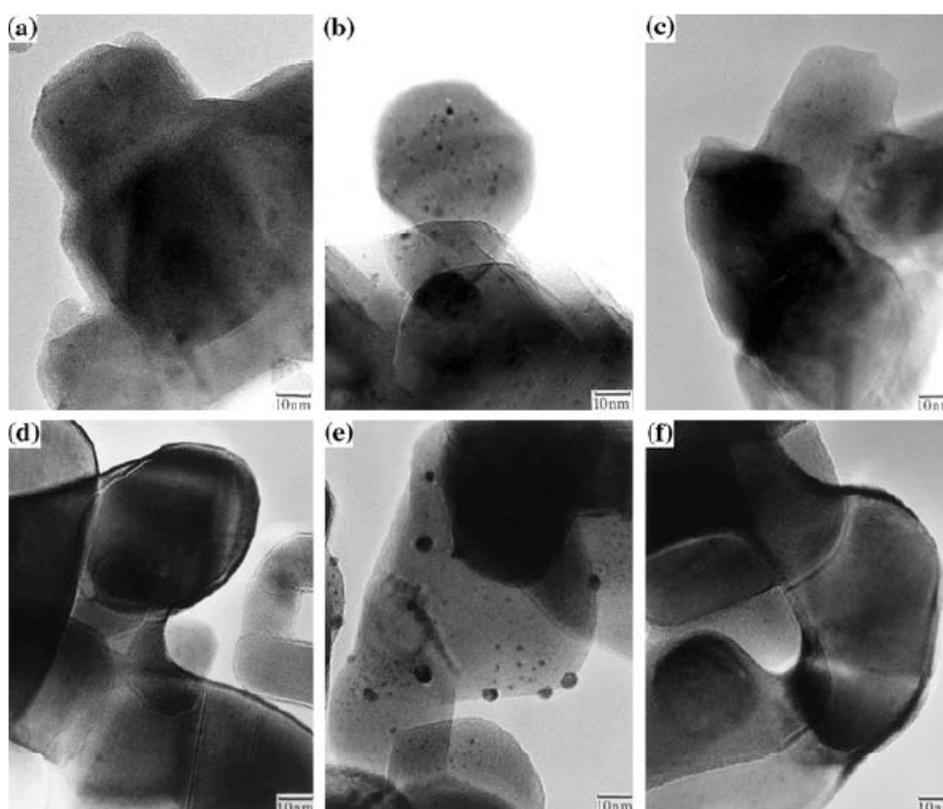
Fig. 2.27. TEM photographs of Rh and Pt on perovskite: a) $CaTiRhO_3$ after oxidation b) $CaTiRhO_3$ after reduction c) $CaTiRhO_3$ after re-oxidation d) $CaTiPtO_3$ after oxidation e) $CaTiPtO_3$ after reduction f) $CaTiPtO_3$ after re-oxidation, demonstrating the self-regeneration function of Rh and Pt perovskites. [M. Taniguchi 2007]

Therefore, precious metal-containing perovskite is labelled as "intelligent" as it maintains high catalytic activity even when subjected to harsh conditions thanks to its self-regeneration function. The core the self-regenerative technology lies in the formation of the metal-perovskite solid solution under oxidizing condition and the segregation of metal under reducing conditions to form either nanoparticles or metallic clusters. [H. Tanaka 2006]. Hence, the self-regenerative mechanism is dependent heavily on the precious metal-perovskite interaction and some aspects should be taken into account when it comes to the design of an intelligent catalyst. That is to say, the oxide consisted of perovskite components should be able to capture and release precious metals in a reversible manner under redox

environment and at the same time preserve the stability of the perovskite structure itself even at high temperature. [H. Tanaka 2006]

Mechanism of the suppression of the agglomeration and growth of palladium particles of the intelligent catalyst with self-regenerative function in comparison with conventional catalyst is presented in Fig. 2.28.
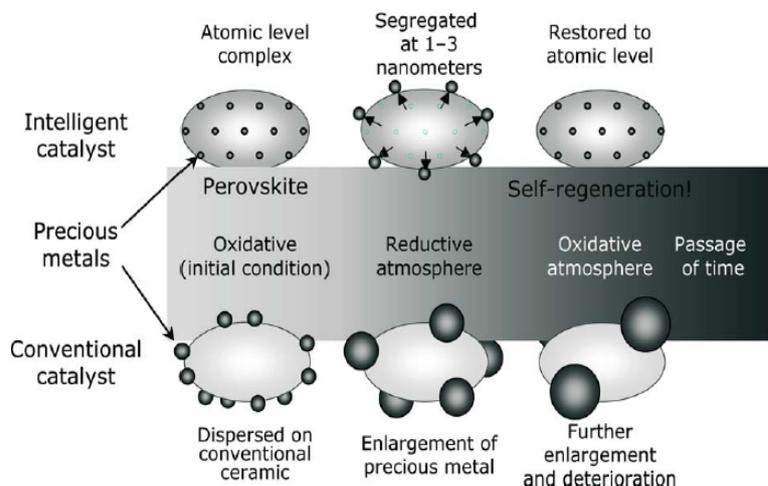
Fig. 2.28. Comparison of palladium behavior in intelligent catalyst possessing self-regenerative function with that in conventional catalyst [H. Tanaka 2005].

Up to now, self-regeneration function has been identified in many intelligent catalysts, most of which are based upon platinum, palladium or rhodium hosted in $LaFeO_3$, $LaAlO_3$, $CaTiO_3$, $CaZrO_3$, $SrTiO_3$, $SrZrO_3$, $BaTiO_3$, $BaZrO_3$ perovskite [H. Tanaka 2006]. However, contrary to most previous claims, recent studies manifested that the dislodged noble metal is not completely reintegrated into the perovskite crystal, casting doubt on the self-regeneration theory. [S. Keav 2014] Likewise, M. B. Katz found that the cyclical process of platinum-doped $CaTiO_3$ perovskite mostly arose from bulk rather than surface re-dispersion and only a few nanometers (measured from free surface) of perovskites with self-regeneration function are potentially useful as a host or support for precious metals in any practical embodiment of the original self-regenerating TWC concept. [M.B. Katz 2012]

2.8. Synthesis of perovskite: from conventional methods to more sophisticated technologies with controllable microstructure

2.8.1. Solid state process

2.8.1.1. Solid-solid method

Solid-solid method, also known as ceramic method, was introduced in the 1970s as the first approach to prepare perovskite[R.J.H. Voorhoeve 1976; Y. Teraoka 1985]. Oxides, hydroxides or carbonates solids are mixed together to undergo reactions through solid-solid diffusion. The obtained compounds is then subjected to heat treatment at high temperature (typically higher than 1000°C)[R.J.H. Voorhoeve 1976]. This simple method requires high-

temperature processing and long reaction time. It has thereby been considered not suitable for catalysis application owing to the poor textural properties of the products because of the growth and agglomeration of particles caused by thermal treatment at high temperature.[S. Royer 2005 b]

2.8.1.2. Reactive grinding method

Reactive grinding method refers to mechanosynthesis, also known as mechanochemical processing (MCP). The first systematic investigation on chemical effects of mechanical action was conducted by M.C. Lea[L. Takacs 2003, 2004]. Mechanosynthesis starts with mixing the precursors(usually in the form of powder) with appropriate proportions and subsequent loading of the above powder mixture, together with grinding media (i.e. steel, zirconia or tungsten carbide) into a reactor in which reactants are subjected to repeated milling for the requisite length of time to get final products[B. Gangdev 2014]. Mechanosynthesis is characterized by the implementation of mechanical energy provided by high-energy ball milling to trigger chemical reactions at quasi room temperature.[B. Peter 2008]. A low reaction temperature allows this technique to reduce significantly the particle size of products and consequently gives rise to higher specific surface area and enhanced density of surface defects expected to be active sites for redox reactions. It should be noticed that some key factors, including the ratio of ball-to-precursor, milling time, milling atmosphere etc. will have a great influence on the particle size of products. In most of the cases, a certain number of additives such as NaCl, LiCl, ZnO can be used for the purpose of further improving specific surface area of perovskite. In such circumstance, additional leaching steps become indispensable to remove additives by means of appropriate liquid solution depending on the nature of employed additives.

2.8.1.3. Microwave crystallization

A variety of perovskites synthesized by microwave crystallization have been reported[Y. Liu 2001; A. Kaddouri 2006; R. Ran 2007] The advantages of microwave can be exemplified: Firstly, many reaction have been observed to occur faster under microwave irradiation and reaction kinetics could be increased by 1-2 orders of magnitude thanks to either the reduction of energy barrier or thermal effect[C.H. Lin 1997; P.D. Ramesh 1996]. Secondly, the limited use of organic solvent makes it more ecologically friendly. In addition, since the initial heating is done rapidly, it consumes less energy and saves cost. Generally speaking, microwave synthesis is faster, cleaner and more energy efficient route compared to conventional methods. However, reagents must have a high dielectric constant or ionic conductivity in order to absorb microwave energy, restricting to a great extent the applicability of microwave technology [I.S. Yakovleva 2013].

2.8.2. Solution-based method

Wet-chemistry synthetic routes are believed to be approaches that are more convenient, more sustainable and less energy-consuming. Unlike solid-state methods, more precise

process control is possible in wet-synthesis routes, which yields better textural properties and homogeneity of the products. [S. Diodati 2014]

2.8.2.1. Sol-gel method

In his patent published in 1967, Pechini invented a method for the preparation of alkaline earth titanates,zirconates and niobates by way of resin intermediates.[M.P. Pechini 1967]. The principle of this method is based on the ability of certain alpha-hydroxycarboxylic acids such as citric,lactic and glycolic acids to form stable polybasic acid chelates with several cations (i.e. titanium, zirconium and niobium) in an aqueous-organic medium. When heated with polyhydroxy alcohol(i.e. ethylene glycol), a polymeric gel with homogeneous distribution of cations is formed as a result of polyesterification of the above chelates. After a thermal treatment at relatively low temperature, excessive organic constituents are removed and desired oxides are obtained. [M.P. Pechini 1967; A.M. Huízar-Félix 2012]. The nature of gel varies depending on the method of drying step: a xerogel is the product of solvent extraction done through thermal evaporation. In contrast, supercritical conditions result in an aerogel.

2.8.2.2. Mechanism of sol-gel method

Various factors, such as the type of employed organic acid, the solution characteristic, the ratio of organic acid to metal ions and the decomposition/calcination temperature, have influences on the product properties. Among common organic acids capable of complexing metals, citric acid was known to be able to form the most stable precursors with metal ions and make them most resistant to autooxydation. Hence, citric acid is most widely used as the complexing agent in sol-gel route. In spite of the fact that specific surface area of perovskites prepared by citric acid complexation is a bit lower than those prepared by polyacrylic acid under same conditions, the enhanced homogeneity and uniformity of ions on the material surface often leads to better catalytic activity for CO oxidation[S. Royer 2014]. What's more, it should be mentioned that the ratio of complexing agent to metal ions impacts greatly the composition and property of the product.The effect of CA/metal ions ratio on $LaMnO_{3+\delta}$ was studied by H. Taguchi [H. Taguchi 1997]. It was shown that gel formation was possible in the molar range from 0.0023 to 0.015 mol of citric acid and the composition of gel was dependent on the citric acid proportion in the initial mixture. P. Courty [P. Courty 1973] discovered that the content of residual carbon in the final product was affected deeply by the citric acid proportion. The higher proportion of citric acid was, the lower content of residual carbon would be. The author attributed this phenomenon to the fact that the combustion of residual carbon was facilitated by higher citric acid proportion leading to diminished apparent density and subsequently augmented porosity. Besides, effect of thermal treatment temperature and time was also examined by the same author. It was found that higher temperature as well as longer treatment time gave rise to bigger size and better crystallinity of perovskite particles. Residual carbon content in the final product plummeted as the decomposition temperature rose in the range of 0-1000°C yet stabilized above 1000°C. [P. Courty 1973]

Another important factor during synthesis is the solvent utilized. As a matter of fact, the characteristic of solvent is linked directly to the dissolution of metallic salts as well as the following complexation and gelation process. A wide variety of solvents have been reported, including both inorganic (i.e. water) and organic ones(i.e. ethanol, propanol, ethylene glycol, diethylene glycol). A. Kahoul [A. Kahoul 2000] gave a detailed comparison of water and propanol on the physico-chemical properties of $La_{1-x}Ca_xCoO_3$ perovskites. He claimed that cobaltite synthesized using propanol as solvent exhibited single perovskite phase, larger SSA and higher electrical conductivity values compared to those prepared using water. H. Aono [H. Aono 2011] prepared precursors of fine perovskite-type materials by using a series of complex solvents composed of water-organic solvent with various constituents and content. According to his result, pure $LaFeO_3$ perovskite phase was obtained even calcined at temperature as low as 350°C by using a water-ethylene glycol mixed solvent.

In some cases, Ethylene Glycol (EG) is employed to improve product property. EG has been proven as a stabilizer of the CA-metal chelate, leading to a lessened gel combustion rate. Surface crystallinity of material could be ameliorated due to the addition of EG, contributing to a better catalytic activity. M. Mohsennia [M. Mohsennia 2017] studied the impact of ethylene/citric acid ratio(EG/CA ratio) on the catalytic activity of $La_{0.7}Ba_{0.3}Co_xNi_{1-x}O_3$ nanocatalyst. The author argued that the catalytic activity of LBCNs can be strongly affected by the EG/CA ratio through distinctive complexing mechanism and a higher EG/CA ratio results in a better catalytic activity for CO oxidation [M. Mohsennia 2017]

The main drawback of sol-gel route is, however, the release of undesired gases such as NO_x during solvent evaporation and drying processes.

2.8.2.3. Co-precipitation method

The co-precipitation method is based on simultaneous precipitation of precursors in a liquid medium with the presence of precipitating agent. The advantages of co-precipitation lie in its simplicity, wide variability ,low cost and easily scalable to industrial level[F. Huang 2018]. Many metal salts could serve as precursors, such as hyroxides, carbonates and oxalates. Water, ammonia, urea, oxalic acid are often used as precipitating agents.[M.K. Mahata 2014; H-I. Hsiang 1996; D.K. Patel 2010; M. Cernea 2009; M.E.V. Costa 1999]. Driven by the principle of reduction of Gibbs free energy of a supersaturated solution, precursors will undergo nucleation, growth, coarsening and/or agglomeration processes, resulting in precipitates which are subjected to further processing (washing, drying, calcination) in order to get final products [G. Cao 2004]. The simultaneous precipitation of multiple species present in the solution is a prerequisite for the success of synthesis. Moreover, PH value of solution and types of precipitating agent plays a decisive role in the precipitation process. By utilizing *N*, *N*-dimethylacetamide (DMAC) as solvent and tetramethylammonium hydroxide (TMAOH) as precipitating agent, Huang and co-workers [F. Huang 2018] reported a facile co-precipitation method to synthesize $La_{0.6}Sr_{0.4}MnO_3$ perovskite catalyst with high surface area of 48m^2/g and excellent catalytic activity for methane oxidation. The author ascribed the reason of this result to the better compositional homogeneity of precipitates caused by lower crystallization temperature. L. Djoudi [L. Djoudi 2015] synthesized successfully $LaAl_{1-x}Ni_xO_{3-\delta}$ ($0 \leq x \leq 0.6$) perovskite via co-precipitation method by employing nitrate

salts of lanthanum, aluminum and nickel as cations precursors and sodium hydroxide as base precipitating agent. Final products showed pure perovskite phase and good crystallinity.

Nevertheless, this method has some inherent disadvantages: Firstly, the solubility and compatibility of precursors must be ensured to form oxides with expected compositions. Further, the quality of products is susceptible to many operational parameters such as pH value, co-precipitation rate, washing, drying and thermal treatment temperature. What's more, addition of inappropriate precipitating agent or poor mixing may induce ununiformed temperature distribution in certain part of the solution, resulting in agglomeration of precipitates and heterogeneity in composition.

2.8.2.4. Auto-combustion method

In the past decade, auto-combustion method has been extensively applied as a reference method to synthesize numerous catalytic materials [K.C. Patil 2002; Y.V. Tyurkin 1997]. This method is characterized by its merits in terms of simplicity, short synthesis time as well as the ease of up-scaling. Precursors can be nitrates or oxides. Organic reagents, such as citric acid, oxalic acid, tartaric acid, urea, glycine, are used as fuel [J. Chandradass 2010]. Auto-combustion is triggered when the gel is heated by a heat source, resulting in the removal of organic matter. Perovskite phase is then formed either directly through heating or through further calcination.

Three atmospheric conditions are involved in auto-combustion: namely, oxidizing atmosphere (fuel-deficient), reducing atmosphere (fuel-rich) and stoichiometric atmosphere. It is worth mentioning that the ratio of fuel/oxidizer has a substantial influence on the released heat and subsequently maximum temperature of the combustion reaction process. Thus, a suitable fuel/oxidizer ratio is very essential to guarantee the purity of crystalline phase [A. Civera 2003].

Despite the fact that the auto-combustion method has been used to synthesize a broad variety of materials, improvement of operational parameters is still demanded for commercial applications. Parameters influencing the combustion reaction, such as type of fuel, fuel/oxidizer ratio, use of excess oxidizer, and water content of the precursor mixture, need to be optimized towards desirable particle size distribution and crystallinity of products [L.E. Shea 1996].

2.8.2.5. Flame Spray Pyrolysis method

Flame spray pyrolysis, also known as flame aerosol synthesis, is a technology consisting of producing nanoparticle aerosol by feeding either liquid or vapor precursors into a high-temperature flame. Some key parameters, including precursor concentration, flame temperature, fuel, mixing, oxidant, entrainment, precursor/dispersion flow rate ratio (P/D) and precursor solution composition, affect significantly product properties and particularly primary particle and crystallite sizes related directly to catalytic performance.[R. Koirala 2016]. It is regarded as a time-saving, energy-efficient synthesis approach as it combines feeding of precursors, mixing, in-situ calcination in a fast single step without neither the need of solvent-intensive washing nor post thermal treatment typical of those made by other wet-

chemistry methods. Unlike batch process, it offers the possibility of continuous production of nanoparticles in industrial scale. Equally important, catalytic features of flame-made materials such as particle size and crystallinity, SSA could be tuned to achieve better performance. Synthesis of perovskite was first reported by J.H. Brewster [J.H. Brewster 1997] .By spraying an aqueous mixture comprising of barium acetate and titanium lactate into a H_2/air flame, $BaTiO_3$ perovskite was successfully synthesized. A series of $La_{1-x}M_xCoO_3$ (M=Ce, Eu) was prepared by spraying aqueous feed composed of metal acetate/nitrate/citrate into a H_2/O_2 flame, resulting in pure perovskite phase with SSA up to $25 m^2/g$.[R. Leanza 2000]. The same methodology has been applied to the successful synthesis of a broader range of perovskites with formula of $LaBO_3$ (B=Co, Mn, Fe).[I. Rossetti 2001]. Organic liquid feed has been reported to be effective to increase dramatically the SSA of products. G.L.Chiarello proposed a technique based on organic liquid feed to synthesize cobaltites. SSA of $LaCoO_3$ was improved to as high as 64 m^2/g by employing a mixed solvent of alcohols + propionic acid. [G.L.Chiarello 2007].

Notwithstanding, some disadvantages still One of its mains shortcomings stem from the high cost of suitable precursors and highly specialized facility. Since the synthesis is completed in a single step, it is sometimes not easy to get rid of the temples frequently used in the synthesis of macroporous material, thus not suitable for the preparation of materials with porous structure. In addition, conditions of precursor mixing must be well controlled as respect to explosive precursors and in certain cases an incomplete combustion could occur.[R. Koirala 2016]

2.8.2.6.   Solvothermal/Hydrothermal method

A solvothermal reaction refers to any chemical reaction which takes place under temperature and pressure above ambient temperature and pressure in a sealed vessel in the presence of a solvent. It is specifically called hydrothermal reaction in the case of water as solvent [M.A. Gomes 2016; K. Byrappa 2001]. It relies on the solvation of precursors (usually soluble metal salts) to form target product in an aqueous medium. Some mineralizers, such as hydroxides, carbonates, halides are often added to assist the solubilization of precursor salts and have a considerable impact on the final particle size and morphology [K. Byrappa 2001]. One the biggest advantages of solvothermal method arises from the fact that it enables the preparation of inorganic materials at temperatures well below those required for solid-state or sol-gel method and in most of the cases post-annealing treatment could be omitted. [M.A. Gomes 2016]. Application of hydrothermal method to the synthesis of titanate perovskites $ATiO_3$ (A = Ca, Sr, Ba, etc.) have been widely reported[H. Xu 2006; J. Xu 2014; M.-H. Um 2000; S. Zhang 2004]. Furthermore, microwave has been reported beneficial to the improvement of physico-chemical and catalytic properties of perovskite-type oxides during hydrothermal aging step [N. Miniajluk 2015]. Kaddouri et al. [A. Kaddouri 2009] found that microwave-assisted hydrothermal synthesis led to enhanced methane combustion actitivy of La-Ce-Mn-O perovskite. The author claimed that the strong interaction between well dispersed cerium oxide species and $LaMnO_3$ host structure was responsible for the good performance of as-prepared material.

2.8.2.7. Spray/freeze drying method

Spray drying refers to a technique involving a rapid vaporization of the solvent contained in small droplets of required solutions of cations whilst slow sublimation of the solvent is employed in the case of freeze drying [P. Cousin 1990]. Freeze drying relies on spraying the solution in the form of fine droplets into liquid nitrogen followed by sublimation of the solvent in the absence of liquid phase [D.M. Roy 1977]. The first step of freezing aims at a minimum segregation of diluted salts and as a consequence an intimate mixing of ions can be attained [D.D. Athayde 2016]. Both spray drying and freeze drying allow excellent control over purity levels and compositions, generating particles with adequate homogeneity. [P. Cousin 1990]. Reports regarding perovskite preparation using these techniques are not scarce, exemplified by the synthesis of $La_{1-x}Sr_xCo_{1-y}Fe_yO_{3-\delta}$ [O. Büchler 2007] by spray drying and the synthesis of Sr_2CoTeO_6 and $La_{0.9}Sr_{0.1}Ga_{0.8}Mg_{0.2}O_{2.85}$ by freeze drying[O.S.M. Luis 2005; K. Traina 2007]

Reference

[A.K. Agarwal 2007] A.K. Agarwal. Prog. Energy Combust. Sci. 2007, 33, 233-271.

[J.R. Anderson 1975] J.R. Anderson, Structure of Metallic Catalysts, Academic Press, London, 1975.

[H. Aono 2011] Hiromichi Aono, Jun Izumi, Musashi Tomida, Yoshihiko Sadaoka. Materials Chemistry and Physics, 2011, 130:973-979.

[H. Arai 1986] H. Arai, T. Yamada, K. Eguchi, T. Seiyama. Applied Catalysis, 1986, 26: 265–276.

[D.D. Athayde 2016] Daniel D. Athaydea, Douglas F. Souzaa, Alysson M.A. Silvaa, Daniela Vasconcelos, Eduardo H.M. Nunes, João C. Diniz da Costa, Wander L. Vasconcelos. Ceramics International, 2016, 42:6555–6571.

[R. Auer 2002] R. Auer, F.C. Thyrion. Industrial & Engineering Chemistry Research, 2002, 41:680-690.

[S. Bernal 1998] S. Bernal, J.J. Calvino, M.A. Cauqui, J.A. Perez Omil, J.M. Pintado, J.M. Rodriguez-Izquierdo. Applied Catalysis B: Environmental, 1998, 16:127-138.

[J. Bickel 2016] J. Bickel, B. Odendall, G. Eigenberger, U. Nieken. Chemical Engineering Science, 2017, 160:34–53.Catalysis Today, 2015, 258:525–534.

[H. Birgersson 2004 a] Henrik Birgersson, Lars Eriksson, Magali Boutonnet, Sven G. Jaras. Applied Catalysis B: Environmental, 2004, 54:193–200.

[H. Birgersson 2004 b] Henrik Birgersson, Magali Boutonnet, S. Jaras, Lars Eriksson. Topics in Catalysis, 2004, 30/31:433-437.

[M. Bosomoiu 2008] Magdalena Bosomoiu, Grigore Bozga, Daniela Berger, Cristian Matei. Applied Catalysis B: Environmental, 2008, 84:758–765.

[J.H. Brewster 1997] J.H. Brewster, T.T. Kodas. AIChE Journal, 1997, 43:2665–2669.

[I.D. Brown 1992] I.D. Brown. Modeling the structures of La_2NiO_4. Zeitschrift für Kristallographie, 1992, 199:255–272.

[O. Büchler 2007] O. Büchler, J.M. Serra, W.A. Meulenberg, D. Sebold, H.P. Buchkremer. Solid State Ionics, 2007, 178:91–99.

[H. Burtscher 2005] H. Burtscher. Journal of Aerosol Science, 2005, 36:896-932.

[K. Byrappa 2001] K. Byrappa, M. Yoshimura. Handbook of hydrothermal technology. A technology of crystal growth and materials processing. Noyes Publications, New Jersey; William Andrew Publishing, New York, 2001.

[A. Cao 2010] Anmin Cao, Rongwen Lu, Götz Veser. Physical Chemistry Chemical Physics, 2010, 12:13499–13510.

[G. Cao 2004] Guozhong. Cao. Ying Wang. Imperial College Press, USA, 2004.

[M. Castagnola 2011] Castagnola M., Caserta J., Chatterjee S., Chen H. et al. SAE Technical Paper, 2011, 2011-01-1329.

[G. Cavataio 2009] G. Cavataio, J. Girard, C. Lambert. SAE Technical Paper, 2009, 2009-01-0897.

[M. Cernea 2009] M. Cernea. Journal of Optoelectronics and Advanced Materials, 2009, 11:1191–1195.

[T. Chan 2013] T. Chan, E. Meloche, J. Kubsh, R. Brezny et al. SAE International Journal of Fuels and Lubricants, 2013, 6(2):350-371.

[J. Chandradass 2010] J. Chandradass, M. Balasubramanian, K.H. Kim. Materials and Manufacturing Processes, 2010, 25:1449–1453.

[L.F. Chen 2005] L.F. Chen, G. González, J.A. Wang, L.E. Noren, A. Toledo, et al. Applied Surface Science, 2005, 243:319–328.

[T. Cheng 2017] Tianqiong Cheng, Jianli Wang, Suning Wang, Yajuan Cui, Hailong Zhang, Shuang Yan, Shandong Yuan, Yaoqiang Chen. Applied Surface Science, 2017, 426:745–754.

[Y.M. Chiang 1997] Y.M. Chiang, D. Birnie, W.D. Kingery. Physical Ceramics: Principles for Ceramic Science and Engineering, John Wiley & Sons, 1997.

[G.L. Chiarello 2007] G.L. Chiarello, I. Rossetti, L. Forni, P. Lopinto, G. Migliavacca. Applied Catalysis B: Environmental, 2007, 72:227-232.

[P. Ciambelli 2001] P. Ciambelli, S. Cimino, L. Lisi, et al. Applied Catalysis B: Environmental, 2001, 33:193–203.

[A. Civera 2003] A. Civera, M. Pavese, G. Saracco, V. Specchia. Catalysis Today, 2003, 83: 199–211.

[M.E.V. Costa 1999] M.E.V. Costa, P.Q. Mantas. Journal of the European Ceramic Society, 1999, 19:1077–1080.

[P. Courty 1973] Ph. Courty, H. Ajot, Ch. Marcilly, B. Delmon. Powder Technology, 1973, 7:21-38.

[P. Cousin 1990] P. Cousin, R.A. Ross. Materials Science and Engineering: A, 1990, 130:119-125.

[L. D'Souza 2007] L. D'Souza, L. Jiao, J.R. Regalbuto, J.T. Miller, A.J. Kropf. Journal of Catalysis, 2007, 248:165–174.

[J. Deng 2018] Jie Deng, Yi Zhou, Shanshan Li, Lei Xiong, Jianli Wang, Shandong Yuan, Yaoqiang Chen. Journal of Industrial and Engineering Chemistry, 2018, 64:219–229.

[P. Dimopoulos Eggenschwiler 2009] Dimopoulos Eggenschwiler P., Tsinoglou D.N., Seyfert J. et al. Experiments in Fluids, 2009, 47:209-222.

[S. Diodati 2014] Stefano Diodati, Luca Nodari, Natile Marta Maria et al. European Journal of Inorganic Chemistry, 2014, 2014:875-887.

[L. Djoudi 2015] Lynda Djoudi, Mahmoud Omari. Journal of Inorganic and Organometallic Polymers and Materials, 2015, 25: 796–803.

[H. Du 2015] Haiwei Du, Xi Lin, Zhemi Xu, Dewei Chu. Journal of Materials Science, 2015, 50:5641–5673.

[D. Duprez 2001] D. Duprez, C. Descorme, T. Birchem, E. Rohart. Topics in Catalysis, 2001, 16/17:49-56.

[B.C. Enger 2008] Bjørn Christian Enger, Rune Lødeng, Anders Holmen. Applied Catalysis A: General, 2008, 346:1–27.

[European Environment Agency report] European Environment Agency, European Union emission inventory report, 1990–2011 under the UNECE Convention.

[A. Eyssler 2011] Arnim Eyssler, Alexander Winkler, Peter Mandaliev, Paul Hug, Anke Weidenkaff, Davide Ferri. Applied Catalysis B: Environmental, 2011, 106: 494–502.

[D.W. Fickel 2010] D.W. Fickel, R.F. Lobo. Journal of Physical Chemistry C, 2010, 114:1633-1640.

[D.W. Fickel 2011] D.W. Fickel, E. D'Addio, J.A. Lauterbach, R.F. Lobo. Applied Catalysis B: Environmental, 2011, 102:441–448.

[R.M.J. Fiedorow 1976] R.M.J. Fiedorow, S.E. Wanke. Journal of Catalysis, 1976, 43:34-42.

[R.M.J. Fiedorow 1997] R.M.J. Fiedorow, S.E. Wanke. Applied Catalysis B: Environmental, 1997, 14: 249-259.

[J.L.G. Fierro 1990] J.L.G. Fierro. Catalysis Today, 1990, 8:153–174.

[D. Fino 2003] D. Fino, N. Russo, G. Saracco, V. Specchia. Journal of Catalysis, 2003, 217:367–375.

[K. Foger 1985 a] K. Foger, H. Jaeger. Journal of Catalysis, 1985, 92:64-78.

[K. Foger 1985 b] K. Foger, D. Hay, H. Jaeger. Journal of Catalysis, 1985, 96:154-169.

[B. Gangdev 2014] Brinda Gangdev, Femina Patel. International Conference on Multidisciplinary Research & Practice. ISSN 2321-2705. 2014, 1:606-608.

[I. Gekas 2009] I. Gekas, A. Vressner, K. Johansen. SAE Technical Paper, 2009, 2009-01-0626.

[P. Gélin 2002] Patrick Gélin, Michel Primet. Applied Catalysis B: Environmental, 39 (2002) 1–37.

[V.M. Goldschmidt 1926] V. M. Goldschmidt. Die Naturwissenschaften, 1926, 21:477−485.

[M.A. Gomes 2016] Maria A. Gomes, Alvaro S. Lima, Katlin I.B. Eguiluz, Giancarlo R. Salazar-Banda. Journal of Materials Science, 2016, 51:4709–4727.

[J.B. Goodenough 1970] J.B. Goodenough, J. M. Longo, In Landolt-Bronstein New Series; Hellwege, K. H., Helwege, A. M., Eds.; Springer-Verlag: Berlin, 1970, Vol. 4, part a, pp:126.

[J.B. Goodenough 1974] J.B. Goodenough. In Solid State Chemistry. Rao C.N.R., Ed.; Marcel Dekker: New York, 1974, pp:215.

[P. Granger 2001] P. Granger, J.J. Lecomte, L. Leclercq, G. Leclercq. Applied Catalysis A: General, 2001, 208: 369–379.

[P. Granger 2004] P. Granger, P. Malfoy, G. Leclercq. Journal of Catalysis, 2004, 223:142-151.

[P. Granger 2017] P. Granger. Catalysis Science & Technology, 2017, 7:5195–5211.

[D. Greenwell 2013] D. Greenwell. Optimisation of Three Way Filter (TWFTM) Coatings and Systems for Euro 6, Advanced Emission Control Concepts for Gasoline Engines. May 2013. (Bonn).

[B. Guan 2014] Bin Guan, Reggie Zhan, He Lin, Zhen Huang. Applied Thermal Engineering, 2014, 66:395-414.

[B. Guan 2015] Bin Guan, Reggie Zhan, He Lin, Zhen Huang. Journal of Environmental Management. 2015, 154:225-258.

[N. Guilhaume 1997] N. Guilhaume, M. Primet. Journal of Catalysis, 1997, 165:197–204.

[A. Gurupatham 2009] A. Gurupatham and Y. He. SAE International Journal of Fuels and Lubricants, 2009, 1(1):1387-1396.

[K.F. Hansen 2014] K.F. Hansen. Development of Gasoline Particulate Filters. 3rd International Conference Advanced Emission Control Concepts for Gasoline Engines. May 2014. (Düsseldorf).

[X. Hao 2011] X. Hao, S. Barnes, J.R. Regalbuto. Journal of Catalysis, 2011, 279:48–65.

[D. Hari Prasad 2012] D. Hari Prasad, S.Y. Park, E.O. Oh, H. Ji, H.R. Kim, K.J. Yoon, J.W. Son, J.H. Lee. Applied Catalysis A: General, 2012, 447–448:100–106.

[Y. He 2009] Y. He, D. Brown, S. Lu et al. SAE Technical Paper, 2009, 2009-01-0274.

[S. Hernandez 2012] S. Hernandez, G.A. Blengini, N. Russo, D. Fino. Industrial & Engineering Chemistry Research, 2012, 51:7584–7589.

[W.Y. Hernández 2015] W.Y. Hernández, M.N. Tsampas, C. Zhao, A. Boreave, F. Bosselet, P. Vernoux. Catalysis Today, 2015, 258:525–534.

[H-I. Hsiang 1996] H-I. Hsiang, F-S. Yen, Y-H. Chang. Journal of Materials Science, 1996, 31:2417–2424.

[F. Huang 2018] Fei Huang, Xiucheng Sun,Yong Zheng,Yihong Xiao,Ying Zheng. Materials Letters, 2018, 210: 287-290.

[J.L. Hueso 2008] J.L. Hueso, A. Caballero, M. Ocana, A.R. González-Elipe. Journal of Catalysis, 2008, 257:334–344.

[A.M. Huízar-Félix 2012] A.M. Huízar-Félix, T. Hernández, S. de la Parra, J. Ibarra, B. Kharisov. Powder Technology, 2012, 229:290–293.

[L. Jiao 2008] L. Jiao, J.R. Regalbuto. Journal of Catalysis, 2008, 260:329–341.

[R. Jiménez 2010] R. Jiménez, R. Zamora, G. Pecchi, X. García, A.L. Gordon. Fuel Processing Technology, 2010, 91:546–549.

[T.V. Johnson 2010] T.V. Johnson. Review of Diesel Emissions and Control. 2010, SAE Technical Paper, 2010-01-0301.

[T.V. Johnson 2014] T.V. Johnson. Review of Emerging Trends on Gasoline Emissions Control, 3rd International Conference Advanced Emission Control Concepts for Gasoline Engines. May 2014. (Düsseldorf).

[A. Kaddouri 2006] A. Kaddouri, S. Ifrah. Catalysis Communications, 2006, 7:109–113.

[A. Kaddouri 2009] A. Kaddouri, P. Gelin, N. Dupont. Catalysis Communications, 2009, 10:1085–1089.

[A. Kahoul 2000] A. Kahoul, A. Hammouche, F. Naamoune, P. Chartier, G. Poillerat, J.F. Koenig. Materials Research Bulletin, 2000, 35:1955–1966.

[J. Kašpar 2000] Jan Kašpar. Mauro Graziani. Paolo Fornasiero. Handbook on the Physics and Chemistry of Rare Earths, Chapter 184 Ceria-containing three-way catalysts. 2000, 29:159-267.

[J. Kašpar 2003] Jan Kašpar, Paolo Fornasiero. Catalysis Today, 2003, 77:419–449.

[M.B. Katz 2012] Michael B. Katz, Shuyi Zhang, Yingwen Duan, Hongjie Wang, Minghao Fang, Kui Zhang, Baihai Li, George W. Graham, Xiaoqing Pan. Journal of Catalysis, 2012, 293:145–148.

[A. Kawakami 2012] A. Kawakami, T. Mizutani, Y. Shibagaki, K. Yuuki, H. Sakamoto, C. Vogt, T. Kuki, W. Heuss, P. Kattouah, M. Makino. SAE Technical Papers, 2012, 2012-01-0843.

[S. Keav 2014] S. Keav, S.K. Matam, D. Ferri, A. Weidenkaff. Catalysts, 2014, 4: 226–255.

[C.P. Khattak 1979] C.P. Khattak., F.F.Y. Wang. In Handbook of the Physics and Chemistry of Rare Earths; Gschneider, K. A. Jr.; Eyring, L., Eds.; North-Holland Publisher: Amsterdam, 1979, pp:525.

[J. Kirchnerova 2002] Jitka Kirchnerova, Mihai Alifanti, Bernard Delmon. Applied Catalysis A: General, 2002, 231:65–80.

[D.B. Kittelson 1998] D.B. Kittelson. Journal of Aerosol Science, 1998, 29,575-588.

[A. Klimkowicz 2014] A. Klimkowicz, K. Świerczek, A. Takasaki, B. Dabrowski. Solid State Ionics, 2014, 257:23–28.

[R. Koirala 2016] Rajesh Koirala, Sotiris E. Pratsinis, Alfons Baiker. Chemical Society Reviews, 2016, 45:3053-3068.

[G. Kremenić 1985] Gojko Kremenić, José M. L. Nieto, Juan M. D. Tascón, Luis G. Tejuca. Journal of the Chemical Society, Faraday Transactions 1: Physical Chemistry in Condensed Phases. 1985, 81:939-949.

[T. Körfer 2008] T. Körfer. SAE Technical Paper, 2013-24-0163.

[L. Lan 2018 a] Li Lan, Shanhu Chen, Hongmei Li, Hanmei Li, Wanxia Wu, Jie Deng, Yaoqiang Chen. Journal of Industrial and Engineering Chemistry, 2018, 58:246–257.

[L. Lan 2018 b] Li Lan, Chaoyang Yan, Shanhu Chen, Hongmei Li, Dacheng Li, Jinfeng Wang, Yongxiang Cheng, Yaoqiang Chen. Journal of the Taiwan Institute of Chemical Engineers, 2018, 85:98–105.

[R. Leanza 2000] R. Leanza, I. Rossetti, L. Fabbrini, C. Oliva, L. Forni. Applied Catalysis B: Environmental, 2000, 28:55–64.

[T.J. Lee 1984] T.J. Lee, Y.G. Kim. Journal of Catalysis, 1984, 90:279-291.

[J.H. Lee 2009] Jong H. Lee, Michael J. Paratore, David B. Brown. SAE International Journal of Fuels and Lubricants, 2009, Vol. 1, No. 1, pp:96-101.

[H. Lee 2015] Heesoo Lee, Dae-Hoon Lee, Young-Hoon Song, Won Choon Choi, Yong-Ki Park, Do Heui Kim. Chemical Engineering Journal-Lausanne, 2015, 259:761–770.

[Dongkyu Lee 2017] Dongkyu Lee and Ho Nyung Lee. Materials, 2017,10:368.

[H. Lieske 1983] H. Lieske, G. Lietz, H. Spindler, J. Völter. Journal of Catalysis, 1983, 81:8-16.

[G. Lietz 1983] G. Lietz, H. Lieske, H. Spindler, W. Hanke, J. Völter. Journal of Catalysis, 1983, 81:17-25.

[C.H. Lin 1997] C.H. Lin, H.Y. Chang, I.N. Lin. IEEE Transactions on Magnetics, 1997, 33:3415-3417.

[Y. Liu 2001] Ya-Fei Liu, Xing-Qin Liu, Guang-Yao Meng. Materials Letters, 2001, 48:176–183.

[Lu Liu 2016] Lu Liu, Daniel D. Taylor, Efrain E. Rodriguez, Michael R. Zachariah. Chemical Communications, 2016, 52:10369-10372.

[P. Lucena 1999] P. Lucena, J.M. Vadillo, J.J. Laserna. Analytical Chemistry, 1999, 71:4385–4391.

[O.S.M. Luis 2005] O.S.M. Luis, P,C. Jon, L. Luis, et al. Journal of Materials Chemistry, 2005, 15:183-193.

[M.K. Mahata 2014] M.K. Mahata, K. Kumar, V.K. Rai. Spectrochimica Acta Part A: Molecular and Biomolecular Spectroscopy, 2014, 124:285–291.

[M.M. Maricq 2007] M.M. Maricq. Journal of Aerosol Science, 2007, 38:1079-1118.

[M. Markova-Velichkova 2013] M. Markova-Velichkova, T. Lazarova, V. Tumbalev et al. Chemical Engineering Journal, 2013, 231:236–244.

[F. Matei 2013] F. Matei, C. Jiménez-Borja, J. Canales-Vázquez, S. Brosda, F. Dorado, J.L. Valverde, D. Ciuparu. Applied Catalysis B: Environmental, 2013, 132–133: 80– 89.

[S. Matsumoto 2004] Shinichi Matsumoto. Catalysis Today, 2004, 90:183-190.

[S.K. Meher 2013] S.K. Meher, M. Cargnello, H. Troiani, T. Montini, G.R. Rao, P. Fornasiero. Applied Catalysis B: Environmental, 2013, 130-131:121-131.

[N. Miniajluk 2015] N. Miniajluk, J. Trawczynski, M. Zawadzki, P.E. Tomaszewski, W. Mista. Catalysis Today, 2015, 257:26–34.

[A. Mishra 2017] A. Mishra, R. Prasad. Bulletin of Chemical Reaction Engineering & Catalysis, 2017, 12 (3): 469-477.

[M. Mohsennia 2017] Mohsen Mohsennia, Bahareh Niknahad, Ali Eliassi. Journal of Sol-Gel Science and Technology, 2017, 82:458–467.

[C. Morgan 2012] C. Morgan. Three Way Filters (TWF^{TM}) for Particulate Number Control, Advanced Emission Control Concepts for Gasoline Engines. 2012, Stuttgart.

[M. Naseri 2011] M. Naseri, S. Chatterjee, M. Castagnola et al. SAE International Journal of Engines, 2011, 4(1):1798-1809.

[E. Ngan 2011] E. Ngan, P. Wetzel, JR J. McCarthy et al. SAE Technical Paper, 2011, 2011-01-2197.

[Y. Nishihata 2002] Y. Nishihata, J. Mizuki, T. Akao, H. Tanaka, M. Uenishi, M. Kimura, T. Okamoto, N. Hamada. Nature, 2002, 418:164-167.

[Y. Nishihata 2005] Y. Nishihata, J. Mizuki, H. Tanaka, M. Uenishi, M. Kimura. Journal of Physics and Chemistry of Solids, 2005, 66:274–282.

[Y. Noboru 1981] Yamazoe Noboru, Teraoka Yasutake, Seiyama Tetsuro. Chemistry Letters, 1981, 10:1767–1770.

[M. Ozawa 2017] Masakuni Ozawa, Masahiro Takahashi-Morita, Katsutoshi Kobayashi, Masaaki Haneda. Catalysis Today, 2017, 281: 482–489

[M. Pacella 2018] M. Pacella, A. Garbujo, J. Fabro, M. Guiotto, Q. Xin, M.M. Natile P. Canu, P. Cool, A. Glisenti. Applied Catalysis B: Environmental, 2018, 227:446–458.

[D.K. Patel 2010] D.K. Patel, B. Vishwanadh, V. Sudarsan, R. Vatsa, S.K. Kulshreshtha. Journal of the American Ceramic Society, 2010, 94:482–487.

[K.C. Patil 2002] K.C. Patil, S.T. Aruna, T. Mimani. Current Opinion in Solid State and Materials Science, 2002, 6:507–512.

[M.P. Pechini 1967] Maggio P. Pechini. 1967, U.S. Patent, Patent No. 3,330,697.

[M.A. Pena 2001] M.A. Pena, J.L.G. Fierro. Chemical Reviews, 2001, 101:1981−2017.

[G. Perin 2017] G. Perin, J. Fabro, M. Guiotto, Q. Xin, M.M. Natile, P. Cool, P. Canu, A. Glisenti. Applied Catalysis B: Environmental, 2017, 209: 214–227.

[B. Peter 2008] Balaz Peter. Mechanochemistry in Nanoscience and Minerals Engineering, Springer-Verlag: Berlin, Heidelberg, 2008.

[L.M. Petkovic 2011] L.M. Petkovic, V. Utgikar, S.N. Rashkeev. Journal of Physical Chemistry C, 2011, 115: 8709–8715.

[S. Philipp 2013] S. Philipp, R. Hoyer, F. Adam, S. Eckhoff, R. Wunsch, C. Schoen and G. Vent, SAE Technical Papers, 2013, vol. 2, code 97364.

[W. Piock 2011] W. Piock, G. Hoffman, A. Berndorfer, P. Salemi and B. Fusshoeller. SAE International Journal of Engines, 2011, 4:1455–1468.

[R. Prasad 2010] R. Prasad, V.R. Bella. Bulletin of Chemical Reaction Engineering & Catalysis, 2010, 5:69-86.

[A. Raj 2016] A. Raj. A review of mobile and stationary source emissions abatement technologies for natural gas engines. Johnson Matthey Technology Review, 2016, 60(4): 228–235.

[P.D. Ramesh 1996] P.D. Ramesh, P. Sarin, S. Jeevan, K.J. Rao. Journal of Materials Synthesis and Processing, 1996, 4:163–173.

[R. Ran 2007] Rui Ran, Duan Weng, Xiaodong Wu, Jun Fan, Liang Qing. Catalysis Today, 2007, 126:394–399.

[K.G. Rappé 2014] K.G. Rappé. Industrial & Engineering Chemistry Research, 2014, 53:17547−17557.

[J.R. Regalbuto 1999] J.R. Regalbuto, A. Navada, S. Shadid, M.L. Bricker, Q. Chen. Journal of Catalysis, 1999, 184:335–348.

[Z.D. Ristovski 2012] Z.D. Ristovski, B.M. Miljevic, N.C. Surawski et al. Respirology, 2012, 17, 201-212.

[D. Rose 2013] D. Rose, J. Jamison, T. Boger, and R. Kataria. SAE Technical Paper, 2013, 2013-26-0051.

[I. Rossetti 2001] I. Rossetti, L. Forni. Applied Catalysis B: Environmental, 2001, 33:345–352.

[D.M. Roy 1977] D.M. Roy, S.O. Oyefesobi. Journal of the American Ceramic Society-Discussions and Notes, 1977, 60:178-180.

[S. Royer 2005 a] S. Royer, H. Alamdari, D. Duprez, S. Kaliaguine. Applied Catalysis B: Environmental, 2005, 58:273–288.

[S. Royer 2005 b] Royer S., Bérubé F., Kaliaguine S. Applied Catalysis A: General, 2005, 282(1):273-284.

[S. Royer 2014] Sebastien Royer, Daniel Duprez, Fabien Can, Xavier Courtois, Catherine Batiot-Dupeyrat, Said Laassiri, Houshang Alamdari. Chemical Reviews, 2014, 114:10292−10368.

[N. Russo 2005] N. Russo, D. Fino, G. Saracco, V. Specchia. Journal of Catalysis, 2005, 229: 459–469.

[C. Saito 2011] C. Saito, T. Nakatani, Y. Miyairi et al. SAE Technical Paper, 2011, 2011-01-0814.

[A. Satsuma 2012] Atsushi Satsuma, Masatoshi Yanagihara, Junya Ohyama, Kenichi Shimizu. Catalysis Today, 2013, 201:62– 67.

[Z. Say 2014] Z. Say, M. Dogac, E.I. Vovk, Y.E. Kalay, C.H. Kim, W. Li, E. Ozensoy. Applied Catalysis B: Environmental, 2014, 154–155:51–61.

[M. Schreier 2004] Marc Schreier, John R. Regalbuto. Journal of Catalysis, 2004, 225:190–202.

[L.E. Shea 1996] L.E. Shea, J. McKittrick, O.A. Lopez. Journal of the American Ceramics Society, 1996, 79, 3257–3265.

[M. Shen 2009] M. Shen, M. Yang, J. Wang, J. Wen, M. Zhao, W. Wang. Journal of Physical Chemistry C, 2009, 113:3212-3221.

[M. Shen 2012] Meiqing Shen, Liying Song, Jun Wang, Xinquan Wang. Catalysis Communications, 2012, 22:28–33.

[W.G. Shim 2011] W.G. Shim, S.C. Jung, S.G. Seo, S.C. Kim. Catalysis Today, 2011,164:500–506.

[S. Liu 2015] Shuang Liu, Xiaodong Wu, Duan Weng, Rui Ran. Journal of Rare Earths, 2015, 33:567-590.

[K. Simmance 2019] Kerry Simmance, David Thompsett, WeiliangWang, Benedicte Thiebaut. Catalysis Today, 2019, 320:40–50.

[M. Stoukides 1981] M. Stoukides, C.G. Vayenas. Journal of Catalysis, 1981, 69:18-31.

[J.E. Stulga 1980] J.E. Stulga, P. Wynblatt, J.K. Tien. Journal of Catalysis, 1980, 62:59-69.

[V. Szabo 2003] V. Szabo, M. Bassir, AVan Neste, S. Kaliaguine. Applied Catalysis B: Environmental, 2003, 43:81-92.

[H. Taguchi 1997] Hideki Taguchi, Shin-ichiro Matsu-ura, Mahiko Nagao et al. Journal of Solid State Chemistry, 1997, 129:60-65.

[L. Takacs 2003] Laszlo Takacs. Bulletin for the History of Chemistry, 2003, 28:26-34.

[L. Takacs 2004] Laszlo Takacs. Journal of Materials Science, 2004, 39:4987-4993.

[H. Tanaka 2004 a] H. Tanaka, M. Uenishi, M. Taniguchi, M. Kimura, Y. Nishihata and J. Mizuki. 2004. Poster Session 6–119, ICC 13th, Paris, 2004, July 11–16.

[H. Tanaka 2004 b] H. Tanaka, M. Taniguchi, N. Kajita, M. Uenishi, I. Tan, N. Sato, K. Narita, M. Kimura. Topics in Catalysis, 2004, 30:389-396.

[H. Tanaka 2005] Hirohisa Tanaka. Catalysis Surveys from Asia, 2005, 9:63-74.

[H. Tanaka 2006] Hirohisa Tanaka, Masashi Taniguchi, Mari Uenishi, Nobuhiko Kajita, Isao Tan, Yasuo Nishihata, Junichiro Mizuki, Keiichi Narita, Mareo Kimura, Kimiyoshi Kaneko. Angewandte Chemie International Edition, 2006, 45:5998-6002.

[W.Y. Tang 2013] W.Y. Tang, D. Younger, M. Santamaria, S. Kumar. SAE International Journal of Engines, 2013, 6(2):862-872.

[M. Taniguchi 2004] M. Taniguchi, M. Uenishi, I. Tan, H. Tanaka, M. Kimura, Y. Nishihata, J. Mizuki. SAE Paper, 2004, 2004-01-1272.

[M. Taniguchi 2007] Masashi Taniguchi, Hirohisa Tanaka, Mari Uenishi, Isao Tan, Yasuo Nishihata, Junichiro Mizuki, Hiromasa Suzuki, Keiichi Narita, Akimasa Hirai, Mareo Kimura. Topics in Catalysis, 2007, 42–43:367-371.

[K.C. Taylor 1984] K.C. Taylor, Automobile catalytic converters, in: J.R. Anderson, M. Boudart (Eds.), Catalysis—Science and Technology, Springer, Berlin, 1984, Chapter 2, pp:119–170.

[L.G. Tejuca 1989] L.G. Tejuca, J.L.G. Fierro, J.M.D. Tascón. Advances in Catalysis, 1989, 36:237–328.

[L.G. Tejuca 1993] In Properties and applications of perovskite-type oxides. L.G. Tejuca, J.L.G. Fierro, Marcel Dekker. Inc.: NEW YORK, 1993.

[P. Tennison 2004] P. Tennison, C. Lambert, M. Levin. SAE Technical Paper, 2004, 2004-01-1291.

[Y. Teraoka 1985] Yasutake Teraoka, Hua-Min Zhang, Noboru Yamazoe. Chemistry Letters, 1985, 14:1367-1370.

[G. Tonetto 2001] G. Tonetto, M.L. Ferreira, D.E. Damiani. Journal of Molecular Catalysis A: Chemical, 2001, 171:123–141.

[K. Traina 2007] K. Traina, M.C. Steil, J.P. Pirard, C. Henrist, A. Rulmont, R. Cloots, B. Vertruyen. Journal of the European Ceramic Society, 2007, 27:3469–3474.

[D.R. Tree 2007] D.R. Tree, K.I. Svensson. Progress in Energy and Combustion Science, 2007, 33, 272-309.

[A. Trovarelli 1996] Alessandro Trovarelli. Catalysis Reviews-Science and Engineering, 1996, 38:439-520.

[Y.V. Tyurkin 1997] Y.V. Tyurkin, L.A. Chesalov, E.N. Luzhkova. Reaction Kinetics and Catalysis Letters, 1997, 60:279-284.

[M. Uenishi 2005] M. Uenishi, M. Taniguchi, H. Tanaka, M. Kimura, Y. Nishihata, J. Mizuki, T. Kobayashi. Applied Catalysis B: Environmental, 2005, 57:267-273.

[M.-H. Um 2000] M.-H. Um, H. Kumazawa. Journal of Materials Science, 2000, 35: 1295-1300.

[M. Václavík 2017] Marek Václavík, Marie Plachá, Petr Kočí, Miloš Svoboda, Thomas Hotchkiss,Vladimír Novák, David Thompsett. Materials Characterization. 2017, 134:311-318.

[R.J.H. Voorhoeve 1974] R.J.H. Voorhoeve, J.P. Remeika, L.E. Trimble. Materials Research Bulletin, 1974, 9:1393–1404.

[R.J.H. Voorhoeve 1975] R.J.H. Voorhoeve, J.P. Remeika, L.E. Trimble et al. Journal of Solid State Chemistry, 1975, 14: 395–406.

[R.J.H. Voorhoeve 1976] R.J.H. Voorhoeve, J.P. Remeika, L.E. Trimble. Annals of the New York Academy of Sciences, 1976, 272:3–21.

[R.J.H. Voorhoeve 1977] R.J.H. Voorhoeve. Advanced Materials in Catalysis. Academic Press: New York, 1977.

[E. Vouitsis 2003] E. Vouitsis, L. Ntziachristos, Z. Samaras. Progress in Energy and Combustion Science, 2003. 29: 635-672.

[A. Vressner 2010] A. Vressner, P. Gabrielsson, I. Gekas et al. SAE Technical Paper, 2010, 2010-01-1216.

[X. Wang 2012] X. Wang, Y.X. Zhang, Q. Li, Z.P. Wang, Z.L. Zhang. Catalysis Science & Technology, 2012, 2:1822–1824.

[J.H. Wang 2015] Jihui Wang, Hong Chen, Zhicheng Hu, Mingfa Yao, Yongdan Li. Catalysis Reviews-Science and Engineering, 2015, 57(1):79-144,

[P. Whitaker 2011] P. Whitaker, P. Kapus, M. Ogris, P. Hollerer. SAE Technical Paper, 2011, 2011-01-1219.

[A. Williams 2006] A. Williams, R.L. McCormick, R.R. Hayes et al. SAE Technical Paper, 2006, 2006-01-3280.

[H. Xu 2006] H. Xu, S. Wei, H. Wang, M. Zhu, R. Yu, H. Yan. Journal of Crystal Growth, 2006, 292:159-164.

[J. Xu 2014] J. Xu, Y. Wei, Y. Huang, J. Wang, X. Zheng, Z. Sun, L. Fan, J. Wu. Ceramics International, 2014, 40:10583-10591.

[I.S. Yakovleva 2013] I.S. Yakovleva, A.N. Nadeev, E.Yu. Gerasimov, D.V. Ivanov, L.S. Dovlitova, E.F. Sutormina, N.F. Saputina, G.S. Litvak, L.A. Isupova. Kinetics and Catalysis, 2013, 54:119–129.

[M. Yashima 1994] M. Yashima, H. Arashi, M. Kakihana and M. Yoshimura. Journal of the American Ceramic Society, 1994, 77:1067–1071.

[D.Y. Yoon 2015] Dal Young Yoon, Young Jin Kim, Ji Hyun Lim, Byong K. Cho, Suk Bong Hong, In-Sik Nam, Jin Woo Choung. Journal of Catalysis, 2015, 330: 71–83.

[R. Zhan 2010] R. Zhan, S. Eakle, P. Weber. SAE Technical Paper, 2010, 2010-01-0365.

[S. Zhang 2004] S. Zhang, J. Liu, Y. Han, B. Chen, X. Li. Materials Science and Engineering: B, 2004, 110:11-17.

[Y. Zhang-Steenwinkel 2004] Y. Zhang-Steenwinkel, L.M. van der Zande, H.L. Castricum, A. Bliek. Applied Catalysis B: Environmental, 2004, 54:93–103.

[Q. Zheng 2015] Qinghe Zheng, Robert Farrauto, Michel Deeba, Ioannis Valsamakis. Catalysts, 2015, 5:1770-1796.

[Q. Zheng 2019] Qinghe Zheng, Marty Lail, Kelly Amato, Jonathan Todd Ennis. Catalysis Today, 2019, 320: 30-39.

[X. Zhu 2013] X. Zhu, H.-R. Cho, M. Pasupong, J.R. Regalbuto. ACS Catalysis, 2013, 3:625–630.

Chapter III. Experimental methods and techniques

3.1. Synthesis protocols

Different synthesis protocols were adopted to fabricate perovskite catalysts depending on specific needs.

3.1.1. Conventional Citric Method (CCM)

Conventional Citric Method (CCM) was used for the synthesis of bare perovskite. This method is based upon the sol-gel route proposed by Taguchi [H. Taguchi 1997] using citric acid as the chelating agent. Metal nitrate precursors were dissolved in an aqueous solution and then mixed with equal molar amount of citric acid (n(citric acid)=n (sum of metal nitrates)). The as-prepared solution was transferred to evaporation flask and subject to rotative evaporation with moderate conditions (heating temperature of 60°C, rotating velocity of 30 rpm) in order to form a gel. The mixture was then dried in a static oven at 80°C for 48 hours and a mushroom-like solid was obtained. The solid was finally calcinated at 600°C for 8 hours to get perovskite products (Fig. 3.1.).

This simple technique allows products with high homogeneity and medium yield. Thus it is suitable for the synthesis of perovskite material in a lab-scale. The main shortage of CCM lies in the low specific surface area and poor pore structure which restrains the improvement of the textural properties of the catalyst.
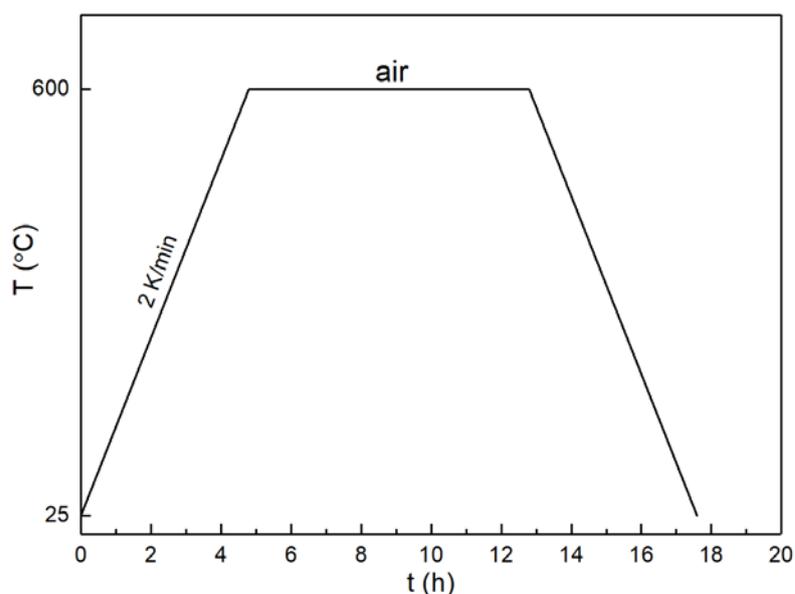
Fig. 3.1. Calcination procedure for bare perovskite

3.1.2. Macro-Structuring Method (MSM)

Macro-structuring method was used to synthesize perovskite three-dimensionally ordered macroporous (3DOM) structure. This method involves a surfactant-templating strategy to improve the textural properties of the perovskite. Previous studies have demonstrated that introduction of a surfactant during synthesis process would result in the generation of mesoporous or macroporous walls beneficial to the improvement of physicochemical properties of the catalyst.[C.X. Liu 2008; H.N. Li 2009; Y. Liu 2012] The interconnected and regular pore structure and large specific surface area would allow better mass transfer and enhanced catalytic activity for soot oxidation.

In our experiment, 3DOM perovskite was synthesized by Colloidal Crystal Templating (CCT) approach adapted from the protocol proposed by Feng [N. Feng 2017]. Monodisperse polymethyl methacrylate (PMMA) spheres were firstly packed into colloidal crystals by centrifugal forces. The obtained matter was dried at 60°C for 12 hours and then sieved to acquire PMMA template with diameters between 1 mm and 1.5 mm. Nitrate precursors with appropriate ratios were dissolved in a mixed solution consisting of 40 vol.% methanol and 60 vol.% ethylene glycol. The mixture was stirred overnight with a stirring velocity of 300 rpm. Then, the PMMA template was soaked in the solution for 6 hours followed by vacuum filtration to remove excess solution. The obtained solid was dried at room temperature in a drying chamber containing silicone gel until complete dryness. The as-prepared mixture was calcinated in a tubular furnace oven following protocol depicted in Fig. 3.2.
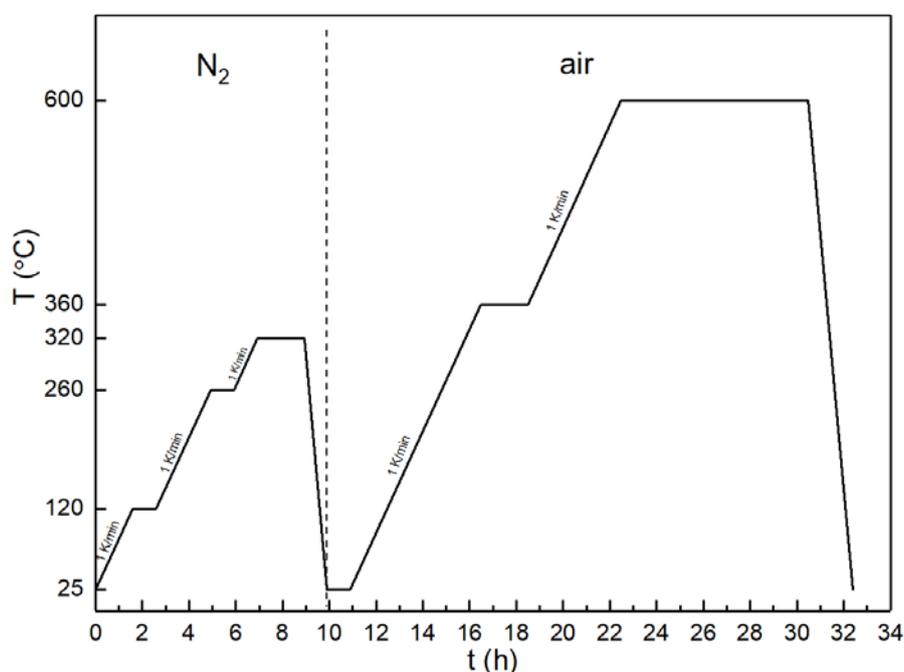
Fig. 3.2. Calcination procedure used for Macro-Structuring Method (MSM)

3.1.3. Incipient Wet Impregnation Method (IWIM)

Noble metal was loaded on bare perovskite by Incipient Wet Impregnation Method (IWIM). $Rh(NO_3)_3 \cdot xH_2O$ and $Pd(NO_3)_2 \cdot xH_2O$ were used as precursors for loading Rh and Pd on perovskite support respectively. At first, the weighed nitrate precursor was dissolved in an aqueous solution and transferred to a volumetric flask of 250 ml. 1.00 g bare perovskite was put into an evaporation flask of 100 ml. An accurate amount of noble metal solution was then

added to the solid followed by diluting with 30 ml ultra-pure water. Afterwards, the abovementioned flask containing the mixture was mounted on a rotative evaporator to undergo evaporation with moderate velocity until complete dryness. The obtained solid was calcinated following the same protocol depicted in Fig .3.1 except a lower temperature used (400°C for 8 hours instead of 600°C for 8 hours). Finally, the PGM-loaded perovskite was acquired.

3.2. Physicochemical characterisation of solid catalyst

3.2.1. Inductively Coupled Plasma Atomic Emission Spectroscopy (ICP-AES)

Inductively Coupled Plasma Atomic Emission Spectroscopy (ICP-AES) was performed at REALCAT platform in order to examine elemental composition of the catalyst. 20 mg sample was digested in aqua regia and then heated at 110°C for 100 min. After diluting with ultra-pure water, the sample was pumped into a nebulizer and then introduced to the plasma flame. Intensity of the characteristic wavelength emitted by a certain element was measured by a photomultiplier and concentration of the element was computed by comparing the intensities of the characteristic lines of the element with that of the standard sample.

3.2.2. X-ray diffraction

X-ray diffraction (XRD) experiment was performed at room temperature using Bruker AXS D8 diffractometer (Cu K_α source, λ=0.154 nm). Principle of XRD is based upon Bragg equation:

$$2d\sin\theta = n\lambda \qquad (eq.\,3-1)$$

Where
d − spacing between diffracting planes
θ − incident angle of the incoming beam
λ − wavelength of the beam
n − integer

Diffraction data were collected in the 2θ range of 5-120 degree with a step of 0.02 degree. Unit cell parameters were calculated by means of Rietveld refinement. Crystal size was calculated by Williamson-Hall approach using LaB_6 as standard. Standard deviations were obtained by Bérar correction.

3.2.3. H₂-TPR

Reducibility of catalysts was evaluated by means of H_2 Temperature-Programmed Reduction (H₂-TPR) experiment using Micromeritics AutoChem 2920. 50 mg sample was exposed to diluted hydrogen atmosphere (5 vol.% H_2/He) with a flowrate of 50ml/min and underwent heating from room temperature to 1000°C with a heating rate of 5 K/min. A thermal conductive detector was employed to monitor the evolution of hydrogen concentration. Hydrogen consumption was obtained by calculating the difference between reference material and the sample. A cold trap containing iso-ethanol was used to catch the water produced during reaction.

3.2.4. O$_2$-TPD

Oxygen mobility of catalysts was investigated through O$_2$ Temperature-Programmed Desorption (O$_2$-TPD) experiment using Micromeritics AutoChem2920. At first, 50 mg sample was exposed to pure oxygen and heated to 600°C with a heating rate of 10 K/min and then kept at 600°C during 1h. After cooling down to room temperature, the aforementioned sample was exposed to pure helium and reheated to 1000°C with a heating rate of 10 K/min. Desorbed oxygen was captured by a thermal conductive detector. A mass spectroscopy was linked to the detector to identify precisely the desorbed species during temperature rise.

3.2.5. N$_2$-physisorption

Textural properties of catalysts were examined by N$_2$-physisorption using Micromeritics Tristar analyser. Prior to measurement, a degasing procedure under vacuum during 4 hours was adopted to get rid of impurities attached to the sample. Specific surface area (SSA) was obtained according to Brunauer-Emmett-Teller (BET) theory and pore size distribution was acquired based upon Barret-Joyner-Halenda (BJH) theory. It should be mentioned that characteristic information related to catalyst pores, including pore size distribution, pore volume and average pore size, were deducted from the desorption process.

3.2.6. Raman spectroscopy

Raman spectroscopy analysis was conducted using Renishaw 2000 Laser Raman Spectrometer. Raman spectra were collected using an Ar$^+$ ion laser in confocal mode (excitation wavelength of 532 nm) combined with a Peltier-cooled CCD detector. A 50× long working distance objective was employed for focusing the excitation bean on the sample. Neutral density filters were used to reduce laser power in order to avoid sample damage.

3.2.7. X-ray Photoelectron Spectroscopy (XPS)

X-ray photoelectron spectroscopy analysis was performed with a Kratos Axis Ultra spectrometer. This instrument is equipped with a monochromatised Al Kα source (15 mA, 14 KV) and a charge compensation gun. The instrumental work function was calibrated to Au 4f$_{7/2}$ metallic god with binding energy of 83.95 ev. The recorded spectra were charged corrected by attributing C 1s spectral component a binding energy of 285.0 ev. Spectra analysis was carried out using Casa XPS software. A Gaussion(70)-Lorentzian(30) line profile was adopted for peak deconvolution . Calculation of surface atomic composition was conducted by relative sensitivity factor analysis method using Shirley background type.

3.2.8. Scanning Electron Microscopy (SEM)/ Energy-dispersive X-ray spectroscopy (EDS)

Morphology of catalysts was investigated by Scanning Electron Microscopy (SEM) using a Hitachi S-4700 Cold Field Emission Gun Scanning Electron Microscope operating at an acceleration voltage of 15kV with an resolution of 1.5 nm. Two secondary detectors

were included: one above the objective lens and the other below. Energy-dispersive X-ray Spectroscopy (EDS) is a useful technique for conducting elemental analysis or chemical characterization of a sample. Oxford EDS system was employed to analyze elemental composition of the prepared catalysts.

3.2.9. Chemisorption

Pulse chemisorption technique was used to examine the dispersion of noble metal on the surface of the support. 200 mg sample was firstly heated to 300℃ under diluted hydrogen (5 vol.% H_2/He) with a heating rate of 10 K/min and then reduced at 300℃ for 2 hours. Afterwards, the said sample was purged with pure argon at 300℃ for 1 hour and cooled down under argon to room temperature. Chemisorption was carried out by injecting 10 pulses of hydrogen with an interval of 5 minutes under argon with a flowrate of 50 ml/min. Dispersion of noble metal on the surface was computed assuming an overall stoichiometry of M:H_2=1:1 (M=Pd, Rh). Particle size was estimated assuming a hemispherical geometry.

3.3. Catalytic activity measurements

3.3.1. Experimental setup and protocols

Catalytic performance tests were carried out in the lab-scale experimental set-up illustrated in Fig. 3.3.
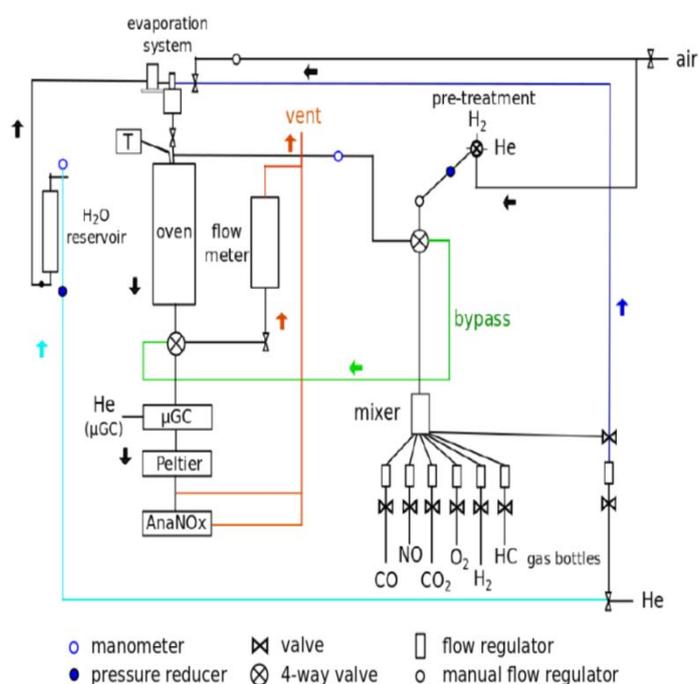
Fig. 3.3. Schematic demonstration of catalytic test setup. Left: real scene; Right: Process instrumentation diagram (with permission from A. Schön 2015)

Fixed bed reactor was employed on 200 mg catalysts in powder form sieved between 100-200 μm. Equal amount of SiC was added to the catalyst to acquire better performance of mass and heat transfer. Composition of inlet gas mixture is shown in Table 3.1. Successive

temperature-programmed reaction experiments were conducted in stoichiometric, lean and rich condition in the temperature range of 100-550 °C. Different test procedures were adopted depending on the composition of catalyst. The composition of outlet gas was monitored by a Thermo Scientific Model 42i-HL chemiluminescence NO_x analyser (denoted as AnalNOx in Fig. 3.3.) and an Agilent 490 Micro Gas Chromatography for the purpose of quantification of N_2, N_2O, O_2, CO, C_3H_6 and C_3H_8. The total feed flowrate was fixed to12 L h^{-1}, corresponding to a Gas Hourly Space Velocity (GHSV) of 60000 mL h^{-1} g^{-1}. It must be emphasized that such operating condition has been verified by previous researcher that can ensure the exclusion of influence of outer diffusion on the evaluation of catalytic performance.

Table 3.1. Composition of inlet gas mixture during temperature-programmed experiment

Gas (vol.%)	NO	CO	C_3H_6	C_3H_8	H_2	O_2	CO_2	H_2O	He
Stoichiometric	0.1	0.7	0.0450	0.0225	0.2333	0.7318	15	10	balance
Lean	0.1	0.5	0.0300	0.0150	0.1667	0.9048	15	10	balance
Rich	0.1	0.9	0.0600	0.0300	0.3000	0.5486	15	10	balance

Conversion of CO, C_3H_6, C_3H_8, O_2 can be expressed as:

$$X_A = \frac{X_{A0} - X_A}{X_{A0}} \times 100\% \qquad (eq.\,3-2)$$

Conversion of NO in stoichiometric and lean condition can be expressed as Eq.3-3 by taking into account only N_2 and N_2O as reduction products:

$$X_{NO} = \frac{2(N_2 + N_2O)}{NO_{inlet}} \times 100\% \qquad (eq.\,3-3)$$

Conversion of NO in rich condition was calculated according to eq.3-4:

$$X_{NO} = \frac{X_{NO_{inlet}} - X_{NO}}{X_{NO_{inlet}}} \times 100\% \qquad (eq.\,3-4)$$

Ammonia amount was estimated according to mass balance of nitrogen:

$$NH_3 = NO_{inlet} - NO_{outlet} - 2N_2 - 2N_2O \qquad (eq.\,3-5)$$

Selectivity of N_2, N_2O and NH_3 were calculated by Eq.3-6, Eq.3-7 and Eq.3-8 respectively:

$$S_{N_2} = \frac{2N_2}{2(N_2 + N_2O) + NH_3} \qquad (eq.\,3-6)$$

$$S_{N_2O} = \frac{2N_2O}{2(N_2 + N_2O) + NH_3} \qquad (eq.\,3-7)$$

$$S_{NH_3} = \frac{NH_3}{2(N_2 + N_2O) + NH_3} \qquad (eq.\,3-8)$$

Yield of N_2, N_2O and NH_3 were calculated by Eq.3-9, Eq.3-10 and Eq.3-11 respectively

$$Y_{N_2} = X_{NO}S_{N_2} \qquad (eq.\,3-9)$$

$$Y_{N_2O} = X_{NO}S_{N_2O} \qquad (eq.\,3-10)$$

$$Y_{NH_3} = X_{NO}S_{NH_3} \qquad (eq.\,3-11)$$
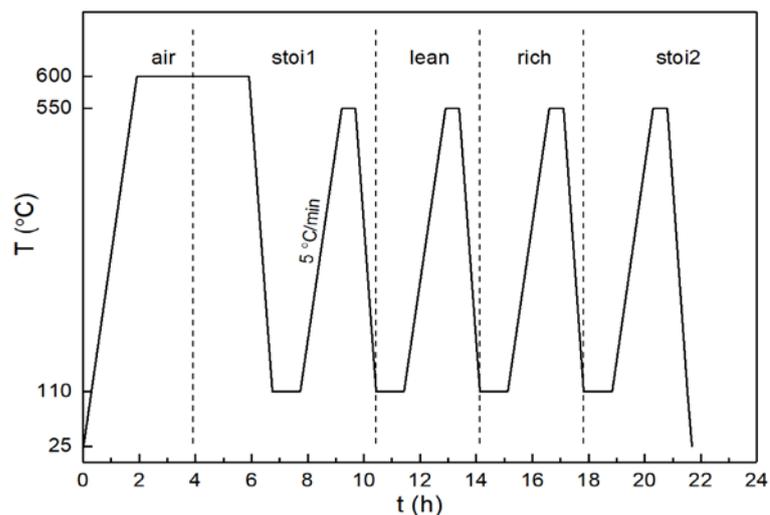
Fig. 3.4. Procedure A. Experimental protocol employed for bare perovskite catalyst

Procedure A was employed for testing bare perovskite. A preliminary thermal treatment was done at 600°C under air during 2h and then under stoichiometric feed during 2 h. After cooling down to 110°C, the catalyst was successively exposed to stoichiometric1 (denoted as stoi1), lean, rich and stoichiometric2 (denoted as stoi2, return test) atmosphere. A heating rate of 5 K/min and cooling rate of 10 K/min were adopted during heating-up and cooling-down respectively. The plateau corresponding to the maximum temperature (550°C) was kept for 0.5 hour to allow enough time for the stabilization of reaction. A waiting time of 1 h was spared before launching the heat-up process to guarantee homogeneous mixture of the feed stream.
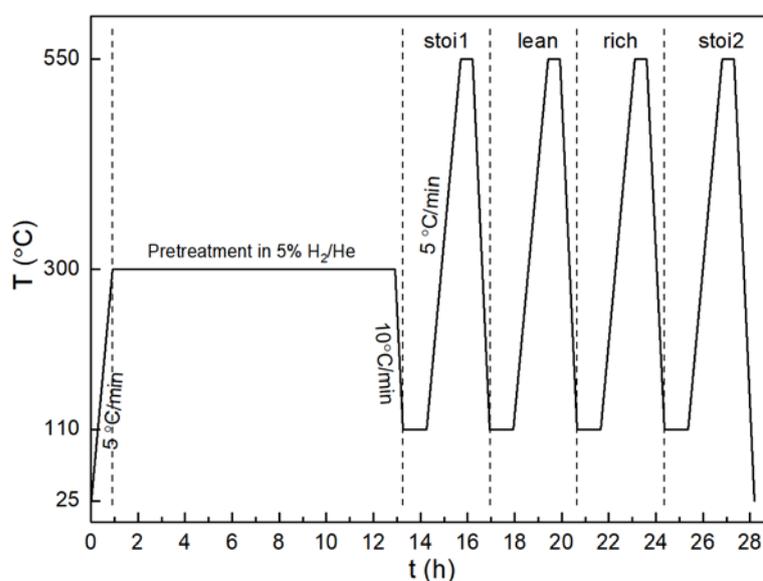
Fig. 3.5. Protocol B. Experimental protocol for PGM-loaded perovskite catalyst

Protocol B was used to perform catalytic test for the PGM-loaded perovskite catalyst. It involves a thermal pretreatment at 300 °C under diluted hydrogen during 12 hours before

proceeding to stoi1, lean, rich and stoi2 in a sequential order. Such thermal pretreatment aims to process the raw surface of the catalyst, beneficial to the redispersion of noble metal on the surface and stabilization of noble metal species in oxidized state. The same heating rate and cooling rate as protocol A were employed during each temperature-programed step.

3.3.2. Estimation of reaction rate and kinetic parameters

Reaction rate of oxidation of CO and C_3H_6 were calculated at appropriated temperature assuming a plug-flow reactor model. Given the low concentration of CO and C_3H_6 compared to O_2, a first-order reaction with respect to CO and C_3H_6 was adopted for the calculation of kinetic parameters. [J.L. Hueso 2009; G. Parravano 1953; A. Schön 2015]

Rate constant of oxidation reaction can be calculated in the equation 3-12:

$$k(T) = \frac{Q_0}{m_{catalyst}} \ln\left(\frac{1}{1 - X_A(T)}\right) \qquad (eq. 3 - 12)$$

where

$k(T) -$ rate constant corresponding to temperature $T, m^3\ g^{-1}\ s^{-1})$

$Q_0 -$ total volumetric feed flowrate, m^3/s

$m_{catalyst} -$ caatalyst weight, mg

$X_A(T) -$ conversion of reactant A corresponding to a certain temperature T

Specific reaction rate ($r_{specific}$) was calculated according to Eq.3-13:

$$r_{specific}(T) = k(T)\frac{F_{A0}}{Q_0}\left(1 - X_A(T)\right) \qquad (eq. 3 - 13)$$

where

$r_{specific}(T) -$ specific reaction rate of reactant A at a given temperature $T, mol\ s^{-1}g^{-1}$

$k(T) -$ rate constant corresponding to temperature $T, m^3\ g^{-1}\ s^{-1})$

$F_{A0} -$ inlet molar flowrate of reactant $A, mol\ s^{-1}$

$Q_0 -$ total volumetric feed flowrate, m^3/s

$X_A(T) -$ conversion of reactant A corresponding to a given temperature T

Intrinsic reaction rate ($r_{intrinsic}$) was calculated by Eq.3-14:

$$r_{intrinsic}(T) = \frac{r_{specific}(T)}{SSA} \qquad (eq. 3 - 14)$$

$r_{intrinsic}(T) -$ intrinsic reaction rate of reactant $A\ , mol\ s^{-1}m^{-2}$

$SSA -$ specific surface area of the catalyst, m^2/g

Arrhenius plots were drawn by taking into account the temperature range in which the conversion of CO or C_3H_6 oxidation remained less than 40% in the light-off curves. Pre-exponential factor (A) and apparent energy (E_{app})can accordingly be deduced:

$$E_{app} = -Ra, \quad kj\ mol^{-1} \qquad\qquad (eq. 3 - 15)$$

$$A = e^b, \quad m^3s^{-1}g^{-1}, \qquad\qquad (eq. 3 - 16)$$

where a and b represents the slope and the intercept extrapolated from the Arrhenius plot.

Reference

[N. Feng 2017] Nengjie Feng, Chong Chen, Jie Meng et al. Catalysis Science & Technology, 2017,7:2204-2212.

[J.L. Hueso 2009] J.L. Hueso, D. Martínez-Martínez, A. Caballero et al. Catalysis Communications, 2009, 10:1898–1902.

[H.N. Li 2009] H.N. Li, L. Zhang, H.X. Dai, H. He. Inorganic Chemistry, 2009, 48:4421-4434.

[C.X. Liu 2008] C.X. Liu, L. Zhang, J.G. Deng, Q. Mu, H.X. Dai, H. He. Journal of Physical Chemistry C, 2008, 112:19248-19256.

[Y. Liu 2012] Yuxi Liu, Hongxing Dai, Yucheng Du et al. Journal of Catalysis, 2012, 287:149-160.

[G. Parravano 1953]G. Parravano. Journal of the American Chemical Society, 1953, 75, 6:1497-1498.

[A. Schön 2015] A. Schön. Development of alternative 3-way catalysts: Fe-based perovskites with low noble metal content. Thesis, 2015.

[H. Taguchi 1997] Hideki Taguchi, Shin-ichiro Matsu-ura, Mahiko Nagao. Journal of Solid State Chemistry, 1997, 129:60-65.

.

PART A

Benchmark Three-Way PGM-doped Catalysts

Chapter IV. PGM-doped reference Three-Way-Catalysts: Pd/Ce$_x$Zr$_{1-x}$O$_2$

Chapter IV. PGM-doped reference Three-Way-Catalysts: Pd/Ce$_x$Zr$_{1-x}$O$_2$

This first chapter will be devoted to reference supported catalysts on ceria-zirconia mixed oxides recognized as efficient Three-Way-Catalyst (TWC). Among, the different active precious metal, palladium is usually the cheapest one in comparison with platinum and rhodium but not the most active especially towards the selective reduction of NO to nitrogen. Generally, rhodium is privileged because NO dissociates on its surface more readily. However, Pd-only catalysts can be efficient to regulate CO and unburnt hydrocarbons. Traditionally, commercial Pt-Rh standard systems are usually set up but in more modern configurations a front Pd-only monolith can be incorporated [M. Pilar Gonzales-Marcos 2012]. One challenging question is related to the development of cheapest Pd-TWC free of rhodium which could reasonable fulfill the near future more stringent standard limitation. In practice, the oxidation state of palladium can strongly influence its catalytic performances and is still under debate [M. Pilar Gonzales-Marcos 2012]. Several investigations reported that PdO exhibited higher activity [C. Thomas 2006; M.F. Luo 2006] but the thermal stability of PdO was found as a crucial parameter to monitor appropriately the oxidation state of palladium when the redox nature of the atmosphere changes.

Currently, ceria itself sharply improves the Oxygen-Storage-Capacity of TWC associated to the Ce^{4+}/Ce^{3+} redox couple but exhibit serious drawback due to its low thermal stability inducing loss of OSC properties. Zirconium incorporation has been found to strengthen thermal stability, durability and jointly to stabilize the dispersion of PGM particles [A. Iglesias 2004; Y. Cui 2018; Q. Wang 2011 a-b]. The current running temperature conditions also affect the stability of the supported active phase depending on the atmosphere in typical cycling conditions. By way of illustration Lupescu et al. [J.A. Lupescu 2016] that significant deteriorations of the catalyst take place in rich conditions because strong metal support interaction induces a loss of exposed Pd surface but also in lean aging conditions which favor PdO particle sintering.

The use of Ce$_x$Zr$_{1-x}$O$_2$ solid solutions can stabilize the dispersion of Pd. The intrinsic properties of the support can be also profitably used to promote the removal of CO through the Water-Gas shift and reforming reactions thank to the creation of new active sites at the metal support interface [J. Kašpar 2004].

Cerium-Zirconium mixed oxides with variable cerium/zirconium ratio have been extensively studied as potential substitutes for conventional ceria in the formulation of three way catalyst (TWC) because of their extraordinary oxygen storage/release capacity. [T. Murota 1993; G. Colón 1998; A. Trovarelli 2002; B. de Rivas 2011; N. Guillén-Hurtado 2012] One of the biggest advantages of such mixed oxide system lies in the enhanced catalytic properties after redox and thermal treatment, especially at high temperature. [M. Fernández-García 2002] According to previous studies, optimal properties (such as oxygen storage capacity (OSC), resistance to thermal sintering) can be achieved on Ce-Zr solid solution with tetragonal symmetry and Ce/Zr ratio close to 1:1. [M. Yashima 1994 a-b; G. Vlaic 1999] Basically, three types of tetragonal phases co-exist: the stable *t* phase and

metastable *t'* and *t''* phase [M. Yashima 1993, 1994 a-b]. Although Ce-Zr mixed oxide with Ce/Zr ratio equivalent to 1:1 is thermodynamically unstable below 1200°C, metastable structure (*t'* phase and *t''* phase) is often involved in catalytic application because of better stabilization by small particle size [J. Kašpar 1999].

However, these catalytic performances can be intimately related to the selected method for their preparation with the aim to monitor properly the Pd-support interface. Based on this several methodologies have been already investigated such as co-precipitation, supercritical drying, sol-gel, micro-emulsion and impregnation methods. Wang et al. [Q. Wang 2010, 2011 a] showed that the supercritical drying and micro-emulsion routes led to the best properties with a widening of the operating window. These enhancements were related to smaller crystallite size jointly with specific surface area improvement and better thermal stability. Nevertheless, remarkable properties in terms of redox properties and thermal stability were obtained on TWC simply prepared by co-precipitation combined with hydrothermal treatment [J. Deng 2018]. The gain observed on the resulting catalytic properties of Pd/Ceria-zirconia catalysts has been ascribed to the stabilization of a larger proportion of Pd^{2+}.

This chapter will provide a comparative study of supported 0.5 wt.% Pd on ceria-zirconia mixed oxide. Ce$_x$Zr$_{1-x}$O$_2$ solid solutions were prepared according to a classical co-precipitation method and a Flame-Spray-Pyrolysis FSP methods. It is generally accepted that co-precipitation can lead to catalytic materials having high specific surface area but they currently lose specific surface area when they are exposed to high temperature. FSP method involves high temperature which in principle should lead to higher thermal resistance and can also lead to high specific surface area, i.e. 80 m^2/g after calcination at 900°C [W.J. Stark 2003]. This technique offers a high production rate [R. Mueller 2003] but optimization is not trivial for controlling the nucleation and condensation of nano-sized crystallites further avoiding their agglomeration. FSP synthesis of bare Ce$_{0.5}$Zr$_{0.5}$O$_2$ and Pd-modified Ce$_{0.5}$Zr$_{0.5}$O$_2$ samples were conducted by Lurederra, a Spanish small company involved in the European H2020-Partial-PGMs project. Co-precipitated samples were supplied by Johnson Matthey. Elemental analysis is summarized in Table 4.1. showing in all case Zr-rich composition irrespective of the selected preparation methods.

Table 4.1. Elemental analysis of reference Three Way Catalyst

Catalyst	Atomic composition (%)				Ce/Zr
	Ce	Zr	O	Pd	
bare Ce$_{0.5}$Zr$_{0.5}$O$_2$-COP	6.19	11.29	82.51	-	0.55
bare Ce$_{0.5}$Zr$_{0.5}$O$_2$-FSP	8.41	14.40	77.19	-	0.58
Pd/Ce$_{0.5}$Zr$_{0.5}$O$_2$ -COP	7.78	11.41	80.65	0.16	0.68
Pd/Ce$_{0.5}$Zr$_{0.5}$O$_2$-FSP	4.59	8.72	86.60	0.09	0.53

4.1. Structural properties

4.1.1. XRD analysis

Currently, X-ray diffraction pattern on CeO$_2$ (not reported in Fig. 4.1) exhibits intense (111), (200), (220) and (311) reflection at 2 θ values of 28.5°, 33.0°, 47.4°, 56.2°, corresponding to the cubic structure of CeO$_2$ (JCPDS 34-0394). For ZrO$_2$, generally the main reflection appears at 2θ values of 30.2°, 35.3°, 50.2°, 60.1° which characterizes a tetragonal structure (JCPDS 81-15). In the particular case of Ce$_x$Zr$_{1-x}$O$_2$ solid solution, shifts on the 2θ values can occur indicating that cerium is partially substituted by zirconium. As seen in Fig. 4.1, reference catalysts prepared by coprecipitation showed a tetragonal structure (PDF 04-014-8800, space group P4$_2$/nmc) with the most intense peak appearing at 2θ = 29.3° degree. In contrast, flame spry pyrolysis gave rise to crystals with co-existence of both cubic and tetragonal structure. There are some debates regarding the occurrence of metastable phases (*t'* and *t''*) as the Ce/Zr ratio is maintained close to 1:1. [J. Kašpar 1999] [T. Montini 2009] It is generally accepted that for Ce$_x$Zr$_{1-x}$O$_2$ system, lower Ce content, for x < 0.1, would favor the structure with the monoclinic symmetry whereas higher Ce content (x > 0.8) would be beneficial to the stabilization of cubic structure. For intermediate compositions with 0.1 < x <0.8, the phase composition is uncertain with the possibility of either single phase or co-existence of multiple phases (including stable *t* and metastable *t'* and *t''*). Indeed, phase boundaries depend heavily on the particle size and smaller crystallite size would favor the stabilization of tetragonal structure.[R.C. Garvie 1978] It should be mentioned that PdO$_x$ was not detectable by XRD due to the low Pd loading amount.
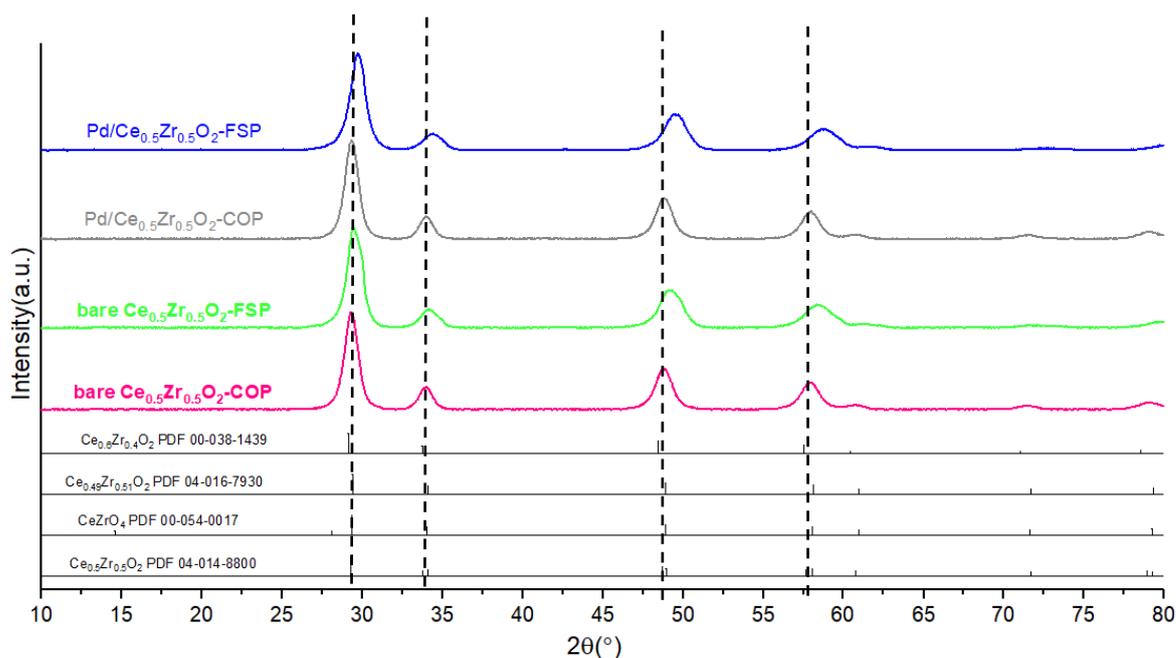
Fig. 4.1. X-ray diffractogram for reference TWC. Pink: bare Ce$_{0.5}$Ze$_{0.5}$O$_2$-COP; Green: bare Ce$_{0.5}$Ze$_{0.5}$O$_2$-FSP; Grey: Pd/ Ce$_{0.5}$Ze$_{0.5}$O$_2$-COP; Blue: Pd/ Ce$_{0.5}$Ze$_{0.5}$O$_2$-FSP.

4.1.2. Raman spectroscopy

The Raman spectra of bare and Pd-doped Ce$_{0.5}$Ze$_{0.5}$O$_2$ prepared by co-precipitation and Flame-Spray-Pyrolyis are reported in Fig. 4.2. As observed, quite similar spectral features characterized both catalysts with broad Raman lines appearing at 302 cm^{-1}, 468 cm^{-1} and 633 cm^{-1} instead of 312 cm^{-1}, 460 cm^{-1} and 632 cm^{-1} on FSP samples. An additional 251 cm^{-1} Raman line appears in on this latter system. According to literature [J. Jehng 1998], this additional peak is frequently observed in supported ceria specimens whose nature is unclear. It might be ascribed either to a localized vibration mode or an impurity-derived vibration mode.[M. Fernández-García 2002]. Exceptionally, less intense Raman lines appear on Pd/Ce$_{0.5}$Ze$_{0.5}$O$_2$-FSP which might be explained by the presence of oxygen vacancies in high concentration arising from the strong interaction between ceria-zirconia occurring at high temperature.[P. Esteves 2011]

Ceria-zirconia mixed oxides can be stabilized into different crystallographic structures depending on the composition and crystallite size. Regarding single oxides, a monoclinic structure for ZrO$_2$ should correspond to 18 active modes (9Ag + 9Bg) associated to a space group P21/c space group, On the other hand, 6 Raman active modes (A1g + 2B1g + 3E2g) agree with a tetragonal structure characterized by a P4$_2$/*nmc* space group. Generally, a prominent Raman line characterize the fluorite cubic structure of CeO$_2$ (465 cm^{-1}) corresponding to the Raman active mode F2g. By examining Raman spectra in Fig. 4.2., they essentially characterize a tetragonal structure in agreement with elemental analysis showing Ce/Zr ratios lower than the unity [P. Fornasiero 1996]. Only slight shift on the position of the F2g active mode are discernible on Ce$_{0.5}$Zr$_{0.5}$O$_2$ in comparison with current value in CeO$_2$ which could also suggest a marginal contribution of cubic structure in Ce-Zr FSP and Pd/Ce-Zr FSP.

The Raman line near 300 cm^{-1} can be explained by the displacement of oxygen atoms from their ideal fluorite lattice positions by the zirconium insertion into the CeO$_2$ lattice with the formation of the pseudo-cubic (*t''*) phase [M. Yashima 1994 a-b; S. Letichevsky 2005]. The Raman line near 155 cm^{-1} can be assigned to *t*-ZrO$_2$ phase [F. Zhang 2006]. Sharp broadening is observed on the 490 cm^{-1} Raman line especially on un-doped Pd ceria-zirconia mixed oxide irrespective of the preparation method which could be originated by crystallites size and increasing concentration of crystal defects essentially oxygen vacancies [M. Teng 2009]. The 620 cm^{-1} Raman line has been previously related to a non-degenerate Raman inactive longitudinal of CeO$_2$ reflecting disturbances of the local M-O bond chemistry leading to the relaxation of its symmetry [W. Mista 2004 ; B. Zhao 2010 a-b; B.M. Reddy, 2008]. This latter spectral feature reflects the presence of oxygen vacancies in the ceria lattice
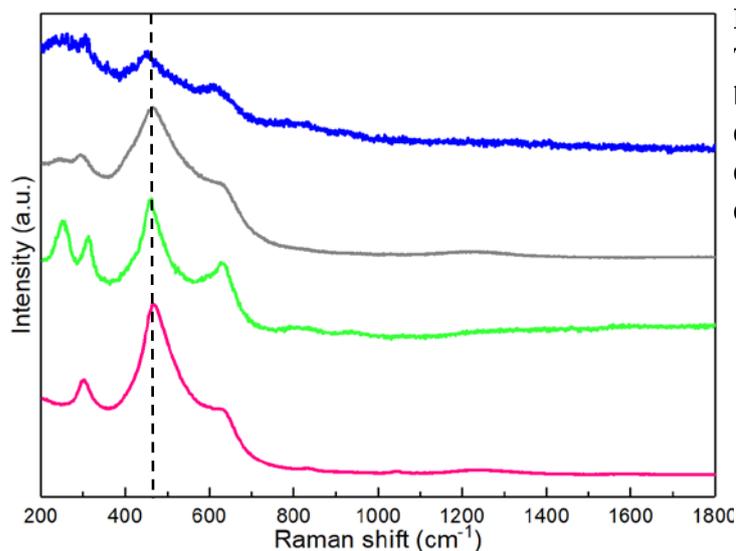
Fig. 4.2. Raman spectra for reference TWC (532 nm wavelength). Pink: bare $Ce_{0.5}Ze_{0.5}O_2$-COP; Green: bare $Ce_{0.5}Ze_{0.5}O_2$-FSP; Grey: Pd/$Ce_{0.5}Ze_{0.5}O_2$-COP; Blue: Pd/$Ce_{0.5}Ze_{0.5}O_2$-FSP.

4.1.3. Scanning Electron Microscopy coupled with EDS

Morphology of the reference TWC has been investigated by Scanning Electronic Microscopy coupled with Energy-dispersive X-ray Electronic spectroscopy. Images of Pd/$Ce_{0.5}Zr_{0.5}O_2$–COP are shown in Fig. 4.3. It can be seen that palladium dispersion on Ce-Zr support prepared by coprecipitation method is highly uniform without significant agglomeration of PdO$_x$ particles. Although it is possible that PdO$_x$ particles might be too small to be observed, one can still assume that the high homogeneity of Pd dispersion on the Ceria-Zirconia support made by coprecipitation method would allow a greater amount of active sites on the surface of the catalyst as well as enhanced thermal stability against sintering. In addition, other species including Ce, Zr and O are present in a highly homogeneous state without marked irregularity.

On the contrary, Pd dispersion on the Ceria-Zirconia support prepared by flame spray pyrolysis method is relatively uneven with reduced uniformity. SEM images (Fig. 4.4, last picture) confirmed the co-existence of Pd-rich zones (blank spot regions) and Ceria-Zirconia-rich zones. This may be linked with the agglomeration of small PdO$_x$ particles during thermal treatment of the feed solution. Besides, highlighted areas are identified for Ce, Zr and O species, suggesting that the Ce/Zr ratio of the Ceria-Zirconia solid solution prepared by flame spray pyrolysis is variable in different part of the mixed oxide. The inhomogeneity of Ceria-Zirconia support would facilitate the enrichment of PdO$_x$ on the Cerium-rich regions of the support due to the strong interaction between the two entities, which may constitute another possible explanation for the irregular dispersion of Pd on the Ceria-Zirconia support.
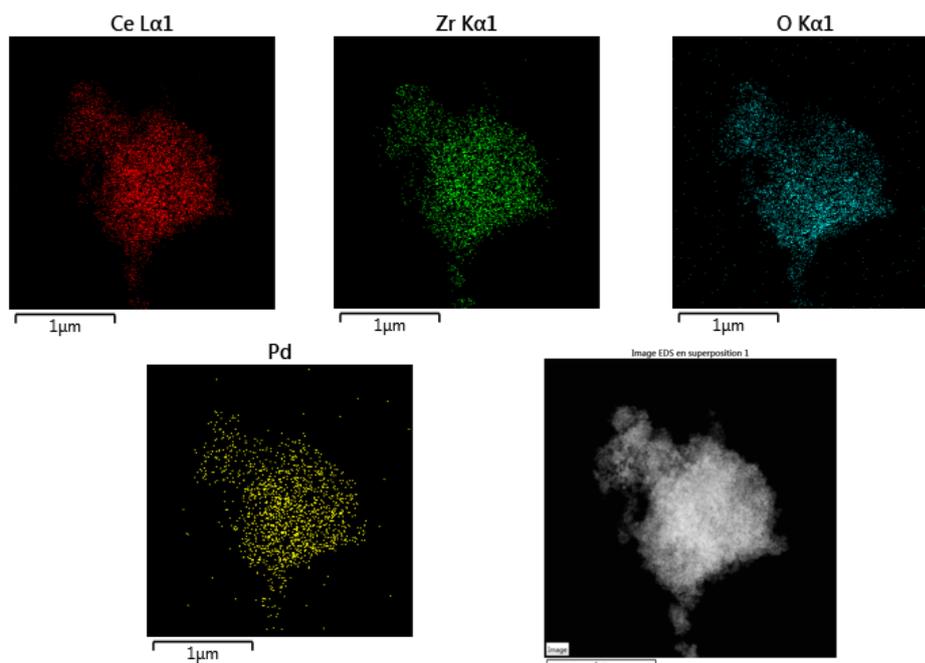
Fig. 4.3. Scanning Electronic Microscopy and Energy-dispersive X-ray spectroscopy images for Pd/Ce$_{0.5}$Zr$_{0.5}$O$_2$ –COP.
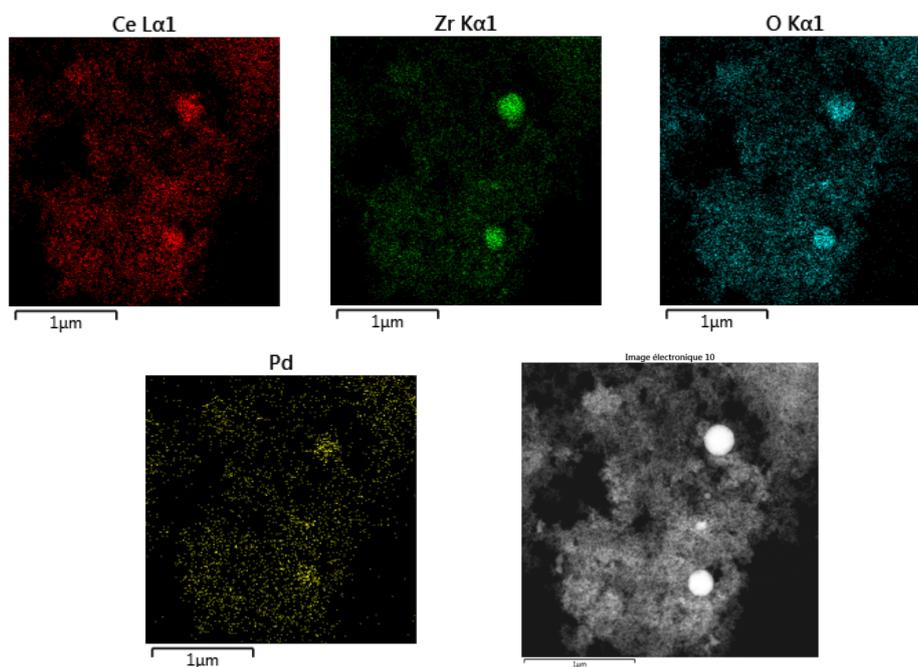
Fig. 4.4. Scanning Electronic Microscopy and Energy-dispersive X-ray spectroscopy images for Pd/Ce$_{0.5}$Zr$_{0.5}$O$_2$-FSP.

4.1.4. Reducibility

Redox properties of the reference TWC were examined from H$_2$-TPR experiment. Hydrogen consumption profiles vs. temperature are illustrated in Fig. 4.5. Bare CeO$_2$-ZrO$_2$ solid solution prepared by coprecipitation exhibited two consecutive peaks in the temperature range of 350-800°C, which are ascribed to reduction of surface and reduction of bulk of the

ceria-zirconia solid solution respectively the estimates of H/Ce is in agreement with the reduction of Ce^{4+} to Ce^{3+}. This is in conformity with previous investigations [H.C. Yao 1984]. Contrary to coprecipitation, bare CeO$_2$-ZrO$_2$ solid solution prepared by flame spray pyrolysis showed weak reducibility with faint intensity of reduction peak and the least hydrogen uptake quantity (0.62 mmol/g, Table 4.2.). In comparison with bare ceria-zirconia solid solution, Pd incorporation to ceria-zirconia solid solution resulted in a marked shift of reduction peaks towards low temperature region. It has been reported by some authors that when exposed to hydrogen Pd^{n+} present in palladium oxide can be easily reduced to metallic Pd^0 at room temperature.[N. Hickey 2001; R.A. Daley 2005]. In our observation, a rough estimate of H/Pd^{n+} ratio (not shown) of the Pd-loaded ceria-zirconia lead to much higher value than the expected for the H/Pd = 2, suggesting that consumption of hydrogen below 150°C should be reasonably attributed to the sum of both reduction of Pd^{n+} species and partial reduction of Ce$_{0.5}$Zr$_{0.5}$O$_2$. One tentative proposal might be that the strong interaction between Pd and the ceria-zirconia support would trigger the spillover of adsorbed hydrogen from Pd particles to support, leading to a more reducible Ce^{4+} species present in the interface between precious metal and support. Previous surveys claimed that PdO$_x$ species are in close contact with ceria-zirconia support and that the interface between Pd and support is the main active sites during H$_2$-TPR experiment. [S. Lin 2014] The splitting of reduction peak below 150°C may be accounted for by the concurrent yet independent reduction of Pd^{n+} and Ce^{4+} species. Surprisingly, the greatest hydrogen uptake was observed on bare ceria-zirconia prepared by coprecipitation method, which may arise from the contribution of highly reducible Ce^{4+}/Ce^{3+} in the bulk of the solid solution.

Returning to the low temperature reduction process, it is noticeable that the reduction is delayed on Pd/ CeO$_2$-ZrO$_2$-COP in comparison to Pd/ CeO$_2$-ZrO$_2$-COP. Such observations are consistent previous investigations which reported that PdO reduces to metallic Pd particles near 60-90°C on Pd/Ce-Zr-O systems [B. Zhao 2010 a, b]. In practice, the reduction temperature might depend on several parameters such as the nature of support materials interacting with PdO and the particle size. Generally, well-dispersed PdO reduces at higher temperature than larger ones (100°C instead of T≤50°C for large PdO clusters [H. Muraki 1989; I. Halasz 1992]. As the consequence the fact that PdO reduce more readily on Pd/ CeO$_2$-ZrO$_2$-FSP than on Pd/ CeO$_2$-ZrO$_2$-COP could be an indication that larger PdO particle forms on Pd/ CeO$_2$-ZrO$_2$-FSP which seems in reasonable agreement with STEM-EDS analysis.

Table 4.2. H$_2$-TPR analysis of reference TWC.

Catalyst composition	H$_2$ total consumption (mmol g^{-1})^a	H/Ce	T$_{max}$ of reduction peaks(°C)	
bare Ce$_{0.5}$Zr$_{0.5}$O$_2$-COP	7.10	1.05	375.8	611.3
bare Ce$_{0.5}$Zr$_{0.5}$O$_2$-FSP	0.62	0.09	-	533.1
Pd/Ce$_{0.5}$Zr$_{0.5}$O$_2$ -COP	1.05	0.15	109.2	370.9
Pd/Ce$_{0.5}$Zr$_{0.5}$O$_2$-FSP	0.89	0.13	77.2	430.1

Note : a H$_2$ total consumption was calculated in the temperature range of 50-800°C
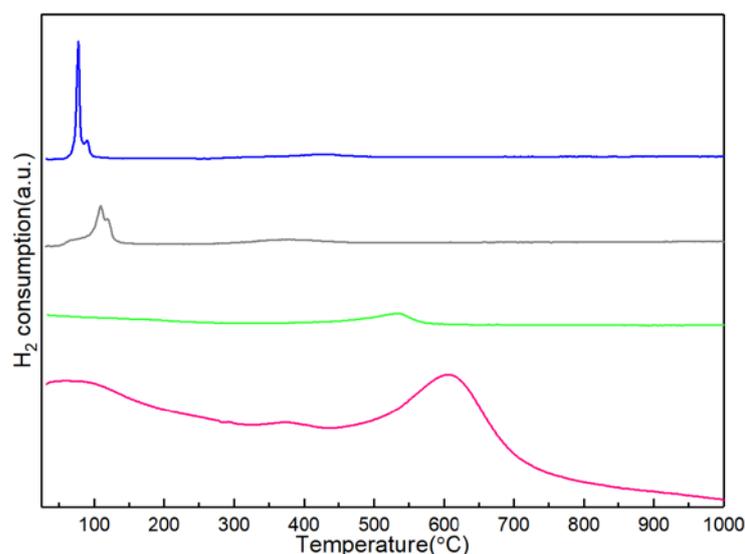
Fig. 4.5. H$_2$ consumption curves plotted against temperature for reference TWC. Pink: bare Ce$_{0.5}$Ze$_{0.5}$O$_2$-COP; Green: bare Ce$_{0.5}$Ze$_{0.5}$O$_2$-FSP; Grey: Pd/ Ce$_{0.5}$Ze$_{0.5}$O$_2$-COP; Blue: Pd/ Ce$_{0.5}$Ze$_{0.5}$O$_2$-FSP.

4.1.5. O$_2$-Temperature-Programmed Desorption experiments

Oxygen mobility of the reference TWC is investigated by O$_2$-TPD experiment. O$_2$ desorption profiles vs. temperature are reported in Fig. 4.6. Bare Ceria-Zirconia prepared by co-precipitation method demonstrated limited surface oxygen mobility with an onset of α-oxygen desorption temperature above 300°C. Further, Pd-loading on the Ceria-Zirconia COP led to a significant shift of α-oxygen desorption towards lower temperature region (below 200°C) with larger desorbed α-oxygen quantity. In contrast, discrepancies between bare Ceria-Zirconia FSP and Pd/Ceria-Zirconia FSP seemed not remarkable in terms of staring temperature of α-oxygen desorption, although a slight increase of desorbed α-oxygen quantity was observed on the latter which may be reasonably associated with incorporation of Pd. CeO$_2$-based catalysts are well-known for their exceptional OSC and high oxygen mobility. Introduction of Zr in the ceria lattice promotes OSC which may be explained by the generation of structural defects responsible for the enhancement of oxygen mobility. The presence of anionic vacancies is believed to be linked with the formation of highly reactive superoxide species upon oxygen adsorption. [D. Duprez 2001] It should be emphasized that both surface oxygen mobility and lattice oxygen mobility contribute to the OSC due to the fact that OSC is not only a surface phenomenon but also involves the diffusion of lattice oxygen atoms. [D. Duprez 2001] It has been observed that Zr substitution in ceria led to a distortion of the oxygen lattice stemming from the decrease of the coordination number of Zr^{4+} cations since surrounding oxygen atoms are driven out of the bonding distances, leading to improved mobility of oxygen atoms[G. Vlaic 1997, 1998, 1999]. The unique feature of Ce$_x$Zr$_{1-x}$O$_2$ mixed oxides is that promotion of OSC is attributed not only to the contribution of surface oxygen mobility but also to the involvement of bulk oxygen atoms. [Y. Madier 1999] However, in our experiment, desorption of bulk oxygen was only observed at high temperature (above 850°C) for all prepared reference catalysts, which is out of the operating

temperature range of TWC. This phenomenon indicates that OSC of the abovementioned reference catalysts is mainly governed by surface oxygen mobility under exposure to oxidizing/reducing atmosphere.
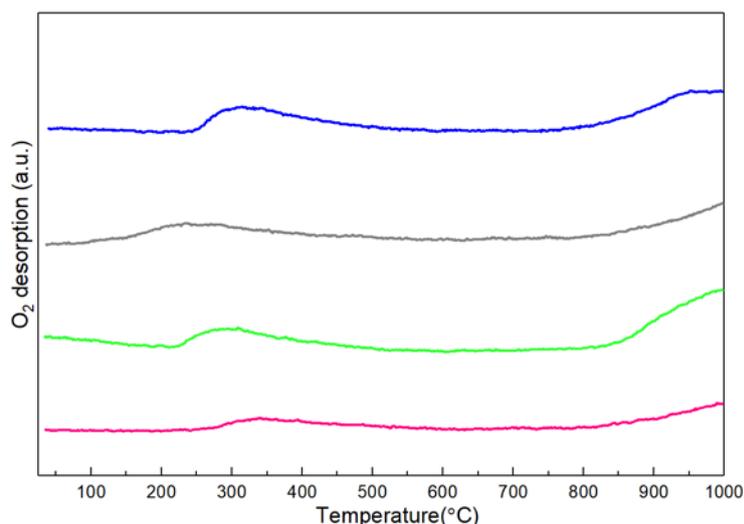
Fig. 4.6. O$_2$-Temperature-Programmed Desorption profiles plotted against temperature for reference TWC. Pink: bare Ce$_{0.5}$Ze$_{0.5}$O$_2$-COP; Green: bare Ce$_{0.5}$Ze$_{0.5}$O$_2$-FSP; Grey: Pd/Ce$_{0.5}$Ze$_{0.5}$O$_2$-COP; Blue: Pd/Ce$_{0.5}$Ze$_{0.5}$O$_2$-FSP.

4.2. Surface properties

4.2.1. Textural properties from N$_2$-physisorption

Ceria-zirconia solid solution prepared by coprecipitation method showed adsorption isotherms of type IV (see Figs. 4.7.) with obvious hysteresis loops in the relative pressure range of 0.6-1.0. A multilayer adsorption on a uniform surface is thus assumed to take place on these solids. In contrast, isotherm of flame spray pyrolysis is characterized by a steep ascent of adsorption curve and then a sharp descent of desorption curve at high relative pressure region with narrow hysteresis loop. A specific, reversible multilayer adsorption process within broadened pores is likely to occur considering the larger pore diameter observed for solid prepared by FSP method (Table 4.3.). Nevertheless, condensation effect cannot be completely ruled out in light of the unapparent hysteresis phenomenon. In this case, an isotherm of combination of type II and type IV is ascribed to solid made by FSP method. As shown in Fig. 4.7.(B), it is noticeable that solid prepared by COP method had a very narrow pore size distribution in contrast to the wide pore size distribution associated with FSP method. This reflects that coprecipitation method yields solid particles with better granule uniformity compared to FSP method. To resolve such problem, synthesis process involving various parameters (i.e. precursor type, solution feed velocity, residence time, flame temperature, etc.) need to be further optimized in order to generate product with more desirable particle regularity.

As shown in Table 4.3., the reference catalysts presented high surface area. The ceria-zirconia solid solution produced by coprecipitation method was around 70 m^2/g. It is worth noting that solid prepared by flame spray pyrolysis method gave rise to a high specific surface area as well as remarkably increased average pore diameter and pore volume.
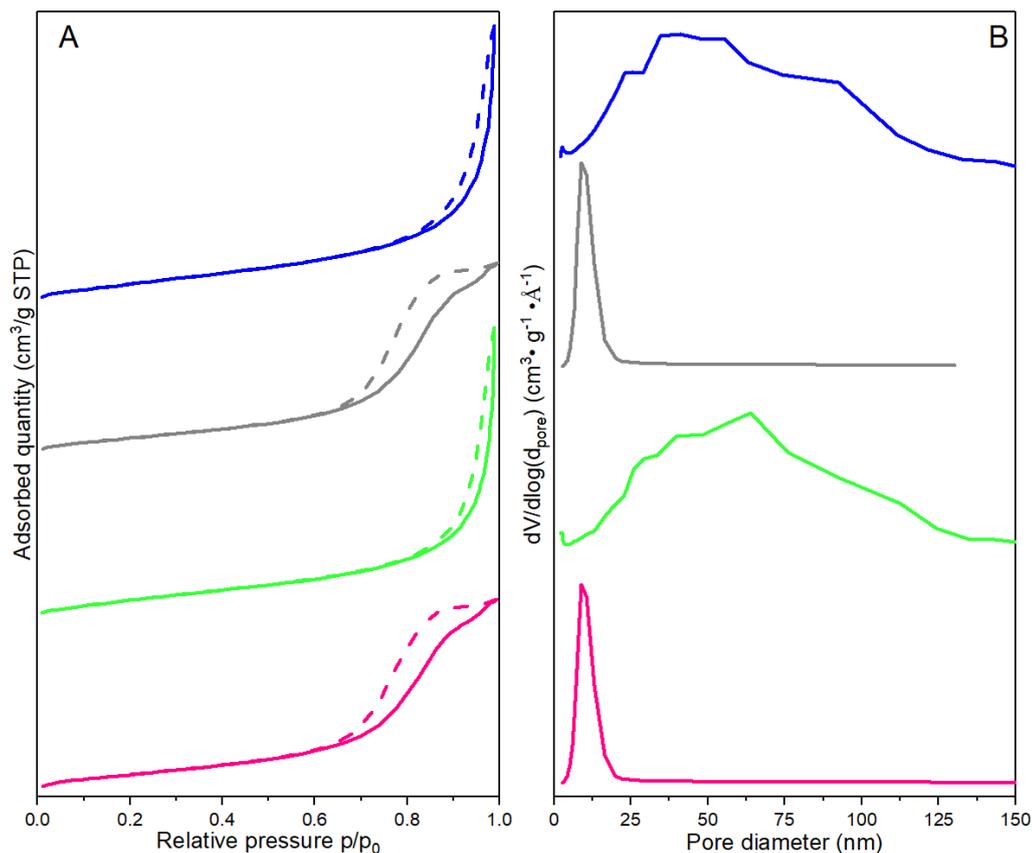
Fig. 4.7. Textural properties of reference TWC. A-Adsorption isotherms solid: adsorption; dash: desorption   B-pore size distribution calculated from desorption process. Pink: bare Ce$_{0.5}$Ze$_{0.5}$O$_2$-COP; Green: bare Ce$_{0.5}$Ze$_{0.5}$O$_2$-FSP; Grey: Pd/ Ce$_{0.5}$Ze$_{0.5}$O$_2$-COP; Blue: Pd/ Ce$_{0.5}$Ze$_{0.5}$O$_2$-FSP.

Table 4.3. Textural properties of reference TWC.

Catalyst	SSA (m^2/g) [a]	Average pore diameter (nm)[b]	Pore volume (cm^3/g)
bare Ce$_{0.5}$Zr$_{0.5}$O$_2$-COP	73.9	8.7	0.22
bare Ce$_{0.5}$Zr$_{0.5}$O$_2$-FSP	113.6	15.10	0.49
Pd/Ce$_{0.5}$Zr$_{0.5}$O$_2$ -COP	71.8	8.9	0.23
Pd/Ce$_{0.5}$Zr$_{0.5}$O$_2$-FSP	152.6	13.6	0.58

Note: a Specific surface area calculated by BET method
        b Average pore diameter calculated from BJH desorption

4.2.2. Surface composition from XPS analysis

Photopeaks of Ce 3d, Zr 3d, O 1s and Pd 3d (combined with Zr 3p) of the reference catalysts are displayed in Fig. 4.8. On one hand, positions of Zr 3d remained almost unaffected regardless of preparation method employed (Table 4.4.). The stable Zr 3d$_{5/2}$ photopeak recorded at B.E. value approximately equal to 182 eV emphasize the presence of Zr^{4+} species. On the other hand, more complex features usually characterize the Ce 3d photopeak which can be decomposed into different components u', u'', u''' and v, v', v'', v''' [F. Le Normand 1989]. The contributions appearing at 898.5 ev, 901 ev and 917 eV manifest a greater stabilization of Ce^{4+} species. Slight shift of Ce 3d$_{5/2}$ core level towards

higher B.E. value (882.7 ev) was observed on Pd/Ce$_{0.5}$Zr$_{0.5}$O$_2$ FSP catalyst, which may be an indication of segregation of CeO$_2$ on the examined surface. [P. Esteves 2011]. It must be emphasized that identification of Pd oxidation state is difficult due to the strong interference of Zr 3p photopeaks that share overlapped regions with Pd 3d photopeaks. Nevertheless, the Pd 3d photopeak appears more distinctly on Pd/Ce$_{0.5}$Zr$_{0.5}$O$_2$-FSP near 338.1 eV. Even if the intensity strongly attenuates on Pd/Ce$_{0.5}$Zr$_{0.5}$O$_2$-FSP a rather similar B.E. seems to be discernible. Semi-quantitative analysis has not been reported with regard to the low expected accuracy. Nevertheless it is obvious that the concentration of Pd at the surface of Pd/Ce$_{0.5}$Zr$_{0.5}$O$_2$-FSP is lower than that expected on Pd/Ce$_{0.5}$Zr$_{0.5}$O$_2$-COP which could be inherent to the preparation method inducing more Pd aggregation or embedded oxidic species in the matrix of the support with respect to small Pd aggregates accessible at the surface.

It is worthwhile to note that higher B.E. values are obtained in comparison with those currently expected for PdO in the range 336.1-336.9 eV [E.M. Slavinskaya 2011]. Higher B.E. values near 338 eV could reflect the stabilization of Pd^{4+} as reported elsewhere [E.M. Slavinskaya 2011; K. Otto 1992; M. Moroseac 2004] and/or the formation of PdO$_y$ with $1 < y < 2$ due to the diffusion of oxygen in PdO [W. Huang 2009]. Previous investigation explained that high B.E. observed on Pd 3g can reflect either electron transfer depending on the extent of interaction with the support or particle size then stabilizing electron deficient Pd$^{\delta+}$ species with $\delta > 2$.
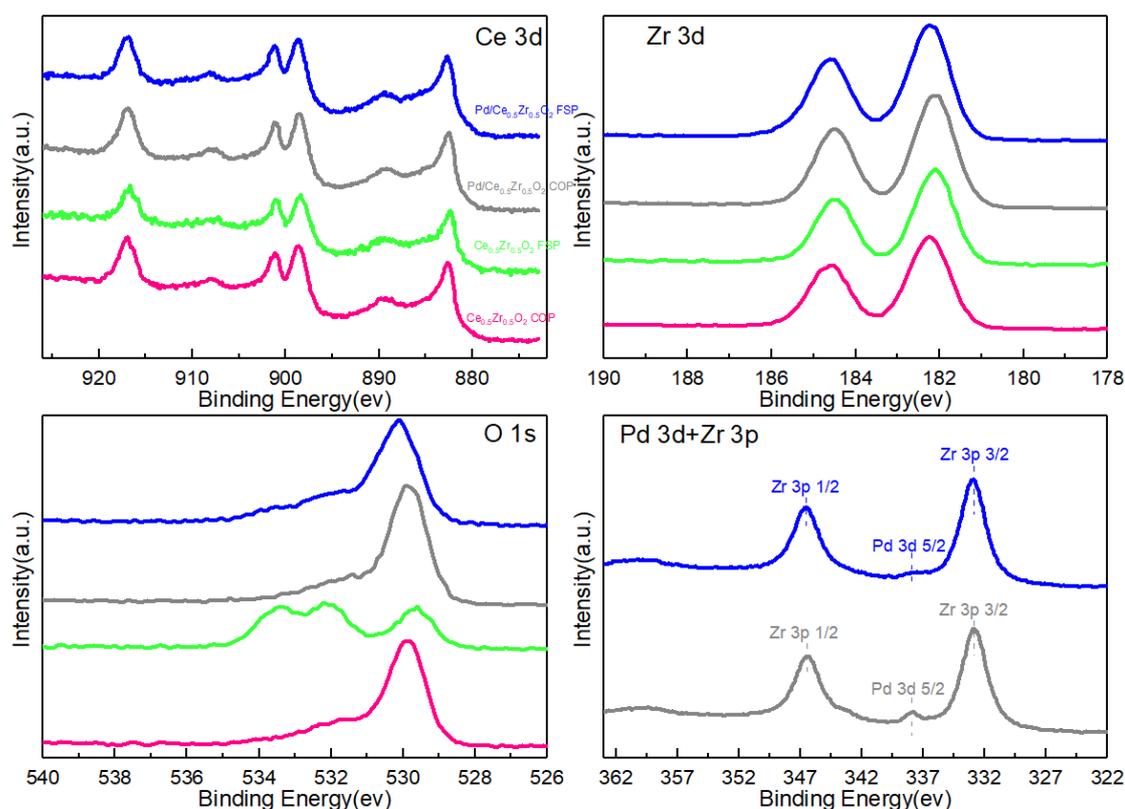
Fig. 4.8. Characteristic of photopeak Ce 3d, Zr 3d, O 1s and Pd 3d (inseparate with Zr 3p). Pink: bare Ce$_{0.5}$Ze$_{0.5}$O$_2$-COP; Green: bare Ce$_{0.5}$Ze$_{0.5}$O$_2$-FSP; Grey: Pd/ Ce$_{0.5}$Ze$_{0.5}$O$_2$-COP; Blue: Pd/ Ce$_{0.5}$Ze$_{0.5}$O$_2$-FSP.

Table 4.4. Binding energy of each element

Catalyst	Ce 3d	Zr 3d	Pd 3d	O 1s	C 1s
Ce$_{0.5}$Zr$_{0.5}$O$_2$ COP	882.7	182.2	-	529.8	285.0
Ce$_{0.5}$Zr$_{0.5}$O$_2$ FSP	882.4	182.1	-	532.2	285.0
Pd/Ce$_{0.5}$Zr$_{0.5}$O$_2$ COP	882.5	182.1	338.1	529.9	285.0
Pd/Ce$_{0.5}$Zr$_{0.5}$O$_2$ FSP	882.7	182.2	338.1	530.1	285.0

Table 4.5. Surface atomic composition calculated from XPS analysis

Catalyst	Atomic ratio (%)					Ce/Zr
	Ce 3d	Zr 3d	Pd 3d	O 1s	C 1s	
Ce$_{0.5}$Zr$_{0.5}$O$_2$ COP	5.78	10.49	-	45.17	38.55	0.55
Ce$_{0.5}$Zr$_{0.5}$O$_2$ FSP	1.06	2.19	-	19.21	77.54	0.48
Pd/Ce$_{0.5}$Zr$_{0.5}$O$_2$ COP	6.76	13.46	unknown[a]	50.02	29.76	0.50
Pd/Ce$_{0.5}$Zr$_{0.5}$O$_2$ FSP	4.56	9.82	unknown[a]	36.88	48.73	0.46

Note : a Palladium content unable to calculate because of interference from Zirconium 3p photopeak

4.3. Catalytic activities of bare and Pd-doped Ce$_{0.5}$Zr$_{0.5}$O$_2$

4.3.1. Oxidative properties

Ceria-Zirconia solid solution is characterized by some unique advantages, including favoring noble metal dispersion, promoting thermal stability and facilitating reactions involved in three-way catalytic converter such as water-gas shift, steam reforming as well as CO and HC oxidation. [A.S. Wörz 2003; G. Li 2012; M. Konsolakis 2007; J. Wang 2008; M. Aryanpour 2013; X. Liang 2008] As reported elsewhere [S. Lin 2014] some debate can arise related to the nature of active sites and the oxidation state of palladium stabilized in reaction conditions. Indeed, catalysts were all calcined prior to reaction at a reasonable temperature which should not favor the thermal decomposition of PdO to metallic species. On the other hand, it was found that they can reduce at very low temperature when they are exposed to hydrogen. As a consequence, one cannot exclude even in stoichiometric conditions that a significant fraction of PdO can reduce to metallic Pd^0 especially in the particular case of weak interaction preferentially on Pd/Ce$_{0.5}$Zr$_{0.5}$O$_2$. Probably this reduction process will speed up in rich conditions corresponding a predominant segregation of metallic Pd^0 in interaction with a reduce support corresponding to the predominance of Ce^{3+} and anionic vacancies.

As displayed in Figs. 4.9. and 4.10., bare Ceria-Zirconia manifested moderate activity for both oxidation of CO and HC and reduction of NO in stoichiometric conditions. In sharp contrast, incorporation of 0.5 wt.% Pd on the Ceria-Zirconia support led to sharp improvement of catalytic activity in lean, rich and stoichiometric conditions.

Pd/Ce$_{0.5}$Zr$_{0.5}$O$_2$-COP gave rise to a markedly promotional effect in terms of CO and HC oxidation. Highly dispersed PdO$_x$ capable of adsorbing/releasing oxygen is assumed to be accountable for the fast initiation of CO oxidation during cold-start process. Also, the

aforementioned catalyst showed the best activity for propene oxidation in stoichiometric condition, although minor deactivation illustrated by the retardation of the light-off curve during the STO2 experiment was noticed. As discussed, a greater stabilization of oxidized Pd^{n+} species on Pd/Ce$_{0.5}$Zr$_{0.5}$O$_2$-COP is believed to play a key role in the rapid occurrence of HC oxidation at low temperature region due to greater supply of oxygen released from adsorption sites of Pd^{n+} [M. Fernández-Garcia 2000] It is obvious that in comparison with flame spray pyrolysis, Pd/Ceria-Zirconia prepared by coprecipitation method showed better activity for CO and C$_3$H$_6$ oxidation in stoichiometric conditions, which is related to the highly homogeneous dispersion of Pd on the support and reinforced stabilization of PdO$_x$ confirmed by the SEM/EDS analysis. Moreover, better Pd dispersion would be favorable for the spillover of oxygen from Pd^{n+} to Ce^{4+} active sites, further boosting oxidation of CO and C$_3$H$_6$. This is in good accordance with H$_2$-TPR result that Pd/Ceria-Zirconia made by coprecipitation method is endowed with the greatest hydrogen consumption at low temperature range (below 200°C), suggesting that the spillover of hydrogen to the support surface was conspicuously intensified on this catalyst. Last but not least, it is generally accepted that CO oxidation over Pd-based catalyst follows Langmuir-Hinshwood mechanism and could be promoted dramatically by the presence of water due to the enhancement of bulk oxygen diffusion in CeO$_2$ [R. Rajasree 2004]. However, the presence of excessive water vapor leads to the formation of palladium hydroxide which is one of the main factors accountable for catalyst deactivation.[C. F. Cullis 1976]

Compared to C$_3$H$_6$, it is found that C$_3$H$_8$ oxidation only exhibited moderate enhancement over Pd-loaded Ceria-Zirconia catalysts. This may be explained by the weak adsorption of propane on palladium or elevated energy barrier required for the cracking C-H bond.

It is important not to overlook the fact that although the Pd/Ceria-Zirconia synthesized by flame spray pyrolysis presented the highest specific surface area, oxidation of CO and HC remained inferior to that of coprecipitation in stoichiometric condition,. This indicates that oxidation of CO and HC is not solely determined by the specific surface area but more impacted by some other factors such as dispersion degree of Pd on Ceria-Zirconia support, crystallite size and stabilization of Pd^{n+} species (i.e. Pd(+IV))
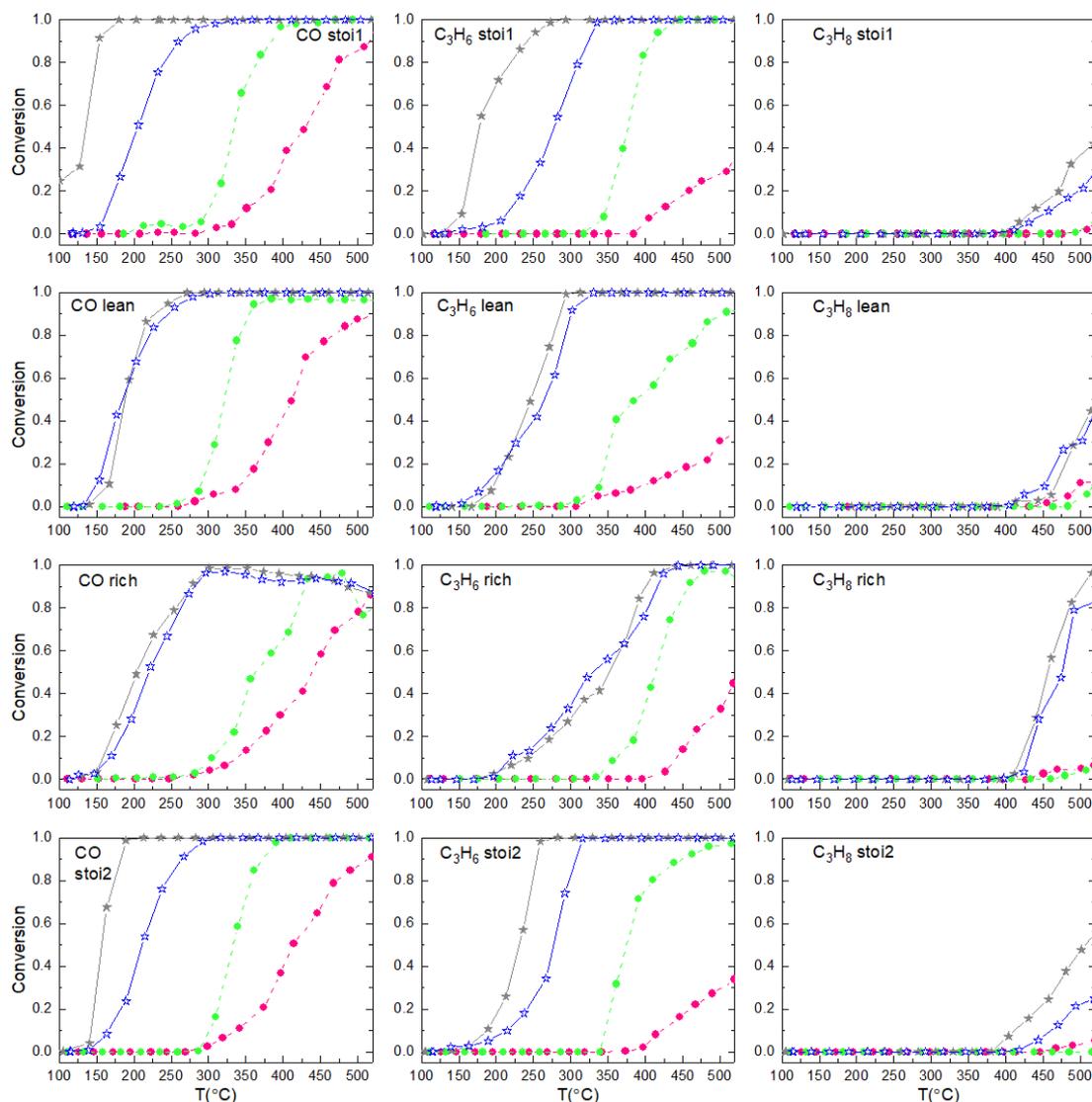
Fig. 4.9. Catalytic oxidation performance of reference TWC. Pink circle dash line: bare Ce$_{0.5}$Ze$_{0.5}$O$_2$-COP (●); Green circle dash line: bare Ce$_{0.5}$Ze$_{0.5}$O$_2$-FSP (●); Grey star solid line: Pd/ Ce$_{0.5}$Ze$_{0.5}$O$_2$-COP (★); Blue star solid line: Pd/ Ce$_{0.5}$Ze$_{0.5}$O$_2$-FSP (☆).

4.3.2. Reductive properties

It can been in Fig. 4.10. that Pd/Ceria-Zirconia prepared by coprecipitation shows the highest activity for NO reduction in lean, rich and stoichiometric conditions. No remarkable loss of activity was observed from STO2 TPR experiments although decreased NO conversion at low temperature was noticeable.

Some authors argued that oxygen vacancies present in the proximity of Pd-CZ interface due to the strong interaction between Pd and support is beneficial to NO reduction during light-off process. [J.H. Holles 2000; A. Martínez-Arias 2001] NO reduction by H$_2$ often occurs in the cold-start period prior to other main reactions. [J. Wang 2015] The main drawback for NO/H$_2$ reaction over Pd-based catalysts resides in the low selectivity of N$_2$, especially at low temperature [K. Paredis 2011; D.C. Chambers 2001] This could explain the high concentration of nitrous oxide at low temperature. On the other hand, formation of

ammonia is not observed which can be an indication that the density chemisorbed nitrogen atoms is rather low which still corroborates the preferential production of N$_2$O.

$$2NO + H_2 \rightarrow N_2O + H_2O \qquad (eq.\, 4-1)$$
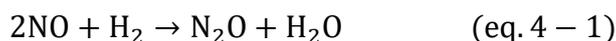
NO reduction over Ceria-Zirconia mixed oxides involves following reactions:[J. Velasco 2001]

$$2NO + Ce_2O_3 \rightarrow N_2O + 2CeO_2 \qquad (eq.\, 4-2)$$
$$N_2O + Ce_2O_3 \rightarrow N_2 + 2CeO_2 \qquad (eq.\, 4-3)$$
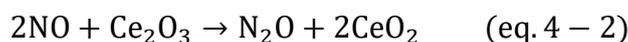
Velasco claimed that NO reduction over Ce-Zr mixed oxides is not directly related to the specific surface area of the catalyst and that the loss of surface area does not necessarily lead to decreased activity for NO reduction. [J. Velasco 2001] The same author further found that selectivity to N$_2$ strongly depends on the oxidation of the mixed oxide: the more rapid the oxidation rate, the higher selectivity to N$_2$.[J. Velasco 2001] From Fig. 4.11., it is noticeable that for Pd/Ceria-Zirconia synthesized by coprecipitation method N$_2$O was mainly produced at low temperature while formation of N$_2$ was favored at high temperature, both in STO1 and STO2. More N$_2$O was observed in the temperature range of 350-500°C over Pd/Ceria-Zirconia prepared by flame spray pyrolysis in STO1, which is probably related to the inhomogeneous dispersion of Pd on support surface. Selectivity of N$_2$ and N$_2$O showed similar evolution over the aforementioned catalysts in STO2 experiments, suggesting presumably that NO reduction over aged catalyst follow comparable pathways.

Another point which is worth noting is that none of the reference catalysts showed significant sintering after exposure to cyclic thermal treatment. It is apparent that NO conversion was maintained in the return test without marked loss of activity. It is reported that deactivation of CeO$_2$-based catalysts are associated with two major phenomena: the first is the sintering on the noble metal particles resulting in the loss of metal surface area; the second resides in the loss of CeO$_2$ surface area causing the weakening of OSC. [J. Kašpar 1999] In our study, the reference catalysts demonstrated good thermal stability and resistance against ageing, essential for the preservation of catalytic performance for long-term use.
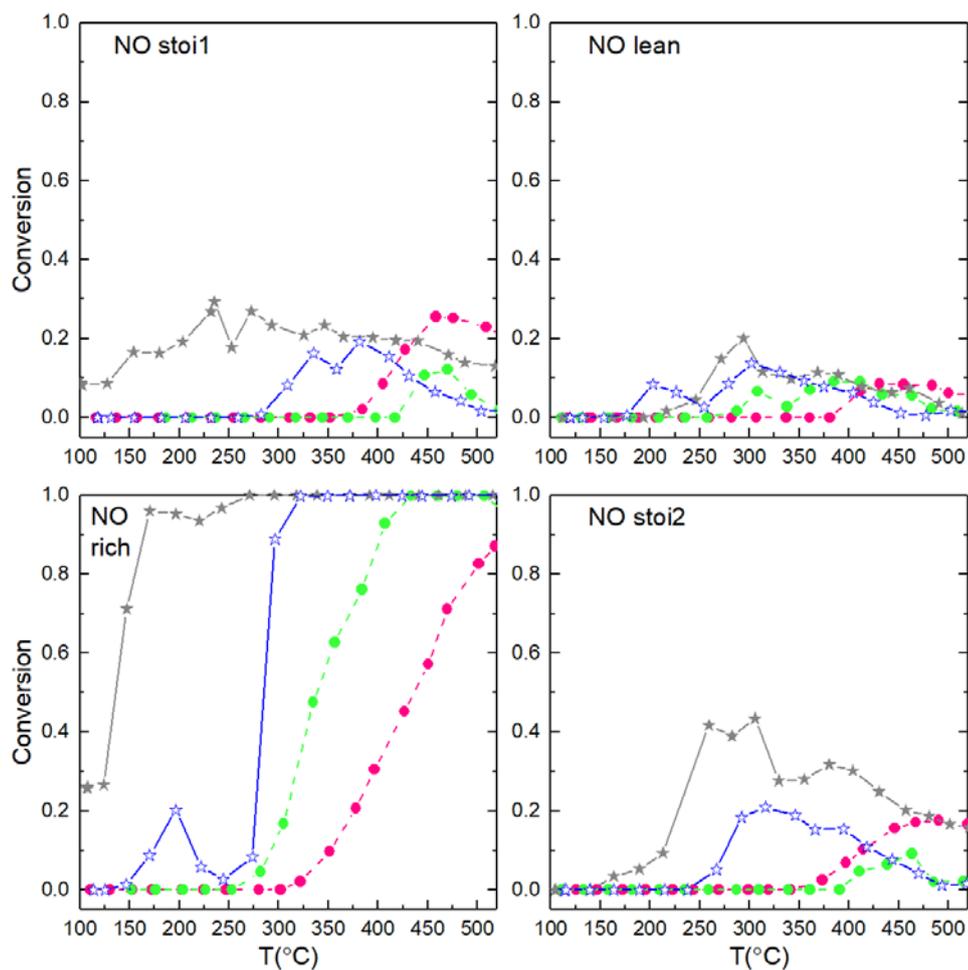
Fig. 4.10. Catalytic reduction performance of reference TWC. Pink circle dash line: bare Ce$_{0.5}$Ze$_{0.5}$O$_2$-COP (●); Green circle dash line: bare Ce$_{0.5}$Ze$_{0.5}$O$_2$-FSP (●); Grey star solid line: Pd/ Ce$_{0.5}$Ze$_{0.5}$O$_2$-COP (★); Blue star solid line: Pd/ Ce$_{0.5}$Ze$_{0.5}$O$_2$-FSP (☆).
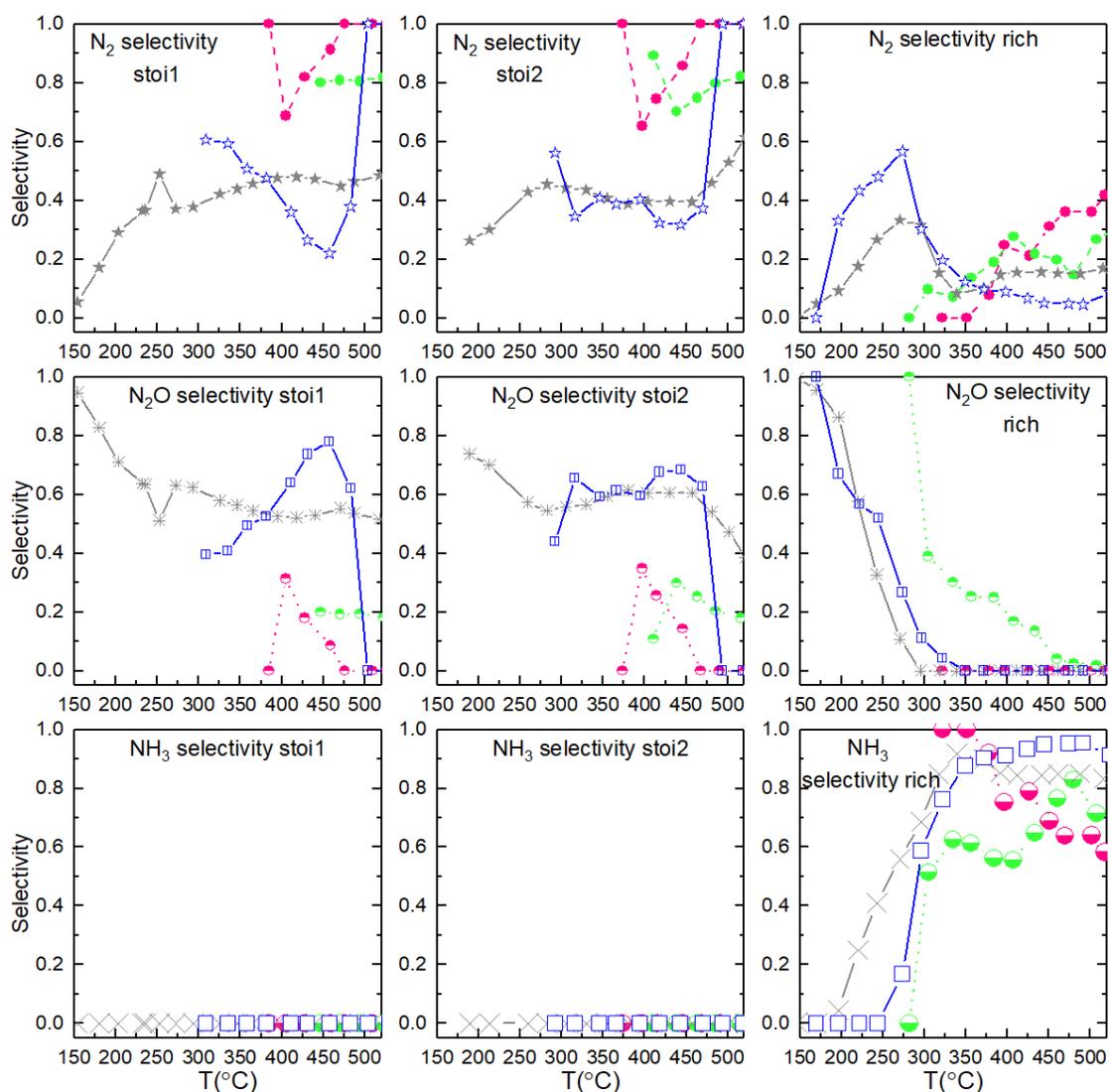
Fig. 4.11. Selectivity of N$_2$, N$_2$O and NH$_3$ in stoichiometric and rich conditions. Pink circle dash line: N$_2$ selectivity of bare Ce$_{0.5}$Ze$_{0.5}$O$_2$-COP (●); Pink up-shaded circle dash line: N$_2$O selectivity of bare Ce$_{0.5}$Ze$_{0.5}$O$_2$-COP (◓); Pink down-shaded circle (big mark) dash line: NH$_3$ selectivity of bare Ce$_{0.5}$Ze$_{0.5}$O$_2$-COP (◒); Green circle dash line: N$_2$ selectivity of bare Ce$_{0.5}$Ze$_{0.5}$O$_2$-FSP (●); Green up-shaded circle dash line: N$_2$O selectivity of of bare Ce$_{0.5}$Ze$_{0.5}$O$_2$-FSP (◓); Green down-shaded circle (big mark) dash line: NH$_3$ selectivity of bare Ce$_{0.5}$Ze$_{0.5}$O$_2$-FSP (◒); Grey star solid line: N$_2$ selectivity of Pd/ Ce$_{0.5}$Ze$_{0.5}$O$_2$-COP (★); Grey eight-spoked asterisk solid line: N$_2$O selectivity of Pd/ Ce$_{0.5}$Ze$_{0.5}$O$_2$-COP (✳); Grey multiplication sign (big mark): NH$_3$ selectivity of Pd/ Ce$_{0.5}$Ze$_{0.5}$O$_2$-COP (✕); Blue star solid line: N$_2$ selectivity of Pd/ Ce$_{0.5}$Ze$_{0.5}$O$_2$-FSP (☆); Blue barred-square solid line: N$_2$O selectivity of Pd/ Ce$_{0.5}$Ze$_{0.5}$O$_2$-FSP (⊞); Blue square (big mark) solid line: NH$_3$ selectivity of Pd/ Ce$_{0.5}$Ze$_{0.5}$O$_2$-FSP (□).

4.4. Conclusion

This chapter was dedicated to the comparison of benchmark PGM catalysts which will be further used as reference TWC. These reference systems are essentially composed of low

content in Pd (0.5 wt.%) in interaction with ceria-zirconia mixed oxides recognized for their exceptional OSC properties and their better thermal properties which ensures a greater stabilization of Pd dispersion. As a matter of fact particular attention was paid to the preparation of the ceria-zirconia mixed oxides and the resulting interactions with dispersed palladium species. Two preparation routes were selected thanks to collaboration with Lurederra and Johnson Matthey which developed Flame-Spray-Pyrolysis and Co-precipitation methods respectively. As found the best catalytic performances were observed on Pd/Ce$_{0.5}$Zr$_{0.5}$O$_2$ prepared by coprecipitation. Clearly this catalyst outperforms the performance recorded on the sample obtained by Flame-Spray-Pyrolysis especially in lean and rich conditions whereas they behave quite similarly in lean conditions. This comparison likely emphasized the better OSC properties resulting from the coprecipitation in spite of their lower specific surface area which tends to demonstrate that the OSC properties would likely depends on the microstructure to speed up bulk oxygen diffusion and also the specific interaction of palladium capable of weakening the Ce-O bond.

Clearly no significant change on the crystallographic structure was detected. Ceria-zirconia mixed oxide from XRD and Raman spectroscopy. On the other hand, redox properties after palladium incorporation are altered differently likely due to better Pd dispersion observed from STEM-EDS analysis on Pd/Ce$_{0.5}$Zr$_{0.5}$O$_2$-COP corresponding to a greater stabilization of Pd^{2+}. More reducible species on Pd/Ce$_{0.5}$Zr$_{0.5}$O$_2$-FSP associated to larger clusters of PdO weakly interacting with the support could explain the lower catalytic performance in stoichiometric and rich conditions partly due to a loss of Pd-Ce interface useful to promote OSC properties.

Reference

[M. Aryanpour 2013] M. Aryanpour, A. Khetan, H. Pitsch. ACS Catalysis, 2013,3:1253-1262.

[D.C. Chambers 2001] Dean C Chambers, Dennys E Angove, Noel W Cant. Journal of Catalysis, 2001, 204:11-22.

[G Colón 1998] G. Colón, M. Pijolat, F. Valdivieso et al. Journal of the Chemical Society, Faraday Transactions, 1998, 94:3717-3726.

[Y. Cui 2018] Y. Cui, L. Lan, Z. Shi, S. Yuan, Y. Chen, Y. Dan. Journal of Industrial and Engineering Chemistry, 2018, 60:102-103.

[C.F. Cullis 1976] C.F. Cullis, T.G. Nevell. Proceedings of the Royal Society A: Mathematical, Physical and Engineering Sciences, 1976, 349:523-534.

[R.A. Daley 2005] R.A. Daley, S.Y. Christou, A.M. Efstathiou et al. Applied Catalysis B: Environmental, 2005, 60:117-127.

[B. de Rivas 2011] B. de Rivas, R. López-Fonseca, M.A. Gutiérrez-Ortiz et al. Applied Catalysis B: Environmental, 2011, 101:317-325.

[J. Deng 2018] J. Deng, Y. Zhou, S. Li, L. Xiong, J. Wang, S. Yuan. Journal of Industrial and Engineering Chemistry, 2018, 64:219-229.

[D. Duprez 2001] D. Duprez, C. Descorme, T. Birchem et al. Topics in Catalysis, 2001,16/17:49-56.

[P. Esteves 2011] P. Esteves, Y. Wu, C. Dujardin et al. Catalysis Today, 2011, 176:453-457.

[M. Fernández-Garcia 2000] M. Fernández-Garcia, A. Martínez-Arias, A. Iglesias-Juez, C. Belver, A.B. Hungria, J.C. Conesa, J. Soria, Journal of Catalysis , 2000, 194:385-392.

[M. Fernández-García 2002] M. Fernández-García, A. Martínez-Arias, A. B. Hungría et al. Physical Chemistry Chemical Physics, 2002, 4:2473-2481.

[J.R. Ferraro 1994] J.R. Ferraro and K. Nakamoto. Introductory Raman Spectroscopy, Academic Press, New York, 1994.

[P. Fornasiero 1996] P. Fornasiero, G. Balducci, R. Di Monte, J. Kaspãr, V. Sergo, G. Gubitosa, A. Ferrero, M. Graziani. Journal of Catalysis, 1996, 164:173-183.

[R.C. Garvie 1978] R.C. Garvie. Journal of Physical Chemistry. 1978,82:218-224.

[J. Velasco 2001]Juan R. González-Velasco, Miguel A. Gutiérrez-Ortiz, Jean-Louis Marc et al. Applied Catalysis B: Environmental, 2001, 33:303-314.

[N. Guillén-Hurtado 2012] N. Guillén-Hurtado, A. Bueno-López, A. García-García. Journal of Materials Science, 2012, 47:3204-3213.

[I. Halasz 1992] I. Halasz, A. Brenner. Applied Catalysis A: General, 1992, 82:51-63.

[N. Hickey 2001] N. Hickey, P. Fornasiero, J. Kaspar et al. Journal of Catalysis, 2001, 200:181-193.

[J.H. Holles 2000] J.H. Holles, M.A. Switzer, R.J. Davis. Journal of Catalysis, 2000, 190:247-260.

[W. Huang 2009] W. Huang, Z. Zuo, P. Han, Z. Li, T. Zhao. Journal of Electron Spectroscopy and Related Phenomena, 2009, 173:88-95.

[A. Iglesias 2004] A. Iglesias, A. Martinez-Arias, M. Fernandez-Garcia. Journal of Catalysis, 2004, 221:148-161.

[J. Jehng 1998] Jih-Mirn Jehng. Journal of Physical Chemistry B, 1998, 102:5816-5822.

[J. Kašpar 1999]J. Kašpar, P. Fornasiero, M. Graziani. Catalysis Today, 1999, 50:285-298.

[J. Kašpar 2004] J. Kaspar, P. Fornasiero, N. Hickey, Catalysis Today, 2003, 77:419-449.

[M. Konsolakis 2007] M. Konsolakis, I.V. Yentekakis. Journal of Hazardous Materials, 2007, 149:619-624.

[F. Le Normand 1989] F. Le Normand, J. El Fallah, L. Hilaire, P. Légaré, A. Kotani, J.C. Parlebas. Solid State Communications, 1989, 71(11):885-889.

[S. Letichevsky 2005] S. Letichevsky, C.A. Tellez, R.R. de Avillez, M.I.P. da Silva, M.A. Fraga MA, L.G. Appel. Applied Catalysis B: Environmental, 2005, 58:203-210.

[G. Li 2012] G. Li, Q. Wang, B. Zhao, R. Zhou. Fuel, 2012, 92:360-368.

[X. Liang 2008] X. Liang, X. Wang, Y. Zhuang, B. Xu, S. Kuang, Y. Li. Journal of the American Chemical Society, 2008, 130: 2736-2737.

[S. Lin 2014] Siyu Lin, Linyan Yang, Xue Yang et al. Applied Surface Science, 2014, 305:642-649.

[M.F. Luo 2006] M.F. Luo, Z.Y. Pu, M. He, J. Jin, L.Y. Jin. Journal of Molecular Catalysis A: Chemical, 2006, 260:152-156.

[J.A. Lupescu 2016] J.A. Lupescu, J.W. Schwank, G.B. Fisher, X. Chen, S.L. Peczonczyck, A.R. Drews. Applied Catalysis B: Environmental, 2016, 185:189-202.

[Y. Madier 1999] Y. Madier, C. Descorme, A.M. Le Govic and D. Duprez, Journal of Physical Chemistry B, 1999, 103:10999-11006.

[A. Martínez-Arias 2001] A. Martínez-Arias, M. Fernández-García, A. Iglesias-Juez, A.B. Hungría, J.A. Anderson, J.C. Conesa, J. Soria. Applied Catalysis B: Environmental, 2001, 31: 51-60.

[S. Matsumoto 2004] S. Matsumoto. Catalysis Today, 2004, 90:183-190.

[W. Mista 2004] W. Mista, T. Rayment, J. Hanuza, L. Macalik. Materials Science-Poland, 2004, 22:153-170.

[T. Montini 2009]Tiziano Montini, Adolfo Speghini, Loredana De Rogatis et al. Journal of the American Chemical Society, 2009, 131:13155-13160.

[M. Moroseac 2004] M. Moroseac, T. Skála, K. Veltruská, V. Matolín, I. Matolínová. Surface Science, 2004, 566:1118-1123.

[R. Mueller 2003] R. Mueller, L. Mädler, S.E. Pratsinis. Chemical Engineering Science, 2003, 58, 1969-1976.

[H. Muraki 1992] H. Muraki, K. Yokota and Y. Fujitani. Applied Catalysis, 1989, 48:93-105.

[T. Murota 1993] T. Murota, T. Hasegawa, S. Aozasa et al. Journal of Alloys and Compounds, 1993, 193:298-299.

[K. Otto 1992] K. Otto, L.P. Haack, J.E. de Vries. Applied Catalysis B: Environmental, 1992, 1 (1), 1-12.

[K. Paredis 2011] Kristof Paredis, Luis K. Ono, Farzad Behafarid et al. Journal of the American Chemical Society, 2011, 133:13455-13464.

[M. Pilar Gonzales-Marcos 2012]M. Pilar Gonzales-Marcos, B. Pereda-Ayo, A. Aranzabal, J.A. Gonzales-Marcos, J.R. Gonzales-Velasco. Catalysis Today, 2012, 180, 88-95.

[R. Rajasree 2004] R Rajasree, J.H.B. J Hoebink, J.C. Schouten. Journal of Catalysis, 2004, 223:36-43.

[B.M. Reddy 2008] B.M. Reddy, P. Bharali, P. Saikia, S.-E. Park, M.W. van den Berg, M. Muhler, W. Grünert. Journal of Physical Chemistry C, 2008, 112:11729-11737.

[E.M. Slavinskaya 2011] E.M. Slavinskaya, O.A. Stonkus, R.V. Gulyaev, A.S. Ivanova, V.I. Zaikovskii, P.A. Kuznetsov, A.I. Boronin. Applied Catalysis A: General, 2011, 401:83-97.

[W.J. Stark 2003] W.J. Stark, M. Maciejewski, L. Mädler, S.E. Pratsinis, A. Baiker. Journal of Catalysis, 2003, 220:35-43.

[M. Teng 2009] M. Teng, L. Luo, X. Yan. Microporous and Mesoporous Materials, 2009, 119:158-164.

[C. Thomas 2006] C. Thomas, O. Gorce, F. Villain, G. Djega-Mariadassou. Journal of Molecular Catalysis A: Chemical, 2006, 249:71-79.

[A. Trovarelli 2002] A. Trovarelli. Catalysis by ceria and related materials. Imperial College Press, London, 2002.

[G. Vlaic 1997] G. Vlaic, P. Fornasiero, S. Geremia, J. Kašpar, M. Graziani. Journal of Catalysis, 1997, 168:386-392.

[G. Vlaic 1998] G. Vlaic, R. Di Monte, P. Fornasiero, E. Fonda, J. Kašpar and M. Graziani. Studies in Surface Science and Catalysis, 1998, 116:185-195.

[G. Vlaic 1999] G. Vlaic, R. Di Monte, P. Fornasiero et al. Journal of Catalysis, 1999, 182: 378-389.

[Q. Wang 2010] Q. Wang, G. Li, B. Zhao, R. Zhou. Applied Catalysis B: Environmental, 2010, 100:516-528.

[Q. Wang 2011 a] Qiuyan Wang, Zhenguo Li, Bo Zhao, Guangfeng Li, Renxian Zhou. Journal of Molecular Catalysis A: Chemical, 2011, 344:132-137.

[Q. Wang 2011 b] Q. Wang, G. Li, R. Zhou. Fuel, 2011, 90:3047-3055.

[J. Wang 2008] J. Wang, M. Shen, Y. An, J. Wang. Catalysis Communications, 2008, 10:103-107.

[J. Wang 2015] Jihui Wang, Hong Chen, Zhicheng Hu et al. Catalysis Reviews: Science and Engineering, 2015, 57:79-144.

[A.S. Wörz 2003] A.S. Wörz, K. Judai, S. Abbet, U. Heiz. Journal of the American Chemical Society. 2003, 125:7964-7970.

[H.C. Yao 1984] H.C. Yao, Y.F. Yu Yao. Journal of Catalysis, 1984, 86:254-265.

[M. Yashima 1993] M. Yashima, K. Morimoto, N. Ishizawa et al. Journal of the American Ceramic Society, 1993, 76:2865-2868.

[M. Yashima 1994 a] M. Yashima, H. Arashi, M. Kakihana et al. Journal of the American Ceramic Society, 1994, 77:1067-1071.

[M. Yashima 1994 b] M. Yashima, H. Arashi, M. Kakihana, M. Yoshimura. Journal of the American Ceramic Society, 1994, 77:1869-1874.

[F. Zhang 2006] F. Zhang, C.H. Chen, J.C. Hanson, R.D. Robinson, I.P. Herman, S.W. Chan. Journal of the American Ceramic Society, 2006, 89:1028-1036.

[B. Zhao 2010 a] B. Zhao, G.F. Li, C.H. Ge, Q.Y. Wang, R.X. Zhou. Applied Catalysis B: Environmental, 2010, 96:338-349.

[B. Zhao 2010 b] B. Zhao, Q.Y. Wang, G.F. Li, R.X. Zhou. Journal of Alloys and Compounds, 2010, 508:500-506.

PART B

PGM-free Perovskite Catalysts

Chapter V. Stoichiometric and non-stoichiometric Ca and Cu doped La$_{1-x}$FeO$_{3\pm\delta}$

Chapter VI. Stoichiometric and non-stoichiometric Ca and Mn doped La$_{1-x}$FeO$_{3\pm\delta}$

Foreword

Versatility of perovkite materials because of accommodation of a wide panel of cations.

First attempt in the use of perovskite-based materials in post-combustion catalysis was pointed out in 1974 highlighting promising oxidative properties to convert CO and unburnt hydrocarbon.[S.C. Sorenson 1974] The development of PGM-undoped perovskite based two-way catalysts at the beginning of the 70s represented a significant breakthrough avoiding an extensive use of Platinum Group Metal (PGM). Their peculiar properties have been more recently used in Diesel Oxidation Catalyst (DOC) for oxidizing NO to NO_2 showing that perovskite can rival with platinum exhibiting higher efficiency. Future developments for three-way application is a challenging issue because NO must be reduced selectively to nitrogen. Up to now, no industrial development regarding bare perovskite emerged slowly despite extensive investigation at the lab-scale. Practical developments were only obtained through the incorporation of low amount of PGM. This discovery was possible because of the self-regenerative behavior of perovskite protecting nano-sized PGM particles to thermal sintering in comparison with alumina support.[Y. Nishihata 2002] Such behavior was possible thanks to fast equilibration of surface composition and oxidation state of active elements on the surface under cycling conditions (lean/rich cycles).

Two major drawbacks usually reside in the development of perovskite based materials related to their inherent low specific surface area and significant imbalance in their redox properties with a much higher capacity to combust hydrocarbons in a large excess of oxygen. Significant improvements in synthesis methods led to specific surface area enhancement and also contributed to lower heterogeneity in composition.[R. Zhang 2006] Sol-gel methods gave rise to a wider panel of catalytic applications not restricted to high temperature application which led to reconsider the potentialities of such variety of materials.

Basically, the ABO_3 structure of perovskite can accommodate a wide number of components in A- and B-site and can stabilize various distorted structures. The stability of the structure depends directly on the geometrical constraints of octahedral and dodecahedral cavities (see Fig. 5.1.). To have a stable BO_6 octahedron, the B^{x+} radii should be higher than 0.51 Å. Insertion of the A cation in the cubo-octahedral cavities of the BO_6 arrangement leads to distortion of the octahedrons and formation of more stable orthorhombic or rhombohedral structures.

The flexibility of these mixed-oxide materials is also related to the creation of electronic imbalance through the substitution of trivalent by divalent cations (see Table 5.1.) which can induce the stabilization of substituted cations in B-site in unusual oxidation state. All these changes can orient differently their catalytic properties. Such strategy has been privileged in this first part with the aim to balance properly the redox properties of those solids. As suggested in Table 5.1. change in the oxidation state can also modify structural properties with expansion/contraction effect of the unit cell.

Table 5.1. Metal cations radii

dodecahedral A site			octahedral B site		
ion	radius (Å)^a	radius (Å)^b	ion	radius (Å)^a	radius (Å)^b
Na^+	1.06	1.32? (IX)	Li^+	0.68	0.74
K^+	1.45	1.60?	Cu^{2+}	0.72	0.73
Rb^+	1.61	1.73	Mg^{2+}	0.66	0.72
Ag^+	1.40	1.30 (VIII)	Zn^{2+}	0.74	0.75
Ca^{2+}	1.08	1.35	Ti^{3+}	0.76	0.67
Sr^{2+}	1.23	1.44	V^{3+}	0.74	0.64
Ba^{2+}	1.46	1.60	Cr^{3+}	0.70	0.62
Pb^{2+}	1.29	1.49	Mn^{3+}	0.66	0.65
La^{3+}	1.22	1.32?	Fe^{3+}	0.64	0.64
Pr^{3+}	1.10	1.14 (VIII)	Co^{3+} (LS)		0.52
Nd^{2+}	1.09	1.12 (VIII)	Co^{3+} (HS)	0.63	0.61
Bi^{3+}	1.07	1.11 (VIII)	Ni^{3+} (LS)		0.56
Ce^{4+}	1.02	0.97 (VIII)	Ni^{3+} (HS)	0.62	0.60
Th^{4+}	1.09	1.04 (VIII)	Rh^{3+}	0.68	0.66
			Ti^{4+}	0.68	0.60
			Mn^{4+}	0.56	0.54

(reprinted with permission from reference [S. Royer 2014]).
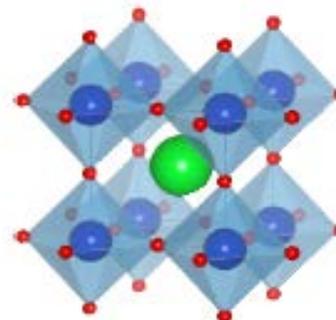
Fig. 5.1. Typical cubic ABO_3 structure: A green, B blue, O red.

How to select A- and B-cations?

A huge number of theoretical data obtained from DFT calculations are accessible in the literature. [R. Pushpa 2013; J. Emmerlich 2014; R. Hammami 2009; Z. Tian 2012]

Among these data some of them can provide important information first for selecting parent perovskite materials then for identifying appropriate dopants for further substitution in A- and B- sites in order to enhance their catalytic properties in the selected application. Hence, in principle a rational selection is possible based on these ab initio calculations. The ability of such materials to create defective sites is also essential since it can modulate originate their intrinsic catalytic properties. This parameter also plays a crucial role in the self-regenerative behavior especially to stabilize the dispersion of precious metal sometime in unusual oxidation state.

Based on these considerations, it was previously found that oxygen vacancies enhance the segregation of precious metal at FeO_2- terminated surfaces while they do not at LaO-terminated surface. Enhanced conductivity of oxygen for $LaFeO_3$ was also demonstrated after Ca doping. The creation of anionic vacancies increases more with La-deficient composition than with Mn-deficient ones. Finally, A-deficient cubic perovskite structure is more stable than the homologues stoichiometric ones.

All those information led to the conclusion that $LaFeO_3$ and particularly La-deficient solids could be efficient candidates for the four-way catalysis application. In addition, the beneficial effect of Ca-doping on the ionic conductivity could also lead to significant improvements on the catalytic properties. The selection of B-site usually recognized as the active catalytic element will be discussed separately in the following two chapters taking partial substitution of iron by copper and manganese respectively.

Chapter V. Stoichiometric and non-stoichiometric Ca and Cu doped $La_{1-x}FeO_{3\pm\delta}$

A wide variety of perovskite composition can be found in literature data. Overall, a series of lanthanum-based oxides $LaBO_3$ (B = Co, Fe, Mn, etc) or La_2BO_4 (B = Cu) have been studied previously in terms of TWC activity. Cobalt has been widely regarded as a carcinogenic hazard for both humans and environment and thus been excluded from this study. According to literatures, copper and iron lanthanates have been widely regarded the most active candidates among the first transition element series for NO reduction using CO as reducing gas. [S.D. Peter 2001]. It was found that the activity of La_2CuO_4 for NO reduction could be enhanced by partial substitution of copper by iron due to the promotion of Cu^{2+} ion dispersion. [S.D. Peter 2001]. Iwamoto has reported that isolated copper led to enhance NO reduction activity [M. Iwamoto 1989]. Since the activity of perovskite-type oxides is mainly governed by B-site metals, promising 3-way catalytic performance was expected to incorporate copper ions into the lanthanum ferrite lattice via B-site substitution.

Hence, partial substitution of La by Ca and Fe by copper has been preferred in this study leading to the following list of samples prepared through a conventional citrate route as described in the experimental section. For sake of clarity, the samples were labeled according to their theoretical composition. Elemental composition measured by inductively coupled plasma-optic emission spectroscopy is reported in Table 5.2.

Table 5.2. Atomic composition of the prepared perovskites from ICP analysis

Theoretical atomic composition	Atomic composition from ICP						
	La (%)	Ca (%)	Ca/La	Fe (%)	Cu (%)	Cu/Fe	A/B
$LaFeO_3$	20.46	-	-	19.97	-	-	1.02
$La_{0.7}FeO_3$	15.33	-	-	22.73	-	-	0.67
$LaFe_{0.9}Cu_{0.1}O_3$	21.42	-	-	19.57	2.17	0.11	0.99
$LaFe_{0.8}Cu_{0.2}O_3$	19.25	-	-	15.88	3.99	0.25	0.97
$LaFe_{0.7}Cu_{0.3}O_3$	20.06	-	-	14.40	6.28	0.44	0.97
$La_{0.7}Fe_{0.9}Cu_{0.1}O_3$	14.19	-	-	18.93	2.11	0.11	0.67
$La_{0.7}Fe_{0.8}Cu_{0.2}O_3$	14.43	-	-	16.95	4.39	0.26	0.68
$La_{0.7}Fe_{0.7}Cu_{0.3}O_3$	15.56	-	-	15.66	6.93	0.44	0.69
$La_{0.6}Ca_{0.1}Fe_{0.8}Cu_{0.2}O_3$	13.25	2.25	0.17	18.08	4.63	0.26	0.68
$La_{0.6}Ca_{0.2}Fe_{0.8}Cu_{0.2}O_3$	12.96	4.31	0.33	17.43	4.47	0.26	0.79
$La_{0.6}Ca_{0.4}Fe_{0.8}Cu_{0.2}O_3$	11.33	7.81	0.69	15.28	3.96	0.26	0.99

5.1. Structural properties

5.1.1. XRD analysis

XRD patterns recorded on the parent perovskites $LaFeO_3$ and $La_{0.7}FeO_3$, calcined at 600°C are reported in Fig. 5.2. They exhibit most intense reflections ascribed to an orthorhombic structure. Positions of the characteristic peaks did not change significantly compared the reference $LaFeO_3$ (JCPDF37-1493) with the strongest reflection recorded near

$2\theta = 32.2°$, (h k l) = (1 2 1) .The relative intensities of diffraction peaks are in accordance with reference JCPDF 37-1493, suggesting that no obvious preferential growth was observed. However, additional weak reflections appear at 2 theta = 33.2 °and 35.6 ° in Fig. 5.2. and 5.4., which reflect the segregation of a minor alpha-Fe$_2$O$_3$ phase. For the La-deficient copper-doped perovskite La$_{0.7}$Fe$_{0.8}$Cu$_{0.2}$O$_3$, additional reflection at $2\theta = 35.6°$, (h k l) = (-1 1 1) and $2\theta=38.8$, (h k l) = (1 1 1) appear assigned of CuO (PDF 04-007-1375) indicating the formation of extra-framework copper oxide species. Lattice parameters of perovskites in Table 5.3., with La-deficiency or copper-doping, did not cause distinct deviations from the stoichiometric LaFeO3 in terms of length of three axes (a, b, c) yet a slight shrinkage of unit cell volume was observed. Such phenomenon is in line with previous results and is possibly associated with lanthanum deficit or substitution of trivalent cations by divalent ones [P. Ciambelli 2001; G. Pecchi 2011]. The orthorhombic perovskite structure seemed not affected by copper doping with no significant deviation on the lattice parameters as a function of copper content. Such weak change could reflect a weak stabilization of Cu^{2+} inside the perovskite lattice and subsequent segregations.
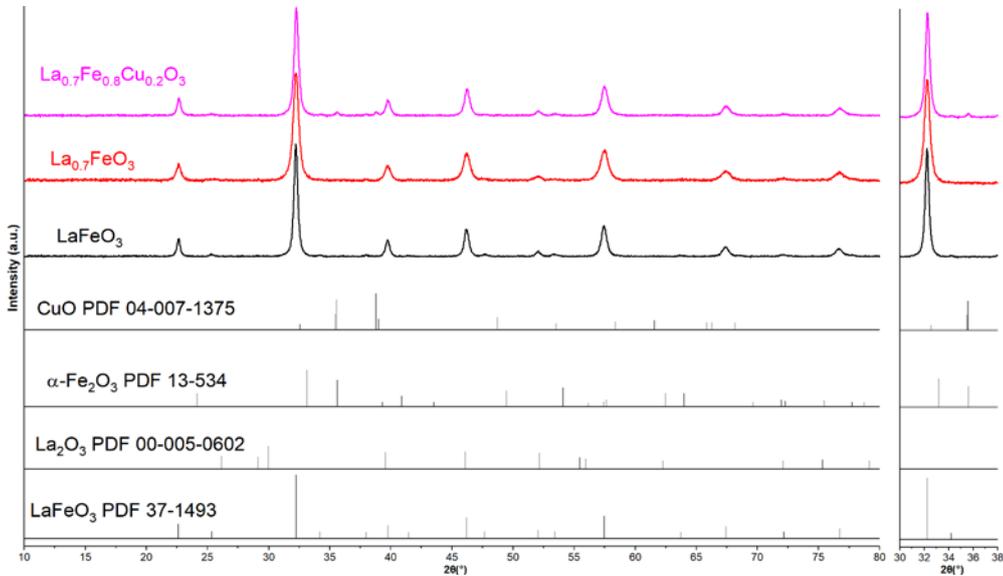
Fig. 5.2. X-ray diffractograms for the parent perovskites La$_{1-x}$FeO$_3$(x = 0, 0.3) and La$_{1-x}$Fe$_{0.8}$Cu$_{0.2}$O$_3$ (x = 0.3)
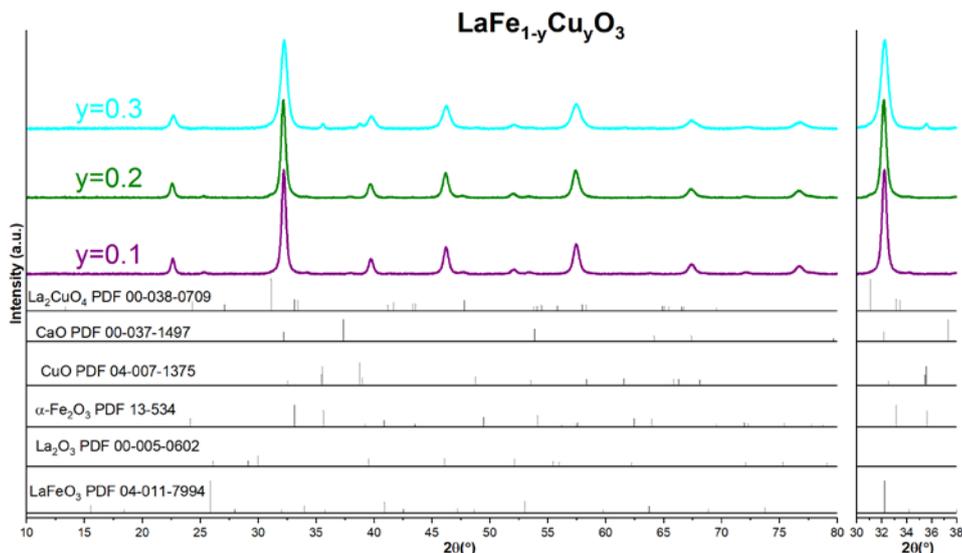
Fig. 5.3. X-ray diffractogram for the stoichiometric perovskite doped with copper LaFe$_{1-y}$Cu$_y$O$_3$ (purple y=0.1; olive y=0.2; cyan y=0.3)

As seen in Fig. 5.3., orthorhombic structure was well preserved for the stoichiometric copper doped perovskites LaFe$_{1-y}$CuyO$_3$ although slight shift towards higher 2θ angles corresponding to (1 2 1) plane was noted when the copper doping content became greater. What's more, apparent segregated phase of CuO existed for y = 0.2 and y = 0.3, testified by the two distinct peaks at 2θ = 35.6° and 2θ = 38.8°, signaling probably that more fraction of Cu^{2+} cations were stabilized as bulk CuO. The contraction of unit cell volume appeared less marked compared to LaFeO$_3$, probably due to the fact that on one hand unit cell tends to shrink originating from replacing Fe^{3+} cation with lower positive charge Cu^{2+} cation in order to meet electroneutrality requirement while on the other hand unit cell expansion might occur because of the introduction of Cu^{2+} cations with greater radius (r(Cu^{2+}) = 0.72 Å, r(Fe^{3+}) = 0.64 Å). In addition, it is worth noting that unit cell volume (Table 5.3.) experienced a sharp decrease from 31.2 nm (for y = 0.1) to 25.7 nm (for y = 0.3).
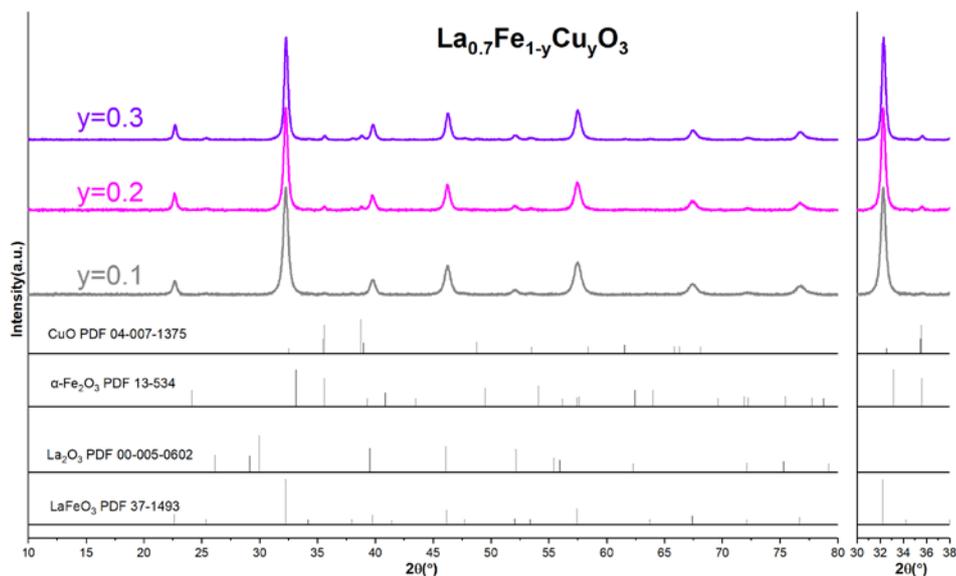
Fig. 5.4. X-ray diffractogram for the La-deficient perovskite doped with copper $La_{0.7}Fe_{1-y}Cu_yO_3$ (grey y=0.1; magenta y=0.2; violet y=0.3)

Compared to the stoichiometric $LaFe_{1-y}Cu_yO_3$, more defective sites exist due to the deficit of A cations and replacement in B site of trivalent cations with cations of lower positive charges. Segregation of iron and copper cations was thereby probably favored by these structural defects. In the meantime, La-deficiency produced greater distortion of the lattice structure, evidenced by the smaller unit cell volume in comparison with their stoichiometric counterparts (Table 5.3.). Besides, La-deficiency seemed favorable to the extraction of copper cation. As illustrated in Fig. 5.4. such trend became more evident when higher copper content was introduced, marked by the stronger intensities of the two diffraction peaks at $2\theta = 35.6°$ and $2\theta = 38.8°$ which could be assigned to cupric oxide (CuO PDF 04-007-1375). However, contrary to the stoichiometric $LaFe_{1-y}Cu_yO_3$, higher copper doping content resulted in greater crystal sizes of the sub-stoichiometric $La_{0.7}Fe_{1-y}Cu_yO_3$.
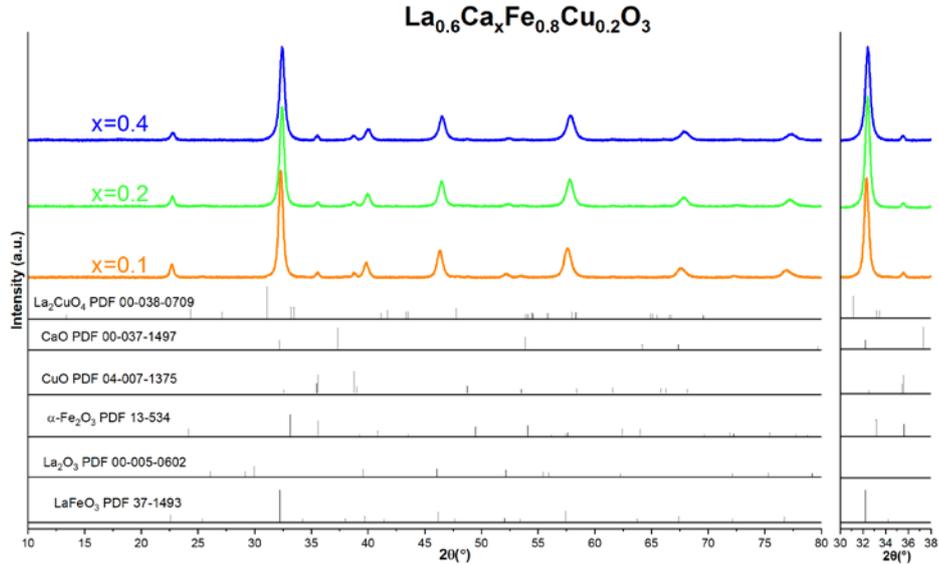
Fig. 5.5. X-ray diffractogram for Ca and Cu co-doped perovskites $La_{0.6}Ca_xFe_{0.8}Cu_{0.2}O_3$ (orange x=0.1; green x=0.2; blue x=0.4)

Fig. 5.5. shows a slight shift of maximum peak intensity towards higher 2θ values was recorded as the Ca doping content increased from 0.1 to 0.4, suggesting lattice distortion was induced by Ca substitution according to Bragg's law $n\lambda = 2d\sin\theta$. In light of the similarity of La^{3+} radius and Ca^{2+} radius ($r(La^{3+}) = 1.36$ Å, $r(Ca^{2+}) = 1.34$ Å), such phenomenon is more likely explained by the stabilization of Fe^{4+} in order to realize charge compensation when La^{3+} cations are partially replaced by more Ca^{2+} cations. This finding is in agreement with previous reports. [Y. Wu 1989; B.P. Barbero 2006]. No significant CaO was identified for all the calcium and copper doped perovskites. However, higher calcium doping content resulted in the attenuation of the two peaks at 2θ = 35.6° and 2θ = 38.8°, probably linked with the inhibition of phase segregation of CuO.

Table 5.3. Structural properties of the iron-based perovskites ABO_3 (A = La, Ca; B = Fe, Cu)

Catalysts	Crystal system	a(Å)	b(Å)	c(Å)	unit cell volume($Å^3$)	Crystallite size (nm)
$LaFeO_3$	orthorhombic	5.560(1)	7.861(0)	5.557(1)	242.88±0.05	29.4
$La_{0.7}FeO_3$	orthorhombic	5.560(0)	7.878(1)	5.535(1)	242.44±0.03	21.7
$LaFe_{0.9}Cu_{0.1}O_3$	orthorhombic	5.561(1)	7.849(1)	5.554(1)	242.49±0.03	31.2
$LaFe_{0.8}Cu_{0.2}O_3$	orthorhombic	5.572(1)	7.837(0)	5.557(1)	242.69±0.02	33.6
$LaFe_{0.7}Cu_{0.3}O_3$	orthorhombic	5.557(0)	7.863(1)	5.533(0)	241.82±0.06	25.7
$La_{0.7}Fe_{0.9}Cu_{0.1}O_3$	orthorhombic	5.557(0)	7.868(1)	5.532(1)	241.90±0.02	24.3
$La_{0.7}Fe_{0.8}Cu_{0.2}O_3$	orthorhombic	5.545(1)	7.857(1)	5.550(1)	241.80±0.05	28.6
$La_{0.7}Fe_{0.7}Cu_{0.3}O_3$	orthorhombic	5.561(0)	7.829(1)	5.543(0)	241.37±0.02	42.3
$La_{0.6}Ca_{0.1}Fe_{0.8}Cu_{0.2}O_3$	orthorhombic	5.544(1)	7.837(1)	5.539(0)	240.66±0.03	32.5
$La_{0.6}Ca_{0.2}Fe_{0.8}Cu_{0.2}O_3$	orthorhombic	5.542(0)	7.785(0)	5.531(0)	238.63±0.03	30.4
$La_{0.6}Ca_{0.4}Fe_{0.8}Cu_{0.2}O_3$	orthorhombic	5.525(0)	7.810(0)	5.436(1)	234.56±0.06	24.4

Note: a) lattice parameters deduced from Rietveld refinement
  b) crystal size was calculated by Williamson-Hall plot method using LaB$_6$ as standard specimen

All the synthesized iron-based perovskite materials exhibited an orthorhombic structure with the space group Pnma. For A^{3+}B^{3+}O$_3$ perovskite, the most symmetric structure observed is R-3C, which results from the slight distortion from the perfect cubic symmetry caused by the rotation of the BO$_6$ octahedra in respect to the cubic structure [M. Johnsson 2005]. Size effects, deviations from the ideal compositions and the Jahn-Teller effect have been identified as the main factors responsible for the distortion. [M. Johnsson 2005]. As for size effects, tolerance factor given by Eq. 5-1.

$$t = \frac{R_A + R_O}{\sqrt{2}(R_B + R_O)} \qquad (eq.\,5-1)$$

Partial substitutions lead to the decrease of A cation radius (r(La^{3+}) = 1.36 Å, r(Ca^{2+}) = 1.34 Å) and the increase of B cation radius (r(Fe^{3+}) = 0.69 Å, r(Fe^{4+}) = 0.585 Å, r(Cu^{2+}) = 0.73 Å), giving rise to a lower t value associated with the tilting of BO$_6$ octahedra yielding a lower symmetry. Besides, the varying iron ion valence is inclined to create oxygen vacancies on the defective perovskites which may cause the deformation of BO$_6$ octahedra (e.g. the formation of FeO$_5$ square pyramids). In some cases, lattice distortion can be induced by Jahn-Teller effect. For the LaFeO$_3$ perovskite with orthorhombic structure, the mean length of Fe-O bond is 2.01 Å with a mean Fe-O-Fe bond angle of 157°[N. Hamada 1997]. The full occupation of d orbitals ($d\varepsilon^3 d\gamma^2$) of one spin direction leads to the G-type Jahn-Teller distorsion. [N. Hamada 1997]. It should be noted that distortion of the compound cannot be attributed to a single factor and that occurrence of the aforementioned 3 factors at the same time is highly possible.

La$_{0.6}$Ca$_x$Fe$_{0.8}$Cu$_{0.2}$O$_{3\pm\delta}$
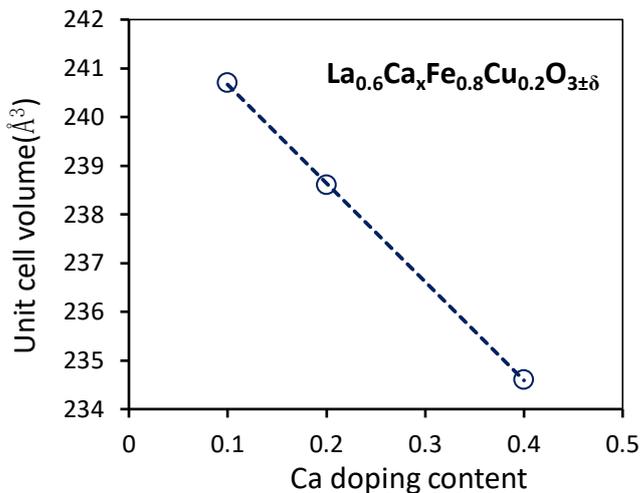
Fig. 5.6. Evolution of unit cell volume plotted against Ca doping content

Significant contraction of unit cell volume was observed as the Ca doping content increased from 0.1 to 0.4, associated with the decrease of crystal size from 32.5 nm to 24.4 nm, presumably stemming from the shortening of interplanar distance. Shrinkage of the unit cell was linked to the sharp decrease of the crystal size as evidenced in Table 5.3., indicating possibly that Ca substitution favors the improvement of resistance to sintering when exposed

to high temperature. A continuous decrease of crystallite size generated by higher Ca^{2+} content indicated that structural disorder caused by calcium doping might play a crucial role in preventing catalyst sintering stemming from crystallite growth under thermal treatment. Such phenomenon seemed in step with previous findings. [P. Ciambelli 2001].

5.1.2. Mössbauer spectroscopy

Mössbauer spectroscopy is a useful technique to investigate the different oxidation states of iron species stabilized in different coordination sites. Hence, it can complement structural information provided from XRD analysis. A typical Fe-O sextet was revealed for the stoichiometric parent perovskite LaFeO$_3$ (Fig. 5.7 (A). black). Further, the spectra became broadened for the La-deficient candidate La$_{0.7}$FeO$_3$ compared to LaFeO$_3$. Isomer shift (IS) in the range of 0.29-0.57 mm s^{-1} correspond to the Fe^{3+} species located in undistorted octahedron centers surrounded by six O^{2-} ions on (0 0 1), (1 0 0) and (0 1 0) faces. The presence of Fe^{4+} species was evidenced for the LaFeO$_3$ perovskite (4.83%. IS=0.072 mm s^{-1}) whereas such high oxidation state of iron was not observed on La-deficient La$_{0.7}$FeO$_3$. Such phenomenon suggests that electroneutrality is merely maintained through oxygen vacancies for the perovskite with A site atom deficiency. On the contrary, the perovskite with 20% copper doping in B site LaFe$_{0.8}$Cu$_{0.2}$O$_3$ yielded a broader spectrum and higher Fe^{4+} ratio (8.59%; Fe^{4+} high spin, IS=0.108 mm s^{-1}; Fe^{4+} low spin, IS=-0.151 mm s^{-1}) compared to LaFeO$_3$, implying that the main mechanism of charge compensation is achieved through both the stabilization of higher valence of A site atom and the oxygen vacancies generated within the lattice. Spectroscopic data are collected in Table 5.4.
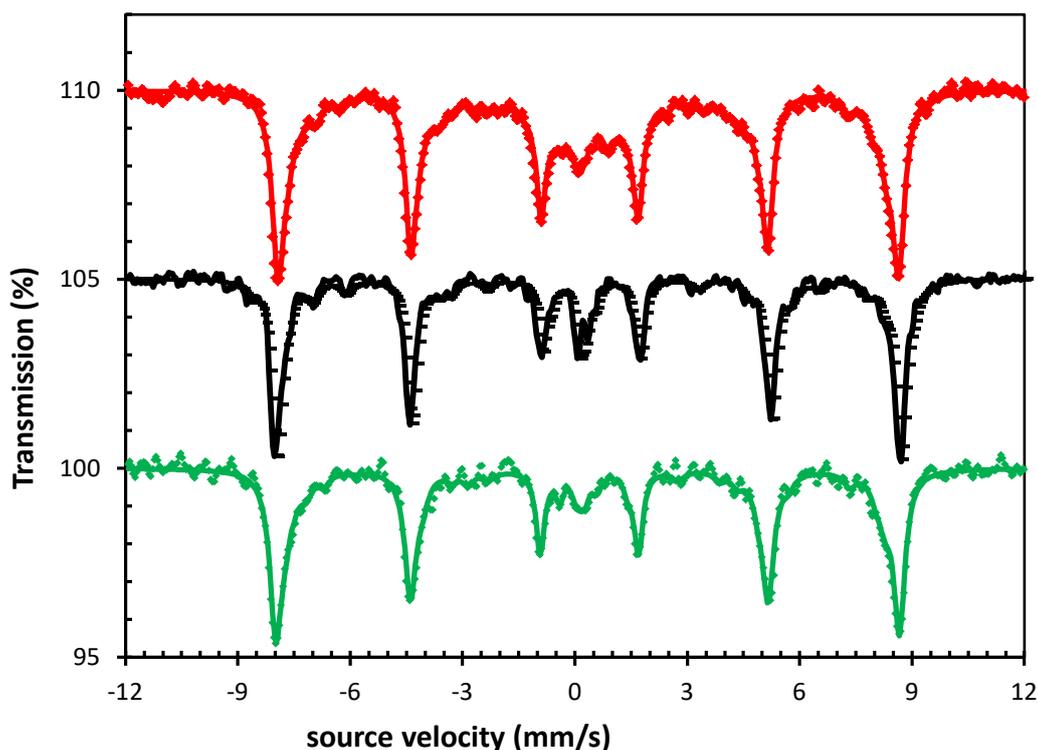
Fig. 5.7 (A). Mössbauer spectra recorded at room temperature. red: La$_{0.7}$FeO$_3$; black: LaFeO$_3$; green: LaFe$_{0.8}$Cu$_{0.2}$O$_3$ (line: calculated values; dot: experimental values)

The candidate $La_{0.7}Fe_{0.8}Cu_{0.2}O_3$ is characterized by both A site atom deficiency and B site substitution at the same time. Compared to the $LaFeO_3$, it is featured by a broadened spectrum and higher ratio of Fe^{3+} (12.88%; IS=0.225 mm s^{-1} and 0.237 mm s^{-1} respectively) located in the tetrahedral center of the Fe-O complex. Similarly to the La-deficient candidate $La_{0.7}FeO_3$, the absence of Fe^{4+} in the $La_{0.7}Fe_{0.8}Cu_{0.2}O_3$ perovskite suggested that charge compensation is presumably provided by mere anionic vacancies.

Significant spectrum broadening was observed when calcium doping was introduced in A site while maintaining copper doping content at 20% in B site (green, Fig. 5.7(B).). As calcium doping increased, higher ratio of Fe^{3+} present in the distorted octahedral center was produced, signifying more tilting of the $[FeO_6]$ octahedron and greater lattice disorder, which agrees with previous results of XRD analysis (Table 5.3.). On one hand, the formation and stabilization of Fe^{4+} could be favored by replacing La^{3+} with lower valence cation Ca^{2+}. An important phenomenon worth noting is that Fe^{4+} species was found to be present only in perovskites with stoichiometric compositions, irrespective of calcium or copper doping. On the other hand, the non-detection of Fe^{4+} for the La-deficient perovskites indicates that electroneutrality is kept through the creation of anionic vacancies, which may improve the oxygen storage capacity closely associated with the redox characteristics of these catalysts. Less structural disorder of the La-deficient perovskites also reflected a greater structural stability compared to $La_{0.6}Ca_{0.4}Fe_{0.8}Cu_{0.2}O_3$, which is in accordance with previous reports [A. Schön 2018;Y. Wu 2012].
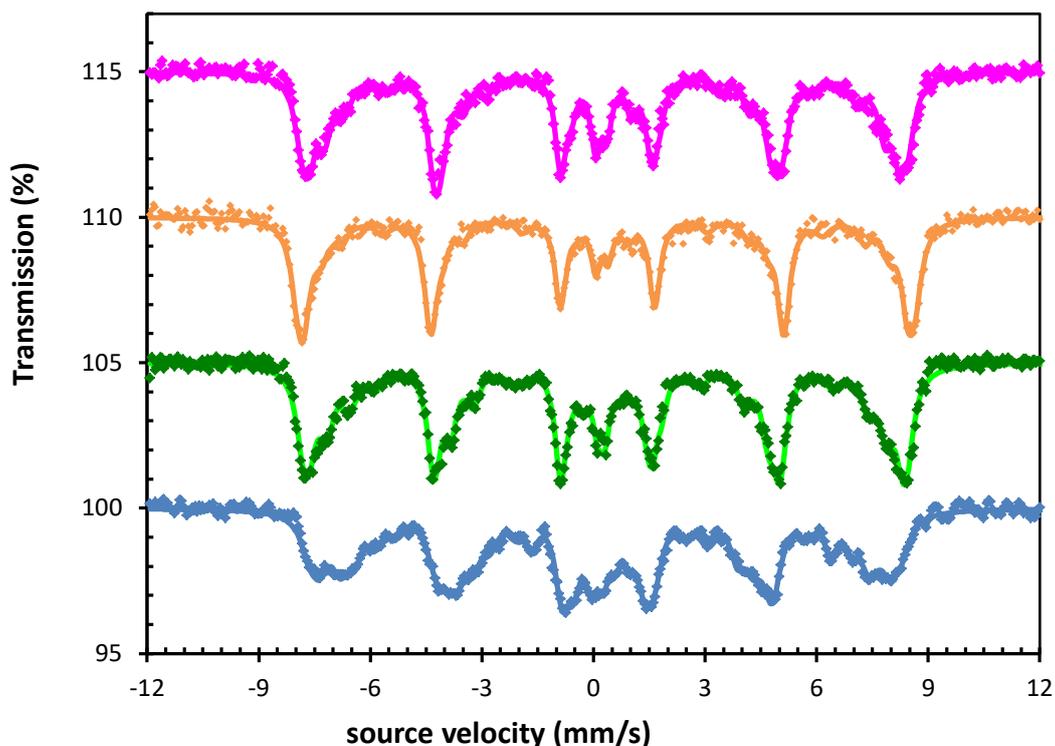
Fig. 5.7(B). Mössbauer spectra recorded at room temperature. magenta: $La_{0.7}Fe_{0.8}Cu_{0.2}O_3$; orange:$La_{0.6}Ca_{0.1}Fe_{0.8}Cu_{0.2}O_3$; green: $La_{0.6}Ca_{0.2}Fe_{0.8}Cu_{0.2}O_3$; blue:$La_{0.6}Ca_{0.4}Fe_{0.8}Cu_{0.2}O_3$

Table 5.4. Iron oxidation states and atomic ratio obtained from Mössbauer spectroscopy analysis for perovskites ABO_3 (A = La, Ca ; B = Fe, Cu).

Catalyst composition	Symmetry and oxidation state of cationic iron species	Relative abundance (at.%)
LaFeO$_3$	Fe^{3+} in undistorted octahedron	78.56
	Fe^{3+} in distorted octahedron	11.35
	Fe^{3+} in tetrahedron	5.26
	Fe^{4+} high spin	4.83
La$_{0.7}$FeO$_3$	Fe^{3+} in undistorted octahedron	92.31
	Fe^{3+} in distorted octahedron	5.58
	Fe^{3+} in tetrahedron	2.11
La$_{0.7}$Fe$_{0.8}$Cu$_{0.2}$O$_3$	Fe^{3+} in undistorted octahedron	76.48
	Fe^{3+} in distorted octahedron	10.64
	Fe^{3+} in tetrahedron	12.88
LaFe$_{0.8}$Cu$_{0.2}$O$_3$	Fe^{3+} in undistorted octahedron	76.62
	Fe^{3+} in distorted octahedron	8.98
	Fe^{3+} in tetrahedron	2.81
	Fe^{4+} high spin	4.41
	Fe^{4+} low spin	4.18
La$_{0.6}$Ca$_{0.1}$Fe$_{0.8}$Cu$_{0.2}$O$_3$	Fe^{3+} in undistorted octahedron	86.25
	Fe^{3+} in distorted octahedron	8.62
	Fe^{3+} in tetrahedron	5.13
La$_{0.6}$Ca$_{0.2}$Fe$_{0.8}$Cu$_{0.2}$O$_3$	Fe^{3+} in undistorted octahedron	86.06
	Fe^{3+} in distorted octahedron	9.05
	Fe^{3+} in tetrahedron	4.89
La$_{0.6}$Ca$_{0.4}$Fe$_{0.8}$Cu$_{0.2}$O$_3$	Fe^{3+} in undistorted octahedron	35.07
	Fe^{3+} in distorted octahedron	12.30
	Fe^{3+} in tetrahedron	35.32
	Fe^{4+} high spin	17.31

5.1.3. SEM-EDS analysis

Scanning electron microscopy analysis was performed on parent stoichiometric and La-deficient benchmarks as well as on the substituted samples by calcium and iron. Energy Dispersive X-ray Spectroscopy was used to analyze the different element leading to atomic composition reported in Table 5.5. Elemental mapping analysis also provides the distribution of these elements on a small volume in accordance with the scale indicated in Fig. 5.8. of the order cubic micrometer. As seen, SEM images reveal different morphology and different degree of aggregation according to the composition. As seen smaller grains are observable on La$_{0.7}$FeO$_3$ compared to the stoichiometric counterpart. Further, substitution with calcium and copper do not lead to more organization in terms of size and morphology of the grain. More interesting is related to the mapping analysis. The scale selected for analyzing LaFeO$_3$ and La$_{0.7}$FeO$_3$ does not reveal strong inhomogeneity in composition in the volume analyzed. An

homogeneous distribution of La and Fe is observable which agree with the prevalence of the orthorhombic structure of the perovskite and the absence of bulk impurities from XRD analysis. On the other hand, the introduction of copper emphasize the fact that Cu(II) species will not be randomly distributed as expected because of exsolution process leading to aggregates which appears more distinctly with a smaller scale on La$_{0.7}$Fe$_{0.8}$Cu$_{0.2}$O$_3$. It is worthwhile to note that no aggregation of lanthanum and iron is discernible which still agrees with XRD analysis underlining the conservation of the orthorhombic structure and the detection of bulk CuO species. TEM-EDS images for Ca-doped samples are recorded at smaller scale of 25 μm. La-deficient samples were analyzed with a particular attention to La$_{0.7}$Ca$_{0.1}$Fe$_{0.8}$Cu$_{0.2}$O$_3$ and La$_{0.7}$Ca$_{0.2}$Fe$_{0.8}$Cu$_{0.2}$O$_3$. Same observations are noticeable on the former sample containing the lowest calcium concentration still revealing the formation of larger spot which increase in density emphasizing a significant formation of extra-framework copper oxide species. On the other hand the reverse tendency is remarkable at increasing calcium concentration suggesting that calcium would slower the exsolution process of copper. Such observations are in qualitative agreement with XRD analysis showing the absence of bulk CaO and lower aggregation of CuO at increasing calcium content. Such tendency seems to be less discernible on La$_{0.6}$Ca$_{0.4}$Fe$_{0.8}$Cu$_{0.2}$O$_3$ despite XRD patterns did not lead to significant detection of bulk CuO species.
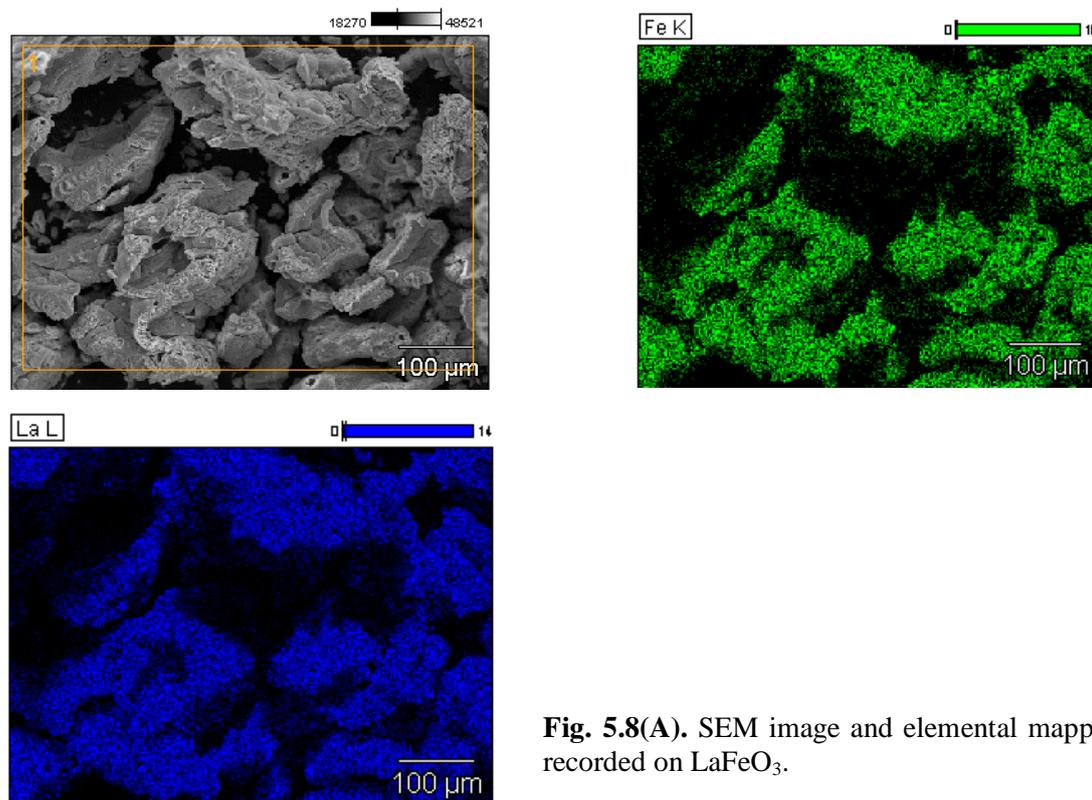
Fig. 5.8(A). SEM image and elemental mapping recorded on LaFeO$_3$.
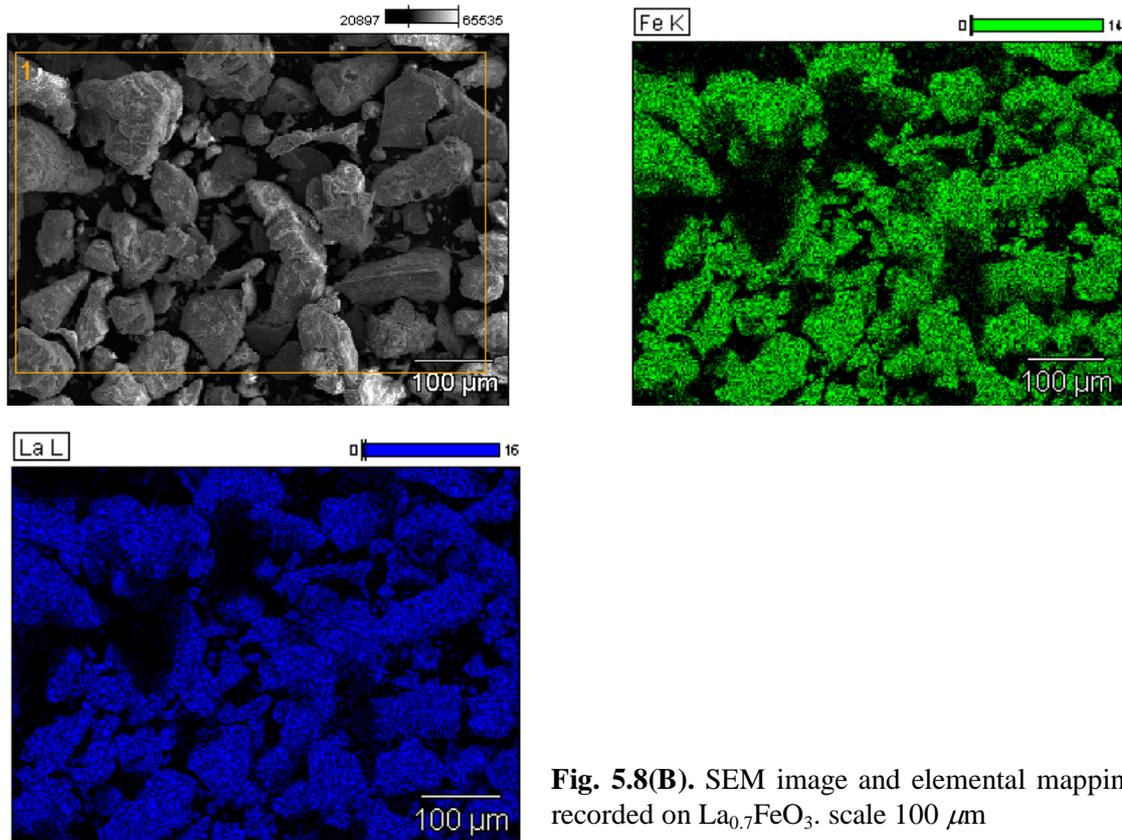
Fig. 5.8(B). SEM image and elemental mapping recorded on La$_{0.7}$FeO$_3$. scale 100 μm
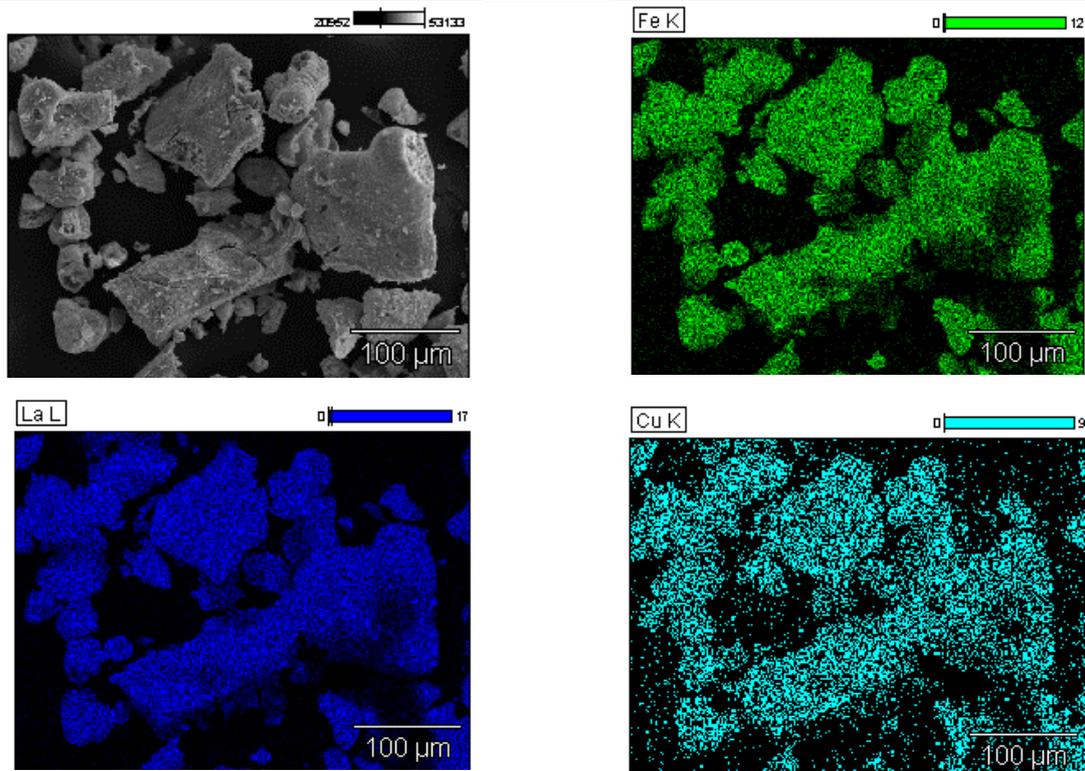
Fig. 5.8(C). SEM image and elemental mapping recorded on La$_{0.7}$Fe$_{0.8}$Cu$_{0.2}$O$_3$ – scale 100 μm.
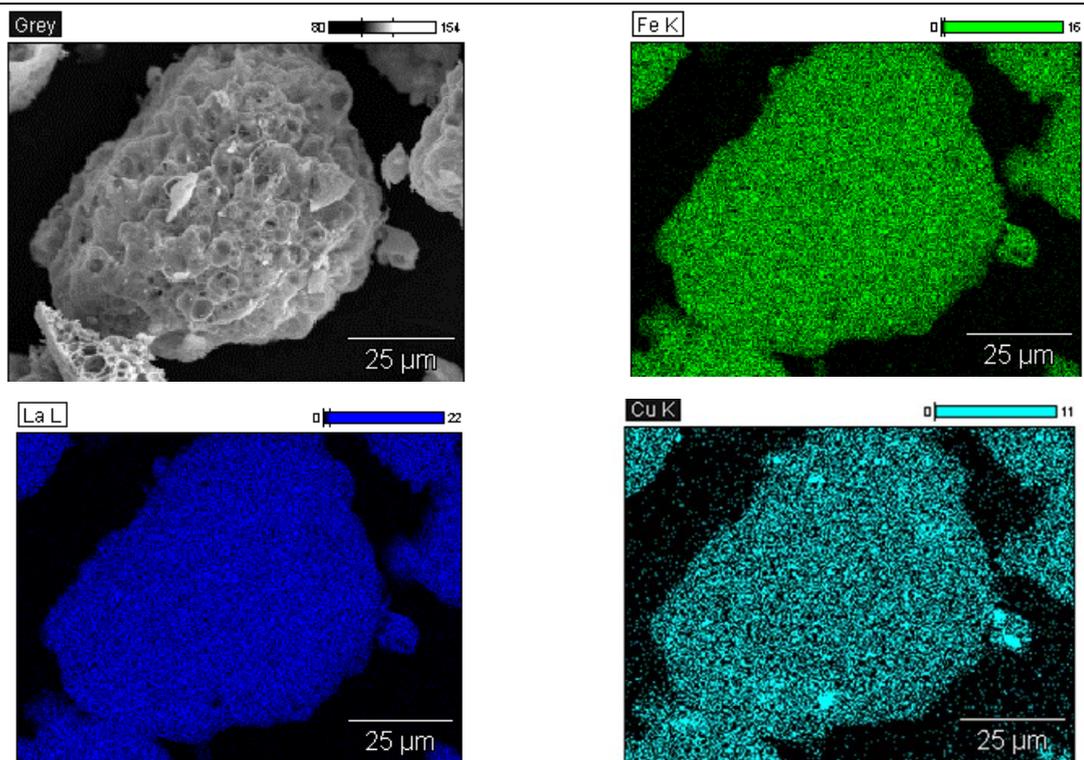
Fig. 5.8(D). SEM image and elemental mapping recorded on La$_{0.7}$Fe$_{0.8}$Cu$_{0.2}$O$_3$ – scale 25 μm.
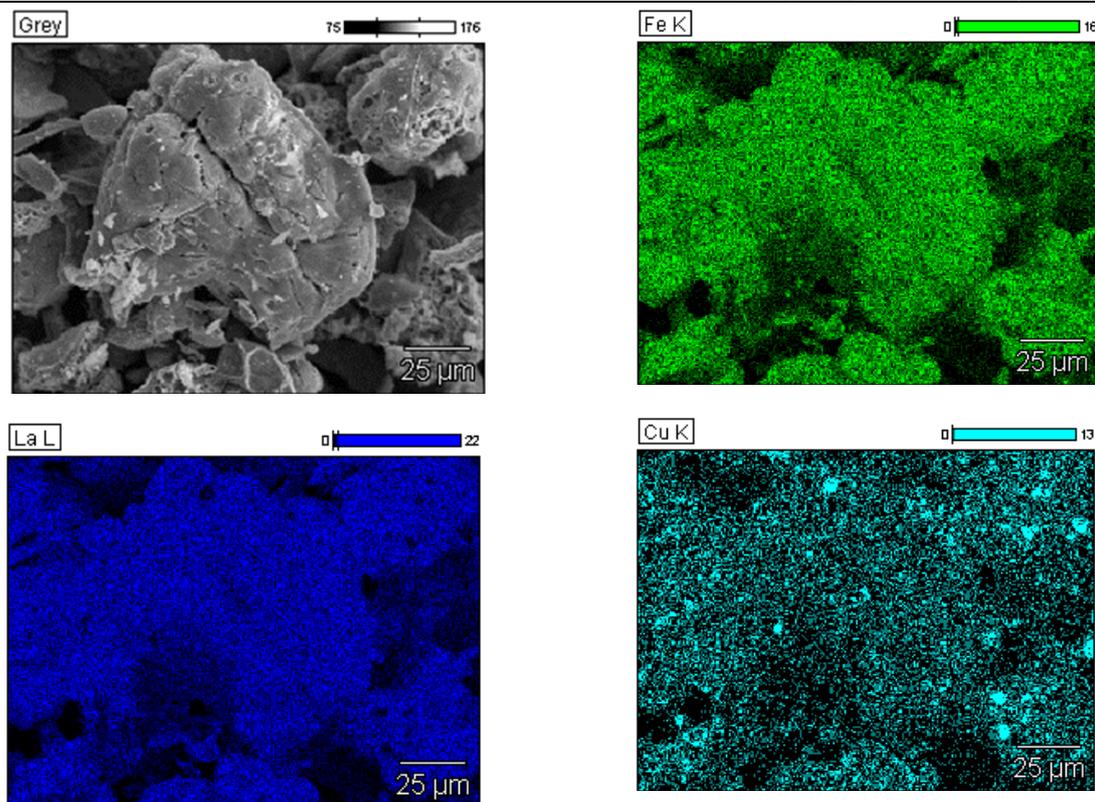
Fig. 5.8(E). SEM image and elemental mapping recorded on $La_{0.6}Ca_{0.1}Fe_{0.8}Cu_{0.2}O_3$ – scale 25 μm.
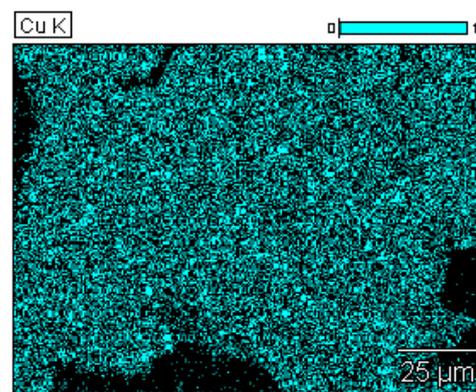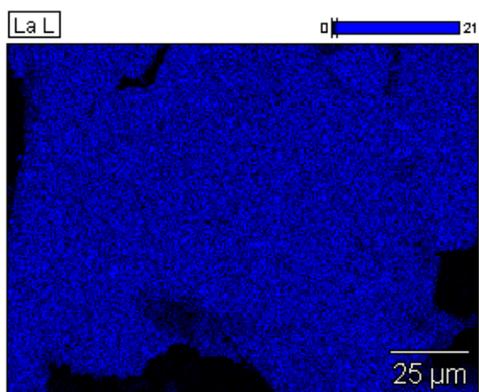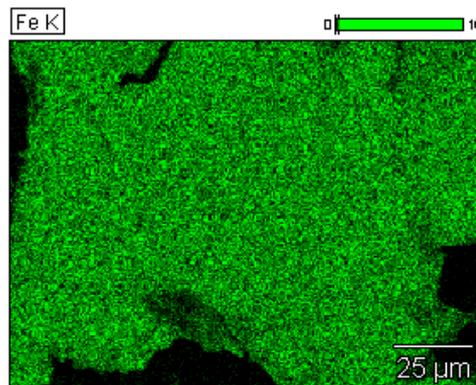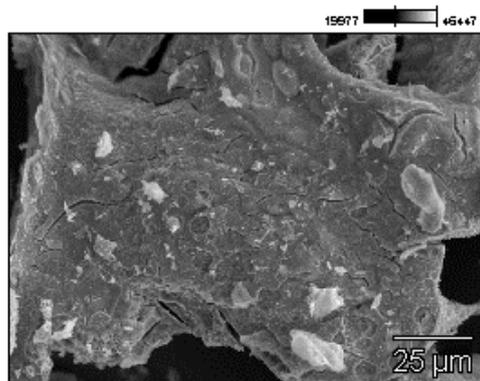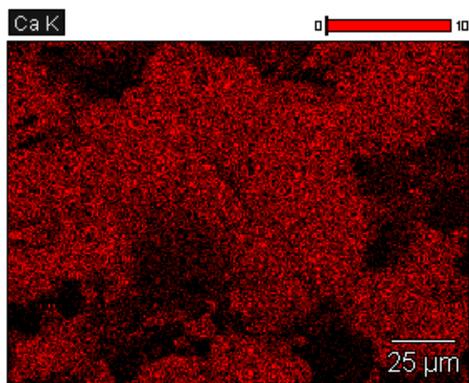
Fig. 5.8(F). SEM image and elemental mapping recorded on on $La_{0.6}Ca_{0.2}Fe_{0.8}Cu_{0.2}O_3$ – scale 25 μm.
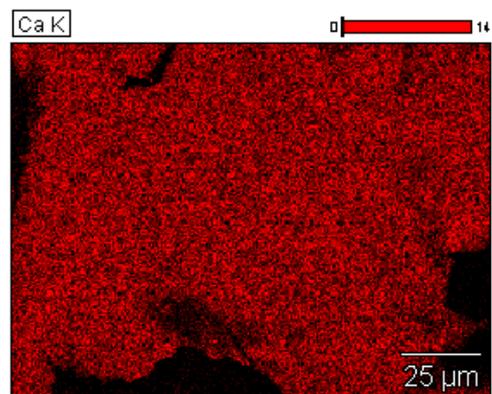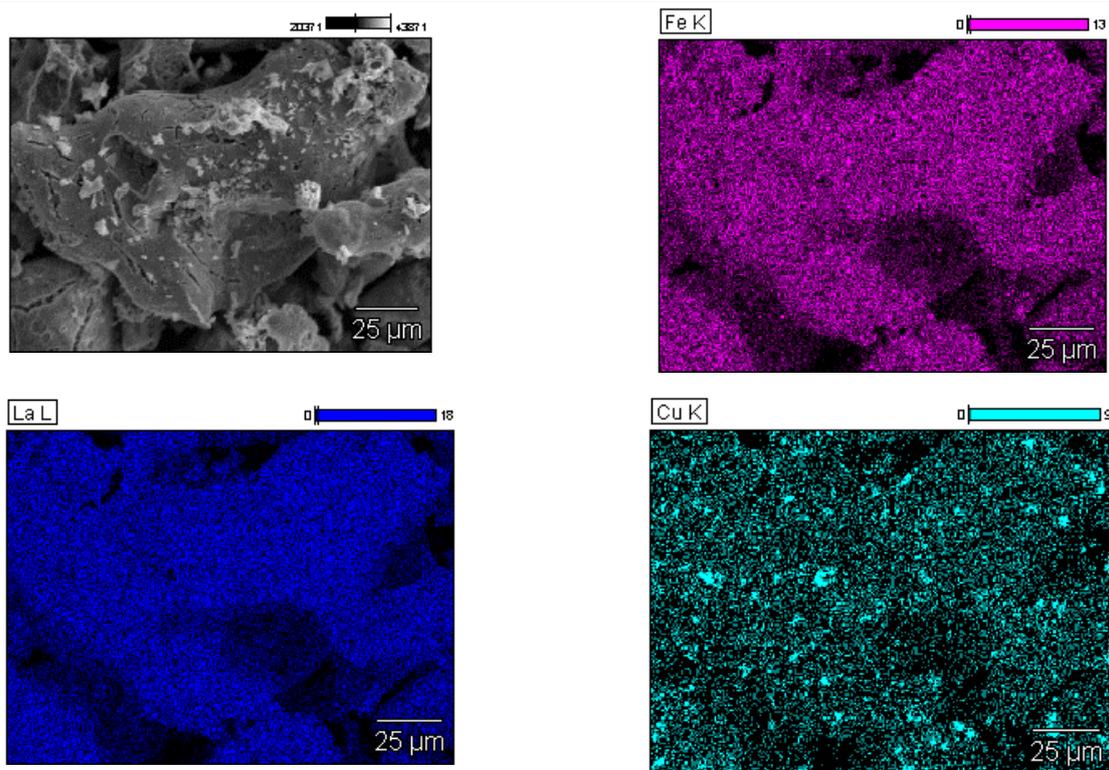
Fig. 5.8(G). SEM image and elemental mapping recorded on on La$_{0.6}$Ca$_{0.4}$Fe$_{0.8}$Cu$_{0.2}$O$_3$ – scale 25 μm.
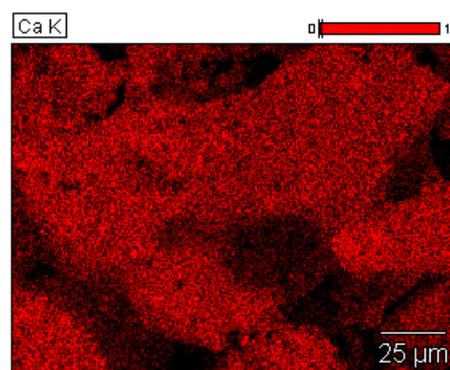
Atomic compositions of the prepared perovskites are presented in Table 5.5. It must be noted that oxygen cannot be analyzed due to the limitation of the EDS instrument. Only elements with atomic number of 11-92 were analyzed. A good consistency is observed for La and Ca. On the other hand, some slight deviations are discernible on copper in comparison with the expected atomic composition especially on La$_{0.6}$Ca$_{0.2}$Fe$_{0.8}$Cu$_{0.2}$O$_3$ corresponding to atomic ratio higher than that calculated on the other samples which could be in rather good agreement with the stronger formation of CuO aggregates.

Table 5.5. Atomic composition of the prepared perovskites from SEM analysis

catalyst	Atomic composition (%)						
	La	Ca	Ca/La	Fe	Cu	Cu/Fe	A/B
LaFeO$_3$	48.56	-	-	51.44	-		0.94
La$_{0.7}$FeO$_3$	37.99	-	-	62.01	-		0.61
La$_{0.7}$Fe$_{0.8}$Cu$_{0.2}$O$_3$	37.14	-	-	50.86	12.00	0.2	0.59
La$_{0.6}$Ca$_{0.1}$Fe$_{0.8}$Cu$_{0.2}$O$_3$	33.14	6.64	0.2	51.20	9.02	0.2	0.66
La$_{0.6}$Ca$_{0.2}$Fe$_{0.8}$Cu$_{0.2}$O$_3$	28.97	11.76	0.4	46.59	12.68	0.3	0.69
La$_{0.6}$Ca$_{0.4}$Fe$_{0.8}$Cu$_{0.2}$O$_3$	26.97	21.87	0.8	43.72	7.45	0.2	0.95

5.1.4. Reducibility

H$_2$-TPR analysis aims to investigate the reducibility of perovskite catalysts. H$_2$ consumptions profiles vs. temperature are shown in Figs. 5.9., 5.10., 5.11. Profiles of the parent LaFeO$_3$ and La$_{0.7}$FeO$_3$ were included as benchmark in each graph in order to provide clearer comparison.

Fig. 5.9. displayed H$_2$ consumption curves for the stoichiometric LaFe$_{1-y}$Cu$_y$O$_3$ perovskites. As discussed previously, the reducibility of perovskites is mainly dependent on B-cations (Here B = Fe or Cu). At first glance, stoichiometric LaFeO$_3$ (black line) seemed unreducible in the temperature range 100-700°C. Regularity of crystal structure makes bulk iron species exist in a stable state and can only be partially reduced at high temperature, evidenced by the unnoticeably progressive H$_2$ consumption above 700°C. By contrast, reducibility of Fe^{3+} in La-deficient La$_{0.7}$FeO$_3$ sample was tremendously enhanced, feature by two broad peaks in the temperature range 300-400°C and 425-625°C. It could be hypothesized a two-step reduction process of extra-framework hematite according to Eqs.5-2 and 5-3 [A. Schön 2015]. The first peak below 300°C should be attributed to the reduction of doped copper species. A small shoulder peak was observed for copper composition y = 0.1 and 0.2, probably ascribed to the reduction of more reducible extra-framework copper oxide species taking place prior to bulk reduction of copper located in B site. Nevertheless, the shoulder peak disappeared for candidate with the highest copper doping y = 0.3, presumably reflecting the simultaneous reduction of both bulk and extracted copper owing to their intense interactions. A marked increase of total H$_2$ uptake was recorded with a rise in copper content (see Table 5.6.), resulting from either the direct introduction of greater amount of copper itself or more stabilized Fe^{4+} species confirmed by Mössbauer spectroscopy.

$$Fe_2O_3 + H_2 \rightarrow 2FeO + H_2O \qquad (eq.\,5-2)$$
$$FeO + H_2 \rightarrow Fe + H_2O \qquad (eq.\,5-3)$$
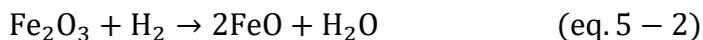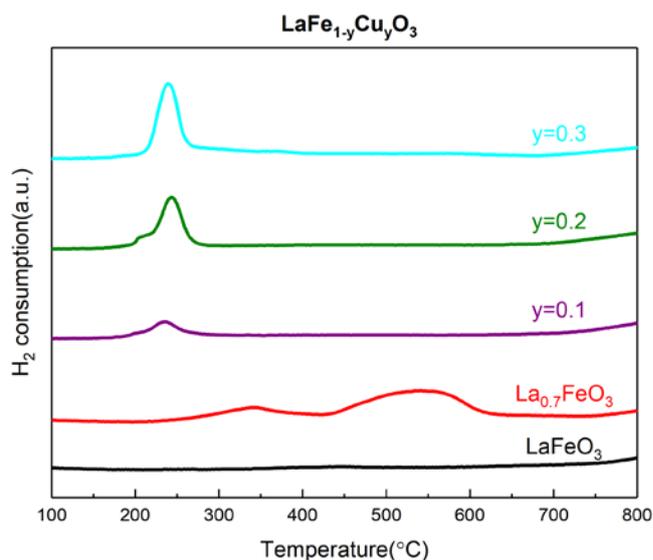
Fig. 5.9. H$_2$ consumption curves plotted against temperature for stoichiometric perovskites doped with copper LaFe$_{1-y}$Cu$_y$O$_3$ purple:y=0.1; olive:y=0.2; cyan:y=0.3.

H$_2$ absorption profiles for the La-deficient perovskites La$_{0.7}$Fe$_{1-y}$Cu$_y$O$_3$ are displayed in Fig. 5.10. Confirmation of the existence of different of oxidic copper species can be made considering the shoulder peaks appearing at T<200°C for all above mentioned three samples. The higher the copper content, the more extraction of copper from the B site, which might be supported by the broadening the shoulder peak. The even shoulder peak of the sample with the highest copper content (y = 0.3) suggested that reduction of different copper species seemed to be more synchronous compared to the Cu composition y = 0.1 and y = 0.2 whose reduction processes occurred in a more separate way marked by the abrupt should peaks. A prominent trend worth noting is that La-deficient perovskites are linked with greater H$_2$ uptake quantity in comparison to the stoichiometric perovskites with equal copper doping content (Table 5.6.), proving that deficit of A-site atoms contribute to the improvement of the overall reducibility of perovskites. Specifically, a reasonable explanation for this phenomenon is that the extraction of copper species out of the bulk is strengthened by La-deficiency, rendering them a higher dispersity and accessibility to reactants, although no Fe^{4+} species were detected.
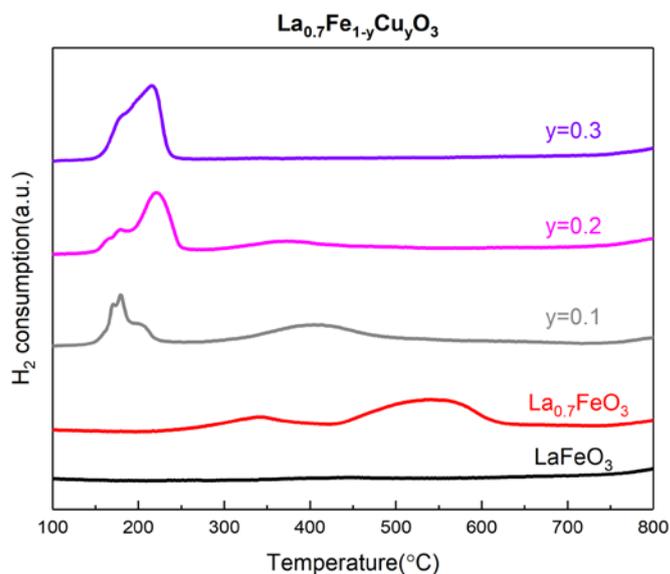
Fig. 5.10. H_2 consumption curves plotted against temperature for La-deficient perovskites doped with copper $La_{0.7}Fe_{1-y}Cu_yO_3$ grey:y=0.1; magenta:y=0.2; violet:y=0.3.

H_2 consumption profiles for perovskites doped with both calcium and copper are shown in Fig. 5.11. Similar to the previous discussed $La_{0.7}Fe_{1-y}Cu_yO_3$, the reduction of bulk copper for the La-deficient candidates x = 0.1 and 0.2 were accompanied with reduction of segregated oxidic copper-containing phases, exhibited by shoulder peaks below 200°C. Less calcium doping content promoted segregation of both iron and copper from the bulk, demonstrated by the higher H_2 consumption in the temperature range 300-650°C and more prominent appearance of shoulder peak below 200°C. The less the calcium content, the greater total H_2 consumption was observed. Less calcium doping content means more A site deficiency, suggesting that defective site number in A site plays a crucial role in the reducibility of the iron-based perovskites. This may account for the greater total H_2 consumption as calcium content diminished (Table 5.6.).
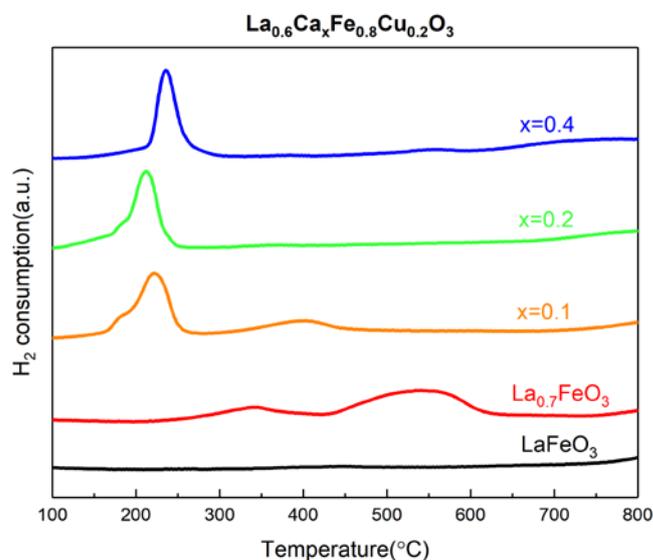
Fig. 5.11. H_2 consumption curves plotted against temperature for calcium and copper co-doped perovskites $La_{0.6}Ca_xFe_{0.8}Cu_{0.2}O_3$ orange:x=0.1; green:x=0.2; blue:x=0.4.

Table 5.6. Detailed H_2-TPR results for perovskites ABO_3 (A = La, Ca; B = Fe, Cu) calcined at T = 600°C.

Catalyst composition	H_2 total uptake (mmol g^{-1})[a]	H_2 uptake Cu(II) red. (mmol g^{-1})[b]	H/B	H/Cu	Extracted Cu^{0} [c]	T_{max} reduction peaks (°C)		
						LT	MT	HT
$LaFeO_3$	-	-	-	-	-	-	-	-
$La_{0.7}FeO_3$	1.45	-	0.58	-	-	-	340	541
$LaFe_{0.9}Cu_{0.1}O_3$	0.29	0.29	0.14	1.4	1.05%	234	-	-
$LaFe_{0.8}Cu_{0.2}O_3$	0.72	0.72	0.35	1.75	3.92%	243	-	-
$LaFe_{0.7}Cu_{0.3}O_3$	1.15	1.15	0.56	1.87	6.79%	239	-	-
$La_{0.7}Fe_{0.9}Cu_{0.1}O_3$	1.26	0.44	0.51	1.76	3.15%	200	404	-
$La_{0.7}Fe_{0.8}Cu_{0.2}O_3$	1.27	0.93	0.52	1.88	6.27%	221	373	-
$La_{0.7}Fe_{0.7}Cu_{0.3}O_3$	1.41	1.41	0.57	1.92	8.58%	215	-	-
$La_{0.6}Ca_{0.1}Fe_{0.8}Cu_{0.2}O_3$	1.44	1.02	0.56	1.97	6.59%	221	403	-
$La_{0.6}Ca_{0.2}Fe_{0.8}Cu_{0.2}O_3$	1.1	1.06	0.43	2.09	6.46%	212	361	-
$La_{0.6}Ca_{0.4}Fe_{0.8}Cu_{0.2}O_3$	1.07	0.99	0.44	2.04	6.21%	236	385	546

[a] total H_2 consumption was calculated taking into account the temperature range 150-700°C.
[b] assuming H_2 consumption at T<300°C was completely ascribed to copper species
[c] extracted Cu^0 means the maximum weight percentage of copper in the solid complex after H_2-TPR experiment assuming that Cu^{2+} was completely reduced to metallic Cu^0

Detailed results of H_2-TPR are presented in Table 5.6. The greatest H_2 total consumption amount was recorded on the La-deficient $La_{0.7}FeO_3$ formulation (1.45 mmol g^{-1}). As shown in Eqs. 5-2 and 5-3), if the two-step reduction of hematite is complete then H_2 consumption at high temperature should be twice higher than that corresponding to the low temperature process. The ratio of H_2 uptake ~2.10 shows a good agreement according to the margin of error. This confirms the complete reduction of the extracted hematite to metallic iron.

Another point worth noting is that since in our experiment the reduction of isolated copper species located in B site of the perovskite and segregated CuO occur quasi simultaneously. It is therefore difficult to distinguish accurately the H_2 consumption corresponding to the reduction of both oxidic copper species. The H/Cu ratio can still be inferred thanks to the similarity of the reduction process from Cu^{2+} to metallic Cu^0.

It is established that reduction of CuO usually occurs at the interface between Cu and CuO and it is often a complex process involving an induction period and the embedding of hydrogen into the bulk of CuO [J.Y. Kim 2003]. However, previous literatures do not agree on the specific routes of the reduction process. Different mechanisms have been proposed by several authors [W.P. Dow 1996; M. Fernandez-Garcia 1998]. It has been proven that reduction of CuO by H_2 is influenced by many factors such as the preparation method, H_2 concentration, gas flowrate, heating rate, etc. The reaction pathways as well as intermediate species are heavily dependent on the experimental conditions. In summary, reduction of CuO could occur in one or two or even three steps depending on the specific experimental conditions.

According to Rodriguez [J. Rodriguez 2003] the reduction of CuO according to a sequential process can involve the following two steps involving the intermediate formation of Cu_2O :

$$Mechanism\ 1-a\ )\quad 2CuO + H_2 \rightarrow Cu_2O + H_2O \qquad\qquad (eq.\ 5-4)$$

$$Mechanism\ 1-b)\quad Cu_2O + H_2 \rightarrow 2Cu^0 + H_2O \qquad\qquad (eq.\ 5-5)$$

Sometimes more than one intermediate, i.e. Cu_4O_3, may be generated. In such case, reduction of CuO to Cu^0 becomes three steps according to Eq. 5-6 [J.Y. Kim 2003].

$$CuO \rightarrow Cu_4O_3 \rightarrow Cu_2O \rightarrow Cu^0 \qquad\qquad (eq.\ 5-6)$$
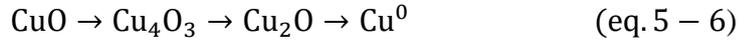
In contrast, one step reduction of CuO (direct reduction) is presented below [J. Rodriguez 2003].

$$Mechanism\ 2\ -\ CuO + H_2 \rightarrow Cu^0 + H_2O \qquad\qquad (eq.\ 5-7\ )$$
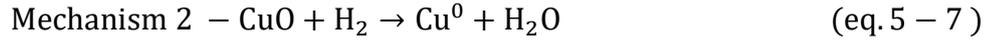
As seen from Eqs. 5-5, 5-6, 5-7, Mechanism 1 and mechanism 2 differ in terms of the presence or non-presence of intermediates. In most cases, these two mechanisms occur simultaneously and compete with each other. According to Kim et coll. [J.Y. Kim 2003], mechanism 1 is favored by limited H_2 supply and faster heating rate during the H_2-TPR experiment. It was argued that by Himelfarb [P.B. Himelfarb 1983] that the intermediate reduction of CuO to Cu_2O (mechanism 1-a) takes place preferentially compared to Cu_2O to Cu^0 (mechanism 1-b) or CuO to Cu^0 (mechanism 2). The same author concluded that regarding mechanism 1(Take the two-step pathway as an example in which Cu_2O is the unique intermediate.) metallic Cu^0 would not be formed until all CuO was reduced to Cu_2O. Kim[J.Y. Kim 2003] believed that mechanism 2 is easier to occur than mechanism 1.From a kinetic point of view, the apparent activation energy for Cu_2O reduction is about 27.4 kcal/mol (mechanism 1-b), while the apparent activation energy for the direct reduction of CuO (mechanism 2) is much less (around 14.5 kcal/mol), which may account for the easier occurrence of the latter. [J.Y. Kim 2003]

$$\left(\frac{H}{Cu}\right)_{max} = 2.0 \qquad\qquad (eq.\ 5-8)$$

Regardless of the specific reduction process, the maximum H/Cu value should be 2.0 in case of complete reduction of Cu^{2+} to metallic Cu^0 Eq. 5-8. Regarding the $LaFe_{1-y}Cu_yO_3$ perovskites, higher copper substitution degree gave rise to higher H/Cu ratio, implying a strengthened reducibility of copper. H/Cu ratio less than 2.0 indicates that Cu^{2+} was not completely reduced to metallic Cu^0 under the given experimental condition (powder, diluted H_2, flowrate = 50 mL/min). Similar results were obtained for $La_{0.7}Fe_{1-y}Cu_yO_3$ perovskites. A striking increase of H/Cu ratio was recorded in La-deficient $La_{0.7}Fe_{1-y}Cu_yO_3$ perovskites in comparison with A-site stoichiometric $LaFe_{1-y}Cu_yO_3$ candidates having the same copper doping content in B site. This is in conformity with previous discussion that copper reducibility was promoted when subjected to La-deficiency environment, displayed by the shift towards lower temperature of the reduction peak of copper in La-deficient perovskites compared to A-site stoichiometric candidates.

As to La$_{0.6}$Ca$_x$Fe$_{0.8}$Cu$_{0.2}$O$_3$, these candidates are characterized by equal copper content in B site (20%). Theoretically, same quantity of H$_2$ consumed by copper should be measured. Thus, the slight variations observed in terms of H$_2$ quantity consumed by copper originate from changes of iron species properties responsible for H$_2$ uptake in the temperature range 300-650°C. Less calcium doping leads to more A site deficiency, resulting in more extracted copper from the bulk which is in agreement with results obtained for La$_{0.7}$Fe$_{1-y}$Cu$_y$O$_3$ candidates. Besides, A site deficiency is beneficial to the enhancement of the overall reducibility of the iron-based perovskite material. This conclusion can be further affirmed by the significant increase of total H$_2$ consumption (from 1.07 to 1.44 mmol g^{-1}).

5.1.5. Oxygen mobility

The oxygen mobility of perovskites was characterized by the Temperature-Programmed Desorption of oxygen (simply as O$_2$-TPD). It is well established that perovskite-type materials are capable of adsorbing and desorbing great amount of oxygen. Typically, two types of oxygen coexist in the perovskites: suprafacial oxygen (α-oxygen) and intrafacial oxygen (β-oxygen). [Y. Noboru 1981] These two oxygen species can be desorbed in different conditions: α-oxygen refers to oxygen species weakly bounded to the surface anion vacancies of the perovskite and are usually desorbed at low-temperature range due to the weak bond energy between adsorbed oxygen species (i.e. O$^-$ or O$_2^-$) and the linking transition metal (B site). Depending on the calcination temperature of the solid, the position of the first α-oxygen desorption peak varies but in most cases is observed below 500°C. For the same material, higher calcination temperature would result in the shift of the α-oxygen desorption peak towards higher temperature zone [S. Kaliaguine 2001]. β-oxygen (i.e. O^{2-}) (sometimes also called lattice oxygen) is present in the bulk of the perovskite and tend to be desorbed at temperature higher than 500°C. The crucial role of β-oxygen lies in their direct participation in catalytic reactions according to Mars-van-Krevelen mechanism [S. Keav 2014] and the desorption of β-oxygen is thereby usually associated with the reduction of B-site transition metal cations in the perovskite. [S. Kaliaguine 2001]. In our case, the oxidation of refractory saturated hydrocarbon can take place at high temperature and involve such species according to an intrafacial mechanism.
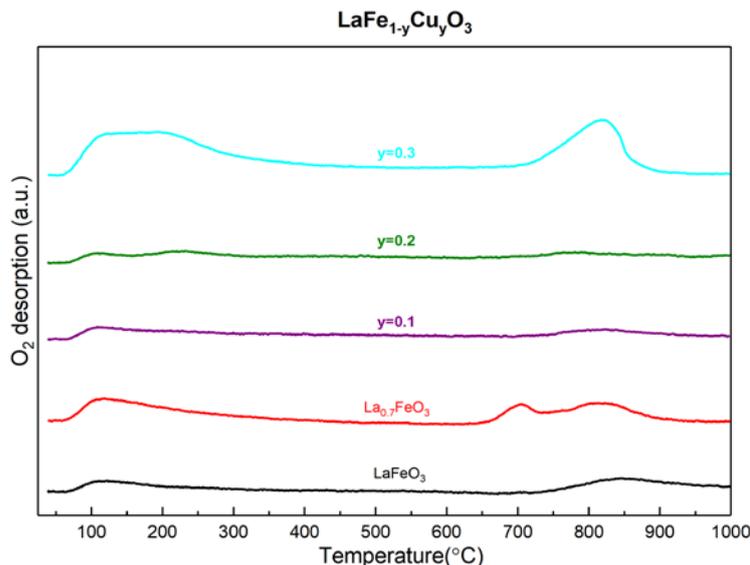
Fig. 5.12. O$_2$-TPD profile of the stoichiometric perovskites doped with copper LaFe$_{1-y}$Cu$_y$O$_3$ purple: y = 0.1; olive: y = 0.2; cyan: y = 0.3.

O$_2$-TPD profiles of the stoichiometric perovskites doped with copper LaFe$_{1-y}$Cu$_y$O$_3$ are shown in Fig. 5.12. As seen, the stoichiometric parent LaFeO$_3$ exhibited limited oxygen storage capacity with the least total oxgyen desorption quantity of 0.12 mmol g^{-1} (Table 5.7.). When the lanthanum content decreased to 70% in A site, a noticeable increase of desorbed O$_2$ quantity was observed both in the low temperature range (<600°C) and in the high temperature range (>600°C) which should be ascribed to α-oxygen and β-oxygen respectively. Slight increase of total oxygen desorption quantity was generated by copper doping y = 0.1 and y = 0.2 on the stoichiometric lanthanum ferrite compared to the parent LaFeO$_3$. Higher copper substitution degree (y = 0.3) led to a substantially larger desorption of both α-oxygen and β-oxygen as well as the subsequent total oxygen desorption amount. Consequently, one can conclude that oxygen mobility of the stoichiometric lanthanum ferrite can be enhanced by copper doping in B site. Structural defects (mainly oxygen vacancies) generated by copper doping may account for this phenomenon. This is in good agreement with previous reports which stated that copper doping in stoichiometric lanthanum ferrite resulted in lower oxygen vacancy formation energy and thus facilitate oxygen mobility of the perovskite [P. Li 2017]. Also, the remarkably increased amount of desorbed α-oxygen recorded on the stoichiometric LaFe$_{0.7}$Cu$_{0.3}$O$_3$ may be attributed to the higher surface area (26.2 m^2/g) as reported in Table 5.8.) compared to those with lower copper substitution degree (y=0.1 and y=0.2).
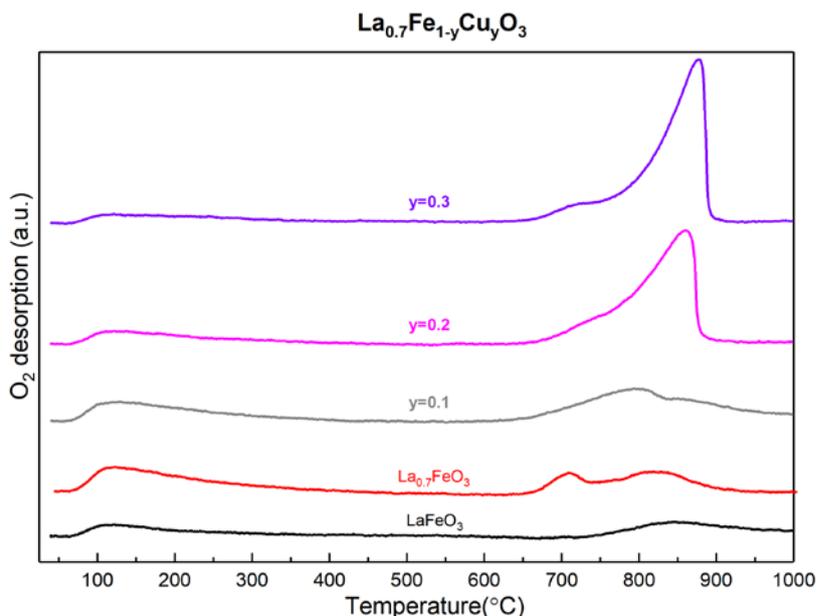
Fig. 5.13. O$_2$-TPD profile of the La-deficient perovskites doped with copper La$_{0.7}$Fe$_{1-y}$Cu$_y$O$_3$ grey: y = 0.1; magenta: y = 0.2; violet: y = 0.3.

O$_2$-TPD profiles for the La-deficient perovskites doped with copper La$_{0.7}$Fe$_{1-y}$Cu$_y$O$_3$ are displayed in Fig. 5.13. In comparison with the parent La$_{0.7}$FeO$_3$, bulk oxygen mobility was tremendously improved for the La-deficient perovskites doped with copper, especially for y = 0.2 and y = 0.3 featured by the dramatic desorption peaks at high temperature range. It is apparent that activation of bulk oxygen was triggered by copper doping. The more copper was doped, the more desorbed amount of β-oxygen became. (Table 5.7.). The greatest amount of β-oxygen desorbed was recorded on the perovskite with the highest copper doping content y=0.3, the experimental value (0.42 mmol/g) of this catalyst being more than 3 times as much as that of the La$_{0.7}$FeO$_3$, Moreover, onset of the lattice oxygen desorption shifted to lower temperature zone as a result of higher copper doping content. Besides, compared to stoichiometric perovskites LaFe$_{1-y}$Cu$_y$O$_3$, La-deficient perovskites manifested a marked augmentation of desorbed β-oxygen at the same copper substitution degree.(Table 5.7.) In brief, it can be assumed that the copper doped La-deficient perovskites might be very promising TWC candidates due to more active lattice oxygen related closely to catalytic reactions.
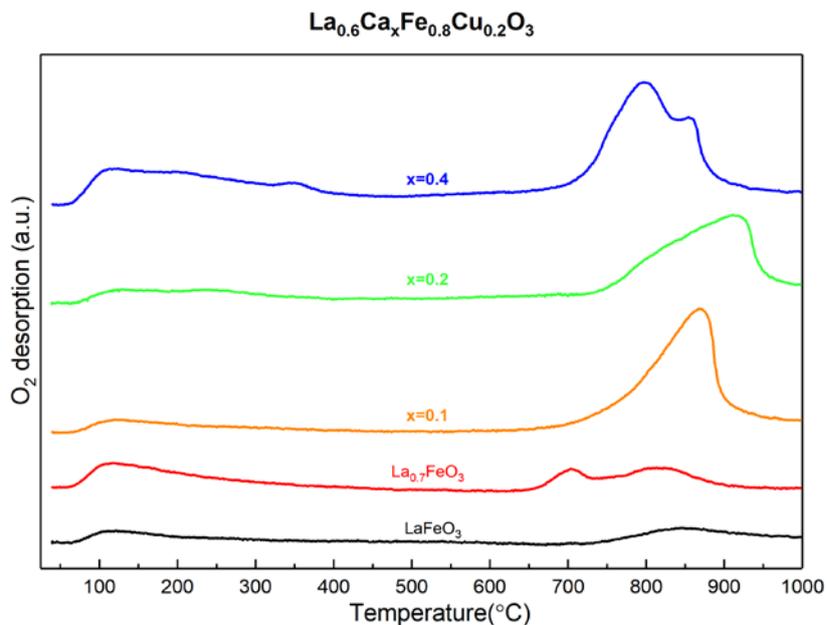
Fig. 5.14. O_2-TPD profile of calcium and copper co-doped perovskites $La_{0.6}Ca_xFe_{0.8}Cu_{0.2}O_3$ orange: x = 0.1; green: x = 0.2; blue: x = 0.4.

O_2-TPD profiles of calcium and copper co-doped perovskites $La_{0.6}Ca_xFe_{0.8}Cu_{0.2}O_3$ are shown in Fig. 5.14. Likewise, these perovskites are endowed with larger amount of desorbed bulk oxygen (Table 5.7.) compared to the parent $La_{0.7}FeO_3$. Nevertheless, onset of bulk oxygen desorption shifted to higher temperature zone (>700°C), implying presumably a detrimental effect of calcium doping in terms of activating lattice oxygen present in the sub-stoichiometric structure (x = 0.1 and x = 0.2). Particular attention should be paid to the stoichiometric co-doped perovskite $La_{0.6}Ca_{0.4}Fe_{0.8}Cu_{0.2}O_3$, which is characterized by the highest amount of both desorbed surface oxygen and desorbed bulk oxygen among all the examined compositions. The former might be explained by the increased number of transition metal sites and oxygen vacancy sites on the surface while the latter seems more linked with the reduced structural stability originating from lattice distortion induced by calcium doping observed from XRD patterns, beneficial to oxygen desorption.

Based upon the above results, one can conclude that oxygen storage capacity of the iron-based perovskites is facilitated by copper doping in B site. Such trend is further reinforced by A-site cationic deficiency and maximized when calcium incorporation is performed on stoichiometric structure.

Table 5.7. Quantitative analysis of O$_2$-TPD experiments

Catalyst	Amount of O$_2$ desorbed (mmol/g)[a]		
	α–O$_2$ [b]	β–O$_2$ [c]	Total O$_2$ desorbed[d]
LaFeO$_3$	0.09	0.03	0.12
La$_{0.7}$FeO$_3$	0.15	0.12	0.27
LaFe$_{0.9}$Cu$_{0.1}$O$_3$	0.09	0.03	0.12
LaFe$_{0.8}$Cu$_{0.2}$O$_3$	0.1	0.03	0.13
LaFe$_{0.7}$Cu$_{0.3}$O$_3$	0.34	0.14	0.48
La$_{0.7}$Fe$_{0.9}$Cu$_{0.1}$O$_3$	0.12	0.16	0.28
La$_{0.7}$Fe$_{0.8}$Cu$_{0.2}$O$_3$	0.09	0.34	0.43
La$_{0.7}$Fe$_{0.7}$Cu$_{0.3}$O$_3$	0.07	0.42	0.49
La$_{0.6}$Ca$_{0.1}$Fe$_{0.8}$Cu$_{0.2}$O$_3$	0.08	0.38	0.46
La$_{0.6}$Ca$_{0.2}$Fe$_{0.8}$Cu$_{0.2}$O$_3$	0.1	0.35	0.45
La$_{0.6}$Ca$_{0.4}$Fe$_{0.8}$Cu$_{0.2}$O$_3$	0.27	0.44	0.71

Note:
[a] Calculated by deconvolution of the O$_2$-TPD curves
[b] Amount of α-O$_2$ was calculated in the temperature range 60-600°C
[c] The amount of β-O$_2$ was calculated in the temperature range 600-1000°C.
[d] Slight quantity of physisorbed O$_2$ was included in the calculation of the amount of total O$_2$ desorbed

Summarizing the data collected from H$_2$-TPR and O$_2$-TPD experiment then tentative explanation can be given to describe the reduction process of cations in B-site and oxygen desorption according to the approach earlier suggested by W. Yang [W. Yang 2012] assuming that reactions follow a Mars-van-Krevelen mechanism. Cu^{2+} surface reduction corresponding to α-O$_2$ desorption (taking the one-step mechanism for example due to the ease of this reaction):

$$\text{(eq. 5-9)}$$
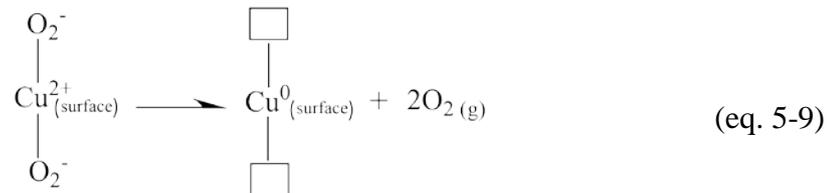
$\square$ −anionic vacancy

Fe^{3+} surface reduction corresponding to α-O$_2$ desorption(consider only the reduction of Fe^{3+} to Fe^{2+} since Fe^{2+} cannot be fully reduced to metallic Fe^0 below 1000°C according to H$_2$-TPR experiment):

$$\text{(eq. 5-10)}$$

$$\text{(eq. 5-11)}$$
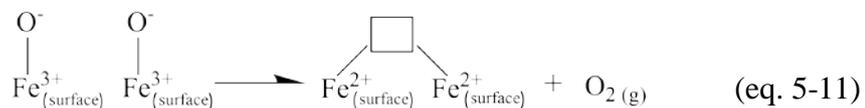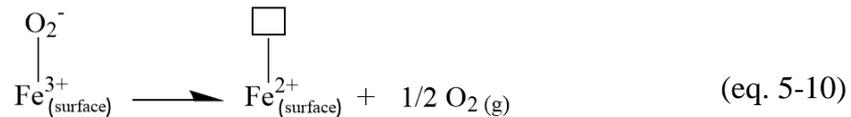
Eqs. 5-10 and 5-11 correspond to reduction of surface iron linked with O_2^- and O^- species respectively. Bulk reduction Cu^{2+} bonded to oxygen lattice corresponding to β-O$_2$ desorption as follows (taking the one-step mechanism for example):

$$\underset{Cu^{2+}_{(bulk)}}{\overset{O^{2-}}{|}} \longrightarrow \underset{Cu^0_{(bulk)}}{\overset{\square}{|}} + O_{2\,(g)} \qquad (eq.\ 5\text{-}12)$$
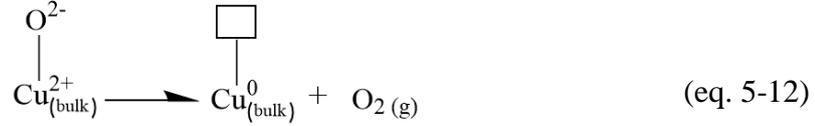
Fe^{3+} bulk reaction corresponding to β-O$_2$ desorption as follows ((consider only the reduction of Fe^{3+} to Fe^{2+}):

$$\underset{Fe^{3+}_{(bulk)}\ Fe^{3+}_{(bulk)}}{\overset{O^{2-}}{\diagup\diagdown}} \longrightarrow \underset{Fe^{2+}_{(bulk)}\ Fe^{2+}_{(bulk)}}{\overset{\square}{\diagup\diagdown}} + 1/2\ O_{2\,(g)} \qquad (eq.\ 5\text{-}13)$$
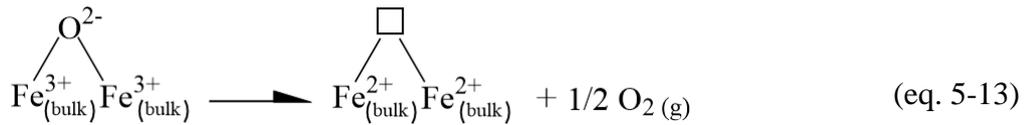
In case of reduction of Fe^{4+} to Fe^{3+} (as a small fraction of Fe^{4+} species is present in the stoichiometric perovskites), reduction process corresponding to α-O$_2$ desorption is written:

$$\underset{Fe^{4+}_{(surface)}}{\overset{O_2^-}{|}} \longrightarrow \underset{Fe^{3+}_{(surface)}}{\overset{\square}{|}} + O_{2\,(g)} \qquad (eq.\ 5\text{-}14)$$

$$\underset{Fe^{4+}_{(surface)}}{\overset{O^-}{|}}\ \underset{Fe^{4+}_{(surface)}}{\overset{O^-}{|}} \longrightarrow \underset{Fe^{3+}_{(surface)}\ Fe^{3+}_{(surface)}}{\overset{\square}{\diagup\diagdown}} + O_{2\,(g)} \qquad (eq.\ 5\text{-}15)$$
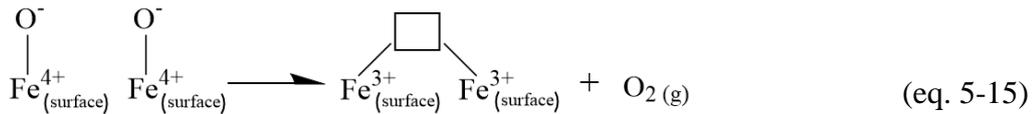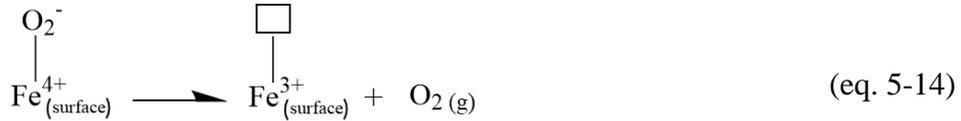
Eqs. 5-14 and 5-15 correspond to O_2^- and O^- species respectively whereas as to β-O$_2$ desorption in Fe^{4+} sites reduction process agrees with Eq. 5-16.

$$\underset{Fe^{4+}_{(bulk)}\ Fe^{4+}_{(bulk)}}{\overset{O^{2-}}{\diagup\diagdown}} \longrightarrow \underset{Fe^{3+}_{(bulk)}\ Fe^{3+}_{(bulk)}}{\overset{\square}{\diagup\diagdown}} + 1/2\ O_{2\,(g)} \qquad (eq.\ 5\text{-}16)$$
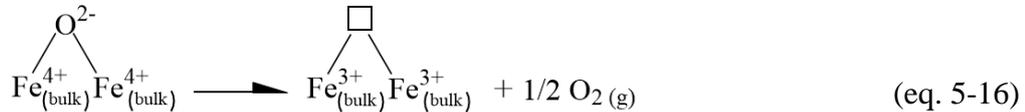
However, it should be mentioned that Eqs. 5-14, 5-15 could only occur in perovskites with stoichiometric composition. For the La-deficient perovskites the reduction of iron associated to oxygen desorption follows exclusively Eqs. 5-10, 5-11, 5-12, 5-13 due to the non-detection of Fe^{4+} species.

To summarize, copper doping in B site led to enhanced bulk oxygen mobility for both stoichiometric LaFe$_{1-y}$Cu$_y$O$_3$ and A-site deficient La$_{0.7}$Fe$_{1-y}$Cu$_y$O$_3$ perovskites. Such trend became more remarkable for the latter, represented by the significantly increased amount of desorbed β-oxygen. Calcium doping appeared beneficial to the enhancement of bulk oxygen mobility, although no evident correlation was found as to the relationship between calcium doping content and desorbed β-oxygen amount. The greatest amount of total oxygen desorbed corresponded to the stoichiometric co-substituted formulation La$_{0.6}$Ca$_{0.4}$Fe$_{0.8}$Cu$_{0.2}$O$_3$,

indicating this perovskite may possess good properties in terms of oxygen storage and release. In addition, the desorption peak above 600 °C of such catalyst shifted towards lower temperature zone, probably suggesting a more active lattice oxygen resulting from the intensification of the synergistic effect of calcium and copper.

5.2. Surface properties

5.2.1. Nitrogen physisorption

Textural properties of the prepared perovskites are examined by nitrogen adsorption method. Values of specific surface area of the materials are displayed in Table 5.8. In view that a relatively high thermal treatment temperature (600°C) was employed during the synthesis process, the as prepared perovskites exhibited low specific surface area, resulting mainly from the agglomeration of the product particles subjected to high temperature and heating duration. This is in accordance with previous reports [J. Yang 2010; N. Choudhary 2018] No obvious correlation between specific surface area and structural composition was observed. The highest specific surface area value was recorded on the substoichiometric parent La$_{0.7}$FeO$_3$, possibly resulting from the role of hematite segregation in preventing particle agglomeration.

Table 5.8. Specific surface area (SSA) of the iron-based perovskite solid ABO$_3$ (A=La, Ca; B= Fe, Cu) synthesized through CCM.

Catalyst	SSA (m^2/g) [a]	S$_{th}$ (m^2/g) [b]	Pore volume (cm^3/g)
LaFeO$_3$	15.5	30.8	0.10
La$_{0.7}$FeO$_3$	35.5	41.7	0.10
LaFe$_{0.9}$Cu$_{0.1}$O$_3$	19.2	29.0	0.09
LaFe$_{0.8}$Cu$_{0.2}$O$_3$	15.3	26.9	0.09
LaFe$_{0.7}$Cu$_{0.3}$O$_3$	26.2	35.2	0.09
La$_{0.7}$Fe$_{0.9}$Cu$_{0.1}$O$_3$	32.2	37.2	0.10
La$_{0.7}$Fe$_{0.8}$Cu$_{0.2}$O$_3$	23.2	31.6	0.10
La$_{0.7}$Fe$_{0.7}$Cu$_{0.3}$O$_3$	15.4	21.4	0.10
La$_{0.6}$Ca$_{0.1}$Fe$_{0.8}$Cu$_{0.2}$O$_3$	22.1	27.8	0.08
La$_{0.6}$Ca$_{0.2}$Fe$_{0.8}$Cu$_{0.2}$O$_3$	21.3	29.8	0.11
La$_{0.6}$Ca$_{0.4}$Fe$_{0.8}$Cu$_{0.2}$O$_3$	32.4	37.1	0.11

Note:

a: SSA derived from N$_2$ physisorption

b: SSA estimated from equation $S_{th} = 6 \times 10^3/(\rho_{perovskite} d_{Rietveld})$

$\rho_{perovskite}$ − density of perovskite, $g \cdot m^{-3}$

$d_{Rietveld}$ − crystallite size calculated from Rietveld refinement, m

Specific surface area is plotted against crystallite size calculated from XRD pattern displayed in Table 5.3. for each perovskite. A general trend shows that higher crystallite size resulted in lower specific surface area although the precise correlation between the two was not determined. The loss of specific surface area is mainly ascribed to the high calcination temperature which accelerates grain aggregation due to the sintering of particles, thus leading to the growth of crystallite.
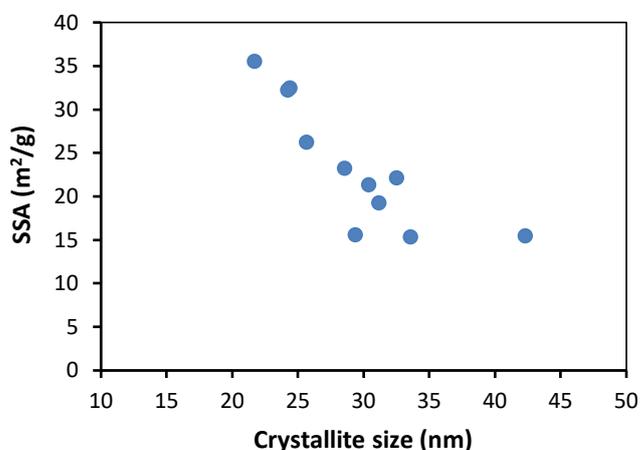
Fig. 5.15. Specific surface area plotted against crystallite size for iron-based perovskites ABO$_3$ (A=La, Ca; B= Fe, Cu).

Isotherms and pore size distribution of several selected perovskites are shown in Fig. 5.16. The isotherms of the measured perovskites follow seemingly the Brunauer type V trend in light of the concave shape without evident "B point" in the low relative pressure range. The interaction between the adsorbent and the adsorbate appeared weak but capillary condensation was still observed at higher relative pressure zone. As general trend, the pore volume and pore size distribution evidence a weak internal pore structure.
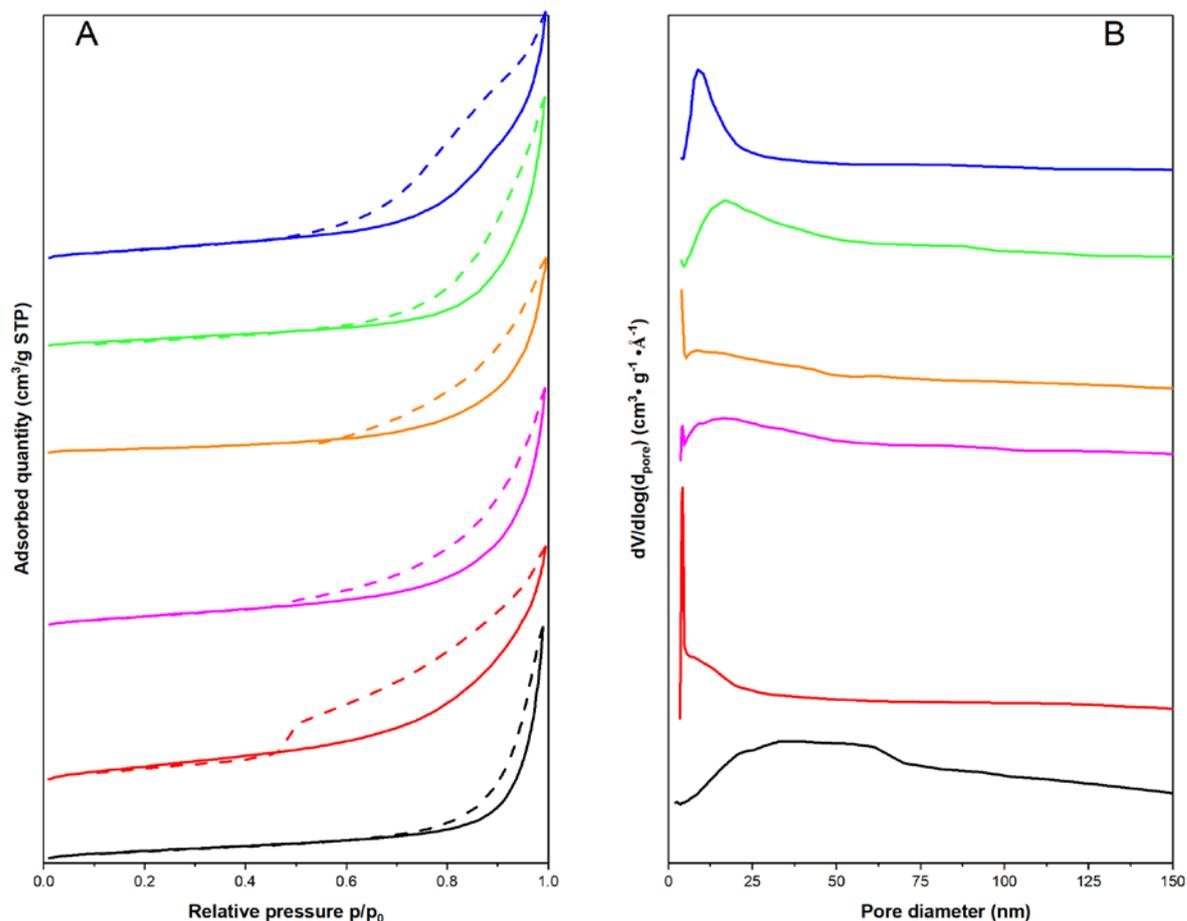
Fig. 5.16. Textural properties of selected perovskites A-Adsorption isotherms solid: adsorption; dash: desorption   B-pore size distribution calculated from desorption process. Black : $LaFeO_3$; Red : $La_{0.7}FeO_3$; Magenta : $La_{0.7}Fe_{0.8}Cu_{0.2}O_3$; Orange : $La_{0.6}Ca_{0.1}Fe_{0.8}Cu_{0.2}O_3$; Green : $La_{0.6}Ca_{0.2}Fe_{0.8}Cu_{0.2}O_3$; Blue : $La_{0.6}Ca_{0.4}Fe_{0.8}Cu_{0.2}O_3$.

5.2.2. XPS analysis

X-ray photoelectron spectroscopic analysis was implemented to analyze the surface on a depth in the range 5-10 nm. For bulk catalysts this resolution can provide information on the oxidation state and the elemental composition representative of the outermost layer. Binding Energy (B.E.) values have been obtained from the characteristic La 3d, Ca 2p, Fe 2p, Cu 2p and O 1s core levels with C 1s used as internal reference at 285 eV. XPS photopeaks are reported in Figs. 5.17.-5.20. and the corresponding B.E. values are collected and compared in Table 5.9. They underline a greater stabilization of La^{3+} and Ca^{2+} on all Ca-substituted samples. The Fe 2p photopeak is usually characterized by the presence of a shake-up satellite structure near 719 eV with only slight deviations in B.E. the Fe $2p_{3/2}$ photopeak which agrees with the predominance Fe^{3+}. On the other hand, more significant perturbations are observable on the Cu $2p_{3/2}$ photopeak with B.E. value varying in the range 932.8 and 934.4 eV. A shake-up satellite structure also appear the range 939-950 eV characteristic of Cu^{2+}. Reduced and oxidized copper species are currently reported near 932.6 and 934.2 eV [F.E. Lopez-Suarez 2009; L. Zhang 2012] Accordingly, the Cu 2p core level near 934 eV, with a more intense shake-up satellite structure reflect a greater stabilization of Cu^{2+} especially on Co-doped

samples. For the series $LaFe_{1-y}Cu_yO_3$, with y =0.1-0.3, lower B.E. values are noticeable associated to an attenuation of the shake-up structure which could reflect the coexistence of Cu^{2+} species and more reduced copper species. Such tendencies are also noticeable on $La_{0.7}Fe_{0.8}Cu_{0.2}O_3$. In order to get more insight into the oxidation state of copper on these samples the Auger line Cu LMM has been examined with kinetic energy values reported in Table 5.11. The Auger parameter can be estimated corresponding to the sum of the B.E. $Cu2p_{3/2}$ and the kinetic energy of the Cu LMM Auger line. The values are collected in Table 5.11. As already reported Auger parameters differ on Cu^0 and Cu(I) shifting from 1851.3 eV to 1849.1 eV. [N.Y. Adonin, 2016; G.G. Jernigan 1994) Lower values have been reported on CuCl near 1847.8 eV [N.Y. Adonin 2016]. By comparing those values with that reported in Table 5.11. one cannot rule out the presence of more reduced copper species coexisting with Cu(II). As a conclusion, more reduced copper species coexist with Cu(II) species in $LaFe_{1-y}Cu_yO_3$. It is worthwhile to note that the Auger line shifts to higher values at increasing copper content which would suggest a more extensive reduced state. It is interesting to note that the Auger lines on $La_{0.6}Ca_xFe_{0.8}Cu_{0.2}O_3$ remains quasi-unchanged with B.E. values near 934.0 eV in agreement with the current value reported for Cu(II). Correlatively, the intensity of the peak satellite is progressively restored on Ca-doped samples which highlight their growth at the expense of more reduced copper species.

The origin of the formation of reduced species is not trivial but has been already observed from XPS analysis [A. Schön 2018; F. Amano 2004]. They have been assigned to extra-framework Cu^{2+} species stabilized as CuO more reducible than Cu^{2+} in octahedral coordination inside the perovskite lattice. Hence, under X-ray beam irradiation, these less stable CuO species would decompose to Cu(I) and Cu^0.
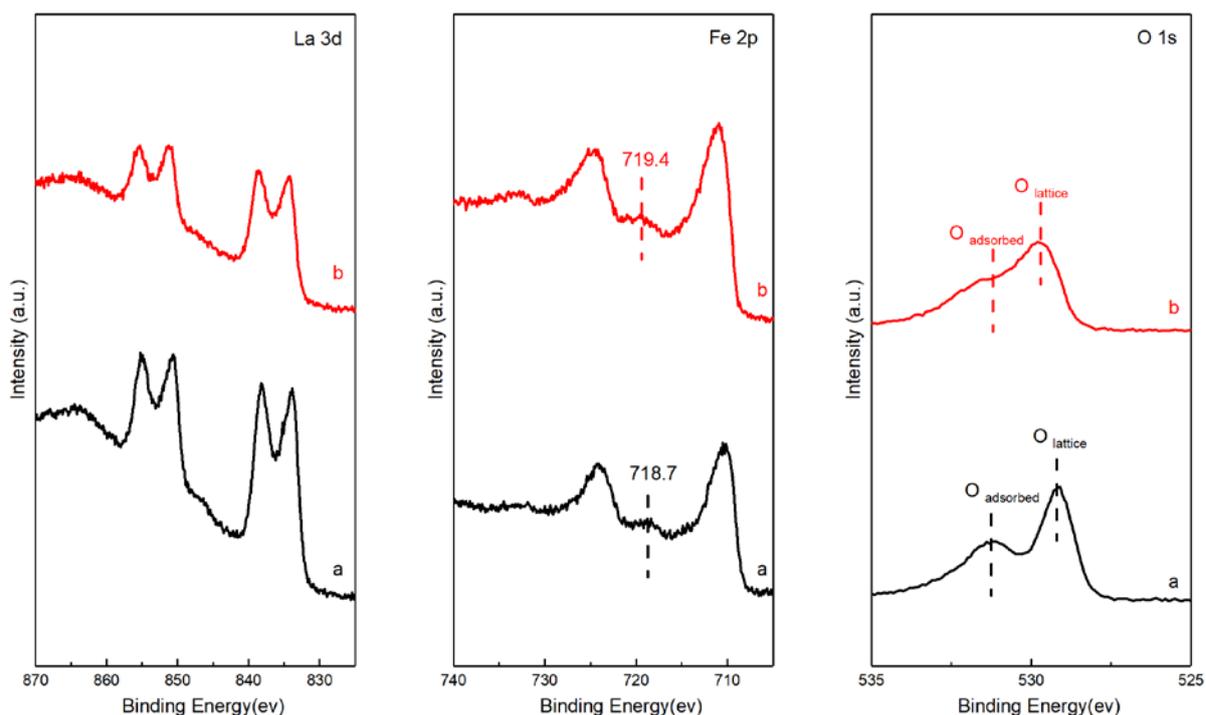
Fig. 5.17. Photopeaks of the parent perovskites $LaFeO_3$ and $La_{0.7}FeO_3$ Black (a): $LaFeO_3$; Red (b): $La_{0.7}FeO_3$.
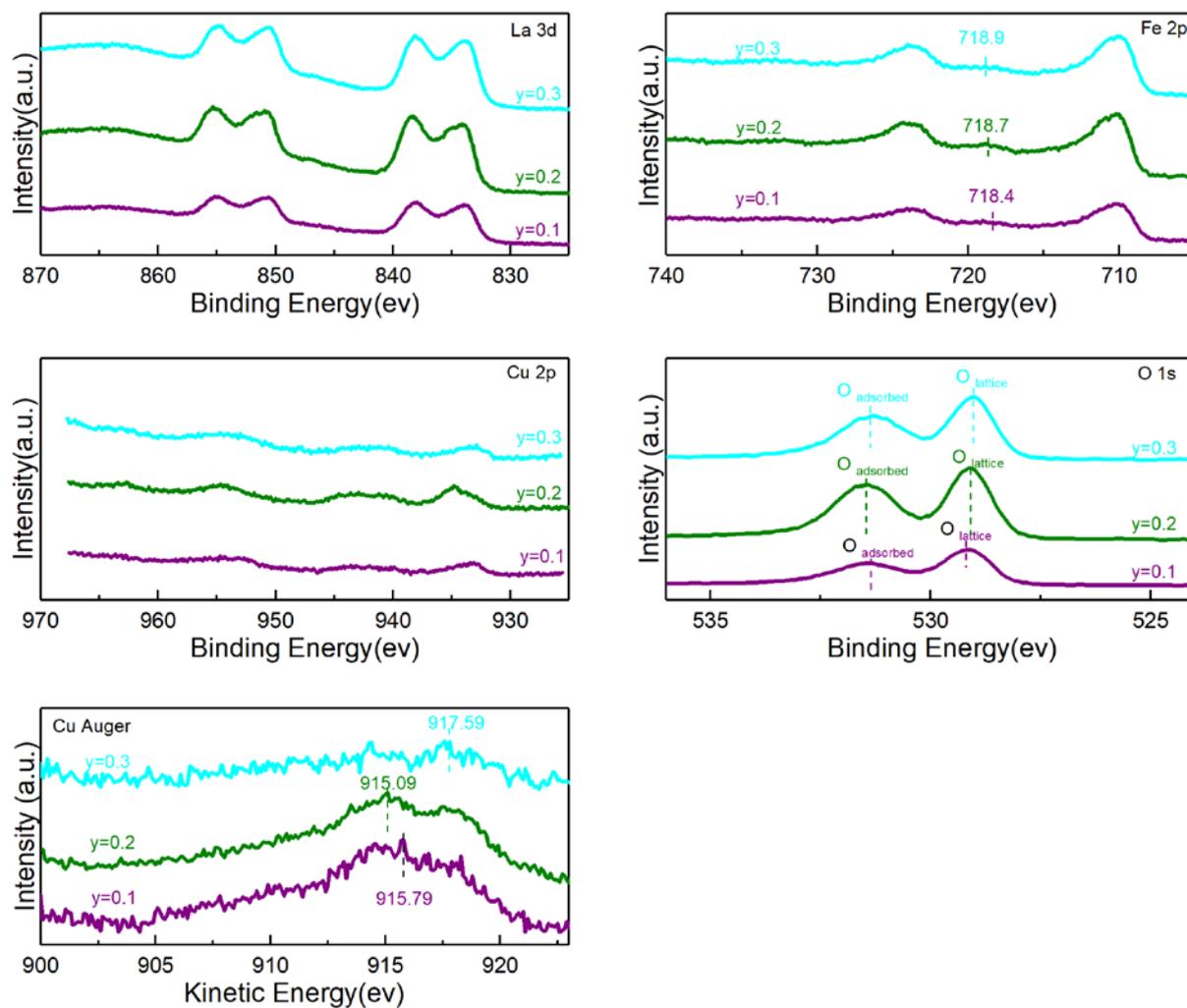
Fig. 5.18. Photopeaks of LaFe$_{1-y}$Cu$_y$O$_3$ La : 3d; Fe : 2p; Cu : 2p; O 1s; Cu Auger. Purple : y = 0.1; olive: y = 0.2; cyan: y = 0.3.
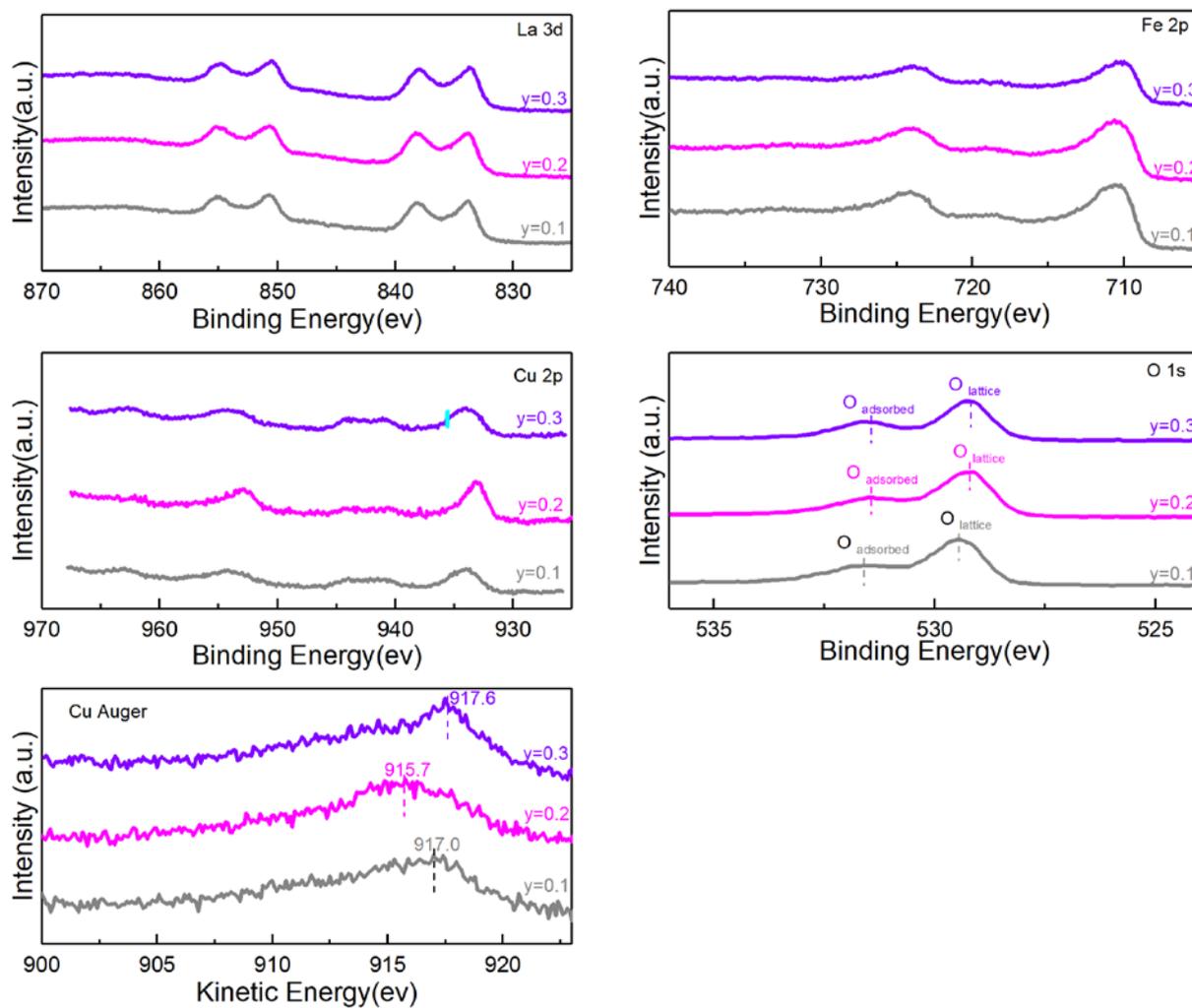
Fig. 5.19. Photopeaks $La_{0.7}Fe_{1-y}Cu_yO_3$ La : 3d; Fe : 2p; Cu : 2p; O 1s; Cu Auger. Grey : y = 0.1; magenta:y = 0.2; violet:y = 0.3.
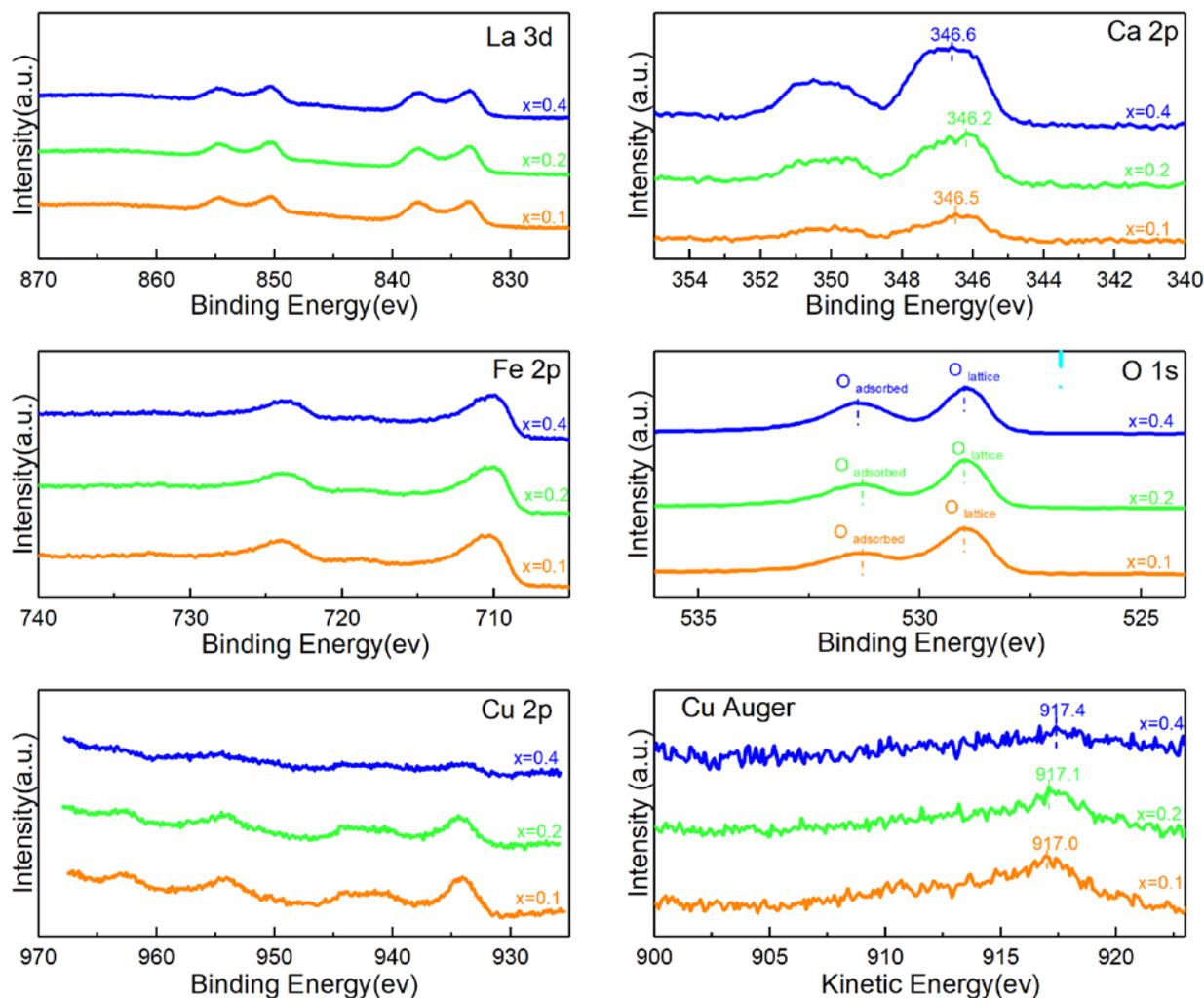
Fig. 5.20. Photopeaks of $La_{0.6}Ca_xFe_{0.8}Cu_{0.2}O_3$ La : 3d; Ca : 2p; Fe : 2p; Cu : 2p; O 1s; Cu Auger. Orange : x = 0.1; green : x = 0.2; blue : x = 0.4.

The semi-quantitative analysis leads to the significant deviation on the surface composition. As illustrated in Table 5.10., usual surface La enrichment is noticeable on the parent stoichiometric $LaFeO_3$ sample which is lowered on La-deficient samples even disappearing on $La_{0.7}FeO_3$ and calcium-doped samples. As a general trend, there is no significant deviation on the surface and bulk ratio La/Ca. On the other hand, significant fluctuations arise on the surface copper concentration, the highest surface concentration being observed on $La_{0.7}Fe_{0.8}Cu_{0.2}O_3$ then decreasing with a rise in Ca loading notably on the stoichiometric $La_{0.6}Ca_{0.4}Fe_{0.8}Cu_{0.2}O_3$ sample. This tendency is consistent with the evolution observed on the Cu LMM Auger peak showing that the bulk diffusion of copper and subsequent surface enrichment is prevented on stoichiometric composition containing high amount of calcium.

Table 5.9. XPS data, B.E. and surface composition of perovskites

Catalyst	Binding energy (eV)							Semi-quantitative analysis		
					O 1s		C 1s			
	La 3d	Ca 2p	Fe 2p	Cu 2p	Adsorbed oxygen	Lattice oxygen	Carbonyl, metal carbonate	O_{ads} (%)	$O_{lattice}$ (%)	CO_3^{2-} (%)
$LaFeO_3$	833.8	-	710.2	-	531.1	529.2	289.0	56.1	43.9	14.7
$La_{0.7}FeO_3$	834.2	-	710.9	-	531.2	529.7	289.1	61.7	38.3	11.5
$LaFe_{0.9}Cu_{0.1}O_3$	833.8	-	710.3	932.9	531.5	529.3	289.3	48.9	51.1	12.6
$LaFe_{0.8}Cu_{0.2}O_3$	833.6	-	709.8	932.8	531.6	529.2	289.3	55.0	45.0	15.9
$LaFe_{0.7}Cu_{0.3}O_3$	833.7	-	709.9	932.9	531.3	529.0	289.2	53.3	46.7	16.5
$La_{0.7}Fe_{0.9}Cu_{0.1}O_3$	833.8	-	710.2	933.7	531.4	529.4	288.7	44.5	55.5	11.3
$La_{0.7}Fe_{0.8}Cu_{0.2}O_3$	833.7	-	710.6	933.1	531.3	529.2	288.9	42.9	57.1	17.7
$La_{0.7}Fe_{0.7}Cu_{0.3}O_3$	833.8	-	710.0	934.0	531.5	529.3	288.9	40.2	59.8	12.6
$La_{0.6}Ca_{0.1}Fe_{0.8}Cu_{0.2}O_3$	833.4	346.5	710.2	934.1	531.2	529.0	288.9	43.9	56.1	12.6
$La_{0.6}Ca_{0.2}Fe_{0.8}Cu_{0.2}O_3$	833.3	346.2	709.9	934.4	531.3	529.0	288.9	46.9	53.2	15.3
$La_{0.6}Ca_{0.4}Fe_{0.8}Cu_{0.2}O_3$	833.5	346.6	709.9	934.1	531.4	529.0	289.3	51.3	48.7	18.9

[a] $O_{adsorbed}+O_{lattice}=1$
[b] $C_{carbonyl}+C_{adventious}=1$
[c] relative abundance of oxygen and carbonyl species was calculated from deconvolution of photopeaks

Table 5.10. Semi-quantitative analysis of XPS data from Figs. 5.17.-5.20.

Catalyst	Surface atomic composition (%)						Atomic ratio		
	La	Ca	Fe	Cu	O	C	Ca/La	Cu/Fe	A/B
$LaFeO_3$	13.37	-	9.99		40.56	36.08	-		1.34
$La_{0.7}FeO_3$	9.17	-	19.12		39.75	31.96	-		0.48
$LaFe_{0.9}Cu_{0.1}O_3$	12.94	-	9.72	1.24	41.51	34.6	-	0.13	1.18
$LaFe_{0.8}Cu_{0.2}O_3$	14.11	-	9.6	2.07	43.46	30.76	-	0.22	1.21
$LaFe_{0.7}Cu_{0.3}O_3$	14.78	-	9.25	1.07	41.8	33.1	-	0.12	1.43
$La_{0.7}Fe_{0.9}Cu_{0.1}O_3$	9.02	-	17.52	2.61	39.37	31.48	-	0.15	0.45
$La_{0.7}Fe_{0.8}Cu_{0.2}O_3$	11.6	-	19.02	3.4	45.13	20.86	-	0.18	0.52
$La_{0.7}Fe_{0.7}Cu_{0.3}O_3$	12.13	-	12.51	3.64	37.81	33.91	-	0.29	0.75
$La_{0.6}Ca_{0.1}Fe_{0.8}Cu_{0.2}O_3$	8.63	1.45	15.64	2.49	38.67	33.12	0.17	0.16	0.56
$La_{0.6}Ca_{0.2}Fe_{0.8}Cu_{0.2}O_3$	9.32	3.02	14.13	2.14	39.73	31.66	0.32	0.15	0.76
$La_{0.6}Ca_{0.4}Fe_{0.8}Cu_{0.2}O_3$	8.73	4.78	12.81	0.98	40.54	32.16	0.55	0.08	0.98

Table 5.11. Auger Cu LMM features recorded on Cu-doped perovskites

Catalyst	KE of Cu Auger strongest line	KE of Cu photoelectron strongest line	Auger parameter
LaFe$_{0.9}$Cu$_{0.1}$O$_3$	914.4	553.2	1847.8
LaFe$_{0.8}$Cu$_{0.2}$O$_3$	916.7	552.0	1851.3
LaFe$_{0.7}$Cu$_{0.3}$O$_3$	917.5	553.8	1850.3
La$_{0.7}$Fe$_{0.9}$Cu$_{0.1}$O$_3$	917.0	552.7	1850.9
La$_{0.7}$Fe$_{0.8}$Cu$_{0.2}$O$_3$	915.8	553.4	1849.0
La$_{0.7}$Fe$_{0.7}$Cu$_{0.3}$O$_3$	917.5	552.6	1851.5
La$_{0.6}$Ca$_{0.1}$Fe$_{0.8}$Cu$_{0.2}$O$_3$	916.9	552.5	1851.0
La$_{0.6}$Ca$_{0.2}$Fe$_{0.8}$Cu$_{0.2}$O$_3$	917.0	552.3	1851.3
La$_{0.6}$Ca$_{0.4}$Fe$_{0.8}$Cu$_{0.2}$O$_3$	917.3	552.7	1851.2

5.3. Catalytic measurements

5.3.1. Temperature-Programmed-Reaction

Catalytic performances were evaluated from Temperature-Programmed-Reaction experiments (TPR). As described in the experimental section, the catalyst samples were systematically pre-heated in air at 600°C and then activated under reaction conditions at the same temperature for 2 hours. Afterwards, four successive ramps of temperature were performed as depicted in Fig. 5.21. Initial (STO1) and final (STO2) TPR experiments in stoichiometric conditions were repeated in order to check changes in catalytic performances due to possible alterations of the catalyst surface (changes in composition and oxidation state of active elements) induced by subsequent lean/rich cycles.
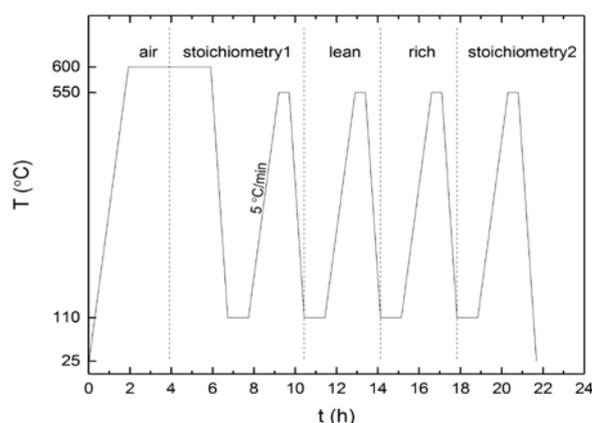
Fig. 5.21. Protocol used for Temperature-Programmed Reaction experiments.

Fig. 5.22. reports, CO, propene and propane conversion profiles vs. temperature on La-deficient La$_{0.7}$Fe$_{1-y}$Cu$_y$O$_3$ and stoichiometric LaFe$_{1-y}$Cu$_y$O$_3$ perovskite samples. As expected weak propane conversion levels are noticeable even in lean conditions and disappearing quasi-completely in rich conditions. The conversion is restored by comparing STO2 and

STO1 conversion profiles highlighting the slight superiority of $LaFeO_3$ (15 m^2/g) whereas $La_{0.7}FeO_3$ (35 m^2/g) exhibits highest propane conversion in lean conditions. Such comparisons reveal the absence of significant beneficial effect induced by the incorporation of copper.

The reactivity of propene is improved with conversion starting above 350°C on STO1 conversion curves. As observed the conversion in rich conditions is also strongly inhibited but in lesser extent with a maximum conversion reaching 55% on $La_{0.7}FeO_3$. Interestingly, the comparison with STO2 conversion curves reveals a slight rate enhancement on $La_{0.7}Fe_{0.9}Cu_{0.1}O_3$ and $La_{0.7}Fe_{0.8}Cu_{0.2}O_3$ at low temperature with conversion starting above 300°C. On the other hand, no gain in activity is discernible from this comparison on $La_{0.7}Fe_{0.7}Cu_{0.3}O_3$. Lean conditions lead to better performance on Cu-substituted perovskite samples especially on $La_{0.7}Fe_{0.8}Cu_{0.2}O_3$.

Clearly much higher conversion levels were observed for CO oxidation on $La_{0.7}Fe_{1-y}Cu_yO_3$ especially on $La_{0.7}Fe_{0.8}Cu_{0.2}O_3$. Its stoichiometric counterpart, i.e. $LaFe_{0.8}Cu_{0.2}O_3$, also shows improved performances compared to the parent $LaFeO_3$ sample. Interestingly, the deviation in conversion observed in STO1 profiles on $La_{0.7}Fe_{0.8}Cu_{0.2}O_3$ and $LaFe_{0.8}Cu_{0.2}O_3$ tends to disappear with superimposed STO2 conversion profiles which underline a greater sensitivity of the La-deficient sample to deactivation. As seen, CO conversion is hardly complete in rich conditions, a slight decrease is even observed on $La_{0.7}Fe_{0.7}Cu_{0.3}O_3$ at high temperature which reflects an extra CO production likely due to the occurrence of partial oxidation and/or reforming reactions of hydrocarbons.

Fig. 5.22. Catalytic oxidation performance of iron-based perovskite solid ABO$_3$ doped with copper (A=La; B= Fe, Cu) black circle: LaFeO$_3$ (●); red circle:La$_{0.7}$FeO$_3$ (●); purple star:LaFe$_{0.9}$Cu$_{0.1}$O$_3$ (★); olive star: LaFe$_{0.8}$Cu$_{0.2}$O$_3$ (★); cyan star:LaFe$_{0.7}$Cu$_{0.3}$O$_3$ (★); grey downward triangle:La$_{0.7}$Fe$_{0.9}$Cu$_{0.1}$O$_3$ (▽); magenta downward triangle: La$_{0.7}$Fe$_{0.8}$Cu$_{0.2}$O$_3$ (▼); violet downward triangle: La$_{0.7}$Fe$_{0.7}$Cu$_{0.3}$O$_3$ (▼).

The conversion profiles vs. T for NO reduction are reported in Fig. 5.23. As observed, a conversion was only measured in rich conditions. Higher conversions are still observable on La$_{0.7}$Fe$_{1-y}$Cu$_y$O$_3$ and La$_{0.7}$Fe$_{0.8}$Cu$_{0.2}$O$_3$ than on parent materials. The best performances observed with higher performances of La$_{0.7}$Fe$_{0.8}$Cu$_{0.2}$O$_3$ at low temperature which seem to be jointly related to surface Cu enrichment and surface La-deficiency as shown from STEM and surface analysis. On the other hand, catalytic performances seem to be weakly dependent on change in specific surface area. A noticeable production of ammonia was deduced from the nitrogen mass balance. This ammonia formation could be related to an over-production of hydrogen due to the occurrence of partial oxidation and reforming reaction of hydrocarbons.
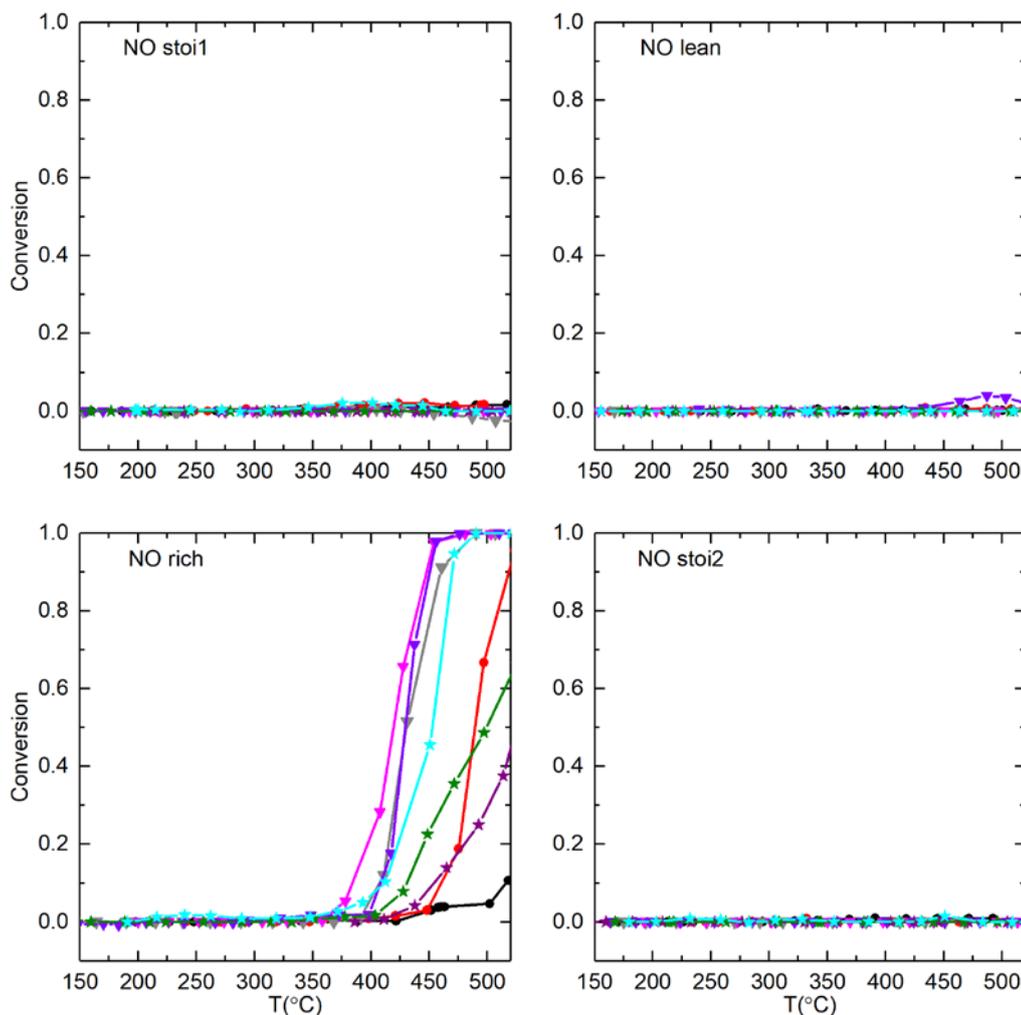
Fig. 5.23. Catalytic reduction performance of iron-based perovskite solid ABO$_3$ doped with copper (A=La; B= Fe, Cu) black circle: LaFeO$_3$ (●); red circle: La$_{0.7}$FeO$_3$ (●); purple star:LaFe$_{0.9}$Cu$_{0.1}$O$_3$ (★); olive star: LaFe$_{0.8}$Cu$_{0.2}$O$_3$ (★); cyan star:LaFe$_{0.7}$Cu$_{0.3}$O$_3$ (★); grey downward triangle:La$_{0.7}$Fe$_{0.9}$Cu$_{0.1}$O$_3$ (▽); magenta downward triangle: La$_{0.7}$Fe$_{0.8}$Cu$_{0.2}$O$_3$ (▼); violet downward triangle: La$_{0.7}$Fe$_{0.7}$Cu$_{0.3}$O$_3$ (▼).

Fig. 5.24. reports CO and propene conversion profiles vs. temperature at different richness on Ca-doped samples. The performances of La$_{0.6}$Ca$_x$Fe$_{0.8}$Cu$_{0.2}$O$_3$ are compared to the parent catalysts showing sharp rate enhancement in propene and CO conversion. It is also worthwhile to note that no significant deviation on the conversion for propene and CO recorded during STO1 and STO2 experiments is noticeable in the temperature range of the experiments. Subsequent comparison with La$_{0.7}$Fe$_{0.8}$Cu$_{0.2}$O$_3$ based on the light-off temperature is useful leading to the following sequence of activity for CO oxidation from STO1 curves for CO oxidation : LaFeO$_3$ < La$_{0.7}$FeO$_3$ < La$_{0.6}$Ca$_{0.4}$Fe$_{0.8}$Cu$_{0.2}$O$_3$ < La$_{0.6}$Ca$_{0.1}$Fe$_{0.8}$Cu$_{0.2}$O$_3$ $\cong$ La$_{0.6}$Ca$_{0.2}$Fe$_{0.8}$Cu$_{0.2}$O$_3$ < La$_{0.7}$Fe$_{0.8}$Cu$_{0.2}$O$_3$ whereas for propene oxidation the following ranking can be established : La$_{0.6}$Ca$_{0.4}$Fe$_{0.8}$Cu$_{0.2}$O$_3$ < LaFeO$_3$ < La$_{0.7}$FeO$_3$ < La$_{0.6}$Ca$_{0.1}$Fe$_{0.8}$Cu$_{0.2}$O$_3$ <

$La_{0.7}Fe_{0.8}Cu_{0.2}O_3$ << $La_{0.6}Ca_{0.2}Fe_{0.8}Cu_{0.2}O_3$. If we repeat this comparison based on the STO2 light-off curves then slight changes are discernible according to the following sequence for CO conversion: $LaFeO_3$ < $La_{0.7}FeO_3$ < $La_{0.6}Ca_{0.4}Fe_{0.8}Cu_{0.2}O_3$ < $La_{0.6}Ca_{0.1}Fe_{0.8}Cu_{0.2}O_3$ $\cong$ $La_{0.6}Ca_{0.2}Fe_{0.8}Cu_{0.2}O_3$ $\cong$ $La_{0.7}Fe_{0.8}Cu_{0.2}O_3$ whereas no significant changes compared to STO1 curves seems to appear for propene conversion highlighting the much faster propene conversion on $La_{0.6}Ca_{0.2}Fe_{0.8}Cu_{0.2}O_3$. At a first glance, calcium substitution could improve the thermal stability limiting the effect of deactivation and drastic changes in surface properties previously observed on $La_{0.7}Fe_{1-y}Cu_yO_3$. According to physicochemical characterization, i.e. XPS and STEM-EDS analysis, extensive segregation of copper at the surface of $La_{0.7}Fe_{0.8}Cu_{0.2}O_3$ could have a detrimental effect on catalytic performance in case of strong agglomeration as illustrated from STO2 experiments. Ca incorporation seems to have a beneficial effect especially on $La_{0.6}Ca_{0.2}Fe_{0.8}Cu_{0.2}O_3$. One can hypothesize that the slower migration process leading to lower formation of CuO aggregates and the preservation of dispersion of segregated copper species and/or stabilized in octahedral coordination inside the perovskite framework could be responsible of the better and more stable performances of $La_{0.6}Ca_{0.2}Fe_{0.8}Cu_{0.2}O_3$.

Regarding NO reduction similar observations as earlier reported appear in Fig. 5.25. with conversion only detected in rich conditions. However, the conversion starts at higher temperature which indicates a slight detrimental effect of calcium on the rate of NO conversion. Interestingly, $La_{0.6}Ca_{0.2}Fe_{0.8}Cu_{0.2}O_3$ does not exhibit the best performances. On the contrary, a strong loss of conversion is observed leading to lower performance than those measured on $La_{0.7}FeCuO_3$. $La_{0.6}Ca_{0.1}Fe_{0.8}Cu_{0.2}O_3$ is the most active system. It shoud be pointed out that all the tested catalysts showed relatively low N_2 Selectivity in rich condtions considering the great amount of ammonia formed above 450 °C.
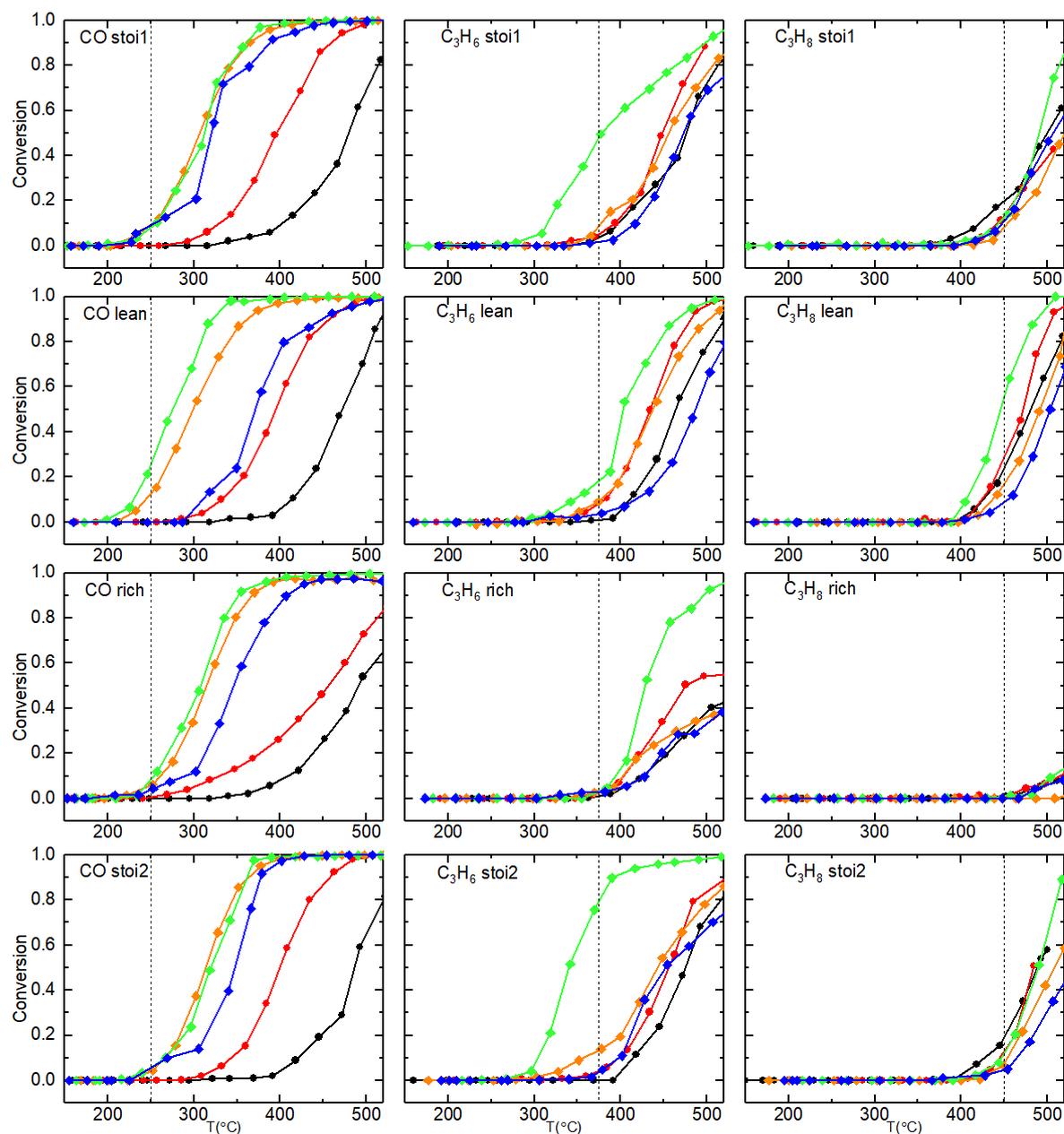
Fig. 5.24. Catalytic oxidation performance of iron-based perovskite solid ABO$_3$ doped with calcium and copper (A=La, Ca; B= Fe, Cu) black circle: LaFeO$_3$; red circle: La$_{0.7}$FeO$_3$; orange diamond : La$_{0.6}$Ca$_{0.1}$Fe$_{0.8}$Cu$_{0.2}$O$_3$; green diamond : La$_{0.6}$Ca$_{0.2}$Fe$_{0.8}$Cu$_{0.2}$O$_3$; blue diamond:La$_{0.6}$Ca$_{0.4}$Fe$_{0.8}$Cu$_{0.2}$O$_3$.
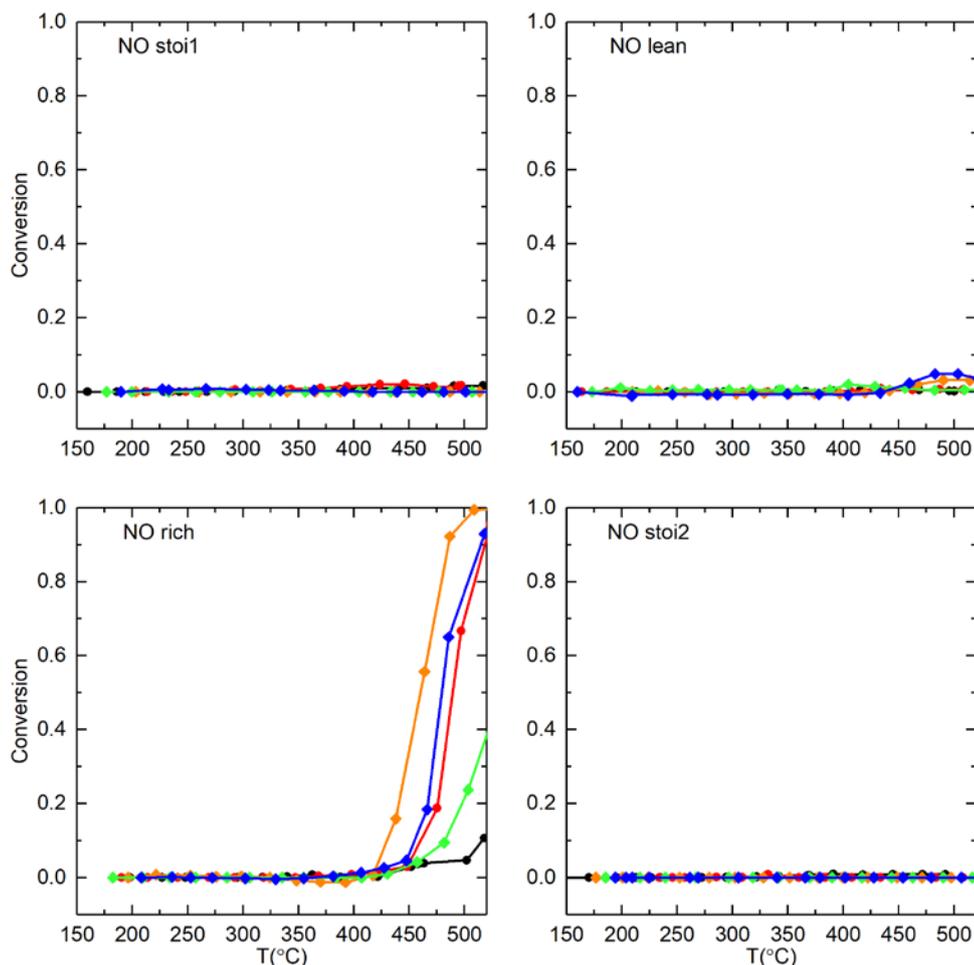
Fig. 5.25. Catalytic reduction performance of iron-based perovskite solid ABO$_3$ doped with calcium and copper (A=La, Ca; B= Fe, Cu) black circle: LaFeO$_3$; red circle: La$_{0.7}$FeO$_3$; orange diamond: La$_{0.6}$Ca$_{0.1}$Fe$_{0.8}$Cu$_{0.2}$O$_3$; green diamond:La$_{0.6}$Ca$_{0.2}$Fe$_{0.8}$Cu$_{0.2}$O$_3$; blue. diamond:La$_{0.6}$Ca$_{0.4}$Fe$_{0.8}$Cu$_{0.2}$O$_3$.

5.3.2. Kinetic analysis

Kinetic analysis has been focused on CO and propene oxidation from transient experiments in stoichiometric conditions with the aim to have a more detailed analysis of the role of Cu and Ca substitution and if La-deficient and stoichiometric composition are affected similarly. The mass balance for a plug flow reactor has been taken into account and a first order kinetics has been assumed in agreement with earlier investigations [A. Schön 2015; J.L. Hueso 2009; G. Parravano 1953]

The estimates of the rate constant k and the specific reaction rates are reported in Tables 5.12. and 5.13. The pre-exponential factor and the apparent activation energy values have been also calculated from the Arrhenius plots ln k vs. the reciprocal temperature (not shown). These calculations took into account conversions lower than 40% from STO1 and STO2 experiments. The order of magnitude of E$_{app}$ values shows that external mass transfer diffusion phenomena should not be prevalent. As these materials do not exhibit significant porosity then internal diffusion phenomena should not occur significantly in our operating conditions. Normalized and specific rates were calculated at 250°C and 375°C from STO1

and STO2 TPR conversion respectively for CO and propene corresponding to conversion lower than 50%.

5.3.2.1.   STO1 experiments

Regarding STO1 experiments, it is interesting to note that different behaviors appear distinctly at low temperature. Indeed, rate measurements show that copper substitution jointly with lanthanum deficiency induces a sharp rate enhancement for CO oxidation in comparison with parent La$_{0.7}$FeO$_3$ and LaFeO$_3$ materials. As seen, a deviation of two orders of magnitude on specific and normalized rates is observed from La$_{0.7}$FeO$_3$ to La$_{0.7}$Fe$_{0.8}$Cu$_{0.2}$O$_3$ which corresponds to an optimal copper content. Such tendency is correlated to a significant lessening of the apparent activation energy from 108 to 72 kJ mol^{-1} respectively. Similar observations characterize Cu-doped stoichiometric perovskites through the comparison of LaFeO$_3$ and LaFe$_{0.7}$Cu$_{0.3}$O$_3$ with a sharp decrease of the activation energy from 121 to 70 kJ mol^{-1}. Contrarily to La-deficient samples a gradual increase of activity is observed on stoichiometric perovskite compositions with a rise in copper content. Subsequent substitution of La by Ca has a significant detrimental effect on the rates in comparison with La$_{0.7}$Fe$_{0.8}$Cu$_{0.2}$O$_3$. A weak calcium dependency of the specific and normalized rate and apparent activation energy is also discernible which does not reveal the existence of optimal composition as previously discussed.

Now regarding propene oxidation, it seems obvious that copper substitution on La$_{0.7}$FeO$_3$ and LaFeO$_3$ does not provoke rate enhancement. A weak detrimental effect is even observed on the stoichiometric perovskite samples corresponding to an increase in E$_{app}$ partly compensated by an increase of the pre-exponential factor. Surprisingly, an opposite behavior is distinguishable with a positive effect of calcium substitution on the specific rate value of La$_{0.6}$Ca$_{0.2}$Fe$_{0.8}$Cu$_{0.2}$O$_3$ accompanied with a lessening of E$_{app}$. On the other hand this effect is restricted to La-deficient samples. As observed, calcium substitution leads to a significant loss of catalytic activity on stoichiometric La$_{0.6}$Ca$_{0.4}$Fe$_{0.8}$Cu$_{0.2}$O$_3$.

5.3.2.2.   STO2 experiments

As previously mentioned this second TPR was implemented to check changes in catalytic feature ascribed to bulk and surface modifications after successive lean/rich exposures. As a matter of fact, the comparison of kinetic data from STO1 experiment can provide general trends which show a relative stability with no strong deactivation based on the comparison of specific and normalized rate. However, a closer examination reveals distinct behavior for CO oxidation at low and high copper content on La-deficient La$_{0.7}$Fe$_{1-y}$Cu$_y$O$_3$ and stoichiometric LaFe$_{1-y}$Cu$_y$O$_3$ samples in connection with an optimal composition observed on the series La$_{0.7}$Fe$_{1-y}$Cu$_y$O$_3$ for y = 0.2 from STO1 experiments. Such a behavior is no longer observed by examining the specific rate values but still persists from the normalized rates. Indeed, for y ≤ 0.2, a slight rate improvement is observed whereas a stabilization or weak loss of activity is discernible for y > 0.2 (y = 0.3). Let us now examine the stoichiometric series LaFe$_{1-y}$Cu$_y$O$_3$ which did not reveal initially optimal copper composition. By examining STO2 rate values, the appearance of an optimal composition is remarkable for y = 0.2. Such comparison would suggest that copper ex-solution plays an important role in determining the density of active copper sites at the surface for CO oxidation. As observed such process would be slower on

stoichiometric compositions but activated after lean/rich cycle then originating well-dispersed copper species. On the other hand, copper extraction and aggregation would occur much faster on La-deficient materials. The evolutions observed after Ca substitution also provide interesting information because in that case a significant lowering of specific and normalized rate is noticeable in comparison to $La_{0.7}Fe_{1-y}Cu_yO_3$ highlighting the detrimental effect of calcium.

Table 5.12. Rate and kinetic parameters related to CO oxidation on substituted perovskite samples

Catalyst	SSA $(m^2\ g^{-1})$	STO1				STO2			
		$r_{spec.}$ $(mol\ s^{-1}g^{-1})^a$	Normalized rate $(mol\ s^{-1}m^{-2})^a$	A $(m^3\ s^{-1}g^{-1})$	E_{app} $(kj\ mol^{-1})$	$r_{spec.}$ $(mol\ s^{-1}g^{-1})^a$	Normalized rate $(mol\ s^{-1}m^{-2})^a$	A $(m^3s^{-1}g^{-1})$	E_{app} $(kj\ mol^{-1})$
$LaFeO_3$	15.5	7.77E-10	5.02E-11	3.56E+03	121	8.93E-10	5.76E-11	2.89E+03	162
$La_{0.7}FeO_3$	35.5	1.60E-08	4.51E-10	3.32E+03	108	6.04E-09	1.70E-10	4.30E+04	123
$LaFe_{0.9}Cu_{0.1}O_3$	19.2	1.68E-08	8.76E-10	3.58E+11	188	5.59E-08	2.91E-09	7.10E+08	156
$LaFe_{0.8}Cu_{0.2}O_3$	15.3	1.57E-08	1.03E-09	4.51E+10	179	1.62E-07	1.06E-08	5.13E+05	120
$LaFe_{0.7}Cu_{0.3}O_3$	26.2	3.98E-07	1.52E-08	1.44E+01	70	1.35E-07	5.14E-09	5.94E+07	141
$La_{0.7}Fe_{0.9}Cu_{0.1}O_3$	32.2	2.09E-07	6.48E-09	1.50E+02	83	4.97E-07	1.54E-08	2.85E+02	82
$La_{0.7}Fe_{0.8}Cu_{0.2}O_3$	23.2	8.02E-07	3.46E-08	5.27E+01	72	4.51E-07	1.94E-08	2.22E+03	91
$La_{0.7}Fe_{0.7}Cu_{0.3}O_3$	15.4	1.83E-07	1.19E-08	5.47E+03	99	2.20E-07	1.43E-08	1.67E+02	83
$La_{0.6}Ca_{0.1}Fe_{0.8}Cu_{0.2}O_3$	22.1	3.96E-07	1.79E-08	7.04E+02	87	1.81E-07	8.18E-09	5.23E+05	119
$La_{0.6}Ca_{0.2}Fe_{0.8}Cu_{0.2}O_3$	21.3	3.94E-07	1.85E-08	3.35E+02	84	2.36E-07	1.11E-08	1.68E+03	93
$La_{0.6}Ca_{0.4}Fe_{0.8}Cu_{0.2}O_3$	32.4	3.98E-07	1.23E-08	1.10E+02	80	2.58E-07	7.97E-09	8.95E-01	60

[a] calculated at T = 250°C for STO1 and STO2.

Note A pre-exponential factor and E_{app} apparent activation energy in agreement with $k = A\ exp(-E_{app}/RT)$

Table 5.13. Rate and kinetic parameters related to C_3H_6 oxidation on substituted perovskite samples

Catalyst	SSA $(m^2\,g^{-1})$	STO1				STO2			
		$r_{spec.}$ $(mol\,s^{-1}\,g{-1})^a$	Normalized rate $(mol\,s^{-1}\,m^{-2})^a$	A $(m^3\,s^{-1}\,g^{-1})$	E_{app} $(kj\,mol^{-1})$	$r_{specific}$ $(mol\,s^{-1}\,g^{-1})^a$	Normalized rate $(mol\,s^{-1}\,m^{-2})^a$	A $(m^3\,s^{-1}\,g^{-1})$	E_{app} $(kj\,mol^{-1})$
$LaFeO_3$	15.5	1.07E-08	6.88E-10	7.11E+03	125	8.26E-09	5.33E-10	1.24E+04	130
$La_{0.7}FeO_3$	35.5	1.73E-08	4.88E-10	7.53E+03	123	1.27E-08	3.57E-10	4.50E+04	134
$LaFe_{0.9}Cu_{0.1}O_3$	19.2	8.60E-10	4.48E-11	1.31E+11	229	2.75E-09	1.43E-10	7.09E+06	170
$LaFe_{0.8}Cu_{0.2}O_3$	15.3	2.93E-09	1.92E-10	1.06E+07	172	3.32E-08	2.17E-09	4.58E+02	160
$LaFe_{0.7}Cu_{0.3}O_3$	26.2	4.40E-08	1.68E-09	4.59E+04	127	5.09E-08	1.94E-09	1.10E+05	130
$La_{0.7}Fe_{0.9}Cu_{0.1}O_3$	32.2	4.50E-08	1.40E-09	2.46E+06	148	1.02E-07	3.17E-09	7.07E+02	98
$La_{0.7}Fe_{0.8}Cu_{0.2}O_3$	23.2	4.93E-08	2.13E-09	3.41E+05	136	1.13E-07	4.89E-09	5.05E+04	121
$La_{0.7}Fe_{0.7}Cu_{0.3}O_3$	15.4	1.10E-08	7.12E-10	6.61E+03	125	4.14E-08	2.69E-09	1.79E+02	97
$La_{0.6}Ca_{0.1}Fe_{0.8}Cu_{0.2}O_3$	22.1	2.98E-08	1.35E-09	2.42E+01	89	1.70E-07	7.71E-09	1.64E+04	114
$La_{0.6}Ca_{0.2}Fe_{0.8}Cu_{0.2}O_3$	21.3	1.19E-07	5.58E-09	1.65E+02	88	3.25E-07	1.52E-08	5.81E+10	84
$La_{0.6}Ca_{0.4}Fe_{0.8}Cu_{0.2}O_3$	32.4	4.72E-09	1.46E-10	9.79E+05	156	1.07E-08	3.32E-10	2.04E+04	116

a calculated at T = 375°C

Note A pre-exponential factor and E_{app} apparent activation energy in agreement with $k = A\,exp(-E_{app}/RT)$

5.3.3. Structure-reactivity relationship

Tentative establishment of structure-reactivity relationship is not trivial by analyzing catalytic measurements showing sometimes opposite behavior after Cu and Ca substitution of La-deficient La$_{0.7}$FeO$_3$ and stoichiometric LaFeO$_3$ perovskite materials. It is remarkable that trends observed for CO oxidation can be no longer observed for hydrocarbon conversion which would suggest that key elementary steps for these two reactions could not refer to the same catalytic functionality.

As earlier discussed, the replacement of trivalent by divalent cations can create significant electronic imbalances and structural distortions. Based on this, charge compensation can be obtained by changes in the valence state of B-sites or the creation of oxygen vacancies. In principle, the appearance of anionic vacancies should be accompanied to a greater oxygen adsorption which can potentially lead to gain in catalytic activity. Starting from iron substitution by copper, changes in ionic radius, i.e. r(Cu^{2+}) = 0.72 Å versus r(Fe^{3+}) = 0.64 Å, should be accompanied to expansion effect of the cell volume. In practice, Rietveld refinement calculations did not show significant changes in the cell volume on LaFe$_{1-y}$Cu$_y$O$_3$ and La$_{0.7}$Fe$_{1-y}$Cu$_y$O$_3$. Several explanations could explain this observation. First, copper ex solution and the detection of bulk extra framework copper species could attenuate this expansion effect. Alternately, it could be counterbalanced by contraction effect due to the creation of oxygen vacancies or the stabilization of Fe^{4+} corresponding to a lower ionic radius of 0.585 Å [T. Caronna 2009]. As shown, some differences appear on La-deficient and stoichiometric perovskite compositions. As illustrated in Figs. 5.2., 5.3., 5.4. distinct reflections assigned to CuO are usually observable on La$_{0.7}$Fe$_{1-y}$Cu$_y$O$_3$ but only discernible on LaFe$_{0.7}$Cu$_{0.3}$O$_3$ for the stoichiometric counterparts. This observation agrees with the stabilization of Fe^{4+} detected from Mössbauer spectroscopy which compensate the lower oxidation state of Cu^{2+} mainly stabilized in octahedral position in LaFe$_{0.8}$Cu$_{0.2}$O$_3$ whereas only Fe^{3+} was observed on La$_{0.7}$Fe$_{0.8}$Cu$_{0.2}$O$_3$ in different tetrahedral and octahedral symmetries. As a consequence, the low temperature reduction process ascribed to an easier reduction of extra framework CuO clusters (below 200°C) strongly attenuates on the stoichiometric LaFe$_{1-y}$Cu$_y$O$_3$. (see Figs. 5.9. and 5.10.) Such an explanation is consistent with SEM measurements and elemental mapping leading observation of larger CuO clusters on La$_{0.7}$Fe$_{0.8}$Cu$_{0.2}$O$_3$. However according to Caronna et al. [T. Caronna 2009] one cannot rule out the formation of anionic vacancies especially on La$_{0.7}$Fe$_{1-y}$Cu$_y$O$_3$. Regarding XPS measurements semi-quantitative analysis La$_{0.7}$Fe$_{1-y}$Cu$_y$O$_3$ underlined a gradual increase of copper concentration from y= 0.1 to 0.3 which is consistent with copper agglomeration at the surface. On the other hand, such tendency does not appear on LaFe$_{1-y}$Cu$_y$O$_3$. Auger line changes in the B.E. values XPS features obtained on La$_{0.7}$Fe$_{1-y}$Cu$_y$O$_3$ and LaFe$_{1-y}$Cu$_y$O$_3$ suggest the coexistence of two oxidic species exhibiting different reducibility. Interestingly, Ca substitution shifts B.E. to higher values corresponding to Cu^{2+} which corresponds to a weaker surface Cu enrichment. Such tendency seems more accentuated on the stoichiometric La$_{0.6}$Ca$_{0.4}$Fe$_{0.8}$Cu$_{0.2}$O$_3$ characterized by the presence of Fe^{4+} suggesting a much greater stabilization of Cu^{2+} in the perovskite framework. Returning the Rietveld refinement calculations, Table 5.3. shows significant contraction effects on the series La$_{0.6}$Ca$_x$Fe$_{0.8}$Cu$_{0.2}$O$_3$ likely due to preferential formation of anionic vacancies on La-deficient

samples. It is remarkable that Ca-substituted samples become less reducible in comparison with La$_{0.7}$Fe$_{1-y}$Cu$_y$O$_3$. Similar observations were previously reported by Nakamura et. al [T. Nakamura 1983] on La$_{1-x}$Sr$_x$CoO$_{3-\delta}$ and led to the conclusion that increasing the perovskites reducibility decreases its ability to refill its oxygen vacancies. Hence, the surface density and stability of anionic vacancies is expected to be higher on La$_{0.6}$Ca$_{0.4}$Fe$_{0.8}$Cu$_{0.2}$O$_3$ than on La$_{0.7}$Fe$_{1-y}$Cu$_y$O$_3$ and LaFe$_{1-y}$Cu$_y$O$_3$.
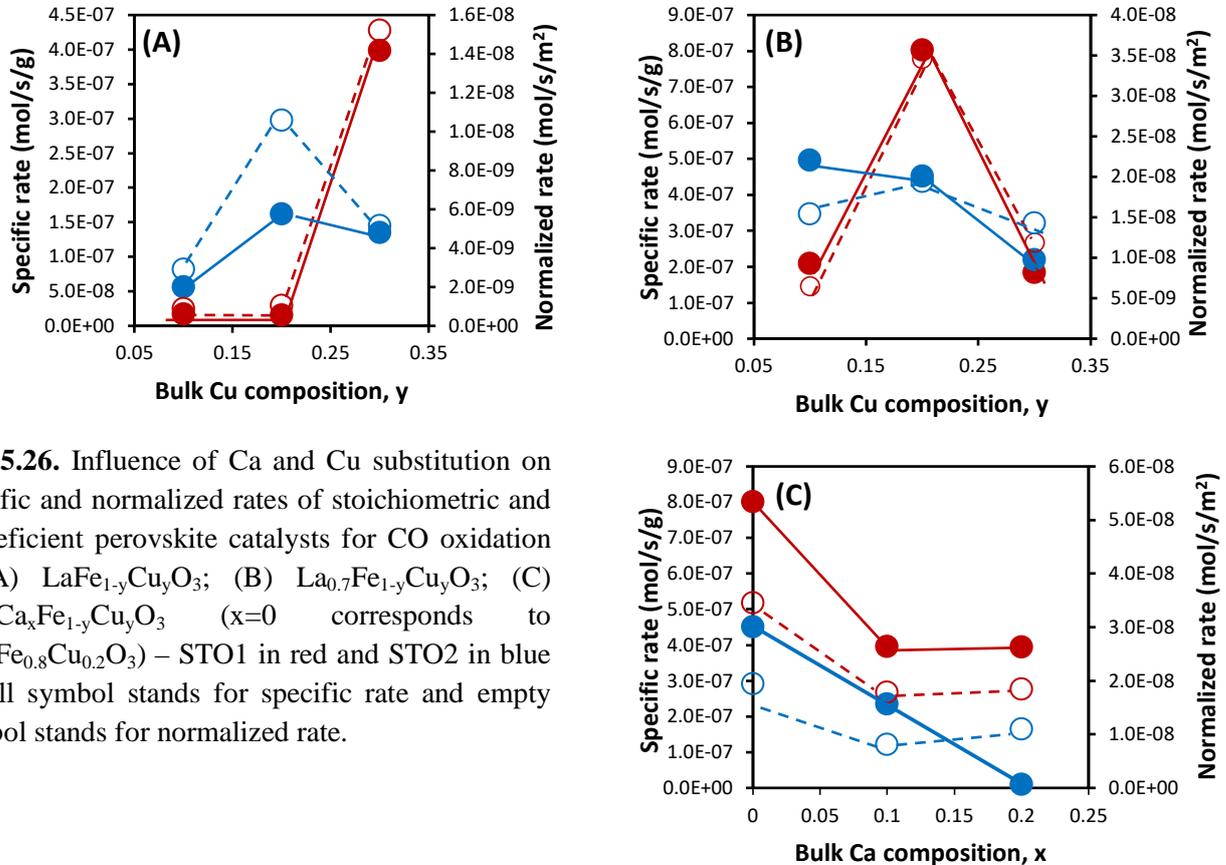
Fig. 5.26. Influence of Ca and Cu substitution on specific and normalized rates of stoichiometric and La-deficient perovskite catalysts for CO oxidation – (A) LaFe$_{1-y}$Cu$_y$O$_3$; (B) La$_{0.7}$Fe$_{1-y}$Cu$_y$O$_3$; (C) La$_{0.6}$Ca$_x$Fe$_{1-y}$Cu$_y$O$_3$ (x=0 corresponds to La$_{0.7}$Fe$_{0.8}$Cu$_{0.2}$O$_3$) – STO1 in red and STO2 in blue – Full symbol stands for specific rate and empty symbol stands for normalized rate.

Now regarding kinetic data in Tables 5.12. and 5.13. it is interesting to note that different behavior affects La-deficient and stoichiometric perovskite after Ca and Cu substitution respectively in A-site and B-site. Figs. 5.26. and 5.27. can resume previous tendencies observed on specific and normalized rate as a function. As observed in Figs. 5.26(B)., an optimal Cu composition for y= 0.2 appears on La-deficient perovskite. Such optimum attenuates from STO2 experiments and even disappears by examining the evolution of the specific rates. On the stoichiometric samples such an optimum was not originally observed but appears on STO2 experiments. Such an evolution is likely governed by the rate of copper extraction and aggregation at the surface, these processes being faster on La$_{0.7}$Fe$_{1-y}$Cu$_y$O$_3$ than LaFe$_{1-y}$Cu$_y$O$_3$ and agree with the increase in the surface Cu/Fe ratio reflecting a significant clustering effect of copper oxide. It is worthwhile to note that no optimum is observed La$_{0.6}$Ca$_x$Fe$_{0.8}$Cu$_{0.2}$O$_3$ which suggests that calcium substitution partially block these processes avoiding significant agglomeration. As a conclusion copper ex solution then diffusing at the surface exhibit a beneficial effect in case of high dispersion. Subsequent

coalescence process leads inevitably to a loss of activity. Such conclusion is in agreement with previous investigation showing that the reduction of Cu^{2+} to Cu^+ is vital for the chemisorption of CO on amorphous CuO highly dispersed on Cu-doped defective perovskite [Y. Yi 2019]

Similar tendency also reproduces for propene except on Ca-substituted with an opposite behavior. Indeed, a significant rate enhancement was asscociated with a rise in calcium content. Merino et al. [N.A. Merino 2005] who substituted La^{3+} by Ca^{2+} into $LaCoO_3$ lattice also observed distinctly an increase in superficial oxygen vacancy densities yielding promoted catalytic activities for propane oxidation.
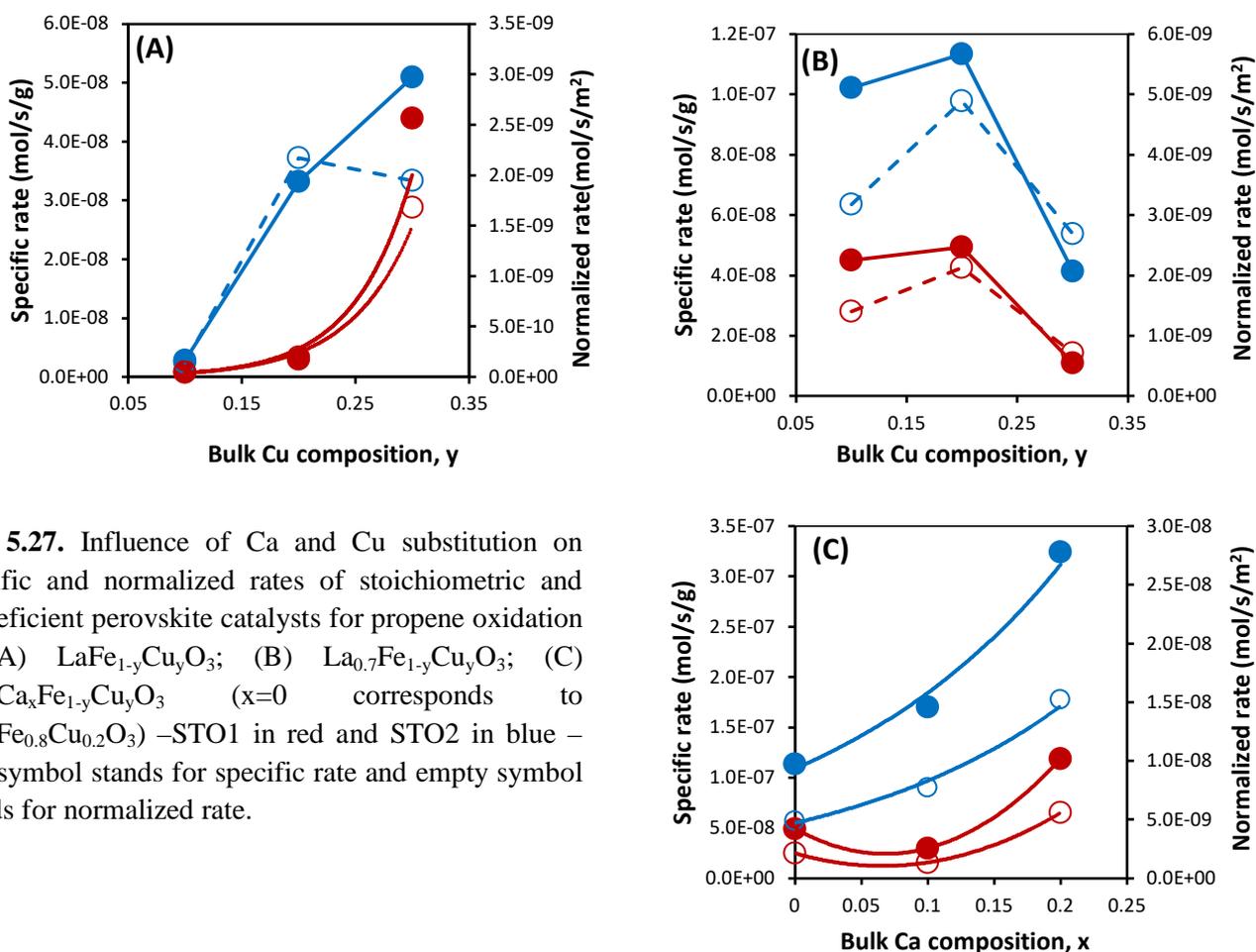
Fig. 5.27. Influence of Ca and Cu substitution on specific and normalized rates of stoichiometric and La-deficient perovskite catalysts for propene oxidation – (A) LaFe$_{1-y}$Cu$_y$O$_3$; (B) La$_{0.7}$Fe$_{1-y}$Cu$_y$O$_3$; (C) La$_{0.6}$Ca$_x$Fe$_{1-y}$Cu$_y$O$_3$ (x=0 corresponds to La$_{0.7}$Fe$_{0.8}$Cu$_{0.2}$O$_3$) –STO1 in red and STO2 in blue – Full symbol stands for specific rate and empty symbol stands for normalized rate.

In general, two mechanisms have been proposed with regard to hydrocarbon oxidation on the perovskite materials: suprafacial mechanism and intrafacial mechanism [R.J.H. Voorhoeve 1977]. The former takes place at lower temperature (T<300°C) involving reaction of hydrocarbons with oxygen species weakly bonded to the anionic sites (e.g. O$^-$). The latter is predominant at higher temperature (T>600°C) when the concentration of adsorbed oxygen species becomes low and bulk oxygen dissociated from the lattice are assumed to be more active in terms of hydrocarbon oxidation. [S. Rousseau 2009]. The synergistic effect on the rate of propene oxidation induced by Ca^{2+} could be associated to dual-site in case of suprafacial reaction mechanism [J. Zhang 2015].

5.4. Conclusion

Conventional sol-gel method yielded lanthanum ferrite with orthorhombic structure. La-deficiency in A-site led to the extra-lattice hematite. Copper substitution in B-site resulted in segregated CuO phase especially at increasing copper content.

Calcium and copper co-doping in A-site and B-site respectively gave rise to the shrinkage of unit cell volume which is probably attributed to the severe distortion of BO$_6$ octahedra induced by the introduction of valiocations. Oxidation state of iron species is sensitive to substitution in A-site and B-site. Stoichiometry in A-site is crucial for the stabilization of Fe^{4+}. Two mechanisms of charge compensation are proposed in response to substitution of La by Ca in A-site and Fe by Cu in B-site: one is the generation of anionic vacancies causing disorder of crystal structure, the other is the stabilization of unusual oxidation state of B-site metal cations evidenced by the greatest amount of Fe^{4+} observed over La$_{0.6}$Ca$_{0.4}$Fe$_{0.8}$Cu$_{0.2}$O$_3$.

Highly dispersed CuO on the surface in strong interaction with perovskite support showed a markedly beneficial impact on CO and C$_3$H$_6$ oxidation in comparison with non-doped LaFeO$_3$ under STOI1 experiment. Such trend was further enhanced by La-deficiency in A-site.

The best composition for CO oxidation corresponds to La$_{0.7}$Fe$_{0.8}$Cu$_{0.2}$O$_3$ in the first stoichiometric condition which may be accounted for by the enhanced adsorption for CO and NO due to CuO segregation.. However, differences induced by copper substitution became less significant in the return test, probably accounted for by the high sensibility related to La-deficient perovskites. CO conversion was hardly complete in rich condition, signifying the occurrence of HC reforming reactions at high temperature. A gain in propene oxidation activity was prominent above 350°C over Cu-substituted perovskites in stoichiometric and lean conditions but severely inhibited in rich conditions. Nevertheless, propane oxidation seemed unaffected by Cu incorporation, with only minor discrepancies observed over catalysts with different copper substitution degrees in stoichiometric, lean and rich conditions. As to Ca and Cu co-doped perovskites, a significant enhancement of reaction rate was observed for CO and C$_3$H$_6$ oxidation compared to parent LaFeO$_3$. It was also found that no marked deviation was discerned in terms of CO and C$_3$H$_6$ conversion recorded during STOI1 and STOI2 experiments, highlighting the fact that Ca and Cu co-doping could improve the stability of lanthanum ferrite thus limiting the effect of deactivation and abrupt changes of surface properties observed notably over La$_{0.7}$Fe$_{1-y}$Cu$_y$O$_3$. Extensive segregation of copper on the surface of La$_{0.7}$Fe$_{0.8}$Cu$_{0.2}$O$_3$ evidenced by XPS and STEM/EDS had a detrimental impact on the oxidation performance in case of severe agglomeration manifested from STOI2 experiment. A hypothesis is therefore put forward that Ca doping would result in slower migration process of copper from lattice to extra solid solution, inhibiting the formation of large CuO aggregates and favoring the preservation of dispersion of segregated copper species or stabilization in octahedral coordination inside the perovskite framework. Thus, an enhanced thermal stability is achieved exhibited in STOI2 experiment over La$_{0.6}$Ca$_x$Fe$_{0.8}$Cu$_{0.2}$O$_3$. A tentative sequence of catalytic oxidation activity based upon light-off temperature in STOI2 experiment is given: for CO oxidation, the order is as follows: LaFeO$_3$

$<$ La$_{0.7}$FeO$_3$ $<$ La$_{0.6}$Ca$_{0.4}$Fe$_{0.8}$Cu$_{0.2}$O$_3$ $<$ La$_{0.6}$Ca$_{0.1}$Fe$_{0.8}$Cu$_{0.2}$O$_3$ $\cong$ La$_{0.6}$Ca$_{0.2}$Fe$_{0.8}$Cu$_{0.2}$O$_3$ $\cong$ La$_{0.7}$Fe$_{0.8}$Cu$_{0.2}$O$_3$. For C$_3$H$_6$ oxidation, the following ranking is established: La$_{0.6}$Ca$_{0.4}$Fe$_{0.8}$Cu$_{0.2}$O$_3$ $<$ LaFeO$_3$ $<$ La$_{0.7}$FeO$_3$ $<$ La$_{0.6}$Ca$_{0.1}$Fe$_{0.8}$Cu$_{0.2}$O$_3$ $<$ La$_{0.7}$Fe$_{0.8}$Cu$_{0.2}$O$_3$ $<<$ La$_{0.6}$Ca$_{0.2}$Fe$_{0.8}$Cu$_{0.2}$O$_3$.

In contrast, NO conversion over Cu-doped perovskites was only noticeable in rich conditions with low N$_2$ selectivity. The production of great amount of ammonia is assumed to occur at high temperature due to the partial oxidation or reforming of hydrocarbons. NO could hardly be reduced in stoichiometric conditions regardless of Cu richness.

Kinetic study showed that CO and C$_3$H$_6$ oxidation followed different trends over substituted lanthanum ferrite perovskite involving different catalytic routes through key elementary steps.

Copper extraction is favorable for the rate enhancement of C$_3$H$_6$ oxidation especially over stoichiometric composition LaFe$_{1-y}$Cu$_y$O$_3$.

For La$_{0.7}$Fe$_{1-y}$Cu$_y$O$_3$, an optimum Cu-doping of y=0.2 is associated with the highest specific and normalized reaction rate both for CO and C$_3$H$_6$ oxidation. Nevertheless, opposite trend was noticeable for CO and C$_3$H$_6$ oxidation over La$_{0.6}$Ca$_x$Fe$_{0.8}$Cu$_{0.2}$O$_3$. On one hand, the decreased rate of CO oxidation over La$_{0.6}$Ca$_x$Fe$_{0.8}$Cu$_{0.2}$O$_3$ was mainly attributed to less reducible Cu^{2+} associated with higher Ca-doping, which is essential for the chemisorption of CO on amorphous CuO or Cu^{2+} located within the center of BO$_6$ octahedra. On the other hand, the remarkable increase of C$_3$H$_6$ oxidation rate linked with higher Ca-doping over La$_{0.6}$Ca$_x$Fe$_{0.8}$Cu$_{0.2}$O$_3$ is presumably accounted for by the greater intensity and stability of oxygen vacancies, leading to a gain in adsorption of C$_3$H$_6$ molecules on the active sites. Another point worth noting is that Ca-doping is beneficial to the dispersion of ex-framework copper in terms of preventing the coalescence of crystallite and the subsequent loss of activity. Such trend is most obvious on La$_{0.6}$Ca$_{0.2}$Fe$_{0.8}$Cu$_{0.2}$O$_3$.

Chapter VI. Stoichiometric and non-stoichiometric Ca and Mn doped La$_{1-x}$FeO$_{3\pm\delta}$

Perovskite structure have been utilized in many oxidative catalytic applications and catalytic end-of-pipe technologies to treat atmospheric pollutants from Diesel exhaust, i.e. Diesel oxidation Catalysts, NO$_x$ Storage Reduction catalysts [J.A. Onrubia 2017; A. Russell 2011; C.H. Kim 2010; N. Russo 2005]. Among the different compositions previously studied, stoichiometric LaMnO$_3$ [J.A. Onrubia 2017; A. Russell 2011] and none-stoichiometry La$_x$MnO$_3$ structures [J. Chen 2013] attracted the interest of several investigators. As example, Chen et al. reported improved performance for NO oxidation to NO$_2$ on La$_{0.9}$MnO$_3$ [J. Chen 2013] ascribed to higher formation of Mn^{4+} related to more catalytically active oxygen species bonded to Mn^{4+}. The catalytic properties of LaMn$_{0.9}$O$_3$ were also examined for methane combustion with improved performances related to specific surface area enhancement jointly to higher density of defective sites [R. Spinicci 2002]. Manganites have been extensively studied in terms of oxidation for light alkanes (C$_2$-C$_7$) and alkenes. [M. Alifanti 2009; V. Roche 2010].

The stabilization of Mn^{4+} at the expense of Mn^{3+} is expected even for stoichiometric LaMnO$_3$ composition. In that case, the over production of positive charges is balanced by an excess of oxygen in the perovskite lattice. Many examples also relate intrinsic redox properties to reversible Mn^{3+}/Mn^{4+} mixed oxidation state with conservation of charges through the creation of cationic vacancies instead of oxygen over-stoichiometry because the perovskite lattice cannot accommodate interstitial oxygen ions [J.A.M. Van Roosmalen 1994]. As already discussed, perovskite structures can accommodate a wide panel of cations in B-site with valency changes in case on non-stoichiometry of B or A cations or La^{3+} substitution by cations having lower oxidation state such as Ca^{2+} or Sr^{2+}. Onrubia et al. [J.A. Onrubia 2017] found that the electronic imbalance due to La^{3+} substitution by Sr^{2+} in Sr-doped LaCoO$_3$ is preferentially compensated by the creation of oxygen vacancies while oxidation state of cobalt remains unchanged. On the other hand, these authors concluded that the same substitution of Sr-doped LaMnO$_3$ is accompanied to an increase of the oxidation state of manganese shifting to Mn^{4+}. For dual site substitution such as La^{3+} by Ca^{2+} and Co^{3+} by Mg^{2+} in B site of parent LaCoO$_3$ material a shift of the oxidation state of +III to +IV is observed for cobalt leading to a beneficial effect for toluene oxidation explained by a prevalent suprafacial oxidation process. In parallel, a reverse detrimental effect is observed with respect to intrafacial oxidation process [J. Zhang 2015]. In this chapter, partial substitution of iron by manganese and lanthanum by calcium will be investigated. As previously seen in chapter V, significant enhancement on the catalytic properties after iron substitution by copper is obtained in agreement with earlier investigation [S.D. Peter 2001] mostly related to partial copper ex solution then stabilized in metallic state. Structural and electronic features induced by the partial substitution of iron by manganese in B-site and lanthanum by calcium in A-site can lead to stabilization of iron in unusual +IV oxidation state. Accordingly two redox couples, Fe^{4+}/Fe^{3+} and Mn^{4+}/Mn^{3+} can coexist and be involved in the overall catalytic process. Leontiou et al. reported a greater stabilization of Fe^{4+} in Sr-doped LaFeO$_3$ by Mössbauer

spectroscopy [A.A. Leontiou 2003]. These authors observed that the highest activity in NO reduction by CO was obtained on the perovskites having the lowest amount of Fe^{4+} and the highest amount of Fe^{3+}. Zhu and Thomas reported an overview dealing with substitution effect in A and B site of perovskite structure for NO decomposition to N_2 [J. Zhu 2009 a, b] recognized as green process for NO_x removal since no additional supply of reducing agent is needed. They reported that understanding the impact of B-site substitution on the overall performance is not trivial due to the coexistence of two redox systems which can be equally involved. The identification the most efficient redox couple remains empirical and is not formally related to a permanent oxidation state or the coexistence of different oxidation states as illustrated in Fig. 6.1.
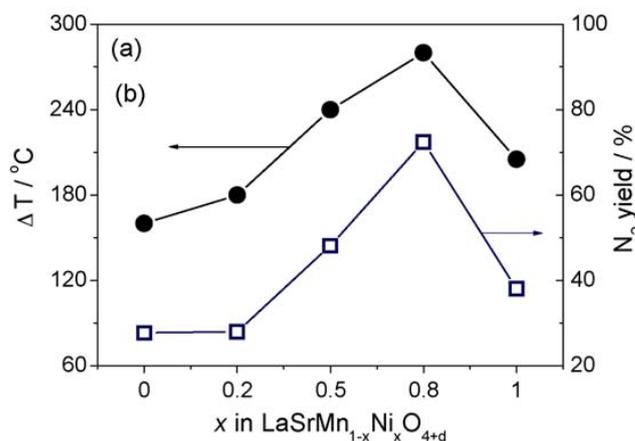
Fig. 6.1. Relationships between the difference in temperature ΔT and NO removal activity: (a) NO decomposition on $LaSrMn_{1-x}Ni_xO_{4+\delta\square}$ in the presence of 2.5 v/v% O_2 at 850°C from [J. Zhu 2009 a]. ΔT stands for the temperature difference of the reduction peaks measured in H_2-TPR experiments.

Despite lower practical examples, the potential interest of perovskite has been already tackled for three-way-conditions but in simulated conditions which are often far from the typical compositions of the exhaust for three-way-conditions. Previous investigations showed that $LaMnO_3$ catalyst can be good candidate for CO [B. Kucharczyk 2008] and hydrocarbon oxidation [S. Cimino 2003] as well as NO reduction [R. Zhang 2006 a-c]. Improved performance in NO reduction by propene have been reported on Cu-substituted $LaMnO_3$ perovskite in stoichiometric or slightly oxidizing conditions related to adsorbed ad-NO_x intermediates through the oxidation of NO by adsorbed oxygen species on anionic vacancies. On the other hand a detrimental effect is observed with a rise in gaseous oxygen concentration because an excessive surface concentration of active oxygen species favors the preferential oxidation of propene [R. Zhang 2006 a-c]. Particular attention was paid in this chapter to the modification of $LaFeO_3$ and $La_{0.7}FeO_3$ as parent materials through manganese substitution. Previous investigations reveal that iron is less active then copper as previously exemplified and the same expectation for manganese should appear. However, iron contributes to the stability giving rise to improved durability [H. Tanaka 2003]. Based on the above considerations the following compositions were prepared according to the citrate method previously described in chapter III.

Table 6.1. Elemental analysis of calcium- and manganese-doped stoichiometric LaFeO$_3$ and none stoichiometric La$_{0.7}$FeO$_3$ perovskites calcined at 600°C.

Theoretical atomic composition	Atomic composition from ICP						
	La (%)	Ca (%)	Ca/La	Fe (%)	Mn (%)	Mn/Fe	A/B
LaFeO$_3$	20.46	-	-	19.97	-	-	1.02
LaMnO$_3$	19.58	-	-	-	18.77	-	1.04
La$_{0.7}$FeO$_3$	15.33	-	-	22.73	-	-	0.67
LaFe$_{0.9}$Mn$_{0.1}$O$_3$	19.33	-	-	17.58	1.87	0.11	0.99
LaFe$_{0.8}$Mn$_{0.2}$O$_3$	19.74	-	-	16.02	4.02	0.25	0.99
LaFe$_{0.7}$Mn$_{0.3}$O$_3$	17.51	-	-	12.58	5.08	0.40	0.99
La$_{0.7}$Fe$_{0.9}$Mn$_{0.1}$O$_3$	13.77	-	-	18.13	1.94	0.11	0.69
La$_{0.7}$Fe$_{0.8}$Mn$_{0.2}$O$_3$	10.62	-	-	12.10	2.96	0.25	0.71
La$_{0.7}$Fe$_{0.7}$Mn$_{0.3}$O$_3$	14.65	-	-	15.00	6.34	0.42	0.69
La$_{0.6}$Ca$_{0.1}$Fe$_{0.8}$Mn$_{0.2}$O$_3$	13.75	2.32	0.02	18.91	4.66	0.25	0.68
La$_{0.6}$Ca$_{0.2}$Fe$_{0.8}$Mn$_{0.2}$O$_3$	11.47	3.92	0.04	15.89	3.92	0.25	0.78
La$_{0.6}$Ca$_{0.4}$Fe$_{0.8}$Mn$_{0.2}$O$_3$	10.97	7.46	0.08	14.67	3.69	0.25	1.00

6.1. Structural properties

6.1.1. XRD analysis

Fig. 6.2. shows the X-ray diffractograms recorded on stoichiometric lanthanum ferrite doped with manganese in B site. Orthorhombic perovskite structure was obtained for all Mn-doped LaFe$_{1-y}$Mn$_y$O$_3$. No additional phase was identified yet slight shift of main peak corresponding to (0 0 2) plane towards lower 2θ values was observed as substitution degree increased from y = 0.1 to 0.3, implying the expansion of interplanar crystal distance generated by incorporation of manganese cations. The width and relative intensity of the doped perovskites remained unchanged compared to reference LaFeO$_3$ (PDF 37-1493). The moderate contraction of unit cell volume, calculated from the Refinement Rietveld method, induced by more Mn-doping (see Table 6.2.) gives a sign that crystal deformation occurred to a limited extent. Higher Mn substitution also prompted lessened crystallite sizes, signaling enhanced textural properties.
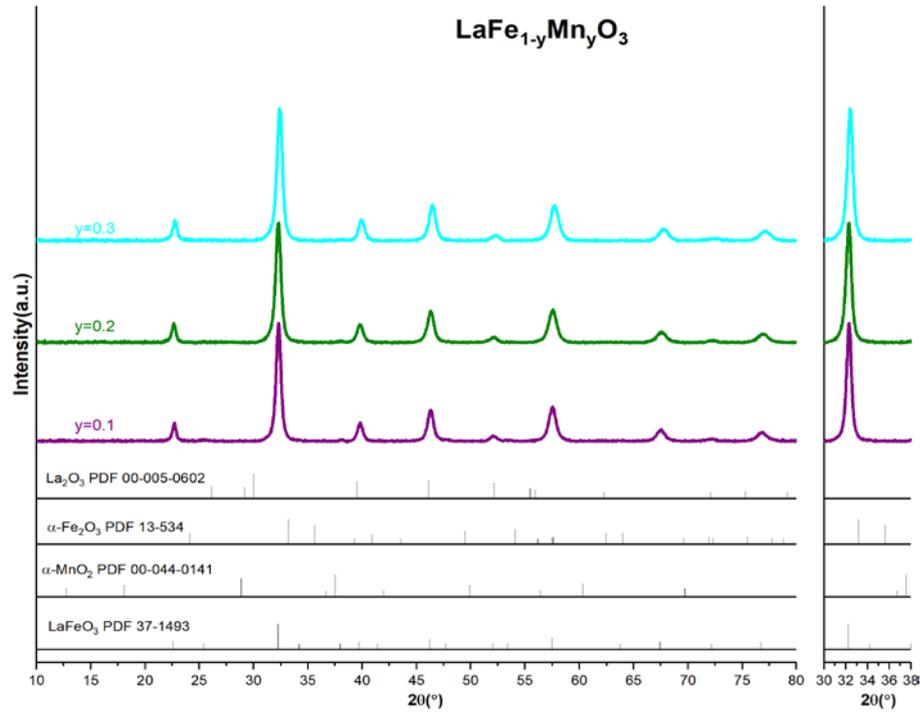
Fig. 6.2. X-ray diffractogram for the stoichiometric perovskite doped with manganese $LaFe_{1-y}Mn_yO_3$ (purple y = 0.1; olive y = 0.2; cyan y = 0.3).

Fig. 6.3. illustrates the X-ray diffractograms of lanthanum ferrites with La-deficiency in A site $La_{0.7}Fe_{1-y}Mn_yO_3$. Perovskite phase with orthorhombic structure was maintained with lanthanum deficiency in A site. Higher Mn-doping content led to minor shift of characteristic peak towards higher 2θ value whereas changes of relative intensity appeared unconspicuous. The narrowing of interplanar spacing reveals that impact of Mn-doping on the La-deficient iron-based perovskite seemed to render the lattice arranged in a sparser array. Combined with the shrinkage of unit cell volume triggered by higher manganese substitution degree (see Table 6.2.), it was believed that anisotropy becomes more notable for the La-deficient perovskites with Mn-doping. Meanwhile, it is not trivial to mention that slight hematite phase ($2\theta = 33.2°$ and $35.6°$) was detected.
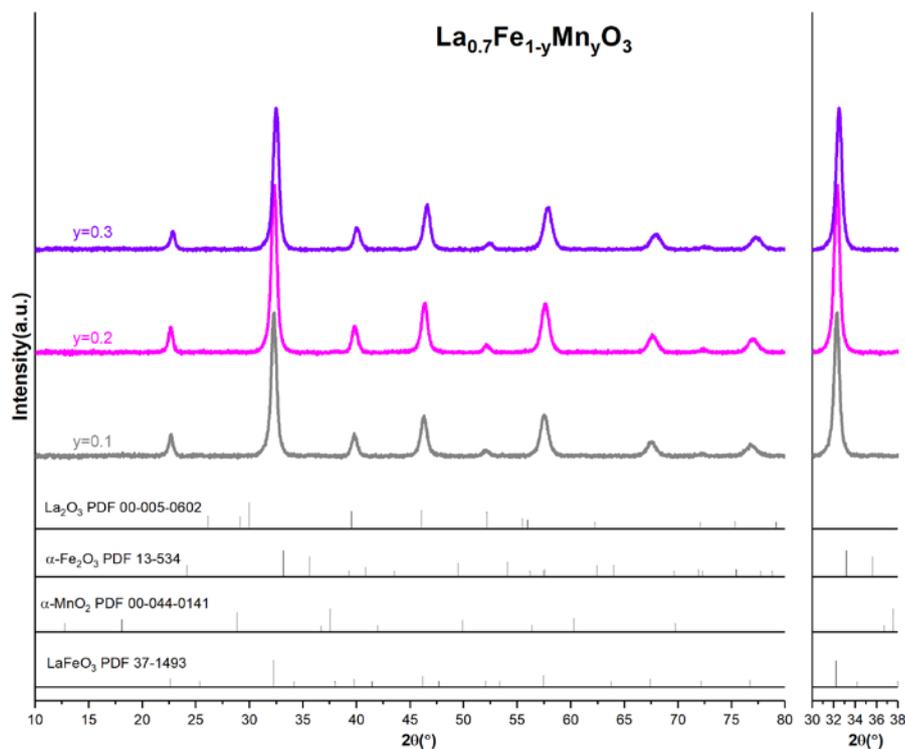
Fig. 6.3. X-ray diffractogram for the La-deficient perovskite doped with manganese $La_{0.7}Fe_{1-y}Mn_yO_3$ (grey y = 0.1; magenta y = 0.2; violet y = 0.3).

According to Fig. 6.4 calcium and manganese co-doping did not prevent the formation of perovskite phase. Neither of them was detected as segregated phase in the form of single oxide (i.e. CaO or MnO_2). Unlike previous findings that presence of extra-framework copper oxide was confirmed as a result of copper doping, manganese doping did not cause significant extraction of lattice manganese species. In light of the radii comparison (Cu^{2+} = 0.72 Å, Fe^{3+} = 0.64 Å, Mn^{3+} = 0.66 Å, Mn^{4+} = 0.56 Å) as well as electronegativity discrepancy (χMn = 1.75, χFe = 1.80, χCu = 1.85, χO = 3.61), it is conceivable that Fe-O-Mn complex has less tendency to dissociate compared to Fe-O-Cu complex due to higher bond dissociation energy of the former favorable for the stabilization of lattice manganese. The striking variations of lattice parameters and shrinkage of unit cell volume brought about by higher calcium substitution degree (see Table 6.2. and Fig. 6.5.) indicates that calcium-doping in A site, alongside manganese doping in B site, resulted in noticeable structural deformation. Although the topology of substituted perovskite is thermodynamically stable, the structure may distort as a result of competing bonding preferences of A and B cations. [L. Ortega-San Martin 2004; A.K. Eriksson 2006]. It was established that π bond (B-O bond) competes with σ bond (A-O bond) within the ABO_3 structure and B-O bond can thus be affected by A site cation.[J. Choy 1994, 1996] Subsequently, BO_6 octahedra tilting, octahedra distortion (i.e. Jahn-Teller distortion), bond length change, cationic displacements (i.e. ferroelectric displacement) and anionic vacancies are the main factors accountable for the structural deformation of substituted perovskites.
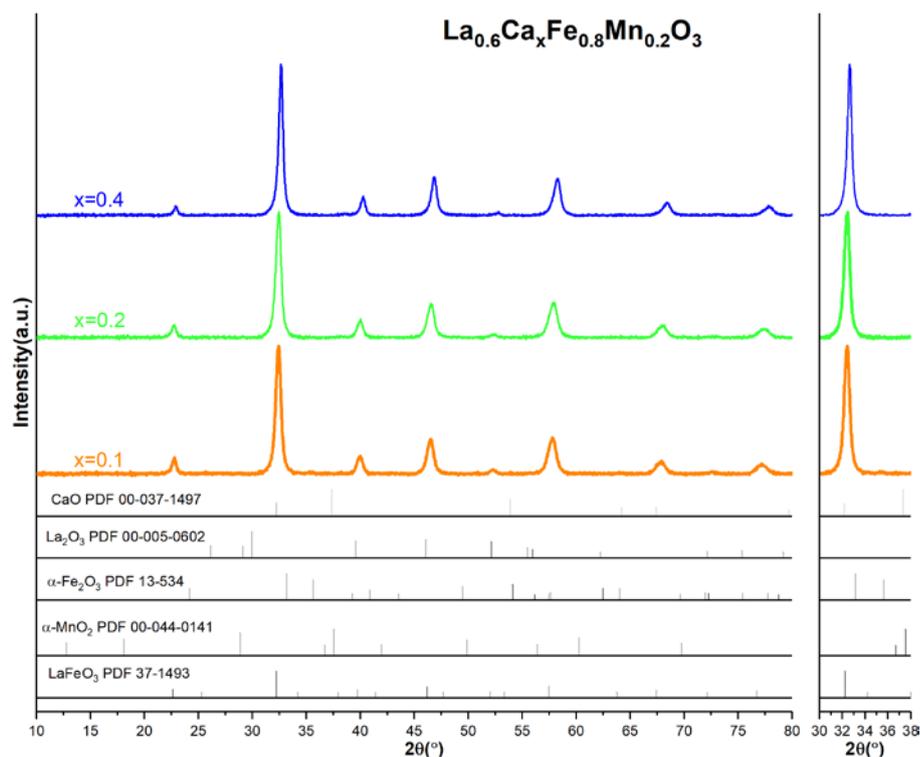
Fig. 6.4. X-ray diffractograms for Ca and Mn co-doped perovskites $La_{0.6}Ca_xFe_{0.8}Mn_{0.2}O_3$ (orange x = 0.1; green x = 0.2; blue x = 0.4).

Table 6.2. Structural properties of the iron-based perovskites ABO_3 (A=La, Ca; B= Fe, Mn)

Catalysts	Crystal system	a(Å)	b(Å)	c(Å)	unit cell volume($Å^3$)	Crystallite size (nm)
$LaFeO_3$	orthorhombic	5.560(1)	7.861(0)	5.557(1)	242.88±0.05	29.4
$La_{0.7}FeO_3$	orthorhombic	5.560(0)	7.878(1)	5.535(1)	242.44±0.03	21.7
$LaFe_{0.9}Mn_{0.1}O_3$	orthorhombic	5.542(0)	7.869(0)	5.532(1)	241.30±0.01	31.9
$LaFe_{0.8}Mn_{0.2}O_3$	orthorhombic	5.554(2)	7.814(1)	5.538(1)	240.33±0.04	31.5
$LaFe_{0.7}Mn_{0.3}O_3$	orthorhombic	5.534(0)	7.828(0)	5.503(1)	238.43±0.01	26.6
$La_{0.7}Fe_{0.9}Mn_{0.1}O_3$	orthorhombic	5.549(0)	7.864(1)	5.531(0)	241.42±0.01	23.8
$La_{0.7}Fe_{0.8}Mn_{0.2}O_3$	orthorhombic	5.547(0)	7.815(0)	5.536(1)	240.07±0.01	20.4
$La_{0.7}Fe_{0.7}Mn_{0.3}O_3$	orthorhombic	5.526(0)	7.800(1)	5.486(0)	236.52±0.03	19.1
$La_{0.6}Ca_{0.1}Fe_{0.8}Mn_{0.2}O_3$	orthorhombic	5.532(1)	7.801(0)	5.519(0)	238.22±0.06	24.8
$La_{0.6}Ca_{0.2}Fe_{0.8}Mn_{0.2}O_3$	orthorhombic	5.540(0)	7.773(1)	5.513(0)	237.46±0.03	23.7
$La_{0.6}Ca_{0.4}Fe_{0.8}Mn_{0.2}O_3$	orthorhombic	5.491(0)	7.764(1)	5.483(0)	233.78±0.05	21.3

Note: a) lattice parameters deduced from Rietveld refinement b) crystal size was calculated by Williamson-Hall plot method using LaB_6 as standard specimen
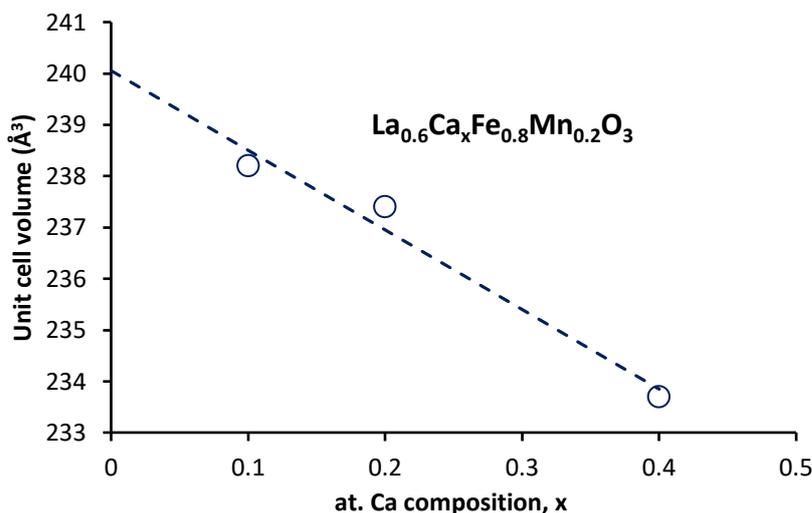
Fig. 6.5. Evolution of unit cell volume vs. Ca content

6.1.2. Mössbauer spectroscopy

Fig.6.6. illustrates Mössbauer spectra of doped perovskites recorded at room temperature. Distortion of $Fe(Mn)O_6$ octahedron from the ideal cubic structure was confirmed by quadruple splitting (ΔFe^{3+}, QS=0.236-0.838 mm/s). A visible broadening of line width could be noticed for the manganese-doped perovskites along with marked quadruple splitting measuring the electrical field gradient at the iron site. Such phenomenon is ascribed to local environment effects that lead to anisotropic deformation of the environment of the Fe (+III) located in the distorted octahedral sites.[T. Hernandez 2001]
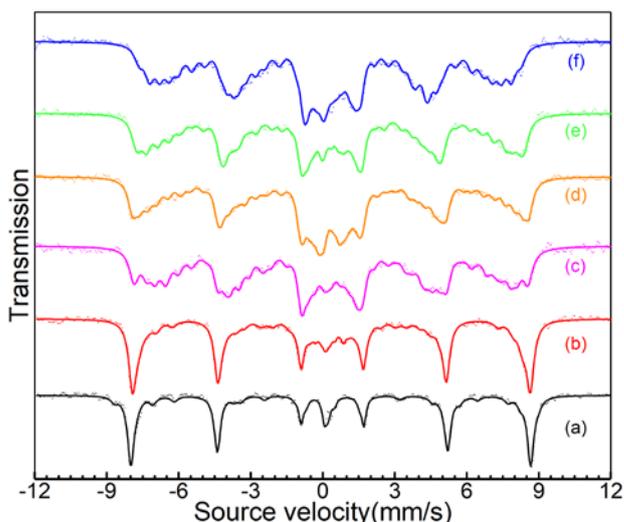
Fig. 6.6. Mössbauer spectra recorded at room temperature a: $LaFeO_3$; b: $La_{0.7}FeO_3$; c: $La_{0.7}Fe_{0.8}Mn_{0.2}O_3$; d: $La_{0.6}Ca_{0.1}Fe_{0.8}Mn_{0.2}O_3$; e: $La_{0.6}Ca_{0.2}Fe_{0.8}Mn_{0.2}O_3$; f: $La_{0.6}Ca_{0.4}Fe_{0.8}Mn_{0.2}O_3$ (line: calculated values; dot: experimental values).

Table 6.3. presents the iron species ratio of selected perovskites deducted from deconvolution of Mössbauer spectrum. The charge state of iron in $La_{0.7}Fe_{0.8}Mn_{0.2}O_3$ is exclusively Fe (+III) while co-existence of Fe^{3+} and Fe^{4+} was observed for candidates with both A site and B site substitution. Mere A site deficiency did not incur unusual oxidation

state of iron species, indicating the charge compensation was effectuated either through alteration of manganese valences or formation of oxygen vacancies or both of them. Presence of high spin Fe^{4+} species seemed more linked with incorporation of A site cations with lower valence regardless of stoichiometry or deficiency in A site.

Isomeric shift (IS) values which are characteristic of Fe (+III) species located in the octahedron sites increased with the amount of calcium doping implying that local distortion of octahedron is associated closely with cation doping in A site. This is in agreement with XRD result that more calcium-doping caused remarkable asymmetry of the crystal structure.

Table 6.3. Atomic ratio of iron species obtained from Mössbauer spectroscopy analysis for perovskites ABO_3 (A = La, Ca; B = Fe, Mn)

Catalyst composition	atomic ratio of iron species	Relative abundance
$LaFeO_3$	Fe^{3+} Undistorted octahedron	78.56%
	Fe^{3+} distorted octahedron	11.35%
	Fe^{3+} tetrahedron	5.26%
	Fe^{4+} high spin	4.83%
$La_{0.7}FeO_3$	Fe^{3+} Undistorted octahedron	92.31%
	Fe^{3+} distorted octahedron	5.58%
	Fe^{3+} tetrahedron	2.11%
	Fe^{4+} high spin	0.00%
$La_{0.7}Fe_{0.8}Mn_{0.2}O_3$	Fe^{3+} (Fe_2O_3 , goethite, ferrihydrite)	12.51%
	Fe^{3+} tetrahedron	16.23%
	Fe^{3+} undistorted octahedron	62.41%
	Fe^{3+} distorted octahedron	8.85%
	Fe^{4+} high spin	0.00%
$La_{0.6}Ca_{0.1}Fe_{0.8}Mn_{0.2}O_3$	Fe^{3+} (Fe_2O_3 , goethite, ferrihydrite)	18.78%
	Fe^{3+} tetrahedron	27.48%
	Fe^{3+} undistorted octahedron	43.30%
	Fe^{3+} distorted octahedron	6.45%
	Fe^{4+} high spin	3.99%
$La_{0.6}Ca_{0.2}Fe_{0.8}Mn_{0.2}O_3$	Fe^{3+} (Fe_2O_3, goethite, ferrihydrite)	10.08%
	Fe^{3+} tetrahedron	41.11%
	Fe^{3+} undistorted octahedron	37.44%
	Fe^{3+} distorted octahedron	8.02%
	Fe^{4+} high spin	3.35%
$La_{0.6}Ca_{0.4}Fe_{0.8}Mn_{0.2}O_3$	Fe^{3+} (Fe_2O_3, goethite, ferrihydrite)	20.20%
	Fe^{3+} tetrahedron	29.43%
	Fe^{3+} undistorted octahedron	38.91%
	Fe^{3+} distorted octahedron	8.74%
	Fe^{4+} high spin	2.72%

6.1.3. SEM-EDS analysis

Scanning electron microscopic measurements were performed on stoichiometric and La-deficient perovskite materials (Fig. 6.7.). As exemplified, large aggregates characterize

$LaMnO_3$ and $La_{0.7}Fe_{0.8}Mn_{0.2}O_3$ then becoming smaller after calcium substitution. However, the absence of morphological organization is noticeable. Elemental analysis from Dispersive X-ray Spectroscopy is summarized in Table 6.4. Data have been compared to those obtained from ICP analysis which indicates no significant deviations which underline homogeneous distribution in the elemental volume analyzed by EDS. Elemental mapping also emphasizes the absence of significant segregation irrespective of the composition. As seen, single phase of calcium and manganese was observed without pronounced inhomogeneity. Back scattered electron (BSE) images revealed no obvious disparity for calcium and manganese located in different zones, further confirming the proposal that incorporation of adventitious cations was achieved through replacement of lanthanum by calcium and iron by manganese rather than formation of extra-lattice oxides dispersed on the perovskite substrate. All these observations match with those obtained from XRD analysis which did not indicate discernible bulk impurities formation assigned to manganese ex solution.
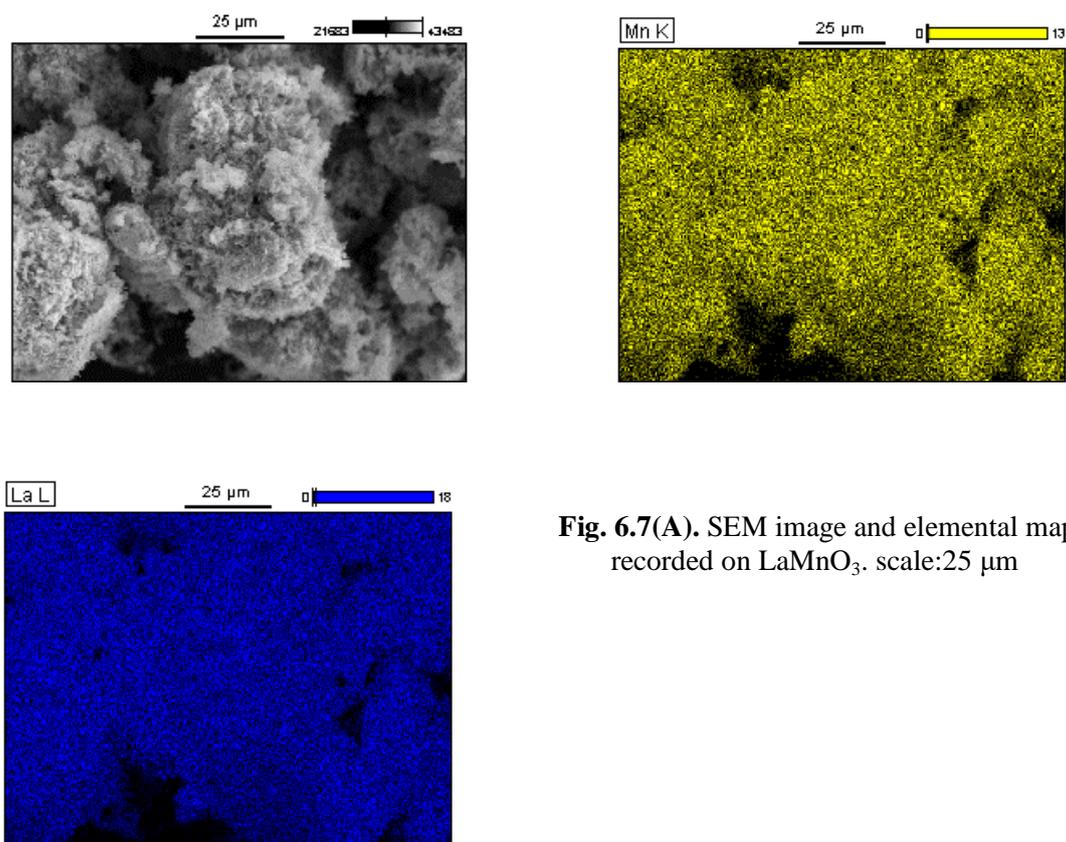
Fig. 6.7(A). SEM image and elemental mapping recorded on $LaMnO_3$. scale:25 μm
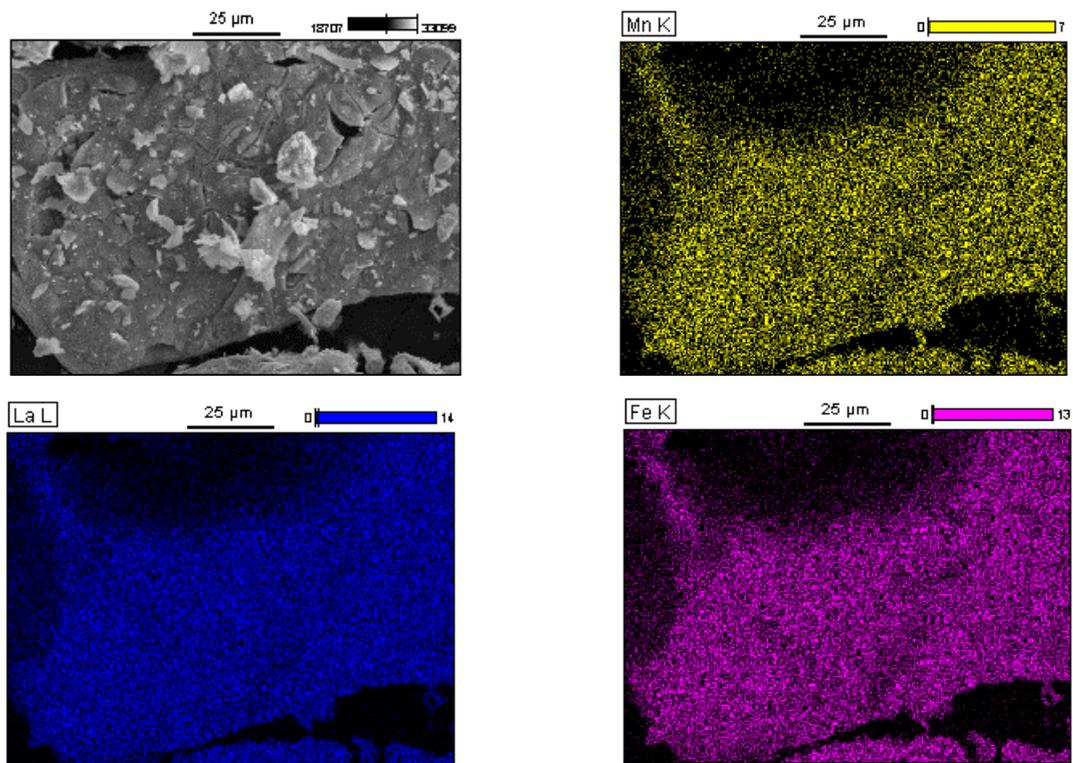
Fig. 6.7(B). SEM image and elemental mapping recorded on $La_{0.7}Fe_{0.8}Mn_{0.2}O_3$. scale:25 µm
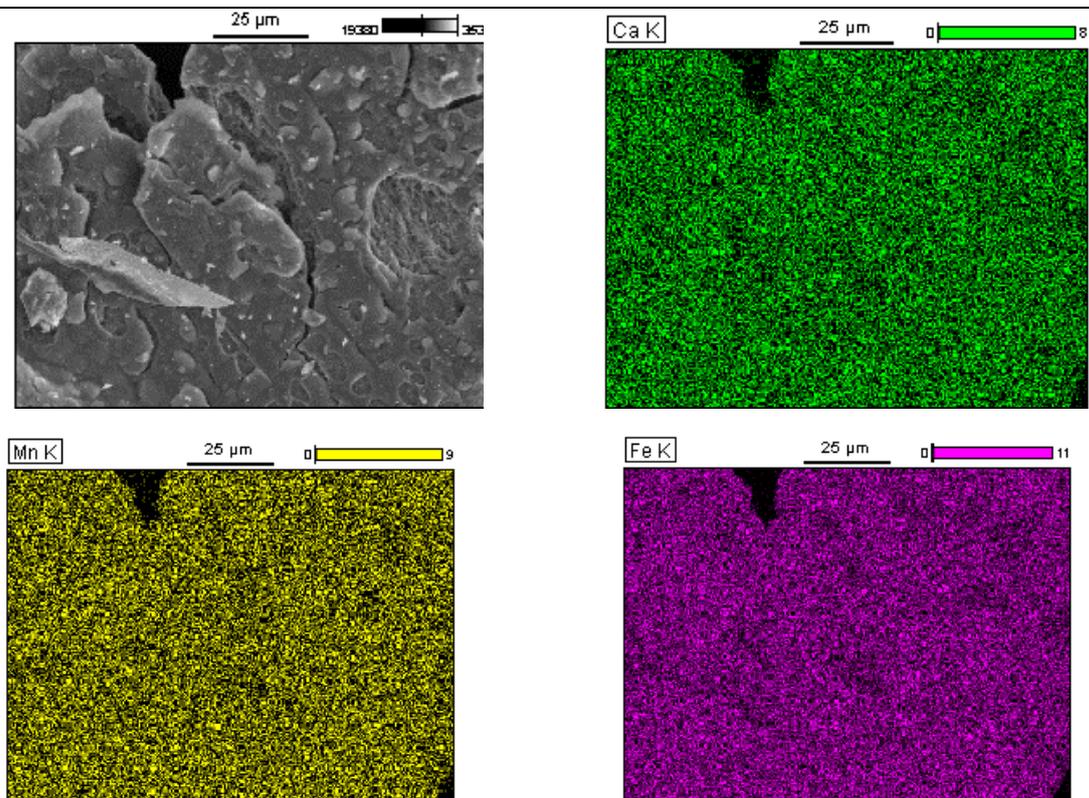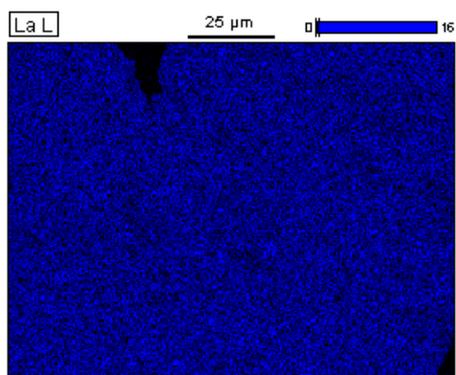
Fig. 6.7(C). SEM image and elemental mapping recorded on $La_{0.6}Ca_{0.1}Fe_{0.8}Mn_{0.2}O_3$. scale:25 μm
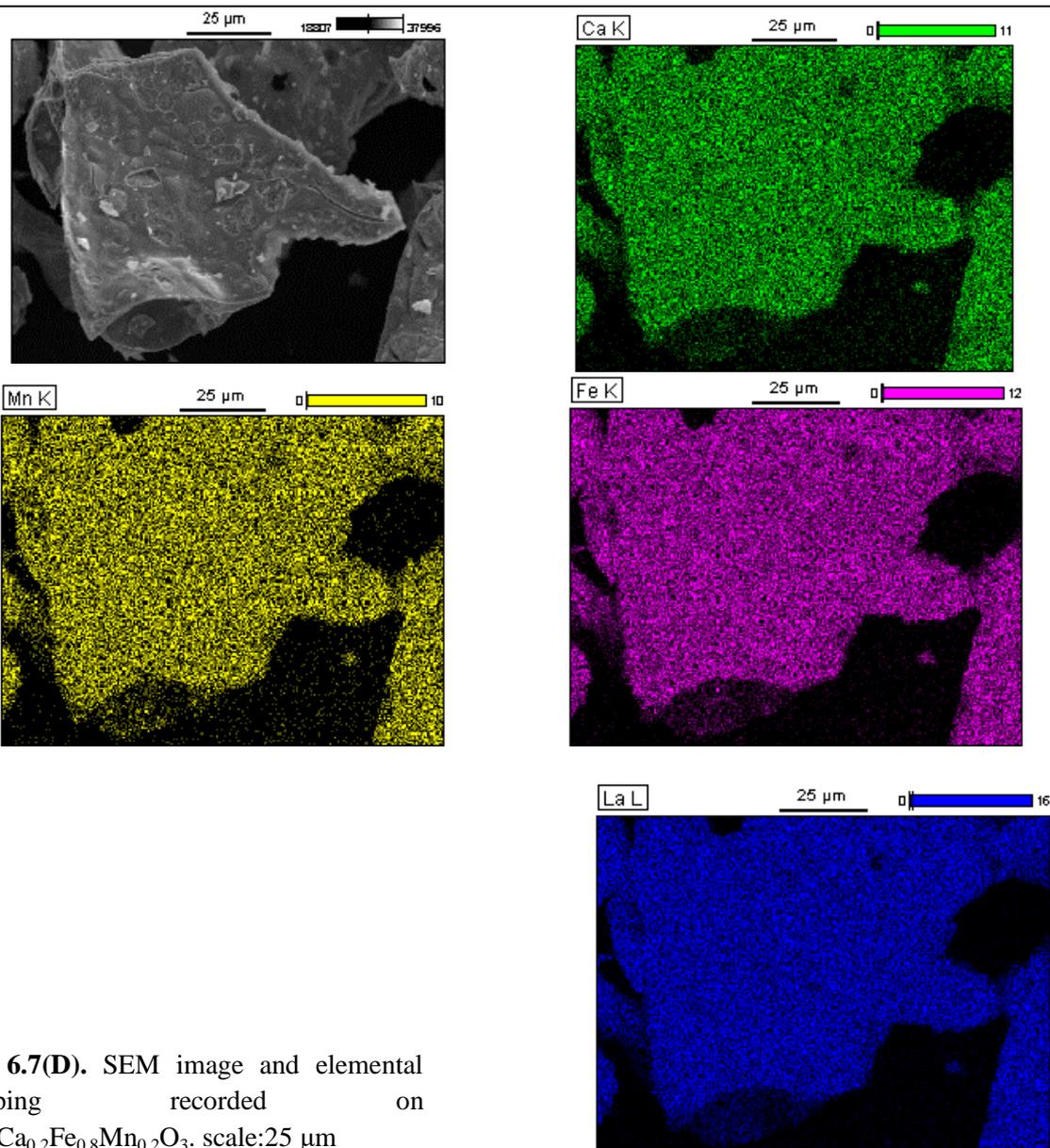
Fig. 6.7(D). SEM image and elemental mapping recorded on $La_{0.6}Ca_{0.2}Fe_{0.8}Mn_{0.2}O_3$. scale:25 μm
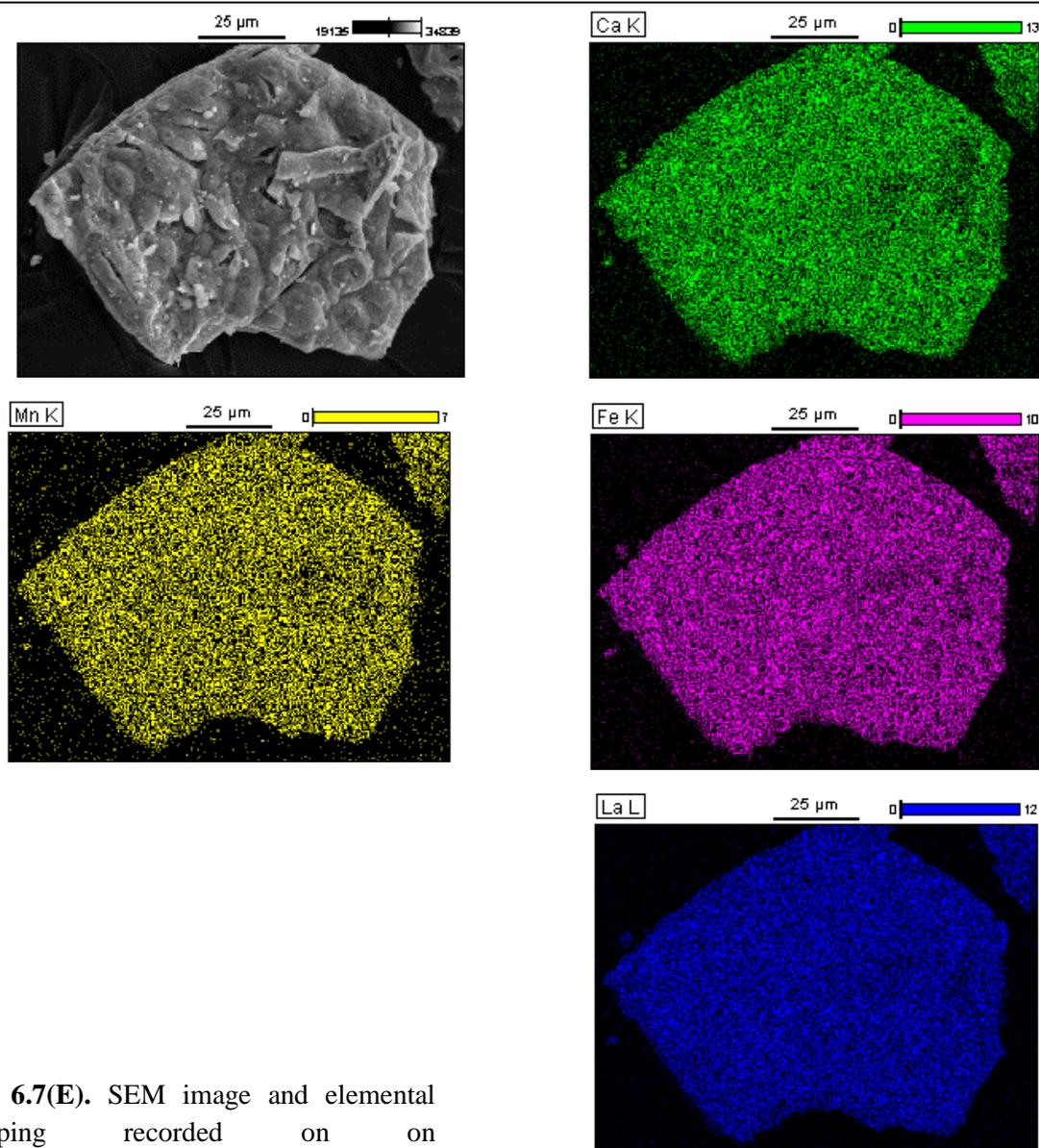
Fig. 6.7(E). SEM image and elemental mapping recorded on on $La_{0.6}Ca_{0.4}Fe_{0.8}Mn_{0.2}O_3$. scale:25 µm

Table 6.4. Atomic composition of the prepared perovskites calculated from EDS analysis

catalyst	Atomic composition (%)				Mn/Fe	A/B
	La	Ca	Fe	Mn		
$LaFeO_3$	48.56	-	51.44	-		0.94 (1.02)
$La_{0.7}FeO_3$	37.99	-	62.01	-		0.61 (0.67)
$La_{0.7}Fe_{0.8}Mn_{0.2}O_3$	37.17	-	49.31	13.52	0.40 (0.40)	0.59 (0.71)
$La_{0.6}Ca_{0.1}Fe_{0.8}Mn_{0.2}O_3$	31.12	6.42	48.51	13.94	0.29 (0.25)	0.60 (0.68)
$La_{0.6}Ca_{0.2}Fe_{0.8}Mn_{0.2}O_3$	29.60	11.24	46.05	13.11	0.28 (0.15)	0.69 (0.78)
$La_{0.6}Ca_{0.4}Fe_{0.8}Mn_{0.2}O_3$	26.32	20.92	40.90	11.86	0.29 (0.25)	0.90 (1.00)

6.1.4. Reducibility

Reducibility of the prepared perovskites was studied from H_2-TPR experiments. As seen in Fig. 6.8, La-deficiency promoted remarkably the reducibility of lanthanum ferrite compared to stoichiometric composition $LaFeO_3$ which was hardly reducible below 700°C. The H_2 consumption profile recorded on stoichiometric lanthanum manganite $LaMnO_3$ exhibit two broad range of hydrogen consumption in the range 250-500°C and above 600°C illustrating to a two steps reduction process of Mn^{4+} to Mn^{2+}. The estimation of the H/Mn ratio, from H_2 uptake ratio in Table 6.5. of 1.25 is slightly overestimated from the theoretical value according to the stoichiometry of Eqs. 6-1 and 6-2, which suggests that manganese could be predominantly stabilized as Mn(+IV) in accompanied with an over stoichiometry of oxygen according to the composition $LaMnO_{3+\delta}$.

$$2MnO_2 + H_2 = Mn_2O_3 + H_2O \qquad (eq.\,6-1)$$

$$Mn_2O_3 + H_2 = 2MnO + H_2O \qquad (eq.\,6-2)$$
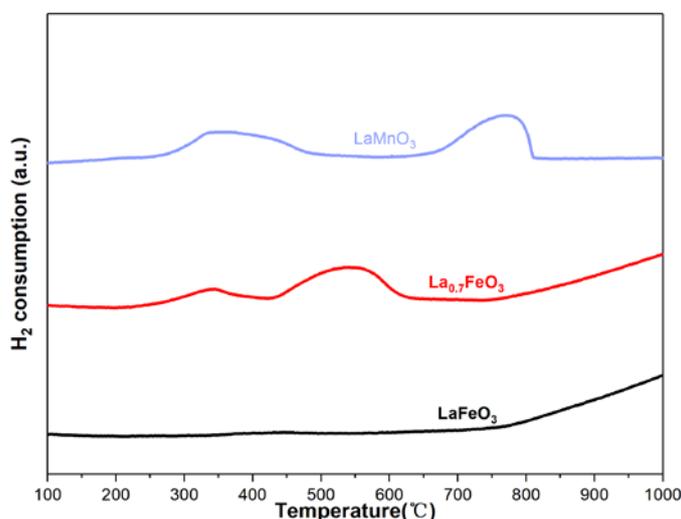
Fig. 6.8. Plots of H_2 consumption curves plotted vs. temperature for reference perovskite black: $LaFeO_3$; Red: $La_{0.7}FeO_3$; Light blue: $LaMnO_3$.

Partial substitution of iron by manganese in the B site of $LaFeO_3$ leads to a much lower reducibility reflected by H/Mn largely under-estimated compared to theoretical values which underlines a greater stabilization of Mn^{4+}/Mn^{3+} in octahedral coordination in the framework of the stoichiometric lanthanum ferrites (see Fig. 6.9.). Bulk iron appeared hardly active below 700°C and can only be partially reduced progressively above 700°C. Increasing the degree of substitution from y = 0.1 to 0.3 is accompanied by a slight increase of H_2 consumed which emphasizes the weak reducibility of the aforementioned compositions indicating that manganese doping in B site plays a quite limited role in affecting the overall redox properties of the stoichiometric perovskites.
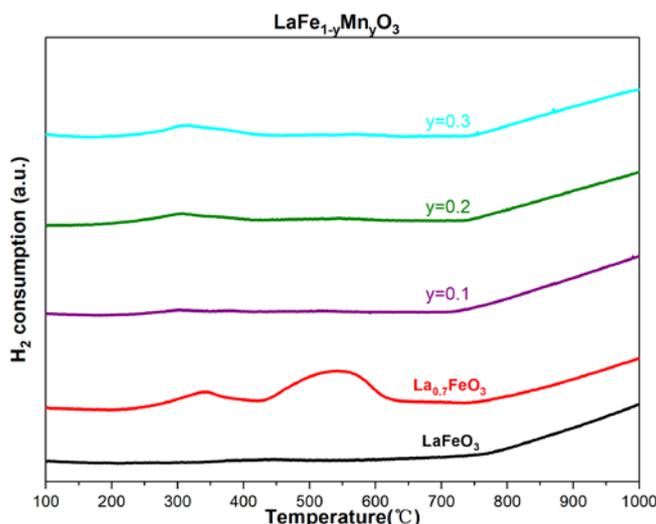
Fig. 6.9. H_2 consumption curves plotted against temperature for stoichiometric perovskites doped with manganese $LaFe_{1-y}Mn_yO_3$ purple: y = 0.1; olive: y = 0.2; cyan: y = 0.3.

Reduction process of La-deficient perovskites with manganese doping in B site shows comparable pattern to that of $La_{0.7}FeO_3$ (Fig. 6.10). Regarding the low temperature reduction process in the range 300-400°C possible overlapping reduction processes may occur ascribed the reduction of Mn^{4+} to Mn^{3+} and extra-lattice hematite to ferrous compound. On the other hand, the second peak at 450-600°C ought to be attributed to a preferential reduction of ferrous species to metallic iron in part. It is worthwhile to note that no extra reduction process takes place above 600°C which could reflect a significant reduction of Mn^{3+} to Mn^{2+}. On the basis of this information, incorporation of valiocations in B site did not prevent the extraction of lattice iron but impacted on the reduction process of hematite characterized by the strengthening of first step (Eq. 5-2) and weakening of second step (Eq. 5-3). As a generally trend, an increase of hydrogen consumption is noticeable below 400°C which reflect improved reducibility on La-deficient perovskite.
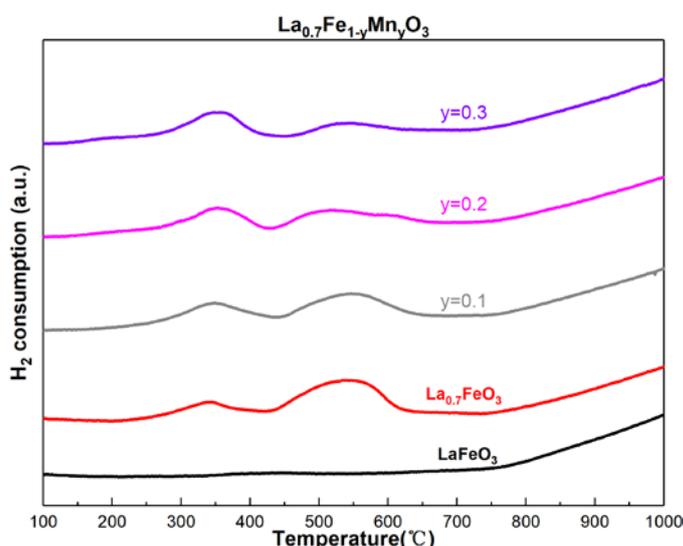
Fig. 6.10. H_2 consumption curves plotted against temperature for La-deficient perovskites doped with manganese $La_{0.7}Fe_{1-y}Mn_yO_3$ grey: y = 0.1; magenta: y = 0.2; violet: y = 0.3.

Modification of redox properties become apparent when calcium and manganese co-doping was implemented, featured by the broadening of reduction peaks and more distinctive separation of reduction processes. Reduction of Mn^{4+} to Mn^{3+} shifted towards lower temperature while reduction of Mn^{3+} to Mn^{2+} was retarded as calcium doping content increased. $La_{0.6}Ca_{0.1}Fe_{0.8}Mn_{0.2}O_3$ boasted the maximum total hydrogen consumption quantity (1.44 mmol/g), comparable to that of $La_{0.7}FeO_3$ (1.45 mmol/g). At a first glance, $La_{0.6}Ca_{0.1}Fe_{0.8}Mn_{0.2}O_3$ mimics the behavior of $La_{0.7}FeO_3$ as illustrated in Fig. 6.11 with preferential reduction of extra lattice iron species. Higher calcium substitution degree results in less hydrogen consumption which suggests that calcium substitution would block the extraction/segregation of hematite. Jointly a H_2 consumption process becomes distinguishable above 700°C which intensifies on the stoichiometric $La_{0.6}Ca_{0.4}Fe_{0.8}Mn_{0.2}O_3$ composition. A broader H_2 consumption is also noticeable characteristic of Mn^{4+} reduction. Clearly, sub-stoichiometric compositions (x = 0.1 and x = 0.2) seemed more analogous to that of $La_{0.7}FeO_3$ characterized by successive reductions of extra-lattice hematite whereas the reduction process of the stoichiometric composition (x = 0.4) is believed to be more connected with lattice manganese species although minor presence of hematite cannot be completely excluded.
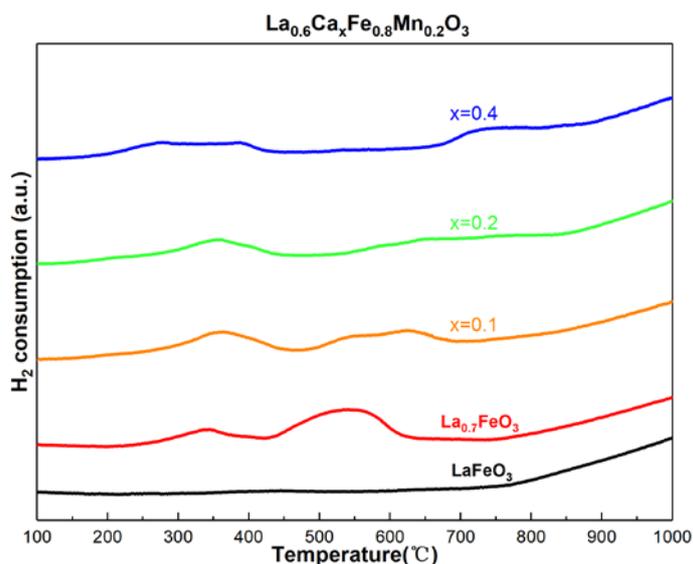
Fig. 6.11. H_2 consumption curves plotted against temperature for calcium and manganese co-doped perovskites $La_{0.6}Ca_xFe_{0.8}Mn_{0.2}O_3$ orange: x = 0.1; green: x = 0.2; blue: x = 0.4.

Table 6.5. presents semi-quantitative exploitation of H_2-TPR profiles for ABO_3 perovskites (A = La, Ca; B = Fe, Mn). In general, manganese doping in B site of the stoichiometric lanthanum ferrites did not give rise to desirable reducibility. Nevertheless, La-deficiency combined with manganese doping led to considerable improvement of reducibility evidenced by the striking augmentation of hydrogen consumption quantity associated with contribution of extra-lattice hematite. Such trend was further bolstered by calcium doping x = 0.1. Yet higher calcium doping yielded less hydrogen consumption due to inhibition of hematite extraction. Surprisingly, the maximum total hydrogen consumption quantity was

recorded on the stoichiometric lanthanum manganite $LaMnO_3$, suggesting probably a better redox property compared to lanthanum ferrites. However, overall performance of this catalyst is estimated to be restrained by its mediocre textural property (SSA=17.8 m^2/g, Table 6.7.).

Table 6.5. H_2-TPR analyses of ABO_3 perovskites (A=La, Ca; B = Fe, Mn)

Catalyst composition	H_2 total consumption (mmmol g^{-1})[a]	H/B[b]	H/Mn[c]	T_{max} of reduction peaks[d] (°C)		
$LaFeO_3$	-	-	-	-	-	>700
$La_{0.7}FeO_3$	1.45	0.58	-	340	541	>700
$LaMnO_3$	2.58	1.25	1.25	351	771	-
$LaFe_{0.9}Mn_{0.1}O_3$	0.14	0.07	0.07	302	520	>700
$LaFe_{0.8}Mn_{0.2}O_3$	0.36	0.17	0.17	306	547	>700
$LaFe_{0.7}Mn_{0.3}O_3$	0.43	0.21	0.21	312	567	>700
$La_{0.7}Fe_{0.9}Mn_{0.1}O_3$	1.15	0.46	-	350	545	>700
$La_{0.7}Fe_{0.8}Mn_{0.2}O_3$	1.16	0.47	-	353	516	>700
$La_{0.7}Fe_{0.7}Mn_{0.3}O_3$	1.02	0.41	-	356	533	>700
$La_{0.6}Ca_{0.1}Fe_{0.8}Mn_{0.2}O_3$	1.44	0.55	-	359	618	>700
$La_{0.6}Ca_{0.2}Fe_{0.8}Mn_{0.2}O_3$	1.15	0.45	-	355	652	>800
$La_{0.6}Ca_{0.4}Fe_{0.8}Mn_{0.2}O_3$	0.77	0.31	-	275	535	>800

a: total H_2 consumption was calculated taking into account the temperature range 150-700 °C
b: B = Fe + Mn
c: H/Mn was only calculated for stoichiometric $LaFe_{1-y}Mn_yO_3$ assuming H_2 uptake below 700°C was solely ascribed to intra-lattice manganese species
d: H_2 uptake below 700 °C was ascribed to extra-lattice hematite and intra-lattice manganese species; while H_2 uptake above 700 °C was ascribed to intra-lattice iron species

6.1.5. Oxygen mobility

Profiles of oxygen temperature programmed desorption vs. temperature of the benchmark catalysts are shown in Fig. 6.12. As discussed previously, activity of both α-oxygen and β-oxygen were enhanced in La-deficient $La_{0.7}FeO_3$ compared to stoichiometric $LaFeO_3$. Compared to lanthanum ferrite, stoichiometric lanthanum manganite $LaMnO_3$ possesses higher bulk oxygen mobility demonstrated by earlier onset of desorption peak and larger desorption quantity of β-oxygen (corresponding to oxygen lattice O^{2-}) whereas α-oxygen could barely be observed due to the lack of surface oxygen vacancies necessary for chemisorbing suprafacial oxygen species. Such an observation seems in rather agreement with H_2-TPR measurements which suggest the storage of interstitial oxygen to equilibrate the stabilization of Mn(+IV) species according to the composition $LaMnO_3$.
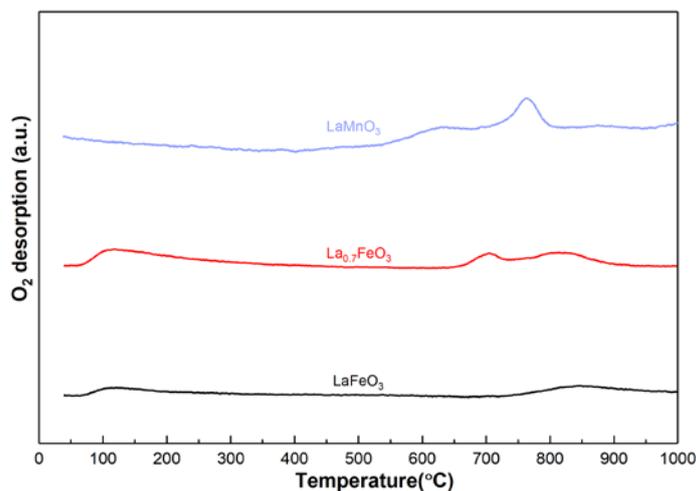
Fig. 6.12. O_2-Temperature-Programmed Desorption profiles vs. T of the reference perovskite catalysts

Manganese doping in B site of stoichiometric lanthanum ferrites resulted in significant enhancement of bulk oxygen mobility (Fig. 6.13.) compared to $LaFeO_3$ in terms of oxygen desorption quantity (see Table 6.6.), which can be explained logically by the creation of more oxygen vacancies deriving from partial replacement of iron cations by manganese cations. Since lattice oxygen desorption occurs usually in accompany with reduction of B site metals, reduction of both iron and manganese cations should be taken into account when it comes to formation of bulk oxygen vacancy in the substituted perovskites.

Lower substitution degrees (y = 0.1 and y = 0.2) leads to an oxygen desorption pattern resembling that of $LaFeO_3$, denoting conceivably a greater impact of iron reduction on the desorption process. Notwithstanding, lattice oxygen desorption process of perovskite with 30% manganese substitution (y = 0.3) displayed discontinuous steps similar to that of $La_{0.7}FeO_3$, signifying presumably the reduction of iron species located in different environment.
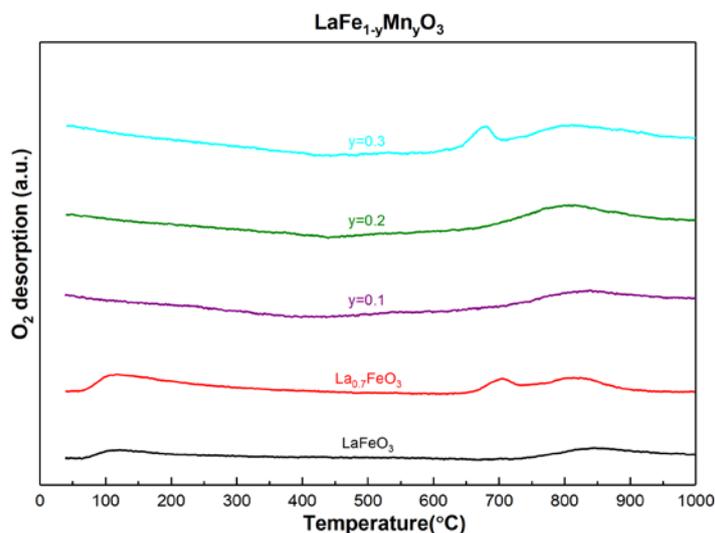
Fig. 6.13. O_2-TPD profile of the stoichiometric $LaFe_{1-y}Mn_yO_3$ perovskites doped with manganese purple: y = 0.1; olive: y = 0.2; cyan: y = 0.3.

When manganese doping was implemented in B site together with La-deficiency in A site Fig. 6.14. it was found that lattice oxygen mobility was tremendously activated manifested by the higher total oxygen desorption quantity at each substitution level. 10%

percent manganese doping generated the largest total oxygen desorption quantity. In comparison with stoichiometric compositions, it is accepted that more oxygen vacancies need to be produced in order to compensate the charge imbalance originating from the loss of A site atoms. This is in good accord with the H$_2$-TPR result that reducibility of B site metals was improved substantially by virtue of La-deficiency. Despite the obvious amelioration of lattice oxygen migration characteristic, surface oxygen seems to be hardly affected by La-deficiency with the lack of observation of marked boost of desorbed α-oxygen quantity. It is thereby assumed that the increased number of oxygen vacancies initiated by synergistic A site deficiency and B site substitution comes mainly from the bulk of the material instead of the surface.
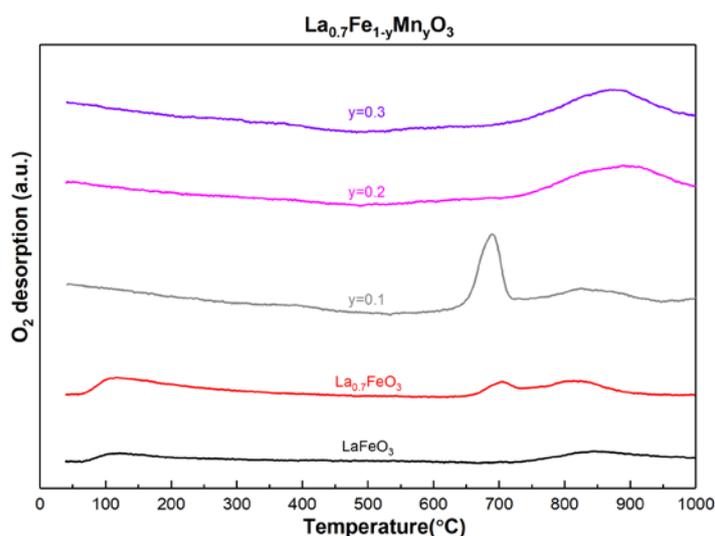
Fig. 6.14. O$_2$-TPD profile of the La-deficient perovskites doped with copper La$_{0.7}$Fe$_{1-y}$Mn$_y$O$_3$ grey: y = 0.1; magenta : y = 0.2; violet: y = 0.3.
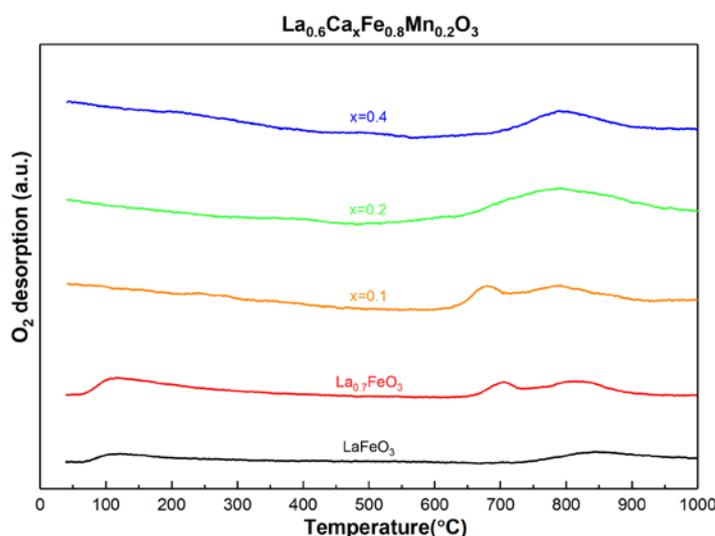
Fig. 6.15. O$_2$-TPD profile of calcium and manganese co-doped perovskites La$_{0.6}$Ca$_x$Fe$_{0.8}$Mn$_{0.2}$O$_3$ orange: x = 0.1; green: x = 0.2; blue: x = 0.4.

10% substitution of calcium in A site of the manganese doped perovskite gave rise to an oxygen desorption pattern similar to that of La$_{0.7}$FeO$_3$ but the two differs in terms of

commencement of temperature and desorbed quantity of lattice oxygen desorption. (Fig. 6.15.) Considering their same deficiency scale (both of them possess 30% deficiency in A site) it can be said that 10% calcium doping is advantageous to the promotion of lattice oxygen mobility marked by slight shift of desorption shoulder peak and larger desorbed quantity of lattice oxygen.

Nevertheless, higher calcium substitution degrees for x = 0.2 and 0.4 led to the inhibition of lattice oxygen mobility owing to less A site deficiency stemming from more calcium doping.

A point which is especially worth noting is that since it is established that characteristic of B site cations is subject to the valence of A site cations, replacement of A site cation by an alkaline earth metal with lower valence would lead to stabilization of unusual oxidation state of B site cations. That is to say, more calcium doping in A site was supposed to incur the increase of oxidation state of either iron or manganese cations in B site. Yet in comparison with La$_{0.7}$FeO$_3$, the total oxygen desorption quantity diminished significantly when 40% calcium doping was implemented, which is contrary to the expectation that the lower the overall valence in A site, the more oxygen vacancies will be generated due to electroneutrality requirement. Thus, it is believed that A site deficiency has a greater impact on the generation of lattice oxygen vacancies than B site substitution with manganese.

Table 6.6. Amount of desorbed oxygen quantity deduced from O$_2$-TPD analysis

Catalyst	β-O$_2$ position (°C)		Amount of O$_2$ desorbed (mmol/g)[a]		
			α-O$_2$ (<600°C) [b]	β-O$_2$ (>600°C) [c]	Total O$_2$ (desorbed)) [d]
LaFeO$_3$	844	-	0.090	0.030	0.120
La$_{0.7}$FeO$_3$	702	820	0.150	0.120	0.270
LaMnO$_3$	629	764	0.004	0.221	0.225
LaFe$_{0.9}$Mn$_{0.1}$O$_3$	838	-	0.024	0.112	0.136
LaFe$_{0.8}$Mn$_{0.2}$O$_3$	800	-	0.016	0.177	0.193
LaFe$_{0.7}$Mn$_{0.3}$O$_3$	677	809	0.008	0.224	0.232
La$_{0.7}$Fe$_{0.9}$Mn$_{0.1}$O$_3$	690	838	0.020	0.265	0.285
La$_{0.7}$Fe$_{0.8}$Mn$_{0.2}$O$_3$	-	896	0.016	0.209	0.226
La$_{0.7}$Fe$_{0.7}$Mn$_{0.3}$O$_3$	-	871	0.021	0.222	0.243
La$_{0.6}$Ca$_{0.1}$Fe$_{0.8}$Mn$_{0.2}$O$_3$	679	788	0.019	0.181	0.200
La$_{0.6}$Ca$_{0.2}$Fe$_{0.8}$Mn$_{0.2}$O$_3$	-	788	0.020	0.257	0.277
La$_{0.6}$Ca$_{0.4}$Fe$_{0.8}$Mn$_{0.2}$O$_3$	-	791	0.037	0.134	0.171

a) Calculated by deconvolution of the O$_2$ desorption curves
b) The amount of α-O$_2$ was calculated in the temperature range 60-600°C
c) The amount of β-O$_2$ was calculated in the temperature range 600-1000°C.
d) Slight quantity of physiosorbed O$_2$ was included in the calculation of the amount of total oxygen desorption quantity

Apart from the contribution of iron reduction, mechanism of oxygen vacancy generation in the manganese doped perovskites becomes more complex because of the coexistence of variable oxidation state of manganese species. One tentative proposal might be that generation of oxygen vacancies was supposed to be more influenced by the reduction of manganese cations due to the fact that iron species present in the lattice only exhibited limited reducibility confirmed by the H$_2$-TPR analysis.

Desorption process of α-oxygen weakly attached to surface manganese species are often linked with reduction of manganese cations and subsequent liberation of oxygen vacancies in the surface according to Eqs.6-3, 6-4, 6-5,6-6.

$$\overset{O_2^-}{\underset{|}{Mn^{4+}_{(surface)}}} \longrightarrow \overset{\square}{\underset{|}{Mn^{3+}_{(surface)}}} + O_{2\,(g)} \qquad \text{(eq. 6-3)}$$

$$\overset{O_2^-}{\underset{|}{Mn^{3+}_{(surface)}}} \longrightarrow \overset{\square}{\underset{|}{Mn^{2+}_{(surface)}}} + O_{2\,(g)} \qquad \text{(eq. 6-4)}$$

$$\overset{O^-}{\underset{|}{Mn^{4+}_{(surface)}}} \overset{O^-}{\underset{|}{Mn^{4+}_{(surface)}}} \longrightarrow Mn^{3+}_{(surface)} \overset{\square}{\diagdown} Mn^{3+}_{(surface)} + O_{2\,(g)} \qquad \text{(eq. 6-5)}$$

$$\overset{O^-}{\underset{|}{Mn^{3+}_{(surface)}}} \overset{O^-}{\underset{|}{Mn^{3+}_{(surface)}}} \longrightarrow Mn^{2+}_{(surface)} \overset{\square}{\diagdown} Mn^{2+}_{(surface)} + O_{2\,(g)} \qquad \text{(eq. 6-6)}$$
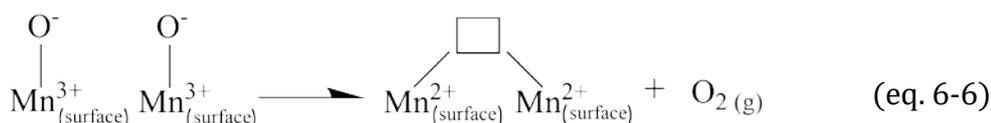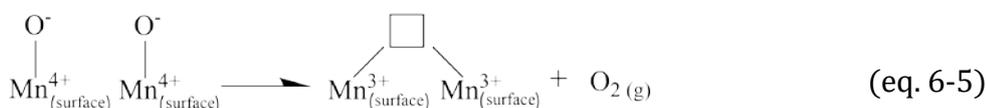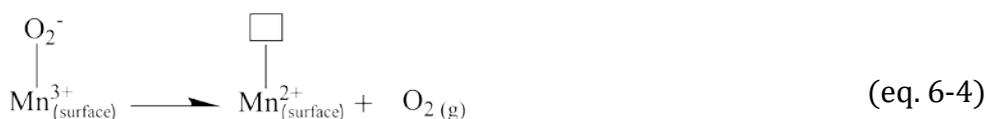
Desorption process of lattice β-oxygen associated with manganese species can be summarized according to Eqs. 6-7, 6-8.

$$Mn^{4+}_{(bulk)} \overset{O^{2-}}{\diagup\diagdown} Mn^{4+}_{(bulk)} \longrightarrow Mn^{3+}_{(bulk)} \overset{\square}{\diagup\diagdown} Mn^{3+}_{(bulk)} + 1/2\, O_{2\,(g)} \qquad \text{(eq. 6-7)}$$

$$Mn^{3+}_{(bulk)} \overset{O^{2-}}{\diagup\diagdown} Mn^{3+}_{(bulk)} \longrightarrow Mn^{2+}_{(bulk)} \overset{\square}{\diagup\diagdown} Mn^{2+}_{(bulk)} + 1/2\, O_{2\,(g)} \qquad \text{(eq. 6-8)}$$
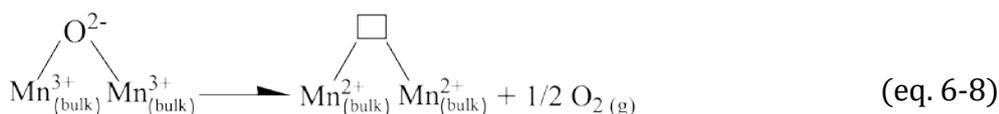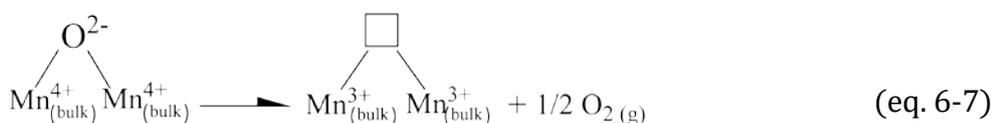
In addition, it must be emphasized that La-deficiency plays a great role in the stoichiometry of oxygen anions. In such case, liberation of oxygen vacancies may not be accompanied by the reduction of B site metals but rather arises from charge compensation in order to maintain electroneutrality.

Indeed, it is considered that manganese doping in B site result in better reducibility of lanthanum ferrite, creating more oxygen vacancies essential for the adsorption of NO and O$_2$ in competition. However, some authors (F. Patcas 2000) pointed out that the ease of reduction, which is desirable from the perspective of intrafacial catalytic reactions, represents

meanwhile a drawback for the stability of catalysts with high substitution degree under reducing atmosphere.

6.2. Surface properties

6.2.1. Nitrogen physisorption

Adsorption isotherms and pore size distribution curves are shown in Figs. 6.16.(A) and 6.16.(B) respectively. The experimental isotherms of lanthanum ferrite doped with calcium and copper exhibited a combination of type III and type V adsorption isotherm characterized by the absence of B-point at low relative pressure zone yet the presence of hysteresis ring at higher relative pressure zone. The former resulted from the weak interaction between adsorbate and perovskite adsorbent while the latter originated from capillary condensation effect. The slight broadening of hysteresis ring recorded on lanthanum-deficient perovskites (curves red, orange, green in Fig. 6.16.-A) compared to stoichiometric ones (curves black and blue) was probably linked with better adsorption properties exhibited by the increased adsorption layers and quantity in the channel Nevertheless, it should be noted that a distinct mesoporous structure cannot be confirmed in the light of the small pore volume of synthesized solids shown in table 6.7.

As illustrated in Table 6.7., the specific surface area of perovskites doped with manganese varied in the range of 26.7-33.8 m^2/g, relatively low due to the high temperature of thermal treatment (T = 600°C) yet slightly higher than those doped with copper. Enlarged SSA combined with decreased crystallite size (Table 6.2.) manifest improved surface properties such as increased active oxygen species and enhanced transport characteristics crucial for oxidation of CO and HC. Besides, adsorption of nitric oxide molecules would be favored by the exposure of more active metal sites on the surface, suggesting that these Mn-doped perovskites could presumably possess better activity with regards to reduction of nitric oxide in stoichiometric atmosphere.

A simple model for depicting the morphology of perovskites and the formation of agglomerates can be used. Such information can be useful to explain their ability to store oxygen. It was earlier stated oxygen availability can be related to a faster diffusion along the grain boundaries. A rough estimation of theoretical surface S$_{th}$ from the crystallite size can be compared to experimental specific surface area (SSA). As reported elsewhere, the S$_{th}$-to-SSA ratio can underline the fraction of surface lost by agglomeration between crystal domains as earlier explained [S. Royer 2005]. As observed in Table 6.7, no significant deviation is discernible which emphasize the fact that changes in SSA is essentially due to the growth of the perovskite crystallites.
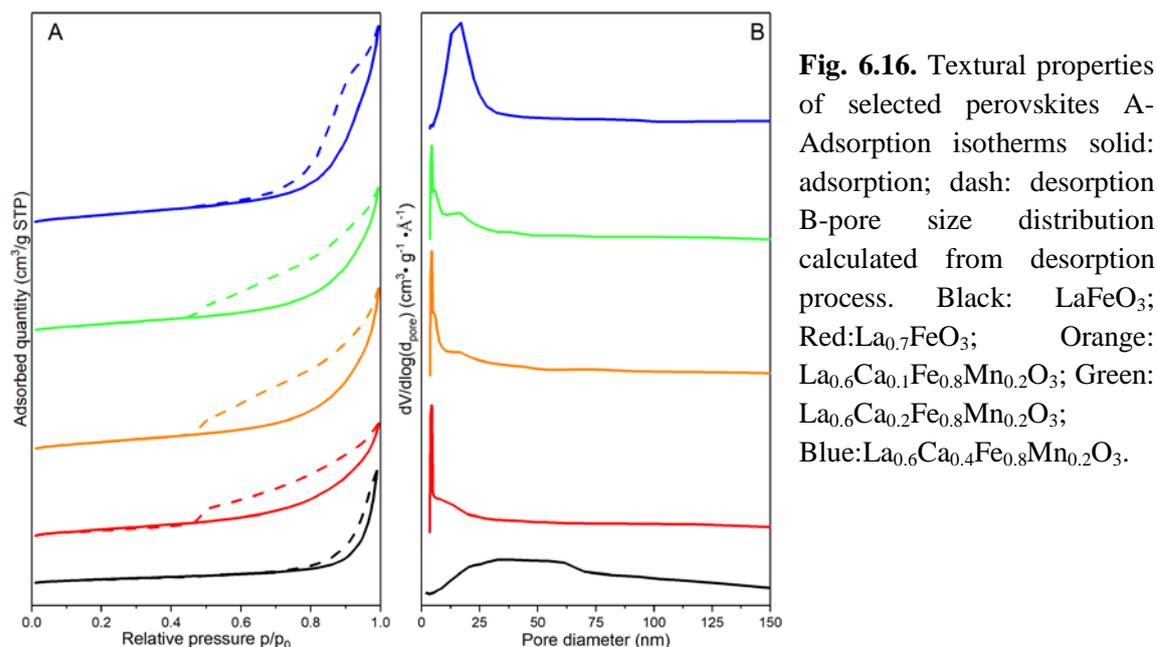
Fig. 6.16. Textural properties of selected perovskites A-Adsorption isotherms solid: adsorption; dash: desorption B-pore size distribution calculated from desorption process. Black: $LaFeO_3$; Red:$La_{0.7}FeO_3$; Orange: $La_{0.6}Ca_{0.1}Fe_{0.8}Mn_{0.2}O_3$; Green: $La_{0.6}Ca_{0.2}Fe_{0.8}Mn_{0.2}O_3$; Blue:$La_{0.6}Ca_{0.4}Fe_{0.8}Mn_{0.2}O_3$.

Table 6.7. Specific surface area (SSA) of the iron-based perovskite solid ABO_3 (A = La, Ca; B = Fe, Mn) synthesized through CCM.

Catalyst	Crystallite size (nm)	SSA (m^2/g) [a]	S_{th} (m^2/g) [b]	Pore volume (cm^3/g)
$LaFeO_3$	29.4	15.5	30.8	0.10
$La_{0.7}FeO_3$	21.7	35.5	41.7	0.10
$LaMnO_3$	38.7	17.8	23.4	0.09
$LaFe_{0.9}Mn_{0.1}O_3$	31.9	26.7	28.4	0.13
$LaFe_{0.8}Mn_{0.2}O_3$	31.5	33.8	28.7	0.17
$LaFe_{0.7}Mn_{0.3}O_3$	26.6	34.4	34.0	0.17
$La_{0.7}Fe_{0.9}Mn_{0.1}O_3$	23.8	28.5	38.0	0.06
$La_{0.7}Fe_{0.8}Mn_{0.2}O_3$	20.4	31.5	44.4	0.09
$La_{0.7}Fe_{0.7}Mn_{0.3}O_3$	19.1	32.4	47.4	0.10
$La_{0.6}Ca_{0.1}Fe_{0.8}Mn_{0.2}O_3$	24.8	32.5	36.5	0.14
$La_{0.6}Ca_{0.2}Fe_{0.8}Mn_{0.2}O_3$	23.7	32.6	38.2	0.13
$La_{0.6}Ca_{0.4}Fe_{0.8}Mn_{0.2}O_3$	21.3	31.8	42.5	0.17

Note:

a: SSA derived from N_2 physisorption

b: SSA estimated from equation $S_{th} = 6 \times 10^3/(\rho_{perovskite} d_{Rietveld})$

$\rho_{perovskite}$ — density of perovskite, $g \cdot m^{-3}$

$d_{Rietveld}$ — crystallite size calculated from Rietveld refinement, m

6.2.2. XPS analysis

Table 6.8. Binding energy of each element and abundance of related oxygen and carbon species

Catalyst	Binding energy (eV)							Relative surf. Comp. O^a			Relative conc. of carbonyl and carbonates (%)[b]
	La 3d	Ca 2p	Fe 2p	Mn 2p	O 1s Ads. oxygen	O 1s Lattice oxygen	C 1s Carbonyl and carbonate	O ads. (%)	O lattice (%)	$\frac{O_{adsorbed}}{O_{lattice}}$	
$LaFeO_3$	833.8	-	710.2	-	531.1	529.2	289.0	56.1	43.9	1.28	14.7
$La_{0.7}FeO_3$	834.2	-	710.9	-	531.2	529.7	289.1	61.7	38.3	1.61	11.5
$LaMnO_3$	833.7	-	-	641.9	531.0	529.2	288.9	52.6	47.4	1.11	12.5
$LaFe_{0.9}Mn_{0.1}O_3$	833.9	-	710.2	641.5	531.4	529.5	289.1	46.9	53.1	0.88	18.2
$LaFe_{0.8}Mn_{0.2}O_3$	834.0	-	710.3	641.7	531.5	529.6	289.0	44.3	55.7	0.80	13.4
$LaFe_{0.7}Mn_{0.3}O_3$	831.4	-	710.2	641.8	531.4	529.6	289.2	48.3	51.7	0.93	21.4
$La_{0.7}Fe_{0.9}Mn_{0.1}O_3$	834.2	-	710.4	641.8	531.5	529.7	289.0	39.3	60.7	0.65	9.8
$La_{0.7}Fe_{0.8}Mn_{0.2}O_3$	834.1	-	710.5	641.7	531.3	529.7	288.8	43.1	56.9	0.76	11.8
$La_{0.7}Fe_{0.7}Mn_{0.3}O_3$	834.2	-	710.3	641.6	531.4	529.7	288.7	50.5	49.5	1.02	12.2
$La_{0.6}Ca_{0.1}Fe_{0.8}Mn_{0.2}O_3$	833.9	346.7	710.6	641.8	531.4	529.6	289.0	47.1	52.9	0.89	13.3
$La_{0.6}Ca_{0.2}Fe_{0.8}Mn_{0.2}O_3$	833.7	346.4	710.2	641.7	531.3	529.4	288.8	52.4	47.6	1.10	13.5
$La_{0.6}Ca_{0.4}Fe_{0.8}Mn_{0.2}O_3$	833.6	346.4	710.2	641.8	531.3	529.0	288.9	42.7	57.3	0.75	14.3

Note:

a $O_{adsorbed} + O_{lattice} = 1$

b $C_{carbonyl} + C_{adventious} = 1$

c relative abundance of oxygen and carbonyl species was calculated from deconvolution of photopeaks

The different characteristic La 3d, Fe 2p, Mn 2p and Ca 2p have been investigated. The corresponding photopeaks are collected in Figs. 6.19., 6.20., 6.21. respectively on $LaFe_{1-y}Mn_yO_3$, $La_{0.7}Fe_{1-y}Mn_yO_3$ and $La_{0.6}Ca_xFe_{0.8}Mn_{0.2}O_3$. Regarding the photopeak La 3d, intense lines of shake-up satellite were observed for all prepared catalysts. Despite minor variations of La 3d peak position, a spin-orbit splitting equal to 16.8 eV between La 3d 5/2 and La 3d 3/2 photopeaks keeps nearly identical for each catalyst regardless of stoichiometry or doping, revealing that the trivalent cation La^{3+} is present as the predominant oxidation state of lanthanum in the complex oxide. The binding energy of La 3d appeared at about 834.0 eV which is characteristic of lanthanum in the perovskite structure, suggesting that perovskite

lanthanum predominates for all catalysts irrespective of composition or stoichiometry (Table 6.8.).

As for Fe 2p photoelectron spectrum, the main photopeak appeared at binding energy near 710.2 eV with a pronounced satellite (718-719 eV) typical of Fe^{3+} cation. Mn 2p 3/2 photopeak usually consists of contribution of two species : Mn^{3+} (B.E = 641.2 eV) and Mn^{4+} (B.E. = 642.5 eV). [H.W. Nesbitt 1998; D. Banerjee 1999, 2001]. Mn^{4+}/Mn^{3+} ratio can be calculated by deconvolution of Mn 2p 3/2 photopeak. For both stoichiometric $LaFe_{1-y}Mn_yO_3$ and substoichiometric $La_{0.7}Fe_{1-y}Mn_yO_3$, higher manganese substitution degree yielded higher Mn^{4+} proportion. But for $La_{0.6}Ca_xFe_{0.8}Mn_{0.2}O_3$, the average oxidation state (AOS) of manganese cations is mainly determined by the overall cationic charge in A site. The O 1s photopeak is usually characterized by two components which have been previously ascribed of surface O lattice species near 529 eV ($O_{lattice}$) and 531 eV (O_{ads}) corresponding to adsorbed oxygen species i.e. O_2^-, O^- or OH groups. The ratio $O_{ads}/O_{lattice}$ can be calculated after spectral decomposition. The corresponding values are reported in Table 6.8. The B.E. values related to Ca 2p mainly characterize Ca^{2+}. B.E. value and semi-quantitative analysis is reported in Tables 6.8. and 6.10. For the La-deficient compositions $La_{0.7}Fe_{1-y}Mn_yO_3$, higher Mn substitution degree resulted in significant increase of $O_{ads}/O_{lattice}$ ratio, indicating that A site deficiency had a great impact on surface oxygen vacancy. Such trend was further strengthened when calcium doping 10% and 20% were implemented, with $O_{ads}/O_{lattice}$ ratio equal to 0.89 and 1.10 respectively. But the $O_{ads}/O_{lattice}$ ratio of the stoichiometric composition $La_{0.6}Ca_{0.4}Fe_{0.8}Mn_{0.2}O_3$ becomes smaller which means A site stoichiometry combined with doping is detrimental to the formation of surface oxygen vacancy.

Mn 3s photopeak provides useful insights on the oxidation state of manganese. Multiplet splitting of Mn 3s peak results from the coupling of non-ionized Mn 3s electrons and 3d valence band electrons [H. Najjar 2013]. Example of Mn 3s peak splitting is given in Fig. 6.17.
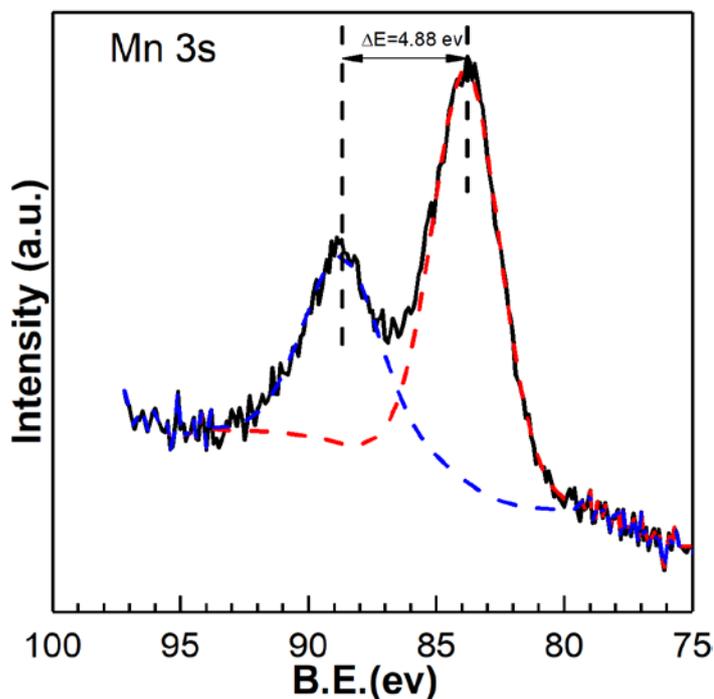
Fig. 6.17. Scheme of multiplet splitting of Mn 3s of $LaMnO_3$ perovskite

Prominent multiplet splitting can be observed for Mn^{2+}, Mn^{3+} and Mn^{4+} while Mn^{5+} is featured by less defined splitting or broadening. The average oxidation state (AOS) of manganese in the perovskite is calculated according Eq. 6-9. [P.S. Bagus 1973, 2004, 2008; Y.S. Jun 2003; J. Junta 1994]

$$\text{Average Oxidation State(AOS)} = 8.956 - 1.126\Delta E_{splitting}(Mn_{3s}) \qquad (eq. 6-9)$$

Table 6.9. Average Oxidation State(AOS) of manganese species in perovskite

Sample	$\Delta E_{splitting}$(Mn 3s)	Mn AOS
$LaMnO_3$	4.88	3.46
$LaFe_{0.9}Mn_{0.1}O_3$	5.77	2.46
$LaFe_{0.8}Mn_{0.2}O_3$	5.31	2.98
$LaFe_{0.7}Mn_{0.3}O_3$	5.28	3.01
$La_{0.7}Fe_{0.9}Mn_{0.1}O_3$	5.06	3.26
$La_{0.7}Fe_{0.8}Mn_{0.2}O_3$	5.12	3.19
$La_{0.7}Fe_{0.7}Mn_{0.3}O_3$	5.26	3.03
$La_{0.6}Ca_{0.1}Fe_{0.8}Mn_{0.2}O_3$	4.95	3.38
$La_{0.6}Ca_{0.2}Fe_{0.8}Mn_{0.2}O_3$	5.28	3.01
$La_{0.6}Ca_{0.4}Fe_{0.8}Mn_{0.2}O_3$	5.62	2.63

The variation of Mn AOS species in perovskite is associated closely with A site atom type and stoichiometry. In general, La-deficiency is beneficial to the increase of Mn AOS. This is in accord with H_2-TPR result that La-deficiency can improve the reducibility of the perovskite. Calcium doping 10% promoted slightly Mn AOS which is supposed to be assigned to the synergistic effect of calcium and manganese. Yet Mn AOS decreased in the stoichiometric composition $La_{0.6}Ca_{0.4}Fe_{0.8}Mn_{0.2}O_3$. It is thereby assumed that reducibility of manganese species located in the lattice is affected primarily by the composition of A site. This is supported by the evolution observed on the Mn AOS vs. total H_2 uptake from H_2-reduction as exemplified in Fig. 6.18 (A). As seen a gradual increase is observed with a rather important dispersion due to possible interference associated to partial reduction of extra framework iron species. On the other hand if the plot is restricted to calcium substituted samples a perfect correlation is observed. The same attempt to correlate Mn AOS with oxygen desorption is reported in Fig. 6.18 (B).
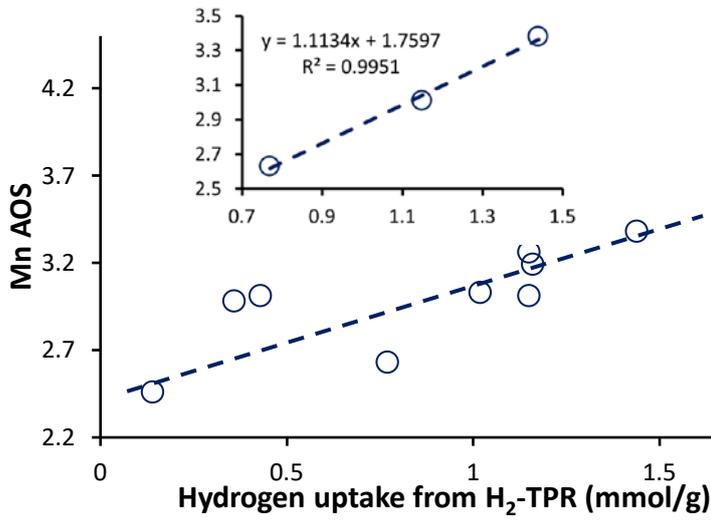
Fig. 6.18(A). Plot of the Mn AOS vs the H$_2$-uptake from temperature programmed experiments.

Inset: $y = 1.1134x + 1.7597$, $R^2 = 0.9951$
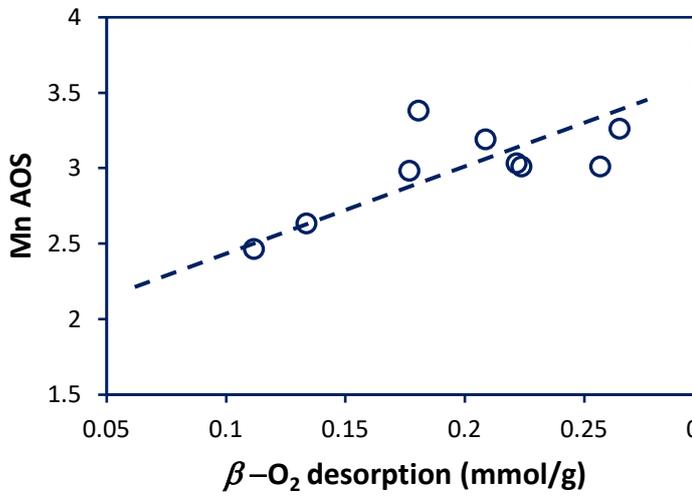
Fig. 6.18(B). Plot of the Mn AOS vs the desorbed β-O$_2$ species from O$_2$-TPD measurements.
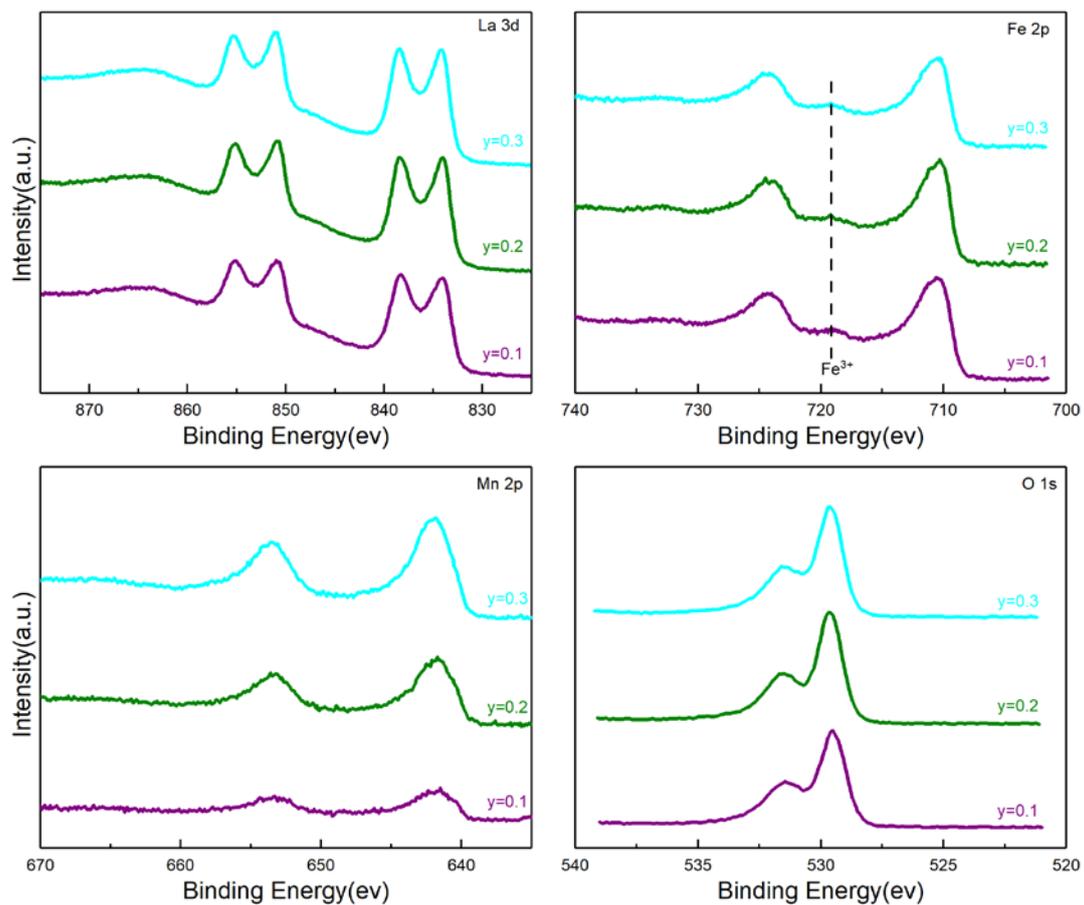
Fig. 6.19. Characteristic La 3d, Fe 2p, Mn 2p and O 1s photopeaks for $LaFe_{1-y}Mn_yO_3$: purple: y = 0.1; olive: y = 0.2; cyan: y =0.3.
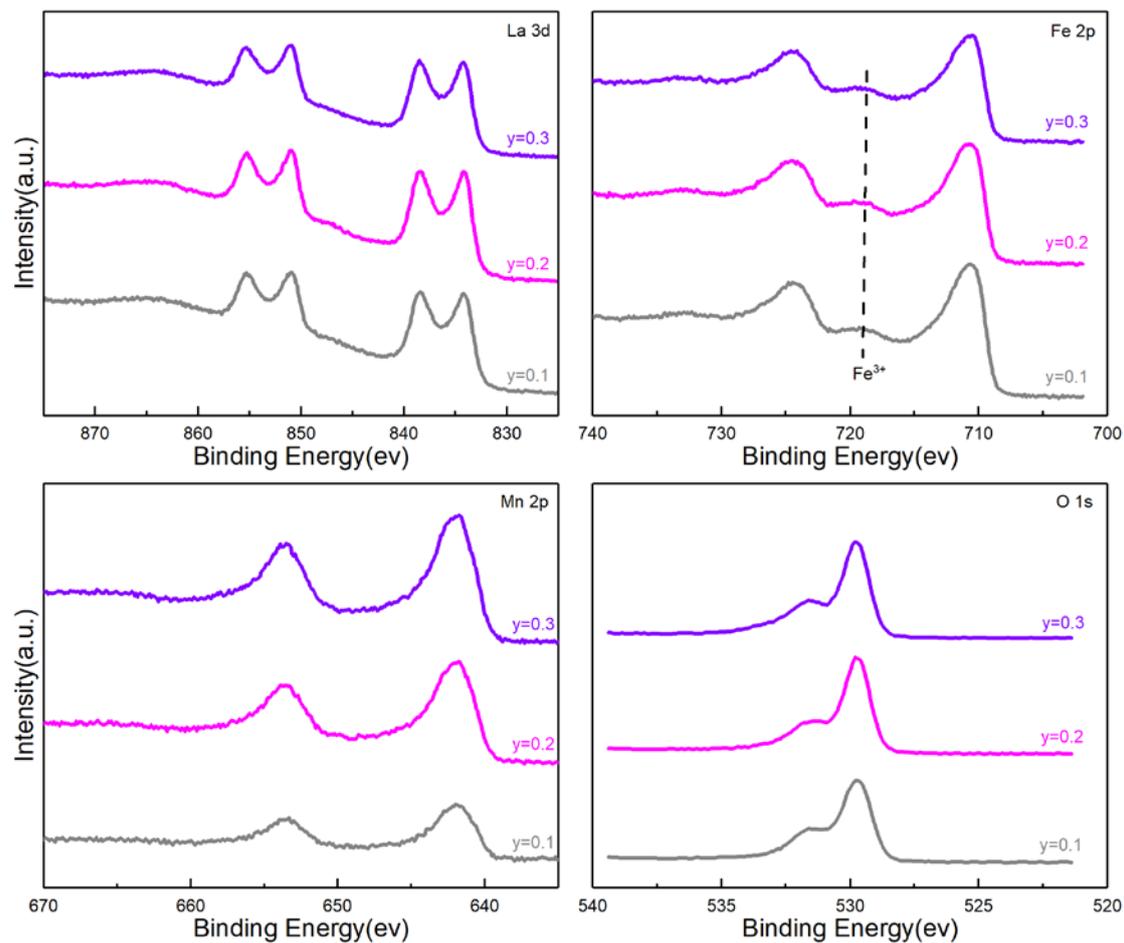
Fig. 6.20. Characteristic La 3d, Fe 2p, Mn 2p and O 1s photopeaks for $La_{0.7}Fe_{1-y}Mn_yO_3$: grey: y = 0.1; magenta: y = 0.2; violet: y = 0.3.
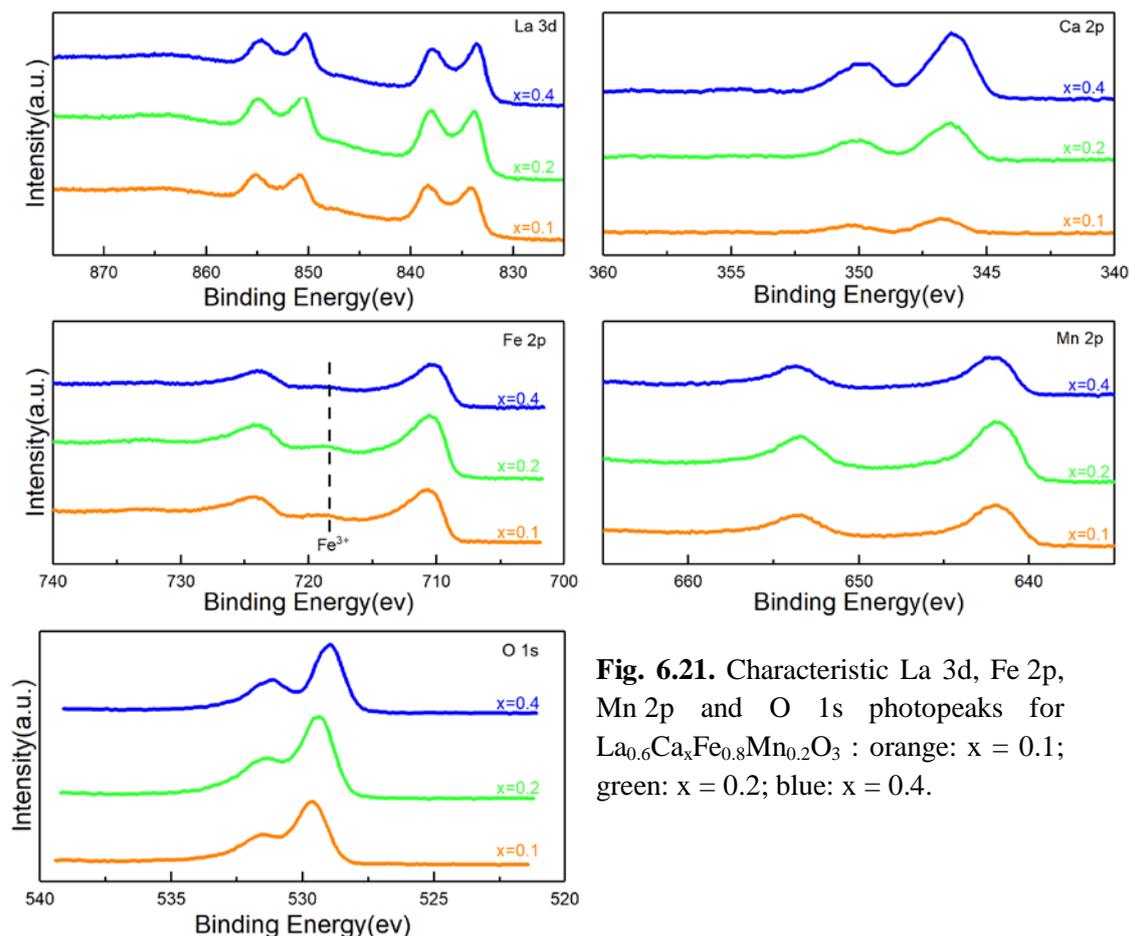
Fig. 6.21. Characteristic La 3d, Fe 2p, Mn 2p and O 1s photopeaks for $La_{0.6}Ca_xFe_{0.8}Mn_{0.2}O_3$: orange: x = 0.1; green: x = 0.2; blue: x = 0.4.

Table 6.10. Surface atomic composition calculated from XPS analysis

Catalyst	Surface atomic composition (%)						Atomic ratio		
	La	Ca	Fe	Mn	O	C	Ca/La	Mn/Fe	A/B
$LaFeO_3$	13.37	-	9.99	-	40.56	36.08	-	-	1.34
$La_{0.7}FeO_3$	9.17	-	19.12	-	39.75	31.96	-	-	0.48
$LaMnO_3$	12.50	-	-	9.27	42.51	35.72	-	-	1.35
$LaFe_{0.9}Mn_{0.1}O_3$	14.41	-	6.36	1.04	44.31	33.88	-	0.16	1.95
$LaFe_{0.8}Mn_{0.2}O_3$	13.63	-	5.35	2.01	42.91	36.10	-	0.38	1.85
$LaFe_{0.7}Mn_{0.3}O_3$	14.62	-	5.21	3.34	45.61	31.22	-	0.64	1.71
$La_{0.7}Fe_{0.9}Mn_{0.1}O_3$	8.58	-	11.09	1.77	41.41	37.14	-	0.16	0.67
$La_{0.7}Fe_{0.8}Mn_{0.2}O_3$	9.21	-	10.43	3.39	43.02	33.94	-	0.32	0.67
$La_{0.7}Fe_{0.7}Mn_{0.3}O_3$	7.89	-	8.16	3.55	40.45	39.94	-	0.44	0.67
$La_{0.6}Ca_{0.1}Fe_{0.8}Mn_{0.2}O_3$	7.06	1.24	9.79	3.09	40.77	38.05	0.18	0.32	0.64
$La_{0.6}Ca_{0.2}Fe_{0.8}Mn_{0.2}O_3$	6.96	2.12	8.56	3.64	44.06	34.66	0.31	0.43	0.74
$La_{0.6}Ca_{0.4}Fe_{0.8}Mn_{0.2}O_3$	7.75	5.28	7.30	2.96	43.04	33.66	0.68	0.41	1.27

Finally, the comparison of semi-quantitative analysis, especially the surface atomic Mn/Fe and A/B ratio with the corresponding relative compositions from elemental analysis (see Table 6.1.) reveals a relative good agreement on the Mn/Fe ratio. This observation seems in good agreement with XRD, SEM-EDS which did not evidence significant segregation processes. On the other hand some deviations appear by examining the A/B ratio which clearly indicates a significant lanthanum surface enrichment on stoichiometric composition. Interestingly, a good convergence is observed by comparing A/B ratios from XPS and ICP analysis.

6.3. Evaluation of the catalytic properties

6.3.1. Oxidative properties

The same experimental protocol was implemented for the characterization of manganite based perovskites. After heating in air at 600°C, four successive temperature programmed reaction experiments were performed in stoichiometric (STO1), lean, rich and stoichiometric (STO2). The investigation of catalytic performances was restricted to stoichiometric and none stoichiometric calcium-doped manganite perovskites in comparison to La$_{0.7}$Fe$_{0.8}$Mn$_{0.2}$O$_3$, La$_{0.7}$FeO$_3$ and LaFeO$_3$ with the aim to understand the role played by the mixed valance Fe^{4+}/Fe^{3+} and Mn^{4+}/Mn^{2+}. The comparison between STO1 and STO2 performance can illustrate possible deviation that could be related to surface changes as previously mentioned. Conversion profiles for CO, propene and propane oxidation are reported in Fig. 6.22. Regarding the activity of those materials in NO reduction, Figs. 6.23., 6.24., 6.25. illustrate changes in conversion, selectivity and yield plotted against temperature respectively.

As observed for CO oxidation the conversion is delayed compared to Cu-doped perovskite (conversion starting above 300°C instead of 200°C on Cu-doped perovskites). On the other hand, this delay is observed neither for propene oxidation nor for propane oxidation. Such comparison emphasizes on Cu-doped perovskites the beneficial effect of reduced copper extra framework species as previously discussed. Hence, one can hypothesize that the catalytic properties of manganite based perovskite materials will be intimately related to their inherent structural properties in terms of accommodation of different oxidation state for manganese and related anionic vacancies through partial substitution of lanthanum by calcium.

Returning to Fig. 6.22., CO oxidation in stoichiometric atmosphere exhibited better activity when lanthanum content was reduced to 70 at.% (La$_{0.7}$FeO$_3$). Subsequent Mn doping showed improved performance with a significant gain in conversion illustrated from the estimation of light-off conversion, T$_{50}$, corresponding to the temperature at half conversion. As seen in Table 6.11 T$_{50}$ shifts from 395 to 360°C. On the other hand, no significant effect of calcium substitution is discernible irrespective of the richness. It is worthwhile to note that STO1 and STO2 curves underlines the same catalytic properties which suggests a rather high stability of the surface properties with no suspected segregation after lean/rich cycle. To summarize, these comparisons seem to demonstrate the cooperative effect of La-deficiency and Mn doping. For propene oxidation, the catalytic behavior totally differs from that observed for CO. The lowest light-off temperature was recorded in La$_{0.7}$Fe$_{0.8}$Mn$_{0.2}$O$_3$ (T$_{50}$ = 405°C in STO1 and T$_{50}$ = 415°C in STO2). A progressive increase in calcium induces a loss of conversion in comparison with La$_{0.7}$Fe$_{0.8}$Mn$_{0.2}$O$_3$ and a lower stability as illustrated from STO2 curves as revealed by the low level of conversion on La$_{0.6}$Ca$_{0.1}$Fe$_{0.8}$Mn$_{0.2}$O$_3$. Neither La-deficiency nor Ca doping had obvious influence on propane oxidation activity, which may be ascribed to the high bond enthalpy of C-H single bond (413 kJ mol^{-1} at 25°C).
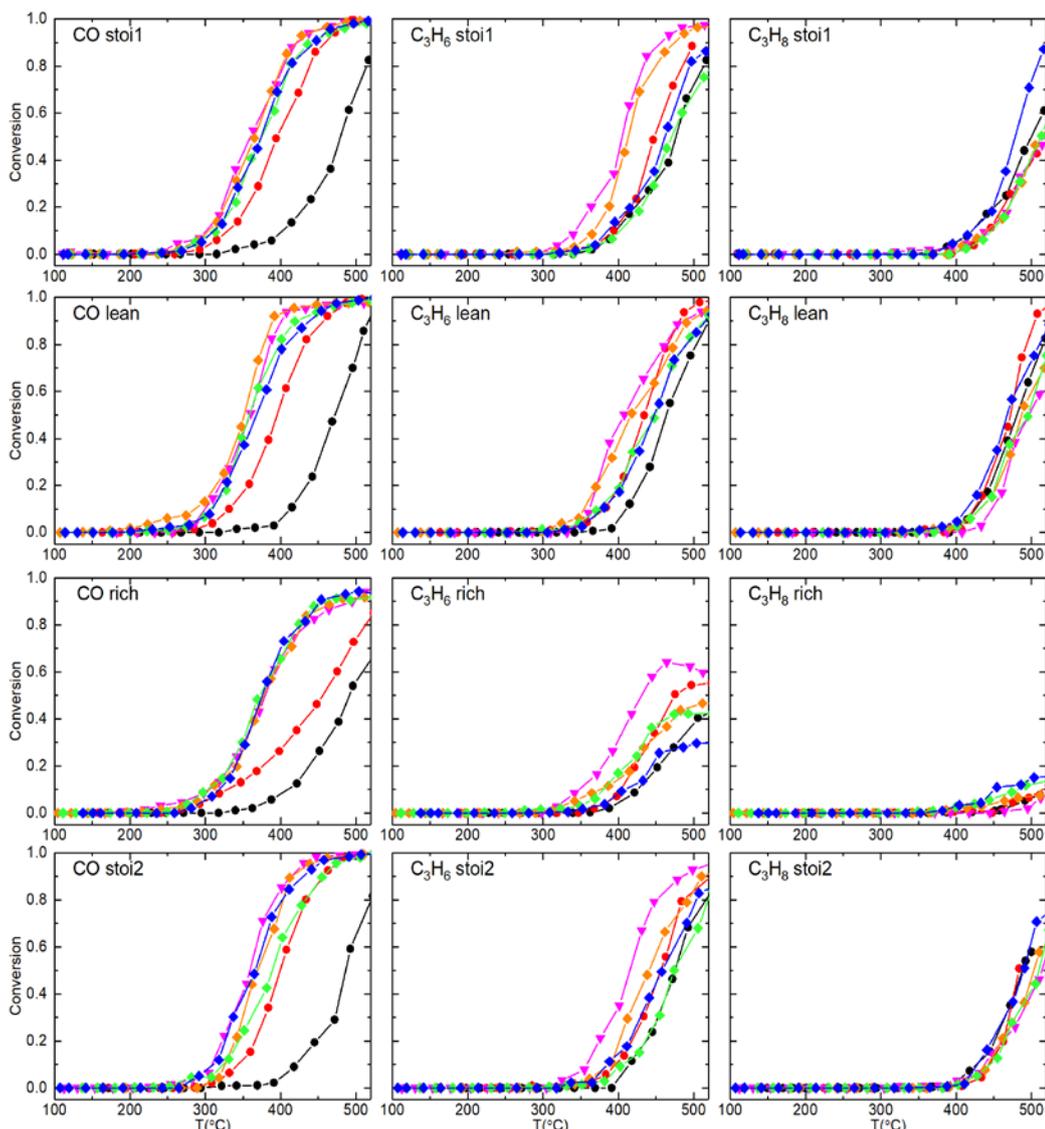
Fig. 6.22. Catalytic oxidation performance of iron-based perovskite solid ABO_3 doped with calcium and manganese (A=La, Ca; B= Fe, Mn) black circle: $LaFeO_3$(●); red circle: $La_{0.7}FeO_3$(●); magenta downward triangle: $La_{0.7}Fe_{0.8}Mn_{0.2}O_3$(▼); orange diamond: $La_{0.6}Ca_{0.1}Fe_{0.8}Mn_{0.2}O_3$(◆); green diamond: $La_{0.6}Ca_{0.2}Fe_{0.8}Mn_{0.2}O_3$(◆); blue diamond: $La_{0.6}Ca_{0.4}Fe_{0.8}Mn_{0.2}O_3$(◆).

Table 6.11. Light-off temperature (T_{50}) of iron-based perovskite solid ABO_3

| Catalyst | Light-off temperature T_{50} (°C) | | | | | |
| | STO1 | | | STO2 | | |
	CO	C_3H_6	C_3H_8	CO	C_3H_6	C_3H_8
$LaFeO_3$	480	477	500	487	475	488
$La_{0.7}FeO_3$	395	448	>520	399	456	483
$La_{0.7}Fe_{0.8}Mn_{0.2}O_3$	360	405	518	359	415	514
$La_{0.6}Ca_{0.1}Fe_{0.8}Mn_{0.2}O_3$	366	413	513	369	441	503
$La_{0.6}Ca_{0.2}Fe_{0.8}Mn_{.2}O_3$	375	471	513	388	475	510
$La_{0.6}Ca_{0.4}Fe_{0.8}Mn_{0.2}O_3$	375	462	479	366	458	490

6.3.2. Kinetics exploitation of TPR conversion curves for CO and propene oxidation

Kinetic exploitation was done based on Temperature-Programmed CO and propene conversions essentially in stoichiometric conditions. This analysis was restricted to Ca-doped perovskites and $La_{0.7}Fe_{0.8}Mn_{0.2}O_3$ in comparison with benchmark $LaFeO_3$ and $La_{0.7}FeO_3$ catalysts. Similarly, the mass balance for a plug flow reactor has been taken into account and a first order kinetics has been assumed in agreement with earlier investigations[A. Schön 2015; J.L. Hueso 2009; G. Parravano 1953]. The estimates of the specific and normalized reaction rates at 320°C and at 375°C for CO and propene oxidation are reported in Tables 6.12. and 6.13. The pre-exponential factor and the apparent activation energy values have been also calculated from the Arrhenius plots ln k vs. the reciprocal temperature (not shown). These calculations took into account conversions lower than 40% from STO1 and STO2 experiments. The order of magnitude of E_{app} values shows that external mass transfer diffusion phenomena should not be prevalent. According to a weak internal porosity, intragranular diffusion should not occur significantly. Kinetic data from STO1 and STO2 conversion curves are reported in Tables 6.12. and 6.13. By examining, these data, different features appear in comparison with those observed on Ca-and Cu-substituted samples. As earlier mentioned, Manganite based perovskites are much less active for CO oxidation. On the other hand, same order of magnitude for the rate of propene oxidation from STO1 and STOI2 are observed. Such differences earlier explained by copper ex solution emphasize the fact that extra framework manganese oxidic species are much less active and/or should not form significantly. It is also remarkable that no significant deviation from STO1 to STO2 experiments is discernible with comparable rate values and also slight variation on the apparent activation energy values. As a consequence, those data can be discussed globally emphasizing the fact that these samples could be more stable than those previously evaluated on the Ca- and Cu-substituted perovskites. Clearly the catalytic activity poorly depends on the specific surface area but mainly on the surface composition. As seen, La-deficiency ($La_{0.7}FeO_3$) and subsequent manganese substitution have a beneficial effect on the reaction rate for CO and propene oxidation which is related to a lessening of apparent activation energy more distinctly for CO oxidation. Regarding Ca-substituted samples, a slight detrimental effect of Ca is noticeable which seems to alter more significantly propene oxidation.

Table 6.12. Rate and kinetic parameters related to CO oxidation on subituted perovskite samples

Catalyst	SSA ($m^2\,g^{-1}$)	STO1					STO2			
		$r_{specific}$ ($mol\,s^{-1}\,g^{-1}$)[a]	Normalized rate ($mol\,s^{-1}\,m^{-2}$)[a]	A ($m^3\,s^{-1}\,g^{-1}$)	E_{app} ($kj\,mol^{-1}$)	$r_{specific}$ ($mol\,s^{-1}\,g^{-1}$)[a]	Normalized rate ($mol\,s^{-1}\,m^{-2}$)[a]	A ($m^3\,s^{-1}\,g^{-1}$)	E_{app} ($kj\,mol^{-1}$)
$LaFeO_3$	15.5	1.00E-08	6.47E-10	3.56E+03	121.4	1.20E-08	7.76E-10	2.89E+03	162.4
$La_{0.7}FeO_3$	35.5	3.35E-07	9.44E-09	3.32E+03	107.9	1.84E-07	5.17E-09	4.30E+04	123.3
$La_{0.7}Fe_{0.8}Mn_{0.2}O_3$	31.5	7.77E-07	2.47E-08	2.01E+03	99.1	7.78E-07	2.47E-08	3.59E+03	102.4
$La_{0.6}Ca_{0.1}Fe_{0.8}Mn_{0.2}O_3$	32.5	7.24E-07	2.23E-08	2.97E+03	102.2	2.71E-07	8.35E-09	3.16E+03	104.3
$La_{0.6}Ca_{0.2}Fe_{0.8}Mn_{0.2}O_3$	32.6	5.55E-07	1.70E-08	2.20E+03	102.1	3.97E-07	1.22E-08	3.33E+03	106.6
$La_{0.6}Ca_{0.4}Fe_{0.8}Mn_{0.2}O_3$	31.8	5.48E-07	1.72E-08	8.22E+03	108.9	5.57E-07	1.75E-08	2.90E+03	102.6

a calculated at T = 320°C

Note: A pre-exponential factor and E_{app} apparent activation energy in agreement with $k = A\,exp(-E_{app}/RT)$

Table 6.13. Rate and kinetic parameters related to C_3H_6 oxidation on susbituted perovskite samples

Catalyst	SSA $(m^2\,g^{-1})$	STO1					STO2			
		$r_{specific}$ $(mol\,s_{-1}\,g_{-1})^a$	Normalized rate $(mol\,s^{-1}\,m^{-2})^a$	A $(m^3\,s^{-1}g^{-1})$	E_{app} $(kj\,mol^{-1})$	$r_{specific}$ $(mol\,s^{-1}\,g^{-1})^a$	Normalized rate $(mol\,s^{-1}\,m^{-2})^a$	A $(m^3\,s^{-1}g^{-1})$	E_{app} $(kj\,mol^{-1})$
$LaFeO_3$	15.5	1.07E-08	6.88E-10	7.11E+03	125	8.26E-09	5.33E-10	1.24E+04	129.6
$La_{0.7}FeO_3$	35.5	1.73E-08	4.88E-10	7.53E+03	122.6	1.27E-08	3.57E-10	4.50E+04	134
$La_{0.7}Fe_{0.8}Mn_{0.2}O_3$	31.5	6.70E-08	2.13E-09	1.76E+03	106.7	5.56E-08	1.76E-09	8.92E+03	117.1
$La_{0.6}Ca_{0.1}Fe_{0.8}Mn_{0.2}O_3$	32.5	3.95E-08	1.22E-09	6.60E+06	154.6	2.04E-08	6.28E-10	1.72E+05	139
$La_{0.6}Ca_{0.2}Fe_{0.8}Mn_{0.2}O_3$	32.6	1.28E-08	3.92E-10	6.42E+04	136	7.71E-09	2.36E-10	4.16E+03	123
$La_{0.6}Ca_{0.4}Fe_{0.8}Mn_{0.2}O_3$	31.8	1.79E-08	5.62E-10	1.95E+03	115.4	9.97E-09	3.13E-10	4.05E+05	145.4

a calculated at T = 375°C

Note: A preexponential factor and E_{app} apparent activation energy in agreement with k = A exp(-E_{app}/RT)

6.3.3. Reductive properties

Regarding NO reduction, it is remarkable that substituted manganites exhibit higher catalytic properties than that reported on Cu-doped perovskite in Chapter V. It is particularly true in stoichiometric conditions with maximum conversion reaching ~30% on $La_{0.7}Fe_{0.8}Mn_{0.2}O_3$ and $La_{0.6}Ca_{0.1}Fe_{0.8}Mn_{0.2}O_3$ whereas a lack of NO conversion appeared on Cu-doped samples. As exemplified, these two samples preserve a low activity in NO reduction in lean conditions. At a first glance this observation suggests that the most selective reducing agent could be propene but as CO conversion takes place in the same range of temperature one cannot totally rule out the participation of the NO-CO reaction. Now, regarding Fig. 6.24., both catalysts exhibit the same selectivity behavior during STO1 and STO2 experiment: At low temperature where NO conversion remained low N_2O forms predominantly and then diminishes at the expense of nitrogen with a rise in temperature. Let us note that the absence of optimum in N_2O production curve could reflect mainly the occurrence of concurrent reaction pathways for N_2 and N_2O production with a minor contribution of sequential reduction of N_2O to N_2. A different behavior is noticeable in rich conditions because ammonia extensively forms above 425°C. It is also remarkable that the conversion curves on $La_{0.7}Fe_{0.8}Mn_{0.2}O_3$, $La_{0.6}Ca_{0.1}Fe_{0.8}Mn_{0.2}O_3$, and $La_{0.6}Ca_{0.2}Fe_{0.8}Mn_{0.2}O_3$ are superimposed underlining comparable properties towards NO reduction. However, some divergences appear at increasing temperature with $La_{0.7}Fe_{0.8}Mn_{0.2}O_3$ exhibiting the highest performances in NO conversion but also the poorest selectivity associated to extensive production of ammonia.

Fig. 6.23. Catalytic reduction performance of iron-based perovskite solid ABO_3 doped with calcium and manganese (A=La, Ca; B= Fe, Mn) black circle: $LaFeO_3(\bullet)$; red circle: $La_{0.7}FeO_3(\bullet)$;

magenta downward triangle: $La_{0.7}Fe_{0.8}Mn_{0.2}O_3$(▼); orange diamond: $La_{0.6}Ca_{0.1}Fe_{0.8}Mn_{0.2}O_3$(◆);
green diamond: $La_{0.6}Ca_{0.2}Fe_{0.8}Mn_{0.2}O_3$(◆); blue diamond: $La_{0.6}Ca_{0.4}Fe_{0.8}Mn_{0.2}O_3$(◆).

Fig. 6.24. Selectivity for $La_{0.7}Fe_{0.8}Mn_{0.2}O_3$ (magenta) and $La_{0.6}Ca_{0.1}Fe_{0.8}Mn_{0.2}O_3$ (orange) in stoi1, stoi2 and rich conditions. Magenta solid line solid square $La_{0.7}Fe_{0.8}Mn_{0.2}O_3$ N_2 selectivity (■);Magenta dash line hollow square $La_{0.7}Fe_{0.8}Mn_{0.2}O_3$ N_2O selectivity(□); Magenta dot line big semi-solid square $La_{0.7}Fe_{0.8}Mn_{0.2}O_3$ NH_3 selectivity (◧); Orange solid line solid circle $La_{0.6}Ca_{0.1}Fe_{0.8}Mn_{0.2}O_3$ N_2 selectivity(●); Orange dash line hollow circle $La_{0.6}Ca_{0.1}Fe_{0.8}Mn_{0.2}O_3$ N_2O selectivity(○); Orange dot line big semi-solid circle $La_{0.6}Ca_{0.1}Fe_{0.8}Mn_{0.2}O_3$ NH_3 selectivity(◑).
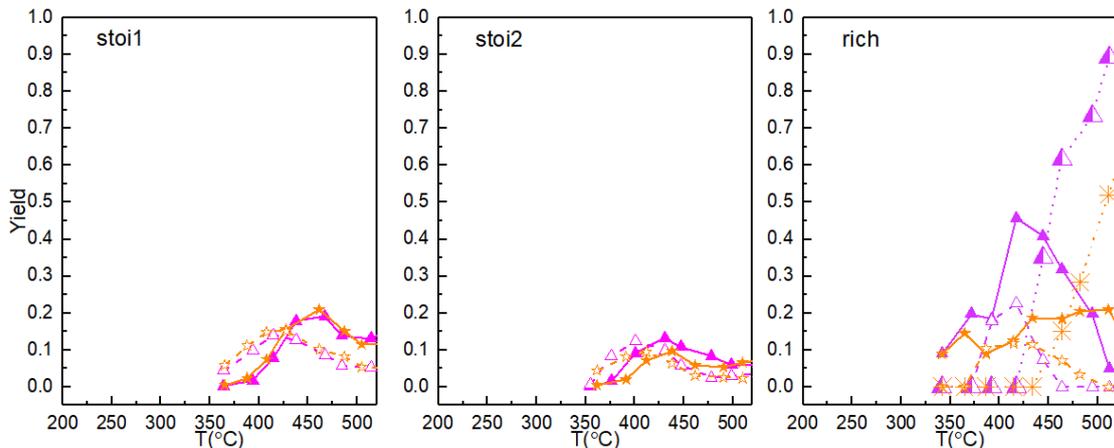
Fig. 6.25. Yield for $La_{0.7}Fe_{0.8}Mn_{0.2}O_3$ (magenta) and $La_{0.6}Ca_{0.1}Fe_{0.8}Mn_{0.2}O_3$ (orange) in stoi1, stoi2 and rich conditions. Magenta solid line solid triangle $La_{0.7}Fe_{0.8}Mn_{0.2}O_3$ N_2 yield(▲); Magenta dash line hollow triangle $La_{0.7}Fe_{0.8}Mn_{0.2}O_3$ N_2O yield (△) ; Magenta dot line big semi-solid triangle $La_{0.7}Fe_{0.8}Mn_{0.2}O_3$ NH_3 yield(▲); Orange solid line solid star $La_{0.6}Ca_{0.1}Fe_{0.8}Mn_{0.2}O_3$ N_2 yield(★); Orange dash line hollow star $La_{0.6}Ca_{0.1}Fe_{0.8}Mn_{0.2}O_3$ N_2O yield(☆); Orange dot line big asterisk $La_{0.6}Ca_{0.1}Fe_{0.8}Mn_{0.2}O_3$ NH_3 yield(✳).

Typically, NO_x reduction in lean conditions is believed to take place through either NO_x storage reduction (NSR) or Selective Catalytic Reduction (SCR). NSR catalysts comprise of precious metals, NO_x storage components and support metal oxides (i.e. $Pt/BaO/Al_2O_3$ as the most typical NSR catalyst) [Y. Li 2001;W.S. Epling 2006]. Detailed information about NSR

catalysts development and reaction mechanisms can be found in relevant references.[G. Liu 2011; S. Roy 2009; N. Takahashi 1996]. SCR process is generally assumed to occur with the presence of reducers. The most studied reducers are HC, CO, H$_2$. Depending on the operating temperature and reactive atmosphere, removal of NO can be achieved through several routes, including Hydrocarbon Selective Catalytic Reduction (HC-SCR), CO-NO reaction route or Hydrogen-NO reaction (H$_2$-SCR). HC-SCR route is mostly likely involved in NO reduction in lean conditions. Wei [M.D. Wei 2000] proposed that NO-reduction activity in the NO-C$_3$H$_8$-O$_2$ reaction system is primarily determined by the strength of B-O bond or redox property of B cations. It has been reported that C$_3$H$_8$ can act as effective reducer below 400°C in lanthanum manganite with Sr doping in A site but severe inhibitory effect of oxygen on NO reduction was also observed at temperature above 400°C [X. Wu 2004]. In our experiment, C$_3$H$_8$ and C$_3$H$_6$ are chosen as representative HC components. According to our observations, C$_3$H$_8$ can only be activated at high temperature (T > 400°C) regardless of reactive atmosphere. The low C$_3$H$_8$ conversion in lean condition suggested that C$_3$H$_8$ only had limited impact on NO reduction in reducing atmosphere. On the other hand, propene seems to be more efficient to reduce NO in lean or stoichiometric conditions as evidenced on La$_{0.7}$Fe$_{0.8}$Mn$_{0.2}$O$_3$ and La$_{0.6}$Ca$_{0.1}$Fe$_{0.8}$Mn$_{0.2}$O$_3$. Two reaction mechanisms have been put forward with regard to NO removal in lanthanum manganite suggesting that C$_3$H$_6$ would firstly be adsorbed on the electron-deficient location of active site to form an intermediate at low temperature according to Eq. 6-10.

$$(eq.\ 6\text{-}10)$$
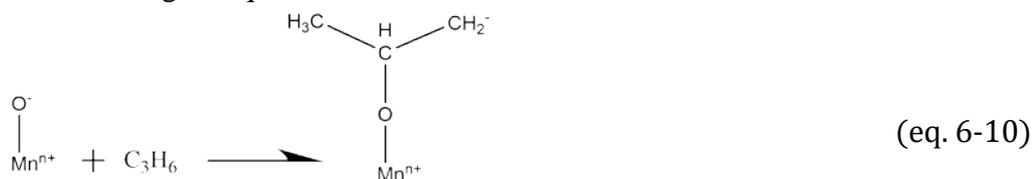
Then the intermediate would react with surrounding α-oxygen, producing CO$_2$ and H$_2$O accompanied by the reduction of Mn^{n+} in agreement with Eq. 6-11.

$$(eq.\ 6\text{-}11)$$
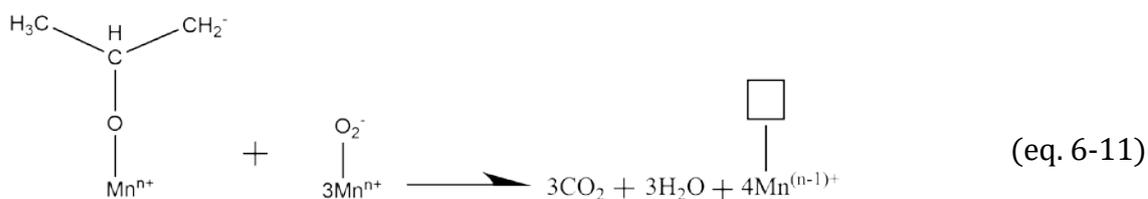
Different, reaction pathways can be proposed for NO conversion depending on the reaction temperature and the richness on the exhaust. Improved performance in NO reduction by propene have been reported on Cu-substituted LaMnO$_3$ perovskite in stoichiometric or slightly oxidizing conditions related to the formation of adsorbed ad-NO$_x$ intermediates through the oxidation of NO by adsorbed oxygen species on anionic vacancies according to Eq. 6-12. Hence, NO removal could occur through the intermediate formation of organonitrite species [R. Zhang 2006 b] then reduced by the reactive intermediate produced from Eq. 6-10, this latter step being rate-determining for the C$_3$H$_6$-SCR process. Hence, competitive reactions which would orient differently the selectivity in lean and stoichiometric

conditions could be governed by the concentration of α-oxygen. A detrimental effect on the rate of NO conversion is clearly observed in lean conditions with a rise in gaseous oxygen concentration because of an excessive surface concentration of active oxygen species which favors the preferential oxidation of propene [R. Zhang 2006 b].

(eq. 6-12)
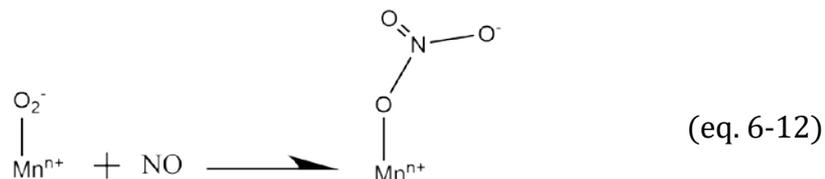
As mentioned, CO could also act as reducing agent leading to nitrogen (Eq. 6-13) but also N_2O (Eq. 6-14) from incomplete reduction. Let us note that both products can be also obtained with propene as reducing agent. Anyway, CO has been considered in the following reactions.

$$2NO + 2CO \rightarrow N_2 + 2CO_2 \qquad\qquad (eq. 6-13)$$

$$2NO + CO \rightarrow N_2O + CO_2 \qquad\qquad (eq. 6-14)$$

As observed in Fig. 6.24., N_2O production happens at lower temperature on $La_{0.7}Fe_{0.8}Mn_{0.2}O_3$ and $La_{0.7}Ca_{0.1}Fe_{0.8}Mn_{0.2}O_3$ which seems consistent with previous observations on $LaFeO_3$ and $LaMnO_3$. Voorhoeve et al. [R.J.H. Voorhoeve 1977; A.K. Ladavos 1992; Y. Teraoka 1996] suggested that N_2O production (step Eq. 6-21) could involve NO dissociation according to step (Eq. 6-15) which is generally assumed slow. Alternately, N_2O can form without prior NO dissociation according to Eq. (6-18) which could be prevalent at low temperature.

$$NO_{ads} \rightarrow N_{ads} + O_{ads} \qquad\qquad (eq. 6-15)$$
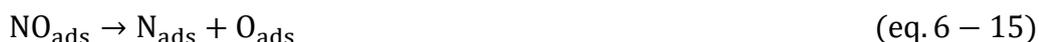
N_2 formation predominates at higher temperature (T > 250°C for $LaFeO_3$ and $LaMnO_3$) with the formation of adsorbed CO_2 as rate-determining step Eq. (6-16) [R.J.H. Voorhoeve 1977; A. K. Ladavos 1992; R. Zhang 2008]:

$$CO_{gas} + O_{ads} \rightarrow CO_{2\,ads} \qquad\qquad (eq. 6-16)$$

According to Ferri [D. Ferri 1998], H_2-SCR over perovskite oxides $LaAA'BO_{3+\delta}$ (A=La,Ce, Eu, Sr; B=Mn, Fe, Co, Ni) involves several elementary reactions:

$$NO + \square \quad\rightarrow\quad NO_{ads} \qquad\qquad (eq. 6-17)$$

$$NO_{ads} + NO \rightarrow N_2O + O_{ads} \qquad\qquad (eq. 6-18)$$

$$2NO_{ads} \quad\rightarrow\quad 2N_{ads} + O_2 \qquad\qquad (eq. 6-19)$$

$$2N_{ads} \quad\rightarrow\quad N_2 + + 2\square \tag{eq. 6-20}$$

$$NO_{ads} + N_{ads} \rightarrow N_2O + \square \tag{eq. 6-21}$$

$$2NO_{ads} \quad\rightarrow\quad 2N_2 + 2\square \tag{eq. 6-22}$$

$$CO + O_{ads} \quad\rightarrow\quad CO_2 + \square \tag{eq. 6-23}$$
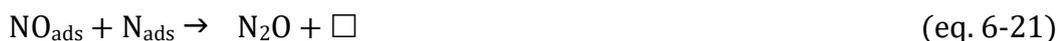
Eqs. (6-18) and (6-21) are predominant at low temperature (T < 275°C) where production of N_2O is facilitated, while Eq. (6-22) would be favored at high temperature (T > 275°C) with more active sites available and less NO_{ads} concentration. Let us note that the production of ammonia above 400°C suggest the involvement of step (Eq. 6-19) the resulting production of N_{ads} would be preferentially hydrogenated to form ammonia instead of N_2 through the recombination of two chemisorbed nitrogen atoms. The production of ammonia can be reasonably explained if a source of hydrogen is available. Previous finding [A. Schön 2018] shows that in rich conditions an extra production takes place assigned to reforming or partial oxidation of hydrocarbons.

6.3.4. Structure-reactivity relationship

Despite some similarities appear, it seems obvious that Ca- and Mn-substituted samples behave differently than Ca- and Cu-substituted catalysts. The same evolutions observed on kinetic parameters, i.e. specific, normalized rate and apparent activation energy on La-deficient, then subsequently substituted by manganese and calcium for CO and propene oxidation differ from previous observations on Cu-substituted perovskites. Regarding calcium incorporation, a slight inhibiting effect on the reaction rate is observable on $La_{0.6}Ca_xFe_{0.8}Mn_{0.2}O_3$ at increasing Ca content whereas optimal Ca composition was previously observed for propene oxidation on $La_{0.6}Ca_{0.2}Fe_{0.8}Mn_{0.2}O_3$. Probably the most significant observation is related to NO reduction in stoichiometric and more weakly in lean conditions which sharply develops in rich conditions according to the following sequence : $La_{0.7}Fe_{0.8}Mn_{0.2}O_3 > La_{0.6}Ca_{0.2}Fe_{0.8}Mn_{0.2}O_3 > La_{0.6}Ca_{0.1}Fe_{0.8}Mn_{0.2}O_3$.

As described, similar structural changes are induced by calcium insertion accompanied with still a sharp contraction effect of the cell volume which accentuates for stoichiometric compositions. This contraction effect seems in rather good agreement with the stabilization of Fe^{4+} detected from Mössbauer spectroscopy to compensate charge imbalance and corresponding to a lower ionic radius of 0.585 Å and/or the creation of oxygen vacancies [T. Caronna 2009]. Such effect could be also equally explained by the stabilization of Mn^{4+} instead of Mn^{3+} corresponding similarly to a reduction of cationic radius from 0.66 to 0.56 Å for Mn^{4+} as explained by Onrubia et al. [J.A. Onrubia 2017] who privileged this latter explanation in $La_{1-x}Sr_xMnO_3$ perovskites, instead of the formation of anionic vacancies, for the interpretation of higher catalytic properties in NO reduction found on Sr-doped perovskites. Clearly, our results differ from those obtained by these authors because, La^{3+} substitution by Ca^{2+} lead to lower rates in NO conversion, the most active sample being $La_{0.7}Fe_{0.8}Mn_{0.2}O_3$. It is worthwhile to note that the same ranking is also observation for CO and propene oxidation.

Quantitative comparisons between H_2 uptake from H_2-TPR experiments and O_2 desorption, reflecting oxygen mobility, is not evident. Interestingly, H_2 uptake diminishes at increasing Ca doping which could contradict a greater formation of Mn^{4+} at a first glance. In practice we demonstrate that calcium also blocks the formation of more reducible hematite. Regarding O_2-TPD experiments, O_2 desorption is promoted on La-deficient perovskites more prone to form anionic vacancies and occurs more readily on $La_{0.6}Ca_xFe_{0.8}Mn_{0.2}O_3$ with x = 0.1 and 0.2 which means more favorable conditions for stabilizing anionic vacancies at lower temperature. On the other hand, opposite trends are observed on the stoichiometric $La_{0.6}Ca_{0.4}Fe_{0.8}Mn_{0.2}O_3$ compositions. Nakamura et. al [T. Nakamura 1983] proposed on $La_{1-x}Sr_xCoO_{3-\delta}$ that increasing the perovskites reducibility decreases its ability to refill its oxygen vacancies which suggest that a poorer activity could be expected in case of intrafacial mechanism. Such a statement and all aforementioned observations cannot fully explain the higher activity observed on $La_{0.7}Fe_{0.8}Mn_{0.2}O_3$ for oxidation and reduction reaction which would suggest that the catalytic features mainly depend on the surface properties according to a suprafacial mechanism in stoichiometric and lean conditions and open the debate on the involvement of the mixed oxidation states Fe^{4+}/Fe^{3+} and Mn^{4+}/Mn^{3+}.

Tables 6.14. and 6.15. compares kinetic data with physicochemical properties. An important information arises from the comparison of $La_{0.7}FeO_3$ and $LaFeO_3$ which clearly demonstrates that the gain in catalytic properties observed on the former composition cannot be formally explained by the presence of Fe^{4+} in the bulk and/or at the surface which a fortiori rules out any participation of Fe(+IV) in Ca-doped samples. Subsequent, improvements on $La_{0.7}Fe_{0.8}Mn_{0.2}O_3$ both for oxidation and reduction reactions emphasize the prevalent role of high oxidation state of manganese corresponding to higher rates and lower activation barriers for CO and propene oxidation. Mössbauer spectroscopy did not detect for this sample the presence of Fe^{4+} which seems in relative agreement with previous investigation reported by Leontiou et al. [A.A. Leontiou 2003] who observed that the highest activity in NO reduction by CO was obtained on the perovskites having the lowest amount of Fe^{4+} and the highest amount of Fe^{3+}.

As shown Ca substitution leads to lower rates accompanied with an increase in E_{app} which reflects a detrimental effect of calcium. Interestingly, a significant decrease in the manganese average oxidation state is noticeable with a predominant stabilization of Mn(+III). Such a tendency could be responsible for the slight increase observed in Mn/Fe surface composition. Accordingly, a slight aggregation/segregation of small clusters of Mn_2O_3 or MnO could occur. Alternately, this evolution on the relative surface concentration of manganese could be related to lower hematite segregation due to the stabilizing effect of calcium maintaining iron in octahedral position of the perovskite stabilized as Fe^{4+}.

To summarize, A-site deficiency coupled to manganese doping in B site result in better reducibility of lanthanum ferrite that could create more oxygen vacancies essential for the adsorption of NO and O_2 in competition. In parallel, manganese stabilizes as Mn^{4+} which suggests a cooperation between iron and manganese to stabilize Mn^{4+} at the vicinity of anionic vacancies. Clearly, Ca doping has a detrimental impact because electronic imbalance would be more compensated by an increase of the oxidation state of Fe^{3+} to Fe^{4+} as observed from Mössbauer spectroscopy which could explain the smallest $O_{ads}/O_{lattice}$ ratio for the stoichiometric composition $La_{0.6}Ca_{0.4}Fe_{0.8}Mn_{0.2}O_3$. Hence, low anionic vacancies jointly with

low Mn AOS can reasonably explain the low catalytic performance of this catalyst both for oxidation and reduction reaction.

.

Table 6.14. Comparison between physicochemical and catalytic properties for CO oxidation

Catalysts	Unit cell ($\mathring{A}^3$)	Fe^{4+}/Fe^{3+}	H_2 uptake (mmol/g)	Mn AOS	$O_{ads}/O_{latt.}$	Mn/Fe	STO1			STO2		
							$r_{specific}$ (mol s^{-1} g^{-1})^a	Normalized rate (mol s^{-1} m^{-2})^a	E_{app} (kj mol^{-1})	$r_{specific}$ (mol s^{-1} g^{-1})^a	Normalized rate (mol s^{-1} m^{-2})^a	E_{app} (kj mol^{-1})
$LaFeO_3$	242.88	4.83	0		1.28		1.00E-08	6.47E-10	121.4	1.20E-08	7.76E-10	162.4
$La_{0.7}FeO_3$	242.44	0	1.45		1.61		3.35E-07	9.44E-09	107.9	1.84E-07	5.17E-09	123.3
$La_{0.7}Fe_{0.8}Mn_{0.2}O_3$	240.07	0	1.16	3.19	0.76	0.32	7.77E-07	2.47E-08	99.1	7.78E-07	2.47E-08	102.4
$La_{0.6}Ca_{0.1}Fe_{0.8}Mn_{0.2}O_3$	238.22	3.99	1.44	3.38	0.89	0.32	7.24E-07	2.23E-08	102.2	2.71E-07	8.35E-09	104.3
$La_{0.6}Ca_{0.2}Fe_{0.8}Mn_{0.2}O_3$	237.46	3.35	1.15	3.01	1.10	0.43	5.55E-07	1.70E-08	102.1	3.97E-07	1.22E-08	106.6
$La_{0.6}Ca_{0.4}Fe_{0.8}Mn_{0.2}O_3$	233.78	2.72	0.77	2.63	0.75	0.41	5.48E-07	1.72E-08	108.9	5.57E-07	1.75E-08	102.6

^{a} calculated at T = 320°C

Table 6.15. Comparison between physicochemical and catalytic properties for propene

Catalyst	Unit cell ($\mathring{A}^3$)	Fe^{4+}/Fe^{3+}	H_2 uptake (mmol/g)	Mn AOS	$O_{ads}/O_{latt.}$	Mn/Fe	STO1			STO2		
							$r_{specific}$ (mol s$_{-1}$ g$_{-1}$)^a	Normalized rate (mol s^{-1} m^{-2})^a	E_{app} (kj mol^{-1})	$r_{specific}$ (mol s^{-1} g^{-1})^a	Normalized rate (mol s^{-1} m^{-2})^a	E_{app} (kj mol^{-1})
$LaFeO_3$	242.88	4.83	0		1.28		1.07E-08	6.88E-10	125.0	8.26E-09	5.33E-10	129.6
$La_{0.7}FeO_3$	242.44	0	1.45		1.61		1.73E-08	4.88E-10	122.6	1.27E-08	3.57E-10	134.0
$La_{0.7}Fe_{0.8}Mn_{0.2}O_3$	240.07	0	1.16	3.19	0.76	0.32	6.70E-08	2.13E-09	106.7	5.56E-08	1.76E-09	117.1
$La_{0.6}Ca_{0.1}Fe_{0.8}Mn_{0.2}O_3$	238.22	3.99	1.44	3.38	0.89	0.32	3.95E-08	1.22E-09	154.6	2.04E-08	6.28E-10	139.0
$La_{0.6}Ca_{0.2}Fe_{0.8}Mn_{0.2}O_3$	237.46	3.35	1.15	3.01	1.10	0.43	1.28E-08	3.92E-10	136.0	7.71E-09	2.36E-10	123.0
$La_{0.6}Ca_{0.4}Fe_{0.8}Mn_{0.2}O_3$	233.78	2.72	0.77	2.63	0.75	0.41	1.79E-08	5.62E-10	115.4	9.97E-09	3.13E-10	145.4

^{a} calculated at T = 375°C

6.4. Conclusion

Lanthanum ferrite perovskite with orthorhombic structure was obtained by conventional citric method. Such crystal structure was maintained without remarkable phase transition when partial substitution in A or B site was carried out. Contrary to previous observation that Cu-doping gave rise to extra copper solution, Mn doping in B-site did not result in significant phase segregation irrespective of Mn doping degree or A-site composition. A reasonable explanation is that Fe-O-Mn complex has less tendency to dissociate in comparison with Fe-O-Cu complex due to the higher bond dissociation energy of the former beneficial for the stabilization of lattice manganese. Ca and Mn co-doping in A-site and B-site respectively led to the contraction of unit cell volume but perovskite structure remained unaffected. Mössbauer spectroscopy confirmed that stabilized Fe^{4+} is linked with partial substitution of La by Ca in A-site. However, more Ca doping in A-site exhibited a detrimental effect on the reducibility illustrated by H$_2$-TPR curve as well as on the oxygen mobility evidenced by O$_2$-TPD profiles. Mn-doping on lanthanum ferrite yielded higher specific surface area compared to Cu-doping. Average oxidation state (AOS) of doped Mn species depends heavily on A-site composition. It was noted that Mn^{4+}/Mn^{3+} ratio altered in response to the variation of chemical composition of the solid and that La-deficiency favored the increase of Mn AOS. A direct correlation between H$_2$ uptake and Mn AOS as well as between desorbed β-oxygen quantity and Mn AOS was found, suggesting that reducibility and oxygen mobility of the Mn-doped lanthanum ferrite perovskite is mainly governed by manganese species instead of iron species.

With regard to oxidative properties, Mn-doped lanthanum ferrite exhibited delayed light-off curves compared to Cu-doped candidates. The best formulation for both CO and C$_3$H$_6$ oxidation based on T$_{50}$ in STOI2 corresponds to La$_{0.7}$Fe$_{0.8}$Mn$_{0.2}$O$_3$. Minor deviation between STOI1 and STOI2 underlines the high stability of the surface properties with no obvious segregation after lean/rich cycle. But oxidation of propane is still characterized by a slow light-off which could hardly be observed below 380°C. Kinetic results showed that in comparison with Cu-doped perovskites, Mn-doping on lanthanum ferrite led to weakened activity for CO oxidation yet the reaction rate for C$_3$H$_6$ oxidation in STOI1 and STOI2 stayed in the same order of magnitude. In addition, oxidation activity of Mn-doped perovskites is mainly determined by surface composition instead of specific surface area. La-deficiency led to lessened apparent activation energy in favor of enhancement of CO and C$_3$H$_6$ oxidation. A slight inhibition of reaction rate is related with Ca-doped compositions, implying a detrimental influence of Ca on oxidation of CO and C$_3$H$_6$.

Mn-doped lanthanum ferrite manifested improved catalytic activity in terms of NO reduction compared to Cu-doped perovskites. It is apparent that a maximum NO conversion in stoichiometric conditions reached around 30% on La$_{0.7}$Fe$_{0.8}$Mn$_{0.2}$O$_3$ and La$_{0.6}$Ca$_{0.1}$Fe$_{0.8}$Mn$_{0.2}$O$_3$. A similar selectivity behavior of the aforementioned catalysts was observed: N$_2$O formed predominantly in low temperature (T<425°C) corresponding to low NO conversion, whereas great amount of N$_2$ was produced at the expense of N$_2$O at high temperature (T>425°C). It is believed that N$_2$O and N$_2$ production followed concurrent reaction pathways instead of a sequential reduction of N$_2$O to N$_2$. However, an evident discrepancy of NO conversion and selectivity in rich condition is noticeable: at low

temperature (T<350°C) $La_{0.7}Fe_{0.8}Mn_{0.2}O_3$, $La_{0.6}Ca_{0.1}Fe_{0.8}Mn_{0.2}O_3$, and $La_{0.6}Ca_{0.2}Fe_{0.8}Mn_{0.2}O_3$ showed comparable properties towards NO reduction. (Figs. 6.23. and 6.24.) Significant divergences appeared as temperature increased. $La_{0.7}Fe_{0.8}Mn_{0.2}O_3$ exhibited the highest performances for NO conversion but also the poorest selectivity related to substantial production of ammonia above 450°C. In contrast, two zones with different reaction mechanisms can be noticed on $La_{0.6}Ca_{0.2}Fe_{0.8}Mn_{0.2}O_3$: the first zone was identified in the temperature range of 300°C<T<480°C where anionic vacancies are assumed crucial for the adsorption of NO and oxygen in competition play a dominating role for NO reduction; the second zone above 480°C is associated with the transition of active sites from anionic vacancies to B-site cations (i.e. Fe, Mn) of perovskite involving the adsorption and dissociation of NO through multiple routes. $La_{0.6}Ca_{0.1}Fe_{0.8}Mn_{0.2}O_3$ displayed a delay in terms of NO reduction but higher N_2 selectivity at increasing temperature. The extra production of hydrogen stemming from partial oxidation or reforming reaction of hydrocarbons is assumed to be responsible for the extensive formation of ammonia in rich conditions at high temperature (T>450°C). (Fig. 6.24.) Moreover, it should not overlook the fact NO conversion in lean conditions remained limited and unsatisfactory on the aforementioned catalysts although a remarkable improvement of NO reduction was achieved in stoichiometric conditions.

To sum up, A-site deficiency combined with Mn-doping in B-site has been proven favorable for NO reduction especially in stoichiometric conditions. Ca-doping in A-site has a detrimental impact on NO reduction, which might be explained by the lower Mn AOS associated with faint reducibility and oxygen mobility as illustrated in Fig.6.18(A) and Fig.6.18(B). However, considering the non-PGM composition of these transition metal-based catalysts, the conspicuous enhancement of NO conversion especially under stoichiometric conditions seems quite encouraging as it offers a feasible solution for further optimization of these perovskite-type materials for the purpose of meeting stringent emission control standards.

Reference

[N.Y. Adonin 2016] N.Y. Adonin, S. Prikhod'ko, A.Y. Shabalin, I.P. Prosvirin, V.I. Zaikovskii, D.I. Kobubey, D.A. Zyuzin, V.N. Parmon, A.A. Monin, I.A. Bykova, P.O. Martynov, S.L. Rusakov, P.A. Storozhenko. Journal of Catalysis, 2016, 338:143-153.

[M. Alifanti 2009]M. Alifanti, G. Bueno, V. Parvulescu et AL. Catalysis Today, 2009, 143:309-314.

[F. Amano 2004] F. Amano, T. Tanaka, T. Funabiki. Journal of Molecular Catalysis A: Chemical, 2004, 221:89-95.

[P.S. Bagus 1973] P.S. Bagus, A.J. Freeman, F. Sasaki. Physical Review Letters, 1973, 30:850-853.

[P.S. Bagus 2004] P.S. Bagus, R. Broer, E.S. Ilton. Chemical Physics Letters, 2004, 394:150-154.

[P.S. Bagus 2008] P.S. Bagus, R. Broer, E.S. Ilton. Journal of Electron Spectroscopy and Related Phenomena, 2008, 165:46-49.

[D. Banerjee 1999] D. Banerjee, H.W. Nesbitt. Geochimica et Cosmochimica Acta, 1999, 63:3025-3038.

[D. Banerjee 2001] D. Banerjee, H.W. Nesbitt. Geochimica et Cosmochimica Acta, 2001, 65:1703-1714.

[B.P. Barbero 2006] B.P. Barbero, J. Andrade Gamboa, L.E. Cadus. Applied Catalysis B: Environmental, 2006, 65:21-30.

[T. Caronna 2009] T. Caronna, F. Fontana, I. Natali Sora, R. Pelosato. Materials Chemistry and Physics, 2009, 116:645-648.

[J. Chen 2013] J. Chen, M. Shen, X. Wang, G. Qi, J. Wang, W. Li. Applied Catalysis B: Environmental, 2013, 134–135:251-257.

[N. Choudhary 2018] Nisha Choudhary, Mukesh Kumar Verma, Narayan Dutt Sharma et al. Journal of Sol-Gel Science and Technology, 2018, 86:73-82.

[J. Choy 1994] Jin-Ho Choy, Jae-Hyun Park, Seung-Tae Hong, Dong-Kuk Kim. Journal of solid state chemistry, 1994, 111:370-379.

[J. Choy 1996] Jin-Ho Choy, Seung-Tae Hong, Kyoung-Shin Choi. Journal of the Chemical Society, Faraday Transactions, 1996, 92:1051-1059.

[P. Ciambelli 2001] P. Ciambelli, S. Cimino, L. Lisi et al. Applied Catalysis B: Environmental, 2001, 33:193-203.

[S. Cimino 2003] S. Cimino, L. Lisi, S. De Rossi, M. Faticanti, P. Porta. Applied Catalysis B: Environmental , 2003, 43: 397-406.

[W.P. Dow 1996] W.P. Dow,Y.P. Wang and T.J. Huang. Journal of Catalysis, 1996, 160:155-170.

[J. Emmerlich 2014] J. Emmerlich, B.M. Linke, D. Music, J.M. Schneider. Solid State Ionics, 2014, 255:108-112.

[W.S. Epling 2006] William S. Epling, Aleksey Yezerets, Neal W. Currier. Catalysis Letters, 2006, 110:143-148.

[A.K. Eriksson 2006] A.K. Eriksson, S.-G. Eriksson, S.A. Ivanov, C.S. Knee, J. Eriksen, H. Rundlöff , M. Tseggai. Materials Research Bulletin. 2006, 41:144-157.

[M. Fernandez-Garcia 1998] M. Fernandez-Garcia, I. Rodriguez-Ramos, P. Ferreira-Aparicio and A. Guerro-Ruiz. Journal of Catalysis, 1998, 178:253-263.

[D. Ferri 1998] Davide Ferri, Lucio Forni, Mark A. P Dekkers, Ben E Nieuwenhuys. Applied Catalysis B: Environmental, 1998, 16:339-345.

[N. Hamada 1997] Noriaki Hamada, Hideaki Sawada, Igor Solovyev, Kiyoyuki Terakura. Physica B: Condensed Matter, 1997, 237-238, Pages 11-13.

[R. Hammami 2009] R. Hammami, N. Harrouch Batis, H. Batis, C. Minot. Solid State Science, 2009, 11: 885-893.

[T. Hernandez 2001] T. Hernandez, F. Plazaola, T. Rojo , J.M. Barandiaran. Journal of Alloys and Compounds, 2001, 323-324:440-443.

[P.B. Himelfarb 1983] P.B. Himelfarb, F.E. Wawner, A. Bieser, S.N. Vines. Journal of catalysis, 1983, 83:469-471.

[J.L. Hueso 2009] J.L. Hueso, D. Martínez-Martínez, A. Caballero et al. Catalysis Communications, 2009, 10:1898-1902.

[M. Iwamoto 1989]Masakazu Iwamoto, Hidenori Yahiro, Yoshihiro Mine, Shuichi Kagawa. Chemistry Letters, 1989, 18:213-216.

[G.G. Jernigan 1994] G.G. Jernigan, G.A. Somorjai. Journal of Catalysis, 1994, 147: 567-577.

[M. Johnsson 2005] Mats Johnsson, Peter Lemmens. Crystallography and Chemistry of Perovskites. Cornell University. 2005, arXiv:cond-mat/0506606 [cond-mat.str-el]

[Y.S. Jun 2003] Y.S. Jun, S.T. Martin. Environmental Science & Technology, 2003, 37:2363-2370.

[J. Junta 1994] J. Junta, M.F. Hochella. Geochimica et Cosmochimica Acta, 1994, 58:4985-4999.

[S. Kaliaguine 2001] S. Kaliaguine, A. van Neste, V. Szabo, J.E. Gallot, M. Bassir, R. Muzychuk. Applied Catalysis A: General, 2001, 209, 345-358.

[S. Keav 2014] Sylvain Keav, Santhosh Kumar Matam, Davide Ferri, Anke Weidenkaff. Catalysts, 2014, 4:226-255.

[J.Y. Kim 2003] J.Y. Kim, J.A. Rodriguez, J.C. Hanson et al. Journal Of The American Chemical Society, 2003, 125(35):10684-10692.

[C.H. Kim 2010] C.H. Kim, G. Qi, K. Dahlberg, W. Li. Science, 2010, 327:1624-1627.

[B. Kucharczyk 2008] B. Kucharczyk, W. Tylus, Applied Catalysis A: General, 2008, 335:28-36.

[A.K. Ladavos 1992] A.K. Ladavos, P.J. Pomonis. Applied Catalysis B: Environmental, 1992, 1:101-116.

[A.A. Leontiou 2003] A.A. Leontiou, A.K. Ladavos, P.J. Pomonis. Applied Catalysis A: General, 2003, 241:133-141.

[Yuejin Li 2001] Yuejin Li, Stan Roth, Joe Dettling, Tilman Beutel. Topics in Catalysis, 2001, 16:139-144.

[P. Li 2017] Peixin Li, Runduo Zhanga, Ning Liu, Sébastien Royer. Applied Catalysis B: Environmental, 2017, 203:174-188.

[G. Liu 2011] Gang Liu, Pu-Xian Gao. Catalysis Science & Technology, 2011, 1:552-568.

[F.E. Lopez-Suarez 2009] F.E. Lopez-Suarez, S. Parres-Esclapez, A. Bueno-Lopez et al. Applied Catalysis B: Environmental, 2009, 93:82-89.

[N.A. Merino 2005] N.A. Merino, B.P. Barbero, P. Grange, L.E. Cadus. Journal of Catalysis, 2005, 231:232-244.

[H. Najjar 2013] Hend Najjar, Jean-François Lamonier, Olivier Mentré et al. Catalysis Science & Technology, 2013, 3:1002-1016.

[T. Nakamura 1983] T. Nakamura, M. Misono, Y. Yoneda. Journal of Catalysis, 1983, 83:151-159.

[H.W. Nesbitt 1998] H.W. Nesbitt, D. Banerjee, American Mineralogist, 1998, 83:305-315.

[Y. Nishihata 2002] Y. Nishihata, J. Mizuki, T. Akao, H. Tanaka, M. Uenishi, M. Kimura, T. Okamoto, N. Hamada. Nature, 2002, 418:164-167.

[Y. Noboru 1981] Yamazoe Noboru, Teraoka Yasutake, Seiyama Tetsuro. Chemistry Letters, 1981, 10, 1767-1770.

[J.A. Onrubia 2017] J.A. Onrubia, B. Pereda-Ayo, U. De-La-Torre, J.R. González-Velasco, Applied Catalysis B: Environmental, 2017, 213:198-210.

[L. Ortega-San Martin 2004] L. Ortega-San Martin, J.P. Chapman, E. Hernandez-Bocanegra et al. Journal of Physics: Condensed Matter, 2004, 16:3879-3888.

[G. Parravano 1953] G. Parravano. Journal of the American Chemical Society.1953, 75, 1497-1498.

[F. Patcas 2000] F. Patcas, F.C. Buciuman, J. Zsako. Thermochimica Acta, 2000, 360:71-76.

[G. Pecchi 2011] G. Pecchi, M.G. Jiliberto, A. Buljan, E.J. Delgado. Solid State Ionics, 2011, 187:27-32.

[S.D. Peter 2001] S.D. Peter, E. Garbowski, V. Perrichon, B. Pommier, M. Primet. Applied Catalysis A: General, 2001, 205:147-158.

[R. Pushpa 2013] R. Pushpa, D. Daniel, D.P. Butt. Solid State Ionics, 2013, 249-250:184-190.

[V. Roche 2010] V. Roche, R. Revel, P. Vernoux. Catalysis Communications, 2010, 11:1076-1080.

[J. Rodriguez 2003] J. Rodriguez, J. Kim, J. Hanson et al. Catalysis Letters, 2003,85:247-254.

[S. Rousseau 2009] S. Rousseau, S. Loridant, P. Delichere et al. Applied Catalysis B: Environmental, 2009, 88: 438-447.

[S. Roy 2009] Sounak Roy, Alfons Baiker. Chemical Reviews, 2009, 109 (9), 4054-4091.

[S. Royer 2005] S. Royer, F. Bérubé, S. Kaliaguine. Applied Catalysis A: General, 2005, 282: 273-284.

[S. Royer 2014] Sebastien Royer, Daniel Duprez, Fabien Can, Xavier Courtois, Catherine Batiot-Dupeyrat, Said Laassiri, Houshang Alamdari. Chemical Reviews, 2014, 114:10292-10368.

[A. Russell 2011] A. Russell, W.S. Epling, Catalysis Reviews, 2011, 53:337-423.

[N. Russo 2005] N. Russo, D. Fino, G. Saracco, V. Specchia. Journal of Catalysis, 2005, 229:459-469.

[A. Schön 2015] A. Schön, C. Dujardin, J.P. Dacquin, P. Granger. Catalysis Today, 2015, 258:543-548.

[A. Schön 2015] A. Schön. Development of alternative 3-way catalysts: Fe-based perovskites with low noble metal content. Thesis, 2015.

[A. Schön 2018] A. Schön, J.P. Dacquin, P. Granger, C. Dujardin. Applied Catalysis B: Environmental, 2018, 223:167-176.

[S.C. Sorenson 1974] S.C. Sorenson, J.A. Wronkiewicz, L.B. Sis, G.P. Wirtz. American Ceramic Society Bulletin, 1974, 53:446-449.

[R. Spinicci 2002] R. Spinicci, A. Delmastro, S. Ronchetti, A. Tofanari. Materials Chemistry and Physics, 2002, 78:393-399.

[N. Takahashi 1996]Naoki Takahashi, Hirofumi Shinjoh, Tomoko Iijima et al. Catalysis Today, 1996, 27:63-69.

[H. Tanaka 2003] H. Tanaka, N. Mizuno, M. Misono. Applied Catalysis A: General, 2003, 244:371-382.

[Y. Teraoka 1996] Yasutake Teraoka, Hiroshi Nii, Shuichi Kagawa, Kjell Jansson and Mats Nygren. Journal of Materials Chemistry, 1996, 6 (1):97-102.

[Z. Tian 2012] Z. Tian, K. Inagaki, Y. Morikawa. Current Applied Physics, 2012, 12:s105-s109.

[J.A.M. Van Roosmalen 1994] J.A.M. Van Roosmalen, E.H.P. Cordfunke, R.B. Helmholdt, H.W. Zandbergen, Journal of Solid State Chemistry, 1994, 110:100-105.

[R.J.H. Voorhoeve 1977] R.J.H.Voorhoeve, In Advanced Materials in Catalysis, J.J. Burton, R. L. Garten (Eds.) Academic Press, New York, 1977:129.

[M.D. Wei 2000] M.D. Wei, Y. Teraoka, S. Kagawa. Materials Research Bulletin, 2000, 35:521-530.

[Y. Wu 1989] Y. Wu, T. Yu, B. Dou, C. Wang, X. Xie, Z. Yu, S. Fan, L. Wang. Journal of Catalysis, 1989, 120, 88-107.

[X. Wu 2004] X. Wu, L. Xu, D. Weng, Catalysis Today, 2004, 90, 199-206.

[Y. Wu 2012] Y. Wu, X. Ni, C. Beaurain, C. Dujardin, P. Granger. Applied Catalysis B: Environmental, 2012, 125:149-157.

[J. Yang 2010] Jun Yang, Runsheng Li, Junyi Zhou et al. Journal of Alloys and Compounds, 2010, 508:301-308.

[W. Yang 2012] Wei Yang, Runduo Zhang, Biaohua Chen, Nicolas Bion, Daniel Duprez, Sébastien Royer. Journal of Catalysis, 2012, 295:45-58.

[Y. Yi 2019] Y. Yi, H. Liu, B. Chu, Z. Qin, L. Dong , H. He, C. Tang, M. Fan, Li Bin. Chemical Engineering Journal, 2019, 369:511-521.

[J.S. Yoon 2014] J.S. Yoon, Y-S Lim, B.H. Choi, H.J. Hwang. International Journal of Hydrogen Energy, 2014,39:7955-7962

[H. Zhan 2015] Haijuan Zhan, Feng Li, Chunling Xin, Ning Zhao, Fukui Xiao, Wei Wei, Yuhan Sun. Catalysis Letters, 2015, 145:1177-1185.

[R. Zhang 2006 a] R. Zhang, A. Villanueva, H. Alamdari, S. Kaliaguine. Applied Catalysis B: Environmental, 2006, 64:220-233.

[R. Zhang 2006 b] Runduo Zhang, Adrian Villanueva, Houshang Alamdari, Serge Kaliaguine. Applied Catalysis A: General, 2006, 307:85-97.

[R. Zhang 2006 c] R. Zhang, A. Villanueva, H. Alamdari, S. Kaliaguine. Journal of Molecular Catalysis A, 2006, 258: 22-34.

[R. Zhang 2008] Runduo Zhang, Houshang Alamdari, Serge Kaliaguine. Applied Catalysis A: General, 2008, 340:140-151.

[L. Zhang 2012] Lili Zhang, Yulun Nie, Chun Hu, Jiuhui Qu. Applied Catalysis B: Environmental, 2012, 125:418-424.

[J. Zhang 2015] Jingyi Zhang, Dongdong Tan, Qingjie Meng, Xiaole Weng, Zhongbiao Wu. Applied Catalysis B: Environmental, 2015, 172–173:18–26.

[J. Zhu 2009 a] J. Zhu, A. Thomas. Applied Catalysis B: Environmental, 2009, 92:225-233.

[J. Zhu 2009 b] J. Zhu, D. Xiao, J. Li, X. Yang. Catalysis Letters, 2009, 129:240-246.

PART C

PGM-doped Perovskite Catalysts: PGM loading combined with Ca and Cu substitution

Chapter VII. Palladium incorporation to stoichiometric and non-stoichiometric Ca and Cu doped La$_{1-x}$FeO$_{3\pm\delta}$

Chapter VIII. Rhodium incorporation to Stoichiometric and non-stoichiometric Ca and Cu doped La$_{1-x}$FeO$_{3\pm\delta}$

Foreword

Results obtained on doped ferrite perovskites showed relative good performances for CO and propene oxidation but exhibits low activity to transform NO to nitrogen. Only rich conditions allowed significant NO conversion accompanied with a significant production of undesired ammonia above 450°C. Such trend was recently reported through the comparison of perovskites of general formula AA'BB'O$_3$ with A=La, A'=Ca, Sr, Y, Ce; B = B' = Mn, Fe, Co, Ni) with a commercial bimetallic Pd-Rh three-way-catalyst. After calcination in mild condition, the residual performances were much lower than those obtained on the commercial benchmark system under simulated gasoline exhaust feed [K. Simmance 2019] showing that PGM-free perovskite structures cannot meet specific requirements for TWC applications.

In practice, the incorporation of low amount of precious metals is usually requested to reach acceptable level of NO$_x$ conversion near stoichiometric conditions. Numerous investigations already reported the beneficial effect of low loaded PGM three-way catalysts with also significant gain obtained on the rate of CO and propene oxidation [Y. Nishihata 2002; A. Schön 2018; A. Eyssler 2011]. Comparative investigations pointed out the importance of the strategy employed for the introduction of precious metals according to a classical wet impregnation or during the sol-gel synthesis. Based on this two different sequential or one pot synthesis different behavior can be obtained. Indeed in the former case precious metals are expected more accessible but less stable towards sintering while the opposite behavior is expected when this one is embedded in the perovskite lattice. Let us note that starting from impregnated samples, Eyssler et al. [A. Eyssler 2011] found it was possible to re-disperse and favor the incorporation of palladium in the perovskite lattice according to the calcination temperature. Accordingly more thermally stable Pd^{n+} species dissolved in the perovskite form at the expense of PdO-like particle recognized less resistant to deactivation during repeated lean/rich cycles. Similar strategy was also optimized through appropriate redox cycles to strengthen the interaction between PGM particles and the perovskite substrate [J.P. Dacquin 2010, 2011]. All these approaches are inspired of the so-called self-regenerative behavior of PGM-doped perovskite. This concept was earlier introduced by Nishihata et al. [Y. Nishihata 2002] starting with palladium embedded in the perovskite structure substituted in octahedral position. It was shown that reversible processes can take place under cycling conditions at high temperature leading to extraction of Pd^{2+} to form nano-sized metallic palladium species in rich conditions and then recovering their initial position after switching to lean conditions. This dynamic process was found to protect palladium to thermal sintering. This concept was earlier verified on Pt and Rh-based systems.

This part will be dedicated to the influence of palladium and rhodium incorporation on ferrite perovskite described in Chapter V. The protocol used for the evaluation of their catalytic properties should be relevant especially to check if reverse processes can take place during the successive stoichiometric (STO1)/lean/rich/stoichiometric (STO2). Even if the final temperature is moderate the examination of STO1 and STO2 performance will provide some insights into possible surface reconstructions modifying the degree of dispersion of palladium and rhodium.

Chapter VII. Palladium incorporation to stoichiometric and non-stoichiometric Ca and Cu doped La$_{1-x}$FeO$_{3\pm\delta}$

Particular attention will be paid to the incorporation of low amount of palladium onto perovskite substrates. A classical wet impregnation method was implemented according to the protocol earlier depicted in chapter III. Impregnated samples were systematically calcined in air at 400°C to decompose the precursor and redisperse PdO$_x$ species. As moderate calcination temperature was selected significant diffusion in the bulk structure is not expected. Hence, a preferential segregation of PdO-like species should occur at large extent. Elemental compositions from ICP analysis are reported in Table 7.1. showing slight deviations on most of the palladium composition except on Pd/La$_{0.7}$FeO$_3$ corresponding to a slightly underestimated Pd/(A+B) ratio. A good agreement is also observed on the Ca/La, Cu/Fe and A/B ratio compared to the theoretical values which seem to indicate an acceptable reproducibility in the deposition method as well as in the perovskite synthesis as previously pointed out.

The impact of palladium on the oxidation and reduction reaction has been compared to a benchmark Pd/Ce$_x$Zr$_{1-x}$O$_2$ TWC supplied by Johnson Matthey and described in Chapter IV. Conversion and rates will be discussed in light of bulk and surface physicochemical characterization with the aim to understand if palladium behaves independently or generate cooperative effects with the perovskite support which could originate synergistic effect on the rates on CO, C$_3$H$_6$ and NO conversion.

Table 7.1. Elemental analysis of 0.5 wt.% Pd-perovskite ABO$_{3\pm\delta}$ with A = La, Ca and B = Fe, Cu.

Catalysts	Atomic composition (%)					Ca/La	Cu/Fe	Pd/(A+B) ×10^{-3}	A/B
	La	Ca	Fe	Cu	Pd				
Pd/LaFeO$_3$	19.75	-	20.68	-	0.16	-	-	3.96	0.96
Pd/La$_{0.7}$FeO$_3$	17.21	-	25.09	-	0.10	-	-	2.36	0.69
Pd/LaFe$_{0.9}$Cu$_{0.1}$O$_3$	22.94	-	20.78	2.30	0.24	-	0.11	5.21	0.99
Pd/LaFe$_{0.8}$Cu$_{0.2}$O$_3$	19.83	-	16.13	4.01	0.20	-	0.25	5.00	0.98
Pd/LaFe$_{0.7}$Cu$_{0.3}$O$_3$	20.80	-	14.86	6.36	0.21	-	0.43	5.00	0.98
Pd/La$_{0.7}$Fe$_{0.9}$Cu$_{0.1}$O$_3$	19.45	-	25.27	2.77	0.18	-	0.11	3.79	0.69
Pd/La$_{0.7}$Fe$_{0.8}$Cu$_{0.2}$O$_3$	17.56	-	20.47	4.98	0.17	-	0.24	3.95	0.69
Pd/La$_{0.7}$Fe$_{0.7}$Cu$_{0.3}$O$_3$	19.66	-	20.07	8.18	0.17	-	0.41	3.55	0.70
Pd/La$_{0.6}$Ca$_{0.1}$Fe$_{0.8}$Cu$_{0.2}$O$_3$	13.29	2.02	17.70	4.57	0.13	0.15	0.26	3.46	0.69
Pd/La$_{0.6}$Ca$_{0.2}$Fe$_{0.8}$Cu$_{0.2}$O$_3$	12.52	4.01	16.93	4.26	0.19	0.32	0.25	5.04	0.78
Pd/La$_{0.6}$Ca$_{0.4}$Fe$_{0.8}$Cu$_{0.2}$O$_3$	13.27	8.66	18.36	4.45	0.20	0.65	0.24	4.47	0.96

First verification from XRD analysis did not reveal appreciable change on the structural properties. The typical orthorhombic structure is preserved, copper extra-framework species still persists irrespective of the perovskite composition, i.e. stoichiometric and none stoichiometric composition. On the other hand, no additional reflection was observed assigned to bulk detectable PdO_x species. Rietveld refinement calculation did not lead to additional comments as those already reported related to calcium addition which induces sharp contraction effects notable on the stoichiometric composition $La_{0.6}Ca_{0.4}Fe_{0.8}Cu_{0.2}O_3$. At this stage, no significant deviation on the cell volume is attributable to diffuse Pd^{2+} species inside the bulk structure of the perovskite. Nonetheless, the very low Pd loading makes any hypothetical conclusion unestablished.

As a matter of fact, the most significant effect is likely expected in terms of surface reducibility and mobility of oxygen species which can depend on the extent of palladium dispersion and different type of interactions with the perovskite structure and/or extra framework CuO species earlier identified. These different properties have been closely examined in the subsequent sub-chapters.

7.1. Reducibility

The same procedure was used than that earlier described consisting in heating the calcined samples in diluted hydrogen (5 vol.% H_2 in He) up to 1000°C. H_2-consumption profiles vs. temperature are reported in Fig. 7.1., 7.2. and 7.3. They have been compared with those previously obtained on bare perovskite materials.

As seen no additional reduction peak appears for $Pd/LaFeO_3$. As earlier found $LaFeO_3$ was found unreducible. A multi-step reduction process was recorded for $Pd/La_{0.7}FeO_3$, displaying a weak reduction process at 165°C and then a more intense and broader peak at 478°C. The lowest temperature reduction process (undetected on bare perovskites) could be attributed to the reduction of Pd^{2+} to Pd^0 in agreement with the value calculated for H/Pd ratio (see Table 7.2.) while the second reduction process is likely linked to the reduction of extra-lattice hematite as reported elsewhere in chapter V. It is noticeable that hematite reducibility was enhanced evidently by palladium deposition characterized by the downward shift of reduction peaks (compared to reduction peaks registered at 340°C and 541°C respectively for pure $La_{0.7}FeO_3$ perovskite). A marked low temperature reduction peak (below 100°C) was observed for Pd-impregnated $LaFe_{1-y}Cu_yO_3$ which could be assigned to the reduction of Pd^{2+} to Pd^0 which still matches with H/Pd ~2. It is also noticeable that a slight shift of the additional reduction processes taking place at higher temperature on $Pd/LaFe_{1-y}Cu_yO_3$ is moderate.
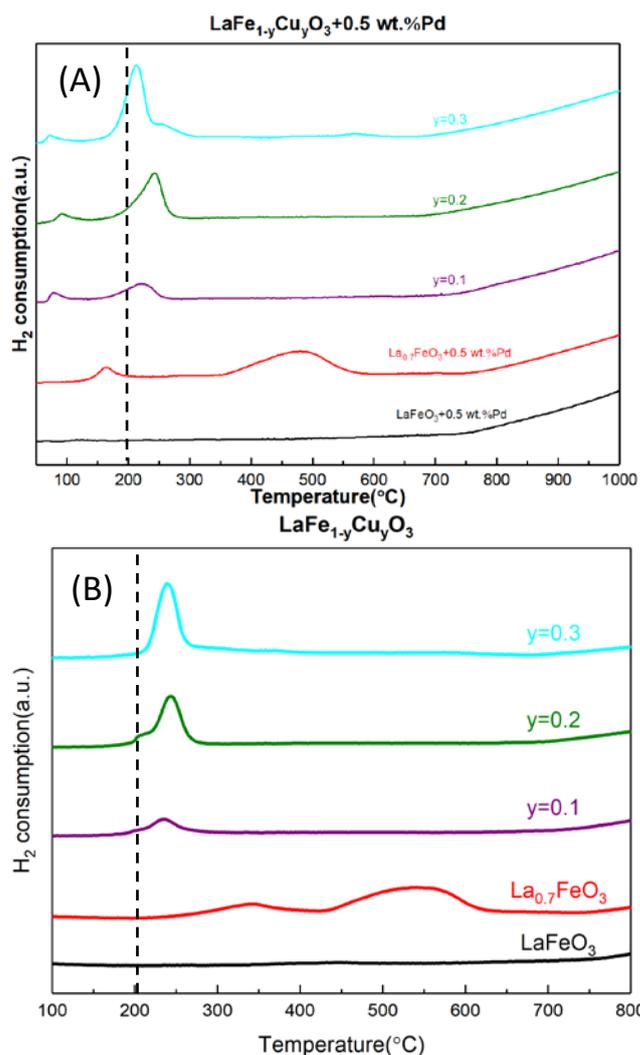
Fig. 7.1. H_2 consumption curves plotted against temperature for doped-Pd (A) and un-doped stoichiometric $LaFe_{1-y}Cu_yO_3$ (B) purple: y = 0.1; olive: y = 0.2; cyan: y = 0.3.

Similarly to stoichiometric compositions, Pd incorporation does not induce a much faster reduction of the La-deficient perovskite substrate (see Fig. 7.2.). Indeed, the H_2 uptake slightly vary likely within the margin of error and the shift observed on the low temperature reduction process near 200°C is moderately disturbed. In the particular case of the composition $LaFe_{0.9}Cu_{0.1}O_3$ a delay on the reduction process is even observed which could suggest weak interaction of metallic Pd species with the perovskite substrate limiting current enhancing effect due to hydrogen spill-over or a possible delay of their reduction thanks to a greater stabilization in case of weakly embedded Pd^{2+} species in the perovskite structure. Let us note that the weak reduction process below 100°C previously ascribed to the reduction of Pd^{2+} to metallic species has disappeared except on $La_{0.7}Fe_{0.8}Cu_{0.2}O_3$.
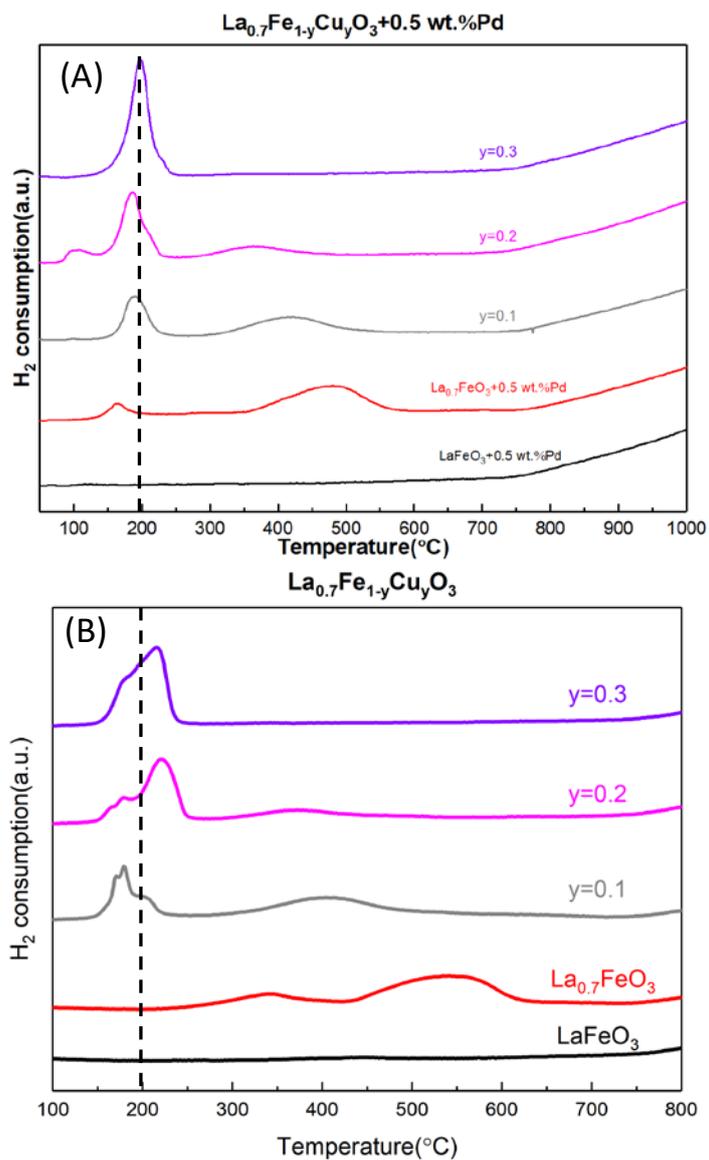
Fig. 7.2. H_2 consumption curves plotted against temperature for Pd-doped (A) and undoped La-deficient $La_{0.7}Fe_{1-y}Cu_yO_3$ (B) grey: y = 0.1; magenta: y = 0.2; violet: y = 0.3.
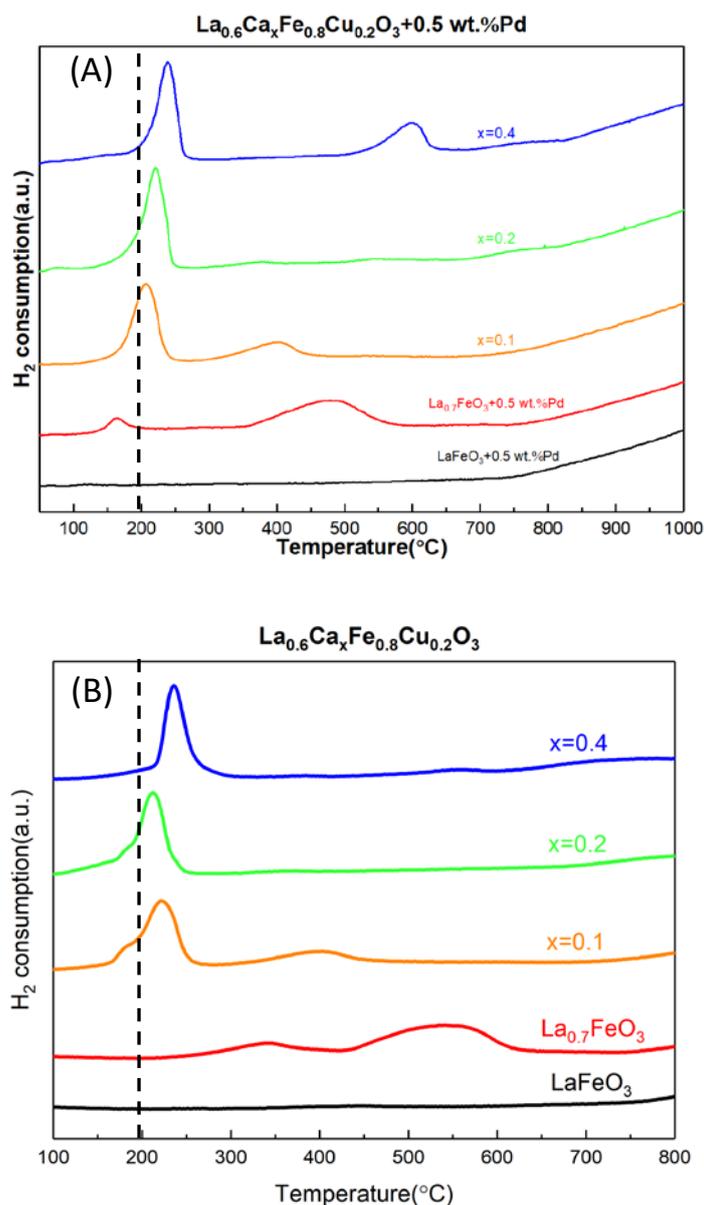
Fig. 7.3. H_2 consumption curves plotted against temperature for Pd-doped (A) and undoped La-deficient $La_{0.6}Ca_xFe_{0.8}Cu_{0.2}O_3$ (B) grey: y = 0.1; magenta: y = 0.2; violet: y = 0.3.

Fig. 7.3. illustrates H_2-TPR profiles recorded on $Pd/La_{0.6}Ca_xFe_{0.8}Cu_{0.2}O_3$ which still reproduce comparable observation except on $Pd/La_{0.6}Ca_{0.4}Fe_{0.8}Cu_{0.2}O_3$. As seen in Table 7.2., calcium and copper co-doping resulted in the greatest total hydrogen consumption amount and H/M ratio among all studied catalysts. On the other hand, the comparison of the H_2 consumption profiles does not reveal distinct changes at low temperature with no significant effect on the intense signal near 200°C. The lack of PdO reduction process below 100°C is still noticeable. Probably the most relevant observation is related to the emergence of a high reduction process near 600°C on the stoichiometric lanthanum composition. At this stage, it seems not easy to identify without ambiguity the origin of such reduction process. Nonetheless, one can hypothesize that specific interaction of metallic/oxidic Pd species with the perovskite structure could originate this extra-reduction process based on the comparison with the bare sample.

As a general trend, the reducibility of PdO_x clusters can be significantly altered by the nature of the support especially on reducible materials. For instance the reduction of PdO to metallic Pd particles was previously observed in the temperature range 60-90°C on Pd/Ce-Zr-O systems [B. Zhao 2010 a, 2010 b]. In addition, the reducibility of PdO particles can be also closely dependent on their particle size. Indeed, numerous investigations found that well-dispersed PdO reduces above 100°C whereas the reduction of larger PdO particles would occur for T≤ 50°C [H. Muraki 1989; G. Chen 1983; I. Halasz 1992]. Accordingly, the appearance of reduction peak near 80°C on $Pd/LaFe_{1-y}Cu_yO_3$ ascribed dispersed PdO_x species jointly with a slightly faster reduction of the perovskite would suggest a moderate metal-support interaction. In case of much more stronger interaction a significant delay would be expected which could suggest that the reduction of Cu^{2+} in the range 200-250°C could overlap the reduction of Pd^{2+} to metallic Pd^0. Accordingly, one can reasonably explain the total absence of shift to lower temperature of the overall reduction process especially on the stoichiometric composition $La_{0.6}Ca_{0.4}Fe_{0.8}Cu_{0.2}O_3$.

Table 7.2. Detailed H_2-TPR results for perovskites ABO_3+0.5 wt.%Pd (A = La, Ca; B = Fe, Cu)

Catalyst	H_2 total uptake (mmol g^{-1})[a]	H/Pd	H/M[b]	T_{max} reduction peaks (°C)		
				1st	2nd	3rd
$Pd/LaFeO_3$	0.002	-	0.072	-	127	-
$Pd/La_{0.7}FeO_3$	0.084	0.15	0.153	72	165	478.2
$Pd/LaFe_{0.9}Cu_{0.1}O_3$	0.329	1.87	1.445	98	224	-
$Pd/LaFe_{0.8}Cu_{0.2}O_3$	0.783	2.00	1.818	90	242	-
$Pd/LaFe_{0.7}Cu_{0.3}O_3$	1.215	1.92	1.896	73	213	566.2
$Pd/La_{0.7}Fe_{0.9}Cu_{0.1}O_3$	1.072	0.29	1.903	98	190	413.8
$Pd/La_{0.7}Fe_{0.8}Cu_{0.2}O_3$	1.241	2.65	1.695	98	187	362.7
$Pd/La_{0.7}Fe_{0.7}Cu_{0.3}O_3$	1.495	0.19	1.975	61	198	-
$Pd/La_{0.6}Ca_{0.1}Fe_{0.8}Cu_{0.2}O_3$	1.659	-	2.278	88	207	395.5
$Pd/La_{0.6}Ca_{0.2}Fe_{0.8}Cu_{0.2}O_3$	1.663	1.16	2.738	72	221	376.2
$Pd/La_{0.6}Ca_{0.4}Fe_{0.8}Cu_{0.2}O_3$	2.043	-	2.838	65	239	598.8

[a] total H_2 consumption was calculated taking into account the temperature range 50-700°C.
[b] M=Cu+Pd. Assuming H_2 consumption at T<300°C was ascribed to Pd(+II) and Cu(+II) species.
[c] on Pd undoped perovskite systems.

7.2. Oxygen mobility

As earlier discussed such experiments allow to differentiate surface labile oxygen species which desorbed at the lowest temperature and lattice oxygen species with desorption taking place at much higher temperature.

Chapter VII. Palladium incorporation to stoichiometric and non stoichiometric Ca and Cu doped $La_{1-x}FeO_{3\pm\delta}$

In general, the former oxygen species labeled α-O_2 is derived from the desorption of chemisorbed O_2^-, O^- species on surface oxygen vacancies [B. Levasseur 2009]. In the particular case on ferrite based perovskite subsequent desorption is accompanied by a reduction of the oxidation state of iron from +IV to +III according to Eqs. (7-1) and (7-2). This desorption process generally occurs below 700°C in the temperature range 400-700°C according to the composition of the perovskite. Iron insertion can delay this desorption process taking place in the upper temperature range compared to copper insertion.

$$\text{eq. (7-1)}$$

$$\text{eq. (7-2)}$$
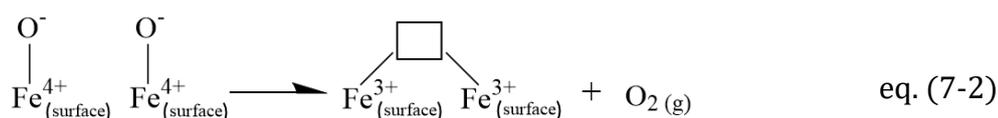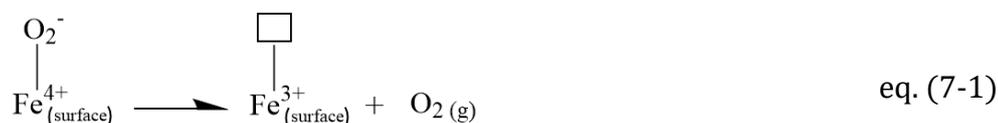
Above 700°C, the desorption of oxygen lattice labeled β-O_2 takes place in agreement with Eq. (5-16) as earlier described.

$$\text{eq. (7-3)}$$
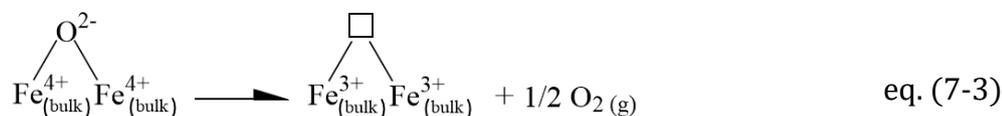
As seen, the profiles on $Pd/LaFe_{1-y}Cu_yO_3$ do not characterize a strong desorption of oxygen with respect to quantitative analysis summarized in Table 7.3. In agreement with data reported in Fig. 7.4, the reference $Pd/LaFeO_3$ and $Pd/La_{0.7}FeO_3$ show very limited oxygen mobility with desorbed oxygen hardly observed below 1000°C. The role of copper doping in terms of oxygen desorption quantity appears quite feeble which suggests a significant extracted fraction which would no longer weaken the B-O bond. Only the highest copper substitution degree ($y = 0.3$) exhibited pronounced lattice oxygen desorption although a slight shift of onset of peak position towards lower temperature zone is noticeable compared to non-PGM $LaFe_{1-y}Cu_yO_3$. Below 700°C broad and weak signal appear indicating surface oxygen desorption process which demonstrated slightly increased intensities on Pd-doped samples but still correspond to weak desorption process.
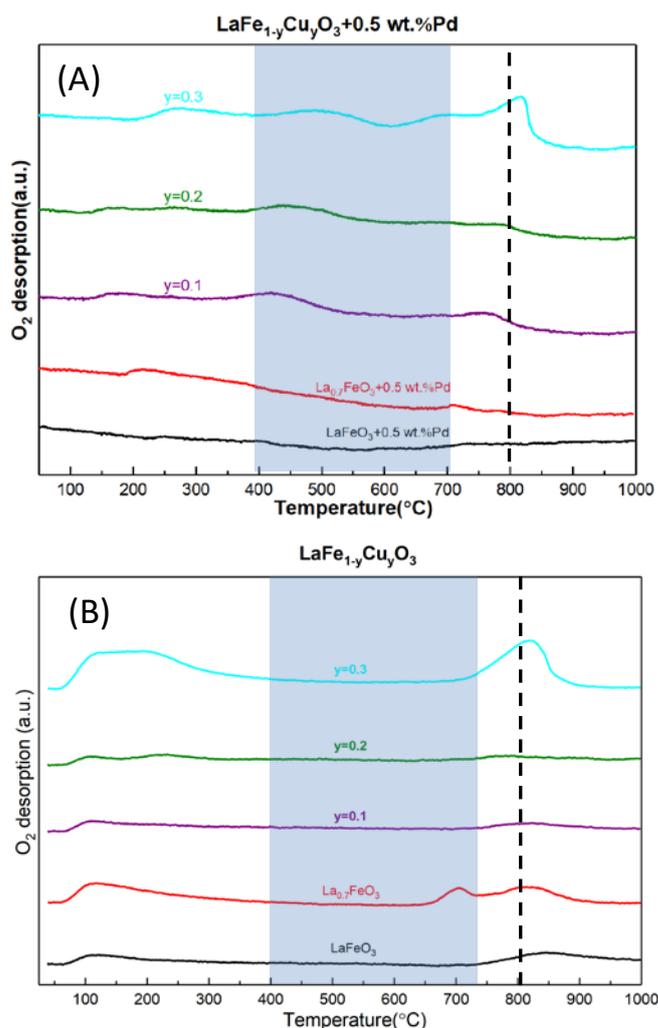
Fig. 7.4. O$_2$-TPD profiles of Pd-doped (A) and un-doped (B) stoichiometric perovskites LaFe$_{1-y}$Cu$_y$O$_3$. Purple: y = 0.1; olive: y = 0.2; cyan: y = 0.3.

Impact of copper doping on the La-deficient composition La$_{0.7}$Fe$_{1-y}$Cu$_y$O$_3$ becomes more significant (Fig. 7.5.). The higher copper substitution degree, the more desorbed oxygen quantity was produced. As discussed previously, the enhancement of bulk oxygen mobility is mainly related to the generation of oxygen vacancies arising from structural defects as well as the incorporation of cations with lower valences. Yet no strong effect of palladium on oxygen mobility of aforementioned perovskite can be witnessed.
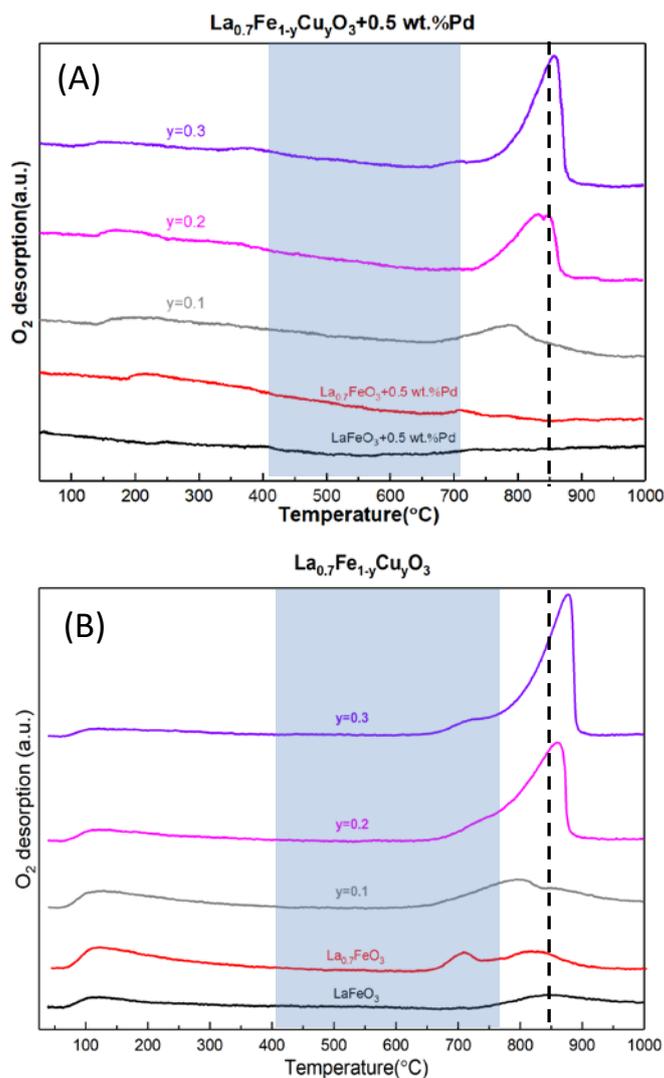
Fig. 7.5. O_2-TPD profiles of Pd-doped (A) and un-doped (B) $La_{0.7}Fe_{1-y}Cu_yO_3$. Purple: y = 0.1; olive: y = 0.2; cyan: y = 0.3.

Total desorbed oxygen quantity was conspicuously facilitated when calcium and copper doping was implemented at the same time (Fig. 7.6.). The most significant observation is related to a prominent extra desorption on $Pd/La_{0.6}Ca_{0.4}Fe_{0.8}Cu_{0.2}O_3$ below 700°C. This process is accompanied to less intense and broad desorption peaks characterized by two apparent maxima at 779°C and 836°C. Let us note that similar observations were already discussed on the bare $La_{0.6}Ca_{0.4}Fe_{0.8}Cu_{0.2}O_3$. Subsequent assignment is not trivial because the intense oxygen desorption near 700°C correspond to the frontier between Oads and Olattice species. Nonetheless, H_2-TPR observation can provide significant argument in connection with the high temperature reduction process observed at 600°C. In this temperature domain bulk reduction process takes places instead of surface reduction. As discussed this process underlines the specific role played by palladium which could be also reflected by this prominent desorption process in case of partial diffusion and weakening of the B-O bond.
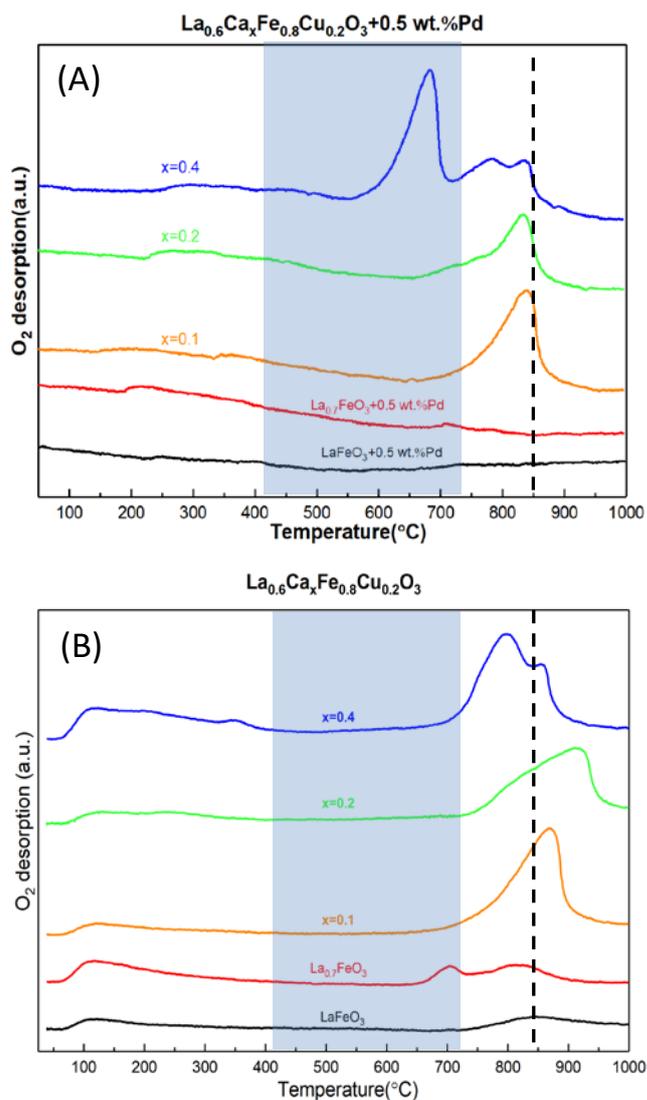
Fig. 7.6. O_2-TPD profiles of Pd-doped (A) and un-doped (B) $La_{0.6}Ca_xFe_{0.8}Cu_{0.2}O_3$. Purple: x = 0.1; olive: x = 0.2; cyan: x = 0.4.

Table 7.3. Quantitative analysis of O_2-TPD experiments

Catalyst	Amount of O_2 desorbed (mmol/g)[a]		
	α-O_2[b]	β-O_2[c]	Total oxygen desorbed [d]
Pd/LaFeO$_3$	weak	weak	weak/0.12 [e]
Pd/La$_{0.7}$FeO$_3$	0.0015	weak	weak/0.27 [e]
Pd/LaFe$_{0.9}$Cu$_{0.1}$O$_3$	0.18	0.06	0.24/0.12 [e]
Pd/LaFe$_{0.8}$Cu$_{0.2}$O$_3$	0.21	0.06	0.27/0.13 [e]
Pd/LaFe$_{0.7}$Cu$_{0.3}$O$_3$	0.21	0.18	0.39/0.48 [e]
Pd/La$_{0.7}$Fe$_{0.9}$Cu$_{0.1}$O$_3$	0.15	0.15	0.30/0.28 [e]
Pd/La$_{0.7}$Fe$_{0.8}$Cu$_{0.2}$O$_3$	0.12	0.39	0.51/0.43 [e]

Pd/$La_{0.7}Fe_{0.7}Cu_{0.3}O_3$	0.15	0.51	0.66/0.49 [e]
Pd/$La_{0.6}Ca_{0.1}Fe_{0.8}Cu_{0.2}O_3$	0.15	0.45	0.60/0.46 [e]
Pd/$La_{0.6}Ca_{0.2}Fe_{0.8}Cu_{0.2}O_3$	0.15	0.36	0.51/0.45 [e]
Pd/$La_{0.6}Ca_{0.4}Fe_{0.8}Cu_{0.2}O_3$	0.12	0.93	1.05/0.71 [e]

[a] Calculated by deconvolution of the O_2-TPD curves
[b] Amount of α-O_2 was calculated in the temperature range 60-600°C
[c] Amount of β-O_2 was calculated in the temperature range 600-1000°C.
[d] Slight quantity of physisorbed O_2 was included in the calculation of the amount of total O_2 desorbed.
[e] Results obtained from O_2-TPD on bare perovskite materials

7.3. Surface analysis through XPS measurements

Previous XPS analyses were reported in chapter V on bare perovskites. Similar experiments were performed on Pd-impregnated samples calcined at 400°C. The same La 3d, Ca 2p, Fe 2p, Cu 2p and O 1s photopeaks are reported in Figs. 7.7.-7.9. In this section particular attention was also paid to the Pd 3d core level. Binding Energy values are reported in Table 7.5. Only slight variations are noticeable on the characteristic photopeak of lanthanum and calcium mainly stabilized as La^{3+} and Ca^{2+}. Regarding the B-site, B.E. values and the appearance of satellite structures respectively near 719 eV and 941 eV characterize the predominance of Fe^{3+} and Cu^{2+} respectively. For copper species, isolated Cu^{2+} in octahedral coordination and extra framework CuO-like species can coexist as earlier discussed. The characteristic photopeak Pd 3d leads to B.E. values in the range 336.5-337.5 eV. Only slight deviations are observed which in all cases agree with a predominant stabilization of Pd^{2+}. Although these B.E. are slightly higher than those currently reported for PdO, one cannot strictly rule out a possible stabilization of palladium in unusual oxidation state as already stated [E.M. Slavinskaya 2011; K. Otto 1992; M. Moroseac 2004; W. Huang 2009]. Nonetheless, this slight shift to higher binding energy value could reflect a strengthening of the Pd-perovskite interaction and/or a particle size dependency. In the frame of this discussion, only particular spectral features arise on the Pd 3d photopeak for $La_{0.7}Fe_{0.7}Cu_{0.3}O_3$ with the growth of a shoulder at higher B.E. Tentative decomposition led to two components as summarized in Table 7.4. assigned respectively to Pd^{2+} and Pd^{4+}. It is reported that highly oxidized hydroxide species Pd^{4+} could appear at position of B.E. in the range of 337.9-338.5 eV.[L.S. Kibis 2009, 2012; K.S. Kim 1974]. Although PdO_2 is unstable in anhydrous form, previous studies have shown that Pd^{4+} nanoparticles can be stabilized by surrounding oxide matrix. [L.S. Kibis 2009; K. Otto 1992; Y. Sohn 2010].

Table 7.4. Deconvolution of Pd 3d photopeak of Pd/$La_{0.7}Fe_{0.7}Cu_{0.3}O_3$

Pd oxidation state	B.E. (eV)	Abundance(%)
+II	337.1	28.3
+IV	338.0	71.7

Semi quantitative analysis provides useful information especially when surface compositions are compared to bulk compositions from elemental analysis. These data are reported in Table 7.6. As seen, surface and bulk Ca/La, Cu/Fe ratios are of the same order of magnitude with minor changes likely within the margin of error. Slight changes are also discernible which agree with surface lanthanum enrichment for stoichiometric composition whereas bulk and surface compositions are comparable for La-deficient compositions. As a matter of fact, the most important discrepancies are observed by comparing bulk and surface Pd/(A+B) ratio (Table 7.7.). As seen a sharp surface palladium enrichment is noticeable irrespective of the composition except for $Pd/La_{0.6}Ca_{0.4}Fe_{0.8}Cu_{0.2}O_3$. As seen, the surface Pd concentration is considerably lowered converging to the bulk composition and indicating the absence of significant gradient in concentration from the core to the surface. It is useful to compare this observation with previous behavior of this specific sample revealed from H_2-TPR and O_2-TPD experiments with the appearance of an extra-reduction process at high temperature and prominent oxygen desorption below 700°C. As a matter of fact, all these information could suggest that Pd^{2+} partly diffuses in the perovskite structure becoming less reducible and then enhancing the bulk/surface oxygen mobility. Subsequent hydrogen titration experiments provide complementary information. Even if no clear evolution can be observed low dispersion are observed even extremely low on the stoichiometric $La_{0.6}Ca_{0.4}Fe_{0.8}Cu_{0.2}O_3$ whereas the counterpart reference stoichiometric sample $Pd/LaFeO_3$ led to appreciable H_2 uptake which underlines strong changes in the reducibility of oxidic palladium species. Possible overestimation of H_2 uptake on $Pd/LaFeO_3$ could be partly due to spill-over process. However, one can hypothesize that this effect could be negligible due to the weak reducibility of $LaFeO_3$. Hence, in this latter case we can conclude that more reducible PdO species would weakly interact with the perovskite substrate. Such statement seems also in rather good agreement with surface Pd/(A+B) ratio abnormally high except on $Pd/La_{0.6}Ca_{0.4}Fe_{0.8}Cu_{0.2}O_3$ with a good convergence with elemental composition as mentioned. This emphasizes the hypothesis that Pd could be randomly distributed whereas strong surface Pd enrichment would reflect more significant PdO aggregation especially on $Pd/LaFeO_3$.
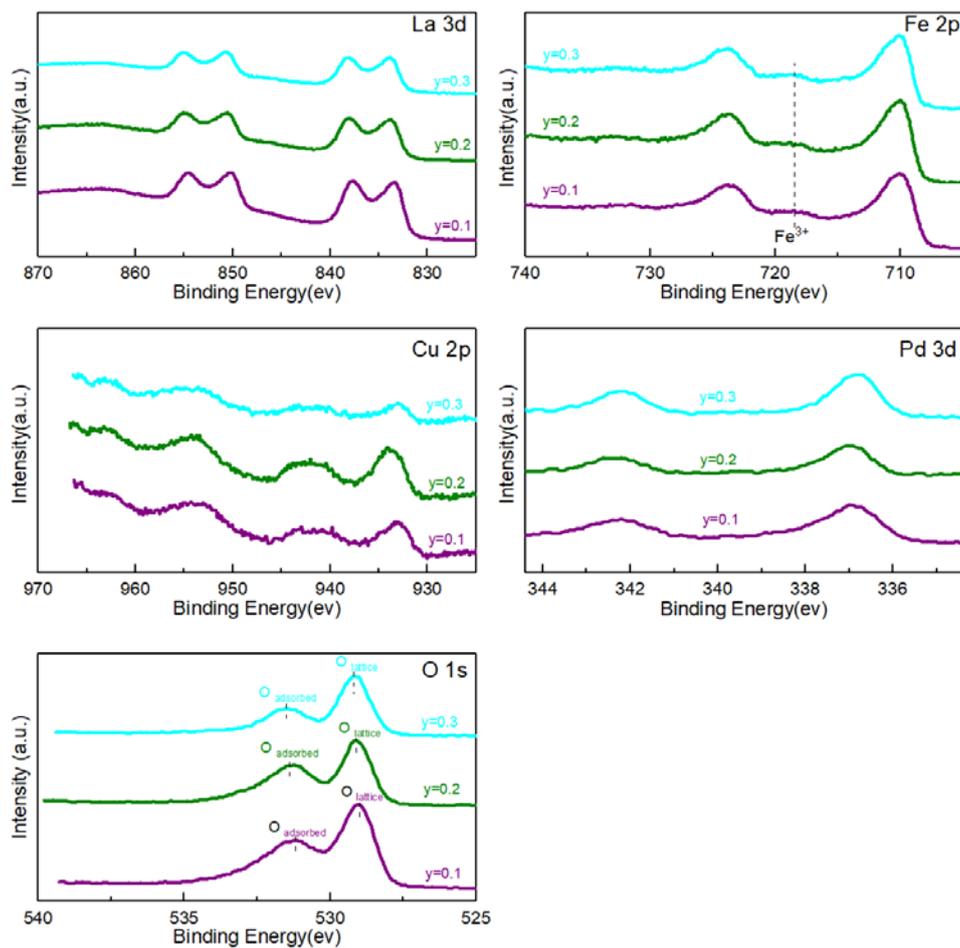
Fig. 7.7. Characteristic La 3d, Fe 2p, Cu 2p, Pd 3d and O 1s photopeaks for $Pd/LaFe_{1-y}Cu_yO_3$: purple: y = 0.1; olive: y = 0.2; cyan: y =0.3.
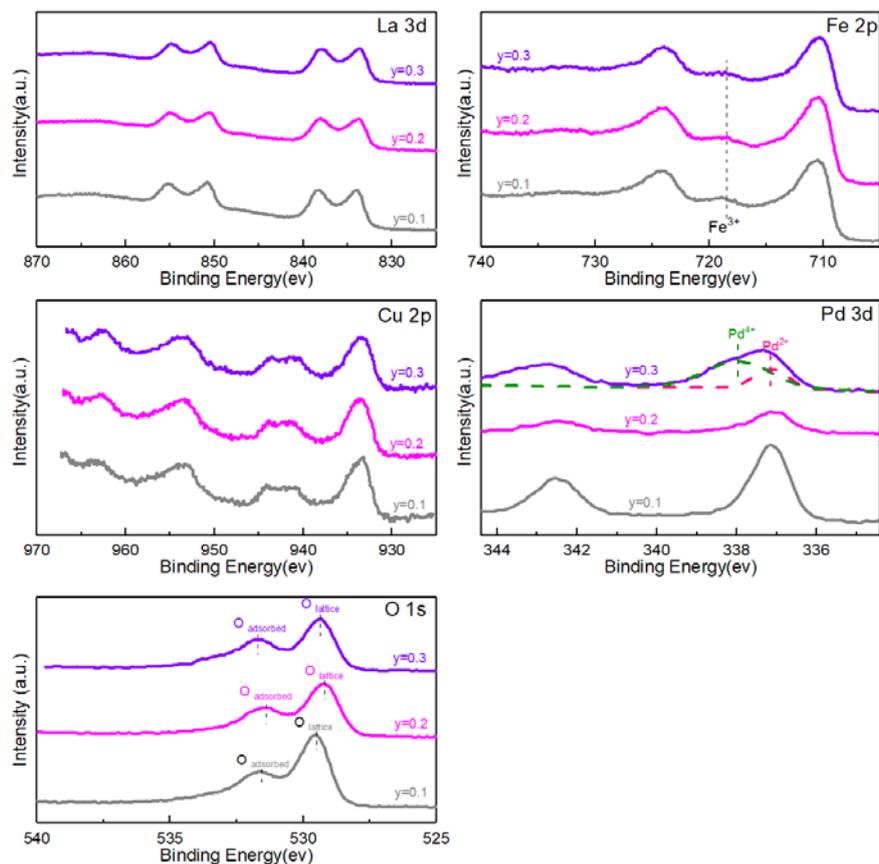
Fig. 7.8. Characteristic La 3d, Fe 2p, Cu 2p, Pd 3d and O 1s photopeaks for La$_{0.7}$Fe$_{1-y}$Cu$_y$O$_3$+0.5 wt.%Pd : grey: y = 0.1; magenta: y = 0.2; violet: y = 0.3.
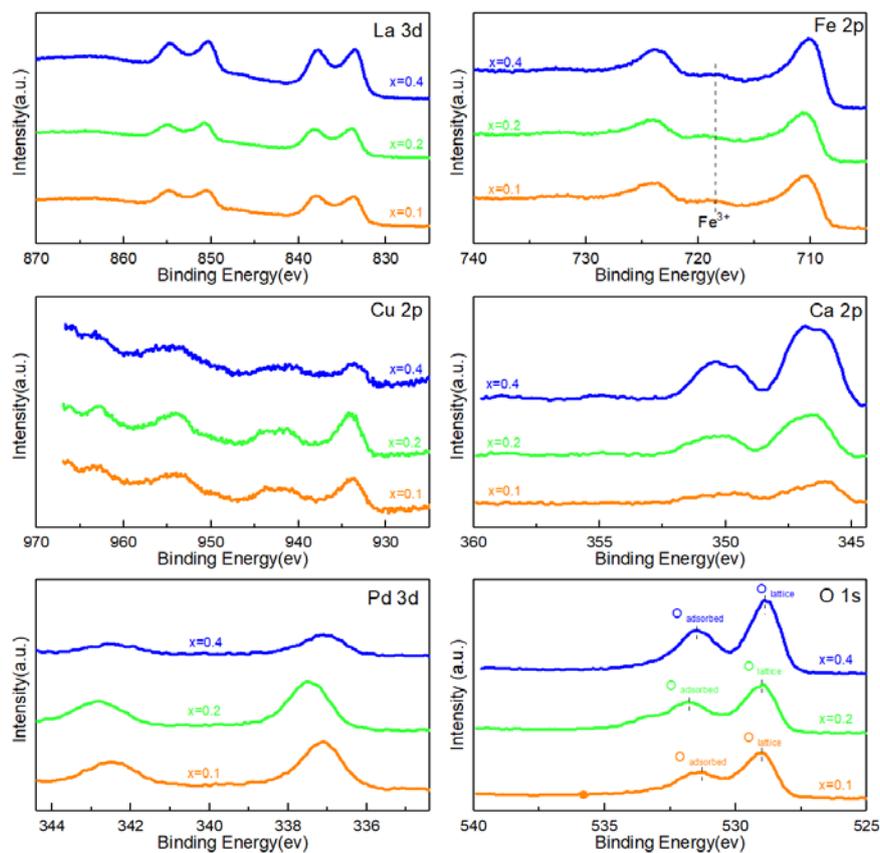
Fig. 7.9. Characteristic La 3d, Fe 2p, Cu 2p, Ca 2p, Pd 3d and O 1s photopeaks for La$_{0.6}$Ca$_x$Fe$_{0.8}$Cu$_{0.2}$O$_3$+0.5 wt.%Pd : orange: x = 0.1; green: x = 0.2; blue: x = 0.4.

Table 7.5. Binding energy of each element and abundance of related oxygen species.

Catalyst	Binding energy (eV)							Relative surf. Comp. O[a]		
						O 1s		O ads. (%)	O lattice (%)	$\dfrac{O_{adsorbed}}{O_{lattice}}$
	La 3d	Ca 2p	Fe 2p	Cu 2p	Pd 3d	Ads. oxygen	Lattice oxygen			
$Pd/LaFeO_3$	834.1	-	710.2	-	337.1	531.7	529.5	50.8	49.2	1.03
$Pd/La_{0.7}FeO_3$	834.1	-	710.4	-	336.8	531.5	529.5	54.0	46.0	1.17
$Pd/LaFe_{0.9}Cu_{0.1}O_3$	833.4	-	709.8	933.0	337.0	531.2	529.0	57.7	42.3	1.36
$Pd/LaFe_{0.8}Cu_{0.2}O_3$	833.8	-	710.0	934.1	337.1	531.4	529.1	56.4	43.6	1.29
$Pd/LaFe_{0.7}Cu_{0.3}O_3$	834.0	-	710.1	933	336.7	531.5	529.2	40.2	59.8	0.67
$Pd/La_{0.7}Fe_{0.9}Cu_{0.1}O_3$	833.9	-	710.5	933.3	337.1	531.5	529.5	54.9	45.1	1.22
$Pd/La_{0.7}Fe_{0.8}Cu_{0.2}O_3$	833.7	-	710.4	933.5	336.9	531.4	529.2	48.8	51.2	0.95
$Pd/La_{0.7}Fe_{0.7}Cu_{0.3}O_3$	833.6	-	710.2	933.4	337.4	531.7	529.3	58.1	41.9	1.39
$Pd/La_{0.6}Ca_{0.1}Fe_{0.8}Cu_{0.2}O_3$	833.6	346.0	710.2	933.6	337.1	531.3	529.0	52.8	47.2	1.12
$Pd/La_{0.6}Ca_{0.2}Fe_{0.8}Cu_{0.2}O_3$	833.9	346.4	710.4	933.9	337.5	531.8	529.0	57.1	42.9	1.33
$Pd/La_{0.6}Ca_{0.4}Fe_{0.8}Cu_{0.2}O_3$	833.5	346.8	710.2	933.6	337.1	531.5	528.9	46.8	53.3	0.88

[a] $O_{adsorbed} + O_{lattice} = 1$

[b] relative abundance of oxygen species was calculated from deconvolution of O 1s photopeak

Table 7.6. Surface atomic composition calculated from XPS analysis.

Catalyst	Surface atomic composition (%)							Atomic ratio			
	La	Ca	Fe	Cu	Pd	O	C	Ca/La	Cu/Fe	Pd/(A+B) $\times 10^{-3}$	A/B
Pd/LaFeO$_3$	11.35	-	7.90	-	0.70	43.91	36.14	-	-	36.4/3.96 [a]	1.44/0.96 [a]
Pd/La$_{0.7}$FeO$_3$	9.18	-	10.84	-	0.46	45.41	34.10	-	-	22.9/2.36 [a]	0.85/0.69 [a]
Pd/LaFe$_{0.9}$Cu$_{0.1}$O$_3$	14.89	-	8.79	1.33	0.45	46.78	27.77	-	0.15/0.11 [a]	18.0/5.21 [a]	1.47/0.99 [a]
Pd/LaFe$_{0.8}$Cu$_{0.2}$O$_3$	13.87	-	6.31	2.07	0.36	45.06	32.33	-	0.33/0.25 [a]	16.2/5.00 [a]	1.66/0.98 [a]
Pd/LaFe$_{0.7}$Cu$_{0.3}$O$_3$	14.55	-	7.26	0.86	0.62	43.37	33.35	-	0.12/0.43 [a]	27.3/5.00 [a]	1.79/0.98 [a]
Pd/La$_{0.7}$Fe$_{0.9}$Cu$_{0.1}$O$_3$	9.28	-	11.36	2.32	0.81	43.14	33.09	-	0.20/0.11 [a]	35.2/3.79 [a]	0.68/0.69 [a]
Pd/La$_{0.7}$Fe$_{0.8}$Cu$_{0.2}$O$_3$	9.65	-	9.45	2.44	0.31	42.18	35.97	-	0.26/0.24 [a]	14.4/3.95 [a]	0.81/0.69 [a]
Pd/La$_{0.7}$Fe$_{0.7}$Cu$_{0.3}$O$_3$	8.89	-	6.30	2.10	0.68	37.07	44.96	-	0.33/0.41 [a]	39.3/3.55 [a]	1.06/0.70 [a]
Pd/La$_{0.6}$Ca$_{0.1}$Fe$_{0.8}$Cu$_{0.2}$O$_3$	9.91	1.30	10.89	1.75	0.53	45.02	30.61	0.13/0.15 [a]	0.16/0.26 [a]	22.2/3.46 [a]	0.89/0.69 [a]
Pd/La$_{0.6}$Ca$_{0.2}$Fe$_{0.8}$Cu$_{0.2}$O$_3$	6.09	1.61	6.55	1.38	0.35	34.24	49.78	0.26/0.32 [a]	0.21/0.25 [a]	22.4/5.04 [a]	0.97/0.78 [a]
Pd/La$_{0.6}$Ca$_{0.4}$Fe$_{0.8}$Cu$_{0.2}$O$_3$	9.99	3.54	9.10	0.70	0.12	44.37	32.18	0.35/0.62 [a]	0.080.24 [a]	5.1/4.47 [a]	1.380.96 [a]

a bulk ratio from elemental analysis

Table 7.7. Pd dispersion comparison

Catalyst	SSA (m^2/g)	Pd dispersion (%)	Pd/(A+B) $\times 10^{-3}$
$Pd/LaFeO_3$	15.5	17.2	36.4/3.96 [a]
$Pd/La_{0.7}FeO_3$	35.5	0.5	22.9/2.36 [a]
$Pd/LaFe_{0.9}Cu_{0.1}O_3$	19.2	1.8	18.0/5.21 [a]
$Pd/LaFe_{0.8}Cu_{0.2}O_3$	15.3	1.3	16.2/5.00 [a]
$Pd/LaFe_{0.7}Cu_{0.3}O_3$	26.2	7.3	27.3/5.00 [a]
$Pd/La_{0.7}Fe_{0.9}Cu_{0.1}O_3$	32.2	1.2	35.2/3.79 [a]
$Pd/La_{0.7}Fe_{0.8}Cu_{0.2}O_3$	23.2	0.4	14.4/3.95 [a]
$Pd/La_{0.7}Fe_{0.7}Cu_{0.3}O_3$	15.4	11.4	39.3/3.55 [a]
$Pd/La_{0.6}Ca_{0.1}Fe_{0.8}Cu_{0.2}O_3$	22.1	1.1	22.2/3.46 [a]
$Pd/La_{0.6}Ca_{0.2}Fe_{0.8}Cu_{0.2}O_3$	21.3	1.4	22.4/5.04 [a]
$Pd/La_{0.6}Ca_{0.4}Fe_{0.8}Cu_{0.2}O_3$	32.4	0.7	5.1/4.47 [a]

[a] calculated from elemental analysis

7.4. Catalytic properties

7.4.1. Oxidative properties

Among the different catalysts prepared and characterized, we have deliberately made a selection with respect to the catalytic performances of the bare perovkites. Probably the parent $LaFeO_3$ sample can still serve as reference. Fig. 7.10. compares the conversion profiles vs. temperature obtained on bare and Pd-doped perovskite materials. Previous observations in Chapter V, led to the conclusion that copper extraction on $La_{0.7}Fe_{0.8}Cu_{0.2}O_3$ can lead to rate enhancement in CO conversion especially in stoichiometric conditions. But this beneficial effect is suppressed in rich conditions. As a matter of fact, a careful monitoring of copper clustering process to avoid the growth of less reactive CuO clusters is not an easy task. Calcium incorporation seems to be an appropriate strategy to slower copper segregation. Similar tendency also reproduces for propene. But in this particular case, rate calculations showed that Ca induces a significant rate enhancement with a rise in calcium content. As exemplified in Fig. 7.10., one can notice the superiority of $La_{0.6}Ca_{0.2}Fe_{0.8}Cu_{0.2}O_3$ compared to $La_{0.7}Fe_{0.8}Cu_{0.2}O_3$. The synergistic effect on the rate of propene oxidation due to calcium insertion has been preliminary explained through the involvement of dual-site in case of suprafacial reaction mechanism [J. Zhang 2015]. Accordingly, we have privileged Ca-doped samples in the evaluation of catalytic properties with the aim to evaluate the specific role played by palladium as a function of the degree of interaction with the perovskite support. As observed in Fig. 7.10. a sharp increase in the conversion of propene and CO is remarkable.

Chapter VII. Palladium incorporation to stoichiometric and non stoichiometric Ca and Cu doped $La_{1-x}FeO_{3\pm\delta}$

The TPR performances of Pd-doped perovskite based materials have been also compared to that obtained on the benchmark $Pd/Ce_xZr_{1-x}O_2$ supplied by Johnson Matthey containing the same amount of palladium but characterized by a better dispersion (D_{Pd} = 46.2%) on a classical OSC material exhibiting a much larger specific surface area (71.8 m^2/g). As a general trend, superior performances are observable for CO and propene oxidation which could be related to better oxygen storage properties compared to perovskite systems. On the other hand, $Pd/La_{0.6}Ca_{0.4}Fe_{0.8}Cu_{0.2}O_3$ was found more active for propane oxidation except in rich conditions with surprisingly a conversion almost nil. It is worth to note that in these reaction conditions Pd deposited on La-deficient perovskite is more active.

For CO oxidation, during STO1 experiments, all the palladium loaded perovskites exhibited similar behaviors with T_{50} near 220°C. On the one hand, deactivation was observed during STO2 experiments for the La-deficient $Pd/La_{0.6}Ca_{0.1}Fe_{0.8}Cu_{0.2}O_3$ and $Pd/La_{0.6}Ca_{0.2}Fe_{0.8}Cu_{0.2}O_3$. On the other hand, palladium loading on the stoichiometric composition $Pd/La_{0.6}Ca_{0.4}Fe_{0.8}Cu_{0.2}O_3$ showed better stability with a lower increase of T_{50} values..

The best activity for propene oxidation in stoichiometric atmosphere corresponds to the palladium loading on the stoichiometric composition $Pd/La_{0.6}Ca_{0.4}Fe_{0.8}Cu_{0.2}O_3$ (T_{50} = 262°C in STO1 and T_{50} = 285°C in STO2). Palladium loading on La-deficient composition $Pd/La_{0.6}Ca_{0.1}Fe_{0.8}Cu_{0.2}O_3$ and $Pd/La_{0.6}Ca_{0.2}Fe_{0.8}Cu_{0.2}O_3$ exhibited noticeable loss of activity in STO2 although an enhanced performance for propene oxidation was initially seen in the first stoichiometric atmosphere.
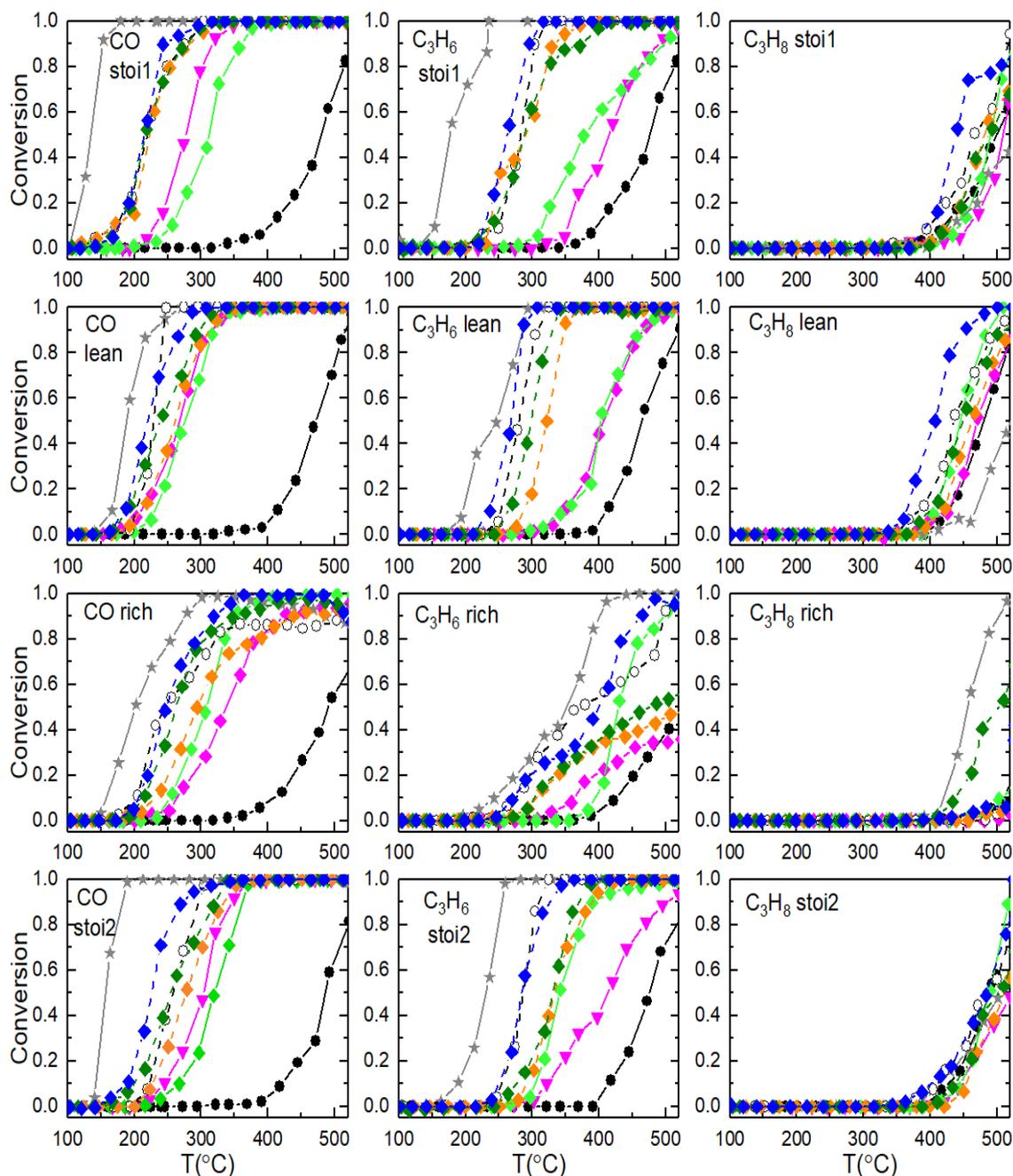
Fig. 7.10. Catalytic oxidation performance of iron-based perovskite solid ABO$_3$ (A=La, Ca; B= Fe, Cu) +0.5 wt.%Pd. Grey star solid line(★):commercial reference catalyst; black circle solid line: LaFeO$_3$(●); magenta downward triangle solid line: La$_{0.7}$Fe$_{0.8}$Cu$_{0.2}$O$_3$(▼); green diamond solid line:La$_{0.6}$Ca$_{0.2}$Fe$_{0.8}$Cu$_{0.2}$O$_3$(◆); blank circle dash line: Pd/LaFeO$_3$ (○); orange diamond dash line: Pd/La$_{0.6}$Ca$_{0.1}$Fe$_{0.8}$Cu$_{0.2}$O$_3$ (◆); olive diamond dash line: Pd/La$_{0.6}$Ca$_{0.2}$Fe$_{0.8}$Cu$_{0.2}$O$_3$ (◆); blue diamond dash line: Pd/La$_{0.6}$Ca$_{0.4}$Fe$_{0.8}$Cu$_{0.2}$O$_3$ (◆).

7.4.2. Reductive properties

Regarding NO reduction, the best performances in the absence of palladium was observed on La$_{0.6}$Ca$_{0.1}$Fe$_{0.8}$Cu$_{0.2}$O$_3$ (see Fig. 7.11.) as depicted in chapter V demonstrating

that low amount of calcium and La-deficiency would promote the conversion of NO in rich conditions.
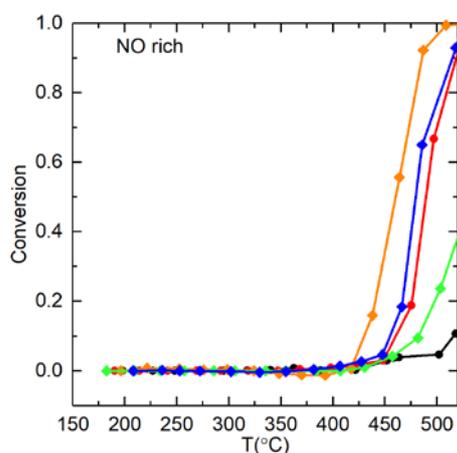
Fig. 7.11. Catalytic reduction performance of iron-based perovskite solid ABO_3 doped with calcium and copper (A=La, Ca; B= Fe, Cu) black circle: $LaFeO_3$; red circle: $La_{0.7}FeO_3$; orange diamond: $La_{0.6}Ca_{0.1}Fe_{0.8}Cu_{0.2}O_3$; green diamond: $La_{0.6}Ca_{0.2}Fe_{0.8}Cu_{0.2}O_3$; blue. diamond: $La_{0.6}Ca_{0.4}Fe_{0.8}Cu_{0.2}O_3$.

It is interesting to note that a different sequence of reactivity can be established after palladium impregnation. As seen in Fig. 7.12. the best performances correspond to stoichiometric $Pd/LaFeO_3$ and $Pd/La_{0.6}Ca_{0.4}Fe_{0.8}Cu_{0.2}O_3$ compositions during STO1 highlighting the prominent role played by palladium. It is remarkable that higher conversion levels are recorded on $Pd/La_{0.6}Ca_{0.4}Fe_{0.8}Cu_{0.2}O_3$ than on the benchmark $Pd/Ce_xZr_{1-x}O_2$ catalyst. This is particularly true above 400°C with a marked increase in NO_x conversion. STO2 conditions led to different behaviors associated with a slight deactivation and the suppression of the low temperature conversion temperature both on benchmark and Pd-impregnated perovskites which could be partly ascribed to NO_x storage properties. On the other hand, the conservation of the NO_x conversion is noticeable at high temperature on all catalytic systems.

In rich conditions the performances of $Pd/Ce_xZr_{1-x}O_2$ in NO reduction largely exceed those measured on $Pd/LaFeO_3$ and $Pd/La_{0.6}Ca_{0.4}Fe_{0.8}Cu_{0.2}O_3$ which still retain higher performances than those observed on Pd-impregnated La-deficient perovskites. However, in these conditions a significant loss of nitrogen selectivity occurs in favor of ammonia production especially at high temperature. As already explained an extra-production of hydrogen from reforming reactions can explain an over-hydrogenation of chemisorbed nitrogen atoms to form ammonia. As shown, the slight decrease in CO conversion seems in agreement with extra CO and H_2 production as earlier discussed.
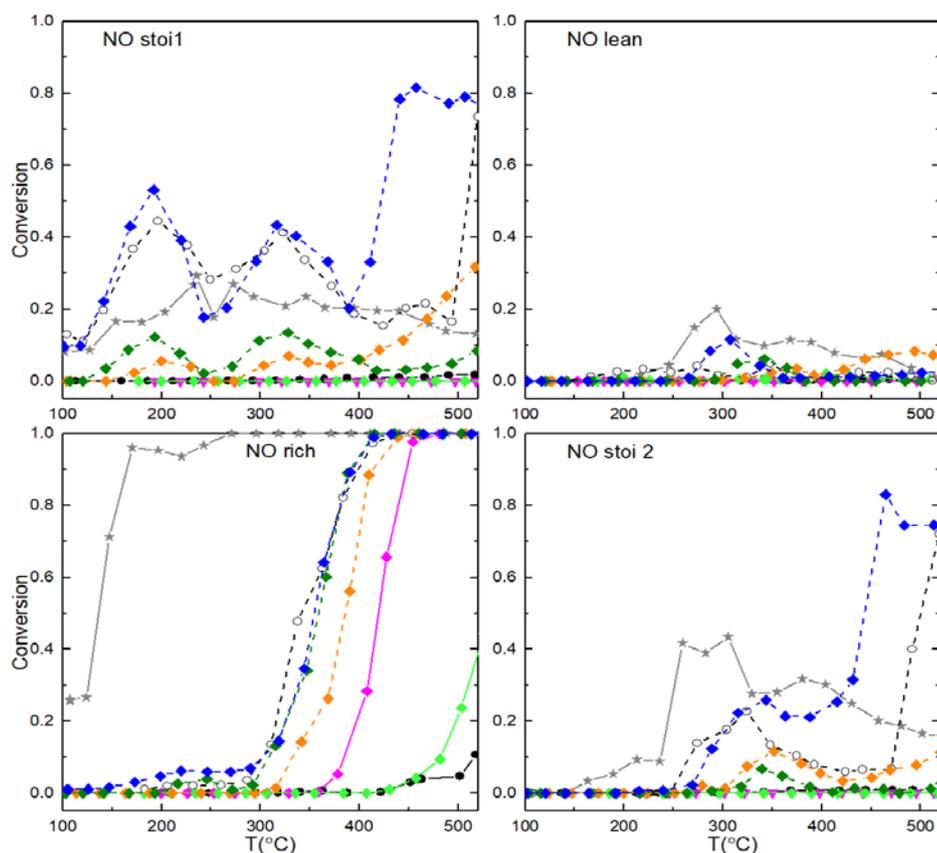
Fig. 7.12. Catalytic reduction performance of iron-based perovskite solid ABO_3 (A=La, Ca; B= Fe, Cu) +0.5 wt.%Pd. Grey star solid line(★):commercial reference catalyst; black circle solid line: $LaFeO_3$(●); magenta downward triangle solid line: $La_{0.7}Fe_{0.8}Cu_{0.2}O_3$(▼); green diamond solid line:$La_{0.6}Ca_{0.2}Fe_{0.8}Cu_{0.2}O_3$(◆); blank circle dash line: $Pd/LaFeO_3$ (○);orange diamond dash line: $Pd/La_{0.6}Ca_{0.1}Fe_{0.8}Cu_{0.2}O_3$ (◆); olive diamond dash line: $Pd/La_{0.6}Ca_{0.2}Fe_{0.8}Cu_{0.2}O_3$ (◆); blue diamond dash line: $Pd/La_{0.6}Ca_{0.4}Fe_{0.8}Cu_{0.2}O_3$ (◆).

The key point develops in chapter V to explain stronger CO but also NO adsorption was related to copper segregation at the surface of $La_{0.7}Fe_{0.8}Cu_{0.2}O_3$. This probably explains why this perovskite composition exhibited the best properties in terms of CO oxidation and NO reduction. As calcium inhibits copper segregation then one can explain the sharp gain in NO reduction rate thanks to palladium particles segregated at the surface. Subsequent discussion on possible cooperative effect of the support is not easy. As seen $LaFeO_3$ is quasi-completely inactive with weak ability to create defective site from which catalytic activity could potentially originate. Based on this, the highest dispersion from hydrogen chemisorption experiment is likely related to Pd metallic particles weakly interacting with the perovskite. Accordingly, the catalytic properties in terms of NO reduction could involve predominantly palladium species mostly in their metallic state. But the same explanation is not so obvious on $Pd/La_{0.6}Ca_{0.4}Fe_{0.8}Cu_{0.2}O_3$. As explained the very low Pd dispersion on this catalysts could be related either to very large and reducible PdO_x species or alternately to unreducible isolated Pd^{2+} species diluted in the perovskite support and/or in strong interaction at the surface/subsurface. Subsequent weakening of the B-O would favor the formation of anionic vacancies. Based on this, the reaction mechanism for NO reduction could be totally different.

Indeed, on $Pd/LaFeO_3$ preferential NO adsorption and dissociation would occur on nearest neighbor Pd sites whereas NO adsorbed on isolated Pd^{2+} species would dissociate on a nearest neighbor anionic vacancy promoted on $Pd/La_{0.6}Ca_{0.4}Fe_{0.8}Cu_{0.2}O_3$. In practice, it is expected that these two borderline cases would coexist and their predominance depends on the degree of dispersion and related reducibility of Pd^{2+} and perovskite structure.

The examination of the selectivity behavior can complement these explanations, especially the production of N_2O on $Pd/LaFeO_3$ and $Pd/La_{0.6}Ca_{0.4}Fe_{0.8}Cu_{0.2}O_3$. As seen in Fig. 7.14, the subsequent desorption and transformation of N_2O is delayed on $Pd/LaFeO_3$ which seems in rather good agreement with a stronger NO adsorption on metallic Pd particles. On the other hand, more weakly bonded NO species would facilitate the subsequent transformation on N_2O $Pd/La_{0.6}Ca_{0.4}Fe_{0.8}Cu_{0.2}O_3$. Regarding the selectivity behavior in rich conditions, a strong detrimental effect on the production of nitrogen is noticeable (see Fig. 7.13.). Probably, a more extensive reduction occurs in these operating conditions, irrespective of the catalysts compositions which promotes an over-reduction of dissociated nitrogen into ammonia. Let us note that the benchmark catalyst leads to a higher level of ammonia in the whole range of temperature (Fig. 7.15.).
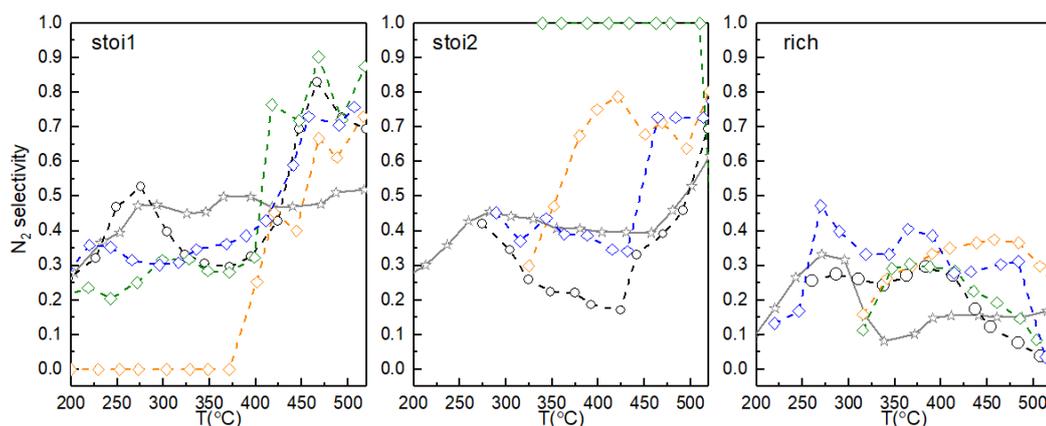
Fig. 7.13. Nitrogen selectivity of tested catalysts in stoichiometric(first and return) and rich atmosphere. Grey star solid line:commercial reference catalyst (☆); blank circle dash line: $Pd/LaFeO_3$ (○);orange diamond dash line: $Pd/La_{0.6}Ca_{0.1}Fe_{0.8}Cu_{0.2}O_3$ (◇);green diamond dash line: $Pd/La_{0.6}Ca_{0.2}Fe_{0.8}Cu_{0.2}O_3$ (◇); blue diamond dash line: $Pd/La_{0.6}Ca_{0.4}Fe_{0.8}Cu_{0.2}O_3$ (◇).
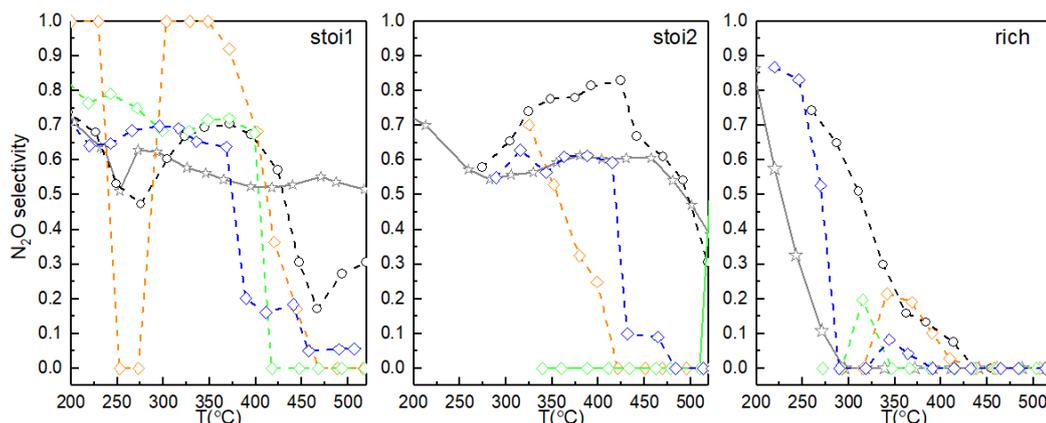
Fig. 7.14. Nitrous oxide selectivity of tested catalysts in stoichiometric(first and return) and rich atmosphere. Grey star solid line: commercial reference catalyst (☆); blank circle dash line: Pd/LaFeO$_3$ (◯);orange diamond dash line: Pd/La$_{0.6}$Ca$_{0.1}$Fe$_{0.8}$Cu$_{0.2}$O$_3$ (◇);green diamond dash line: Pd/La$_{0.6}$Ca$_{0.2}$Fe$_{0.8}$Cu$_{0.2}$O$_3$ (◇); blue diamond dash line: Pd/La$_{0.6}$Ca$_{0.4}$Fe$_{0.8}$Cu$_{0.2}$O$_3$ (◇).
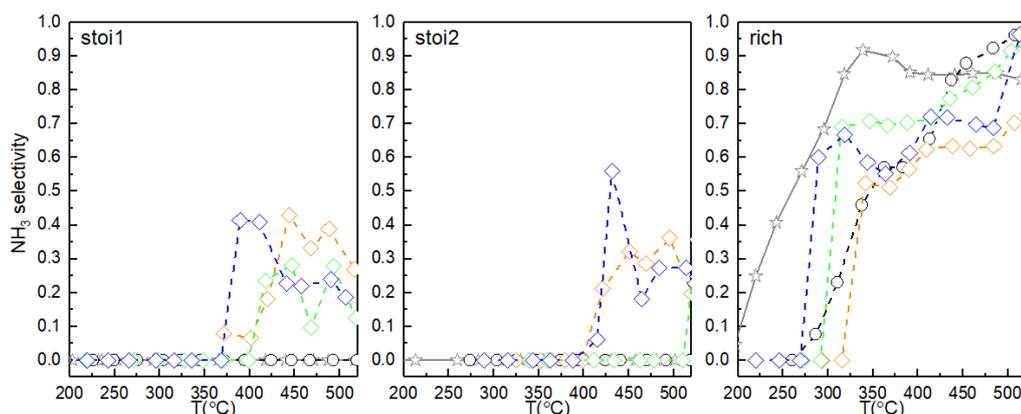
Fig. 7.15. Ammonia selectivity of tested catalysts in stoichiometric(first and return) and rich atmosphere. Grey star solid line: commercial reference catalyst (☆); blank circle dash line: Pd/LaFeO$_3$ (◯); orange diamond dash line: Pd/La$_{0.6}$Ca$_{0.1}$Fe$_{0.8}$Cu$_{0.2}$O$_3$ (◇); green diamond dash line: Pd/La$_{0.6}$Ca$_{0.2}$Fe$_{0.8}$Cu$_{0.2}$O$_3$ (◇); blue diamond dash line: Pd/La$_{0.6}$Ca$_{0.4}$Fe$_{0.8}$Cu$_{0.2}$O$_3$ (◇).

7.4.3. Kinetics of CO and propene oxidation

Similarly, TPR conversions were exploited according to the same assumptions earlier proposed. In this specific case the conversion of CO and propene occurs more readily than on bare materials with selected temperatures of 200°C for CO and 250°C for propene instead of 250°C and 375°C respectively which clearly highlights the beneficial role played by Pd. Rate calculations, apparent activation energy and the pre-exponential factor of the rate constant k, obtained from the slopes and the intercepts of the Arrhenius plots ln k = f(1/T), are reported in Tables 7.8. and 7.10. for stoichiometric conditions (STO1 and STO2) and Tables 7.9. and 7.11. for lean and rich conditions. As observed, it is obvious that specific and normalized rates are independent of the specific surface area both for CO and propene oxidation which means that performances will depend on dispersed palladium species. On the other hand, the surface composition can play a key role by monitoring the dispersion, the oxidation state of Pd and related catalytic properties. The comparison of the order of magnitude of rates from

STO1 and STO2 values underlines only weak deviations which suggest that deactivation did not occur significantly as previously mentioned. Finally, the evolution of the specific rate and normalized rate is quasi similar both for CO and propene oxidation from $Pd/LaFeO_3$ to $Pd/La_{0.6}Ca_{0.4}Fe_{0.8}Cu_{0.2}O_3$ with a minimum activity usually observed for Pd-impregnated on La-deficient perovskites except for propene oxidation from STO1 experiments showing a gradual increase of the rate with a rise in calcium composition. This comparison differs from previous observations on bare perovskites (see Chapter V) which underlines the prominent role played by Pd.

Figs. 7.16. and Fig. 7.17., respectively for CO and propene oxidation, resume these aforementioned tendencies but also provide useful observations through the comparison with the apparent activation energy values. As exemplified the minimum observed on the specific and also normalized rates corresponds to an optimum for E_{app}. Such optimum could reflect changes in the reaction mechanism as earlier discussed for NO reduction. This could be more obvious for CO oxidation than for propene because both reactions likely compete on the same active sites. Based on this, for the extremum composition corresponding to $Pd/LaFeO_3$ (x = 0) and $Pd/La_{0.6}Ca_{0.4}Fe_{0.8}Cu_{0.2}O_3$ (x = 0.4), different reaction mechanisms would predominate involving single sites mainly composed of Pd atoms on $Pd/LaFeO_3$ or dual mechanism with active site composed of Pd^{2+} at the vicinity of anionic vacancies on $Pd/La_{0.6}Ca_{0.4}Fe_{0.8}Cu_{0.2}O_3$.
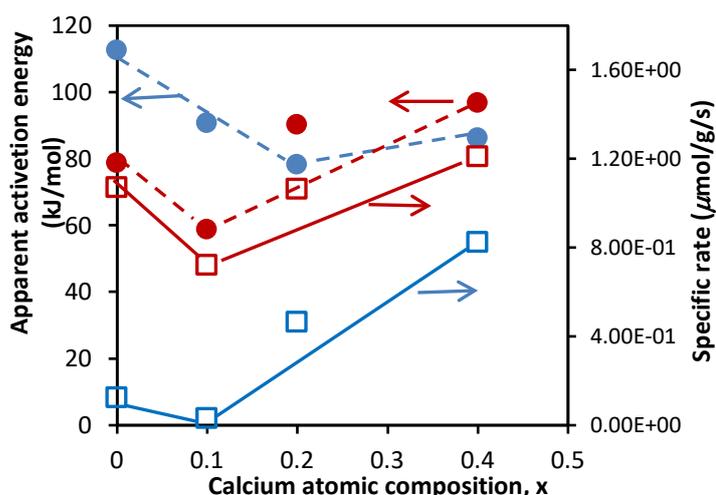
Fig. 7.16. Effect of surface composition of $Pd/LaFeO_3$ (x = 0) and $La_{0.6}Ca_xFe_{0.8}Cu_{0.2}O_3$ (x=0.1, 0.2, 0.4) on the specific rate and apparent activation energy for CO oxidation at 200°C : STO1 experiment in red and STO2 experiment in blue.
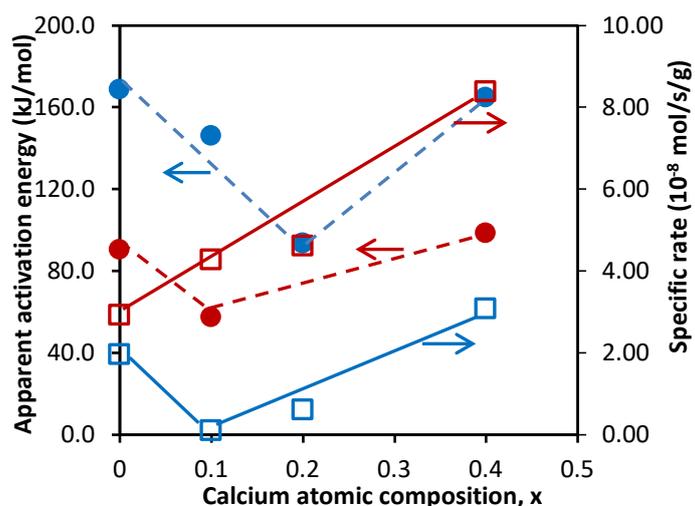
Fig. 7.17. Effect of surface composition of Pd/LaFeO$_3$ (x = 0) and La$_{0.6}$Ca$_x$Fe$_{0.8}$Cu$_{0.2}$O$_3$ (x=0.1, 0.2, 0.4) on the specific rate and apparent activation energy for propene oxidation at 250°C : STO1 experiment in red and STO2 experiment in blue.

Finally, it is interesting to compare kinetic parameters obtained in stoichiometric (STO1 and STO2) with those obtained in lean and rich conditions. As shown, there is no significant deviation observed on the specific and normalized rate. On the other hand, apparent activation energy values in Tables 7.9. and 7.11. strongly differ being much higher both for CO and propene oxidation which probably underlines different type of mechanism in lean and rich conditions.

Table 7.8. Rate and kinetic parameters related to CO oxidation on palladium doped perovskite samples

Catalyst	SSA $(m^2 g^{-1})$	STO1				STO2			
		$r_{spec.}$ $(mols^{-1}g^{-1})^a$	Normalized rate $(mols^{-1}m^{-2})^a$	A $(m^3s^{-1}g^{-1})$	E_{app} $(kJ.mol^{-1})$	$r_{spec.}$ $(mols^{-1}g^{-1})^a$	Normalized rate $(mols^{-1}m^{-2})^a$	A $(m^3s^{-1}g^{-1})$	E_{app} $(kJ\ mol^{-1})$
Pd/LaFeO$_3$	16.1	1.07E-06	6.67E-08	5567	78.7	1.23E-07	0.76E-08	1254203	112.6
Pd/La$_{0.6}$Ca$_{0.1}$Fe$_{0.8}$Cu$_{0.2}$O$_3$	23.9	0.72E-06	3.02E-08	14	58.7	3.08E-08	0.13E-08	5000	90.8
Pd/La$_{0.6}$Ca$_{0.2}$Fe$_{0.8}$Cu$_{0.2}$O$_3$	22.7	1.065E-06	4.67E-08	44824	90.2	4.65E-07	2.05E-08	709	78.3
Pd/La$_{0.6}$Ca$_{0.4}$Fe$_{0.8}$Cu$_{0.2}$O$_3$	34.3	1.21E-06	3.53E-08	251038	96.8	8.23E-07	2.40E-08	11585	86.2

Note: pre-exponential factor and E_{app} apparent activation energy in agreement with $k = A\ exp(-E_{app}/RT)$
[a] calculated at T = 200°C for STO1 and STO2.

Table 7.9. Rate and kinetic parameters related to CO oxidation on palladium doped perovskite samples

Catalyst	SSA $(m^2 g^{-1})$	LEAN				RICH			
		$r_{spec.}$ $(mols^{-1}g^{-1})^a$	Normalized rate $(mols^{-1}m^{-2})^a$	A $(m^3s^{-1}g^{-1})$	E_{app} $(kJ.mol^{-1})$	$r_{spec.}$ $(mols^{-1}g^{-1})^a$	Normalized rate $(mols^{-1}m^{-2})^a$	A $(m^3s^{-1}g^{-1})$	E_{app} $(kJ\ mol^{-1})$
Pd/LaFeO$_3$	16.1	2.47E-07	1.54E-08	1.47E+18	221.1	4.99E-07	3.10E-08	5.81	78.2
Pd/La$_{0.6}$Ca$_{0.1}$Fe$_{0.8}$Cu$_{0.2}$O$_3$	23.9	2.15E-07	9.00E-09	450.7	77.8	1.99E-07	8.33E-09	312.6	80.2
Pd/La$_{0.6}$Ca$_{0.2}$Fe$_{0.8}$Cu$_{0.2}$O$_3$	22.7	5.31E-07	2.34E-08	1.74	51.1	2.97E-07	1.31E-08	7.83	60.4
Pd/La$_{0.6}$Ca$_{0.4}$Fe$_{0.8}$Cu$_{0.2}$O$_3$	34.3	7.71E-07	2.25E-08	12.6	57.2	3.70E-07	1.08E-08	23.0	63.6

[a] calculated at T = 200°C for LEAN and RICH.

Table 7.10. Rate and kinetic parameters related to C_3H_6 oxidation on palladium doped perovskite samples

Catalyst	SSA (m^2g^{-1})		STO1					STO2		
		$r_{spec.}$ $(mols^{-1}g^{-1})^a$	Normalized rate $(mols^{-1}m^{-2})^a$	A $(m^3 s^{-1}g^{-1})$	E_{app} $(kj\,mol^{-1})$	$r_{specific}$ $(mol\,s^{-1}g^{-1})^a$	Normalized rate $(mols^{-1}m^{-2})^a$	A $(m^3 s^{-1}g^{-1})$	E_{app} $(kJmol^{-1})$
Pd//LaFeO$_3$	16.1	2.92E-08	1.81E-09	2.4E3	90.2	1.96E-08	12.2E-10	6.0E10	168.6
Pd/La$_{0.6}$Ca$_{0.1}$Fe$_{0.8}$Cu$_{0.2}$O$_3$	23.9	4.27E-08	1.79E-09	2.9	57.4	1.01E-09	0.42E-10	4.0E7	146.1
Pd/La$_{0.6}$Ca$_{0.2}$Fe$_{0.8}$Cu$_{0.2}$O$_3$	22.7	4.64E-08	2.03E-09	5.7E3	93.4	6.01E-09	2.65E-10	1.3E3	93.6
Pd/La$_{0.6}$Ca$_{0.4}$Fe$_{0.8}$Cu$_{0.2}$O$_3$	34.3	8.38E-08	2.44E-09	4.4E4	98.6	3.08E-08	8.97E-10	3.1E10	164.8

[a] calculated at T = 250°C for STO1 and STO2

Table 7.11. Rate and kinetic parameters related to C_3H_6 oxidation on palladium doped perovskite samples

Catalyst	SSA $(m^2 g^{-1})$		LEAN					RICH		
		$r_{spec.}$ $(mols^{-1}g^{-1})^a$	Normalized rate $(mols^{-1}m^{-2})^a$	A $(m^3s^{-1}g^{-1})$	E_{app} $(kJ.mol^{-1})$	$r_{spec.}$ $(mols^{-1}g^{-1})^a$	Normalized rate $(mols^{-1}m^{-2})^a$	A $(m^3s^{-1}g^{-1})$	E_{app} $(kJ\,mol^{-1})$
Pd/LaFeO$_3$	16.1	1.28E-08	7.95E-10	4.7E+10	166.5	1.51E-08	9.35E-10	0.39	55.1
Pd/La$_{0.6}$Ca$_{0.1}$Fe$_{0.8}$Cu$_{0.2}$O$_3$	23.9	2.33E-09	9.75E-11	5.3E+10	178.1	4.95E-09	2.07E-10	3.20	70.1
Pd/La$_{0.6}$Ca$_{0.2}$Fe$_{0.8}$Cu$_{0.2}$O$_3$	22.7	6.91E-09	3.01E-10	5.1E8	138.6	3.66E-09	1.61E-10	0.41	61.2
Pd/La$_{0.6}$Ca$_{0.4}$Fe$_{0.8}$Cu$_{0.2}$O$_3$	34.3	4.65E-08	1.36E-09	6.3E7	132.2	1.20E-08	3.51E-10	0.05	46.9

[a] calculated at T = 250°C for LEAN and RICH.

7.5. Conclusion

Incorporation of 0.5 wt.% palladium to lanthanum ferrite perovskite did not cause significant deformation of the perovskite structure. No detectable PdO_x crystal phase was identified by XRD due to the quite low Pd loading amount. On the other hand, the dispersion and oxidation state of palladium likely change according to the perovskite composition. Indeed, noticeable changes appears on the catalytic properties when palladium is dispersed on stoichiometric and none stoichiometric substrates.

Compared to non-PGM ferrite based perovskite, Pd loading resulted in improved reducibility and oxygen mobility illustrated by the increased H_2 uptake and desorbed O_2 quantity. Ca-doping further strengthened this trend. A H/M (M=Cu+Pd) ratio higher than theoretical value 2.0 during H_2-TPR experiment is associated with $Pd/La_{0.6}Ca_xFe_{0.8}Cu_{0.2}O_3$, probably implying the occurrence of spillover process due to Pd incorporation. Particular attention should be paid to $Pd/La_{0.6}Ca_{0.4}Fe_{0.8}Cu_{0.2}O_3$ which is characterized by the greatest H_2 consumption and O_2 desorption quantity yet the lowest Pd content on the surface. For the aforesaid catalyst, the high homogeneity of Pd distribution across the substrate could be attributable to the strong interaction between Pd and perovskite support. As a result, an enhanced reducibility of B-site cations as well as lattice oxygen mobility was achieved, as illustrated by the additional reduction process between 500-600°C in Fig.7.3.(A) and lattice oxygen desorption process between 550-750°C in Fig.7.6(A).

Pd loading on the Ca and Cu co-doped perovskite showed a remarkable improvement for CO and C_3H_6 oxidation in comparison with bare perovskites. Similar oxidative behavior in STOI1 was observed on $Pd/La_{0.6}Ca_xFe_{0.8}Cu_{0.2}O_3$ irrespective of Ca richness, with T_{50} below 220°C for CO oxidation and T_{50} below 280°C for C_3H_6 oxidation. Nevertheless, a marked deactivation in STOI2 was noticeable on $Pd/La_{0.6}Ca_{0.1}Fe_{0.8}Cu_{0.2}O_3$ and $Pd/La_{0.6}Ca_{0.2}Fe_{0.8}Cu_{0.2}O_3$. On the contrary, $Pd/La_{0.6}Ca_{0.4}Fe_{0.8}Cu_{0.2}O_3$ demonstrated improved stability with only a minor loss of activity recorded in the return test. The inhibition of agglomeration of Pd particles was probably ascribed to the strong interaction between Pd and perovskite support, which accounts for the high thermal stability of $Pd/La_{0.6}Ca_{0.4}Fe_{0.8}Cu_{0.2}O_3$. Kinetic analysis revealed that the specific and normalized reaction rates of CO and C_3H_6 oxidation are independent of the specific surface area but rely heavily on the surface composition of the catalyst. Compared to non-PGM perovskite, the marked increase of reaction rate highlights the beneficial role of Pd in terms of promoting oxidative properties. The optimum composition for CO and C_3H_6 oxidation corresponds to $Pd/LaFeO_3$ and $Pd/La_{0.6}Ca_{0.4}Fe_{0.8}Cu_{0.2}O_3$. However, different mechanisms function on the aforesaid candidates. Indeed, if $La_{0.6}Ca_{0.4}Fe_{0.8}Cu_{0.2}O_3$ was found highly reducible with improved OSC properties, $LaFeO_3$ exhibits an opposite behavior being quasi-unreducible and exhibiting much poorer OSC properties. Such differences can influence the extent of Pd dispersion and its reducibility with a larger distribution of oxidic Pd species in interaction with reactive oxygen or anionicvacancies on the support whereas metallic Pd particles would predominate on $LaFeO_3$. As a consequence, reaction mechanism on $Pd/LaFeO_3$ could preferentially involved single active sites consisting of metallic Pd atoms while a dual mechanism

involving active sites composed of Pd^{2+} species at the vicinity of anionic vacancies could occour on $Pd/La_{0.6}Ca_{0.4}Fe_{0.8}Cu_{0.2}O_3$.

Compared to bare perovskite, NO conversion in stoichiometric condition was significantly improved thanks to Pd incorporation. The highest NO conversion reached 52% in STOI1 and 24% in STOI2 respectively in the temperature range of 150-400°C. It was found that Pd loading on perovskite with stoichiometric compositions in A-site showed the highest activity for NO reduction: $Pd/LaFeO_3$ and $Pd/La_{0.6}Ca_{0.4}Fe_{0.8}Cu_{0.2}O_3$. The aforesaid catalysts exhibited higher NO conversion compared to commercial benchmark $Pd/Ce_{0.5}Ze_{0.5}O_2$ in STOI1 but a loss of low temperature NO conversion was also prominent in STOI2 due to deactivation. Nevertheless, different mechanisms of NO reduction are involved on the aforementioned catalysts. Since $LaFeO_3$ possesses weak ability to create defective sites, it is conceivable NO reduction would take place on metallic Pd^0 particle weakly interacting with $LaFeO_3$ support. In this case, adsorption of NO and subsequent dissociation of adsorbed NO occurs predominantly on Pd^0 surface. As for $Pd/La_{0.6}Ca_{0.4}Fe_{0.8}Cu_{0.2}O_3$, the extremely low Pd dispersion evidenced by hydrogen chemisorption experiment demonstrates that presence of Pd is either in the form of large and reducible PdO_x species or alternately as unreducible isolated Pd^{2+} species diluted in the perovskite support. Accordingly, the strong metal-support interaction would result in the weakening of B-O bond, favorable for the creation of anionic vacancies. As a result, NO adsorption occurs in the oxidized Pd^{n+} site and dissociates preferentially on the closest anionic vacancies. Moreover, Pd-loaded perovskite presented N_2 selectivity at low temperature inferior to that of the benchmark $Pd/Ce_{0.5}Ze_{0.5}O_2$ in both STOI1 and STOI2. In rich conditions, the formation of great amount of ammonia is quite pronounced, which is related to the production of hydrogen arising from partial oxidation or reforming of hydrocarbons.

Chapter VIII. Rhodium incorporation to stoichiometric and non-stoichiometric Ca and Cu doped $La_{1-x}FeO_{3\pm\delta}$

A similar approach was adopted for rhodium addition through a classical wet impregnation approach. The precursors obtained after impregnation were calcined in air at 400°C. As previously explained for palladium, surface re-dispersion is expected through this thermal treatment but one cannot strictly rule out the possibility that marginally oxidic rhodium species can diffuse inside the perovskite lattice depending on the extent of defective sites which are crucial for that surface vs. bulk diffusion. As previously demonstrated, the reducibility in this borderline case can be strongly affected because a stronger metal-support interaction can lower the reducibility and alter the related performances and corresponding reaction mechanism. The rhodium content in that case has been significantly lowered to preserve the cost efficiency of those catalytic materials.

Elemental analysis of rhodium loaded perovskites $ABO_{3\pm\delta}$ is shown in Table 8.1. The real composition of the rhodium loaded perovskites is essentially in good agreement with theoretical compositions. As seen, minor variations of rhodium content is observed with regard to the expected value (theoretical Rh content equals to 0.1 wt.%). The measured compositions probably vary within the margin of error excepted for $Rh/La_{0.7}FeO_3$ with an abnormally low Rh/(A+B) ratio.

Table 8.1. Elemental analysis of rhodium loaded perovskite $ABO_{3\pm\delta}$

Catalyst	Atomic composition (%)					Ca/La	Cu/Fe	A/B	Rh/(A+B)×10⁻³
	La	Ca	Fe	Cu	Rh				
$Rh/LaFeO_3$	13.72	-	13.75	-	0.03	-	-	1.00	1.02
$Rh/La_{0.7}FeO_3$	18.46	-	25.91	-	0.04	-	-	0.71	0.96
$Rh/LaFe_{0.9}Cu_{0.1}O_3$	21.34	-	19.15	2.08	0.04	-	0.11	1.00	1.05
$Rh/LaFe_{0.8}Cu_{0.2}O_3$	21.09	-	16.9	4.21	0.05	-	0.25	1.00	1.13
$Rh/LaFe_{0.7}Cu_{0.3}O_3$	20.31	-	14.22	6.07	0.05	-	0.43	1.00	1.19
$Rh/La_{0.7}Fe_{0.9}Cu_{0.1}O_3$	20.14	-	25.5	2.86	0.05	-	0.11	0.71	0.96
$Rh/La_{0.7}Fe_{0.8}Cu_{0.2}O_3$	19.75	-	22.48	5.76	0.04	-	0.26	0.70	0.80
$Rh/La_{0.7}Fe_{0.7}Cu_{0.3}O_3$	17.49	-	17.37	7.68	0.04	-	0.44	0.70	0.99
$Rh/La_{0.6}Ca_{0.1}Fe_{0.8}Cu_{0.2}O_3$	18.95	3.01	24.85	6.4	0.05	0.16	0.26	0.70	0.98
$Rh/La_{0.6}Ca_{0.2}Fe_{0.8}Cu_{0.2}O_3$	16.49	5.27	21.69	5.47	0.05	0.32	0.25	0.80	0.95
$Rh/La_{0.6}Ca_{0.4}Fe_{0.8}Cu_{0.2}O_3$	12.39	7.66	16.23	4.19	0.03	0.62	0.26	0.98	0.85

We checked from X-ray analysis (not shown) the absence of reflections characteristic of bulk detectable RhO_x species. This result was expected likely due to highly dispersed RhO_x

species but more probably to the low Rh content below the detection limit of this technique. As aforementioned, the reducibility of oxidic rhodium species can depend on the strength of interaction with the support. To this end, H$_2$-TPR and O$_2$-TPD can be useful to investigate this interaction because it can alter both the reducibility as well as oxygen mobility.

8.1. Reducibility

As seen from Fig. 8.1., Rh deposition on LaFeO$_3$ did not generate considerable hydrogen consumption, with the lowest total hydrogen uptake quantity observed (0.003 mmol/g, Table 8.2.). This tendency is in agreement with previous observations on the bare material found unreducible. In comparison with PGM-free perovskite La$_{0.7}$FeO$_3$, Rh/La$_{0.7}$FeO$_3$ is characterized by the ease of the extra-network hematite demonstrated by the significant shift of the reduction peaks towards lower temperature. The broadening of the reduction peak in the range of 150-300°C is noticeable on the Rh/LaFe$_{1-y}$Cu$_y$O$_3$ although the peak position seems hardly affected compared to PGM-free LaFe$_{1-y}$Cu$_y$O$_3$, suggesting that rhodium loading only has little impact on the reduction process of Cu^{2+} to metallic copper. The H/M ratio (see Table 8.2.) estimated on Rh/LaFe$_{1-y}$Cu$_y$O$_3$ remains less than 2.0, indicating an incomplete reduction of both Cu^{2+} and Rh^{3+}. Higher copper doping gave rise to greater hydrogen consumption quantity. The most prominent observation is likely related to the growth of a high temperature H$_2$ consumption which intensifies on Rh/LaFe$_{0.7}$Cu$_{0.3}$O$_3$. it should be emphasized that this reduction process was not earlier detected on the bare sample. Hence, one can hypothesize that this could reflect a bulk reduction process closely related to partial diffusion of rhodium.
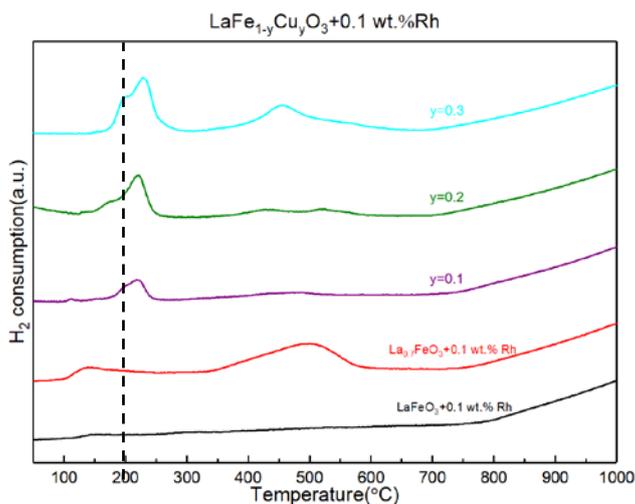
Fig. 8.1. H$_2$ consumption curves plotted against temperature for stoichiometric Rh/ LaFe$_{1-y}$Cu$_y$O$_3$ purple:y=0.1; olive:y=0.2; cyan:y=0.3.
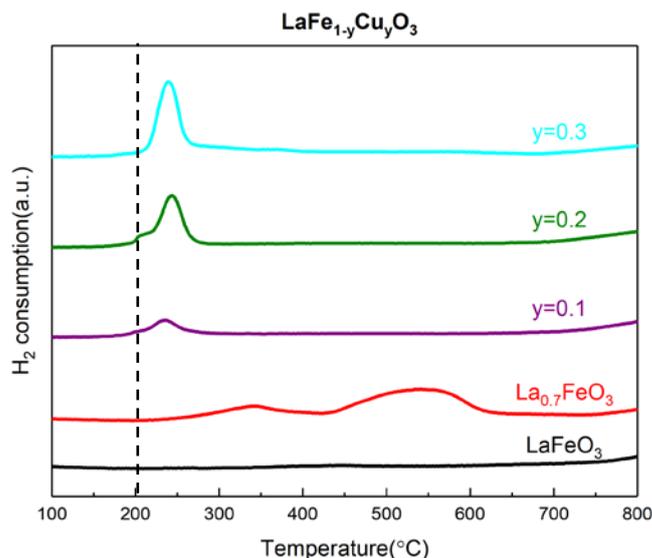
Fig. 8.2. H$_2$ consumption curves plotted against temperature for stoichiometric perovskites doped with copper LaFe$_{1-y}$Cu$_y$O$_3$ purple:y=0.1; olive:y=0.2; cyan:y=0.3.

Previous observations on bare La-deficient La$_{0.7}$Fe$_{1-y}$Cu$_y$O$_3$ samples proved that deficit of A-site atoms improves of the overall reducibility of perovskites partly explained by copper and iron extraction. Mössbauer spectroscopy did not reveal the presence of unusual Fe (+IV) on these samples to compensate electronic imbalances created by partial substitution of Fe^{3+} by Cu^{2+} that could explain such improved reducibility. Fig. 8.3. and Fig. 8.4. reveal the same trends which does not underline a strong impact of Rh on the overall reducibility of the solids. As seen, the reduction of oxidic copper species takes place at le lowest temperature. Probably the reduction of RhO$_x$ and CuO occur simultaneously with significant overlapping which could explain changes on the relative intensity and apparent maxima of the contribution at low temperature. The reduction of extra framework iron species is observable in the range 300-600°C. Interestingly, such reduction process is no longer noticeable on Rh/La$_{0.7}$Fe$_{0.7}$Cu$_{0.3}$O$_3$ which suggests that the extraction of iron would occur more slowly at increasing copper content. Nevertheless, the evolution observed on the H$_2$ uptake did not indicate that this sample becomes less reducible. An important observation comes from the comparison of Rh/LaFe$_{0.7}$Cu$_{0.3}$O$_3$ and Rh/La$_{0.7}$Fe$_{0.7}$Cu$_{0.3}$O$_3$. As shown in the former sample an extra-reduction process was evidenced possibly ascribed to Rh incorporation. It is worthwhile to note that this reduction process does note take place on Rh/La$_{0.7}$Fe$_{0.7}$Cu$_{0.3}$O$_3$ above 400°C.
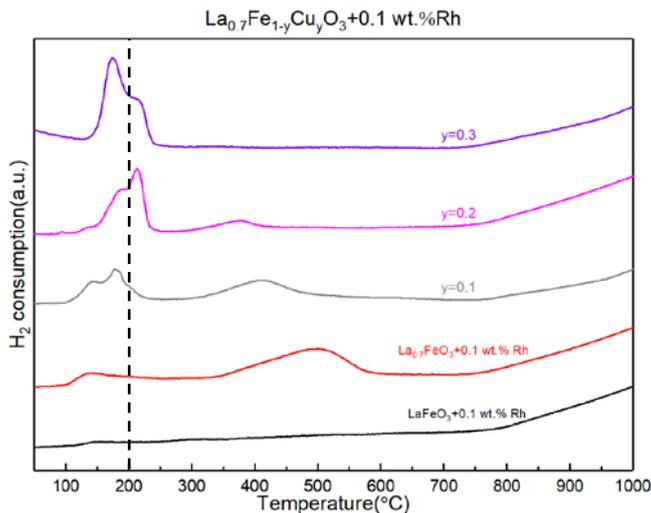
Fig. 8.3. H$_2$ consumption curves plotted against temperature for Rh/La$_{0.7}$Fe$_{1-y}$Cu$_y$O$_3$ grey: y = 0.1; magenta: y = 0.2; violet: y = 0.3.
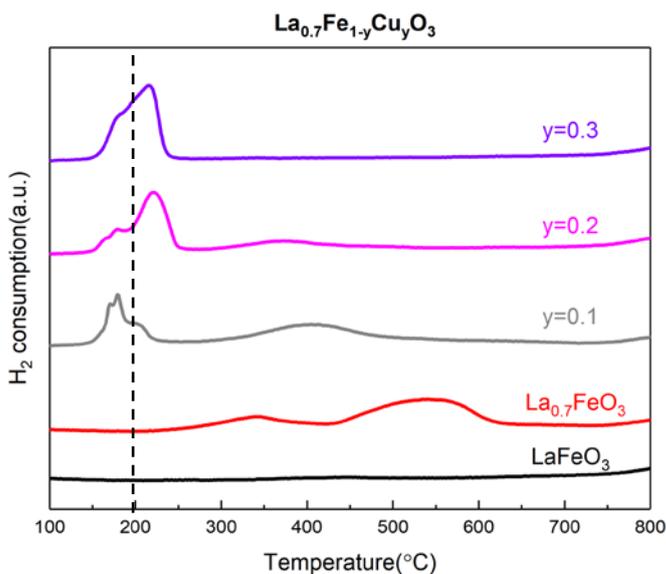
Fig. 8.4. H$_2$ consumption curves plotted against temperature for La-deficient perovskites doped with copper La$_{0.7}$Fe$_{1-y}$Cu$_y$O$_3$ grey: y = 0.1; magenta: y = 0.2; violet: y = 0.3.

According to Fig. 8.5., rhodium loading on La$_{0.6}$Ca$_{0.1}$Fe$_{0.8}$Cu$_{0.2}$O$_3$ caused the splitting of the reduction peak below 300℃ caused the splitting of the the overlap of Rh^{3+} and Cu^{2+} reduction processes. For Rh/La$_{0.6}$Ca$_{0.2}$Fe$_{0.8}$Cu$_{0.2}$O$_3$ and Rh/La$_{0.6}$Ca$_{0.4}$Fe$_{0.8}$Cu$_{0.2}$O$_3$, the H/M ratio reached close to the maximum value 3.0. In addition, the largest hydrogen consumption was observed on Rh/La$_{0.6}$Ca$_{0.4}$Fe$_{0.8}$Cu$_{0.2}$O$_3$. As a matter of fact, this latter composition exhibits a peculiar behavior already mentioned on Rh/LaFe$_{0.7}$Cu$_{0.3}$O$_3$ corresponding to stoichiometric perovskite compositions. Indeed, the same high temperature reduction process is observable above 500°C. Given that this composition is associated with the most pronounced unit cell contraction, it is thereby assumed that crystal defects resulting from introduction of calcium and copper could be beneficial to rhodium diffusion thus improving the overall reducibility of sample.
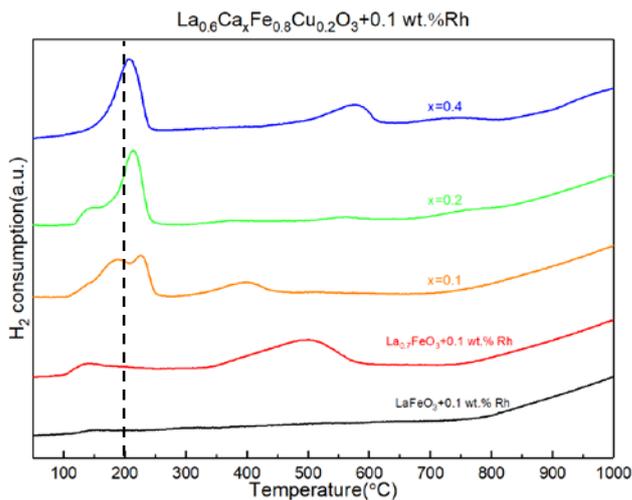
Fig. 8.5. H$_2$ consumption curves plotted against temperature for Rh/La$_{0.6}$Ca$_x$Fe$_{0.8}$Cu$_{0.2}$O$_3$ orange:x=0.1; green:x=0.2; blue:x=0.4.
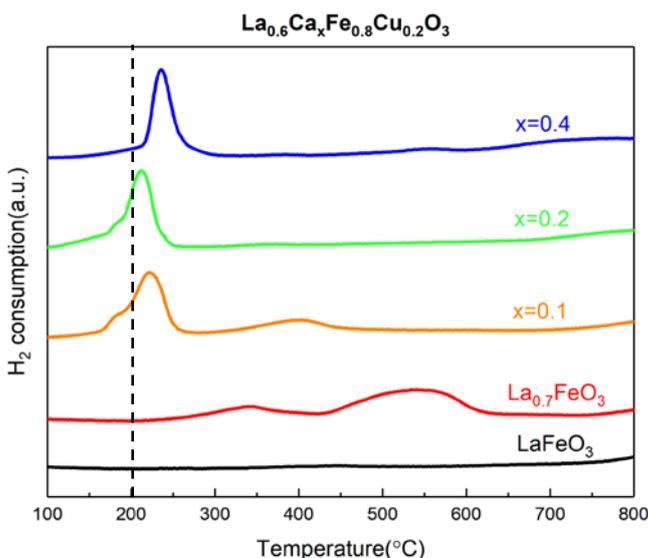
Fig. 8.6. H$_2$ consumption curves plotted against temperature for calcium and copper co-doped perovskites La$_{0.6}$Ca$_x$Fe$_{0.8}$Cu$_{0.2}$O$_3$ orange:x=0.1; green:x=0.2; blue:x=0.4.

Semi-quantitative exploitation is summarized in Table 8.2. Total H$_2$ uptakes are reported showing that calcium incorporation improves the reducibility. It is not easy to decompose the overall profile into different components because probably significant overlapping must be taken into account. Accordingly, a rough estimation of the H/M (with M = Cu, Fe and Rh) ratio has been done with values reported in Table 8.2. As seen, a continuous increase is observable up to a maximum values obtained on Rh/La$_{0.6}$Ca$_{0.4}$Fe$_{0.8}$Cu$_{0.2}$O$_3$. This evolution is in relative agreement with previous observations related to the formation of more reducible extra framework oxidic iron species on La-deficient composition while they are unreducible in octahedral coordination in the perovskite lattice of the stoichiometric LaFeO$_3$. Hence, they can contribute on the H/M ratio. In parallel, the reduction of Cu^{2+} and Rh^{3+} occur but is usually incomplete with H/M lower those expected in case of complete reduction of Rh^{3+} and Cu^{2+}. Calcium substitution provides interesting observations because for the stoichiometric compositions the reduction of extra framework iron species is no longer observed which means that the highest H/M values reflect a greater reducibility of Rh^{3+} and Cu^{2+} stabilized both in the state of RhO$_x$ and or CuO weakly interacting with the perovskite and/or isolated Rh^{3+} and Cu^{2+} in strong interaction inside the perovskite lattice.

Table 8.2. Detailed H_2-TPR results for perovskites ABO_3+0.1 wt.%Rh (A = La, Ca; B = Fe, Cu)

Catalyst	H_2 total uptake (mmol g^{-1})^a	H/M^{b,c}	T_{max} reduction peaks (°C)		
			1st	2nd	3rd
Rh/LaFeO$_3$	0.003	0.617	149.8	-	-
Rh/La$_{0.7}$FeO$_3$	1.656	-	138.7	500.6	-
Rh/LaFe$_{0.9}$Cu$_{0.1}$O$_3$	0.621	1.672	111.2	219.5	477.9
Rh/LaFe$_{0.8}$Cu$_{0.2}$O$_3$	1.101	1.703	127.9	220.6	521.8
Rh/LaFe$_{0.7}$Cu$_{0.3}$O$_3$	1.920	1.783	155	229.9	454.2
Rhd/La$_{0.7}$Fe$_{0.9}$Cu$_{0.1}$O$_3$	1.467	2.519	178.1	406.1	-
Rh/La$_{0.7}$Fe$_{0.8}$Cu$_{0.2}$O$_3$	1.484	2.416	95.1	213.8	374.2
Rh/La$_{0.7}$Fe$_{0.7}$Cu$_{0.3}$O$_3$	1.680	2.265	174.4	-	-
Rh/La$_{0.6}$Ca$_{0.1}$Fe$_{0.8}$Cu$_{0.2}$O$_3$	1.884	2.591	226.2	398.3	-
Rh/La$_{0.6}$Ca$_{0.2}$Fe$_{0.8}$Cu$_{0.2}$O$_3$	1.717	2.994	214.2	371.4	557.4
Rh/La$_{0.6}$Ca$_{0.4}$Fe$_{0.8}$Cu$_{0.2}$O$_3$	2.247	2.996	208.3	576.4	-

Note :

a Total H_2 consumption was calculated taking into account the temperature range 50-700°C.

b Individual reduction peak at temperature below 180°C was ascribed to Rh(+III)

c M = Cu+Rh. Assuming H_2 consumption at T<300°C was ascribed to Rh(+III) and Cu(+II) species

8.2. Oxygen mobility

Previous experiments showed that Oxygen TPD can characterize low temperature desorption processes labeled α-O_2 corresponding to desorption of chemisorbed O^{2-}/O^- species on surface oxygen vacancies whereas desorption taking place at much higher temperature is related to lattice oxygen desorption β-O_2. Accordingly, such experiments can complement information given by H_2-TPR experiments regarding the role of rhodium to activate at lower temperature α-O_2 and β-O_2 processes at higher temperature. Indeed, a convergence between these two types of experiments could be useful to identify rhodium in different coordination state corresponding to weak or strong interaction.

The comparison of Figs. 8.7.(A) and (B) is useful to underline the influence of Rh deposited on $LaFe_{1-y}Cu_yO_3$. As a general trend for all samples oxygen desorption is weak but becomes more distinguishable on $LaFe_{0.7}Cu_{0.3}O_3$ with a prominent desorption peak ascribed to β-O_2 with similar maximum temperature in the presence and in the absence of rhodium. On this specific sample, but also for lower Cu content, one can observe that the presence of Rh is accompanied to broad and weak signal at lower temperature which corresponds to α-O_2. Based on this comparison, rhodium would slightly activate the desorption of suprafacial oxygen.
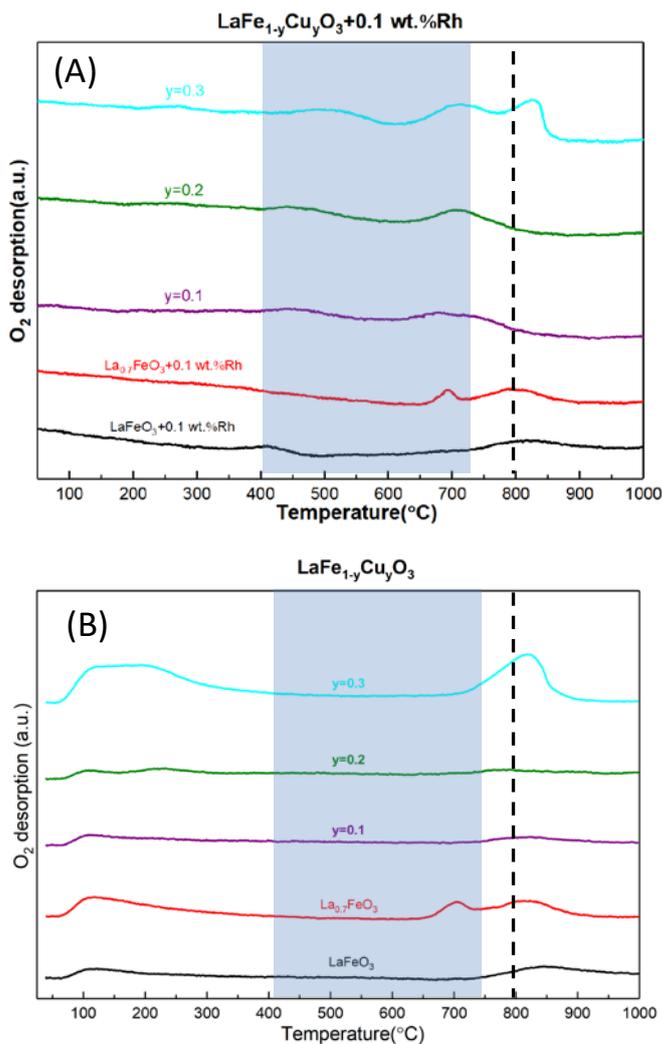
Fig. 8.7. O$_2$-TPD profiles on Rh-doped LaFe$_{1-y}$Cu$_y$O$_3$ (A) and LaFe$_{1-y}$Cu$_y$O$_3$ (B) : purple: y = 0.1; olive: y = 0.2; cyan: y = 0.3.

Oxygen desorption profiles vs. temperature recorded on Rh/La$_{0.7}$Fe$_{1-y}$Cu$_y$O$_3$ do not reveal additional feature. The influence of Rhodium is weak on O$_2$ desorption. As seen in Fig. 8.8. similar patterns to those of PGM-free perovskites are obtained which essentially underlines a prominent β-O$_2$ desorption process.

Ca substitution provides more interesting information. Regarding the parent materials and the La-deficient composition containing the lowest amount of calcium, i.e. La$_{0.6}$Ca$_{0.1}$Fe$_{0.8}$Cu$_{0.2}$O$_3$, it is obvious that Rh incorporation has only a weak impact on the bulk oxygen mobility in comparison with PGM-free perovskites (Fig.8.9(B).). Subsequent increase in Ca content (La$_{0.6}$Ca$_{0.2}$Fe$_{0.8}$Cu$_{0.2}$O$_3$) clearly shows a shift of β-O$_2$ desorption to lower temperature. But the most significant change appears when rhodium is dispersed on the stoichiometric La$_{0.6}$Ca$_{0.4}$Fe$_{0.8}$Cu$_{0.2}$O$_3$ perovskite because an additional desorption process takes place at lower temperature in the range 550-700°C. It is not easy to ascribe this extra desorption but according to the literature data it should match with β-O$_2$ instead of α-O$_2$ desorption. It is therefore proposed that Rh loading on the stoichiometric composition La$_{0.6}$Ca$_{0.4}$Fe$_{0.8}$Cu$_{0.2}$O$_3$ makes the iron cations in B site more reducible which could be related

to a greater stabilization of unusual Fe^{4+} species detected from Mössbauer spectroscopy, resulting in a better lattice and surface oxygen mobility. This observation seems in rather good agreement with the appearance of an extra-reduction process on this sample in the temperature range 550-700°C.
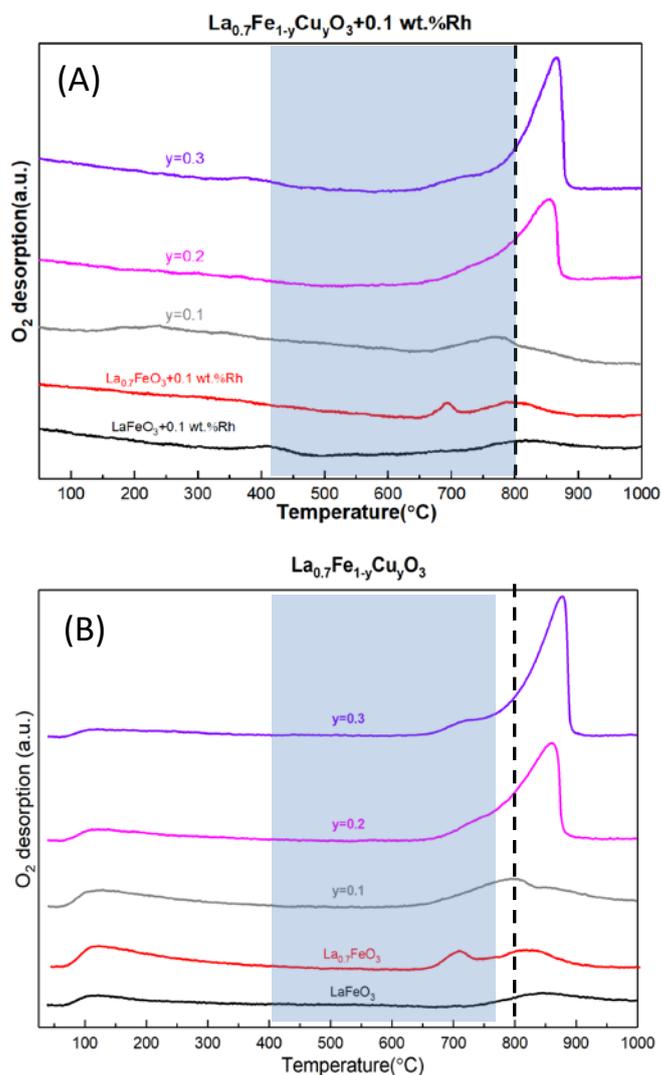
Fig. 8.8. O$_2$-TPD profiles of Rh-doped (A) and un-doped (B) La$_{0.7}$Fe$_{1-y}$Cu$_y$O$_3$. Purple: y = 0.1; olive: y = 0.2; cyan: y = 0.3.
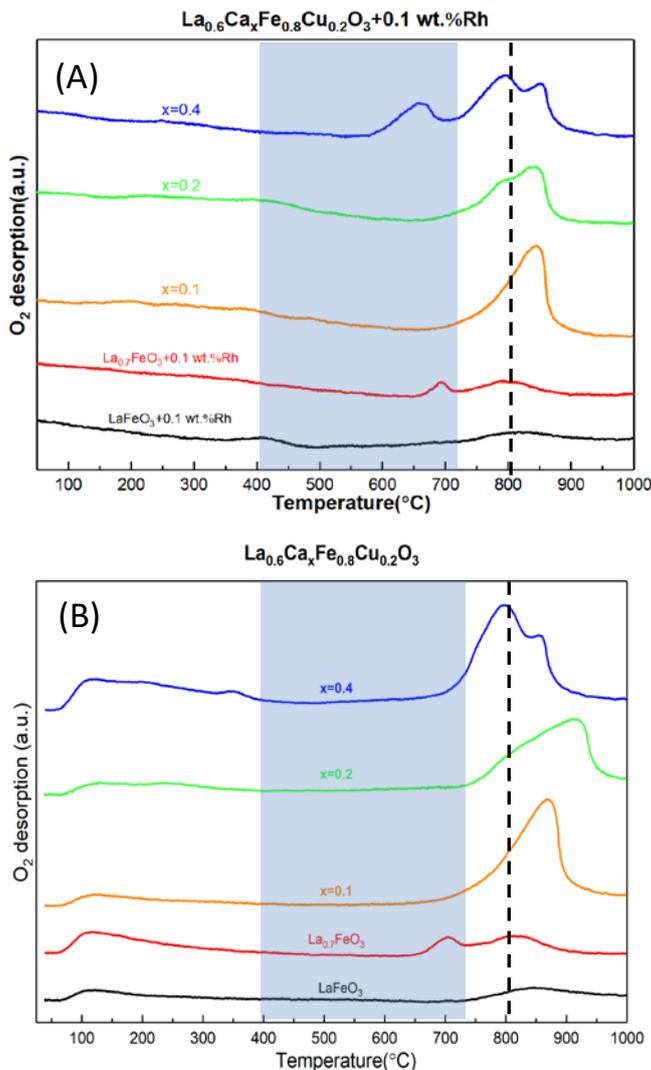
Fig. 8.9. O_2-TPD profiles of Rh-doped (A) and un-doped (B) $La_{0.6}Ca_{1-x}Fe_{0.8}Cu_{0.2}O_3$. Purple: x = 0.1; olive: x = 0.2; cyan: x = 0.4.

8.3. Surface analysis through XPS measurements

Surface properties of Rh-loaded perovskites were investigated using X-ray Photoelectron Spectroscopy. Rh 3d, La 3d, Ca 2p, Fe 2p, Cu 2p and O 1s core levels were investigated. The corresponding photopeaks are reported in Figs. 8.10.-8.12. Binding energy and relative surface compositions of oxygen species are collected in Table 8.3. Surface atomic composition of each element is shown in Table 8.4.

La $3d_{5/2}$ photopeak exhibits a typical doublet at B.E. value around 833.0-834.0 eV, suggesting the presence of stable La^{3+} in the composite materials. The shake-up satellite at B.E. value around 719 eV revealed the preferential stabilization of Fe^{3+} species. The presence of Cu^{2+} species was confirmed by the photopeak at B.E. value around 933 eV combined with the shake-up satellite at B.E. 938-948 eV while the marked difference of peak intensity highlighted the variation of surface copper content which is strongly dependent on the structural composition and doping degree of the substituted perovskite, especially for the Ca and Cu co-doped compositions (Fig. 8.12.). The photopeak at B.E. 346 eV is typical of Ca^{2+} species. The presence of Rh^{3+} can be confirmed by the photopeak at B.E. around 309 eV.

Regarding the photopeak O 1s, two components are distinguishable : The most intense contribution at low B.E. 528.7-530 eV is ascribed to lattice oxygen while the shoulder in the range of 531.0-532.0 eV can be attributed to suprafacial oxygen species (i.e. O$^-$, O$_2^-$)[A. Schön 2018]. Semi-quantitative analysis reveals the same tendencies as those discussed on the bare samples. As shown a surface lanthanum enrichment is usually observed on stoichiometric perovskite composition. The atomic Cu/Fe is not significantly modified after Rh addition. As a matter of fact, surface and elemental compositions strongly deviate mainly for Rh/(A+B) ratio. In all cases, a sharp surface rhodium enrichment occurs but not in the same extent. Indeed, this trend accentuates when rhodium is deposited on La-deficient perovskite compositions and could be related to a greater aggregation of RhO$_x$ weakly interacting. As preliminary discussed in the case of Pd supported catalysts, the well-dispersed RhO$_x$ species could be more reducible due to stronger interaction with the perovskite support. In order to get more insight into the chemical environment of rhodium and related reducibility, H$_2$ titration measurements allowed the determination of the metallic dispersion. As exemplified in Table 8.5., a clear tendency appears showing that higher Rh dispersions are obtained on the series LaFe$_{1-y}$Cu$_y$O$_3$ whereas a significant loss of dispersion is noticeable on La$_{0.7}$Fe$_{1-y}$Cu$_y$O$_3$. Such comparison seems in rather good agreement with the evolution observed on Rh/(A+B) values which increase for La-deficient support materials indicating a greater agglomeration of RhO$_x$ in weak interaction. Based on this comparison it seems obvious that La-deficiency does not promote Rh dispersion and seems to be in rather good agreement with O$_2$-TPD observations which show that desorption of suprafacial oxygen is promoted by well-dispersed metallic Rh species preferentially on LaFe$_{1-y}$Cu$_y$O$_3$ whereas no beneficial effect is noticeable when rhodium is poorly dispersed on La-deficient perovskites.

It is interesting to note that the series Rh/La$_{0.6}$Ca$_x$Fe$_{0.8}$Cu$_{0.2}$O$_3$ obeys different observations. As seen the metal dispersion decreases with a rise in Ca composition reaching a minimum value on Rh/La$_{0.6}$Ca$_{0.4}$Fe$_{0.8}$Cu$_{0.2}$O$_3$. On the contrary a lowering of the Rh/(A+B) ratio can be distinguished which contradict previous tendency. While we cannot exclude the formation of large RhO$_x$ clusters on Rh/La$_{0.6}$Ca$_{0.4}$Fe$_{0.8}$Cu$_{0.2}$O$_3$, the lowest dispersion in this series could reflect the coexistence of well-dispersed RhO$_x$ or less reducible isolated Rh^{3+} in strong interaction with the perovskite support which could match with lower Rh/(A+B) ratio. Such explanation seems to be in rather good agreement with H$_2$-TPR measurements in Fig. 8.5. which highlight an extra reduction process above 500°C on Rh/La$_{0.6}$Ca$_{0.4}$Fe$_{0.8}$Cu$_{0.2}$O$_3$ which could be assigned to Rh^{3+} species. Accordingly, the selected H$_2$ pre-treatment in H$_2$ at 300°C prior to chemisorption measurements is probably unable to reduce these oxidic Rh species preserving their integrity and explaining underestimated Rh dispersion.

Finally, let us note that this explanation also corroborates O$_2$ desorption features which show that the extra desorption of oxygen occurring in the range 600-700°C on Rh/La$_{0.6}$Ca$_{0.4}$Fe$_{0.8}$Cu$_{0.2}$O$_3$ could be the consequence of rhodium insertion in the first layer of the perovskite structure rather than the stabilization of Fe^{4+} with more labile Fe^{4+}-O species. Such explanation seems to be more satisfactorily because in this last case the same behavior would be expected on LaFeO$_3$ also capable of stabilizing Fe^{4+} as demonstrated from Mössbauer spectroscopy.
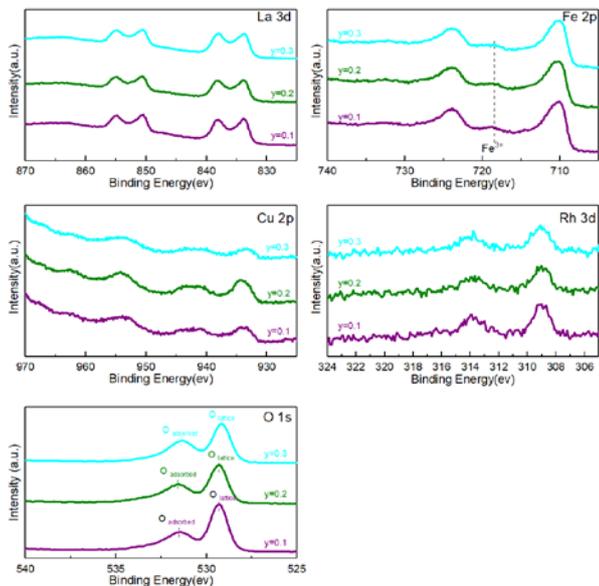
Fig. 8.10. Characteristic La 3d, Fe 2p, Cu 2p, Rh 3d and O 1s photopeaks for $Rh/LaFe_{1-y}Cu_yO_3$: purple: y = 0.1; olive: y = 0.2; cyan: y =0.3.
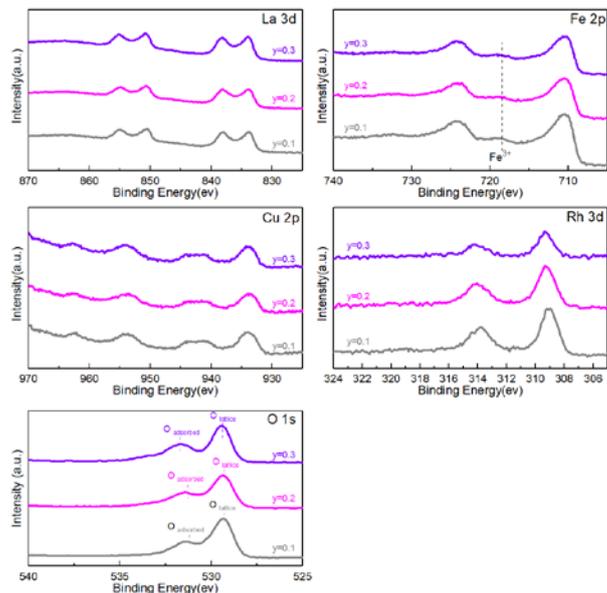
Fig. 8.11. Characteristic La 3d, Fe 2p, Cu 2p, Rh 3d and O 1s photopeaks for $Rh/La_{0.7}Fe_{1-y}Cu_yO_3$ grey: y = 0.1; magenta: y = 0.2; violet: y = 0.3.
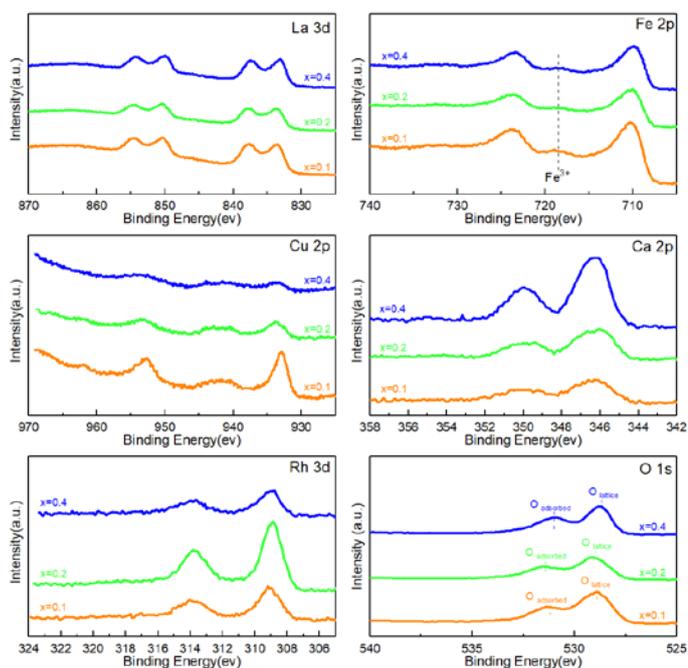
Fig. 8.12. Characteristic La 3d, Fe 2p, Cu 2p, Ca 2p, Rh 3d and O 1s photopeaks for $Rh/La_{0.6}Ca_xFe_{0.8}Cu_{0.2}O_3$: orange: x = 0.1; green: x = 0.2; blue: x = 0.4.

Table 8.3. Binding energy of each element and abundance of oxygen species

Catalyst	Binding Energy (eV)							Relative surf. Comp. O[a]		
						O 1s				
	La 3d	Ca 2p	Fe 2p	Cu 2p	Rh 3d	Ads. oxygen	Lattice oxygen	$O_{ads.}$ (%)	$O_{lattice}$ (%)	$\dfrac{O_{adsorbed}}{O_{lattice}}$
$Rh/LaFeO_3$	833.8	-	710.2	-	309.4	531.4	529.3	51.7	48.3	$1.07/1.28^c$
$Rh/La_{0.7}FeO_3$	834.0	-	710.5	-	309.2	531.0	529.5	55.6	44.4	$1.25/1.61^c$
$Rh/LaFe_{0.9}Cu_{0.1}O_3$	833.8	-	710.0	933.4	309.0	531.5	529.3	45.4	54.6	$0.83/0.96^c$
$Rh/LaFe_{0.8}Cu_{0.2}O_3$	833.9	-	710.0	933.6	309.0	531.6	529.3	50.4	49.6	$1.02/1.22^c$
$Rh/LaFe_{0.7}Cu_{0.3}O_3$	833.6	-	710.1	933.3	309.1	531.4	529.1	51.0	49.0	$1.04/1.14^c$
$Rh/La_{0.7}Fe_{0.9}Cu_{0.1}O_3$	833.8	-	710.4	934.1	309.0	531.2	529.3	43.0	57.0	$0.75/0.80^c$
$Rh/La_{0.7}Fe_{0.8}Cu_{0.2}O_3$	833.8	-	710.2	933.4	309.3	531.3	529.3	52.5	47.5	$1.11/0.75^c$
$Rh/La_{0.7}Fe_{0.7}Cu_{0.3}O_3$	833.9	-	710.2	933.6	309.4	531.7	529.4	51.5	48.5	$1.06/0.67^c$
$Rh/La_{0.6}Ca_{0.1}Fe_{0.8}Cu_{0.2}O_3$	833.5	346.3	710.1	932.9	309.2	531.2	528.9	39.4	60.6	$0.65/0.78^c$
$Rh/La_{0.6}Ca_{0.2}Fe_{0.8}Cu_{0.2}O_3$	833.5	346.0	710.0	933.9	308.9	531.4	529.0	44.6	55.4	$0.81/0.88^c$
$Rh/La_{0.6}Ca_{0.4}Fe_{0.8}Cu_{0.2}O_3$	833.0	346.1	709.5	933.4	308.8	531.0	528.7	54.5	45.5	$1.20/1.05^c$

Note:

a $O_{adsorbed} + O_{lattice} = 1$

b relative abundance of oxygen species was calculated from deconvolution of O 1s photopeak

c on bare perovskites

Table 8.4. Surface atomic composition calculated from XPS analysis

Catalyst	Surface atomic composition (%)							A/B	Cu/Fe	Rh/(A+B) $\times 10^{-3}$
	O	La	Fe	Rh	C	Cu	Ca			
$Rh/LaFeO_3$	45.05	12.01	8.31	0.26	34.37	0.00	-	1.45	-	12.64
$Rh/La_{0.7}FeO_3$	46.18	10.58	14.38	0.83	28.04	0.00	-	0.74	-	33.05
$Rh/LaFe_{0.9}Cu_{0.1}O_3$	43.81	13.48	7.68	0.19	33.43	1.42	-	1.48	0.18	8.42
$Rh/LaFe_{0.8}Cu_{0.2}O_3$	40.56	11.96	6.68	0.18	38.61	2.01	-	1.38	0.30	8.81
$Rh/LaFe_{0.7}Cu_{0.3}O_3$	43.67	14.33	6.84	0.22	33.91	1.03	-	1.82	0.15	9.95
$Rh/La_{0.7}Fe_{0.9}Cu_{0.1}O_3$	46.40	10.44	14.20	0.65	25.20	3.11	-	0.60	0.22	23.53
$Rh/La_{0.7}Fe_{0.8}Cu_{0.2}O_3$	41.64	10.03	10.19	0.60	35.17	2.38	-	0.80	0.23	26.43
$Rh/La_{0.7}Fe_{0.7}Cu_{0.3}O_3$	40.67	10.50	8.38	0.30	37.68	2.48	-	0.97	0.30	13.81
$Rh/La_{0.6}Ca_{0.1}Fe_{0.8}Cu_{0.2}O_3$	43.03	10.22	12.13	0.44	30.69	2.20	1.29	0.80	0.18	17.18
$Rh/La_{0.6}Ca_{0.2}Fe_{0.8}Cu_{0.2}O_3$	42.36	9.50	8.53	1.12	34.43	1.81	2.25	1.14	0.21	50.51
$Rh/La_{0.6}Ca_{0.4}Fe_{0.8}Cu_{0.2}O_3$	44.94	10.62	9.75	0.43	29.22	0.88	4.18	1.39	0.09	16.76

Table 8.5. Metallic dispersion of rhodium measured by H_2 chemisorption analysis

Catalyst	Metal dispersion (%)	Metallic Surface Area (m²/g metal):	Rh/(A+B) $\times 10^{-3}$
$Rh/LaFeO_3$	12.92	56.87	12.64/1.02[a]
$Rh/La_{0.7}FeO_3$	5.01	22.03	33.05/0.96[a]
$Rh/LaFe_{0.9}Cu_{0.1}O_3$	15.31	67.40	8.42/1.05[a]
$Rh/LaFe_{0.8}Cu_{0.2}O_3$	21.75	95.74	8.81/1.13[a]
$Rh/LaFe_{0.7}Cu_{0.3}O_3$	22.52	99.11	9.95/1.19[a]
$Rh/La_{0.7}Fe_{0.9}Cu_{0.1}O_3$	10.85	47.74	23.53/0.96[a]
$Rh/La_{0.7}Fe_{0.8}Cu_{0.2}O_3$	2.40	10.57	26.43/0.80[a]
$Rh/La_{0.7}Fe_{0.7}Cu_{0.3}O_3$	6.29	27.68	13.81/0.99[a]
$Rh/La_{0.6}Ca_{0.1}Fe_{0.8}Cu_{0.2}O_3$	10.38	45.71	17.18/0.98[a]
$Rh/La_{0.6}Ca_{0.2}Fe_{0.8}Cu_{0.2}O_3$	4.60	20.25	50.51/0.95[a]
$Rh/La_{0.6}Ca_{0.4}Fe_{0.8}Cu_{0.2}O_3$	2.64	11.64	16.76/0.85[a]

Note : a calculated from elemental analysis.

8.4. Catalytic properties

8.4.1. Oxidative properties

Similarly to palladium, the investigation of catalytic properties has been restricted to supported rhodium catalysts on Ca-subsituted perovskites, $La_{0.7}Fe_{0.8}Cu_{0.5}O_3$, $La_{0.7}FeO_3$ and $LaFeO_3$. Conversion and selectivity has been compared to those obtained on bare perovskites as well as on the benchmark $Pd/Ce_{0.5}Zr_{0.5}O_2$ catalyst provided by Johnson Matthey. Conversion curves for CO, propene and propane oxidation measured at different richness from lean to rich conditions are reported in Fig. 8.13. Particular attention was also paid to stoichiometric conditions with two TPR experiments STO1 and STO2 corresponding to more stabilized surfaces after equilibration of surface composition and oxidation state of the active elements.

First comments arise by examining the catalytic behavior of the benchmark $Pd/Ce_xZr_{1-x}O_2$: A remarkable low activity is observed for CO oxidation in stoichiometric conditions which surprisingly outperforms that measured in lean condition in the presence of a slight excess of oxygen. It is also worth to note that the conversion obtained in rich condition is only slightly delayed at the initial stage of the reaction. The same reactivity sequence is observed for propene with conversion taking place at higher temperature. On the hand, it clearly appears that propene conversion in rich conditions is strongly inhibited and probably goes through different reaction pathways than in lean or stoichiometric conditions in conjunction with the slow decrease in CO conversion which likely corresponds to extra production of CO through propene reforming reaction in rich atmosphere. Finally, the residual conversion of propane is low especially in lean and stoichiometric conditions.

However, remarkably propane conversion occurs more readily in rich condition likely due to reforming instead of total oxidation reaction similarly to propene. The comparison of STO1 and STO2 conversion profiles only shows a slight deactivation.

Regarding perovskite-supported rhodium catalysts, it clearly appears that the benchmark system has superior performances. Such a trend was reasonably expected because palladium is more recognized for its oxidative properties whereas rhodium should convert more readily NO. Anyway, acceptable conversions were obtained especially for propane oxidation where Rh-loaded perovskites rival with the benchmark system except in rich condition. For CO oxidation, the best systems are $Rh/La_{0.7}Fe_{0.8}Cu_{0.2}O_3$, $Rh/La_{0.6}Ca_{0.1}Fe_{0.8}Cu_{0.2}O_3$ and $Rh/La_{0.6}Ca_{0.2}Fe_{0.8}Cu_{0.2}O_3$ in stoichiometric and rich atmosphere. However, there is no gain in conversion due to Rh addition in lean condition. For propene oxidation, the same tendencies as those described on the benchmark system are noticeable and still revealing a complete inactivity of rhodium to convert propene in lean conditions. The evolution of propene conversion in rich conditions correspond to the existence of two ranges of temperatures which clearly appear on $Rh/La_{0.6}Ca_{0.4}Fe_{0.8}Cu_{0.2}O_3$ and correspond to a concomitant production of CO with a rise in temperature previously ascribed to the intervention of reforming and/or partial reactions. It is worthnoting that these operating conditions are quite specific because in stoichiometric conditions the superior performances of $Rh/La_{0.7}Fe_{0.8}Cu_{0.2}O_3$, $Rh/La_{0.6}Ca_{0.1}Fe_{0.8}Cu_{0.2}O_3$ are evidenced. Slight deactivation of Rh-loaded catalysts was noted from STO2 experiments.

As a conclusion while the catalytic behavior was found strongly influenced by Rh addition to the perovskite substrate, it seems obvious that the perovskite composition impact more importantly the catalytic behavior when rhodium is incorporated. As already stated in chapter V., extraction and partial segregation of copper and redispersion at the surface has a beneficial effect in case of careful monitoring to avoid strong agglomeration for CO and propene oxidation. Reasonably we retrieve in this study the best compromise when Rh is supported on $La_{0.7}Fe_{0.8}Cu_{0.2}O_3$, and $La_{0.6}Ca_{0.1}Fe_{0.8}Cu_{0.2}O_3$. Ca-doping insures a better control of copper extraction avoiding surface aggregation. However, TPR measurements evidence different reaction routes for propene conversion in rich conditions and in these conditions $Rh/La_{0.6}Ca_{0.4}Fe_{0.8}Cu_{0.2}O_3$ is the most active catalyst at low temperature corresponding to totally different surface properties. As a matter of fact, segregation of extra framework CuO species on $Rh/La_{0.7}Fe_{0.8}Cu_{0.2}O_3$, and $Rh/La_{0.6}Ca_{0.1}Fe_{0.8}Cu_{0.2}O_3$ could induce contraction effects on RhO_x species then facilitating their aggregation into larger RhO_x clusters. This process can lead to more reducible oxidic rhodium species due to weaker interactions with the perovskite. This could explain the superior oxidative properties of Rh supported on $La_{0.7}Fe_{0.8}Cu_{0.2}O_3$, and $La_{0.6}Ca_{0.1}Fe_{0.8}Cu_{0.2}O_3$. On the other hand, surface characterization led to different surface properties for $Rh/La_{0.6}Ca_{0.4}Fe_{0.8}Cu_{0.2}O_3$ because calcium at high concentration blocks copper extraction process then suppressing their detrimental effect on the rhodium dispersion. As explained from H_2-TPR, O_2-TPD, XPS and H_2-chemisorption measurement one cannot totally rule out partial diffusion of rhodium thanks to the promotion of defective sites on this catalyst.

By examining literature data it is recognized that high Rh dispersion and strong interaction with a reducible support improve the performance in hydrocarbon reforming by

minimizing deactivation phenomena. [V. Shanmugam 2018; T.B. Shoynkhorova 2018] Yentekakis et al. suggested for the dry reforming that well-dispersed Rh$_2$O$_3$ in strong interaction with ceria-zirconia support can be destabilized under reaction conditions with high oxygen lability due to O$_2$−backspillover that weakens the Rh-O bond. Hence greater activity and stability would be related to metallic Rh^0 at the vicinity of anionic vacancies which could adsorb and dissociate CO$_2$. [I.V. Yentekakis 2019]
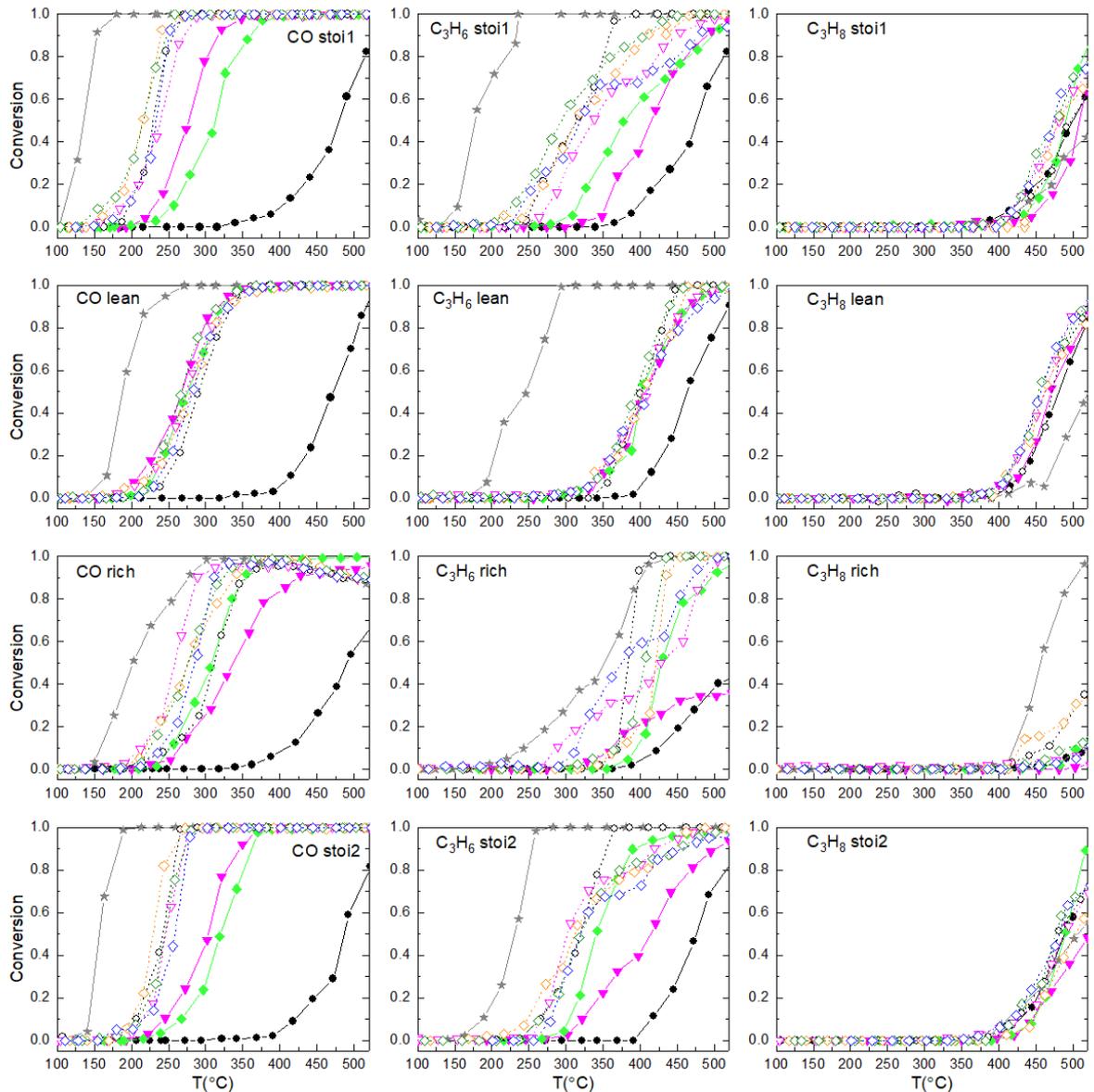
Fig. 8.13. Catalytic oxidation performance of iron-based perovskite solid ABO$_3$ (A=La, Ca; B= Fe, Cu) +0.1 wt.%Rh. Grey star solid line: commercial reference catalyst(★); black circle solid line: LaFeO$_3$(●); magenta downward triangle solid line: La$_{0.7}$Fe$_{0.8}$Cu$_{0.2}$O$_3$(▼); green diamond solid line:La$_{0.6}$Ca$_{0.2}$Fe$_{0.8}$Cu$_{0.2}$O$_3$(◆); black hollow circle dash line: LaFeO$_3$+0.1 wt%.Rh(○0;magenta downward hollow triangle dash line: La$_{0.7}$Fe$_{0.8}$Cu$_{0.2}$O$_3$+0.1 wt.%Rh (▽); orange diamond dash line: La$_{0.6}$Ca$_{0.1}$Fe$_{0.8}$Cu$_{0.2}$O$_3$+0.1 wt.%Rh(◇); olive diamond dash line: La$_{0.6}$Ca$_{0.2}$Fe$_{0.8}$Cu$_{0.2}$O$_3$+0.1 wt.%Rh(◇); blue diamond dash line: La$_{0.6}$Ca$_{0.4}$Fe$_{0.8}$Cu$_{0.2}$O$_3$+0.1wt.%Rh(◇).

8.4.2. Reductive properties

Compared to palladium, the reduction of NO on Rh-loaded perovskites starts at lower temperature demonstrating improved performances during the cold start of engine. It is also worthwhile to note that these systems outperform the benchmark catalyst except in rich conditions.

Conversion profiles vs. temperature recorded from STO1 and STO2 experiments exhibit a maximum near 310°C corresponding to a conversion of 52% and 55% respectively. The following ranking can be established from STO1 at this temperature: Rh/La$_{0.6}$Ca$_{0.4}$Fe$_{0.8}$Cu$_{0.2}$O$_3$~Rh/La$_{0.6}$Ca$_{0.2}$Fe$_{0.8}$Cu$_{0.2}$O$_3$> Rh/LaFeO$_3$ > Rh/La$_{0.6}$Ca$_{0.1}$Fe$_{0.8}$Cu$_{0.2}$O$_3$ ~ Rh/La$_{0.7}$Fe$_{0.8}$Cu$_{0.2}$O$_3$ > Pd/Ce$_x$Zr$_{1-x}$O$_2$. At increasing temperature the highest conversion values is recorded on Rh/La$_{0.6}$Ca$_{0.2}$Fe$_{0.8}$Cu$_{0.2}$O$_3$. After successive lean/rich cycles, STO2 sequence led to convergent conversion irrespective of the perovskite composition. At higher temperature an increase of the activity in NO conversion is discernible on Rh/La$_{0.6}$Ca$_{0.2}$Fe$_{0.8}$Cu$_{0.2}$O$_3$ and Rh/LaFeO$_3$ whereas they decline on the other samples. Based on this comparison it is noticeable that different tendencies were observed on Rh-loaded perovskite catalysts because the most efficient system corresponded to Rh/La$_{0.6}$Ca$_{0.4}$Fe$_{0.8}$Cu$_{0.2}$O$_3$ in the whole temperature range of this study.

Regarding the performances in rich conditions the following reactivity sequence can be established: Rh/La$_{0.7}$Fe$_{0.8}$Cu$_{0.2}$O$_3$ > Rh/La$_{0.6}$Ca$_{0.4}$Fe$_{0.8}$Cu$_{0.2}$O$_3$ >> Rh/La$_{0.6}$Ca$_{0.2}$Fe$_{0.8}$Cu$_{0.2}$O$_3$ ~ Rh/LaFeO$_3$ > Rh/La$_{0.6}$Ca$_{0.1}$Fe$_{0.8}$Cu$_{0.2}$O$_3$. As a general trend Rh/La$_{0.6}$Ca$_{0.4}$Fe$_{0.8}$Cu$_{0.2}$O$_3$ and Rh/La$_{0.6}$Ca$_{0.2}$Fe$_{0.8}$Cu$_{0.2}$O$_3$ seem to have the best compromise.

The physicochemical features can differ according to the perovskite composition with different surface distributions in terms of metallic rhodium particles, electrophilic rhodium species, defective sites, i.e. anionic vacancies, depending on the lability of surface oxygen species. The proportion of large metallic Rh species is apparently more important on La-deficient materials which also contain less suprafacial oxygen. On the other hand the lower dispersions of Rh/La$_{0.6}$Ca$_{0.4}$Fe$_{0.8}$Cu$_{0.2}$O$_3$ and Rh/La$_{0.6}$Ca$_{0.2}$Fe$_{0.8}$Cu$_{0.2}$O$_3$ could suggest less accessible metallic Rh species, larger proportion of electrophilic Rh and a greater extent of suprafacial oxygen which can lead to the creation of anionic vacancies. Regarding the literature data, Peden et al. demonstrated the structure-sensitivity of the NO/CO on single and polycristalline rhodium catalysts [C.H.F. Peden 1995]. In this latter case, they found that large Rh particles behave like more open Rh (110) surface with high TOF values. On the other hand, small polycrystalline particles behave like close-packed compact Rh (111) surface. Based on this comparison, Rh/La$_{0.7}$Fe$_{0.8}$Cu$_{0.2}$O$_3$ should in principle exhibit the best performance. In practice it is true only in rich conditions. Indeed, in lean conditions the best performances were obtained on Ca-substituted sample where greater extent metallic Rh sites should coexist with anionic vacancies. Accordingly, the active sites could have a different composition where more dispersed Rh^0 combined with anionic vacancies could assist the dissociation of chemisorbed NO molecules [P. Granger 2002].
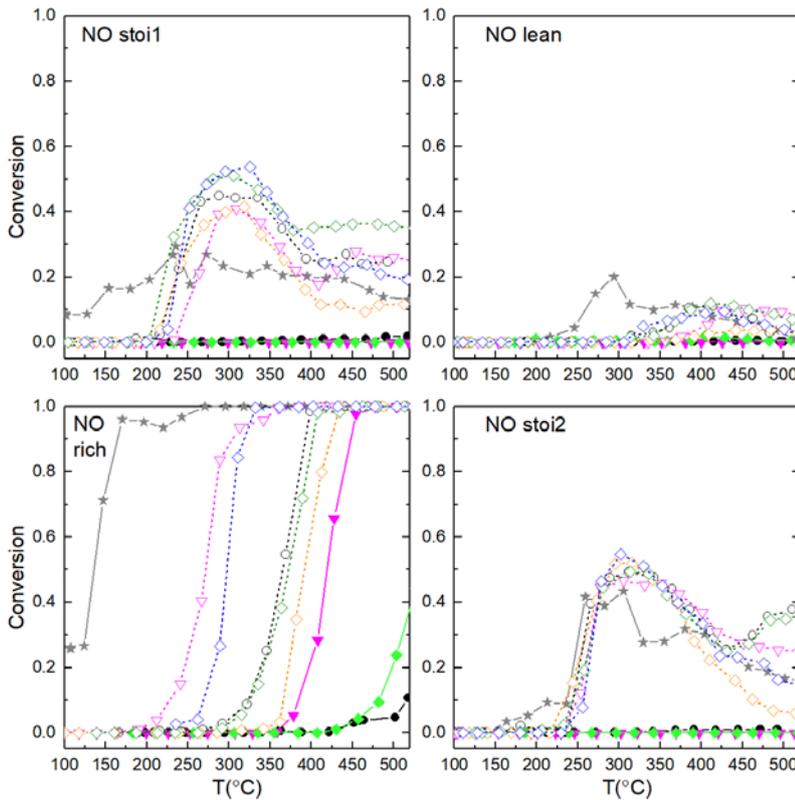
Fig. 8.14. Catalytic reduction performance of iron-based perovskite solid ABO$_3$ (A=La, Ca; B= Fe, Cu) +0.1 wt.%Rh. Grey star solid line: commercial reference catalyst (★); black circle solid line: LaFeO$_3$(●); magenta downward triangle solid line: La$_{0.7}$Fe$_{0.8}$Cu$_{0.2}$O$_3$(▼); green diamond solid line:La$_{0.6}$Ca$_{0.2}$Fe$_{0.8}$Cu$_{0.2}$O$_3$(◆); black hollow circle dash line: LaFeO$_3$+0.1 wt%.Rh(○); magenta downward hollow triangle dash line: La$_{0.7}$Fe$_{0.8}$Cu$_{0.2}$O$_3$+0.1 wt.%Rh(▽); orange diamond dash line: La$_{0.6}$Ca$_{0.1}$Fe$_{0.8}$Cu$_{0.2}$O$_3$+0.1 wt.%Rh(◇); olive diamond dash line: La$_{0.6}$Ca$_{0.2}$Fe$_{0.8}$Cu$_{0.2}$O$_3$+0.1 wt.%Rh(◇); blue diamond dash line: La$_{0.6}$Ca$_{0.4}$Fe$_{0.8}$Cu$_{0.2}$O$_3$+0.1wt.%Rh (◇).

The comparison of Pd/Ce$_x$Zr$_{1-x}$O$_2$ with Rh-loaded perovskite catalysts in terms of selectivity behavior underlines the specific role of rhodium. As seen in Figs. 8.15. and 8.16., the magnitude of changes of nitrogen selectivity is weak on the benchmark catalyst. N$_2$O is jointly formed in lean and stoichiometric conditions. In the particular case of rhodium both N$_2$ and N$_2$O also form in such operating conditions but to different extent. As shown the production of N$_2$O occurs predominantly at low temperature with a quasi-exclusive production of N$_2$O on Rh/La$_{0.6}$Ca$_{0.1}$Fe$_{0.8}$Cu$_{0.2}$O$_3$ and Rh/La$_{0.7}$Fe$_{0.8}$Cu$_{0.2}$O$_3$. A rise in temperature leads progressively to a predominant production of nitrogen, this phenomenon occurring more readily on Rh/LaFeO$_3$ stabilizing at 80%. Clearly, selectivity enhancement is observed compared to the benchmark above 375°C. Such selectivity behavior is typical of metallic rhodium sites. Previous kinetic investigations revealed that NO strongly adsorbed on Rh^0 [P. Granger 1998]. At high NO coverage, the low probability to find two nearest-neighbor sites for the dissociation of adsorbed NO molecules leads to low N coverages and a preferential reaction between N and NO to form N$_2$O. At increasing temperature, NO desorption releases vacant sites and the dissociation is accelerated then increasing the N coverage. In such case, the production of N$_2$ can occur more readily through the recombination of two nitrogen atoms.
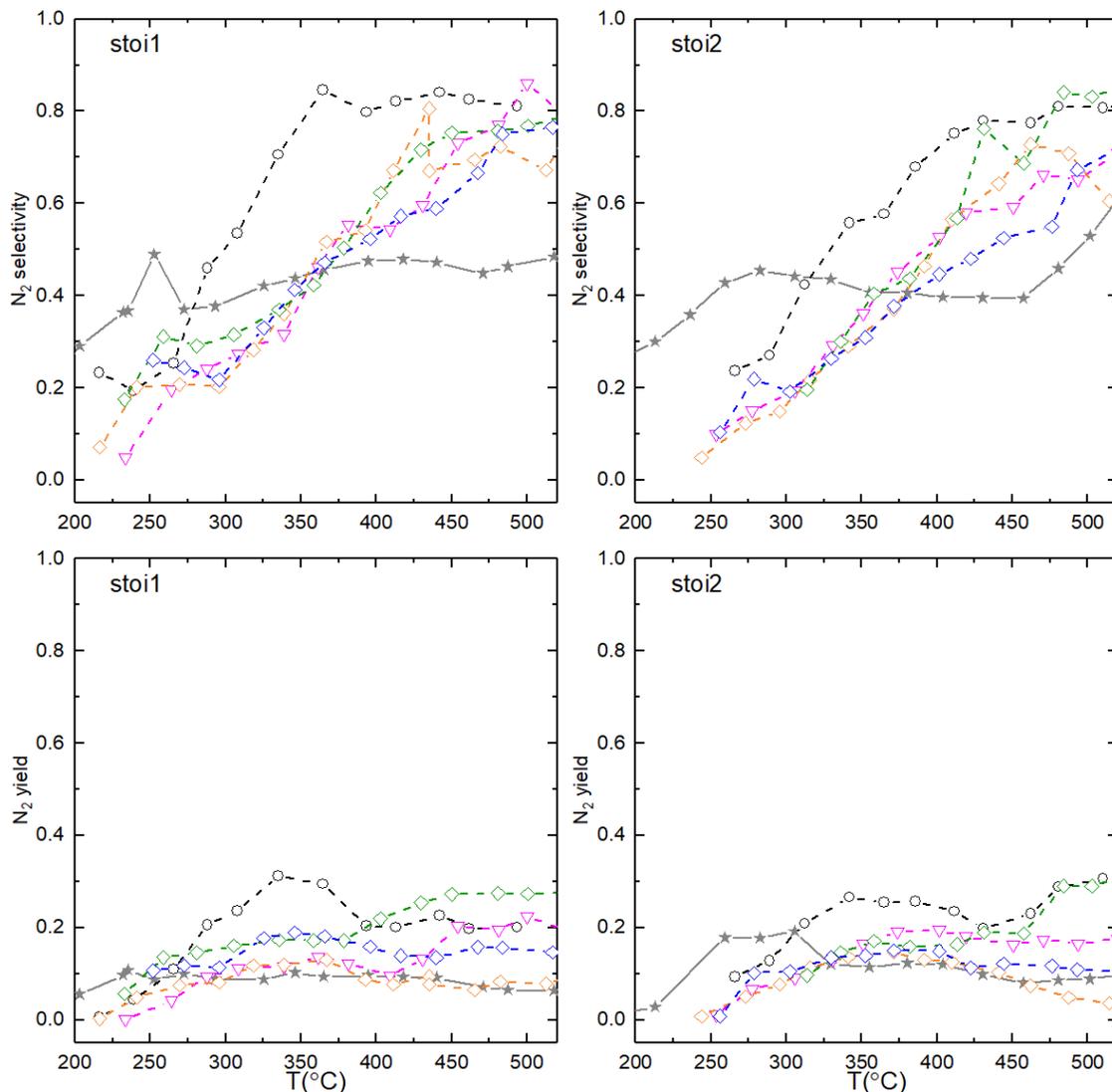
Fig. 8.15. N$_2$ selectivity and yield in stoichiometric atmosphere of iron-based perovskite solid ABO$_3$ (A=La, Ca; B= Fe, Cu) +0.1 wt.%Rh. Grey star solid line: commercial reference catalyst (★); black hollow circle dash line: LaFeO$_3$+0.1 wt%.Rh(○); magenta downward hollow triangle dash line: La$_{0.7}$Fe$_{0.8}$Cu$_{0.2}$O$_3$+0.1 wt.%Rh (▽); orange diamond dash line: La$_{0.6}$Ca$_{0.1}$Fe$_{0.8}$Cu$_{0.2}$O$_3$+0.1 wt.%Rh(◇); olive diamond dash line: La$_{0.6}$Ca$_{0.2}$Fe$_{0.8}$Cu$_{0.2}$O$_3$+0.1 wt.%Rh(◇); blue diamond dash line: La$_{0.6}$Ca$_{0.4}$Fe$_{0.8}$Cu$_{0.2}$O$_3$+0.1wt.%Rh(◇).

Fig. 8.16. N_2O selectivity and yield in stoichiometric atmosphere of iron-based perovskite solid ABO_3 (A=La, Ca; B= Fe, Cu) +0.1 wt.%Rh. Grey star solid line: commercial reference catalyst(★); black hollow circle dash line: $LaFeO_3$+0.1 wt%.Rh(◯); magenta downward hollow triangle dash line: $La_{0.7}Fe_{0.8}Cu_{0.2}O_3$+0.1 wt.%Rh (▽); orange diamond dash line: $La_{0.6}Ca_{0.1}Fe_{0.8}Cu_{0.2}O_3$+0.1 wt.%Rh(◇); olive diamond dash line: $La_{0.6}Ca_{0.2}Fe_{0.8}Cu_{0.2}O_3$+0.1 wt.%Rh(◇); blue diamond dash line: $La_{0.6}Ca_{0.4}Fe_{0.8}Cu_{0.2}O_3$+0.1wt.%Rh(◇).

Fig. 8.17. Selectivity of N$_2$, N$_2$O and NH$_3$ in rich atmosphere of iron-based perovskite solid ABO$_3$ (A=La, Ca; B= Fe, Cu) +0.1 wt.%Rh. Grey star solid line: commercial reference catalyst(☆); black hollow circle dash line: LaFeO$_3$+0.1 wt%.Rh(○); magenta downward hollow triangle dash line: La$_{0.7}$Fe$_{0.8}$Cu$_{0.2}$O$_3$+0.1 wt.%Rh (▽); orange diamond dash line: La$_{0.6}$Ca$_{0.1}$Fe$_{0.8}$Cu$_{0.2}$O$_3$+0.1 wt.%Rh(◇); olive diamond dash line: La$_{0.6}$Ca$_{0.2}$Fe$_{0.8}$Cu$_{0.2}$O$_3$+0.1 wt.%Rh(◇); blue diamond dash line: La$_{0.6}$Ca$_{0.4}$Fe$_{0.8}$Cu$_{0.2}$O$_3$+0.1wt.%Rh(◇).

With regard to the selectivity in rich condition, an outstanding observation comes from the comparison of Rh-loaded perovskite catalysts with the benchmark Pd/Ce$_x$Zr$_{1-x}$O$_2$. As seen the production of undesired ammonia on this latter catalyst is much higher in the whole temperature range. As a matter of fact, ammonia production is significantly delayed on Rh/perovskite especially on Rh/La$_{0.6}$Ca$_{0.1}$Fe$_{0.8}$Cu$_{0.2}$O$_3$ and Rh/LaFeO$_3$. However, it occurs more readily on Rh/La$_{0.7}$Fe$_{0.8}$Cu$_{0.2}$O$_3$ and Rh/La$_{0.6}$Ca$_{0.4}$Fe$_{0.8}$Cu$_{0.2}$O$_3$ which could suggest that is this operating conditions Rh/La$_{0.6}$Ca$_{0.4}$Fe$_{0.8}$Cu$_{0.2}$O$_3$ would recover a more marked metallic state. Additional information are provided by the examination of the selectivity behavior. It is noticeable the shape of the selectivity vs. temperature profile differs from that observed on the same catalysts in stoichiometric conditions. As seen a volcano-type curve is usually observed for the plots N$_2$O selectivity vs. temperature which reflect a two steps process associated to the production and the subsequent reduction of N$_2$O to N$_2$ as earlier discussed on PGM-based catalysts [P. Granger 1998, 2004]. It seems obvious that the comparison with the selectivity profiles in Fig. 8.16. suggest that the formation of N$_2$O is retarded on Rh/La$_{0.6}$Ca$_{0.4}$Fe$_{0.8}$Cu$_{0.2}$O$_3$ and probably the re-adsorption of N$_2$O is facilitated leading to a fast subsequent dissociation resulting ultimately in N$_2$ formation. Clearly Rh/LaFeO$_3$ and Rh/La$_{0.7}$Fe$_{0.8}$Cu$_{0.2}$O$_3$ behave differently with a larger production of NO with a selectivity governed by the strength of adsorption of NO on metallic Rh particle. Hence the peculiar selectivity behavior of Rh/La$_{0.6}$Ca$_{0.4}$Fe$_{0.8}$Cu$_{0.2}$O$_3$ and Rh/ La$_{0.6}$Ca$_{0.2}$Fe$_{0.8}$Cu$_{0.2}$O$_3$ could be explained by the assistance of anionic vacancies at the vicinity of adsorbed or re-adsorbed N$_2$O molecules which would dissociate more readily on anionic vacancies more extensively formed in rich condition than in lean condition.

8.4.3. Kinetics of CO and propene oxidation

The exploitation of TPR conversions led to the estimates of the rate and kinetic parameters for CO and propene oxidation in Tables 8.6.-8.7. for stoichiometric conditions (STO1 and STO2). Similarly to palladium based catalysts, the evolution of the specific rate does not depend on the specific surface area but obeys more reasonably to the surface composition and rhodium dispersion. Some comparisons with rhodium-free catalysts are useful (see Chapter V., Table 5.8., Table 5.9.) in order to check the related importance of rhodium to activate both reactions. Of course, sharp differences in terms of reaction rates are discernible because they were recorded at much lower temperature on bare samples. They also correspond to a significant lowering of the apparent activation energy which demonstrates that Rh incorporation leads to the creation of new active sites which combine Rh as aforementioned. The comparison of the order of magnitude of rates from STO1 and STO2 values underlines only weak deviations which suggests that deactivation did not occur significantly. Finally, rather similar tendencies found on Pd-based catalyst are observable but less accentuated than on Pd catalysts. Anyway, lower activities for CO and propene oxidation are observable on $Rh/La_{0.7}Fe_{0.8}Cu_{0.2}O_3$. However, the weak maxima observed on the specific and normalized rate values cannot be easily related to the evolution observed on the apparent activation energies. Such observations emphasize the fact that rhodium has a more marked effect of the reduction of NO and a greater cooperative effect with the support to control the rate of NO reduction and selectivity to produce nitrogen in stoichiometric conditions.

Table 8.6. Rate and kinetic parameters related to CO oxidation on Rh-loaded perovskite samples

Catalyst	SSA $(m^2\ g^{-1})$	STO1				STO2			
		$r_{spec.}$ $(mol\ s^{-1}g^{-1})^a$	Normalized rate $(mol\ s^{-1}m^{-2})^a$	A $(m^3\ s^{-1}g^{-1})$	E_{app} (kJ/ mol)	$r_{spec.}$ $(mol\ s^{-1}g^{-1})^a$	Normalized rate $(mol\ s^{-1}m^{-2})^a$	A $(m^3s^{-1}g^{-1})$	E_{app} (kj mol^{-1})
$Rh/LaFeO_3$	15.9	5.57E-07	3.50E-08	6.01E07	122.7	3.36E-07	2.11E-08	1.13E10	136.7
$Rh/La_{0.7}Fe_{0.8}Cu_{0.2}O_3$	23.9	6.72E-07	2.81E-08	172	70.7	2.42E-07	1.01E-08	1.63E08	131.4
$Rh/La_{0.6}Ca_{0.1}Fe_{0.8}Cu_{0.2}O_3$	22.6	1.18E-06	5.22E-08	9525	83.7	4.59E-07	2.03E-08	1.06E08	125.4
$Rh/La_{0.6}Ca_{0.2}Fe_{0.8}Cu_{0.2}O_3$	22	1.19E-06	5.42E-08	63	63.2	2.88E-07	1.31E-08	9.51E09	144.6
$Rh/La_{0.6}Ca_{0.4}Fe_{0.8}Cu_{0.2}O_3$	33.2	5.57E-07	1.68E-08	5067	84.8	2.71E-07	8.15E-09	6403	89.8

Note: a calculated at T = 200°C for STO1 and STO2.

pre-exponential factor and E_{app} apparent activation energy in agreement with $k = A \exp(-E_{app}/RT)$

Table 8.7. Rate and kinetic parameters related to C_3H_6 oxidation on Rh-loaded perovskite samples

Catalyst	SSA $(m^2\,g^{-1})$	STO1					STO2			
		$r_{spec.}$ $(mol\,s^{-1}g^{-1})^a$	Normalized rate $(mol\,s^{-1}m^{-2})^a$	A $(m^3\,s^{-1}g^{-1})$	E_{app} (kJ/mol)		$r_{spec.}$ $(mol\,s^{-1}g^{-1})^a$	Normalized rate $(mol\,s^{-1}m^{-2})^a$	A $(m^3\,s^{-1}g^{-1})$	E_{app} (kJ/mol)
Rh/LaFeO$_3$	15.9	1.68E-08	1.05E-09	2.4	59.8		1.35E-08	8.51E-10	3112.4	95.5
Rh/La$_{0.7}$Fe$_{0.8}$Cu$_{0.2}$O$_3$	23.9	7.18E-09	3.00E-10	7.4	68.1		5.08E-09	2.12E-10	40892.0	106.0
Rh/La$_{0.6}$Ca$_{0.1}$Fe$_{0.8}$Cu$_{0.2}$O$_3$	22.6	3.64E-08	1.61E-09	1.4	57.7		2.62E-08	1.16E-09	200.9	80.8
Rh/La$_{0.6}$Ca$_{0.2}$Fe$_{0.8}$Cu$_{0.2}$O$_3$	22.0	5.72E-08	2.60E-09	1.0	54.6		1.41E-08	6.39E-10	80.7	79.0
Rh/La$_{0.6}$Ca$_{0.4}$Fe$_{0.8}$Cu$_{0.2}$O$_3$	33.2	4.47E-08	1.35E-09	0.2	49.0		1.99E-09	5.99-11	2.8	63.4

Note: a calculated at T = 250°C

pre-exponential factor and E_{app} apparent activation energy in agreement with k = A exp($-E_{app}$/RT)

8.5. Conclusion

0.1 wt.% rhodium loading on lanthanum ferrite perovskite was carried out by means of wet impregnation approach. As already observed for palladium addition, low amount of rhodium loading did not cause notable structural alteration of the perovskite support. The initial orthorhombic crystal structure and bulk composition ratio of the bare perovskite were maintained. The main change are related to surface modification governed by the dispersion and the oxidation state of rhodium as earlier discussed for palladium.

Obvious changes of reducibility engendered by rhodium incorporation have been noticed during H$_2$-TPR experiment. For the Rh/La$_{0.7}$FeO$_3$, the reduction process of extracted hematite shifted to lower temperature region compared to bare La$_{0.7}$FeO$_3$, demonstrating the beneficial role played by Rh. For the Rh/LaFe$_{1-y}$Cu$_y$O$_3$, an extra reduction process in the temperature range of 350-650°C was noticed, which was associated with partial diffusion of Rh across the support. Such trend intensified as Cu doping increased. Rh loading on La-deficient perovskite La$_{0.7}$Fe$_{1-y}$Cu$_y$O$_3$ caused the earlier onset of hematite reduction although no significant impact on copper reduction was observed. By contrast, Rh loading on La$_{0.6}$Ca$_x$Fe$_{0.8}$Cu$_{0.2}$O$_3$ not only induces a more reducible copper species but also gave rise to a considerable increase of H$_2$ uptake (Table 8.2.). The H/M ratio close to 3.0 means that Rh^{3+} present on the Ca and Cu co-doped perovskite was almost thoroughly reduced to metallic Rh^0. Particular attention should be paid to Rh/La$_{0.6}$Ca$_{0.4}$Fe$_{0.8}$Cu$_{0.2}$O$_3$ which is featured by the greatest H/M ratio, reflecting an improved reducibility of both Rh^{3+} and Cu^{2+} stabilized either in the status of RhO$_x$ and CuO in weak interaction with support or as isolated Rh^{3+} and Cu^{2+} cations interacting intensely with the support within the lattice.

Mobility of suprafacial oxygen was only enhanced to a very limited extent thanks to Rh loading, evidenced by the weak α-O$_2$ desorption irrespective of the bulk composition of the support. Notwithstanding, it was found that lattice oxygen mobility was triggered especially on Rh/La$_{0.6}$Ca$_{0.4}$Fe$_{0.8}$Cu$_{0.2}$O$_3$ which is related to the promotion of reducibility of B site cations owing to Rh incorporation resulting in a greater intensity and accessibility of anionic vacancies.

Surface enrichment of Rh is confirmed by XPS on all examined catalysts, with the highest surface Rh content corresponding to Rh/La$_{0.6}$Ca$_{0.2}$Fe$_{0.8}$Cu$_{0.2}$O$_3$. It was found that Rh dispersion is closely dependent on the composition of perovskite support. Rh loading on stoichiometric compositions Rh/LaFe$_{1-y}$Cu$_y$O$_3$ resulted in higher Rh dispersion but mostly in the form of metallic Rh^0. On the contrary, Rh/La$_{0.7}$Fe$_{1-y}$Cu$_y$O$_3$ is featured by a loss of Rh dispersion probably owing to the agglomeration of RhO$_x$ in weak interaction with support. As a result, a gain in terms of reducibility and lattice oxygen mobility is attained. (Fig. 8.5. and Fig. 8.9(A).) Compared to 0.5 wt.% Pd loading, 0.1 wt.% Rh loading exhibited slightly slower light-off for CO and C$_3$H$_6$ oxidation but better activity in terms of NO conversion and N$_2$ selectivity in STOI1 and STOI2. For CO and C$_3$H$_6$ oxidation, the best systems are Rh/La$_{0.7}$Fe$_{0.8}$Cu$_{0.2}$O$_3$, Rh/La$_{0.6}$Ca$_{0.1}$Fe$_{0.8}$Cu$_{0.2}$O$_3$ and Rh/La$_{0.6}$Ca$_{0.2}$Fe$_{0.8}$Cu$_{0.2}$O$_3$ in stoichiometric and rich atmosphere. In lean conditions, no significant gain of oxidation was obtained by Rh loading. Extra framework CuO is assumed to induce agglomeration of RhO$_x$ clusters leading to a more reducible Rh^{n+} species accountable for the oxidative performance.

In addition, slight deactivation is observed for both CO and C_3H_6 oxidation in STOI2. Kinetic study showed that specific and normalized reaction rate does not rely on the specific surface area of the catalyst but rather depends on the surface composition and Rh dispersion.

With regard to NO reduction, Rh-loaded perovskite catalysts outperformed the commercial benchmark catalyst in stoichiometric conditions. It was found that Rh-loaded perovskite catalysts yielded a highest NO conversion near 310°C corresponding to 52% and 55% in STOI1 and in STOI2 respectively. The following ranking can be established from STO1 near 310 °C: $Rh/La_{0.6}Ca_{0.4}Fe_{0.8}Cu_{0.2}O_3 \sim Rh/La_{0.6}Ca_{0.2}Fe_{0.8}Cu_{0.2}O_3 > Rh/LaFeO_3 > Rh/La_{0.6}Ca_{0.1}Fe_{0.8}Cu_{0.2}O_3 \sim Rh/La_{0.7}Fe_{0.8}Cu_{0.2}O_3 > Pd/Ce_xZr_{1-x}O_2$. It is also noticeable that NO conversion in STOI2 manifested similar profiles featured by a convergence in the temperature range of 250-450°C without marked discrepancies. What's more, Rh-loaded perovskite catalysts presented higher N_2 selectivity at high temperature region than that of the benchmark catalyst in stoichiometric condition although poorer N_2 selectivity at low temperature region should not be neglected due to the formation of N_2O during the cold start process. Such selectivity behavior is typical of NO reduction on metallic Rh^0 site.

In general, the most effective system corresponded to $Rh/La_{0.6}Ca_{0.4}Fe_{0.8}Cu_{0.2}O_3$ in the whole temperature range in view of a compromise between oxidative and reductive properties.

Reference

[G. Chen 1983] G. Chen, W.T. Chou and C.T. Yeh. Applied Catalysis A: General, 1983, 8:389-397.

[J.P. Dacquin 2010] J.P. Dacquin, M. Cabié, C.R. Henry, C. Lancelot, C. Dujardin, S.R. Raouf, P. Granger. Journal of Catalysis, 2010, 270:299-309.

[J.P. Dacquin 2011] J.P. Dacquin, C. Lancelot, C. Dujardin, P. Granger. Journal of Physical Chemistry C, 2011, 115, 1911-1921.

[A. Eyssler 2011] A. Eyssler, A. Winkler, P. Mandaliev, P. Hug, A. Weidenkaff, D. Ferri. Applied Catalysis B: Environmental, 2011, 106:494-502.

[P. Granger 1998] P. Granger, J.-J. Lecomte, C. Dathy, L. Leclercq, G. Leclercq. Journal of Catalysis, 1998, 175:194-203.

[P. Granger 2002] P. Granger, L. Delannoy, J.-J. Lecomte, C. Dathy, L. Leclercq, G. Leclercq. Journal of Catalysis, 2002, 207:202-212.

[P. Granger 2004] P. Granger, P. Malfoy, G. Leclercq. Journal of Catalysis, 2004, 223:142-151.

[I. Halasz 1992] I. Halasz, A. Brenner. Applied Catalysis A: General, 1992, 82:51-63.

[W. Huang 2009] W. Huang, Z. Zuo, P. Han, Z. Li, T. Zhao. Journal of Electron Spectroscopy and Related Phenomena, 2009, 173:88-95.

[L.S. Kibis 2009] L.S. Kibis, A.I. Titkov, A.I. Stadnichenko, S.V. Koscheev, A.I. Boronin. Applied Surface Science, 2009, 255 (22), 9248−9254.

[L.S. Kibis 2012] Lidiya S Kibis, Andrey I Stadnichenko, Sergei V Koscheev, Vladimir I Zaikovskii, Andrei I Boronin. Journal of Physical Chemistry C, 2012, 116 (36):19342-19348.

[K.S. Kim 1974] K.S. Kim, A.F. Gossmann, N. Winograd. Analytical Chemistry, 1974, 46 (2):197-200.

[B. Levasseur 2009] B. Levasseur, S. Kaliaguine. Applied Catalysis B: Environmental, 2009, 88, 305-314.

[M. Moroseac 2004] M. Moroseac, T Skála, K. Veltruská, V. Matolín, I. Matolínová. Surface Science, 2004, 566:1118-1123.

[H. Muraki 1989] H. Muraki, K. Yokota and Y. Fujitani. Applied Catalysis, 1989, 48:93-105.

[Y. Nishihata 2002] Y. Nishihata, J. Mizuki, T. Akao, H. Tanaka, M. Uenishi, M. Kimura, T. Okamoto, N. Hamada. Nature, 2002, 418:164-166.

[K. Otto 1992] K. Otto, L.P. Haack, J. E. Devries. Applied Catalysis B: Environmental, 1992, 1 (1), 1-12.

[C.H.F. Peden 1995] C.H.F. Peden, D.N. Belton, S.J. Schmieg. Journal of Catalysis, 1995, 155:204-218.

[A. Schön 2018] A. Schön, J.P. Dacquin, P. Granger, C. Dujardin. Applied Catalysis B: Environmental, 2018, 223:167-176.

[V. Shanmugam 2018] V. Shanmugam, R. Zapf, V. Hessel, H. Pennemann, G. Kolb. Applied Catalysis B: Environmental, 2018, 226:403-411.

[T.B. Shoynkhorova 2018] T.B. Shoynkhorova, P.A. Simonov, D.I. Potemkin, P.V. Snytnikov, V.D. Belyaev, A.V. Ishchenko, D.A. Svintsitskiy, V.A. Sobyanin. Applied Catalysis B: Environmental, 2018, 237: 237-244.

[K. Simmance 2019] K. Simmance, D. Thompsett, W. Wang, B. Thiebaut. Catalysis Today, 2019, 320:40-50.

[E.M. Slavinskaya 2011] E.M. Slavinskaya, O.A. Stonkus, R.V. Gulyaev, A.S. Ivanova, V.I. Zaikovskii, P.A. Kuznetsov, A.I. Boronin. Applied Catalysis A:General, 2011, 401:83–97.

[Y. Sohn 2010] Y. Sohn, D. Pradhan, K.T. Leung. ACS Nano, 2010, 4 (9):5111-5120.

[I.V. Yentekakis 2019] I.V. Yentekakis, G. Goula, M. Hatzisymeon, I. Betsi-Argyropoulou, G. Botzolaki, K. Kousi, D.I. Kondarides, M.J. Taylor, C.M.A. Parlett, A. Osatiashtianic, G. Kyriakou, J. Pedro Holgado, R.M. Lambert. Applied Catalysis B: Environmental, 2019, 243: 490-501.

[R. Zhang 2006] R.D. Zhang, H. Alamdari, S. Kaliaguine. Journal of Catalysis, 2006, 242:241-253.

[J. Zhang 2015] Jingyi Zhang, Dongdong Tan, Qingjie Meng, Xiaole Weng, Zhongbiao Wu. Applied Catalysis B: Environmental, 2015, 172-173:18-26.

[B. Zhao 2010 a] B. Zhao, Q.Y. Wang, G.F. Li, R.X. Zhou. Journal of Alloys and Compounds, 2010, 508:500-506.

[B. Zhao 2010 b] B. Zhao, G.F. Li, C.H. Ge, Q.Y. Wang, R.X. Zhou. Applied Catalysis B: Environmental, 2010, 96:338-349.

PART D

PGM-doped Perovskite Catalysts: PGM loading combined with Ca and Mn substitution

Chapter IX. Rhodium incorporation to stoichiometric and non-stoichiometric Ca and Mn doped La$_{1-x}$FeO$_{3\pm\delta}$

Chapter IX. Rhodium incorporation to stoichiometric and non-stoichiometric Ca and Mn doped La$_{1-x}$FeO$_{3\pm\delta}$

Foreword

Chapter VI. revealed that manganese doping on lanthanum ferrite not only showed improved activity for CO and C$_3$H$_6$ oxidation but also for NO conversion in stoichiometric conditions. Enhancement of NO reduction activity is more noticeable on La-deficient composition which is mainly related to better reducibility and oxygen mobility resulting from introduction of Mn^{n+} species. Although the catalytic activity of Mn-doped perovskite appears less satisfactory compared to commercial TWC in terms of NO conversion and nitrogen selectivity, it provides a promising alternative to reduce hazardous nitric oxide while reducing significantly the amount of PGMs.

Palladium and rhodium meet the requirement of remaining metallic status under most operating conditions while restricting the formation of volatile oxides which may probably result in metal loss. [M.V. Twigg 2005][G.J.K. Acres 2004] Palladium is accepted to form stable oxide and it is catalytically active in oxidation reactions. Rhodium is widely recognized as an indispensable element to ensure NO$_x$ reduction which is usually associated with the reversible transformation between metallic rhodium and cationic rhodium species. Metallic rhodium is assumed to provide accessible sites for hydrogen adsorption and dissociation with low activation energy [G. Chen 2010].

Interaction between rhodium and perovskite can be illustrated as follows: Under oxidizing conditions, rhodium oxide (Rh$_2$O$_3$) can be readily formed according to Eq. (9-1) which can easily react with perovskite through reaction (9-2):

$$2Rh \ + \ 3/2 \ O_2 \ = Rh_2O_3 \qquad\qquad (eq. \, 9-1)$$

$$Rh_2O_3 + ABO_3 = Rh_2O_3 \cdot ABO_3 \qquad\qquad (eq. \, 9-2)$$

The aboementioned complex can undergo subsequent reduction process under reducing conditions (i.e. hydrogen as a reducer) :

$$Rh_2O_3 \cdot ABO_3 + 2H_2 = 2Rh + 3H_2O + ABO_3 \qquad (eq. \, 9-3)$$
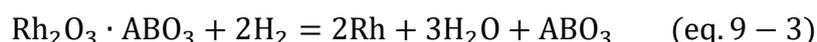
Oxidation of metallic rhodium (Eq. 9-1) is quite important in NO$_x$ reduction reaction and can be made available rapidly when oxidizing conditions return to slightly reducing conditions. [M.V. Twigg 2007]. The re-reduction of Rh$_2$O$_3$-perovskite solid solution (Eq. 9-3) is believed to be a comparatively slow process due to the lack of active centers necessary for the dissociation of reductant species (especially hydrogen) and it can thus be accelerated by

the presence of small quantity of other metallic species capable of providing active sites required for hydrogen dissociation. [M.V. Twigg 2007].

Interactions between manganese species and precious metals have been studied by some authors.[Eugenia Pocoroba 2000] [X. Wei 2010; A.Eyssler 2012; Y. Lu 2013] Ability of Rh for CO dissociation is reported to be remarkably enhanced by manganese [Guochang Chen 2010]. Also, it is reported that the reduction of a second surface metal oxide species in close contact with noble metals can be accelerated accountable for the improved reducibility of Mn oxides with the presence of Rh. [H. Treviño 1995; V. Schünemann 1995; B.J. Kip 1987].

Previous studies demonstrated that NO_x adsorption on the Mn-based perovskites could be remarkably boosted by the presence of palladium. [Z. Say 2014]. Several reasons are accountable for this phenomenon: Firstly, the reduction-induced morphological changes such as surface reconstruction would favor the increase of specific surface area advantageous to NO_x adsorption. Secondly, presence of palladium would strengthen the interaction between NO_x and perovskite capable of activating N-O linkage favorable for the reduction of NO_x to N_2 and N_2O. Moreover, electronic changes (partial or total reduction of B-site cation), compositional alterations occurring on the catalyst surface, reduction of PdO species to metallic Pd^0 as well as the generation of oxygen defects on perovskite surface functioning as anchoring sites for NO_x species are other possible factors responsible for the increased uptake of NO_x adsorption.[Z. Say 2014; I. Twagirashema 2007 a, b; M. Pirez-Engelmann 2004].

One of the toughest challenges associated with precious metals is the easy aggregation of small particles at high temperature leading to sintering of active species and the degradation of their catalytic activity. To tackle this problem, precious metals are supposed to move back and forth between the B site in the perovskite structure and the metal lattice under repeated oxidizing/reducing atmosphere. [Y. Nishihata 2002]. The so-called "self-recovery" mechanism is assumed to restrain metallic particles from growing and allows a better resistance to ageing when exposed to severe operating conditions. [H. Tanaka 2004; H. Tanaka 2006 a, b].

In this chapter, various physicochemical properties and catalytic performance of the Rh-loaded perovskite together with Ca and Mn doping will be discussed in an attempt to provide fundamental understanding related to the impact of nature of A-site and B-site cations and PGM incorporation on TWC system. Improved activity for NO reduction especially in stoichiometric conditions is expected for the Rh-loaded perovskites.

Table 9.1. Elemental analysis of rhodium loaded perovskite $ABO_{3\pm\delta}$

Catalyst	Atomic composition (%)					Ca/La	Mn/Fe	A/B	Rh/(A+B) $\times10^{-3}$
	La	Ca	Fe	Mn	Rh				
$Rh/LaFeO_3$	13.72	-	13.75	-	0.03	-	-	1.00	1.02
$Rh/La_{0.7}FeO_3$	18.46	-	25.91	-	0.04	-	-	0.71	0.96
$Rh/La_{0.6}Ca_{0.1}Fe_{0.8}Mn_{0.2}O_3$	15.03	2.38	19.62	4.93	0.04	0.16	0.25	0.71	0.92
$Rh/La_{0.6}Ca_{0.2}Fe_{0.8}Mn_{0.2}O_3$	15.38	4.95	19.94	4.99	0.04	0.32	0.25	0.82	0.89
$Rh/La_{0.6}Ca_{0.4}Fe_{0.8}Mn_{0.2}O_3$	14.23	9.21	18.51	4.63	0.04	0.65	0.25	1.01	0.78

Elemental analysis produced results essentially in accordance with theoretical values. Rhodium content is close to expected amount (0.1 wt.%) while Ca/La and Mn/Fe ratio were in good agreement with presumed values depending on the Ca and Mn doping degree. It is thereby supposed that rhodium incorporation did not induce a significant alteration of structural composition of the perovskite support. Particular attention should be paid to Rh/(A+B) ratio on the doped perovskite support which slightly varies within the margin of error revealing equivalent Rh composition varying within the margin of error.

Additional XRD analysis showed that bulk RhO_x was hardly detectable in fresh sample. However, given the low amount of loaded rhodium (0.1 wt.%), the possibility of presence of Rh^{n+} cannot be totally excluded. Rhodium species together with B-site cations (Fe and Mn) is thus supposed to be the key factor that impacts the redox properties of the composite materials.

9.1. Reducibility

Reduction of Rh^{n+} is generally believed to take place at low temperature.[S. Cimino 2006]. Similarly to palladium, low reduction temperature of Rh_2O_3 to metallic rhodium species in weak interaction with the perovskite support could assist subsequent reduction processes. Clearly, the same features appear on $Rh/La_{0.7}FeO_3$ and $Pd/La_{0.7}FeO_3$ associated with a sharp shift to lower temperature of the first step of hematite reduction (below 200°C, Fig. 9.1.). Additional reduction processes take place at higher temperature on Ca-substituted samples becoming more distinguishable on $Rh/La_{0.6}Ca_{0.4}Fe_{0.8}Mn_{0.2}O_3$ in the range of 200-400°C, 450-650°C and above 700°C previously ascribed to Mn^{4+} to Mn^{3+}, extra-lattice hematite to ferrous compound and Mn^{3+} to Mn^{2+} reduction processes. As earlier discussed the reduction of unusual Fe^{4+} species not detected on $Rh/LaFeO_3$ is also hardly detected when Rh is deposited on Ca-substituted perovskites. One cannot rule out the possibility that surface defective sites on perovskite support could accommodate Rh^{3+} species. Indeed, the H/M ratio ($M=Rh^{n+}+Mn^{n+}$) less than 3.0 when the consumption of hydrogen below 300°C is ascribed to contributions of Rh^{n+} and Mn^{n+} (Table 9.2.) suggests that the average oxidation state of rhodium is lower than 3 which may signify that a fraction of rhodium species is not reducible in the tested temperature range and could correspond to strengthening interactions.

$La_{0.6}Ca_xFe_{0.8}Mn_{0.2}O_3+0.1$ wt.%Rh
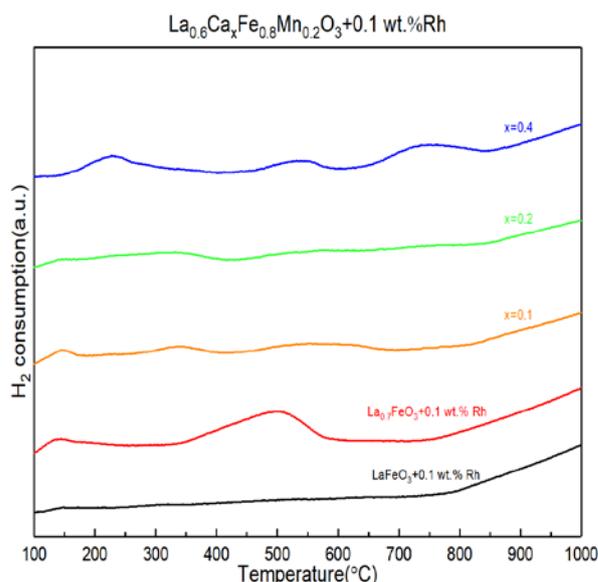
Fig. 9.1. H_2 consumption curves plotted against temperature for $Rh/La_{0.6}Ca_xFe_{0.8}Mn_{0.2}O_3$ orange: x = 0.1; green: x = 0.2; blue: x = 0.4.

Table 9.2. Detailed H_2-TPR results for perovskites $ABO_3+0.1$ wt.%Rh (A = La, Ca; B = Fe, Mn).

Catalyst	H_2 total uptake (mmol g^{-1})[a]	H/M[b]	T_{max} reduction peaks (°C)		
			1st	2nd	3rd
$Rh/LaFeO_3$	<0.01	0.62	150	-	-
$Rh/La_{0.7}FeO_3$	1.66	-	139	501	-
$Rh/La_{0.6}Ca_{0.1}Fe_{0.8}Mn_{0.2}O_3$	0.69	1.32	144	336	556
$Rh/La_{0.6}Ca_{0.2}Fe_{0.8}Mn_{0.2}O_3$	0.91	1.76	142	307	541
$Rh/La_{0.6}Ca_{0.4}Fe_{0.8}Mn_{0.2}O_3$	1.48	1.95	100	229	532

Note :

a Total H_2 consumption was calculated taking into account the temperature range 50-700°C.

b M=Mn+Rh. Assuming H_2 consumption at T<300°C was ascribed to oxidic Rh and Mn species

9.2. Oxygen mobility

O_2-TPD profiles vs. temperature for $Rh/La_{0.6}Ca_xFe_{0.8}Mn_{0.2}O_3$ are collected in Fig. 9.2. As seen, a minor increase of desorbed suprafacial oxygen of the Rh-loaded perovskites was observed while desorption characteristic of intrafacial oxygen seemed unaffected with respect to non-PGM perovskites (Fig. 6.15.). Such phenomenon could be accounted for by the oxygen enrichment surrounding metallic rhodium centers. It is established that metallic rhodium can adsorb oxygen species to provide sufficient active oxygen species required for CO and hydrocarbon oxidation. Besides, desorption of suprafacial oxygen is also associated with reduction of B site transition metals. Manganese cations are assumed more reducible thanks to the spillover effect caused by rhodium incorporation, which may partly explain the shift of reduction peaks of Mn^{n+} towards lower temperature zone shown in Table 9.2. compared with non-PGM perovskites (see Table 6.5.).

Returning to previous observations on Rh-doped $La_{0.6}Ca_xFe_{0.8}Cu_{0.2}O_3$ it is obvious that weak desorption appears on Rh/$La_{0.6}Ca_xFe_{0.8}Mn_{0.2}O_3$ in comparison with this former series. This is particularly true on the stoichiometric perovskite composition as support, i.e. Rh/$La_{0.6}Ca_{0.4}Fe_{0.8}Cu_{0.2}O_3$ which exhibits high oxygen mobility as described in Fig. 8.9.(A). This result would suggest that the defective sites at the surface of the perovskite would accommodate a lower extent of isolated Rh species capable of improving surface oxygen mobility.
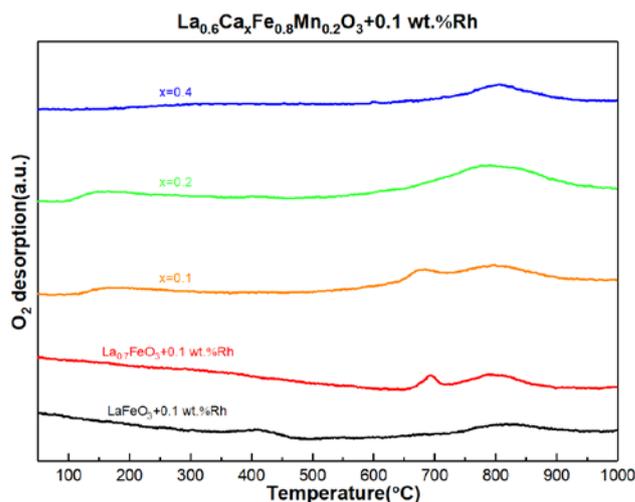
Fig. 9.2. O_2 desorption curves plotted against temperature for Rh/$La_{0.6}Ca_xFe_{0.8}Mn_{0.2}O_3$ orange: x = 0.1; green: x = 0.2; blue: x = 0.4.

9.3. Surface analysis

La 3d, Fe 2p, Mn 2p, Ca 2p, Rh 3d and O 1s photopeaks for $La_{0.6}Ca_xFe_{0.8}Mn_{0.2}O_3$ are collected in Fig. 9.3. B.E. values corresponding to these photopeaks were calibrated by using C 1s core level at 285.0 eV as internal reference. Positions of La 3d 5/2 in the range of 833.4 -834.0 eV with a distance of around 4.4 eV between the main line and satellite mainly characterize La^{3+}. Since La has a tendency to form hydroxide or carbonate, contribution of the combination of the two on the spectra cannot be excluded but their intensity remains limited.[G. Tyuliev 2003] Fe 2p photopeak show a profile typical of Fe^{3+} species with a characteristic shake up structure near 719 eV. Slight shift towards higher binding energy of Fe 2p 3/2 photopeak was observed when Ca doping degree increased yet the distance between Fe 2p 3/2 and Fe 2p 1/2 were almost unchanged (13.9 ev) irrespective of Ca content, confirming that oxidation state of iron species were stable in the Rh-loaded perovskites. Intensity of Rh 3d photopeak becomes stronger at higher Ca doping degree. The B.E. values near 309.0 eV characteristic of Rh^{3+} slightly vary likely within the margin of error and a priori do not evidence significant changes on the chemical environment of oxidic rhodium species mainly stabilize as Rh_2O_3.

Data from semi-quantitative analysis are reported in Tables 9.3. and 9.4. As already noticed, a sharp surface La enrichment prevails on stoichiometric compositions whereas bulk and surface La composition on La-deficient materials are comparable showing the absence of gradient concentration. There is no significant deviation on the Mn/Fe in comparison with the

same ratio calculated from elemental analysis still revealing a quite homogeneous distribution from the bulk to the surface. On the other hand, the rhodium content on the surface of catalyst is much higher than in the bulk. This is in agreement with previous hypothesis that Rh migration from bulk to surface could be favored by Ca doping. It is assumed that metallic rhodium particles tend to form cluster on the surface leaving part of bare perovskite surface unoccupied. Redistribution of rhodium is seemingly dependent on Ca doping which may account for the variations of Rh/(A+B) ratio (Table 9.4.). Enrichment of rhodium on the surface is beneficial to the adsorption of oxygen species, which may explain partly the decrease of $O_{adsorbed}/O_{lattice}$ ratio accompanied by higher Ca doping degree (Table 9.3.)
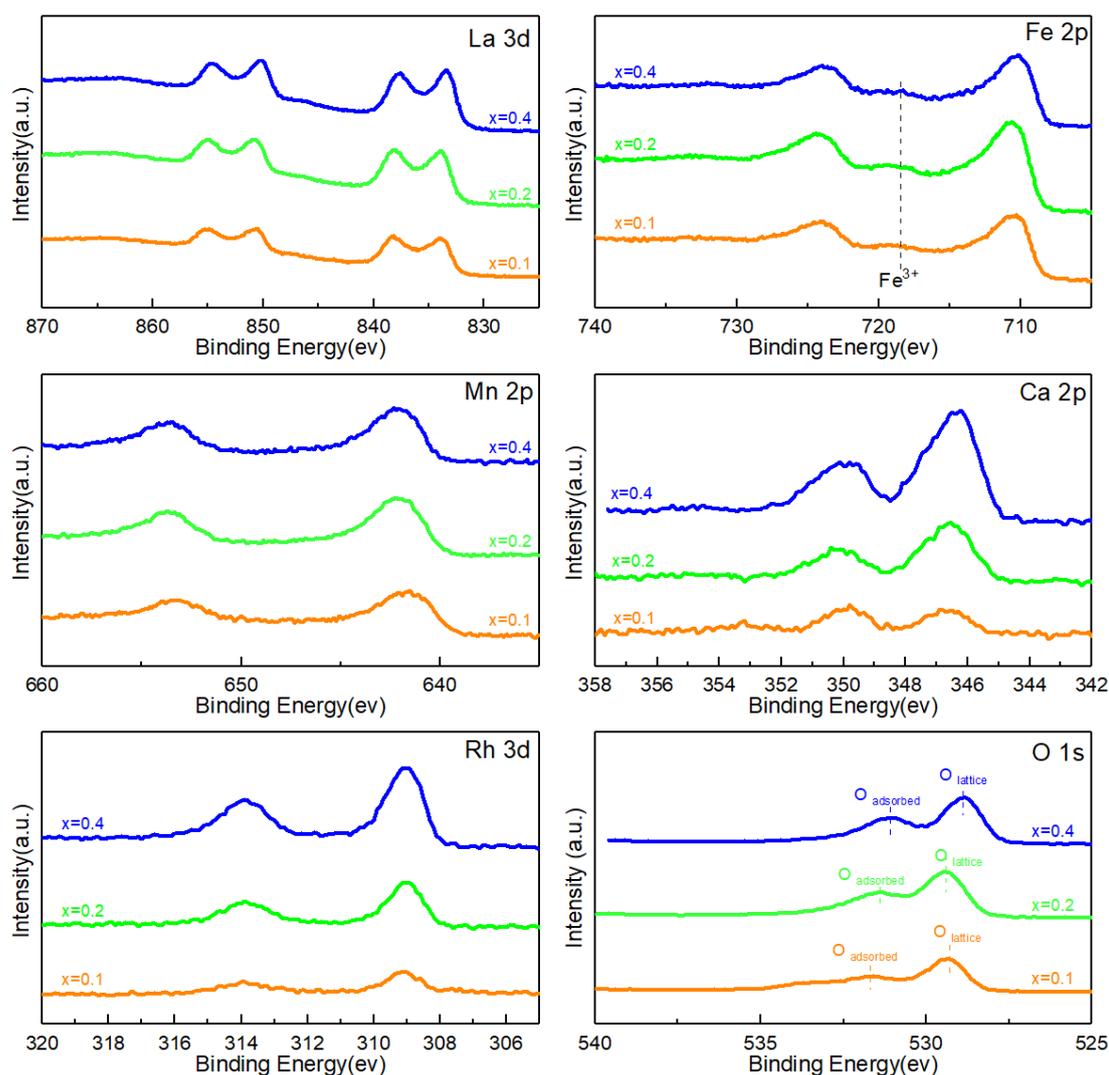
Fig. 9.3. Characteristic photopeaks from XPS analysis recorded on $Rh/La_{0.6}Ca_xFe_{0.8}Mn_{0.2}O_3$ orange: x = 0.1; green: x = 0.2; blue: x = 0.4.

Table 9.3. Binding energy of each element and abundance of oxygen species

| Catalyst | Binding energy (eV) | | | | | | | Relative surf. Comp. O[a] | | |
| | La 3d | Ca 2p | Fe 2p | Mn 2p | Rh 3d | O 1s | | O ads. (%)[b] | O lattice (%)[b] | $\frac{O_{adsorbed}}{O_{lattice}}$ |
						Ads. oxygen	Lattice oxygen			
Rh/LaFeO$_3$	833.8	-	710.2	-	309.4	531.4	529.3	51.7	48.3	1.07
Rh/La$_{0.7}$FeO$_3$	834.0	-	710.5	-	309.2	531.0	529.5	55.6	44.4	1.25
Rh/La$_{0.6}$Ca$_{0.1}$Fe$_{0.8}$Mn$_{0.2}$O$_3$	834.0	349.8	710.3	641.5	309.2	531.7	529.3	60.0	40.0	1.5
Rh/La$_{0.6}$Ca$_{0.2}$Fe$_{0.8}$Mn$_{0.2}$O$_3$	833.9	346.5	710.5	642.2	309.1	531.4	529.4	51.7	48.3	1.07
Rh/La$_{0.6}$Ca$_{0.4}$Fe$_{0.8}$Mn$_{0.2}$O$_3$	833.4	346.2	710.2	642.3	309.1	531.1	528.9	48.4	51.6	0.94

Note:

a O$_{adsorbed}$ + O$_{lattice}$ = 1

b relative abundance of oxygen species was calculated from deconvolution of O 1s photopeak

Table 9.4. Surface atomic composition calculated from XPS analysis

| Catalyst | Surface atomic composition (%) | | | | | | | A/B | Mn/Fe | Rh/ (A+B) ×10^{-3} |
	O	La	Fe	Rh	C	Mn	Ca			
Rh/LaFeO$_3$	45.05	12.01	8.31	0.26	34.37	0.00	-	1.45	-	12.64
Rh/La$_{0.7}$FeO$_3$	46.18	10.58	14.38	0.83	28.04	0.00	-	0.74	-	33.05
Rh/La$_{0.6}$Ca$_{0.1}$Fe$_{0.8}$Mn$_{0.2}$O$_3$	31.30	4.95	5.65	0.18	55.16	1.93	0.84	0.76	0.34	13.46
Rh/La$_{0.6}$Ca$_{0.2}$Fe$_{0.8}$Mn$_{0.2}$O$_3$	42.97	6.98	8.95	0.42	35.35	2.84	2.48	0.80	0.32	19.76
Rh/La$_{0.6}$Ca$_{0.4}$Fe$_{0.8}$Mn$_{0.2}$O$_3$	44.45	7.78	6.48	0.80	32.93	2.66	4.90	1.39	0.41	36.66

To complement XPS data, Rh dispersion was estimated from hydrogen chemisorption on Rh-loaded perovskites as shown in Table 9.5. Rh/(A+B) ratios displayed opposite trends in the bulk and on the surface. It is hypothesized that more Ca doping would lead to the enrichment of rhodium on the surface and subsequently increased amount of surface metallic active sites. Katz proposes that the cyclical movement of precious metals in the PGM-perovskite system stems mostly from bulk rather than surface re-dispersion. [M.B. Katz 2012] Further, the author made an assumption that surface of only a few nanometer depths are potentially useful as a host or support for loading precious metals in any practical embodiment of the original self-regenerating mechanism.[M.B. Katz 2012] In our case, Ca doping seemed to have an inhibiting impact on the dissolution of rhodium within the perovskite substrate yet favorable to the migration of rhodium from bulk to surface. Such explanations seem in relative good agreement with higher Rh dispersion especially on

Rh/La$_{0.6}$Ca$_{0.4}$Fe$_{0.8}$Mn$_{0.2}$O$_3$. Interestingly the reverse behavior was observed on Pd/La$_{0.6}$Ca$_{0.4}$Fe$_{0.8}$Mn$_{0.2}$O$_3$ with very low Pd dispersion likely underestimated based on the fact that unreducible oxidic species could be stabilized by the perovskite structure and then permitting a greater oxygen mobility. Clearly, rhodium and palladium exhibit opposite behavior.

Table 9.5. Metallic dispersion of rhodium measured by H$_2$ chemisorption analysis

Catalyst	Rh dispersion (%)	Metallic Surface Area (m²/g metal)	Rh/(A+B) ×10^{-3}
Rh/LaFeO$_3$	12.92	56.87	12.64[b]/1.02[a]
Rh/La$_{0.7}$FeO$_3$	5.01	22.03	33.05[b]/0.96[a]
Rh/La$_{0.6}$Ca$_{0.1}$Fe$_{0.8}$Mn$_{0.2}$O$_3$	15.23	67.01	13.46[b]/0.92[a]
Rh/La$_{0.6}$Ca$_{0.2}$Fe$_{0.8}$Mn$_{0.2}$O$_3$	5.48	24.11	19.76[b]/0.89[a]
Rh/La$_{0.6}$Ca$_{0.4}$Fe$_{0.8}$Mn$_{0.2}$O$_3$	12.96	57.03	36.66[b]/0.78[a]

Note: a calculated from elemental analysis

           b calculated from XPS experiment

9.4. Catalytic properties

9.4.1. Oxidative properties

A rapid oxidation of CO was observed on Rh-loaded perovskites with a light-off temperature less than 250°C and 300°C in the first and return stoichiometric test respectively (see Table 9.6. and Fig. 9.4.). La-deficient compositions Rh/La$_{0.6}$Ca$_{0.1}$Fe$_{0.8}$Mn$_{0.2}$O$_3$ and Rh/La$_{0.6}$Ca$_{0.2}$Fe$_{0.8}$Mn$_{0.2}$O$_3$ showed improved stability with respect to Rh/La$_{0.6}$Ca$_{0.4}$Fe$_{0.8}$Mn$_{0.2}$O$_3$ which suffered from a loss of activity in the return test. Oxidation of propene presented similar trend but higher light-off temperatures were noticed over the same catalysts (< 350°C in STO1 and <400°C in STO2 see Table 9.6.). It is clear that oxidation activity for CO and C$_3$H$_6$ was significantly enhanced owing to rhodium incorporation compared to bare perovskites. The possible reason may be that active sites on rhodium capable of adsorbing oxygen species provides sufficient adsorbed oxygen atoms and subsequently facilitates the formation and desorption of adsorbed CO$_2$ molecules. However, activity for propane oxidation did not undergo a tremendous rise irrespective of composition variations of the tested catalysts. Scission of C-H bond has been well accepted as the rate-determining step for hydrocarbon activation [R. Burch 1995]. The rate of C-H bond activation is heavily dependent on dispersion of rhodium on the support and the metal-support interaction as well as reaction conditions. Also, inhibiting effect of certain reaction products, such as CO$_2$ and H$_2$O, constitutes another factor responsible for the hindrance to the activation of C-H bond. The best catalytic performance for C$_3$H$_8$ oxidation corresponds to Rh/La$_{0.6}$Ca$_{0.2}$Fe$_{0.8}$Mn$_{0.2}$O$_3$ which has relatively low rhodium dispersion, suggesting that

combustion of C$_3$H$_8$ is more determined by the metal-support interaction rather than by rhodium dispersion.

Fig. 9.4. Catalytic oxidation performance of iron-based perovskite solid ABO$_3$ (A=La, Ca; B= Fe, Mn) +0.1 wt.%Rh. Grey star solid line: commercial reference catalyst(★); black circle solid line: LaFeO$_3$(●); red circle solid line: La$_{0.7}$FeO$_3$ (●); magenta downward triangle solid line: La$_{0.7}$Fe$_{0.8}$Mn$_{0.2}$O$_3$(▼); black hollow circle dash line: LaFeO$_3$+0.1 wt%.Rh(○); orange diamond dash line: La$_{0.6}$Ca$_{0.1}$Fe$_{0.8}$Mn$_{0.2}$O$_3$+0.1 wt.%Rh(◇); green diamond dash line: La$_{0.6}$Ca$_{0.2}$Fe$_{0.8}$Mn$_{0.2}$O$_3$+0.1 wt.%Rh(◇); blue diamond dash line: La$_{0.6}$Ca$_{0.4}$Fe$_{0.8}$Mn$_{0.2}$O$_3$+0.1wt.%Rh(◇).

9.4.2. Reductive properties

Fig. 9.5. Catalytic reduction performance of iron-based perovskite solid ABO$_3$ (A=La, Ca; B= Fe, Mn) +0.1 wt.%Rh. Grey star solid line: commercial reference catalyst(★); black circle solid line: LaFeO$_3$(●); red circle solid line: La$_{0.7}$FeO$_3$ (●); magenta downward triangle solid line: La$_{0.7}$Fe$_{0.8}$Mn$_{0.2}$O$_3$(▼); black hollow circle dash line: LaFeO$_3$+0.1 wt%.Rh(○; orange diamond dash line: La$_{0.6}$Ca$_{0.1}$Fe$_{0.8}$Mn$_{0.2}$O$_3$+0.1 wt.%Rh(◇); green diamond dash line: La$_{0.6}$Ca$_{0.2}$Fe$_{0.8}$Mn$_{0.2}$O$_3$+0.1 wt.%Rh(◇); blue diamond dash line: La$_{0.6}$Ca$_{0.4}$Fe$_{0.8}$Mn$_{0.2}$O$_3$+0.1wt.%Rh(◇).

As for NO reduction, Rh-loaded perovskites exhibits better conversion in terms of NO reduction in the first and return stoichiometric test (Fig. 9.5.). In the temperature range of 300-500°C typical of the operating temperature in the real TWC converter, a maximum NO conversion exceeding 60% was observed on Rh/La$_{0.6}$Ca$_{0.4}$Fe$_{0.8}$Mn$_{0.2}$O$_3$ in the first stoichiometric test and on Rh/La$_{0.6}$Ca$_{01}$Fe$_{0.8}$Mn$_{0.2}$O$_3$and Rh/La$_{0.6}$Ca$_{0.2}$Fe$_{0.8}$Mn$_{0.2}$O$_3$ in the return test, which is surprisingly better than the commercial catalysts, although activity below 200°C remained unsatisfactory because of the slow activation during cold-start process. Regarding Rh/La$_{0.6}$Ca$_{0.4}$Fe$_{0.8}$Mn$_{0.2}$O$_3$, metallic rhodium is supposed to be the major source of

catalytic activity but the facile segregation of metallic rhodium particles on the perovskite surface led to a remarkable loss of initial activity (Table 9.6.).

In lean condition, NO conversion is usually limited due to the competitive reduction between NO$_x$ and large excess of oxygen with reducing gases in oxidizing atmosphere. As a matter of fact, Rh-loaded perovskites displayed comparable maximum NO conversion to that of the commercial catalyst but only at higher temperature region (above 350°C). Activity for NO reduction was hardly observed in low temperature region (below 300°C).

Rh-loaded perovskites showed higher nitrogen selectivity above 350°C in stoichiometric atmosphere whereas nitrous oxides were the main product bellows 350°C. Formation of nitrous oxide has been identified as an important intermediate step in the NO-CO reaction over supported rhodium catalysts. Mechanism of NO reduction by CO is investigated by Cho [B.K. Cho 1994]. It was found that nitrous oxide is the main reduction product at low temperature range (below 300°C, Eq. 9-4) while further decomposition of nitrous oxide at high temperature range (above 300°C) was predominant, leading to the formation of target product nitrogen (Eq. (9-5)):

$$NO_{ads} + N_{ads} \rightarrow N_2O_{ads} + Rh_{ads} \qquad\qquad (eq.\,9-4)$$

$$N_2O_{ads} \rightarrow N_2 + O_{ads} \qquad\qquad (eq.\,9-5)$$

Coverage of surface species may also contribute to the evolution of selectivity for N$_2$ and N$_2$O. Su[Q. Su 2014] argued that dissociation of adsorbed N$_2$O is limited by relatively high fraction of CO coverage on rhodium surface which is the dominating adsorbed species at low temperature region (below 250°C). Alternately, other authors claimed a stronger adsorption of NO than CO which would mostly govern the selectivity. In this case, desorbed N$_2$O would desorb immediately instead of undergoing direct reduction. As temperature increases, fraction of CO and or NO coverage would diminish and dissociation of N$_2$O becomes more rapid leading to higher conversion of N$_2$O to target product N$_2$. In our experiment, the sudden rise of NO conversion in the temperature range of 200-350°C is probably attributed to the increase of vacant site on rhodium, with N$_2$O as the main product. At higher temperature region, active sites of rhodium would mostly covered by adsorbed nitrogen atoms and coverage fraction of adsorbed NO molecules would decrease dramatically in favor of the recombination of adsorbed nitrogen atoms and the subsequent formation of N$_2$. This is in consistence with previous reports elsewhere. [V. P. Zhdanov 1997; J. Nováková 2001]

What's more, it is important not to overlook the ammonia produced above 350°C in stoichiometric conditions. Ammonia formation involves the hydrogenation of adsorbed nitrogen atoms:

$$N_{ads} + xH_{ads} \rightarrow NH_{x_{ads}} \qquad\qquad (eq.\,9-6)$$

Compared to platinum and palladium, rhodium is considered to possess an outstanding attribute in terms of selective reduction of NO$_x$ to N$_2$. In our observation, the onset of ammonia formation on Rh-loaded perovskite catalysts is between 250-300°C in rich condition, slight outperforming that of the commercial catalyst starting at 200°C.

Meanwhile, reduction of NO by H$_2$ is supposed to become more prevalent at elevated temperature favoring the formation of ammonia.[J. Nováková 2001] Given that fact inlet

hydrogen gas is consumed rapidly below 350°C in stoichiometric atmosphere, the hydrogen atoms necessary for the formation of ammonia is hypothesized to come mainly from products of hydrocarbon oxidation, although the possibility of other hydrogen sources stemming from steam reforming reactions could not be fully excluded.

Deactivation mechanism of rhodium in classical TWC operating condition is accepted to be linked with the loss of accessible metallic area stemming from the oxidation of metallic particles (Rh^0) to cationic species (Rh^{3+}) that diffuses into the vacancies of the support.[N. Guilhaume 1997] It is known that the driving force for thermal deactivation of TWC is the reduced surface energy, destroying of pore structure and sintering of complex oxides[D.M. Fernandes 2010]

In our observation, Rh-loading on La-deficient perovskite $Rh/La_{0.6}Ca_{0.1}Fe_{0.8}Mn_{0.2}O_3$ and $Rh/La_{0.6}Ca_{0.2}Fe_{0.8}Mn_{0.2}O_3$ exhibited higher resistance to ageing compared to $Rh/La_{0.6}Ca_{0.4}Fe_{0.8}Mn_{0.2}O_3$. This can be explained by the fact that although rhodium enrichment on the surface gives rise to higher reducibility, it plays a detrimental role in the preservation of catalytic activity subject to alternative oxidizing-reducing atmosphere. La-deficiency can facilitate the re-dispersion of rhodium thanks to crystal defects. As a result, enhanced stability of the catalysts is obtained which explains the phenomenon that both oxidation and reduction activity were maintained in the return test for $Rh/La_{0.6}Ca_{0.1}Fe_{0.8}Mn_{0.2}O_3$ and $Rh/La_{0.6}Ca_{0.2}Fe_{0.8}Mn_{0.2}O_3$.

The self-regenerating mechanism of Rh-loaded perovskite have been proposed in previous studies involving a reversible process of metal dissolution into perovskite structure in oxidizing atmosphere and precipitation in reducing atmosphere. [H. Tanaka 2001, 2006] However, such hypothesis has been questioned by recent studies. STEM studies performed by Katz revealed that movement of precious metal cations during such process was extremely tiny [M.B. Katz 2012]. For perovskite material with primary particle size of 100 nm order of magnitude the movement distance was only within the scale of a few nanometers. In this case, the majority of rhodium particles would dissolve and precipitate entirely within adjacent perovskite particles, thus inaccessible for gas reactants and hardly available for gas-solid catalytic reactions. [S.A. Malamis 2015] Therefore, sintering of rhodium species resulting from particle growth and aggregation cannot be fully ruled out.

Table 9.6. Light-off temperature of Rh-loaded perovskites

Catalyst	Light-off temperature T_{50} (°C)					
	STO1			STO2		
	CO	C_3H_6	C_3H_8	CO	C_3H_6	C_3H_8
$Rh/LaFeO_3$	229	315	500	243	319	481
$Rh/La_{0.6}Ca_{0.1}Fe_{0.8}Mn_{0.2}O_3$	239	330	495	231	301	501
$Rh/La_{0.6}Ca_{0.2}Fe_{0.8}Mn_{.2}O_3$	200	294	429	220	297	445
$Rh/La_{0.6}Ca_{0.4}Fe_{0.8}Mn_{0.2}O_3$	232	302	468	296	377	474

Fig. 9.6. N$_2$, N$_2$O and NH$_3$ selectivity in stoichiometric and rich condition. Grey star solid line: N$_2$ selectivity of commercial reference catalyst (★); orange barred square dash line: N$_2$ selectivity of Rh/La$_{0.6}$Ca$_{0.1}$Fe$_{0.8}$Mn$_{0.2}$O$_3$ (⊡); green barred square dash line: N$_2$ selectivity of Rh/La$_{0.6}$Ca$_{0.2}$Fe$_{0.8}$Mn$_{0.2}$O$_3$ (⊡); blue barred square dash line: N$_2$ selectivity of Rh/La$_{0.6}$Ca$_{0.4}$Fe$_{0.8}$Mn$_{0.2}$O$_3$ (⊡); grey eight-spoked asterisk solid line: N$_2$O selectivity of commercial reference catalyst(✳); orange up-shaded circle dot line: N$_2$O selectivity of Rh/La$_{0.6}$Ca$_{0.1}$Fe$_{0.8}$Mn$_{0.2}$O$_3$ (◓); green up-shaded circle dot line: N$_2$O selectivity of Rh/La$_{0.6}$Ca$_{0.2}$Fe$_{0.8}$Mn$_{0.2}$O$_3$(◓); blue up-shaded circle dot line: N$_2$O selectivity of Rh/La$_{0.6}$Ca$_{0.4}$Fe$_{0.8}$Mn$_{0.2}$O$_3$(◓); grey multiplication sign (big mark) solid line: NH$_3$ selectivity of commercial reference catalyst(✕); orange down-shaded circle (big mark) dash line: NH$_3$ selectivity of Rh/La$_{0.6}$Ca$_{0.1}$Fe$_{0.8}$Mn$_{0.2}$O$_3$ (◒); green down-shaded circle (big mark) dash line: NH$_3$ selectivity of Rh/La$_{0.6}$Ca$_{0.2}$Fe$_{0.8}$Mn$_{0.2}$O$_3$ (◒); blue down-shaded circle (big mark) dash line: NH$_3$ selectivity of Rh/La$_{0.6}$Ca$_{0.4}$Fe$_{0.8}$Mn$_{0.2}$O$_3$(◒).
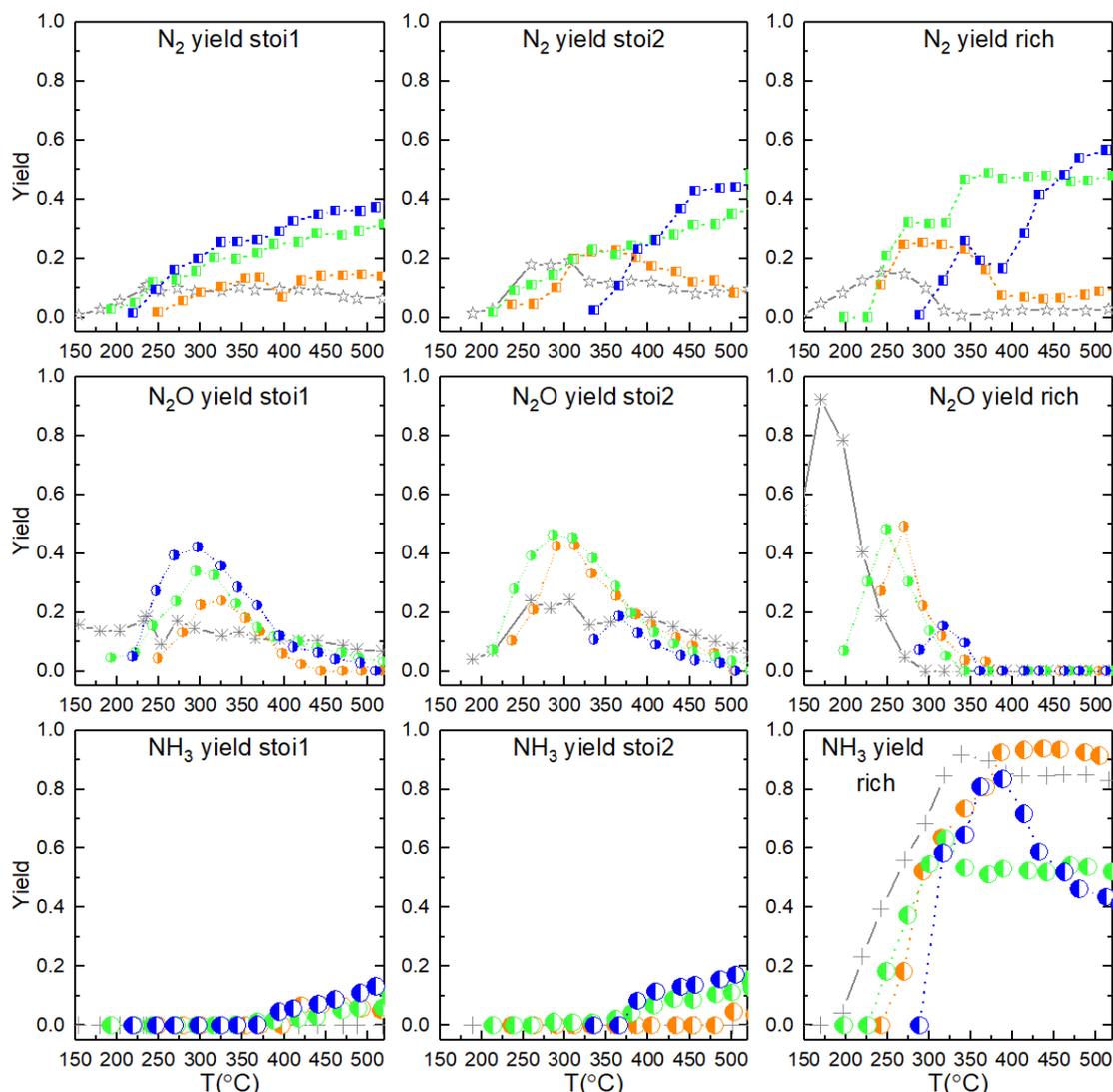
Fig. 9.7. N$_2$, N$_2$O, NH$_3$ yield in stoichiometric and rich condition. Grey star solid line: N$_2$ yield of commercial reference catalyst (☆); orange left-shaded square dash line: N$_2$ yield of Rh/La$_{0.6}$Ca$_{0.1}$Fe$_{0.8}$Mn$_{0.2}$O$_3$ (■); green left-shaded square dash line: N$_2$ yield of Rh/La$_{0.6}$Ca$_{0.2}$Fe$_{0.8}$Mn$_{0.2}$O$_3$ (■); blue left-shaded square dash line: N$_2$ yield of Rh/La$_{0.6}$Ca$_{0.4}$Fe$_{0.8}$Mn$_{0.2}$O$_3$ (■); grey eight-spoked asterisk solid line: N$_2$O yield of commercial reference catalyst(✳); orange right-shaded circle dot line: N$_2$O yield of Rh/La$_{0.6}$Ca$_{0.1}$Fe$_{0.8}$Mn$_{0.2}$O$_3$ (◐); green right-shaded circle dot line: N$_2$O yield of Rh/La$_{0.6}$Ca$_{0.2}$Fe$_{0.8}$Mn$_{0.2}$O$_3$(◐); blue right-shaded circle dot line: N$_2$O yield of Rh/La$_{0.6}$Ca$_{0.4}$Fe$_{0.8}$Mn$_{0.2}$O$_3$(◐); grey plus (big mark) solid line: NH$_3$ yield of commercial reference catalyst (+); orange left-shaded circle (big mark) dot line: NH$_3$ yield of Rh/La$_{0.6}$Ca$_{0.1}$Fe$_{0.8}$Mn$_{0.2}$O$_3$ (◑); green left-shaded circle (big mark) dot line: NH$_3$ yield of Rh/La$_{0.6}$Ca$_{0.2}$Fe$_{0.8}$Mn$_{0.2}$O$_3$ (◑); blue left-shaded circle (big mark) dot line: NH$_3$ yield of Rh/La$_{0.6}$Ca$_{0.4}$Fe$_{0.8}$Mn$_{0.2}$O$_3$ (◑).

9.4.3. Kinetics of CO and propene oxidation

As already described TPR conversion of propene and CO were exploited at low temperature to calculate specific and normalized rate expressed per m^2. According to the mass balance equation of plug flow reaction the rate constants calculated were used to

calculate the pre-exponential factor and the apparent activation energy values from the intercept and the slope of Arrhenius plots. The results are collected in Tables 9.7. and 9.8.

It seems interesting to compare the evolutions observed on the specific and normalized rates vs calcium composition on Rh/La$_{0.6}$Ca$_x$Fe$_{0.8}$Mn$_{0.2}$O$_3$ and Rh/La$_{0.6}$Ca$_x$Fe$_{0.8}$Cu$_{0.2}$O$_3$. This comparison does not highlight drastic changes on the values at least from STO1 experiments which remains of the same order of magnitude and quite comparable on these two series. As observed an optimum was observed for x = 0.2 on the series Rh/La$_{0.6}$Ca$_x$Fe$_{0.8}$Cu$_{0.2}$O$_3$ which seems also prevailing on Rh/La$_{0.6}$Ca$_x$Fe$_{0.8}$Mn$_{0.2}$O$_3$. The comparison based on the STO2 experiments is interesting because the decline in activity compared to STO1 observed on Rh/La$_{0.6}$Ca$_x$Fe$_{0.8}$Cu$_{0.2}$O$_3$ seems to be more limited on Rh/La$_{0.6}$Ca$_x$Fe$_{0.8}$Mn$_{0.2}$O$_3$.
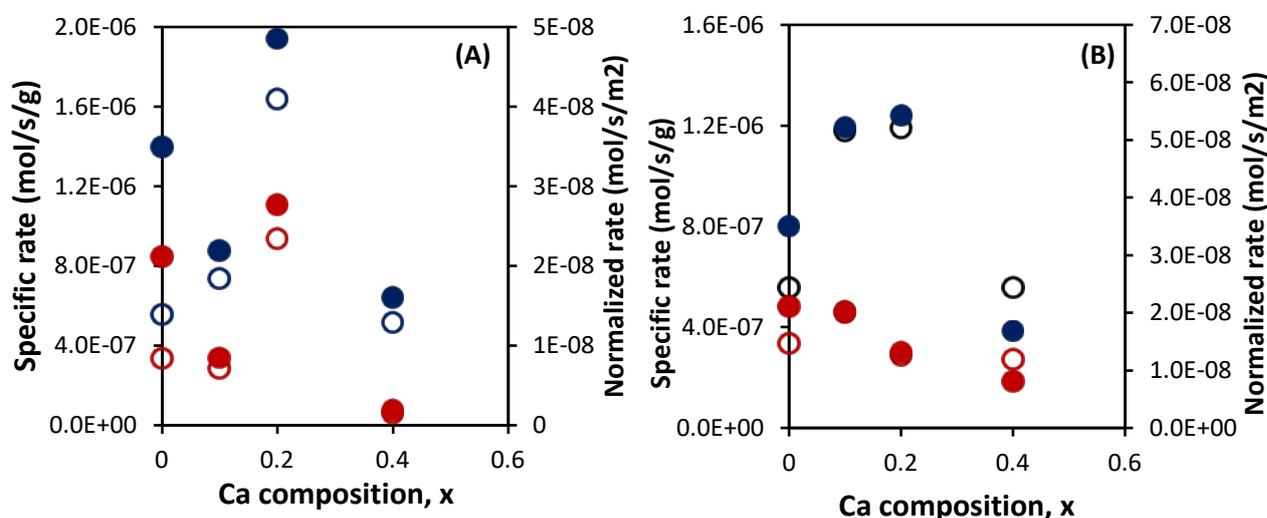
Fig. 9.8. Comparison of specific and normalized rates for CO oxidation measured at 250°C on Rh/La$_{0.6}$Ca$_x$Fe$_{0.8}$Cu$_{0.2}$O$_3$ (A); at 200°C on Rh/La$_{0.6}$Ca$_x$Fe$_{0.8}$Mn$_{0.2}$O$_3$ (B): O specific rate (STO1); O specific rate (STO2); ● normalized rate (STO1); ●; Normalized rate (STO2).

Fig. 9.9. Comparison of specific and normalized rates for propene oxidation measured at 375°C on Rh/La$_{0.6}$Ca$_x$Fe$_{0.8}$Cu$_{0.2}$O$_3$ (A); at 250 °C on Rh/La$_{0.6}$Ca$_x$Fe$_{0.8}$Mn$_{0.2}$O$_3$ (B) : ○ specific rate (STO1); ○ specific rate (STO2); ● normalized rate (STO1); ●; Normalized rate (STO2).

Table 9.7. Rate and kinetic parameters related to CO oxidation in stoichiometric conditions

Catalyst	SSA $(m^2\ g^{-1})$	STO1				STO2			
		$r_{spec.}$ $(mol\ s^{-1}\ g^{-1})^a$	Normalized rate $(mol\ s^{-1}\ m^{-2})^a$	A $(m^3\ s^{-1}g^{-1})$	E_{app} $(kj\ mol^{-1})$	$r_{spec.}$ $(mol\ s^{-1}\ g^{-1})^a$	Normalized rate $(mol\ s^{-1}\ m^{-2})^a$	A $(m^3 s^{-1}g^{-1})$	E_{app} $(kj\ mol^{-1})$
Rh/LaFeO$_3$	15.9	5.57E-07	3.50E-08	6.0E07	122.7	3.36E-07	2.11E-08	1.1E09	136.7
Rh/La$_{0.6}$Ca$_{0.1}$Fe$_{0.8}$Mn$_{0.2}$O$_3$	33.7	7.38E-07	2.19E-08	21.3	61.6	2.85E-07	8.45E-09	3.9E09	141.5
Rh/La$_{0.6}$Ca$_{0.2}$Fe$_{0.8}$Mn$_{0.2}$O$_3$	33.9	1.64E-06	4.85E-08	7.7E04	89.8	9.38E-07	2.77E-08	1.3E06	104.1
Rh/La$_{0.6}$Ca$_{0.4}$Fe$_{0.8}$Mn$_{0.2}$O$_3$	32.3	5.16E-07	1.60E-08	1.3E07	116.4	6.15E-08	1.91E-09	5412	84.1

^{a} calculated at T=200°C

Table 9.8. Rate and kinetic parameters related to C_3H_6 oxidation in stoichiometric conditions

Catalyst	SSA $(m^2\ g^{-1})$	STO1				STO2			
		$r_{spec.}$ $(mols^{-1}g-1)^a$	Normalized rate $(mol\ s^{-1}\ m^{-2})^a$	A $(m^3\ s^{-1}g^{-1})$	E_{app} $(kj\ mol^{-1})$	$r_{specific}$ $(mol\ s^{-1}\ g^{-1})^a$	Normalized rate $(mol\ s^{-1}\ m^{-2})^a$	A $(m^3\ s^{-1}g^{-1})$	E_{app} $(kJ\ mol^{-1})$
Rh/LaFeO$_3$	15.9	1.68E-08	1.05E-09	2.4	59.8	1.35E-08	8.51E-10	3112.4	95.5
Rh/La$_{0.6}$Ca$_{0.1}$Fe$_{0.8}$Mn$_{0.2}$O$_3$	33.7	2.93E-09	8.69E-11	146	82.2	1.90E-08	5.65E-10	5727.6	95.6
Rh/La$_{0.6}$Ca$_{0.2}$Fe$_{0.8}$Mn$_{0.2}$O$_3$	33.9	3.91E-08	1.15E-09	2.8E3	91.2	2.50E-08	7.38E-10	0.4	49.3
Rh/La$_{0.6}$Ca$_{0.4}$Fe$_{0.8}$Mn$_{0.2}$O$_3$	32.3	1.99E-08	6.17E-10	7.8E4	108.6	4.62E-11	1.43E-12	7960.4	110.4

^{a} calculated at T=250°C

9.5. Conclusion

0.1 wt.% rhodium loading on La$_{0.6}$Ca$_x$Fe$_{0.8}$Mn$_{0.2}$O$_3$ led to the improvement of reducibility of Mn^{n+} species located in the B-site of perovskite. The H/M ratio (M=Mn+Rh) less than 3.0 recorded during the H$_2$-TPR experiment suggests that a fraction of Rh is not reducible in the temperature range of 100-1000°C. A weak desorption of both α-oxygen and β-oxygen was observed on Rh/La$_{0.6}$Ca$_x$Fe$_{0.8}$Mn$_{0.2}$O$_3$ regardless of Ca richness. Rh/(A+B) ratios displayed opposite trends in the bulk and on the surface. A hypothesis is put forth that more Ca doping would lead to the enrichment of rhodium on the surface and subsequently increased amount of surface metallic active sites. Contrary to previous observation that migration of Pd from bulk to surface was inhibited by Ca doping, a reverse trend has been observed with regard to Rh-loaded perovskite: the migration of Rh from bulk to the surface was seemingly promoted by higher Ca doping, corroborated by the fact that Rh/La$_{0.6}$Ca$_{0.4}$Fe$_{0.8}$Mn$_{0.2}$O$_3$ corresponds to the highest surface Rh/(A+B) ratio whilst the lowest bulk Rh/(A+B) ratio.

Rh loading on Ca and Mn co-doped perovskites showed superior activity in terms of both oxidation of CO and C$_3$H$_6$ in comparison with the same amount of Rh loading on the Ca and Cu co-doped perovskites. The lowest light-off temperature for CO and C$_3$H$_6$ oxidation was observed on Rh/ La$_{0.6}$Ca$_{0.2}$Fe$_{0.8}$Mn$_{0.2}$O$_3$, corresponding to 200°C in STOI1 and 220°C in STOI2 for CO oxidation and 294°C in STOI1 and 297°C in STOI2 for C$_3$H$_6$ oxidation. A point which is especially to be noted is that activity for C$_3$H$_8$ oxidation of the aforesaid catalyst presented marked enhancement in stoichiometric and lean conditions, outperforming that of the commercial benchmark catalyst. In rich conditions, the above-mentioned catalysts demonstrated comparable light-off profiles.

NO reduction in stoichiometric condition was tremendously promoted thanks to the addition of 0.1 wt% Rh combined with Ca and Mn co-doping on the lanthanum ferrite. In the temperature range of 300-500°C typical of the operating temperature of the TWC system, the highest NO conversion reached 62% in STOI1 on Rh/ La$_{0.6}$Ca$_{0.4}$Fe$_{0.8}$Mn$_{0.2}$O$_3$ and 65% in STOI2 on Rh/ La$_{0.6}$Ca$_{0.2}$Fe$_{0.8}$Mn$_{0.2}$O$_3$ which exceeded that of the commercial benchmark catalyst in the same temperature scope. Rh enrichment caused by Ca doping in A-site is beneficial to NO reduction but is subject to severe deactivation due to the segregation of metallic Rh^0. Defective sites generated by La deficit would favor the re-dispersion of Rh resulting in improved thermal stability. Selectivity behavior of the Rh-loaded perovskite exhibited a NO reduction process on Rh^0 sites, characterized by the fact that N$_2$O was the primary product below 350°C while the production of N$_2$ became predominant above 350°C due to the dissociation of N$_2$O. In rich conditions, less ammonia was produced on Rh-loaded perovskite catalysts compared to the commercial benchmark catalyst.

To sum up, the most effective composition is Rh/ La$_{0.6}$Ca$_{0.2}$Fe$_{0.8}$Mn$_{0.2}$O$_3$ highlighted by the fastest light-off for oxidation of CO, C$_3$H$_6$ and C$_3$H$_8$ and the highest NO conversion in stoichiometric conditions. Another advantage of the aforesaid catalyst lies in the improved thermal stability and resistance to deactivation although NO conversion and N$_2$ selectivity at low temperature remained inferior to that of the commercial benchmark catalyst.

Reference

[G.J.K. Acres 2004] G.J.K. Acres, B. Harrison. Topics in Catalysis, 2004, 28:3-11.

[R. Burch 1995] R. Burch, M.J. Hayes. Journal of Molecular Catalysis A: Chemical, 1995, 100:13-33.

[G. Chen 2010] Guochang Chen, Xiaohui Zhang, Cun-Yue Guo, Guoqing Yuan. Comptes Rendus Chimie, 2010, 13:1384–1390.

[B. K. Cho 1994] B. K. Cho. Journal of Catalysis, 1994, 148:697-708.

[S. Cimino 2006] S. Cimino, G. Landi, L. Lisi et al. Catalysis Today, 2006, 117:454-461.

[A. Eyssler 2012] Arnim Eyssler, Alexander Winkler, Olga Safonova et al. Chemistry of Materials, 2012, 24, 1864−1875.

[D. M. Fernandes 2010] Daniela Meyer Fernandes, Cynthia Fraga Scofield, Arnaldo Alcover Neto. Chemical Engineering Journal, 2010, 160:85-92.

[N. Guilhaume 1997] Nolven Guilhaume and Michel Primet. Journal of Catalysis, 1997, 165:197-204.

[M.B. Katz 2012] Michael B. Katz, Shuyi Zhang, Yingwen Duan et al. Journal of Catalysis, 2012, 293:145–148.

[B.J. Kip 1987] B.J. Kip, E.G.F. Hermans, J.H.M.C. van Wolput, N.M.A. Hermans, J.van Grondelle, R. Prins, Applied Catalysis, 1987, 35:109-139.

[Ye Lu 2013] Ye Lu, Arnim Eyssler, Eugenio H. Otalet al. Catalysis Today, 2013, 208, 42-47.

[S.A. Malamis 2015] Sotirios A. Malamis, Rachael J. Harrington, Michael B. Katz. Catalysis Today, 2015, 258:535–542.

[Y. Nishihata 2002] Y. Nishihata, J. Mizuki, T. Akao et al. Nature, 2002, 418:164-167.

[J. Nováková 2001] J. Nováková, Applied Catalysis B: Environmental, 2001, 30:445-457.

[M. Pirez-Engelmann 2004] M. Pirez-Engelmann, P. Granger, L. Leclercq. G. Leclercq. Topics in Catalysis, 2004, 30: 59-64.

[E. Pocoroba, 2000] Eugenia Pocoroba, E. Magnus Johansson, Sven G. Järås. Catalysis Today, 2000, 59:179-189.

[Z. Say 2014] Zafer Say, Merve Dogac, Evgeny I. Vovk et al. Applied Catalysis B: Environmental, 2014, 154-155:51-61.

[V. Schünemann 1995] V. Schünemann, H. Treviño, G.D. Lei, D.C. Tomczak, W.M.H. Sachtler, K. Fogash, J.A. Dumesic. Journal of Catalysis, 1995, 153:144-157.

[Qingyun Su 2014] Qingyun Su, Liang Xie, Yanbin Li. Canadian Journal of Chemical Engineering, 2014, 92:1579-1586.

[H. Tanaka 2001] H. Tanaka, I. Tan, M. Uenishi, M. Kimura, K. Dohmae, Topics in Catalysis, 2001, 16/17:63-70.

[H. Tanaka 2004] H. Tanaka, M. Taniguchi, N. Kajita et al. Topics in Catalysis, 2004, 30-31:389-396.

[H. Tanaka 2006 a] H. Tanaka, M. Taniguchi, M. Uenishi, N. Kajita, I. Tan, Y. Nishihata, J. Mizuki, K. Narita, M. Kimura, K. Kaneko. Angewandte Chemie Int. Ed. 2006, 45:5998-6002.

[H. Tanaka 2006 b] H. Tanaka, M. Uenishi, M. Taniguchiet al. Catalysis Today, 2006, 117:321-328.

[H. Treviño 1995] H. Treviño, G.D. Lei, W.M.H. Sachtler. Journal of Catalysis, 1995, 154:245-252.

[I. Twagirashema 2007 a] I. Twagirashema, M. Pirez-Engelmann, M. Frere, L. Burylo, L. Gengembre, C. Dujardin, P. Granger. Catalysis Today, 2007, 119:100-105.

[I. Twagirashema 2007 b] I. Twagirashema, M. Frere, L. Gengembre, C. Dujardin, P. Granger, Topics in Catalysis, 2007, 42:171-176.

[M.V. Twigg 2005] M.V. Twigg, Philosophical Transactions: Mathematical, Physical and Engineering Sciences, 2005, 363:1013-1033.

[M.V. Twigg 2007] M.V. Twigg. Applied Catalysis B: Environmental, 2007, 70:2-15.

[G. Tyuliev 2003] G. Tyuliev, D. Panayotov, I. Avramova, D. Stoichev, Ts. Marinova. Materials Science and Engineering: C Materials for Biological Applications, 2003, 23:117-121.

[X. Wei 2010] Xun Wei, Paul Hug, Renato Figi et al. Applied Catalysis B: Environmental, 2010, 94:27-37.

[V.P. Zhdanov 1997] V.P. Zhdanov, B. Kasemo. Surface Science Reports, 1997, 29:31-90.

General conclusion and prospects

General conclusion

The aim of this study is to find alternative materials that could potentially replace the existing PGM-based Three Way Catalysts employed for the post-treatment of gasoline powered engine exhaust gas. Ideally, the substitute material should possess the following attributes:

a. High efficiency for the removal of CO, HC and NO_x under atmosphere in which air-to-fuel ratio fluctuates close to stoichiometric value (14.7)

b. High thermal stability and resistance to deactivation under repeated exposure to lean/rich fluctuation

c. Good activity for soot oxidation in order to eliminate particulate matter stipulated by the Euro6 emission regulations

d. Significant reduction of the usage of PGMs and REEs without impairing significantly the catalytic performance

e. Low-cost, low-toxicity, abundance and easiness for shaping

On the basis of the above considerations, perovskite-type materials provide a possible solution due to their unique advantages. The feasibility of applying perovskite-type materials as an alternative to replace conventional TWC materials was thoroughly investigated in this study.

Previous studies have shown that A-site deficiency combined with B-site substitution on lanthanum ferrite perovskite led to the enrichment of active elements in B-site on the surface and the increase of density of anionic vacancies in favor of the enhancement of reducibility and catalytic activity.[A. Schön 2015] Improvement of physicochemical properties of the perovskite materials is achieved through composition optimization, including creation of non-stoichiometric compositions, partial substitution in A or B site by various transition metals and addition of small amount of PGMs. The ultimate goal is to make the overall three way catalytic performance of perovskite as close to that of the commercial benchmark catalyst as possible whist keeping the usage of PGMs within acceptable levels.

At the beginning, analysis of the physicochemical properties and catalytic performance of commercial benchmark catalysts prepared by different methods were performed. Results showed that $Pd/Ce_{0.5}Zr_{0.5}O_2$ synthesized by co-precipitation method manifested superiority compared to $Pd/Ce_{0.5}Zr_{0.5}O_2$ prepared by Flame Spray Pyrolysis method. A more homogeneous Pd dispersion and faster light-off was observed on the former although a higher specific surface area was noticed on the latter. As discussed, more reducible species on $Pd/Ce_{0.5}Zr_{0.5}O_2$-FSP associated to larger clusters of PdO weakly interacting with the support could explain the lower catalytic performance in stoichiometric and rich conditions partly due to a loss of Pd-Ce interface useful to promote OSC properties.

With regard to the non-PGM bare perovskites, partial substitution of Fe by Cu in B-site of lanthanum ferrite led to the segregation of CuO present outside the perovskite lattice. Such highly dispersed CuO in strong interaction with perovskite substrate is believed as the key

active components responsible for the reducibility of the solid solution. Ca doping in A-site could alleviate the extraction of Cu from the center of BO_6 octahedron and promote the stabilization of unusual oxidation state of Fe^{4+} evidenced from Mössbauer spectroscopy. The synergistic effect of Ca and Cu co-doping resides in the better structural stability of the perovskite lattice, thus avoiding the drastic changes of surface properties and severe deactivation resulting from the agglomeration of small particles observed extensively on La-deficient compositions. In addition, an obvious shrinkage of unit cell volume is induced by Ca and Cu co-doping. Such deformation of crystal structure is regarded as a promoter for the improvement of reducibility and oxygen mobility of the perovskite. By contrast, Mn-doping in B-site of the lanthanum ferrite did not result in significant segregation of MnO_x. Such phenomenon cannot be simply attributed to the discrepancies of cation radii ($Cu^{2+} = 0.72$ Å, $Fe^{3+} = 0.64$ Å, $Mn^{3+} = 0.66$ Å, $Mn^{4+} = 0.56$ Å). A more reasonable explanation would be that Fe-O-Mn complex is less inclined to dissociate compared to Fe-O-Cu complex because of higher bond energy, favoring the stabilization of Mn species within the lattice. Unlike Ca and Cu co-doping, Ca and Mn co-doping has been found detrimental to the reducibility and oxygen mobility of the perovskite. In this case, since Mn^{n+} species serve as the most active components, Mn^{4+}/Mn^{3+} ratio plays a crucial role in determining the redox properties of the catalyst. More Ca doping in A-site led to the decrease of Mn average oxidation state evidenced from XPS experiment, causing subsequently a loss of reducibility and oxygen mobility. Another point worth mentioning is that a slight increase of specific surface area is obtained on Mn-doped lanthanum ferrite in comparison with Cu-doped candidates.

A-site deficit combined with B-site substitution has been proven a successful strategy to lower the light-off temperature of CO and C_3H_6 oxidation in stoichiometric condition. The beneficial role of Cu-doping in terms of CO and C_3H_6 oxidation is more pronounced but NO reduction only occurred in rich conditions and hardly took place in stoichiometric conditions. In contrast, Mn-doping gave rise to conspicuous improvement of NO conversion in stoichiometric condition, with a maximum NO conversion reaching 30% in STOI1 and 23% in STOI2 on $La_{0.7}Fe_{0.8}Cu_{0.2}O_3$ in the temperature scope of 350-500°C. The notable discrepancies observed between Cu and Mn doping originate from the distinct intrinsic mechanisms governing the redox properties of these two systems: On one hand, it is found that the extracted CuO was crucial for the oxidation of CO and C_3H_6 but turned out ineffective for NO reduction in stoichiometric and lean condition due to the lack of active sites for NO adsorption and dissociation. On the other hand, the majority of Mn species exists within the perovskite lattice with variable oxidation states in favor of the generation of adjacent anionic vacancies and the advancement of oxygen mobility. La-deficiency further strengthens this trend. Hence, the reducibility of the Mn-doped perovskite is facilitated in conjunction with remarkable NO conversion exhibited in stoichiometric conditions. It should not ignore the fact that Ca-doping in A-site displayed a deleterious effect on NO conversion which may be linked with the decrease of Mn average oxidation state resulting from the introduction of Ca. Nevertheless, given the non-PGM composition of the bare perovskite catalyst, such restricted improvement of NO reduction makes already a forward step in the design of novel PGM-free materials suitable for the replacement of existing TWC system.

Due to the unsatisfactory activity of bare perovskite catalysts for NO reduction in stoichiometric conditions, addition of small amount of PGMs was adopted with the aim to

improve NO_x removal efficiency especially in stoichiometric conditions. In the conventional Pd-Rh three way catalyst, Pd is widely recognized by its outstanding oxidative properties while Rh could convert more readily NO_x. The combination of Pd or Rh with transition metal-doped perovskite provides thereby a practical plan in order to enhance the redox properties of the latter. Results showed that 0.5 wt.% Pd loading on the stoichiometric composition $La_{0.6}Ca_{0.4}Fe_{0.8}Cu_{0.2}O_3$ gave rise to the best performance in terms of both oxidation and reduction effectiveness in stoichiometric condition. For the aforesaid catalyst, kinetic study suggested that no significant deactivation occurred for oxidation of CO and C_3H_6 in the return test but a remarkable loss of NO conversion at low temperature region was prevalent. Agglomeration of PdO_x is assumed responsible for such deactivation observed in the return test. Compared to Pd loading, Rh incorporation gave rise to comparable oxidative activity but improved reductive activity and resistance to deactivation in stoichiometric conditions. Two systems have been screened out in view of three way catalytic performance and thermal stability: namely $Rh/La_{0.6}Ca_{0.4}Fe_{0.8}Cu_{0.2}O_3$ and $Rh/La_{0.6}Ca_{0.2}Fe_{0.8}Mn_{0.2}O_3$. NO conversion on the aforesaid catalysts outperformed the benchmark catalyst in the temperature range of 250-450°C although a lower N_2 selectivity was prominent at low temperature region. What's more, $Rh/La_{0.6}Ca_{0.2}Fe_{0.8}Mn_{0.2}O_3$ displayed better activity for C_3H_8 oxidation in stoichiometric and lean conditions than the benchmark catalyst. More Rh enrichment on the surface would be beneficial for NO reduction but is also subject to more severe deactivation, as is observed on $Rh/La_{0.6}Ca_{0.4}Fe_{0.8}Mn_{0.2}O_3$ in the first stoichiometric and return test.

Kinetic analysis demonstrated that specific and normalized reaction rates for CO and C_3H_6 oxidation on perovskite catalysts were not dependent on the specific surface area of the solid but more related to the surface composition of the catalyst, suggesting that structural properties played a more significant role in the redox characteristics of perovskite catalysts compared to textural properties.

Selectivity behavior of the PGM-loaded perovskite in stoichiometric conditions presented similar trends: N_2O was the predominant product at low temperature and N_2 became the main reduction product at high temperature. Compared to the commercial benchmark catalyst, the PGM-loaded perovskites exhibited superior N_2 selectivity at high temperature although more N_2O was formed during cold-start process. Another finding is that in rich conditions, less ammonia was produced on the PGM-loaded perovskites in comparison with that of the benchmark catalyst. However, NO conversion in lean conditions remained much more inferior to that of the benchmark catalyst.

Migration of Rh or Pd from surface to bulk was observed on the PGM-loaded perovskites, leading to significant enhancement of lattice oxygen mobility due to strong metal-support interaction. This phenomenon is quite notable on $Pd/La_{0.6}Ca_{0.4}Fe_{0.8}Cu_{0.2}O_3$ and $Rh/La_{0.6}Ca_{0.4}Fe_{0.8}Cu_{0.2}O_3$ compositions.

Dispersion of Pd or Rh on the support is closely associated with the surface composition of the latter. Contrary to previous reports, it is noticed that defective sites in perovskite lattice did not show an obvious promoting effect on Rh dispersion. Stoichiometry and chemical composition of A-site seemed to exert a greater influence on Rh dispersion. Also, the spillover phenomenon is noticed on Pd-loaded perovskites but needs further confirmation by other methods.

In conclusion, ferrite based perovskite materials showed great potential to serve as an alternative for the replacement of conventional TWC. The physicochemical properties of perovskite could be dramatically improved by means of surface and bulk composition optimization. This strategy allows a notable gain in terms of oxidation of CO and C_3H_6. However, the biggest challenge of applying bare perovskites to the TWC system resides in the low NO conversion in atmosphere close to stoichiometric conditions. Addition of small amounts of PGMs could enhance significantly NO conversion in stoichiometric conditions. Loading of 0.5 wt.% Pd or 0.1 wt.% Rh on bare perovskites coupled with composition optimization gave rise to higher NO conversion as well as higher N_2 selectivity than the commercial benchmark catalyst in stoichiometric condition in the temperature scope of 300-500°C typical of the operating temperature range of the TWC system. But NO conversion and N_2 selectivity at low temperature remained inferior to that of the commercial benchmark catalyst. In addition, NO conversion in lean conditions was only promoted to a limited extent by the incorporation of either 0.5 wt.% Pd or 0.1 wt.% Rh, unable to compete with the benchmark catalyst.

Prospects

On the basis of obtained results, amelioration in certain aspects is still attainable to further advance the current study and acquire more insights in terms of the functioning principle of perovskite-type materials in the real TWC system. Regarding the synthesis methods, more advanced approaches could be investigated. The macro-structuring method offers a suitable solution to improve textural properties of perovskite materials through optimization of pore structure and pore size distribution. This method involves the use of polymeric microspheres (i.e. PMMA or PS) as templates upon which the precursors are deposited through appropriate method (i.e. Precursor Infiltration). After calcination at moderate temperature, the template will be removed, leaving ordered network with hierarchical layers within the product. Such so-called Three Dimensionally Ordered Macroporous (3DOM) perovskite materials possess greater specific surface area along with improved pore structure and are thus expected to promote substantially soot oxidation due to better mass and heat transfer efficiency. This conception has already been carried out on the non-stoichiometric composition of $La_{0.7}Fe_{0.8}Cu_{0.2}O_3$ and $La_{0.6}Ca_{0.2}Fe_{0.8}Cu_{0.2}O_3$. For the aforesaid 3DOM perovskites, enhanced reducibility and oxygen mobility as well as textural properties are confirmed by relevant physicochemical characterizations. It will be quite exciting to evaluate the activity for soot oxidation of these 3DOM perovskites in order to design novel materials with Four Way Catalytic performance.

As discussed earlier, the low NO conversion and N_2 selectivity in stoichiometric condition during cold-start process is a major obstacle that prevents the wide application of PGM-loaded perovskite materials as a feasible alternative to replace conventional TWC materials. More PGM loading or simultaneous introduction of multiple types of precious metals with optimal ratio might be a realistic solution to overcome this drawback. Moreover, ageing test will be helpful to elucidate the deactivation mechanisms associated with Pd or Rh after alternate exposure to lean/rich atmosphere.

Finally, a more facile and reliable scale-up needs to be conducted to realize the commercialization of the prototype. Related studies are underway and some encouraging results are already available in the frame of the European H2020-PARTIAL-PGMs project.

List of Figures

List of Figures

List of Figures

Fig. 9.6. N_2, N_2O and NH_3 selectivity in stoichiometric and rich condition. Grey star solid line: N_2 selectivity of commercial reference catalyst (★); orange barred square dash line: N_2 selectivity of $Rh/La_{0.6}Ca_{0.1}Fe_{0.8}Mn_{0.2}O_3$ (▥); green barred square dash line: N_2 selectivity of $Rh/La_{0.6}Ca_{0.2}Fe_{0.8}Mn_{0.2}O_3$ (▥); blue barred square dash line: N_2 selectivity of $Rh/La_{0.6}Ca_{0.4}Fe_{0.8}Mn_{0.2}O_3$ (▥); grey eight-spoked asterisk solid line: N_2O selectivity of commercial reference catalyst(＊); orange up-shaded circle dot line: N_2O selectivity of $Rh/La_{0.6}Ca_{0.1}Fe_{0.8}Mn_{0.2}O_3$ (◓); green up-shaded circle dot line: N_2O selectivity of $Rh/La_{0.6}Ca_{0.2}Fe_{0.8}Mn_{0.2}O_3$(◓); blue up-shaded circle dot line: N_2O selectivity of $Rh/La_{0.6}Ca_{0.4}Fe_{0.8}Mn_{0.2}O_3$(◓); grey multiplication sign (big mark) solid line: NH_3 selectivity of commercial reference catalyst(×); orange down-shaded circle (big mark) dash line: NH_3 selectivity of $Rh/La_{0.6}Ca_{0.1}Fe_{0.8}Mn_{0.2}O_3$ (◒); green down-shaded circle (big mark) dash line: NH_3 selectivity of

List of Tables

List of Tables